DISSERTATION

ADVANCEMENTS IN ORGANOCATALYZED ATOM TRANSFER RADICAL POLYMERIZATION BY INVESTIGATION OF KEY MECHANISTIC STEPS

Submitted by

Daniel Andreas Corbin

Department of Chemistry

In partial fulfillment of the requirements

For the Degree of Doctor of Philosophy

Colorado State University

Fort Collins, Colorado

Spring 2022

Doctoral Committee:

Advisor: Garret Miyake

Richard Finke
Anthony Rappé
Matt Kipper

ABSTRACT

ADVANCEMENTS IN ORGANOCATALYZED ATOM TRANSFER RADICAL POLYMERIZATION BY INVESTIGATION OF KEY MECHANISTIC STEPS

Organocatalyzed atom transfer radical polymerization (O-ATRP) is a controlled radical polymerization method employing organic photoredox catalysts to mediate the synthesis of well-defined polymers. The success of this method derives from its reversible-deactivation mechanism, where polymers are activated by reduction of a chain-end C-Br bond to generate a reactive radical for chain growth, followed by deactivation of the polymer by reinstallation of the dormant bromide chain-end group. As a result, the polymer chain can be grown by reaction of the polymer radical with alkene-based monomers, but undesirable termination and side reactions can be suppressed by minimization of the radical concentration through deactivation.

In this work, key mechanistic steps of O-ATRP are investigated to understand the fundamental limitations of this method and improve upon them. When *N,N*-diaryl dihydrophenazines were investigated, side reactions were identified in which alkyl radicals add to the phenazine core, leading to new core-substituted PC derivatives with non-equivalent catalytic properties. Employing these core-substituted PCs in O-ATRP showed these side reactions can be eliminated to improve polymerization control. In addition, the deactivation step of O-ATRP and related intermediates were studied, which revealed new side reactions that can limit polymerization efficiency as well as influences on the rate of deactivation. Finally, methods to exert control over the deactivation process were developed as a means of improving polymerization outcomes in challenging systems. For example, the intermediate responsible for deactivation was isolated and

added to a polymerization to increase the rate of deactivation and limit side reactions in O-ATRP. Alternatively, a similar outcome could be achieved through *in-situ* electrolysis to increase the concentration of the desired intermediate during the polymerization. Ultimately, this work has yielded insight into important mechanistic processes in O-ATRP that will continue to benefit the development of this method.

ACKNOWLEDGEMENTS

I would first like to thank my committee – Prof. Garret Miyake, Prof. Richard Finke, Prof. Anthony Rappé, and Prof. Matt Kipper – for their guidance throughout the preparation and defense of this dissertation. I would also like to thank the professors at Colorado State University who provided me with guidance and advice throughout my graduate studies, including Prof. Richard Finke, Prof. Melissa Reynolds, Prof. Nancy Levinger, and Prof. Amy Prieto.

In addition, I would like to thank all the graduate students, postdoctoral researchers, and visiting scholars who were a part of the Miyake group during my time in graduate school. This experience would not have been the same without each of you, and I am glad to have gotten to know you and learn from you over the past five years. In particular, I would like to thank Dr. Blaine McCarthy for her constant guidance, support, and encouragement. Watching you work and learning from you has in-part shaped me into the scientist I am today, and I will forever be grateful for having been able to work with you. I would also like to thank Dr. Scott Folkman for teaching me and providing me with new perspectives in life. Without your guidance, much of the work in this dissertation would not have been possible. However, more importantly, your perspectives in life caused me to reevaluate my own goals and strive for a more balance life, and I will always be grateful to you for that. Finally, I would like to thank Dr. Bret Boyle and Dr. Bonnie Buss for their support and encouragement throughout my graduate career. On numerous occasions, your positivity helped me remain motivated in the face of adversity and ultimately helped me to complete the work described in this dissertation.

I would also like to thank all of the individuals I've had the pleasure of working and publishing with over the course of my graduate studies, including Blaine McCarthy, Nicholas

Swisher, Yisrael Lattke, Katrina Puffer, Katherine (Katie) Chism, and Zach van de Lindt. In particular, I would like to thank Katrina, Katie, and Zach, who I mentored at various stages of my career. Each of you taught me valuable lessons in mentorship and remained patient with me as I learned to be an effective mentor. I sincerely hope you got as much out of working with me as I gained from working with you these past years.

Of course, none of this work would have been possible without the guidance of my advisor, Prof. Garret Miyake. Garret, I can honestly say I would not be where I am today without your help, guidance, support, and mentorship. Throughout my graduate studies, you pushed me to achieve things I never thought would be possible. You gave me the tools to become an independent scientist, while also supporting me to pursue my own interests. Even more importantly, you supported me in both success and failure, guiding me as I learned to not only be a better scientist, but also a better person. I will always be grateful for everything you have given me and hope one day I will be able to return the favor.

I also want to thank everyone who played a role in getting me to this point in my life. I would like to thank Jeff Phelps and the faculty of the Governor's School for the Arts in Norfolk, Virginia. The opportunities you gave me altered the trajectory of my life and taught me I could achieve anything I desired through persistence and dedication. I would like to thank Eleni Babcock for being an incredible teacher and educator. Your class was perhaps the first one to truly challenge me, and it ultimately gave me the perseverance and work ethic to be successful in graduate school and in life. In addition, it was in your class that I learned to be an effective writer and communicator. While I didn't appreciate the value of these skills at the time, they have been key factors in my success since then.

I would like to thank Prof. Brycelyn (Bryce) Boardman, Prof. Scott Lewis, and all of the chemistry faculty at James Madison University (JMU). Your incredible dedication to undergraduate students is inspiring and is the reason I ultimately went to graduate school. Prof. Lewis, you were the first person to give me an opportunity in chemistry and were ultimately responsible for my ability to attend JMU. Bryce, I would especially like to thank you for all of your support and guidance throughout my time at JMU. Working with you ultimately gave me the courage to pursue a graduate degree, a path in life I never thought would be available to me. You showed me I could do anything I want with my life, and words cannot express how grateful I am to you for that.

I would like to thank my parents, Dennis and Milena Corbin. Dad, your persistence and courage in the face of adversity is incredible and has given me strength in times of weakness. Every day, you serve as an example of the type of man I hope to become, and I can only hope I will be able to follow in your footsteps. Mom, you are a constant source of inspiration and have taught me to never stop pursuing my dreams. More importantly, you are an example of the type of person I hope to be in life. Your open-mindedness and passion to learn from others is incredible and continues to inspire me to be a better person. I would also like to thank my brother, Nicholas Corbin. Your intelligence and drive are unbelievable. You have already achieved so much, and in doing so you have inspired me to pursue goals I never would have pursued on my own. I am so grateful to have you as my brother and hope I will be able to support you the way you have supported me in your own endeavors.

Finally, I would like to thank my wife, Cassidy Jackson. Over the course of my graduate career, you have never stopped supporting and encouraging me, even as you pursued a Ph.D. of your own. In success and in failure, you have always been by my side. You have pushed me to be

a better person, and you have taught me to get more out of life than I would have on my own. None of this would have been possible without your help. As we now close this chapter of our lives and begin the next one, I am so grateful to have you by my side and cannot wait to discover what the future holds for us.

Thank you to everyone who has helped me reach this point in my life. I hope I have made you proud.

Chapter 2: This dissertation chapter contains the manuscript of an article [Corbin, D. A.; Miyake, G. M. Photoinduced Organocatalyzed Atom Transfer Radical Polymerization (O-ATRP): Precision Polymer Synthesis using Organic Photoredox Catalysis. *Chem. Rev.* **2021**, *122*, 1830–1874.]. This chapter was written primarily by the author of this dissertation under the guidance of Prof. Garret Miyake.

The writing of this chapter was partially supported by the National Institute of General Medical Sciences (Award R35GM119702) of the National Institutes of Health. The content is solely the responsibility of the authors and does not necessarily represent the official views of the National Institutes of Health. The authors are also grateful for support provided by Colorado State University and the Research Corporation for Science Advancement (Cottrell Scholar Award). This work was further supported by funding from the National Science Foundation (Award CHE-2055742). D.A.C. would like to thank Prof. Garret Miyake for his guidance during the writing of this manuscript; Max Kudisch, Cam Chrisman, Mariel Price, Felipe Garcia Alzate, Alexander Green, and Katrina Puffer for helpful feedback during revisions of this manuscript; and Cassidy Jackson for her general support and feedback.

Chapter 3: This dissertation chapter contains the manuscript of a book chapter [Corbin, D. A.; Swisher, N. A.; Miyake, G. M. Fundamentals of Photochemical Redox Reactions. In *Organic Redox Chemistry: Chemical, Photochemical and Electrochemical Syntheses*; Wiley, 2021. DOI: 10.1002/9783527815678.ch3]. Nicholas Swisher wrote the sections on the history of photochemistry, inorganic photoredox catalysts, organic excited state oxidants, and open shell photoredox catalysts.

The writing of this chapter was supported by the National Institute of General Medical Sciences (Award R35GM119702) of the National Institutes of Health. The content is solely the responsibility of the authors and does not necessarily represent the official views of the National Institutes of Health. The authors are also grateful for support provided by Colorado State University. D.A.C. would like to thank N.A.S. and G.M.M. for their guidance during the writing of this chapter, as well Max Kudisch for helpful feedback during revisions of this manuscript, and Cassidy Jackson for her general support during this process.

Chapter 4: This dissertation chapter contains the manuscript of an article [Corbin, D. A.; McCarthy, B. G.; Miyake, G. M. Impacts of Performing Electrolysis during Organocatalyzed Atom Transfer Radical Polymerization. *Polym. Chem.* **2020**, *11*, 4978–4985.]. Blaine McCarthy provided guidance throughout this project and helpful feedback on the organization of the manuscript.

The work described in this chapter was supported by Colorado State University. Research reported in this publication was also supported by the National Institute of General Medical Sciences (Award R35GM119702) of the National Institutes of Health. The content is solely the responsibility of the authors and does not necessarily represent the official views of the National Institutes of Health. B.G.M. acknowledges support from the NSF GRFP. D.A.C. would also like

to thank Dr. Scott Folkman for helpful discussions on electrochemistry, as well as Max Kudisch and Tara Mensch for assistance with the design and assembly of 3D printed photoreactors used in this work.

Chapter 5: This dissertation chapter contains the manuscript of an article [Corbin, D. A.; McCarthy, B. G.; van de Lindt, Z.; Miyake, G. M. Radical Cations of Phenoxazine and Dihydrophenazine Photoredox Catalysts and Their Role as Deactivators in Organocatalyzed Atom Transfer Radical Polymerization. *Macromolecules* **2021**, *54*, 4726–4738.]. Blaine McCarthy synthesized some of the phenoxazine catalysts used in this work. Zach van de Lindt synthesized one of the phenoxazine catalysts used in this work under the guidance of Daniel Corbin.

The work described in this chapter was supported by the National Institute of General Medical Sciences (Award R35GM119702) of the National Institutes of Health. The content is solely the responsibility of the authors and does not necessarily represent the official views of the National Institutes of Health. The authors are grateful for support provided by Colorado State University and the Research Corporation for Science Advancement (Cottrell Scholar Award). B.G.M. acknowledges support from the NSF GRFP. D.A.C. would like to thank Dr. Scott Folkman for helpful discussions of electrochemistry; Dr. Brian Newell, Cassidy Jackson, and Anthony Campanella for assistance with crystallography; and Cassidy Jackson for support throughout this work.

Chapter 6: This dissertation chapter contains the manuscript of an article [Corbin, D. A.; Puffer, K. O.; Chism, K. A.; Cole, J. P.; Theriot, J. C.; McCarthy, B. G.; Buss, B. L.; Lim, C.-H.; Lincoln, S. R.; Newell, B. S.; Miyake, G. M. Radical Addition to N,N-Diaryl Dihydrophenazine Photoredox Catalysts and Implications in Photoinduced Organocatalyzed Atom Transfer Radical Polymerization. *Macromolecules* **2021**, *54*, 4507–4516.]. K.O.P. performed some of the

polymerizations reported in this work. K.A.C. assisted with the synthesis of catalysts used in this work and performed some of the reported polymerizations. J.P.C. developed the synthesis of novel catalysts in this work, characterized them, and investigated the mechanism of catalyst side reactions. J.C.T. performed initial experiments investigating catalyst side reactions during O-ATRP. B.G.M., B.L.B., and S.R.L assisted with the synthesis and characterization of catalysts reported in this work. C.-H.L. performed computational studies to investigate the properties of novel catalysts. B.S.N. collected and refined crystal structures reported in this work.

This work was supported by Colorado State University and the NIH (R35GM119702). This work used the Extreme Science and Engineering Discovery Environment (XSEDE), which is supported by National Science Foundation grant number ACI- 1548562. J.C.T. and B.G.M. are grateful for support from the NSF GRFP. The authors would also like to thank Max Kudisch, Ryan Pearson, Matthew Ryan, and the CSU Central Instrumentation Facility for technical assistance.

DEDICATION

This dissertation is dedicated to my family:

To my parents, Dennis and Milena Corbin, for all the sacrifices you made so I could reach this point in my life.

To my brother, Nicholas Corbin, for your drive and perspectives in life, which have always inspired be to push farther and dream bigger.

And to my wife, Cassidy Jackson, for supporting me, encouraging me, and always pushing me to grow as a person.

This work would not have been possible without you.

TABLE OF CONTENTS

CHAPTER 1.

INTRODUCTION

Thesis Structure

This dissertation describes studies that have sought to expand our knowledge of the mechanism of organocatalyzed atom transfer radical polymerization (O-ATRP). The first study aimed to do so by investigating the impact of electrolysis during O-ATRP on key mechanistic steps. However, limitations in our understanding of the O-ATRP mechanism made this investigation challenging, motivating a deeper investigation of the O-ATRP mechanism. In addition, side reactions in O-ATRP have been probed and discovered to alter the identity of the catalyst in O-ATRP. These side reactions are described and exploited to improve polymerization outcomes in O-ATRP.

The overall structure of this dissertation follows a journal-format style. Select publications from the author's graduate studies have been used to comprise the body of this work, with each chapter being modeled off one published manuscript. The beginning chapters include one review published in *Chemical Reviews* on the development of O-ATRP, as well as a book chapter published in *Organic Redox Chemistry* that described the development and background of photoredox chemistry. The rest of this dissertation is comprised of research articles by the author, including one published in *Polymer Chemistry* and two published in *Macromolecules*. The topics covered in this thesis are presented in five chapters with the following titles:

1. Photoinduced Organocatalyzed Atom Transfer Radical Polymerization (O-ATRP): Precision Polymer Synthesis using Organic Photoredox Catalysis
2. Fundamentals of Photochemical Redox Reactions

3. Impacts of Performing Electrolysis during Organocatalyzed Atom Transfer Radical Polymerization
4. Radical Cations of Phenoxazine and Dihydrophenazine Photoredox Catalysis and Their Role as Deactivators in Organocatalyzed Atom Transfer Radical Polymerization
5. Radical Addition to *N,N*-Diaryl Dihydrophenazines Photoredox Catalysis and Implications in Photoinduced Organocatalyzed Atom Transfer Radical Polymerization

In addition to the topics covered in this dissertation, the author of this work published on other topics during his doctoral work spanning concepts in photochemistry and polymer chemistry. A full list of publications from his doctoral work is provided below:

1. Corbin, D. A.; Miyake, G. M. Photoinduced Organocatalyzed Atom Transfer Radical Polymerization (O-ATRP): Precision Polymer Synthesis using Organic Photoredox Catalysis. *Chem. Rev.* **2021**, *122*, 1830–1874.
2. Corbin, D. A.; Puffer, K. O.; Chism, K. A.; Cole, J. P.; Theriot, J. C.; McCarthy, B. G.; Buss, B. L.; Lim, C.-H.; Lincoln, S. R.; Newell, B. S.; Miyake, G. M. Radical Addition to *N,N*-Diaryl Dihydrophenazine Photoredox Catalysts and Implications in Photoinduced Organocatalyzed Atom Transfer Radical Polymerization. *Macromolecules* **2021**, *54*, 4507–4516.
3. Corbin, D. A.; McCarthy, B. G.; van de Lindt, Z.; Miyake, G. M. Radical Cations of Phenoxazine and Dihydrophenazine Photoredox Catalysts and Their Role as Deactivators in Organocatalyzed Atom Transfer Radical Polymerization. *Macromolecules* **2021**, *54*, 4726–4738.

4. Lattke, Y. M.; Corbin, D. A.; Sartor, S. M.; McCarthy, B. G.; Miyake, G. M.; Damrauer, N. H. Interrogation of O-ATRP Activation Conducted by Singlet and Triplet Excited States of Phenoxazine Photocatalysts. *J. Phys. Chem. A.* **2021**, *125*, 3109–3121.
5. Swisher, N. A.; Corbin, D. A.; Miyake, G. M. Synthesis, Characterization, and Reactivity of N-Alkyl Phenoxazines in Organocatalyzed Atom Transfer Radical Polymerization. *ACS Macro Lett.* **2021**, *10*, 453–459.
6. Corbin, D. A.; Swisher, N. A.; Miyake, G. M. Fundamentals of Photochemical Redox Reactions. In *Organic Redox Chemistry: Chemical, Photochemical and Electrochemical Syntheses*; Wiley, 2021. DOI: 10.1002/9783527815678.ch3.
7. Corbin, D. A.; Miyake, G. M. Making Block Copolymers with the Flip of a Switch. *Chem* **2020**, *6*, 1508.
8. Corbin, D. A.; McCarthy, B. G.; Miyake, G. M. Impacts of Performing Electrolysis during Organocatalyzed Atom Transfer Radical Polymerization. *Polym. Chem.* **2020**, *11*, 4978–4985.
9. Corbin, D. A.; Lim, C.-H.; Miyake, G. M. Phenothiazines, Dihydrophenazines, and Phenoxazines: Sustainable Alternatives to Precious-Metal-Based Photoredox Catalysts. *Aldrichimica Acta.* **2019**, *52*, 7–21.

Motivations

At the beginning of this work in 2017, organocatalyzed atom transfer radical polymerization (O-ATRP) was emerging as a promising controlled radical polymerization (CRP) method for synthesizing polymers with precise structures under mild and metal-free reaction conditions. As with all CRPs, O-ATRP is based on a radical polymerization strategy, where

propagation, or polymer growth, occurs through a carbon-centered radical on a polymer chain reacting with a polymerizable functionality such as an alkene within a monomer molecule. As a result of this reaction, the polymer chain grows by one monomer unit, and the propagating radical is shifted to the end of the polymer chain to enable successive monomer additions. In O-ATRP specifically, this process is mediated by organic (i.e. not containing metal atoms) photoredox catalysts (PCs), many of which are strong reductants in their excited states [$E^o(PC^{\bullet+}/PC^*) < -1.0$ V vs. saturated calomel electrode (SCE)]

Unfortunately, all radical polymerization methods are susceptible to termination reactions, wherein two propagating radicals rapidly undergo irreversible reactions that limit control over the product polymer structure. To overcome these limitations, O-ATRP employs a reversible-deactivation strategy (Figure 1.1), in which dormant polymer chains (P_nBr) are activated for polymer growth by reduction of the chain-end C-Br bond to generate the propagating polymer radical ($P_n\bullet$). Shortly thereafter, the polymer is deactivated by reforming the dormant chain-end C-Br bond, which lowers the propensity of the polymer to undergo termination reactions while still allowing it to be reactivated for future growth. As a result of this process, termination reactions in O-ATRP are suppressed, allowing the structure of the product polymer to be tuned as desired.

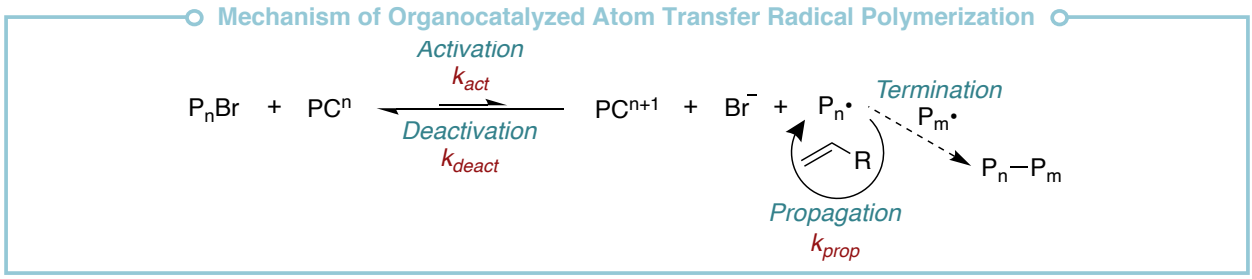

Figure 1.1. *General mechanism of O-ATRP highlighting the activation-deactivation equilibrium that is key to controlling polymer structure.*

When O-ATRP was first introduced in 2014, two organic PCs were reported that could mediate this process: perylene and 10-phenylphenothiazine.[1,2] As neither catalyst was ideal for this application, subsequent research focused largely on identifying superior PCs for O-ATRP and developing design principles for the development of effective catalysts. Our group in particular played a major role in this research, introducing several new families of organic PCs such as *N,N*-diaryl dihydrophenazines,[3-6] phenoxazines,[7-9] dimethyl dihydroacridines.[10] Over the course of this work, several important design principles for effective catalysts were discovered that expedited the development O-ATRP (see Chapters 2 and 3 for more information). However, certain key goals remained elusive despite these advancements in catalyst design. In particular, expanding the monomer scope of O-ATRP has remained challenging, especially with regard to monomers that exhibit large propagation rate constants (k_{prop}). In addition, at the onset of this work, little was known regarding the mechanism of O-ATRP, further complicating efforts to improve this process.

In this dissertation, efforts to address these challenges by understanding key steps in the mechanism of O-ATRP are described. Beginning with Chapter 2, the history, theoretical background, and applications of O-ATRP are discussed in detail. While this chapter provides a brief introduction to photochemistry for the inexperienced reader, additional details on this topic are discussed in greater depth in the subsequent chapter (Chapter 3).

Following these introductory chapters, efforts to understand and control deactivation in O-ATRP are discussed. Given the importance of deactivation in controlling the product polymer structure, we hypothesized improving deactivation in O-ATRP could ultimately enable expanding the monomer scope of this method to monomers with large k_{prop} values. To control deactivation, we first proposed electrochemical methods could be useful (Chapter 4), as electrolysis could be

used to generate the species responsible for deactivation ($PC^{\bullet+}$) from the neutral catalyst (PC). However, this work highlighted important gaps in the field's understanding of deactivation, which ultimately complicated the success of this electrochemically mediated variant of O-ATRP. To address these gaps in our knowledge, we next focused on understanding the reactivity of PC radical cations and their role in deactivation (Chapter 5). Through this work, new side reactions caused by $PC^{\bullet+}$ were identified, and factors influencing deactivation and polymerization control in O-ATRP were elucidated. Finally, a collaboration across several members of the Miyake group is described that probed side reactions in O-ATRP between $PC^{\bullet+}$ and the alkyl radicals at the center of this polymerization process (Chapter 6), which ultimately unveiled a new termination pathway that is unique to O-ATRP.

Combined, this work has provided a foundation for understanding and controlling deactivation and termination pathways in O-ATRP. Practically, we envision the insights gained here will be helpful in future work expanding the monomer and application scope of O-ATRP. In addition, the discoveries detailed in this work regarding PC side reactions and $PC^{\bullet+}$ reactivity will broadly impact the field of photoredox catalysis and could motivate new modes of reactivity in small molecule and polymer synthesis.

REFERENCES

(1) Miyake, G. M.; Theriot, J. C. Perylene as an organic photocatalyst for the radical polymerization of functionalized vinyl monomers through oxidative quenching with alkyl bromides and visible light. *Macromolecules* **2014,** *47*, 8255–8261.

(2) Treat, N. J.; Sprafke, H.; Kramer, J. W.; Clark, P. G.; Barton, B. E.; de Alaniz, J. R.; Fors, B. P.; Hawker, C. J. Metal-free atom transfer radical polymerization. *J. Am. Chem. Soc.* **2014,** *136*, 16096–16101.

(3) Theriot, J. C.; Lim, C. H.; Yang, H.; Ryan, M. D.; Musgrave, C. B.; Miyake, G. M. Organocatalyzed atom transfer radical polymerization driven by visible light. *Science* **2016,** *352*, 1082–1086.

(4) Ryan, M. D.; Theriot, J. C.; Lim, C. H.; Yang, H. S.; Lockwood, A. G.; Garrison, N. G.; Lincoln, S. R.; Musgrave, C. B.; Miyake, G. M. Solvent effects on the intramolecular charge transfer character of *N,N*-diaryl dihydrophenazine catalysts for organocatalyzed atom transfer radical polymerization. *J. Polym. Sci. Part A Polym. Chem.* **2017,** *55*, 3017–3027.

(5) Cole, J. P.; Federico, C. R.; Lim, C. H.; Miyake, G. M. Photoinduced organocatalyzed atom transfer radical polymerization using low ppm catalyst loading. *Macromolecules* **2019,** *52*, 747–754.

(6) Price, M. J.; Puffer, K. O.; Kudisch, M.; Knies, D.; Miyake, G. M. Structure–property relationships of core-substituted diaryl dihydrophenazine organic photoredox catalysts and their application in O-ATRP. *Polym. Chem.* **2021**, *12*, 6110–6122.

(7) Pearson, R. M.; Lim, C. H.; McCarthy, B. G.; Musgrave, C. B.; Miyake, G. M. Organocatalyzed atom transfer radical polymerization using *N*-aryl phenoxazines as photoredox catalysts. *J. Am. Chem. Soc.* **2016,** *138*, 11399–11407.

(8) McCarthy, B. G.; Pearson, R. M.; Lim, C. H.; Sartor, S. M.; Damrauer, N. H.; Miyake, G. M. Structure-property relationships for tailoring phenoxazines as reducing photoredox catalysts. *J. Am. Chem. Soc.* **2018,** *140*, 5088–5101.

(9) Swisher, N. A.; Corbin, D. A.; Miyake, G. M. Synthesis, characterization, and reactivity of *N*-alkyl phenoxazines in organocatalyzed atom transfer radical polymerization. *ACS Macro Lett.* **2021**, *10*, 453–459.

(10) Buss, B. L.; Lim, C.-H.; Miyake, G. M. Dimethyl dihydroacridines as photocatalysts in organocatalyzed atom transfer radical polymerization of acrylate monomers. *Angew. Chem. Int. Ed.* **2020,** *59*, 3209–3217.

CHAPTER 2.

PHOTOINDUCED ORGANOCATALYZED ATOM TRANSFER RADICAL POLYMERIZATION (O-ATRP): PRECISION POLYMER SYNTHESIS USING ORGANIC PHOTOREDOX CATALYSIS

Overview

The development of photoinduced organocatalyzed atom transfer radical polymerization (O-ATRP) has received considerable attention since its introduction in 2014. Expanding on many of the advantages of traditional ATRP, O-ATRP allows well-defined polymers to be produced under mild reaction conditions using organic photoredox catalysts. As a result, O-ATRP has opened access to a range of sensitive applications where the use of a metal catalyst could be of concern, such as electronics, certain biological applications, and the polymerization of coordinating monomers. However, key limitations of this method remain and necessitate further investigation to continue the development of this field. As such, this review details the achievements made to-date as well as future research directions that will continue to expand the capabilities and application landscape of O-ATRP.

Introduction

Atom transfer radical polymerization (ATRP) is a powerful controlled radical polymerization (CRP) method for the synthesis of polymers with targeted molecular weights, narrow molecular weight distributions (low dispersity [$Đ$]), varied chemical compositions, and complex architectures. In this method, a catalyst mediates the reversible activation and deactivation of polymers with halide end-groups, wherein the halide is removed during activation

to generate a reactive polymer radical and then reinstalled during deactivation to yield a "dormant" polymer chain. As a result of this reversible deactivation mechanism, bimolecular radical termination reactions are suppressed, and polymer growth is controlled toward the synthesis of well-defined macromolecules with a range of functionalities and architectures.[1-6]

For the purposes of this review, it is beneficial to define certain metrics of polymerization control that are often considered in ATRP. Commonly, properties such as molecular weight control, $Đ$, and initiator efficiency (I*) are analyzed to evaluate control over a given polymerization. Molecular weight control refers to the ability of the user to target and synthesize polymers of varied molecular weights, commonly through manipulation of the reaction stoichiometry.

For $Đ$, the desirable range in ATRP and other CRPs is between 1.0 and 1.5. The lower limit of $Đ = 1.0$ represents a totally uniform molecular weight distribution (i.e. a single molecular weight is present). Since this value generally cannot be obtained using synthetic chemistry, values as close as possible to 1.0 are sought to indicate a well-controlled polymerization process. Instead, the upper limit of $Đ = 1.5$ represents the lowest $Đ$ theoretically obtainable through a free radical polymerization process.[7] As such, a polymerization that produces a $Đ > 1.5$ is not considered controlled, since a similar $Đ$ could be obtained through an uncontrolled free radical polymerization. In this review, $1.0 < Đ \leq 1.1$ is considered excellent, $1.1 < Đ \leq 1.3$ is considered good, $1.3 < Đ \leq 1.5$ is considered moderate, and $Đ > 1.5$ is considered poor.

Finally, I* represents the theoretical number average molecular weight ([$M_{n,theo}$], based on the reaction stoichiometry) divided by the experimentally determined number average molecular weight ($M_{n,exp}$). When I* = 100%, this value indicates that all the initiators added to the polymerization reaction initiated a single polymer chain, providing the user with control over the

molecular weight of the product polymer. However, if $I^* \neq 100\%$, this value can indicate that side reactions or other undesirable processes are present that may reduce control over the product polymer structure.

In seminal ATRP reports by Matyjaszewski[8] and Sawamoto[9], Cu and Ru catalysts, respectively, were chosen to mediate the polymerization process. In each case, polymers could be obtained with predictable molecular weights and $Đ < 1.5$, indicating the radical polymerization process had been controlled to some degree. In the following years, notable advancements included the development of methods to dramatically lower catalyst loadings in ATRP,[10, 11] as well as strategies to control the polymerization process using external stimuli such as light or electricity.[12-22] In particular, work reported by Fors and Hawker showed a common Ir photoredox catalyst (PC) could be used to mediate the polymerization of methyl methacrylate (MMA), providing the first example of a photoredox catalyzed ATRP method.[15] However, around the same time, concerns surrounding the sustainability of Ir and Ru compounds[23] began motivating the use of organic molecules as more sustainable alternatives to these catalysts.[24-31] As such, shortly after the report by Fors and Hawker, the first examples of organocatalyzed atom transfer radical polymerization (O-ATRP) emerged employing organic PCs to mediate the polymerization of methacrylate monomers *via* an ATRP mechanism.[32, 33]

Due to challenges associated with the reduction of C-X (X = halide) bonds (i.e. the polymer chain-end groups in ATRP), early catalyst systems for O-ATRP primarily focused on PCs that could operate by oxidative quenching of the excited state (PC*). In other words, these early catalysts systems featured strongly reducing excited states that could directly reduce the alkyl halide (Figure 2.1a), leading to the formation of a polymer radical (P_n•) and the catalyst radical cation ($PC^{•+}$). It is hypothesized that deactivation of the polymer radical is mediated by $PC^{•+}$, which

in turn regenerates the neutral ground state of the catalyst (PC). Thus, the general mechanism of ATRP is maintained, but it is mediated using a photoredox catalytic cycle.

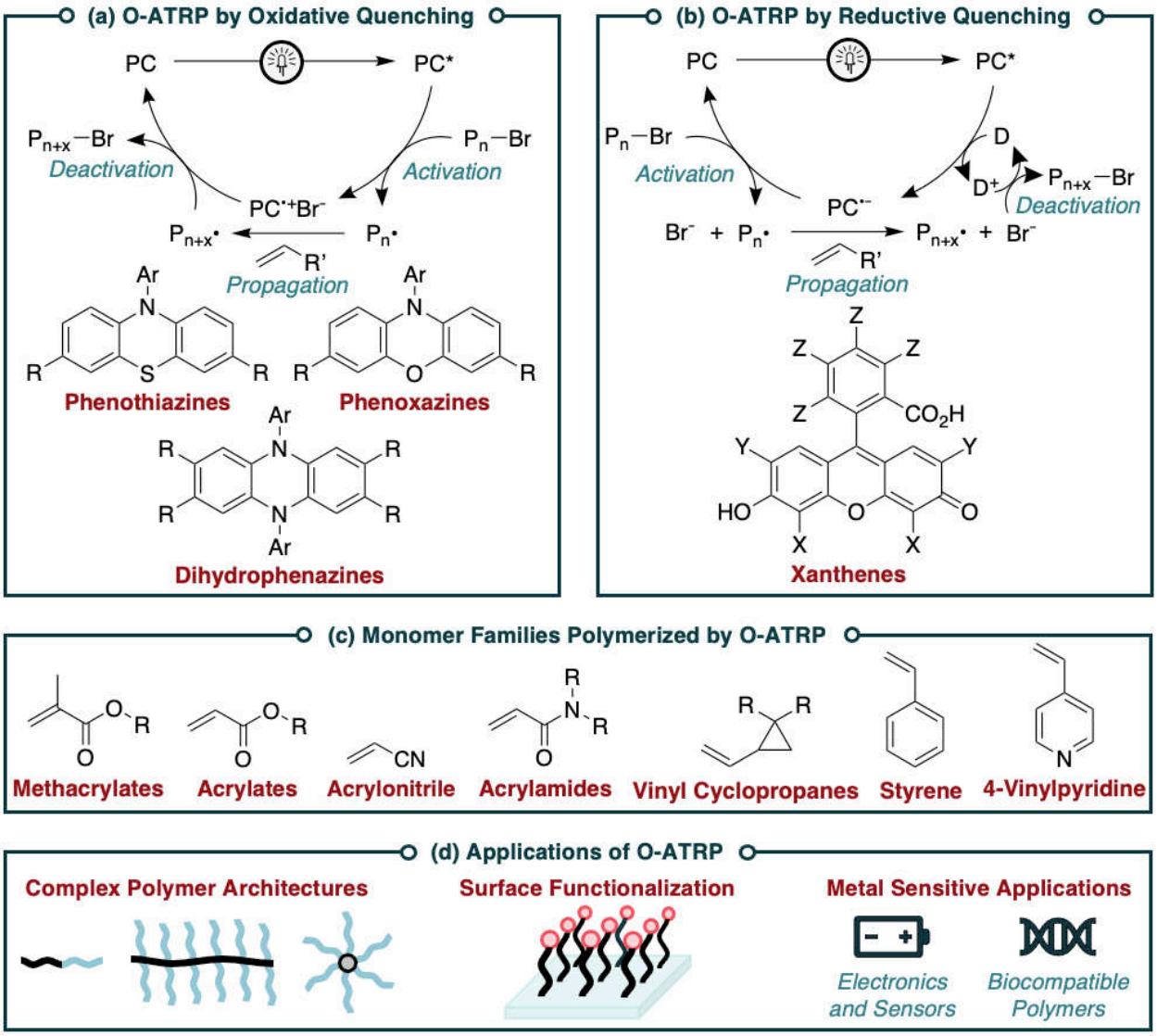

Figure 2.1. *Overview of O-ATRP: (a) the mechanism of O-ATRP by oxidative quenching and common PCs employed therein; (b) the mechanism of O-ATRP by reductive quenching and a common PC family employed in this method; (c) monomer families that have been polymerized by O-ATRP; (d) common applications of O-ATRP.*

In the early development of O-ATRP, much attention was given to the development of strongly reducing PCs, such as phenothiazines[33], dihydrophenazines[34], and phenoxazines[35] (Figure

2.1a). However, work by Park and Choi showed similar polymerizations could also be performed using reductive quenching PCs such as $Ru(bpy)_3^{2+}$ (bpy = 2,2'-bipyridine).[17] Zhang and Cheng quickly showed this method could also be mediated by organic reductive quenching PCs (Figure 2.1b),[36] in which PC* is reduced by an electron donor (D) to generate a catalyst radical anion ($PC^{\bullet-}$) and the donor cation (D^+). Since PC* in these cases is often incapable of directly reducing the alkyl halide, $PC^{\bullet-}$ is formed through the reaction of PC* with a sacrificial electron donor. In turn, activation mediated by $PC^{\bullet-}$ generates the neutral PC, and it is proposed that the D^+ mediates deactivation. As a result, common organic PCs such as xanthenes (Figure 2.1b) can also be used to mediate O-ATRP. While there are certain advantages and disadvantages associated with each class of PCs, these considerations will be discussed in greater detail later in the text (see *Oxidative and Reductive Quenching Mechanisms*).

Relative to other polymerization methods, O-ATRP features several desirable properties that have contributed to its popularity over time. For example, like other ATRP methods,[1, 4] O-ATRP features a simple reaction setup, can produce well-defined polymers, and is tolerant to a wide range of functional groups (Figure 2.1c). Thanks to the use of photoredox catalysis to drive this method, O-ATRP also enjoys added benefits such as mild reaction conditions (e.g. performed at ambient temperatures), as well as spatial and temporal polymerization control through manipulation of the light source in the reaction. In addition, O-ATRP has been employed to access numerous interesting applications, including the synthesis of polymers and copolymers with complex architectures, the functionalization of various surfaces through surface-initiated polymerizations, and the production of materials for electronic and biological applications (Figure 2.1d).

With that said, O-ATRP has experienced several limitations since its inception that continue to attract research efforts. Regarding the mechanism of O-ATRP, significant advancements have been made in understanding PC photophysics, how PC design impacts these photophysical processes, and how these properties can affect activation during the polymerization. However, certain aspects of the O-ATRP mechanism remain poorly understood, especially in the presence of reductive quenching PCs. In addition, while significant advancements have been made in the scope of monomers successfully polymerized by this method, several of these monomers remain poorly controlled. Thus, continued research in this area is necessary to overcome the current limitations of O-ATRP and expand the utility of this method.

To promote progress in this field, this review will provide a comprehensive overview of the development, current status, and applications of O-ATRP. We begin by placing O-ATRP in context relative to other metal-free CRPs to demonstrate why one might choose O-ATRP over other, similar methods. Next, we provide a detailed account of the development of O-ATRP, including its history, common variations of O-ATRP, catalysts reported for this method, and insights gained into its mechanism. With the history of the method in mind, the current status of the field is discussed, including monomers and applications accessible through O-ATRP. Finally, we conclude this review with an opinion overviewing future directions that could expand the capabilities and utility of this method. While other reviews have been written on this topic,[37-46] they have typically focused on specific aspects of this method (ex. catalyst design, applications etc.) rather than providing a complete overview of its development and uses. As such, this review seeks to document O-ATRP in detail, providing a comprehensive discussion of developments and advancements in the field for both new and veteran practitioners.

Metal-free controlled radical polymerizations: O-ATRP in context

While the focus of this review is on O-ATRP, several other metal-free CRPs also exist that warrant comparison. Each method has its own advantages and disadvantages, so this section seeks to place O-ATRP in context relative to these other methods. Since this review is not intended to provide a comprehensive overview of metal-free CRPs, this section will focus only on common methods, including photoinduced electron/energy transfer reversible addition-fragmentation chain-transfer (PET-RAFT), photoiniferter polymerization, nitroxide mediated polymerization, and iodine transfer polymerization.

Beginning with PET-RAFT, this method is the photocatalyzed variant of the more traditional RAFT polymerization first reported by Moad, Rizzardo, and Thang in 1998.[47] As such, PET-RAFT operates by a reversible chain-transfer mechanism, where polymer growth is controlled by transferring the propagating radical from one polymer chain to another (Figure 2.2). In 2014, Boyer and coworkers showed the RAFT process could be mediated by common photoredox catalysts, such as *fac*-[Ir(ppy$_3$)] (ppy = 2-phenylpyridine)[48] and Ru(bpy)$_3$Cl$_2$[49]. While these methods were not metal-free, it was quickly shown that PET-RAFT could also be mediated by organic catalysts, such as 5,10,15,20-tetraphenylporphyrin and related derivatives.[50]

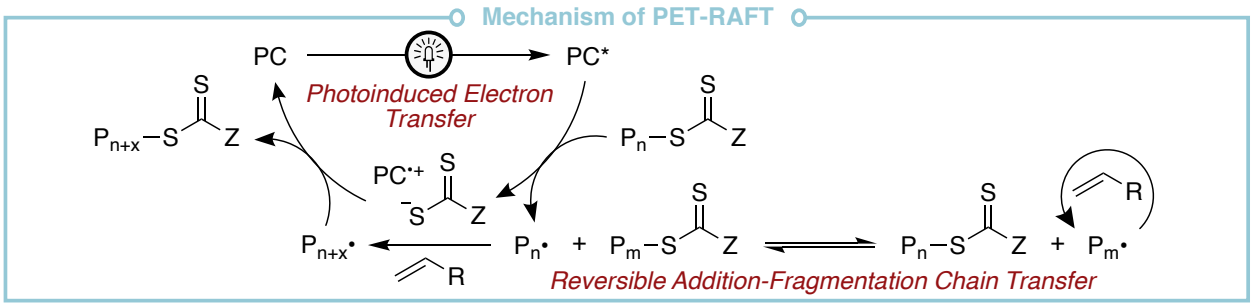

Figure 2.2. *Mechanism of PET-RAFT proceeding through electron transfer.*

Following these seminal reports, the scope of catalysts for PET-RAFT has blossomed and now includes many common organic PCs such as eosin Y, fluorescein, and more.[51] This feature is

one of the great advantages of PET-RAFT, as it can be performed with a wide variety of catalysts – many of which are commercially available – under irradiation spanning the entire visible spectrum and even into the near infrared spectrum,[52] which is less common in O-ATRP. Comparatively, the number of catalysts available for O-ATRP is smaller due to the greater thermodynamic requirements for activating carbon halide bonds, making catalyst selection an advantage in PET-RAFT. In addition, a large number of RAFT chain-transfer agents (CTAs) have been reported over the years, and many are now commercially available, lowering the barrier to use for this method. With that said, CTAs for RAFT are generally more expensive than the alkyl halide initiators commonly employed in O-ATRP, although this can sometimes be offset by the cost of the catalyst (Table 2.1). In addition, since many CTAs are capable of absorbing visible light, their presence on the chain-ends of the product polymer can impart color to the polymer that may be undesirable. As a result, extra steps may be necessary to alter the polymer chain-ends and remove this color from the product.

Closely related to PET-RAFT, iniferter polymerizations can also use CTAs to control polymer growth but without an added photoredox catalyst. Instead, the CTA is directly activated by irradiation to generate reactive radicals, which then initiate and drive the polymerization process. As a result, iniferter polymerizations are remarkably simple, since a single reagent acts as the initiator, chain-transfer agent, and terminator (the ini-fer-ter).[53] In turn, this simplicity can greatly reduce the need for purification of the polymer product, which is often necessary with other polymerization methods such as O-ATRP and PET-RAFT. When these polymerizations are driven by photolysis of the iniferter, they are referred to as photoiniferter polymerizations (Figure 2.3). Importantly, while some RAFT agents can function as iniferters, it should be noted that not all

Table 2.1. *Comparative characteristics of common metal-free controlled radical polymerization techniques.*

Method	Reagents Required	Commercial Availability of Reagents	Cost of Reagents (g^{-1})[a]	Monomer Scope
O-ATRP	Photocatalyst (PC)	Some PCs available, most must be synthesized.	\$500 – \$1,000	Acrylamides, acrylates, acrylonitrile, methacrylates, styrene, vinyl cyclopropanes, 4-vinyl pyridine.
	Alkyl halide initiator	Numerous alkyl bromides and chlorides available for purchase.	\$1 – \$15	
PET-RAFT	PC	Numerous PCs available.	\$10 – \$1,200	Acrylamides, acrylates, methacrylates, styrene, vinyl acetate.
	RAFT agent	Numerous dithiobenzoate, dithiocarbonate, and trithiocarbamate RAFT agents available for purchase.	\$100 – \$300	
Photoiniferter	Iniferter (light absorbing RAFT agent)	Numerous dithiobenzoate, dithiocarbonate, and trithiocarbamate RAFT agents available for purchase.	\$100 – \$300	Acrylates, methacrylates, styrene, vinyl acetate.
NMP	Nitroxide <u>or</u> Alkoxyamine	Some nitroxides and alkoxyamines available, most must be synthesized.	\$30 – \$600	Acrylamides, acrylates, cyclic ketene acetals, 1,3-dienes, styrenes, methyl methacrylate, vinyl acetate, vinyl chloride.
ITP	Initiator	Numerous radical initiators available.	\$1 – \$40	Acrylates, methacrylates, styrene, vinyl acetate, vinyl chloride.
	Alkyl iodide <u>or</u> Alkyl bromide + NaI	Limited availability of alkyl iodides, most must be synthesized. Numerous alkyl bromides available.	\$1 – \$100[b] \$1 – \$15	

[a] *Price ranges determined by a survey of compounds available on sigmaaldrich.com in January 2021 and may vary by supplier.* [b] *2-Iodo-2-methylpropionitrile is sold by TCI for but is not available through Sigma Aldrich.*

iniferters can also serve as CTAs in RAFT polymerizations. One notable example is tetraphenylethane derivatives,[54] which can serve as iniferters but not RAFT CTAs.

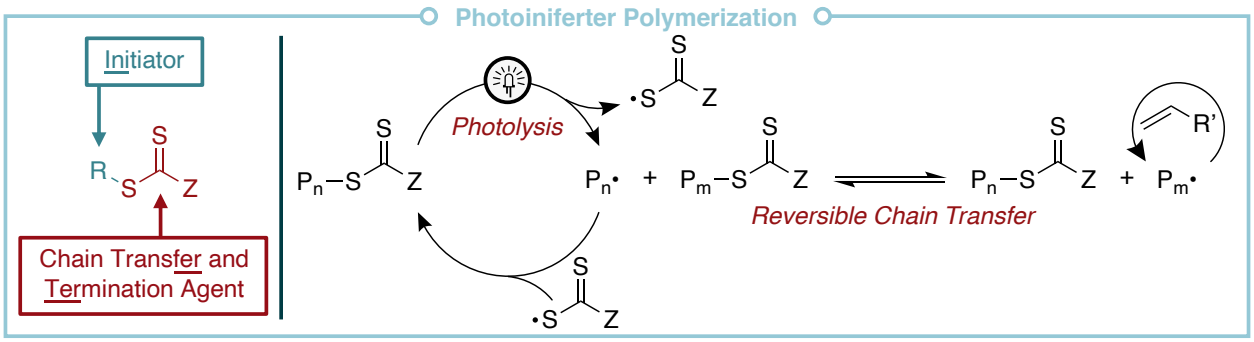

Figure 2.3. *Origin of the name "iniferter" (left) and mechanism of a photoiniferter polymerization using dithiocarbonyl compounds (right).*

Unfortunately, the simplicity of this process can also come at a cost. For instance, the use of high-energy UV light is generally undesirable in organic synthesis, because it can cause side reactions that are less likely under visible light irradiation. In 2002, such side reactions were observed with certain iniferters, which were shown to undergo decomposition under polymerization relevant conditions.[55] To circumvent this issue, one can use visible light absorbing or thermally activated iniferters,[52, 54] although these constraints may also introduce added complexities by changing the chemistry of the iniferter or the polymerization process. For this reason, it is sometimes easier to employ other techniques, such as O-ATRP or PET-RAFT.

Another popular CRP method is nitroxide mediated polymerization (NMP), which employs alkoxyamines to control polymer growth through a reversible deactivation process similar to that found in ATRP. Since NMP typically involves direct homolysis of the polymer chain-end C-O bond (Figure 2.4), it is often performed in the absence of a catalyst. Further, the alkoxy amine can also serve as the initiator in this method, allowing these polymerizations to be performed with minimal reagents and reducing the need for polymer purification. Most commonly, NMP is

performed at elevated temperature using a thermal initiator or thermally activated alkoxyamine initiator,[41, 56-58] although photomediated NMP has also been reported.[59, 60]

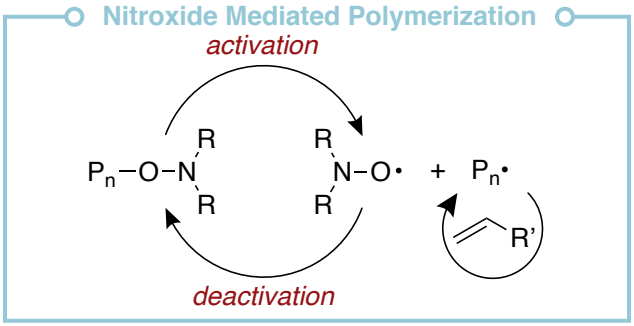

Figure 2.4. *Mechanism of activation and deactivation in a nitroxide mediated polymerization.*

While a number of alkoxyamines have been reported for NMP,[56, 57] most are not commercially available and must be synthesized prior to the polymerization. In addition, many of these compounds are unstable at elevated temperatures. As a result, they must be carefully stored and can sometimes decompose under polymerization conditions, introducing added complications relative to O-ATRP.[57] Nonetheless, NMP remains a powerful controlled polymerization method, especially for sensitive applications where polymer impurities can be detrimental.

Finally, one CRP that is receiving increasing levels of attention is iodine transfer polymerization (ITP). While a number of ITP methods have been reported and discussed elsewhere,[61] here we will focus on two ITP mechanisms operating by degenerative chain-transfer (Figure 2.5a) and reversible complexation (Figure 2.5b). In the first, which was first reported by Tatemoto[62] and later expanded by Matyjaszewski and coworkers in 1995,[63] iodine is transferred from a deactivated polymer to a propagating polymer, such that polymer growth is controlled by distribution of the propagating radical across several polymer chains. As a result, the reaction system is quite simple, as the only reagents necessary for the polymerization to proceed are the

monomer, initiator, and an alkyl iodide that also ultimately serves as an initiator. However, the chain-transfer rate of the alkyl iodide must be matched to the propagation rate of the monomer, which can complicate reaction design.[61]

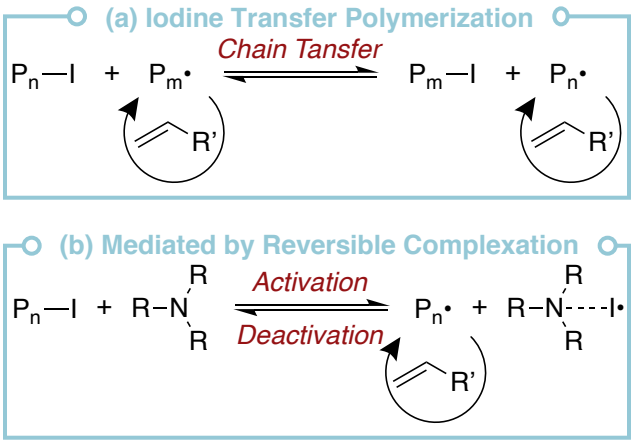

Figure 2.5. *Two common mechanisms of iodine transfer polymerization without (a) and with (b) amines as complexing agents.*

Instead, ITP mediated by reversible complexation employs a complexing agent – often an amine – to assist in the removal of iodine from the polymer chain end to enable propagation. As a result, this mechanism resembles one of reversible deactivation, where the polymer is activated by removal of the iodine and deactivated by regeneration of the C-I bond. When the exchange frequency of the iodine is the limiting factor in a polymerization, this strategy can improve polymerization outcomes by facilitating iodine exchange.[61] However, this method also introduces new reagents to the polymerization, which can complicate the reaction setup and necessitate further purification of the product polymer.

Unfortunately, one limitation of ITP is the lack of commercially available alkyl iodides, possibly because these compounds are often thermally and photochemically unstable. One way this issue has been addressed is through *in-situ* generation of the alkyl iodide, where alkyl bromides

are converted to alkyl iodides through reaction with an iodide source (ex. NaI). Since numerous alkyl bromides are available commercially, this approach can circumvent issues related to the availability of alkyl iodides, although it also complicates the polymerization process. In addition, one must consider the stability of the polymer chain-end, which can also be susceptible to degradation either during or after the polymerization.[61]

In summary, each polymerization method presented here features different advantages and disadvantages that one must consider in choosing a method. Perhaps one final feature that should be considered is the monomer scope of each method (Table 2.1), which may eliminate certain methods depending on the materials one wishes to produce. However, regardless of the specific method chosen, a central theme emerges: metal-free CRPs enable facile access to a range of polymeric materials with tunable compositions, structures, and functionalities. For instances in which O-ATRP may be the best choice, the following sections will provide deeper insight into the mechanism, scope, and applications of this method.

Mechanisms of O-ATRP

General mechanism of ATRP

Regardless of the identity of the catalyst, all ATRP methods operate by the same general mechanism of reversible activation and deactivation (Figure 2.6). During activation, the catalyst (Cat^n) reduces an initiator molecule or a polymer chain-end possessing a C-X bond (X = halide) to generate a reactive, carbon-centered radical. Since this radical can react with functionalities within the monomer, such as alkenes, polymerization propagation can occur to grow the polymer chain. However, radical polymerizations are inherently susceptible to termination processes, wherein the propagating radicals undergo irreversible side reactions such as radical chain-coupling

or disproportionation. From the standpoint of precision polymer synthesis, these side reactions are undesirable because they reduce the user's ability to control the structure of the polymer product.

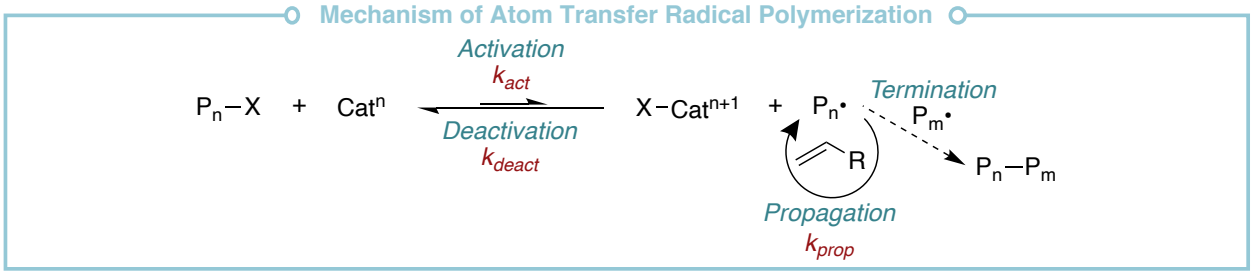

Figure 2.6. *General mechanism of ATRP and key mechanistic steps. For simplicity, only one possible termination pathway is depicted (termination by combination).*

To overcome this limitation, a key feature of ATRP is the formation of a deactivator during the activation step. Often, the deactivator is simply the oxidized catalyst (Cat^{n+1}), though some examples will be presented later where this may not be the case (see *Mechanistic Insights in O-ATRP by Reductive Quenching*). Regardless of the identity of the deactivator, this species mediates the deactivation step of ATRP, in which the C-X polymer chain-end group is reinstalled to generate a "dormant" polymer chain and lower the concentration of radicals in solution. As a result, both the rates of propagation (Eq. 2.1) and termination (Eq. 2.2) are lowered. However, since radical termination reactions are typically bimolecular, the rate of termination is reduced to a greater degree than propagation. Therefore, the net result of deactivation is that termination reactions are suppressed while allowing polymer growth to proceed as desired. Importantly, for effective deactivation to occur, this step should generally be faster than the other steps of the polymerization (i.e. $R_{deact} > R_{act}, R_{prop}, R_{term}$). For further information on the general mechanism of ATRP, we point the reader to other reviews already written on this topic.[1, 3, 4]

$$R_{prop} = k_{prop}[Monomer][P_n\cdot] \quad \text{(Eq. 2.1)}$$

$$R_{term} = k_{term}[P_n\cdot]^2 \quad \text{(Eq. 2.2)}$$

Oxidative and reductive quenching mechanisms

In O-ATRP, organic PCs are used to mediate the ATRP mechanism. As such, it is important to consider the role of the PCs in addition to that of the polymerization. Most commonly, PCs that operate by oxidative quenching (Figure 2.7, bottom) are employed, since such PCs possess strongly reducing excites states [$E_{red}(PC^{\bullet+}/PC^*) \leq$ -1.5 V vs. saturated calomel electrode (SCE)] that are capable of directly reducing the alkyl bromide or chloride in O-ATRP [E^o(C-Br/C-Br$^{\bullet-}$) ~ -0.8 to -0.6 V vs. SCE[34], and E^o(C-Cl/C-Cl$^{\bullet-}$) ~ 0.1 to 0.2 V < E^o(C-Br/C-Br$^{\bullet-}$)[64]]. This mechanism begins when the PC becomes photoexcited by absorption of light to generate the strongly reducing excited state (PC*). This excited state can react with an alkyl halide – either the initiator or the polymer chain-end – to generate the reactive radical for propagation. In addition, the PC radical cation ($PC^{\bullet+}$) is formed along with a halide anion (i.e. Br^- or Cl^-). Together, these ions are used to deactivate the propagating radical, effectively lowering the concentration of radicals in solution and thereby limiting termination reactions. Common PC families that typically operate by this mechanism include phenothiazines,[33] dihydrophenazines,[34] phenoxazines,[35] and dihydroacridines.[65, 66]

PCs that operate by reductive quenching (Figure 2.7, top) are typically insufficiently reducing in PC* to directly reduce the alkyl halide. To circumvent this issue, sacrificial electron donors, such as amines, are oxidized by PC*, generating a more reducing PC radical anion ($PC^{\bullet-}$). If $PC^{\bullet-}$ is thermodynamically capable of reducing the alkyl halide, activation can proceed.

However, since the product of activation is now the neutral PC ground state, deactivation must be mediated by another species. Often, the radical cation of the sacrificial electron donor may be sufficient.

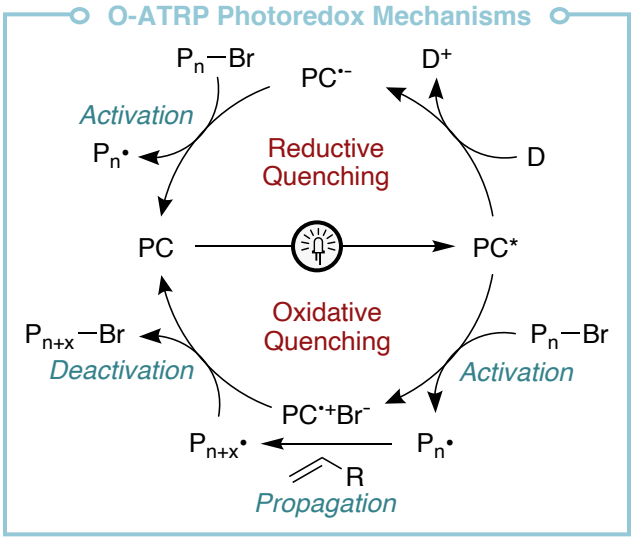

Figure 2.7. *Mechanisms of O-ATRP proceeding through oxidative and reductive quenching mechanisms.*

Comparing these two mechanisms, some advantages and disadvantages with each one become apparent. With oxidative quenching, fewer reagents are required. As a result, the likelihood of side reactions occurring is lowered, and contamination of the polymer product is minimized. However, PCs with strongly reducing excited states are necessary to mediate this mechanism, and such PCs – in particular strongly reducing organic PCs – have historically been rare.[25, 31, 67, 68] Further, while catalyst development in O-ATRP has greatly expanded the availability of strongly reducing organic PCs,[31] only a handful are commercially available.[69-72]

By contrast, many of the PCs commonly employed for reductive quenching – often xanthenes – are commercially available, greatly reducing the barrier to performing O-ATRP by this photoredox mechanism. However, the requirement for a sacrificial electron donor increases

the complexity of the reaction and creates new opportunities for side reactions to occur, such as undesirable hydrogen atom abstractions when amines are used,[73] potentially limiting control over the product polymer structure. Such side reactions may be the reason that better polymerization control is often seen in O-ATRP using oxidative rather than reductive quenching PCs, although similar levels of control are possible in some cases (see *Reductive Quenching Catalysts*). One final consideration is that a sacrificial electron donor may remain in the polymer as an impurity after the polymerization is complete, potentially increasing the need for polymer purification depending on the desired application.

Photocatalysts employed in O-ATRP

Initial photocatalysts

The first examples of O-ATRP were reported simultaneously by the Miyake and Theriot[32] and the Hawker[33] groups in 2014. In the former, perylene (Figure 2.8) was used as a PC and could activate ethyl α-bromophenylacetate (EBP) and catalyze the polymerization of MMA to produce poly(methyl methacrylate) (PMMA) under visible light irradiation. While this catalyst gave only moderate polymerization control – $Đ$ as low as 1.3, initiator efficiency (I^*) ≠ 100% – it also provided the first example of performing O-ATRP using visible light. This feature is desirable because UV light is more likely to cause side reactions by direct activation of other organic molecules in solution. Further, by employing perylene as the PC, high molecular weight polymers (M_n > 100 kDa) could be produced by O-ATRP (M_n = 125 to 273 kDa), and several monomers (methacrylates, acrylates, and styrene) were successfully polymerized.[32]

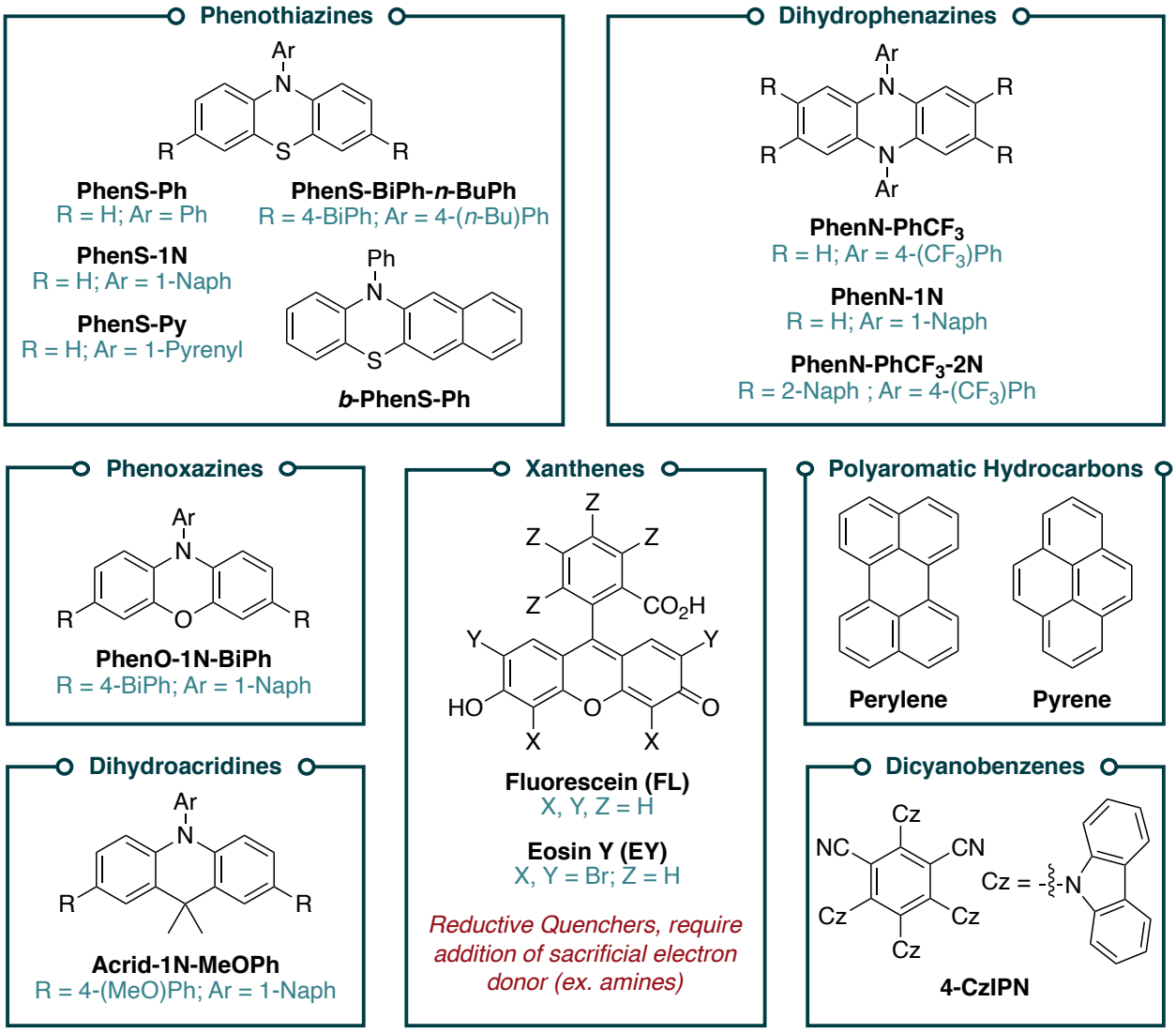

Figure 2.8. *Structures of common PCs and PC families employed in O-ATRP. For phenothiazines, dihydrophenazines, and phenoxazines, the following naming system is used in this review: PhenX-N_aryl-core, where PhenX refers to the identity of the PC core (ex. PhenS = phenothiazine, PhenN = dihydrophenazine, and PhenO = phenoxazine); N_aryl is an abbreviation referring to the N-aryl substituent (ex. 1N = 1-naphthyl); and core is an abbreviation referring to the core substituents (ex. BiPh = 4-biphenyl). For dihydroacridine PCs, PhenX is replaced with Acrid.*

To demonstrate that these polymerizations were driven by light, on/off experiments were performed in which the polymerization was repeatedly stopped and restarted by manipulation of the light source. During each "off" period, conversion remained unchanged, increasing only when the lights were turned on again. Further, a control experiment was performed using orange instead of white light, which could not be

absorbed by the catalyst. Since no polymerization was observed, this experiment suggested that the reaction was in fact driven by light and not simply the heat produced by the light source.[32]

In addition to investigating the role of light in these polymerizations, experiments were also performed to demonstrate that these reactions indeed proceeded through an ATRP mechanism. For example, kinetics experiments showed the polymerization exhibited linear pseudo-first-order kinetics; however, $Đ$ increased throughout the polymerization while M_w decreased, the opposite of what is expected for an ATRP process. Nevertheless, investigation of the chain-end groups by matrix-assisted laser desorption ionization mass spectrometry (MALDI-MS) showed the presence of bromine chain-ends, which enabled the polymers to be chain-extended with various monomers to produce block copolymers. As such, it was concluded that these polymerizations did in fact proceed through an ATRP mechanism mediated by perylene.[32]

Around the same time, Hawker and coworkers reported the first use of phenothiazines to mediate O-ATRP under UV irradiation. Specifically, 10-phenylphenothiazine (PhenS-Ph) exhibited excellent performance, producing PMMA with M_n = 1.3 to 15.4 kDa, $Đ$ as low as 1.2, and I^* ~ 100%. Further, dimethylaminoethyl methacrylate (DMAEMA) – a monomer that can poison metal-based catalysts by coordination – was successfully polymerized with excellent control (M_n = 8.8 kDa, $Đ$ = 1.1), making this the first example to highlight the utility of organocatalysis in ATRP.[33]

By cycling the light source "on" and "off," it was shown that this polymerization reaction was driven by light, and that the reaction could be started and stopped repeatedly without loss of polymerization control. Investigation of chain-end group fidelity in the polymer products was performed using electrospray ionization mass spectrometry (ESI-MS), ^{1}H nuclear magnetic resonance (NMR) spectroscopy, and chain-extension experiments. Together, these experiments demonstrated that this method provided excellent chain-end fidelity, and that the polymers produced by O-ATRP could be further functionalized by other ATRP methods such as $Ir(ppy)_3$ catalyzed photo-controlled ATRP (photoATRP) and Cu ATRP.

Importantly, the compatibility of O-ATRP with other ATRP methods enables unique copolymers to be synthesized by leveraging the complementary strengths of different catalyst systems.[33]

Comparing these two initial catalyst systems, each had associated advantages and disadvantages that would motivate future catalyst development. For example, the superior ability of PhenS-Ph to produce polymers with low *Đ* and near-quantitative *I** was immediately evident and can be attributed to the superior excited state redox properties of this catalyst (Table 2.2). For example, the triplet excited state of PhenS-Ph is far more reducing than that of perylene [$E^o(PC^{\bullet+}/{}^3PC^*)$ = -1.7 V for PhenS-Ph[33] vs. -0.58 V for perylene[74-77], both vs. SCE], which should facilitate more efficient activation of the alkyl bromide [$E^o(C\text{-}Br/C\text{-}Br^{\bullet-})$ ~ -0.8 to -0.6 V vs. SCE[78]] throughout the polymerization. However, PhenS-Ph required irradiation with UV light, whereas perylene was able to operate under visible light irradiation. While UV irradiation was not detrimental in this seminal report, it is more susceptible to initiating side reactions in certain systems. To avoid this possibility, the use of visible light to drive the polymerization is more desirable. As is outlined in the next two sections, addressing this disparity through the design of visible light absorbing, strongly reducing organic PCs was a significant research focus during the early development of O-ATRP.

Dihydrophenazines

One of the first PC families to possess both strongly reducing excited states and visible light absorption was the *N,N*-diaryl dihydrophenazines. First introduced in 2016 by Theriot *et al.*, the dihydrophenazine family was identified as a class of PCs through computational methods and predicted to feature excited state reduction potentials [$E^o(PC^{\bullet+}/{}^3PC^*)$] as low as -2.36 V vs. SCE. As this reduction potential is more than sufficient to reduce the alkyl halides in O-ATRP, a series of four dihydrophenazines with varying *N*-aryl substituents was synthesized and investigated. Substituents were chosen featuring both electron donating groups (EDGs) and electron

withdrawing groups (EWGs) to investigate how the electronics of the *N*-aryl substituent impacts PC properties, which led to the discovery of several important structure-property relationships. For example, the use of EDGs made ^{3}PC* more reducing, while also decreasing the oxidation potential of the PC radical cation [$E^o(PC^{\bullet+}/PC)$]. Instead, EWGs had the opposite effect, increasing $E^o(PC^{\bullet+}/^3PC^*)$ (i.e. making it more positive and ^{3}PC* less reducing) and increasing the oxidation potential of the radical cation.[34]

Interestingly, when these dihydrophenazines were employed in O-ATRP, all four effectively catalyzed the polymerization of MMA. However, PCs with EWGs exhibited superior polymerization control, producing polymers with lower dispersity ($Đ \leq 1.3$) than PCs with EDGs. In particular, 5,10-di(4-trifluoromethylphenyl)-5,10-dihydrophenazine (PhenN-PhCF_3, Figure 2.8) showed good control in the polymerization of MMA, producing PMMA with M_n = 6.0 to 58.6 kDa, $Đ$ as low as 1.1, and I^* ranging from 50% to 85%.[34]

To understand how the identity of the *N*-aryl substituent impacts catalysis, density functional theory (DFT) was used to probe the excited states of each PC. Visualization of the computed singly occupied molecular orbitals (SOMOs) in ^{3}PC* revealed that PCs with EDGs had two SOMOs both located on the dihydrophenazine core in the excited state. Instead, PCs with EWGs featured a lower-lying SOMO localized on the dihydrophenazine core and a higher-lying SOMO on the *N*-aryl substituent (Figure 2.9). This spatial separation of the SOMOs was interpreted as intramolecular charge transfer (ICT) in ^{3}PC*,[34] analogous to metal to ligand charge transfer in transition-metal PCs such as $Ru(bpy)_3^{2+}$.[68, 86]

Table 2.2. Redox properties of photoredox catalysts used in O-ATRP.

		Ground State		Excited State (S_1)		Excited State (T_1)		
Photocatalyst (PC)	Solvent	$E_{1/2}(PC^+/PC)$	$E_{1/2}(PC^-/PC)$	$E^o(PC^+/{}^1PC^*)$	$E^o(PC^-/{}^1PC^*)$	$E^o(PC^+/{}^3PC^*)$	$E^o(PC^-/{}^3PC^*)$	Reference
PhenS-Ph	MeCN	0.68	-	-2.1	-	-1.7	-	33
	DMAc	0.82	-	-1.97	-	-	-	79
PhenS-1N	DMAc	0.83	-	-2.23	-	-	-	79
PhenS-BiPh-*t*-BuPh	DMF	0.76	-	-1.94	-	-	-	78
b-PhenS-Ph	DMAc	0.90	-	-1.92	-	-	-	79
PhenN-$PhCF_3$	MeCN	0.32	-	-1.80	-	-2.06[a]	-	34
PhenN-1N	MeCN	0.23	-	-1.64	-	-2.12[a]	-	34
PhenN-$PhCF_3$-2N	DMAc	0.38	-	-1.84	-	-1.79[a]	-	81
PhenO-1N-BiPh	DMAc	0.65	-	-1.80	-	-1.70[a]	-	35,65
PhenO-2N-PhCN	DMAc	0.69	-	-1.75	-	-1.42[a]	-	65
PhenO-2N-MeOPh	DMAc	0.52	-	-1.81	-	-1.91[a]	-	65
PhenO-2N-Ph_3N	DMAc	0.54	-	-1.83	-	-1.88	-	65
Acrid-1N-MeOPh	DMF	0.71	-	-1.73	-	-1.62[b]	-	74
Perylene	MeCN	0.98	-	-1.87	-	-0.58	-	75,76,77,82
Pyrene	MeCN	1.24	-	-2.12	-	-	-	82
4-CzIPN	MeCN	1.52	-	-2.12	-	-	-	83
Fluorescein	MeCN	0.87	-1.17	-1.55	1.25	-1.07	0.77	83
Eosin Y	MeCN	0.76	-1.08	-1.58	1.23	-1.15	0.83	83
Benzophenone	MeCN	2.39	-1.72	-0.83	1.5	-0.61	1.28	84,85

[a] Value computed by density functional theory, see reference for details. [b] Measured at 77 ºC.

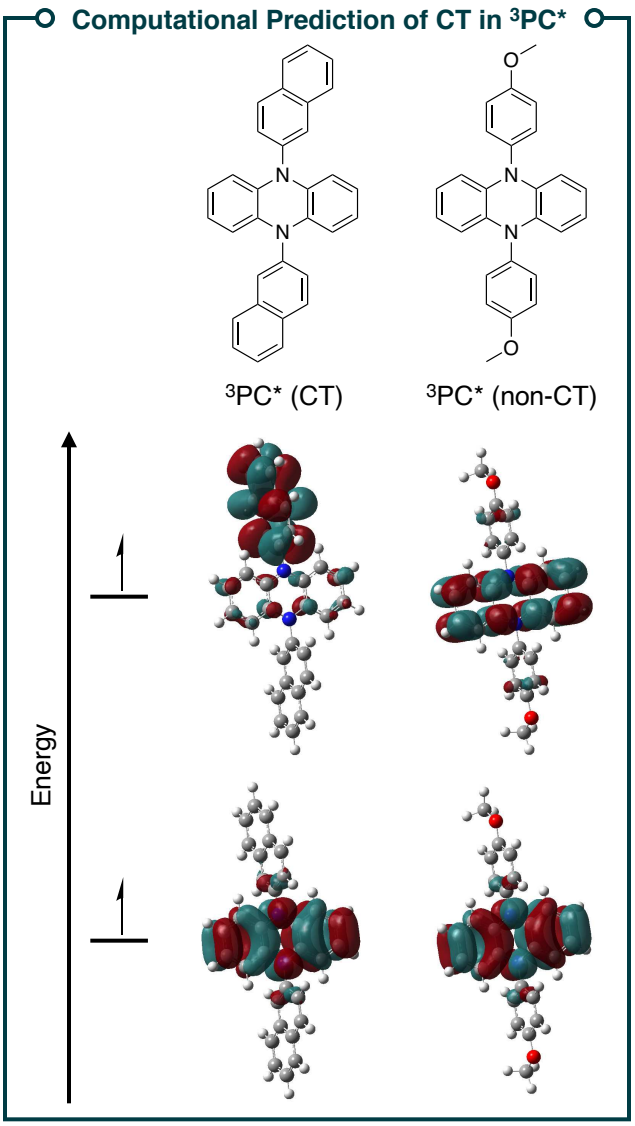

Figure 2.9. *SOMOs of dihydrophenazines with and without ICT in the triplet excited state.*

Since ICT in ^{3}PC* appeared beneficial for catalysis in O-ATRP, new PC targets were explored that also exhibited this computationally predicted property. As a result, two new dihydrophenazines bearing 1-naphthyl (PhenN-1N) and 2-naphthyl *N*-aryl substituents were identified and employed in O-ATRP. Excitingly, both PCs demonstrated excellent polymerization control in the synthesis of PMMA,[34] supporting the importance of ICT as a key design principle

for O-ATRP catalysts.[37] Further, PhenN-2N later became commercially available,[70] reducing the barrier to implementation of this catalyst in future reaction development.

Further functionalization of *N,N*-diaryl dihydrophenazines was later enabled by a synthetic breakthrough allowing for bromination of the dihydrophenazine core. By subjecting the tetrabrominated dihydrophenazine to Suzuki coupling conditions, several new PCs featuring aryl-core substituents were developed with enhanced light absorption – indicated by an increase in molar absorptivity – and further tunable redox properties. Interestingly, while several of these new compounds were still predicted to feature ICT in ^{3}PC*, DFT calculations suggest the ICT state is localized on the core substituents rather than the *N*-aryl substituents.[81] Despite this difference in ICT, the previous trend in polymerization performance[34] was again observed – PCs with ICT excited states displayed better control in O-ATRP than PCs without ICT.[81]

In addition, these core-extended dihydrophenazines exhibited several advantages over their non-core substituted counterparts. For example, core-substitution led to improved control in the polymerization of MMA, as exhibited by the production of polymer with lower $Đ$ and near-quantitative I^*. However, perhaps the most notable improvement in catalysis was the ability of core-substituted phenazines to operate at significantly reduced catalyst loadings without loss of polymerization control. In the case of PhenN-PhCF$_3$-2N (Figure 2.8), PMMA was successfully synthesized with M_n = 7.8 kDa, $Đ$ = 1.1, and I^* = 106% using just 50 ppm of catalyst. By contrast, lowering the concentration of PhenN-PhCF$_3$ from 1000 ppm to 50 ppm resulted in a significant increase in dispersity ($Đ$ = 1.3 at 1000 ppm, 1.66 at 50 ppm), indicating a loss of polymerization control at low catalyst loadings.[81]

Despite these advances in catalyst design, one long-standing challenge in O-ATRP has been the development of catalyst systems or reaction conditions to polymerize a wide variety of

monomers in a controlled fashion. Toward this end, Jessop and Cunningham reported a novel dihydrophenazine catalyst bearing amine-functionalities on the *N*-aryl substituents (Figure 2.10) that proved particularly effective in the polymerization of styrene by O-ATRP (M_n = 17.0 to 18.0 kDa, $Đ$ = 1.1 to 1.2). This report represents the first example of polymerizing styrene by O-ATRP with excellent polymerization control. However, it remains unclear how the properties of this new PC differ from previous dihydrophenazines and how these properties contribute to the controlled polymerization of styrene. As such, further investigation of this catalyst is warranted.[87]

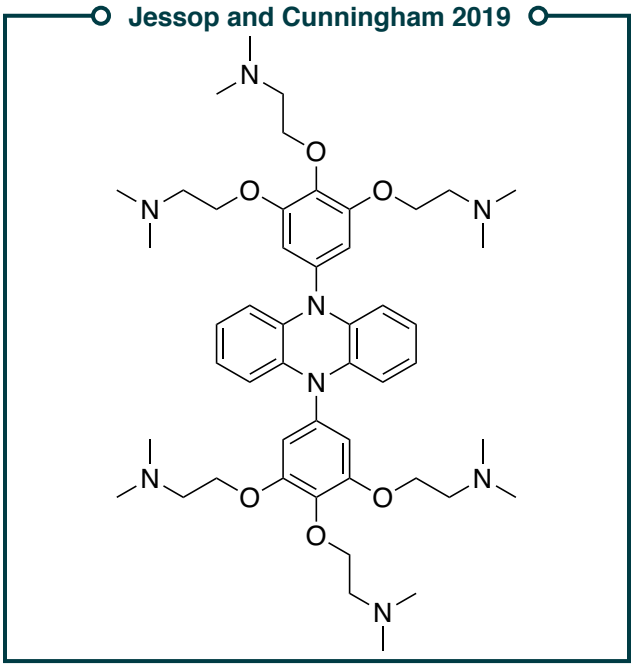

Figure 2.10. *Recyclable dihydrophenazine PC developed by Jessop and Cunningham.*

In addition to the O-ATRP of styrene, catalyst recycling was demonstrated in both organic and aqueous polymerizations by protonation or deprotonation of the amine functionalities and extraction of the catalyst from the polymerization solution. For example, after the polymerization of styrene, carbonated water was added to the reaction to protonate and extract the catalyst from the organic phase, allowing for the catalyst to be reused in subsequent polymerizations. Similarly,

when hydroxyethyl methacrylate (HEMA) was polymerized in water using the protonated catalyst, deprotonation of the PC and addition of toluene to the reaction enabled the catalyst to be recovered post-polymerization.[87]

In an effort to further expand the utility of dihydrophenazine photocatalysts, McCarthy *et al.* investigated the ability of phenazine PCs to mediate the O-ATRP of acrylates. Compared to methacrylates, the polymerization of acrylate monomers is more challenging to control due to their faster propagation, which requires faster deactivation to minimize uncontrolled propagation and termination reactions. Furthermore, reduction of a secondary alkyl bromide for a dormant acrylate-based polymer is more challenging than reduction of a tertiary alkyl bromide for a methacrylate-based polymer. Interestingly, when 5,10-di(2-naphthyl)-5,10-dihydrophenazine (PhenN-2N) was employed, it was discovered that the choice of solvent could significantly impact the success of the polymerization. In general, less polar solvents improved polymerization control (lower $Đ$, higher I^*) relative to more polar solvents, enabling the controlled polymerization of *n*-butyl acrylate (*n*-BuA).[88] For a more detailed explanation of the impact of solvent polarity on PC properties and their ability to mediate a controlled polymerization, please see *Section 3.4.5. – Solvent Effects in O-ATRP.*

It was also discovered that PhenN-2N could undergo core-substitution by the initiator during early polymerization times, leading to the *in-situ* formation of a new catalytic species. Ultimately, the *in-situ* generation of this new core-substituted PC prior to O-ATRP was exploited to produce well-defined poly(*n*-butyl acrylate) with a range of molecular weights (M_n = 7.7 to 17.5 kDa), low dispersity ($Đ$ = 1.1 to 1.4), and moderate-to-excellent initiator efficiencies (I^* = 183% to 93%). Further, this polymerization system was expanded to a number of other acrylate monomers and even to the synthesis of well-defined block copolymers with similar levels of

control, demonstrating the versatility of this new catalyst system.[88] In later work, it was shown that this core-substitution side reaction could be used to generate a series of new phenazine PCs, and that core-substitution could be used to tune several catalytically relevant properties.[89, 90]

Phenothiazines

Following the seminal report by Hawker that employed PhenS-Ph as the PC for O-ATRP,[33] a number of other phenothiazine PCs were developed by variation of the *N*-aryl substituent as well as through core-substitution. One of the first examples of this catalyst development came from Matyjaszewski in 2015, when phenothiazines with 4-methoxyphenyl (PhenS-MeOPh) and 1-naphthyl (PhenS-1N) *N*-aryl substituents were reported for the polymerization of acrylonitrile (AN) by O-ATRP. However, as PhenS-Ph ultimately provided the best control in the polymerization of this monomer, these new PC variants did not receive extensive use.[91] Later in 2016, Matyjaszewski reported several new phenothiazines with *N*-aryl substituents such as 4-chlorophenyl and 2-pyridinyl, as well as the use of PhenS-MeOPh and PhenS-1N in the O-ATRP of MMA. This time, PhenS-1N exhibited better performance than PhenS-Ph, producing PMMA with lower dispersity ($Đ$ = 1.4 vs. 1.5) albeit at relatively low monomer conversions (10% and 16%, respectively).[79]

Despite these efforts to tune PC properties through variation of the *N*-aryl substituent, all of the phenothiazine variants discussed to this point required UV irradiation during O-ATRP. To address this limitation, Matyjaszewski and coworkers developed phenyl benzo[*b*]phenothiazine (*b*-PhenS-Ph, Figure 2.8). Relative to previous phenothiazines, *b*-PhenS-Ph features a larger aromatic core, which redshifts its absorption into the visible range. As a result, this PC was able to mediate the O-ATRP of MMA under 392 nm light, producing PMMA with M_n ranging from

7.3 to 21.7 kDa and $Đ$ = 1.3 to 1.7. However, I^* with this catalyst system was generally low, ranging from 18% to 69% for the polymerization of MMA. Nevertheless, the polymerization could be stopped and restarted several times by manipulating the light source, and block copolymers were successfully synthesized, indicating retention of the bromine chain-ends of the polymers produced.

Similarly, Chen and coworkers sought to develop visible light absorbing phenothiazines, this time using a core-substitution approach[80] similar to that first employed with phenoxazine PCs in 2016.[35] By installing 4-*n*-butylphenyl groups at the 3- and 7- positions of the PC core, phenothiazines with various *N*-aryl substituents were prepared that exhibited strong light absorption tailing into the visible region. In particular, PhenS-BiPh-*n*-BuPh (Figure 2.8) exhibited good control over the polymerization of MMA, producing polymer with M_n = 11.2 kDa, $Đ$ = 1.2, and I^* = 81%. This PC was also explored in the polymerization of other monomers, including acrylates and acrylamides, although these polymerizations were generally less controlled ($Đ > 1.5$) than those of methacrylates.[80]

In addition to these more common phenothiazines, a number of other PCs within this family have been developed by modification of the *N*-aryl group. Indeed, functionalities such as 2-naphthyl,[80] 4-cyanophenyl, 4-trifluoromethylphenyl,[92] 4-triphenylamine,[93] and 1-pyrenyl[94] groups have all been incorporated into novel phenothiazine PCs. However, PhenS-Ph remains perhaps the most popular phenothiazine for O-ATRP, possibly due to its versatility and commercial availability.[69]

Phenoxazines

Another popular class of photocatalysts that has received considerable development is the

phenoxazine family. First introduced in 2016 by Pearson *et al.*, initial interest in this PC family stemmed from the desire to create strongly reducing, visible light absorbing catalysts for O-ATRP. Toward this end, Phenoxazines with various *N*-aryl substituents were synthesized and investigated experimentally and computationally.[35] Given the previous observation that phenazines with EWGs and extended conjugation on the *N*-aryl substituent provided the best polymerization control in O-ATRP,[34] this work primarily investigated PCs with 4-trifluoromethylphenyl (PhenO-PhCF$_3$), 1-naphthyl (PhenO-1N), and 2-naphthyl (PhenO-2N) groups. However, it is interesting to note that computations predicted PhenO-PhCF$_3$ would not undergo ICT in ^{3}PC*, since both computed SOMOs were localized on the phenoxazine core. Supporting this prediction, PhenO-PhCF$_3$ provided only moderate polymerization control in the O-ATRP of MMA (M_n = 6.5 kDa, $Đ$ = 1.5, I* = 86%). Instead, PhenO-1N and PhenO-2N were both predicted to poses ICT excited states, which in turn afforded enhanced polymerization control (M_n = 8.8 kDa, $Đ$ = 1.2, I* = 93% for PhenO-1N; M_n = 10.8 kDa, $Đ$ = 1.1, I* = 77% for PhenO-2N).[35]

Despite these results, initial phenoxazine PCs remained limited by their requirement for UV light to drive their reactivity. In an effort to retain their favorable catalytic properties but also redshift their absorption into the visible spectrum, core-substitution of PhenO-1N was undertaken to install 4-biphenyl substituents at the 3- and 7- positions of the phenoxazine core. The resulting catalyst (PhenO-1N-BiPh, Figure 2.8) exhibited strong visible light absorption, enabling O-ATRP to be performed under white light irradiation. Further, the ability of this catalyst to mediate the controlled polymerization of MMA under various conditions was demonstrated, with polymers produced exhibiting M_n = 3.6 to 21.3 kDa, $Đ$ = 1.1 to 1.3, and I* 98% to 105%. As such, while PhenO-1N-BiPh was not the first PC for O-ATRP with both visible light absorption and a strong excited state reduction potential [$E^o(PC^{\bullet+}/^3PC^*)$ = -1.70 V vs. SCE[95]], it did represent the first

catalyst system that could produce polymer with both low $Đ$ and quantitative I^* under visible light irradiation.[35]

Expanding on this strategy of core-substitution, future development of the phenoxazine family resulted in the installation of a variety of core substituents with both EWGs and EDGs to tune the redox properties of the catalysts. For example, through incorporation of EWGs, $E^o(PC^{\bullet+}/^3PC^*)$ could be increased by as much as 280 mV relative to PhenO-1N-BiPh [$E^o(PC^{\bullet+}/^3PC^*)$ = -1.42 V vs. SCE for 3,7-di(4-cyanophenyl)-2-naphthyl-10-phenoxazine (PhenO-2N-PhCN)]. Similarly, by destabilizing the radical cation of the PC, installation of EWGs was also found to change $E^o(PC^{\bullet+}/PC)$ by as much as 40 mV relative to PhenO-1N-BiPh [$E^o(PC^{\bullet+}/PC)$ = 0.69 V vs. SCE for PhenO-2N-PhCN and 0.65 V vs. SCE for PhenO-1N-BiPh]. Instead, when EDGs were installed on the phenoxazine core, a decrease in both $E^o(PC^{\bullet+}/^3PC^*)$ and $E^o(PC^{\bullet+}/PC)$ was observed. For example, installing 4-methoxyphenyl substituents (PhenO-2N-MeOPh) yielded $E^o(PC^{\bullet+}/^3PC^*)$ = -1.91 V vs. SCE and $E^o(PC^{\bullet+}/PC)$ = 0.52 V vs. SCE, whereas 4-triphenylamine functionalities gave $E^o(PC^{\bullet+}/^3PC^*)$ = -1.88 V vs. SCE and $E^o(PC^{\bullet+}/PC)$ = 0.54 V vs. SCE.[95]

In addition to investigating the impact of core substituents on PC redox properties, this work also probed how different functionalities affect light absorption and ICT within the PC. For example, by systematically increasing the amount of conjugation on the phenoxazine core, it was shown that the absorption of the catalyst could be red-shifted and the molar absorptivity increased to improve visible light absorption. Moreover, computational modelling was employed to visualize the electrostatic potential (ESP)-mapped electron density in phenoxazines with various *N*-aryl and core substituents in an effort to understand ICT in each of these compounds. Notably, these computational results suggested that PCs with biphenyl core substituents could exhibit ICT to the biphenyl group even if the *N*-aryl substituent cannot support ICT. This prediction was then

supported through measurement of the PC emission spectra. In the case of PhenO-2N, a broad, featureless emission was observed with a Stokes shift of 191 nm in DMAc, consistent with ICT to the 2-naphthyl group. Instead, while PhenO-2N-BiPh also displayed a broad, featureless emission – consistent with an ICT state – its Stokes shift was much smaller (82 nm). This difference in emission suggests the nature of the ICT state observed in PhenO-2N-BiPh is distinct from that present in PhenO-2N. Most interestingly, when the *N*-aryl group was changed from 2-naphthyl to phenyl (PhenO-Ph-BiPh), an emission spectrum nearly identical to that of PhenO-2N-BiPh was obtained, suggesting an ICT state localized on the biphenyl moiety of these PCs. Practically, the effect of this ICT state was observed in O-ATRP when PhenO-Ph-BiPh was able to produce well-defined PMMA ($Đ$ = 1.2, I^* = 102%) while PhenO-Ph could not ($Đ$ = 1.5, I^* = 111%).[95]

While Pearson *et al.* and McCarthy *et al.* largely focused on phenoxazines with phenyl and naphthyl *N*-aryl groups,[35, 95] Lee and Son developed a series of phenoxazine PCs with 4-trifluoromethylphenyl *N*-aryl substituents. Again, core-substitution with aromatic functionalities was found to red-shift the absorption of the PCs, as well as increase their molar absorptivity. Further, the installation of EWGs and EDGs was found to tune the redox properties of the PCs,[96] consistent with the trends previously reported.[95] In the O-ATRP of MMA, the catalyst with 4-biphenyl core substituents (PhenO-PhCF_3-BiPh) was ultimately the most successful, producing PMMA with M_n = 7.5 to 12.9 kDa, $Đ$ = 1.2 to 1.5, and I^* = 49% to 92%. In addition, this PC was employed in the synthesis of amphiphilic block copolymers, where bromine-functionalized poly(ethylene glycol) (PEG-Br) was chain-extended with glycidyl methacrylate by O-ATRP.[96]

In an effort to develop water-soluble O-ATRP catalysts, Zhou and Luo employed the core-substitution strategy to add PEG functionalities to PhenO-1N (PhenO-1N-PEG, Figure 2.11). Since PhenO-1N exhibits ICT to the 1-naphthyl group, this strategy should preserve the favorable

catalytic properties of PhenO-1N while increasing its solubility in aqueous solvent systems. Indeed, when PhenO-1N-PEG was employed in the O-ATRP of various monomers, good polymerization control was observed. For PEG methacrylate, polymer with M_n ranging from 26.7 kDa to 67.1 kDa was obtained, with $Đ$ = 1.2 to 1.3 and I^* = 60% to 79%. Further, the polymer was successfully chain-extended, suggesting retention of the bromine chain-end functionality. For the analogous PEG acrylate monomer, similar results were obtained, albeit with slightly reduced polymerization control (M_n = 81.9 kDa, $Đ$ = 1.4, I^* = 51%). In addition, the polymerization of *N*-isopropylacrylamide (NiPAM) was also attempted, although this polymerization did not exhibit the features of a controlled radical polymerization (M_n = 71.4 kDa, $Đ$ = 2.6, I^* = 15%).[97]

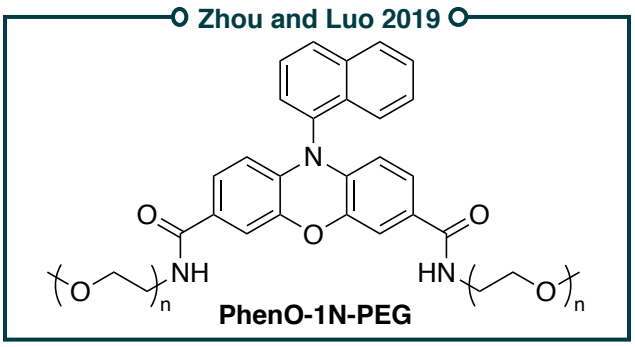

Figure 2.11. *PEG-Functionalized, water soluble phenoxazine.*

By further tuning the *N*-aryl substituent of phenoxazine PCs, Chen and Fang developed PCs for O-ATRP exhibiting thermally activated delayed fluorescence (TADF). In essence, these PCs were developed to feature a small energy gap between S_1 and T_1, allowing reverse intersystem crossing (T_1 to S_1) to take place through thermal excitation. The result should be an increased yield of S_1 that can be used to mediate activation during O-ATRP. In the polymerization of MMA, these PCs with TADF showed moderate polymerization control (M_n = 1.4 to 17.8 kDa, $Đ$ = 1.3 to 1.9, I^* = 6% to 180%).[98]

Finally, the versatility of phenoxazines was demonstrated in 2018 when PhenO-1N-BiPh was shown to mediate the controlled polymerization of MMA under air.[99] Typically, O-ATRP has been performed under an inert atmosphere to avoid possible interference from oxygen. For example, oxygen is known to quench propagating radicals,[100] as well as engage in energy transfer with PCs operating from triplet excited states, since the ground state of oxygen is also a triplet.[101] However, this work showed that under the appropriate conditions, PhenO-1N-BiPh could successfully perform O-ATRP in the presence of oxygen, greatly reducing the complexity of this polymerization system. Key to overcoming this challenge was optimization of the reaction headspace, where it was shown that eliminating the headspace of air enabled the synthesis of well-defined PMMA (M_n = 11.3 kDa, $Đ$ = 1.2, I* = 87%) while the same polymerization with ~18 mL of headspace of air was completely uncontrolled (M_n = 7.6 kDa, $Đ$ = 1.9, I* = 50%). Through the synthesis of block copolymers, support was found for good chain-end fidelity in these polymerizations, suggesting the presence of a small quantity of oxygen does not significantly impact the ATRP process. In addition, similar polymerization results were also obtained with several other phenoxazine PCs,[99] suggesting this strategy can be generalized across the phenoxazine family.

Dihydroacridines

One major limitation of O-ATRP has historically been its narrow monomer scope, especially in comparison to traditional ATRP methods[1, 4]. In an effort to expand this method's scope, acrylates have often been targeted in O-ATRP. However, these monomers present several challenges that make their controlled polymerization difficult. In particular, the propagation rate constants for radical polymerizations of acrylates are typically an order of magnitude larger than

those of methacrylates.[102] As a consequence, faster and more efficient deactivation is necessary to control the propagation of acrylates. Additionally, the bromine chain-end groups of acrylates are more challenging to reduce,[103, 104] impeding activation of the polymer. As such, overcoming these challenges requires strongly reducing PCs that can also mediate deactivation effectively.

One strategy that has been explored to achieve these properties has been the development of novel PCs similar to phenothiazines, phenoxazines, and dihydrophenazines featuring more oxidizing radical cations. The rationale behind this approach is that increasing $E^o(PC^{\bullet+}/PC)$ increases the driving force for deactivation, which might in turn increase the rate of deactivation in O-ATRP. Toward this end, dihydroacridines were developed in 2020, which display excited state reduction potentials [$E(PC^{\bullet+}/^3PC^*)$] ranging from -1.62 V to -1.49 V and oxidation potentials [$E^o(PC^{\bullet+}/PC)$] from 0.71 V to 0.90 V (all vs. SCE). Interestingly, while 9,9-dimethyl-10-(1-naphthyl)-9,10-dihydroacridine (Acrid-1N) does not exhibit electrochemical reversibility, indicating degradation of the radical cation, core-substitution with aryl functionalities stabilizes the radical cation. As a result, core-substituted dihydroacridines such as Acrid-1N-MeOPh (Figure 2.8) can undergo reversible oxidation and subsequent reduction, allowing them to operate as catalysts in O-ATRP. In addition, computational and spectroscopic investigation of these compounds' excited states revealed evidence of excited state ICT, suggesting these compounds would perform favorably in O-ATRP.[65]

To probe the catalytic properties of these new compounds, the O-ATRP of *n*-BuA was attempted using seven dihydroacridine PCs. It was discovered that Acrid-1N-MeOPh gave the best polymerization control, producing polymer with M_n = 10.6 kDa, $Đ$ = 1.5, and I^* = 96% under batch irradiation conditions. Since this PC was the least oxidizing [$E^o(PC^{\bullet+}/PC)$] and most reducing [$E(PC^{\bullet+}/^3PC^*)$] acridine investigated, it was hypothesized that a balance in redox properties was

necessary to ensure efficient deactivation while maintaining the ability of the catalyst to activate the polymer chain-end.[65]

To further improve activation in this polymerization system, it was proposed that the use of a continuous flow reactor would be beneficial,[65] since this reactor design can provide more uniform irradiation of the reaction solution than a batch reactor.[105-108] Consistent with this hypothesis, when a flow reactor was used, Acrid-1N-MeOPh produced poly(*n*-butyl acrylate) with nearly identical molecular weight (M_n = 11.0 kDa) and initiator efficiency (I^* = 97%), but lower dispersity ($Đ$ = 1.4). Through further optimization and the use of bromide salts, improved polymerization control was ultimately demonstrated for *n*-BuA (M_n = 5.4 to 26.4 kDa, $Đ$ = 1.2 to 1.4, and I^* = 44% to 173%) as well as a number of other acrylate monomers.[65]

Through modification of the *N*-aryl and core substituents, Ma and coworkers developed a similar series of dihydroacridines for O-ATRP. Similar to the previous report, the electrochemical reversibility of the acridines was significantly improved by core-substitution with aryl functionalities. However, these compounds exhibited even more strongly oxidizing radical cations [$E^o(PC^{\bullet+}/PC)$ = 0.94 V to 1.02 V vs. SCE], expanding the range of redox potentials accessible by this class of organic PCs. In the O-ATRP of methacrylates, catalysts with 3',5'-trifluoromethyl-4-biphenyl substituents exhibited the best catalytic performance, producing poly(methacrylates) with M_n = 8.9 to 12.2, $Đ$ = 1.1 to 1.6, and I^* = 53% to 105%.[66]

Polyaromatic hydrocarbons

In addition to the phenazines, phenothiazines, phenoxazines, and acridines discussed above, a number of polyaromatic hydrocarbons (PAHs) have been investigated and employed as PCs in O-ATRP. Of course, the first example of such a catalyst in O-ATRP is perylene (see *Initial*

Photocatalysts).[32] Closely related to perylene are anthracene and pyrene, which were explored as organic PCs for O-ATRP by Yilmaz and Yagci in 2016. When anthracene was used under UV irradiation, the polymerization of MMA showed signs of moderate polymerization control (M_n = 4.1 to 19.1 kDa, $Đ$ = 1.4 to 1.5). However, ^{1}H NMR analysis of the reaction before and after irradiation suggested the presence of a side reaction with the anthracene catalyst, which the authors proposed involves substitution of the catalyst by the initiator radical followed by growth of the polymer chain from the PC core.[109]

Instead, pyrene exhibited slightly improved polymerization control, producing PMMA with a range of molecular weights (M_n = 11.0 to 36.0 kDa), moderate dispersity ($Đ$ = 1.4 to 2.1), and moderate initiator efficiencies (I^* = 12% to 112%). Similar polymerization control was observed when pyrene was used to mediate the O-ATRP of other monomers, such as *t*-butyl acrylate (M_n = 107 kDa, $Đ$ = 1.3, I^* = 25%) and styrene (M_n = 2.0 kDa, $Đ$ = 1.3, I^* = 383%). Perhaps the most interesting detail about this catalyst, though, is its propensity to form excimers, or excited state dimers. To probe the role of these excimers in catalysis, Yagci and coworkers performed Stern-Volmer quenching experiments to measure the rates of activation with various ATRP initiators. Under dilute conditions, where excimer formation is disfavored, activation rate constants ranging from 4.4 x 10^7 $M^{-1}s^{-1}$ to 1.1 x 10^8 $M^{-1}s^{-1}$ were obtained. Under high concentrations of pyrene, where excimer formation is favored, activation rate constants ranged from 1.6 x 10^7 $M^{-1}s^{-1}$ to 7.5 x 10^7 $M^{-1}s^{-1}$. As such, both species may contribute to activation during O-ATRP.[109]

In addition to unfunctionalized PAHs such as perylene, anthracene, and pyrene, a number of functionalized PAHs have also been employed as PCs in O-ATRP. For example, 3,4,9,10-tetra-(12-alkoxycarbonyl)-perylene – an ester functionalized perylene bearing alkyl chains – was shown

to mediate the polymerization of MMA under blue light irradiation. Interestingly, while PMMA with similar dispersity ($Đ$ = 1.4 to 1.5) was obtained relative to when perylene was the PC ($Đ$ = 1.3 to 1.9), I* was significantly improved (I* = 86% to 97%) relative to unsubstituted perylene (I* = 2% to 88%).[110] Further, by increasing conjugation within the PAH core (Figure 2.12), it was demonstrated that the absorption of the PC could be red-shifted into the near-IR (NIR) spectrum. As a result, the O-ATRP of MMA could be conducted under NIR irradiation with moderate polymerization control (M_n = 2.2 to 8.7 kDa, $Đ$ = 1.3 to 1.5, I* = 73% to 94%) and under low catalyst loadings (1 to 20 ppm of PC).[111]

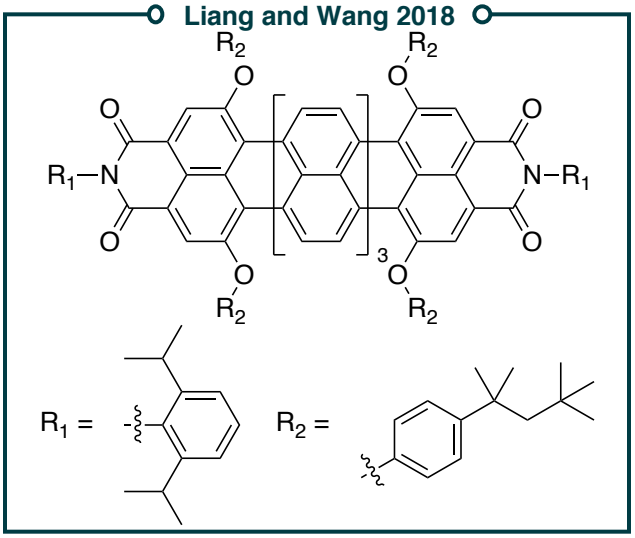

Figure 2.12. *An NIR absorbing PC developed for O-ATRP in 2018 by Liang and Wang.*

More recently, Liao and coworkers developed a strategy to synthesize heteroatom-doped PAHs through the oxidative cyclization of 1,1'-bisnaphthol (BINOL) derivatives. The resulting PAHs could be further functionalized by modification of the BINOL precursor, enabling the installation of alkyl and aryl functionalities on the PAH core. Using computational (DFT) and experimental (cyclic voltammetry) methods, the excited state reduction potentials [$E^o(PC^{\bullet+}/^3PC^*)$]

of the new compounds synthesized were estimated to be roughly -1.6 V vs. SCE, whereas the oxidation potentials of their radical cations [$E^o(PC^{\bullet+}/PC)$] ranged between 0.74 V to 0.82 V vs. SCE. In the O-ATRP of MMA, all of the PCs synthesized provided moderate or good polymerization control (M_n = 10.9 to 19.9 kDa, $Đ$ = 1.1 to 1.3, I^* = 46% to 73%). Most excitingly, these PCs could mediate the O-ATRP of various methacrylates at concentrations as low as 0.05 ppm (M_n = 30.8 kDa, $Đ$ = 1.5), a significantly lower catalyst loading than that employed in early O-ATRP methods (generally 1000 ppm of PC).[112]

Yagci and coworkers also developed a series of heteroatom-containing PAHs for O-ATRP, although in this case they were based on functionalized thienothiophenes. In total, four PC derivatives were synthesized, each with increasing quantities of conjugation that served to red-shift the PC absorption into the visible spectrum. Through fluorescence quenching experiments, the authors demonstrated that one of these derivatives could undergo an excited state reaction with ethyl α-bromoisobutyrate, an alkyl bromide initiator for O-ATRP. However, due to the nature of these experiments, they could not inform whether this reaction proceeded through an electron transfer or energy transfer pathway. Interestingly, less functionalized derivatives exhibited better control in O-ATRP through the production of polymers with lower dispersity ($Đ$ ~ 1.3 vs. 1.7 for more functionalized PC derivatives).[113]

Other oxidative quenching photocatalysts

Several other photocatalysts and dyes have also been explored as catalysts in O-ATRP. For example, Zhang and Cheng investigated 1,2,3,5-tetrakis(carbazole-9-yl)-4,6-dicyanobenzene (4-CzIPN, Figure 2.8) in the O-ATRP of MMA, although this catalyst afforded only moderate polymerization control under optimized conditions (M_n = 19.1 kDa, $Đ$ = 1.5, I^* = 95%).[114] In a

later report, Kim, Gierschner, and Kwon showed 4-CzIPN could produce PMMA with $Đ$ as low as 1.37 (M_n = 24.2 kDa), although with reduced initiator efficiency (I^* = 63%).[115]

In addition, Kim, Gierschner, Kwon, and coworkers explored a number of other PC targets using computational methods. One of these PCs, which can be described as two *N*-phenyl dihydrophenazines sharing a common diphenyl sulfone linker, demonstrated moderate control over the polymerization of styrene, producing poly(styrene) with M_n = 8.7 kDa, $Đ$ = 1.4, and I^* = 90%.[115] Similarly, Zhou and coworkers developed a PC containing two phenothiazine moieties linked at the *N*-aryl positions by 2,7-fluorenone, which was able to produce PMMA with M_n = 3.1 to 10.1 kDa, $Đ$ = 1.4 to 1.7, and I^* = 60% to 95%.[116]

In 2018, Wang and Zhang showed that substituted benzothiadiazoles and benzotriazoles could mediate the polymerization of MMA in the presence of a sacrificial amine. Interestingly, while the addition of an amine did improve polymerization control, the polymerization proceeded even in the absence of added amine. This observation suggests these organic PCs could activate the alkyl halide for growth, but that addition of the amine served to improve deactivation in some manner. While the exact role of the amine in this system remains unclear, ultimately these PCs were shown to produce PMMA with $Đ$ as low as 1.27 and I^* as high as 82%.[117]

In another example, Liao reported the use of substituted BINOLs as PCs in O-ATRP.[118] While some of these BINOLs would later be modified to generate heteroatom-doped PAHs (see *Polyaromatic Hydrocarbons*), they were also shown to be effective O-ATRP catalysts for the synthesis of PMMA with M_n = 10.9 to 48.5 kDa, $Đ$ = 1.2 to 1.6, and I^* = 12% to 76%.

In 2019, Wang and coworkers studied a series of dies in an effort to identify new catalysts for O-ATRP. Ultimately, several derivatives of quinacridone, indigo, and diketopyrrolopyrrole were shown to mediate O-ATRP. However, these PCs generally exhibited poor control in these

polymerizations, producing polymer with $Đ > 1.5$ and $I^* < 90\%$. In part, this poor performance might be attributable to the poor electrochemical reversibility of the catalysts,[119] which could inhibit their radical cations from successfully performing deactivation during O-ATRP. Later in 2020, Yang, He, and Jiang also explored substituted diketopyrrolopyrroles as O-ATRP catalysts. However, the polymers produced from MMA and styrene using these PCs were not characterized. Therefore, conclusions regarding the polymerization performance of these PCs cannot be made.[120]

Also in 2020, Lei disclosed the use of triarylsulfonium hexafluorophosphate salts as PCs in the polymerization of MMA. In general, these PCs exhibited moderate polymerization control. The PMMA produced featured M_n ranging from 4.8 to 17.0 kDa, $Đ = 1.3$ to 1.6, and I^* generally around 100%. Interestingly, the choice of solvent with this catalyst system was particularly important for maintaining a controlled polymerization, with less polar solvent systems resulting in the best performance.[121]

While numerous PCs with varying properties have been reported for use in O-ATRP, one common downfall of many PCs is their ease of synthesis. Often, several-step syntheses are necessary to obtain successful O-ATRP catalysts, creating a barrier to their use. Addressing this issue, work reported by Yang showed that simple benzaldehyde derivatives could effectively mediate O-ATRP under the appropriate conditions.[122] Similarly to benzotriazoles and benzothiadiazoles,[117] these benzaldehydes showed improved polymerization control when used in the presence of sacrificial amines. However, since the polymerization proceeded also in the absence of amines – albeit with poor control ($Đ > 1.5$) – it seems these benzaldehydes can successfully perform activation, whereas the role of the amines is to mediate deactivation of the polymer.[122]

Finally, in 2020 riboflavin derivatives were shown to mediate the O-ATRP of methacrylates. In this report, riboflavin was functionalized to include pendant bromoisobutyrate groups, allowing it to function as both the PC and the initiator in O-ATRP (Figure 2.13). In the polymerization of hydroxyethyl methacrylate (HEMA), this catalyst/initiator system gave good control, yielding poly(HEMA) with M_n = 38.8 kDa, $Đ$ = 1.2, and I% ~ 100%. Similar polymerization control was obtained in the polymerization of poly(ethylene glycol) methyl ether methacrylate (M_n = 116 kDa, $Đ$ = 1.4, I* ~ 100%), albeit with slightly higher dispersity than in the polymerization of HEMA.[123]

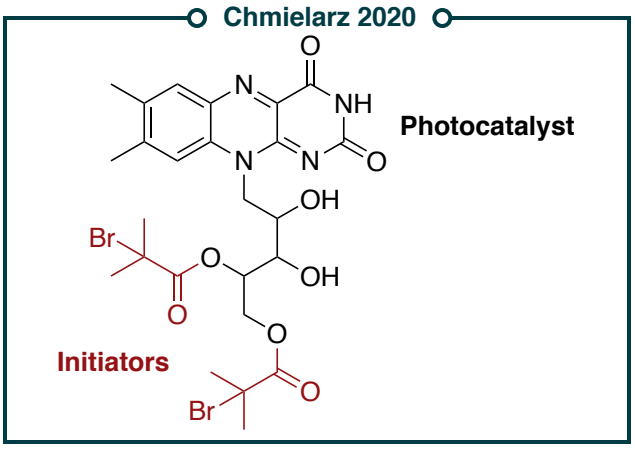

Figure 2.13. *A bifunctional PC and initiator for O-ATRP based on riboflavin.*

Reductive quenching photocatalysts

While the majority of the catalysts employed in O-ATRP are PCs that operate through oxidative quenching (i.e. reduction of the alkyl halide by PC* to generate $PC^{\bullet+}$, see *Section 3.2. – Oxidative and Reductive Quenching Mechanisms*), a number of PCs operating through reductive quenching pathways have also been utilized. The first example of this approach came from Zhang and Cheng, who used fluorescein (FL, Figure 2.8) in the presence of triethyl amine to drive the polymerization of MMA.[36] Unlike previous examples where an uncontrolled polymerization

would proceed to high conversion in the absence of the amine,[117, 122] the catalyst in this report appeared to proceed through a true reductive quenching mechanism. That is, in the absence of added amine, only a small degree of monomer conversion (2.6%) was obtained, indicating ineffective activation from PC*.[36]

In the polymerization of MMA, fluorescein showed moderate polymerization control. In general, PMMA with M_n ranging from about 20 kDa to 60 kDa was produced, with $Đ$ from 1.3 to 1.6 and I^* generally below 50%. Interestingly, similar polymerization control was obtained with styrene, although a monomer conversion of only 10% was achieved in this case. Nevertheless, experiments cycling the light source "on" and "off" showed monomer conversion was directly tied to irradiation of the reaction, and that the polymer M_n and $Đ$ remained constant during "off" periods. Further, MALDI-TOF analysis of the polymers produced by this method showed retention of the Br chain-end group in the polymerization of styrene, suggesting this polymerization proceeds through an ATRP mechanism. However, evidence was also found for significant loss of this chain-end functionality, as chain-extensions of PMMA with MMA and styrene showed a large quantity of unfunctionalized polymer remaining after the reaction. Therefore, while this report showed that O-ATRP could proceed in the presence of a reductive quenching PC, this method provided only moderate control over the polymerization.[36]

Soon after this report, Yilmaz and Yagci also investigated reductive quenching PCs in O-ATRP. In addition to FL, eosin Y (EY) and erythrosin B were also studied and generally provided the best polymerization control in the O-ATRP of MMA. When EY was used as the catalyst, PMMA was obtained with M_n = 8.7 to 22.1 kDa and $Đ$ = 1.3 to 1.9. Instead, erythrosin B gave PMMA with M_n = 13.7 to 90.0 kDa and $Đ$ = 1.2 to 2.5.[124] In addition, Wei and Chen showed eosin Y and rhodamine B could be grafted to cellulose to create recyclable PCs that maintain moderate

control in the polymerization of MMA (M_n = 17.2 to 119 kDa, $Đ$ = 1.3 to 1.6, I* = 3% to 25%).[125] Finally, Zhang and coworkers demonstrated the successful O-ATRP of MMA in the presence of oxygen using fluorescein,[126] paving the way to simplify experimental setups using reductive quenching PCs.

Traditional photoinitiators have also been employed as catalysts in O-ATRP, including thioxanthone, 2-isopropylthioxanthone, benzophenone, and camphorquinone. In each case, moderate polymerization control was observed, with the polymers produced displaying M_n ranging from 4.8 to 17.0 kDa and $Đ$ = 1.3 to 2.0. However, when the light source was cycled "on" and "off," a small degree of monomer conversion was still observed during "off" periods. While the authors attributed this conversion to inefficient deactivation, the cause of this phenomenon remains unknown.[127] Later in 2018, Yi showed that a substituted benzophenone derivative – functionalized to enable its solubility in water – could also mediate the O-ATRP of acrylamide, producing poly(acrylamide) with M_n = 2.7 to 37.5 kDa, $Đ$ = 1.4 to 1.5, and I* = 67% to 97%.[128]

Finally, Chmielarz and coworkers reported on the use of riboflavin as a reductive quenching PC in the presence of ascorbic acid as a sacrificial electron donor. Using this combination, the O-ATRP of a PEG methacrylate was undertaken using bromoisobutyrate-functionalized lignin as an initiator to create star-shaped polymers and copolymers.[129]

Investigations of the O-ATRP mechanism

Since the inception of O-ATRP in 2014, several investigations have sought to better understand the mechanism of this polymerization method. The primary focus of this work has often been understanding O-ATRP mediated by oxidative quenching PCs. As such, the following

sections discuss each step of the oxidative quenching mechanism and are primarily organized according to the order of those mechanistic steps.

Photoexcitation and Photophysical Processes

To truly understand the photophysics of O-ATRP PCs and the factors influencing their properties, it is important first become familiar with photophysical processes that occur upon the absorption of light by a molecule. Here, we will provide a brief introduction to these processes as a foundation for subsequent discussions of PC photophysics. For further information on these topics, we refer the reader to other, more thorough resources on photochemistry.[86, 101, 130-132]

When a molecule absorbs light, it can undergo a number of photophysical processes that are often represented on a Jablonski diagram (Figure 2.14), the first being photoexcitation from a ground state to an excited state. In organic molecules, the ground state is often a singlet state (S_0), and photoexcitation occurs to higher energy singlet states (S_n, $n \geq 1$). In most cases, rapid photophysical processes such as vibrational relaxation and internal conversion cause relaxation to the lowest energy excited state (S_1),[133] so most of the photochemistry of interest occurs from this state. For example, in the absence of a quencher – a species that reacts with the excited state – the PC may undergo fluorescence (radiative relaxation) or internal conversion followed by vibrational relaxation (non-radiative relaxation) to transition from S_1 to S_0. Instead, if a suitable quencher is present, the PC may react with the quencher to initiate a reaction. This process can occur through either electron transfer or energy transfer, although the requirements for each mechanism differ. Further, reactivity from a singlet excited state can be limited by the short lifetime of the singlet excited state – typically picoseconds to nanoseconds. Since bimolecular collisions in solution

typically require at least a few nanoseconds to occur,[86, 134] a short excited-state lifetime can sometimes lead to relaxation prior to reaction with a substrate.

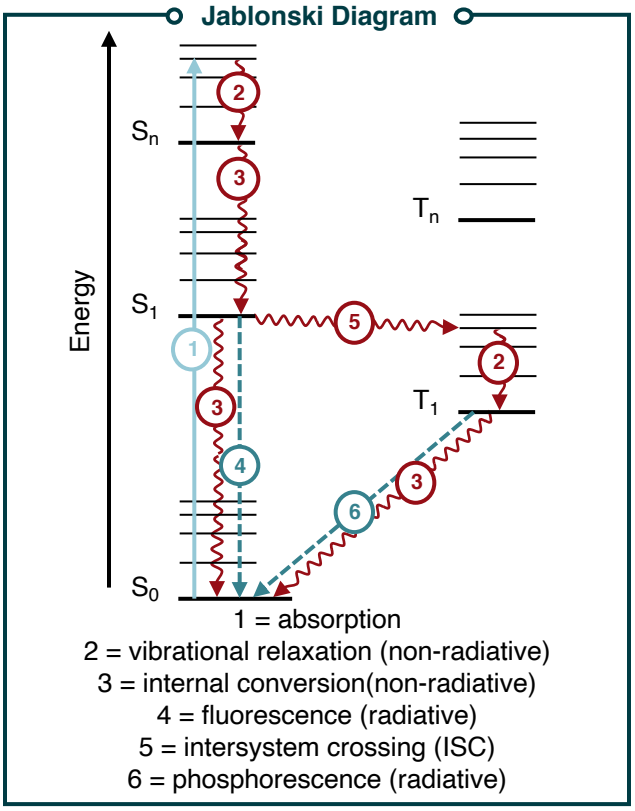

***Figure 2.14**. A general Jablonski diagram depicting common photophysical processes for organic molecules.*

To overcome this limitation, some PCs can access longer-lived triplet excited states (T_n) through intersystem crossing (ISC), where the spin of the excited electron flips. During this process, the PC will transition from S_1 to T_n ($n \geq 1$), followed by rapid non-radiative decay to access T_1. Since a spin-flip is quantum mechanically forbidden, relaxation of T_1 to S_0 is more challenging than S_1 to S_0, lengthening the lifetime of the triplet excited state – typically microseconds or longer. However, since the same is true for the transition from S_1 to T_n, accessing reactivity from the triplet manifold is challenging and requires suitable catalyst design.

To this end, initial investigations of dihydrophenazine PCs yielded some insight into how catalyst structure can impact the triplet yields of these catalysts. During early work with this catalyst family, it was discovered that the identity of the *N*-aryl substituents could greatly influence the catalyst's performance in O-ATRP. Specifically, catalysts with electron withdrawing groups (EWGs) consistently exhibited superior polymerization control (lower $Đ$) than those with electron donating groups (EDGs). Through computational investigations, it was discovered that PCs with EDGs also exhibited spatially separated singly occupied molecular orbitals (SOMOs) in ^{3}PC*, whereas PCs with EDGs did not (Figure 2.9). In turn, it was hypothesized that the presence of EWGs led to ICT in PC* from the phenazine core to the *N*-aryl substituent, which could facilitate ISC and improve the triplet yield of the catalyst. In O-ATRP, the increased formation of ^{3}PC* might improve activation, leading to better polymerization control as observed with some catalysts. To test this hypothesis, new PCs were targeted with 1-naphthyl and 2-naphthyl *N*-aryl substituents, which were also predicted by DFT to feature ICT. When employed in O-ATRP, these catalysts exhibited good polymerization control ($Đ < 1.2$), supporting the importance of this property for effective catalysis.[34]

While this work provided useful guiding principles for future catalyst design, it relied primarily on computational evidence to show how certain *N*-aryl functionalities could impact PC photophysics. In later work, experimental evidence was found to support these theoretical insights, providing a stronger basis for conclusions drawn from this data. Since catalysts with ICT were predicted to feature polar excited states – due to localization of electron density on the *N*-aryl substituent – it was proposed that their emission would be susceptible to solvent polarity. In essence, increasing the polarity of the solvent might stabilize the excited state, leading to a red-shift in the emission of the catalyst. Indeed, when the emission of various phenazines was

compared, PCs with ICT showed significant red-shifting of their emission in more polar solvents, while the emission of a PC without ICT remained essentially unchanged. Additionally, the fluorescence spectra of PCs with ICT showed broad, featureless peaks consistent with a charge transfer excited state, further supporting the conclusions of previous computational investigations.[135] As such, the remaining question became exactly how ICT impacts PC photophysics to improve catalysis.

Motivated by this question, Damrauer and coworkers characterized the photophysics of two phenoxazine PCs – PhenO-1N-BiPh and the analogous *N*-phenyl derivative (PhenO-Ph-BiPh). Through these studies, the authors were ultimately able to propose an energy level diagram mapping the relaxation pathways of these two catalysts (Figure 2.15), yielding insight into the effect of the *N*-aryl substituent on photophysical relaxation processes. In the case of PhenO-Ph-BiPh, photoexcitation of the catalyst leads to the formation of a Franck-Condon singlet state (S_{FC}), which rapidly relaxes to a singlet charge transfer state localized on a biphenyl core substituent ($S_{CT\text{-}BiPh}$). While this charge transfer state enables ISC to an analogous triplet state ($T_{CT\text{-}BiPh}$), this process is in competition with efficient fluorescence from $S_{CT\text{-}BiPh}$ to S_0, making the quantum yield of ISC low ($\Phi = 0.11$).[136]

For PhenO-1N-BiPh, similar behavior is observed upon photoexcitation, ultimately leading to the formation of a similar $S_{CT\text{-}BiPh}$ state. However, the presence of the 1-naphthyl substituent in this catalyst leads to the formation of new intermediate states between $S_{CT\text{-}BiPh}$ and S_0 that significantly impact subsequent relaxation processes. Although the final triplet excited state is similar to that in PhenO-Ph-BiPh ($T_{CT\text{-}BiPh}$), an intermediate singlet state localized on the naphthyl substituent ($S_{CT\text{-}Naph}$) provides more efficient ISC and greater yield of the triplet state ($\Phi = 0.91$). The exact pathway through which this process occurs remains unknown, but it is hypothesized to

occur either through direct relaxation of $S_{CT\text{-}Naph}$ to $T_{CT\text{-}BiPh}$ or through an intermediate dark state (unobservable) localized on the naphthyl ring ($T_{CT\text{-}Naph}$).[136] Regardless of the pathway, the effect is the same – ICT to the naphthyl substituent enables more efficient ISC, increasing the [^{3}PC*] available to engage in catalysis during O-ATRP.

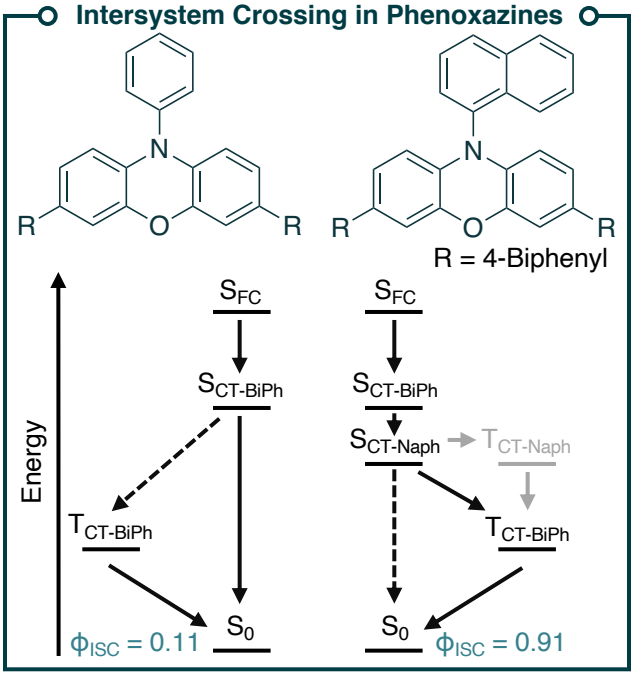

Figure 2.15 *Energy diagrams demonstrating the impact of naphthyl N-aryl substituents on intersystem crossing in phenoxazine PCs dissolved in N,N-dimethylacetamide.*

In later work, Damrauer and coworkers expanded on these studies to investigate the effect of naphthyl connectivity on PC photophysics in these phenoxazines.[137] Since phenoxazines with 1-naphthyl and 2-naphthyl *N*-aryl groups had previously been reported for O-ATRP,[35, 95] this investigation sought to understand whether the location of naphthyl connectivity could impact important catalyst properties. Again, the photophysical relaxation processes of various catalysts were characterized, and it was revealed that the naphthyl connectivity could have a small impact on the energy of the $S_{CT\text{-}BiPh}$ state. In the case of PhenO-2N-BiPh (a 2-naphthyl phenoxazine PC),

the change in naphthyl connectivity results in a slight destabilization of $S_{CT\text{-}Naph}$, leading to an equilibrium between $S_{CT\text{-}Naph}$ and $S_{CT\text{-}BiPh}$. Consequently, ISC becomes less competitive and the yield of ^{3}PC* becomes significantly lower ($\Phi = 0.54$). In addition, the reorganization energy for charge transfer from the *N*-aryl substituent to the PC core during ISC was found to be roughly 10% larger for 2-naphthyl versus 1-naphthyl substituents, presumably due to the larger donor-acceptor distance between the PC core and the 2-naphthyl group. As a result, PCs with 2-naphthyl groups exhibit slower intersystem crossing (smaller k_{ISC}) than those with 1-naphthyl groups.[137] Importantly, both of these observations – excited state energies and reorganization energy – could impact catalysis where formation of ^{3}PC* is critical to the success of the reaction.

Further expanding on these investigations, it was shown that these principles could be applied to other catalyst families to design high triplet yield PCs. Within the phenothiazine family, a series of catalysts was designed with various *N*-aryl functionalities intended to stabilize the S_{CT} state to increasing degrees. Through characterization of the photophysics of these PCs, it was shown that stabilization of this state could be used to increase the yield of ^{3}PC* up to 96%. However, excessive stabilization – through introduction of strong EWGs – could also bypass the triplet manifold and result in efficient nonradiative decay to S_0.[138]

While the work discussed to this point yielded important insights into the photophysics of common O-ATRP catalysts, others have focused their investigations on the impact of external factors on photoexcitation and photoredox catalysis in O-ATRP. For example, Ryan *et al.* probed the impact of light intensity on polymerization control in the presence of perylene and PhenO-1N-BiPh. Interestingly, lowering the intensity of the light source resulted in a gradual decrease in polymerization control. It was hypothesized that this observation was due to decreasing efficiency of activation, which ultimately results in insufficient buildup of the $PC^{\bullet+}$ deactivating species. As

a result, deactivation becomes inefficient and polymerization control is lost at low light intensities. More interesting, however, was the discovery that tolerance to low light intensity could be designed into the catalyst, as PhenO-1N-BiPh operated effectively at lower light intensities than perylene.[139] While the exact reason for this superior performance has not been investigated, one can hypothesize that the stronger excited state reduction potential [$E^o(PC^{\bullet+}/^3PC^*)$] and higher molar absorptivity of PhenO-1N-BiPh are likely beneficial under these conditions.

An investigation by Hawker and coworkers probed various controlled radical polymerizations in the dark to understand how the polymerization process was impacted by manipulation of the light source (i.e. turning it on or off). In this report, the advantage of photoredox catalyzed ATRP over traditional, Cu mediated photoATRP was demonstrated by tracking monomer conversion *in-situ* during periods of irradiation and darkness. When irradiation was ceased, Cu mediated photoATRP still showed slow monomer conversion in the dark, whereas O-ATRP catalyzed by PhenS-Ph stopped immediately in the dark. In addition, when the light source was turned on again, Cu catalyzed photoATRP showed nonlinear, gradually increasing kinetics, whereas O-ATRP with PhenS-Ph immediately exhibited linear pseudo-first-order kinetics.[140]

To understand these differences, it is important to understand how the mechanisms of photoATRP and O-ATRP differ. In photoATRP, irradiation of the reaction solution enables conversion of Cu^{II} to Cu^{I}, a long-lived species capable of mediating O-ATRP in the absence of light. Instead, irradiation in O-ATRP generates a short-lived PC excited state, which rapidly relaxes in the dark to a ground state that is incapable of mediating O-ATRP on its own. This rapid relaxation is supported by the short excited state lifetimes of O-ATRP PCs, as well as kinetic

modeling performed by Guo and Luo[141]. As a result, O-ATRP offers precise temporal control over the polymerization, while photoATRP is generally less responsive on shorter timescales.[140]

Activation

One longstanding question in O-ATRP has been the nature of the catalyst excited state responsible for catalysis. Specifically, is it the singlet state (^{1}PC*) or the triplet state (^{3}PC*) that is most relevant (Figure 2.16)? Indeed, arguments can be made for each one. While ^{3}PC* is likely longer lived, making it more likely to engage in bimolecular reactions in solution, it is generally less reducing than ^{1}PC* due to photophysical relaxation processes. By the same token, ^{1}PC* is more reducing than ^{3}PC*, which increases the driving force for activation, but it may be too short lived to efficiently undergo bimolecular reactions. Therefore, which of these properties is most important in O-ATRP?

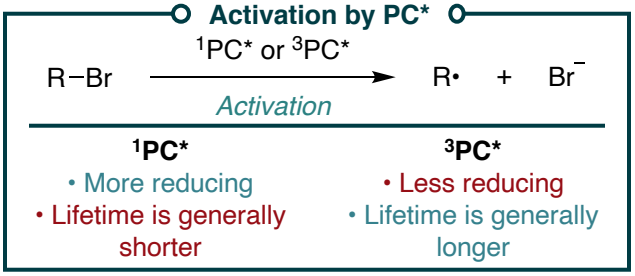

Figure 2.16. *Advantages and disadvantages associated with ^{1}PC* and ^{3}PC* for activation during O-ATRP.*

In 2016, Jockusch and Yagci attempted to answer this question through investigation of methyl phenothiazine (PhenS-Me). In this work, the rate of electron transfer (ET) from ^{1}PC* to several alkyl halides was measured by fluorescence spectroscopy, and that from ^{3}PC* was measured using transient absorption spectroscopy. It was found that the rates of ET were generally

greater for ^{1}PC*, a discovery that is unsurprising given the greater reduction potential of ^{1}PC* relative to ^{3}PC*. However, PhenS-Me exhibited significant ISC to the triplet state ($\Phi \sim 0.6$), suggesting the yield and lifetime of ^{3}PC* could counteract its lower rate of ET. As such, these authors concluded activation in O-ATRP with PhenS-Me most likely occurs from ^{3}PC*, with minor contributions from ^{1}PC*.[142]

In another study, Orr-Ewing and coworkers also investigated activation during O-ATRP, although this time using picosecond transient absorption spectroscopy. In this investigation, ET between methyl-2-bromopropionate and PhenN-PhCF$_3$ or the *N*-phenyl analogue (PhenN-Ph) was targeted, since PhenN-PhCF$_3$ was previously proposed to operate *via* ^{3}PC* while PhenN-Ph was proposed to operate *via* ^{1}PC*. By varying the polarity of the solvent, the authors showed that the rate of ET could be influenced for PhenN-PhCF$_3$ but not PhenN-Ph, consistent with previous suggestions that the ICT nature of the PhenN-PhCF$_3$ excited state made it susceptible to solvent polarity. More importantly, however, these studies revealed PhenN-Ph exhibits faster ET than PhenN-PhCF$_3$, and that both catalysts can perform activation from ^{1}PC*. In turn, this result led the authors to conclude that the most successful catalysts for O-ATRP should feature short ^{1}PC* lifetimes, low yields of ISC, and slow ET to minimize the concentration of radicals in solution.[143]

In later work, this investigation was expanded to include PhenN-2N – another common catalyst in O-ATRP. Again, the results of these investigations suggested ET occurs primarily from ^{1}PC* to the alkyl bromide, contrary to previous suggestions that a triplet excited state may be catalytically active. Further, it was found that ET from PhenN-2N was generally slower than from PhenN-PhCF$_3$ or PhenN-Ph, again suggesting slower rates of ET may be most beneficial for successful O-ATRP (since PhenN-2N is one of the top performing catalysts for this method).[144] These conclusions were further supported in 2021, when these investigations were expanded to a

series of nine PCs spanning three PC families – dihydrophenazines, phenoxazines, and phenothiazines.[145]

It is important to note, however, that these investigations did not consider the effect of deactivation in O-ATRP. Indeed, in the absence of deactivation, slow, inefficient ET would be beneficial to suppress the concentration of propagating radical, which is necessary to limit irreversible termination reactions in O-ATRP. However, the suppression of radicals in O-ATRP is also achieved through the deactivation step of the mechanism. As such, it may be possible to design catalysts with fast and efficient ET that also effectively mediate O-ATRP, as long as those catalysts are capable of performing effective deactivation to control the concentration of propagating radicals. In light of this consideration, it is possible that the superior performance of PCs with ICT such as PhenN-$PhCF_3$ or PhenN-2N may be attributable to their ability to deactivate alkyl radicals rather than their photophysical properties. Instead, PCs such as PhenN-Ph may be less successful in O-ATRP due to the low oxidation potentials of their radical cations [$E^o(PC^{\bullet+}/PC)$], which will impede deactivation.

One other important takeaway from the studies by Orr-Ewing and coworkers is that effective catalysts for O-ATRP – PhenN-$PhCF_3$ and PhenN-2N – exhibited reactivity primarily from a singlet excited state with charge transfer character.[143, 144] Although these studies call into question the role of ^{3}PC* in activation, they do provide support for the importance of PCs exhibiting ICT in the excited state. As such, this property remains an important design principle for the development of new PCs for O-ATRP.

To further probe which excited state is relevant for O-ATRP, Damrauer and coworkers investigated the activation of an alkyl bromide by four phenoxazines with varying *N*-aryl and core substituents. In this study, ET rate constants for both ^{1}PC* and ^{3}PC* were measured, as well as

reaction quantum yields for each excited state. As a result, it was observed that both ^{1}PC* and ^{3}PC* can contribute significantly to activation during O-ATRP, but which one contributes most can depend on a number of factors.[146] Consistent with investigations by Orr-Ewing,[143-145] the driving force for electron transfer (ΔG^o_{ET}) is extremely influential and favors activation from ^{1}PC*, since this state tends to be more reducing than ^{3}PC*. However, the lifetime of the excited state and the yield of ISC (Φ_{ISC}) are also important factors to consider. At low concentrations of quencher (i.e. the alkyl halide) where bimolecular reactions are less likely, when Φ_{ISC} is high, or if the lifetime of ^{3}PC* is long, reactivity from ^{3}PC* can contribute significantly to activation. As such, this work highlights the importance of considering both ^{1}PC* and ^{3}PC* in O-ATRP, as both states can contribute to catalysis.[146] Further, it is worth noting that the relative contributions of ^{1}PC* and ^{3}PC* likely vary from one catalyst family to another, between catalysts within the same family, and even for the same catalyst under different reaction conditions. For example, since dihydrophenazines are typically more reducing in the excited state, feature shorter triplet lifetimes, and lower Φ_{ISC} than phenoxazines,[147] reactivity from ^{1}PC* may be more significant for dihydrophenazines than other catalyst families. In addition, performing polymerizations at low catalyst or initiator concentrations may favor reactivity from ^{3}PC*, since lowering the concentrations of these species will make bimolecular reactions with a short-lived ^{1}PC* more challenging. Another consideration is that O-ATRP reactions are typically performed at high monomer concentrations. During the course of polymerization, the solution viscosity significantly increases, impeding diffusion. Therefore, long-lived excited-state PCs may become more important later in the polymerization relative to at the onset of polymerization.

Regardless of the relative contributions of ^{1}PC* and ^{3}PC*, Matyjaszewski and coworkers showed that activation in O-ATRP likely occurs through a dissociative, outer-sphere electron

transfer mechanism,[79] which is not typically observed in metal-catalyzed ATRP. Moreover, activation in O-ATRP is generally very fast, approaching diffusion limited kinetics for many PCs.[79] This observation has since been supported by others[142-144, 146] and seems to be a general trend for many O-ATRP catalysts. However, due to the short lifetimes of many PCs, the efficiency of activation tends to be low,[79] resulting in an effective rate of activation similar to that observed in metal catalyzed ATRP[4].

Finally, Pearson *et al.* used computational methods to investigate how reorganization of different PC cores during electron transfer can contribute to activation rates during O-ATRP (Figure 2.17). In this work, three catalysts with *N*-phenyl substituents were investigated – PhenO-Ph, PhenN-Ph, and PhenS-Ph. In each case, the reduction potentials and reorganization energies relevant to activation (^{3}PC* to PC$^{\bullet+}$) were computed by DFT, revealing that all three catalysts feature a similar driving force for activation [E^o(PC$^{\bullet+}$/^{3}PC*) ~ -2 V vs. SCE]. However, since PhenS-Ph contains a larger S atom in its core, this catalyst exhibits a significantly larger reorganization energy than PhenO-Ph. As a result, it was predicted PhenS-Ph would exhibit slower activation than PhenO-Ph, suggesting even small structural changes in the PC core can significantly influence catalysis.

Deactivation

One of the most important steps in the mechanism of O-ATRP (and more broadly ATRP as well as all controlled radical polymerizations) is deactivation. In any radical polymerization method, bimolecular radical termination reactions will always be present to some degree, necessitating a method to inhibit these side reactions and maintain control of the polymerization. In O-ATRP, this method involves reversible deactivation of the propagating radical through

installation of a halide on the polymer chain-end. In effect, this process reduces the concentration of radicals to prevent radical-based side reactions while enabling the polymer to be reactivated for future chain growth.

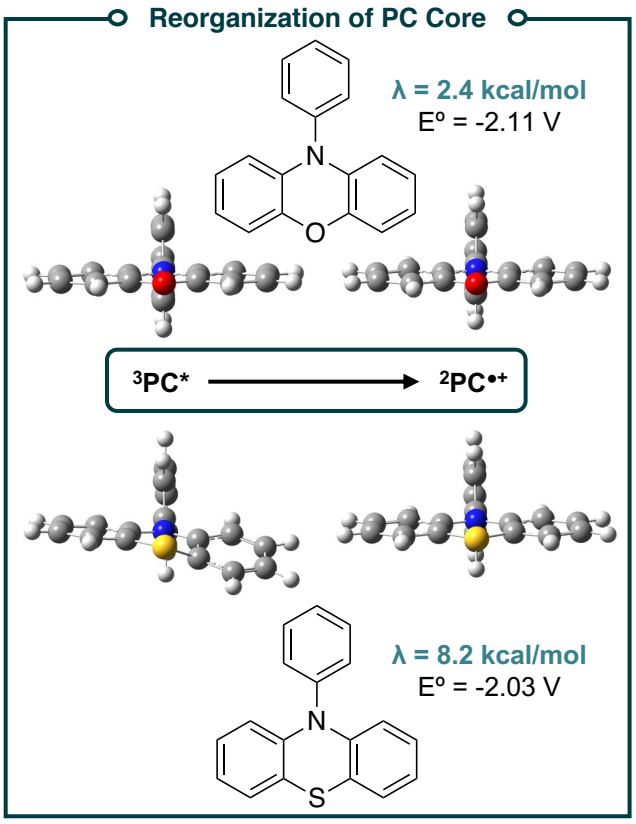

Figure 2.17. *Impact of PC core on reorganization energy (λ) during electron transfer. Key: white = hydrogen, grey = carbon, blue = nitrogen, red = oxygen, yellow = sulfur.*

Despite the importance of this mechanistic step, deactivation remains relatively understudied in comparison to photoexcitation and activation in O-ATRP. In one of the most comprehensive studies of this step, Matyjaszewski and coworkers probed deactivation through the addition of halide salts to the polymerization of MMA in the presence of PhenS-Ph. Hypothesizing that deactivation could be mediated by the radical cation ion pair ($PC^{\bullet+}X^-$, X = Br or Cl), the authors proposed that the addition of halide salts to the polymerization should encourage the

formation of this ion pair. The result would then be more effective deactivation, observable through the lowering of the polymerization rate and improvements in polymerization control (i.e. lower $Đ$, I* closer to 100%).[79]

When this experiment was performed in O-ATRP using EBP as the initiator, a slight decrease in the rate of the polymerization was observed but without any significant improvement in polymerization control, potentially indicating unanticipated complexities in this system. However, a noticeable effect was observed when the initiator was changed to ethyl α-chlorophenylacetate (EClP). In comparison to polymerizations without added Br^-, those with additional Br^- showed significant improvements in I* (75% with added Br^- versus 9% without it). In addition to highlighting the importance of Br^- for deactivation, this experiment suggests deactivation is particularly ineffective in the presence of Cl^-. Further supporting this conclusion, when the authors performed additional polymerizations using EClP, they discovered that PhenS-Ph could activate this initiator, since 55% monomer conversion was observed in 4 h (compared to 15% in the same time without catalyst present). However, the polymerization was completely uncontrolled ($Đ$ = 3.4, I* = 36%), suggesting deactivation with Cl^- had been ineffective.[79]

To gain deeper insight into deactivation in O-ATRP, Matyjaszewski and coworkers then employed computational chemistry to compute the thermodynamic feasibility of five possible deactivation mechanisms (Figure 2.18): two proceeding through an outer-sphere electron transfer [OSET (1) and OSET (2)], one through an inner-sphere electron transfer (ISET), one through dissociative electron transfer (DET), and another by termolecular associative electron transfer [AET (ter)]. The results of these calculations showed that the AET (ter) mechanism is most favorable, but it is important to consider that these calculations only yield insight into the thermodynamics of each mechanism. To understand kinetic contributions, activation energies

computed by DFT were used to estimate rate constants for each deactivation mechanism. The results of these calculations showed that of the five proposed mechanisms, only OSET (2) and AET (ter) could outcompete the rate of termination in the polymerization of MMA. However, the estimated rate of deactivation through AET (ter) was nearly two orders of magnitude larger than through OSET (2), again suggesting deactivation may occur through this termolecular mechanism.[79]

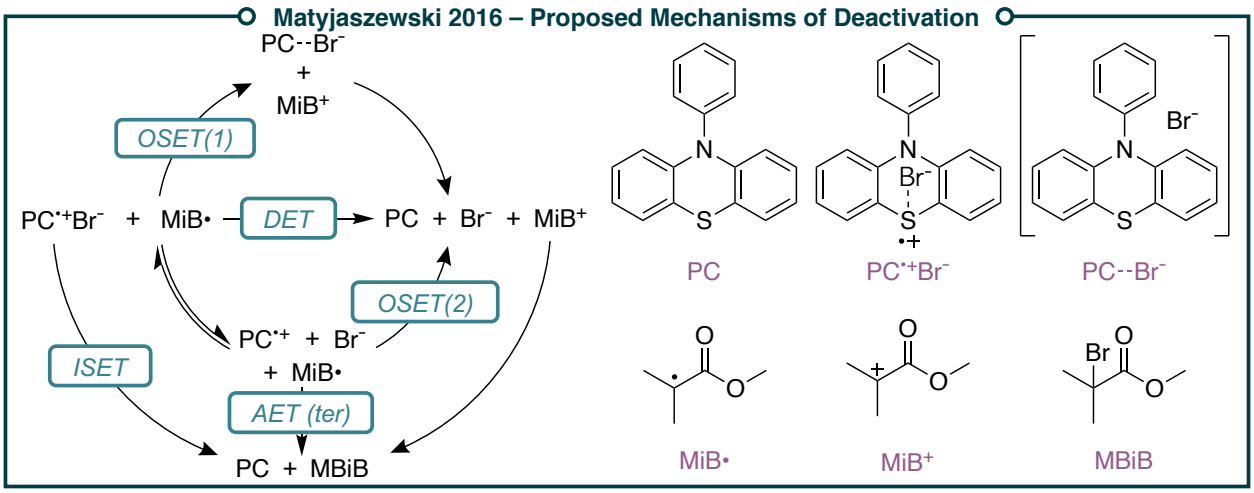

Figure 2.18 *Possible mechanisms of deactivation proposed by Matyjaszewski in 2016 (left) and structures of relevant intermediates (right).*

Later in 2017, Lim *et al.* probed the impact of solvent polarity on ion pairing in $PC^{\bullet+}Br^-$ and the effect of manipulating this variable on polymerization control in O-ATRP. Hypothesizing $PC^{\bullet+}Br^-$ to be the deactivator in O-ATRP, these authors reasoned that lowering the polarity of the reaction solution would favor formation of this ion pair, in turn increasing the rate of deactivation through increasing $[PC^{\bullet+}Br^-]$. To probe the impact of solution polarity, DFT calculations were used to calculate the association free energy (ΔG^o_{assoc}) for a phenazine radical cation (PhenN-1N) and Br^-. Consistent with their expectations, these calculations predicted that ΔG^o_{assoc} would become

increasingly exergonic with decreasing solvent polarity, suggesting this variable could be tuned to manipulate deactivation in O-ATRP. As such, a series of polymerizations was performed with varying ratios of *N,N*-dimethylacetamide (DMAc) and tetrahydrofuran (THF) as the solvent system. Interestingly, the addition of 25% THF improved polymerization control, suggesting decreasing solvent polarity could be beneficial to polymerization outcomes in O-ATRP.[135] Expanding on this work, later reports showed that these results could be generalized to a series of dihydrophenazine PCs and solvent systems,[148] and that tuning solvent polarity could also be used to lower catalyst loadings in O-ATRP[89] (see *Solvent Effects in O-ATRP*).

In work by Guo and Luo, kinetic modeling was employed to understand how changes in activation can impact deactivation during O-ATRP. While one might initially consider these steps to be independent, it is important to remember that the buildup of deactivator during early polymerization times is directly dependent upon activation. As such, activation and deactivation are intimately intertwined, especially early in the reaction (or rather at early times after irradiation is started). Through kinetic modeling, Guo and Luo demonstrated this dependence on activation by showing that [$PC^{\bullet+}$] must surpass a threshold before deactivation can become effective. In order to reach this threshold rapidly, fast and effective activation is necessary. To manipulate this process, control of the reactor light intensity can be crucial, as the authors showed increasing light intensity could improve polymerization control by increasing the rate of activation and therefore the rate of $PC^{\bullet+}$ buildup.[141] Importantly, these results are consistent with previous reports on the effect of light intensity in O-ATRP, which suggested the same link between light intensity, the rate of activation, and efficiency of deactivation.[139]

Finally, work by Corbin *et al.* probed deactivation in O-ATRP by synthesis and investigation of the PC radical cations hypothesized to mediate this process. Through a model

reaction using azobisisobutyronitrile (AIBN) to generate alkyl radicals, evidence was found supporting the ability of a phenazine radical cation to deactivate radicals in the presence of Br^-. Through further investigation of this model reaction, it was also discovered that the oxidation potential of the halide [$E^o(X•/X^-)$, X = Br or Cl] as well as the radical cation [$E^o(PC^{•+}/PC)$] impact the rate of deactivation. By measuring ΔG^o_{assoc} for the formation of $PC^{•+}PF_6^-$ ion pairs, it was found that catalyst structure has a minimal influence on ion pair strength, whereas tuning solvent polarity greatly impacts this property. As such, changing the solvent in O-ATRP may be the most effective approach to manipulating deactivation through ion pairing. Finally, when a radical cation was employed as a reagent in O-ATRP, this strategy yielded improved control in the polymerization of acrylates, further supporting the role of $PC^{•+}$ in deactivation during O-ATRP.

Side reactions

Perhaps the most obvious side reactions in O-ATRP are the termination reactions inherent to any radical polymerization method. Often, termination occurs through one of two common mechanisms: radical coupling (also called combination) or disproportionation. In essence, radical coupling involves the reaction of two propagating radicals, which couple to each other to irreversibly form a C-C bond. Instead, disproportionation involves hydrogen atom abstraction from the carbon *beta* to one propagating radical by a second radical in solution. Since these modes of termination are general to all radical polymerization methods and have been discussed in detail by others,[7, 149, 150] they will not be discussed further in this text. Instead, this discussion will focus on side reactions more unique to O-ATRP.

In 2016, Matyjaszewski and coworkers investigated the ability of the alkyl halide initiator to undergo direct activation under irradiation with UV light. Their results showed that both EBP

and EClP could initiate uncontrolled polymerizations in the absence of a PC, suggesting direct photolysis of the initiator may be a major side reaction in O-ATRP. In the case of EBP, however, addition of a PC to the reaction solution slowed monomer conversion and improved polymerization control, suggesting the presence of an appropriate catalyst can limit this side reaction.[79] In addition, the use of visible light irradiation, which is likely not absorbed by alkyl halides, could also assist in minimizing these side reactions.

Further evidence supporting this side reaction was later presented by Guo and Luo, who used kinetic modeling to show that a small quantity of polymer chains can be generated in O-ATRP through direct photolysis of the initiator. Importantly, their work showed this side reaction can become problematic at low catalyst loadings, where the [$PC^{\bullet+}$] remains limited and deactivation cannot control the propagation of these undesired radicals. As such, a threshold exists – one that likely varies depending on the catalyst and reaction conditions – below which the catalyst is in too low of a concentration to effectively mediate O-ATRP.[141]

Another side reaction in O-ATRP involves substitution of the PC by alkyl radicals during the polymerization.[89, 90] In initial reports on dihydrophenazine catalysts, it was observed that successful PCs could produce PMMA with good dispersity ($Đ < 1.2$) but consistently low initiator efficiency ($I^* = 60\%$ to 80%).[34, 148] Even more interestingly, when one of these dihydrophenazines was further functionalized by installation of aryl core substituents, these new PCs consistently produced polymer with $I^* \sim 100\%$.[81] In turn, these observations motivated the hypothesis that certain O-ATRP catalysts could undergo substitution by the initiator during a polymerization, which would ultimately result in low I^*. The ability of one dihydrophenazine PC (PhenN-2N) to undergo substitution by an alkyl bromide was confirmed by McCarthy *et al.*, which ultimately enabled good control in the polymerization of acrylate monomers. In addition to being isolatable,

this substituted catalyst could be prepared *in-situ* prior to polymerization by pre-irradiation of a catalyst / initiator solution, followed by addition of the monomer and additional initiator to start the polymerization.[88]

After this report, a systematic investigation of this side reaction was performed by Corbin *et al.*, revealing that dihydrophenazine core-substitution can occur *via* a number of alkyl bromide initiators as well as the propagating polymer in O-ATRP. Importantly, substitution by the propagating polymer represents a new termination reaction that was previously unknown in O-ATRP. Through investigation of initiators with different sterics, it was discovered that tertiary bromides could undergo two additions to the catalyst core, whereas secondary bromides could undergo up to four additions to the catalyst core (Figure 2.19). Further, the use of core substituted catalysts in O-ATRP consistently produced polymers with $I^* \sim 100\%$, supporting the hypothesis that low I^* with non-core substituted catalysts is due to an *in-situ* core-substitution side reaction.[89] A similar study was also reported by Zhao, Guo, and coworkers, which investigated the core substitution of dihydrophenazines using various alkyl bromides and benzyl bromide derivatives. Interestingly, this report showed unsubstituted phenoxazines and phenothiazines can undergo similar substitution-based side reactions, suggesting this reactivity is not unique to a single catalyst family.[90]

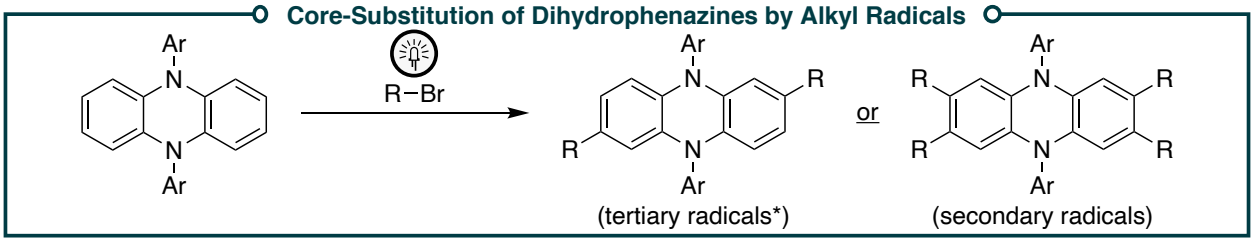

Figure 2.19. *Observed core-substitution of dihydrophenazine PCs by alkyl radicals such as those present during O-ATRP. Note that R-Br can be either an alkyl bromide initiator or the alkyl bromide chain-end group of a polymer. *Only the 2,7 isomer is depicted, though the 2,8 isomer is also formed.*[89]

Finally, in an investigation of deactivation in O-ATRP, several side reactions related to this step were probed and identified. Perhaps most significantly, it was discovered that $PC^{\bullet+}$ can react with DMAc, a common O-ATRP solvent, as well as halides such as Br^- and Cl^-. In both cases, $PC^{\bullet+}$ is reduced *via* single electron transfer to generate the neutral PC, a process that is accelerated in light and that likely impedes deactivation under the appropriate conditions. Since this process can generate halogen radicals (Br• and Cl•), the propensity for these radicals to engage in hydrogen atom abstraction under O-ATRP conditions was evaluated as well. While this possible side reaction was not ruled out, it did not appear to be greatly impacted by the identity of the halide in the presence of MMA. As such, since well controlled PMMA has been synthesized repeatedly in the presence of bromides, these results suggest this side reaction may not be significant in the O-ATRP of MMA.[151]

Solvent effects in O-ATRP

Early in the development of O-ATRP, researchers noted that solvent choice could impact catalyst properties and the outcome of a polymerization. For example, dihydrophenazines exhibiting ICT in the excited state displayed solvatochromic emission from stabilization of the excited state in more polar solvents, suggesting the excited state properties of these PCs are

significantly impacted by changes in solvent polarity. In addition, computational work suggested lowering solvent polarity could encourage formation of the $PC^{\bullet+}Br^-$ ion pair, a species proposed to mediate deactivation in O-ATRP. Together, these results led researchers to believe that performing O-ATRP in lower polarity solvents could improve polymerization control by improving activation (through manipulation of PC*) and deactivation (by encouraging ion pairing in $PC^{\bullet+}Br^-$). Indeed, when O-ATRP was performed with a mixture of DMAc and THF, improved polymerization control was obtained relative to using DMAc as the solvent alone.[135] In a later study, this point was further demonstrated by investigation of O-ATRP in several solvent systems. Interestingly, catalysts with ICT in the excited state were most robust to changes in solvent polarity and ultimately performed best in less polar solvents,[148] consistent with the hypotheses presented in previous work.[135]

While these studies provided important insight into the importance of solvent choice in O-ATRP, the fundamental impacts of solvent polarity on PC properties remained poorly understood for some time. Later in 2020, McCarthy *et al.* performed a systematic investigation of solvent effects on the PhenN-2N catalyst, yielding deeper insight into this phenomenon. Through detailed investigation of PC photophysics in DMAc (more polar) and THF (less polar), these authors identified several important implications of lowering solvent polarity. These included a decrease in nonradiative decay from S_1 to S_0, an increase in intersystem crossing from the singlet to the triplet manifold, and an increase in the lifetimes of both the S_1 and T_1 excited states.[88] Similar results have been reported by Orr-Ewing,[145] and all three effects can be expected to improve activation during O-ATRP by increasing the concentration of excited states available for catalysis. In addition, the $PC^{\bullet+}$ of PhenN-2N was found to be more oxidizing [larger $E^o(PC^{\bullet+}/PC)$] in less polar solvents, presumably due to destabilization of the cation. In turn, this property increases the

driving force for deactivation, which should improve polymerization control in O-ATRP.[88] As such, several synergistic effects exist upon lowering solvent polarity that will ultimately benefit O-ATRP. In both the polymerization of acrylates[88] and the polymerization of MMA at low catalyst loadings[89], these solvent effects were evident.

Finally, in the investigation of radical cations and deactivation in O-ATRP, several solvent effects were identified. As predicted previously through computational studies,[135] solvent polarity was shown to influence ion pairing in radical cation salts ($PC^{\bullet+}PF_6^-$) by increasing ΔG^o_{assoc} with decreasing polarity. In addition, it was found that several radical cations can oxidize O-ATRP solvents, such as DMAc and DMF. As such, to ensure stability of $PC^{\bullet+}$ during O-ATRP, the use of solvents with greater oxidation potentials [$E^o(S^+/S)$, S = solvent] is beneficial. In this work, ethyl acetate was a suitable choice in which radical cation decomposition could be minimized.[151]

One detail that should be noted is that most of the studies presented here have focused on the dihydrophenazine family of PCs. While these investigations can serve as useful guides to choosing solvents for O-ATRP, they may not be generalizable to other catalyst families. Moreover, there may be other solvent considerations that are not directly related to PC properties. For example, in some instances dichloromethane may be a poor solvent choice for O-ATRP, since some PCs may be able to reduce this solvent [$E^o(CH_2Cl_2/CH_2Cl_2^{\bullet-})$ = -2.2 V to -2.5 V vs. SCE[152]], leading to unwanted initiation and termination reactions. In addition, the use of toluene as a solvent could be detrimental to polymerization control, since the benzylic C-H bond in toluene is easily broken and the resulting benzylic radical is stabilized by resonance.[7] As a result, toluene can serve as a chain-transfer agent in radical polymerizations, again causing unwanted initiation and termination of polymer chains. Moving forward, further investigations elucidating the impact of various solvents in O-ATRP will undoubtably be useful to the development of the field. In

particular, studies revealing solvent effects for new catalyst families (i.e. other than dihydrophenazines) or that develop a general guide to understanding solvent effects in O-ATRP could significantly impact the field.

Mechanistic insights in O-ATRP by reductive quenching

Compared to O-ATRP by oxidative quenching, less studies exist on the mechanism of O-ATRP using reductive quenching catalysts. In 2018, Luo and coworkers used kinetic modeling to probe this process, the results of which support the importance of the sacrificial electron donor in these methods. For example, their modelling suggested that in the absence of a donor, no polymerization would occur. This result was consistent with experiments, which also showed no polymerization in the presence of EY without a sacrificial electron donor also present. In addition, it has been proposed that deactivation in these methods is mediated by the radical cation of the sacrificial electron donor – often an amine radical cation. In this work, kinetic modeling predicted the concentration of the donor would remain constant throughout the polymerization, consistent with the donor radical cation being reduced during activation to regenerate the original donor species.[153]

While these studies are insightful and can guide the development of this method, it is important to note they are predicated on a hypothesized mechanism and do not consider alternative mechanisms. As an example, since a single mechanism of deactivation involving the donor radical cation was considered,[153] this modeling cannot reveal the existence other possible deactivating species. As such, further investigation of the mechanism of O-ATRP using reductive quenching PCs, including experimental kinetics to validate this model, is warranted and would likely benefit future development in this field.

Monomers polymerized by O-ATRP

Methacrylates

By far the most common monomers in O-ATRP have been methacrylates (Figure 2.20). First reported in the seminal works by Miyake and Theriot[32] and Hawker[33], MMA has been the monomer of choice for most new O-ATRP methods. Often, it can be polymerized to molecular weights ranging from 1 to 20 kDa with $Đ < 1.2$ and $I^* \sim 100\%$. Hawker showed PhenS-Ph could also polymerize dimethylaminoethyl methacrylate with good control (M_n = 8.8 kDa, $Đ$ = 1.1), highlighting for the first time an advantage of O-ATRP over traditional metal-catalyzed ATRP methods. Since this monomer can coordinate to metal catalysts and alter their catalytic properties, the use of metal-free catalysts in O-ATRP was crucial for its successful polymerization.[33] In addition, both Hawker and Miyake showed other methacrylates could be polymerized in the synthesis of block copolymers with PMMA. In Hawker's case, benzyl methacrylate (BnMA) was used to synthesize PMMA-b-PBnMA, with M_n = 25.9 kDa and $Đ$ = 1.3.[33] Instead, Miyake and Theriot synthesized PMMA-b-PBMA (BMA = *n*-butyl methacrylate) by converting PMMA (M_n = 72.9 kDa, $Đ$ = 1.3) to a block copolymer with M_n = 523 kDa and $Đ$ = 2.6.[32]

In 2016, the monomer scope of O-ATRP was expanded to several other methacrylates using two dihydrophenazine catalysts. These monomers included trimethylsilyl hydroxyethyl methacrylate (M_n = 20.0 kDa, $Đ$ = 1.3, I^* = 86%), diethyleneglycol methyl ether methacrylate (M_n = 21.3 kDa, $Đ$ = 1.4, I^* = 85%), and trifluoroethyl methacrylate (M_n = 54.7 kDa, $Đ$ = 1.1, I^* = 24%).[34] While each of these methacrylates was polymerized with varying $Đ$ and I^* – highlighting differences in polymerization control – the broad array of functionalities within these monomers began demonstrating the excellent functional group tolerance enjoyed by O-ATRP.

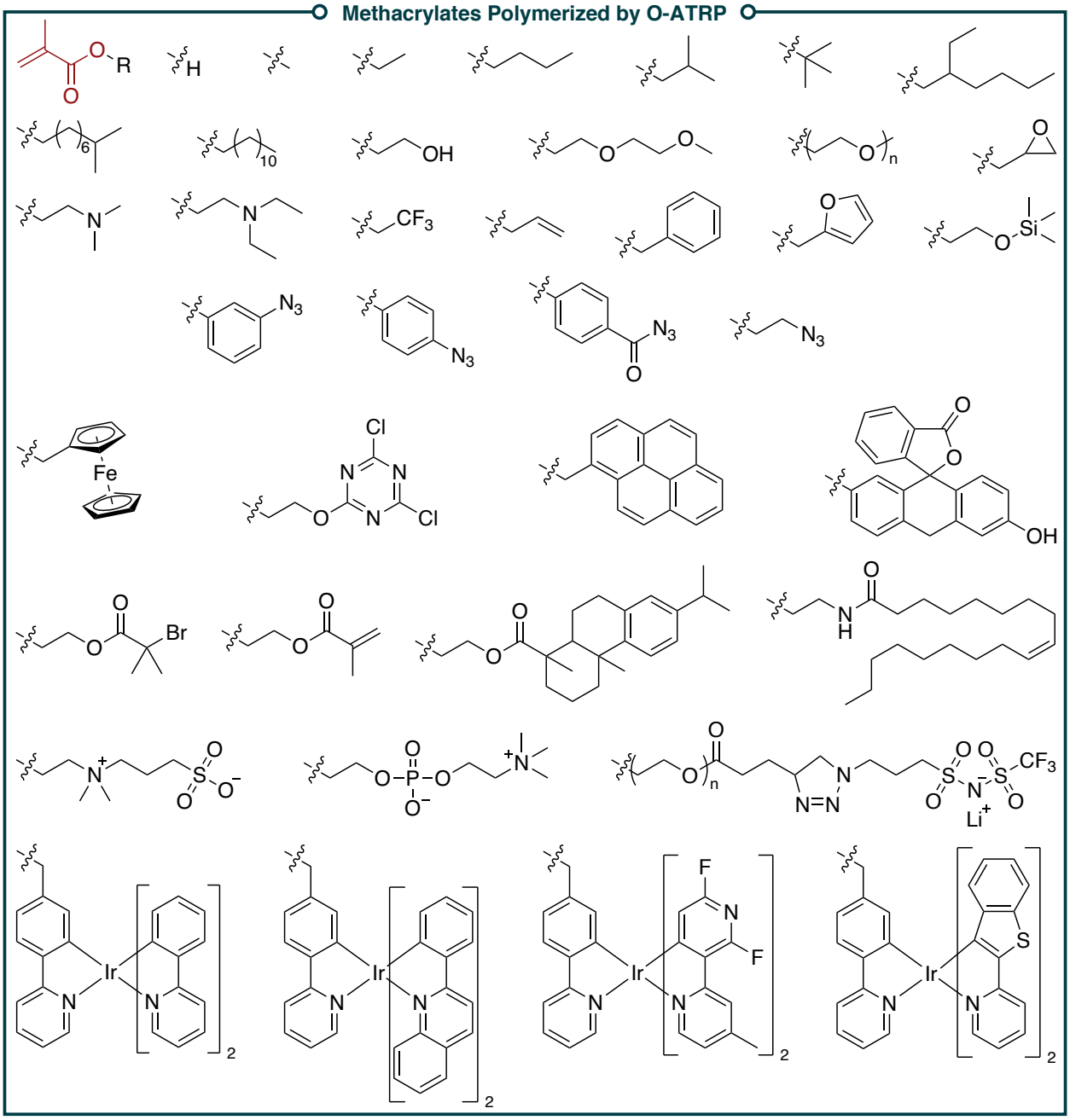

Figure 2.20. *Structures of methacrylate monomers polymerized by O-ATRP.*

Broadly, methacrylates with alkyl chains of various lengths have been well tolerated in O-ATRP. These include methyl methacrylate[32, 33], ethyl methacrylate[154], *n*-butyl methacrylate[32, 154], *i*-butyl methacrylate[35], *t*-butyl methacrylate[80], 2-ethylhexyl methacrylate[155], *i*-decyl

methacrylate[35], and dodecyl methacrylate[155]. Since numerous different catalysts have been employed to achieve this wide monomer scope, a direct comparison of polymerization control across monomers of increasing alkyl chain length is challenging. However, a sense of the effect this group has can be gained from work investigating the polymerization of various methacrylates in continuous flow using a single catalyst. In this case, increasing the chain length generally resulted in a loss of polymerization control, as observed through increasing *Đ* and gradually decreasing *I** (Table 2.3).[155] In part, this loss of polymerization control may be attributable to the increase in the rate of propagation (represented by k_{prop}, Table 2.4), which makes propagation more challenging to control in the absence of sufficient deactivation. However, changes in monomer structure can also be expected to impact other polymerization conditions, such as the reaction solution polarity. Since a number of catalytic properties (ex. PC photophysics, ion pairing, etc.) are susceptible to changes in solution polarity (see *Solvent Effects in O-ATRP*), it is difficult to understand exactly why increasing the length of the methacrylate alkyl chain decreases polymerization control. As such, further investigation of this phenomenon is necessary.

Table 2.3. *Impact of methacrylate alkyl chain length on polymerization control as observed by Ramsey et al..*[155]

Alkyl Chain	M_n (kDa)	*Đ*	*I** (%)
ethyl	7.6	1.2	94
i-butyl	9.9	1.2	96
2-ethylhexyl	16.0	1.4	98
i-decyl	26.5	1.2	56
dodecyl	18.5	1.5	83

Table 2.4. *Free radical propagation rate constants of common vinyl monomers calculated at 30°C.*

Monomer	A^a x 10^{-6} (l mol^{-1} s^{-1})	$E_A{}^b$ (kJ mol^{-1})	$k_{prop}{}^c$ (M^{-1} s^{-1})	Reference
Methacrylate Monomers				
Methacrylic Acid	0.38	16.1	639	156
Methyl Methacrylate	2.67	22.4	369	157
Ethyl Methacrylate	4.06	23.4	377	158
n-Butyl Methcrylate	3.78	22.9	428	158
i-Butyl Methacrylate	2.64	21.8	463	159
2-Ethylhexyl Methacrylate	1.87	20.4	571	159
i-Decyl Methacrylate	2.19	20.8	571	159
Dodecyl Methacrylate	2.50	21.0	602	158
Cyclohexyl Methacrylate	4.88	22.3	701	160
	3.76	21.5	742	161
Benzyl Methacrylate	3.61	21.5	713	161
	8.50	23.2	855	162
i-Bornyl Methacrylate	4.28	22.5	568	161
Glycidyl Methacrylate	4.41	21.9	743	160
	6.02	22.9	682	161
Hydroxyethyl Methacrylate	8.88	21.9	1,500	160
2-Hydroxypropyl Methacrylate	3.51	20.8	915	161
Acrylate Monomers				
Methyl Acrylate	16.6	17.7	14,800	163
n-Butyl Acrylate	15.8	17.3	16,500	164
Dodecyl Acrylate	17.9	17.0	21,100	165
Other Monomers				
Acrylonitrile	-	16.2	1,100	7
Styrene	43.0	32.5	108	166
	4.50	26.0	149	7
Vinyl Acetate	10.0	19.8	3,870	163
	14.7	20.7	3,990	167
1,3-Butadiene	80.5	35.7	57	168
Chloroprene	20.0	26.6	522	169

[a] Arrhenius parameter. [b] Activation energy. [c] Calculated using the Arrhenius parameters and activation energies published in the respective references.

In addition to these alkane-functionalized methacrylates, a number of methacrylates with heteroatom-containing aliphatic groups have been polymerized successfully. These monomers include methacrylic acid[170], 2-hydroxyethyl methacrylate[87], diethylene glycol methyl ether

methacrylate[155], poly(ethylene glycol) methacrylate[97, 122], glycidyl methacrylate[171], and diethylamino ethyl methacrylate[171]. A number of aromatic monomers have also been polymerized, including benzyl methacrylate[33, 35] and furfuryl methacrylate[66, 172], although not as extensively as aliphatic methacrylates.

Exploiting the wide functional group tolerance of O-ATRP, a number of reports have disclosed the polymerization of highly functionalized monomers for various applications. In 2019, Ni and Niu reported the successful polymerization of several azide containing methacrylates with good polymerization control (M_n = 11.9 to 22.6 kDa, $Đ$ = 1.2 to 1.3, I* = 70% to 100%). Using FT-IR, these authors demonstrated the presence of the desired azide functionality within the product polymer, supporting the tolerance of this method to these functional groups.[173]

In other work, researchers disclosed the polymerization of 2-([4,6-dichloro- triazin-2-yl]oxy)ethyl methacrylate[94], pyrenyl methacrylate[94], and even fluorescein-o-methacrylate[174]. In addition, several bifunctional monomers have been reported in O-ATRP, such as allyl methacrylate[171], methacrylate-based inimers (monomers that can also serve as initiators)[175], and dimethacrylate monomers to achieve polymer crosslinking[176]. Due to the complex polymer architectures achieved using such monomers – in particular inimers and dimethacrylates – polymerization control in these systems often cannot be evaluated.

Further highlighting the excellent functional group tolerance of O-ATRP, several research groups have reported the polymerization of metal-containing monomers using this method. In an example from the Hawker group in 2018, methacrylates functionalized using tethered Ir complexes were prepared and grafted to Si surfaces. By tuning the functionalities on each complex, the authors were then able to tune the emission of the resulting films, generating patterned films of various colors under UV irradiation.[177] Similarly, Kong and coworkers disclosed the

polymerization of ferrocenylmethyl methacrylate to generate ferrocene-containing polymers, which were ultimately employed in the detection of lung cancer DNA.[178]

In other reports, the metal-free conditions enabled by O-ATRP have been exploited in the synthesis of polymers for metal-sensitive applications. One such application is in electronics, where residual metal contaminants within the polymer can lead to detrimental side reactions and undesirable material performance. For this reason, O-ATRP was chosen for the synthesis of poly(PEG) methacrylate lithium sulfonyl(trifluoromethylsulfonyl)imide), a single-ion homopolymer electrolyte intended for battery applications.[179] Another area where the elimination of metal contamination can be beneficial is in biological and medical applications. For this reason, O-ATRP was selected for the copolymerization of fluorescein *O*-methacrylate and sulfobetaine methacrylate to generate polymer-based drug delivery vehicles.[174] Similarly, nanodiamonds were surface-functionalized with 2-methacryloyloxyethyl phosphorylcholine – a zwitterionic methacrylate – with the goal of generating new materials for biomedical applications.[180] Importantly, each of these examples highlights the polymerization of monomers with ionic and other functionalities, further highlighting the excellent functional group tolerance enjoyed by O-ATRP.

Finally, Chu and Tang showed that several monomers derived from biomass could also be polymerized by O-ATRP. In this work, the authors synthesized methacrylate-based monomers from soybean oil, rosin acid, and furfural – three biomass feedstocks. Using PhenS-Ph, they showed these monomers could be polymerized with good to moderate control (M_n = 2.5 to 11.0 kDa, $Đ$ = 1.1 to 1.4), again demonstrating the utility of this highly tolerant polymerization method.[172]

Acrylates

Closely related to methacrylate monomers, acrylates (Figure 2.21) have generated significant interest in efforts to expand the monomer scope of O-ATRP. However, several challenges exist in polymerizing this monomer family. For example, acrylates typically exhibit k_{prop} values roughly an order of magnitude larger than methacrylates (Table 2.4). As such, much more efficient deactivation is necessary to maintain polymerization control with this class of compounds. In addition, the C-X (X = Br, Cl) chain-end bonds of acrylates are typically stronger than those of methacrylates (Table 2.5). As a result, activation in the O-ATRP of acrylates is also more challenging. For these reasons, the polymerization of acrylates to form well defined polymers (controlled molecular weights and low $Đ$) while achieving a high I^* using this method was limited for several years.

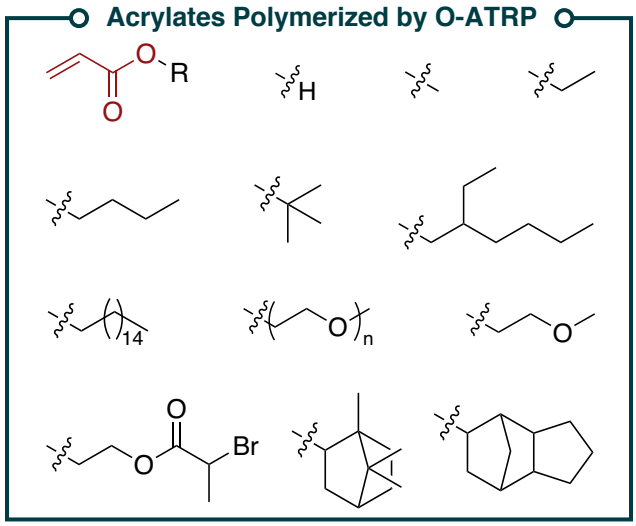

Figure 2.21. *Structures of acrylate monomers polymerized by O-ATRP.*

Table 2.5. *Computed and experimental bond dissociation energies for chain-end C-X (X = Br, Cl) bonds of polymers from common vinyl monomers.*

Monomer	Halide	ΔG°[a] (kcal mol^{-1})	BDE[b] (kcal mol^{-1})
Acrylonitrile	Br	47.2	-
	Cl	55.8	-
Methyl Methacrylate	Br	49.4	-
	Cl	57.4	-
Styrene	Br	50.3	-
	Cl	58.8	-
Methyl Acrylate	Br	51.8	-
	Cl	60.4	-
Vinyl Ketone	Br	53.3	-
	Cl	61.3	-
Dimethyl Acrylamide	Br	54.2	-
	Cl	62.2	-
Vinyl Chloride	Br	55.9	65
	Cl	65.9	79.5
Vinyl Acetate	Br	59.5	-
	Cl	69.4	-
Isobutylene	Br	60.1	70
	Cl	69	84.1
Propylene	Br	61.7	71.5
	Cl	71.2	84.6
Vinyl Ether	Br	63.2	-
	Cl	72.1	-

[a] *Computed in reference 103 by density functional theory at B3P86/6-31G**.* [b] *Determined experimentally in reference 181.*

Highlighting these challenges, many early attempts to polymerize acrylates exhibited moderate or poor polymerization control, as indicated by $Đ$ around or above 1.5 and I^* deviating significantly from 100%. Perhaps the first example of an acrylate polymerized by O-ATRP came in the seminal report by Miyake and Theriot, which used a PMMA macroinitiator (M_n = 72.9 kDa, $Đ$ = 1.3) and *n*-butyl acrylate to synthesize a block copolymer (M_n = 219 kDa, $Đ$ = 1.7). However, as evidenced by the large increase in $Đ$, the polymerization of this monomer was not well controlled.[32] Similarly, Yilmaz and Yagci developed a method for the copolymerization of butyl

acrylate (by O-ATRP) and ε-caprolactone (by ring opening polymerization) using a bifunctional initiator. Again, the copolymerization exhibited signs of poor control (M_n = 30.6 kDa, $Đ$ = 1.7).[182]

In work by Chen and coworkers, a core substituted phenothiazine catalyst was used to polymerize several monomers from sulfonyl halide initiators. Included in these monomers were methyl acrylate and *n*-butyl acrylate. In the case of methyl acrylate, poor polymerization control was observed, primarily through high dispersity ($Đ$ > 1.5). However, the polymerization of this monomer did exhibit linear pseudo-first-order kinetics, linear molecular weight growth, and decreasing $Đ$ throughout the reaction, suggesting some degree of polymerization control may have been present. Instead, the polymerization of *n*-butyl acrylate produced polymers with lower dispersity ($Đ$ = 1.4), although with reduced initiator efficiency (I^* = 82%).[80] Similar results were obtained by Zhou and Lou, who were able to polymerize poly(ethylene glycol) acrylate with moderate control ($Đ$ = 1.4, I^* ~ 50%) using a water soluble phenoxazine catalyst.[97]

It wasn't until 2020 that O-ATRP was able to access a wide range of acrylates in a well-controlled fashion. With the development of dihydroacridine catalysts and enabled through the use of a continuous flow reactor, the polymerization of *n*-butyl acrylate was finally reported with good control (M_n = 2.4 to 45.7 kDa, $Đ$ = 1.2 to 1.4, and I^* ~ 100%). Further, the versatility of this polymerization system was demonstrated through the polymerization of methyl acrylate, ethyl acrylate, *t*-butyl acrylate, 2-ethylhexyl acrylate, and ethylene glycol methyl ether acrylate (Table 2.6). In each case, good or moderate polymerization control was observed, supporting the viability of this method to access a wide range of acrylate monomers.[65]

Table 2.6. *Results from the polymerization of acrylates by Buss et al. using dihydroacridine PCs.*[65]

Monomer	M_n (kDa)	$Đ$	I^* (%)
methyl acrylate	8.1	1.3	81
ethyl acrylate	7.8	1.2	105
t-butyl acrylate	12.1	1.2	88
2-ethylhexyl acrylate	16.8	1.5	104
ethylene glycol methyl ether acrylate	12.3	1.4	117

Shortly after this report, McCarthy *et al.* explored the ability of dihydrophenazine catalysts to also access the polymerization of acrylates. Through their investigations, the authors discovered that tuning the polarity of the reaction solution could greatly impact the polymerization process. In particular, lowering the solvent polarity allowed access to the controlled polymerization of acrylates through modification of a number of important catalytic properties (see *Solvent Effects in O-ATRP*).[88] Additionally, evidence was found for an *in-situ* side reaction involving substitution of the catalyst by the radical initiator. This core-substitution was then performed intentionally through pre-irradiation of a catalyst and initiator solution, followed by addition of the monomer and additional initiator to begin the polymerization. The pre-irradiation step was intended to generate the substituted catalyst prior to polymerization, such that this side reaction wouldn't consume initiator undesirably once the polymerization began. This approach ultimately yielded improved polymerization control (namely I^* closer to 100%), presumably by eliminating this side reaction. In addition, this method was broadly applicable to a number of acrylate monomers, including methyl acrylate (M_n = 9.1 kDa, $Đ$ = 1.2, I^* = 83%), ethyl acrylate (M_n = 9.7 kDa, $Đ$ = 1.2, I^* = 97%), *n*-butyl acrylate (M_n = 7.7 to 17.5 kDa, $Đ$ = 1.1 to 1.4, I^* ~ 100% to 180%), *t*-butyl acrylate (M_n = 10.4 kDa, $Đ$ = 1.2, I^* = 115%), 2-ethylhexyl acrylate (M_n = 12.4 kDa, $Đ$ = 1.2, I^* = 115%), ethylene glycol methyl ether acrylate (M_n = 9.8 kDa, $Đ$ = 1.4, I^* = 127%), isobornyl acrylate (M_n = 10.3 kDa, $Đ$ = 1.3, I^* = 101%), and dicyclopentanyl acrylate (M_n = 15.4 kDa, $Đ$ = 1.4, I^* = 127%).[88]

In work by the Wang group, acrylic acid was polymerized from the surfaces of nanoparticles using O-ATRP mediated by PhenS-Ph. While polymerization control was not evaluated in this report, the successful polymerization of this monomer was verified by FT-IR and transmission electron microscopy.[183] In 2021, Qian, Han, Zhang, and coworkers demonstrated the polymerization of hexadecyl acrylate from functionalized cellulose-based fibers, although polymerization control was again not evaluated.[184] Finally, an acrylate based inimer similar to that reported for methacrylates was employed to synthesize hyperbranched polymers by O-ATRP. Gel permeation chromatography (GPC) analysis of the resulting polymer revealed broad molecular weight distributions throughout the polymerization, suggesting poor control over the polymer molecular weight and $Đ$. While a microemulsion polymerization was also attempted with this monomer to gain better control over the polymerization, it was ultimately unsuccessful as evidenced by the formation of unstable latexes and bimodal molecular weight distributions.[185]

Acrylonitrile

Early in the development of O-ATRP, Matyjaszewski and coworkers reported on the use of various phenothiazine catalysts for the polymerization of acrylonitrile. While several new catalysts were developed for this application – namely phenothiazines with new *N*-aryl substituents – PhenS-Ph was ultimately the most successful. Using PhenS-Ph, the polymerization of acrylonitrile was moderately controlled, with the resulting polymer exhibiting M_n = 1.7 to 4.4 kDa and $Đ$ = 1.4 to 1.9. Further, through the synthesis of a block copolymer with MMA, good chain-end fidelity was demonstrated with this system.[91]

In 2017, Chen and Liu showed EY could also mediate the polymerization of this monomer using a benzenediazonium tetrafluoroborate initiator. In the homopolymerization of acrylonitrile,

moderate polymerization control was again achieved, with the product poly(acrylonitrile) exhibiting M_n = 73 to 153 kDa, $Đ$ = 1.2 to 1.6, and I^* generally below 10%. In addition, these authors synthesized a series of statistical copolymers with acrylonitrile, using monomers such as MMA (5 mol %, M_n = 101 kDa, $Đ$ = 1.3), methyl acrylate (15 mol %, M_n = 93 kDa, $Đ$ = 1.3), *n*-butyl acrylate (5 mol %, M_n = 105 kDa, $Đ$ = 1.4), styrene (5 mol %, M_n = 45 kDa, $Đ$ = 1.2), and itaconic acid (5 mol %, M_n = 74 kDa, $Đ$ = 1.2).[186] In later work, this method was expanded to a number of other photocatalysts, such as rhodamine B, erythrosin B, and fluorescein. However, EY generally gave the best polymerization control and was ultimately chosen for subsequent experiments.[187]

Acrylamides

In addition to acrylates and methacrylates, a handful of acrylamides have been polymerized by O-ATRP (Figure 2.22), although generally without much polymerization control. For example, Li and coworkers used surface-initiated O-ATRP to graft *N*-isopropyl acrylamide (NIPAM) to the surface of SBA-15 nanoparticles. The resulting functionalized nanoparticles exhibited M_n = 13.4 kDa and $Đ$ = 2.3, suggesting poor polymerization control with this monomer. When instead MMA was polymerized in the same system, polymers consistently showed $Đ$ = 1.2 to 1.3, indicating a higher degree of polymerization control with this methacrylate monomer.[188] Around the same time, Yilmaz and Yagci disclosed the concurrent O-ATRP and ring opening polymerization of NIPAM and ε-caprolactone, respectively, using a bifunctional initiator. However, the resulting polymer again exhibited signs of poor polymerization control (M_n = 33.2 kDa, $Đ$ = 1.5).[182] Slightly better polymerization control (M_n = 5.1 to 14.0 kDa, $Đ$ = 1.4 to 1.5) was obtained by Hu and Wang

in their attempts to synthesize block copolymers with NIPAM, although even this system gave $Đ$ near the limit of control ($Đ$ = 1.5).[189]

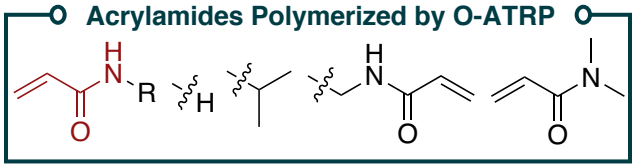

Figure 2.22. *Structures of acrylamide monomers polymerized by O-ATRP.*

In addition to NIPAM, others have attempted the polymerization of acrylamide using O-ATRP. In an early example, researchers employed this monomer for the functionalization of Au electrodes for lead ion detection. Since the resulting polymer was surface-bound, it was not characterized to evaluate polymerization control.[190] In a similar example, Sun and coworkers copolymerized acrylamide and *N,N*-methylene bis-acrylamide – a bifunctional acrylamide crosslinker – to produce molecularly imprinted electrochemical sensors. Again, polymerization control was not evaluated due to the nature of the product polymer.[191] More recently, Swisher *et al.* attempted the polymerization of *N,N*-dimethylacrylamide using newly developed phenoxazine PCs, although this polymerization showed little evidence of a controlled process.[192] Instead, Liu and Yi employed a water-soluble benzophenone derivative for the homopolymerization of acrylamide in water, which gave poly(acrylamide) with M_n = 2.7 to 37.5 kDa, $Đ$ = 1.4 to 1.5, and I^* ~ 70% to 100%.[128] Excitingly, these results suggest acrylamides have potential to be polymerized in a well-controlled fashion, assuming a suitable catalyst system can be developed for this monomer family.

Styrene and 4-vinylpyridine

One common monomer that has largely remained elusive in O-ATRP is styrene, presumably because styrene can be a triplet quencher or because the dormant alkyl halide is more thermodynamically challenging to reduce (Figure 2.23). In 2014, this monomer was first accessed using perylene to synthesize a PMMA / poly(styrene) (PS) copolymer with moderate control (PMMA: M_n = 72.9 kDa, $Đ$ = 1.3; PMMA-b-PS: M_n = 165 kDa, $Đ$ = 1.4).[32] Improved results were obtained by Yilmaz and Yagci, who reported the concurrent copolymerization of styrene and ε-caprolactone through O-ATRP and ring opening polymerization, respectively. In this system, the PC for O-ATRP was again perylene, and the resulting copolymer was obtained with M_n = 14.1 kDa and $Đ$ = 1.2.[182] However, many subsequent catalyst systems have been unable to polymerize styrene in a controlled fashion.

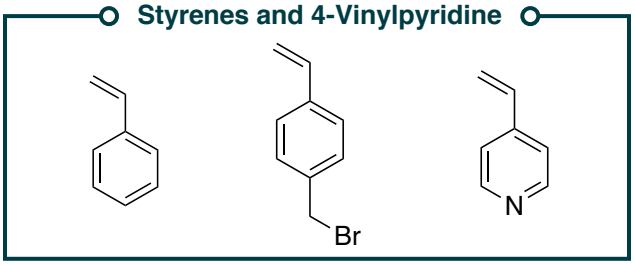

Figure 2.23. *Structures of styrene monomers polymerized by O-ATRP and 4-vinylpyridine.*

In 2018, Kim, Gierschner, Kwon, and coworkers provided one example of styrene being polymerized by O-ATRP with moderate control (M_n = 8.7 kDa, $Đ$ = 1.4, I^* = 90%).[115] However, it wasn't until 2019 in a report by Jessop and Cunningham that styrene was polymerized with the level of control expected for O-ATRP. In this work, the authors developed a new dihydrophenazine PC with pH sensitive functionalities for catalyst recycling. In addition to achieving this goal, they showed this catalyst could mediate the polymerization of styrene with good control (M_n ~ 18 kDa,

$Đ$ = 1.1 to 1.2) for the first time.[87] Unfortunately, it remains unclear how the properties of this phenazine differ from those of other PCs, and why this PC is successful in the polymerization of styrene when others are not. As such, further investigation of this catalyst system is warranted and could reveal important catalyst design principles for accessing new monomers in the future.

In addition to styrene, the analogous 4-vinylpyridine has also been employed in O-ATRP, although with relatively little emphasis on its controlled polymerization. Generally, this monomer has been employed for the production of self-healing hydrogels through grafting to a range of nanoparticle surfaces, and polymerization control has not been evaluated.[193-196] However, work by Nguyen, Truong, and coworkers showed that both PhenS-Py and pyrene can successfully polymerize 4-vinylpyridine to high conversions (up to 92%) with good polymerization control (M_n = 7.2 to 14.5 kDa, $Đ$ = 1.1 to 1.2, I^* = 95% to 102%).[197] As such, the polymerization of 4-vinylpyridine by O-ATRP shows promise and warrants further investigation in the future.

Finally, 4-vinylbenzyl bromide – a styrene-based inimer– has also been polymerized by O-ATRP, this time in a copolymerization with styrene to synthesize styrene-based hyperbranched polymers. Unsurprisingly, when the product polymers were characterized by GPC, they exhibited high dispersity ($Đ$ > 3), although the molecular weight of the polymers did show a dependence on the amount of inimer added to the reaction.

Vinyl cyclopropanes

Another interesting monomer family that has received attention in O-ATRP has been vinylcyclopropanes (Figure 2.24). Notably, these monomers contain coordinating functionalities, which may interact with metal catalysts in traditional ATRP and limit control in their polymerizations.[198-200] In O-ATRP, however, this issue is circumvented by the use of organic

catalysts, which cannot coordinate with these monomers and are therefore better suited for these polymerizations. In 2019, the first application of O-ATRP to vinylcyclopropanes was reported by Chen *et al.* using phenoxazine and dihydrophenazine PCs. The dihydrophenazine PCs – PhenN-2N and PhenN-$PhCF_3$ – showed particularly good control in the polymerization of ethyl vinylcyclopropane, producing polymer with M_n = 11.6 kDa to 79.5 kDa, $Đ$ = 1.1 to 1.4, I* = 91% to 127%. In addition, it was discovered that varying the reaction conditions could provide control over an intramolecular rearrangement of the polymer backbone, although this feature will be discussed further in a subsequent section (see *Metal Sensitive Applications of O-ATRP*).[201]

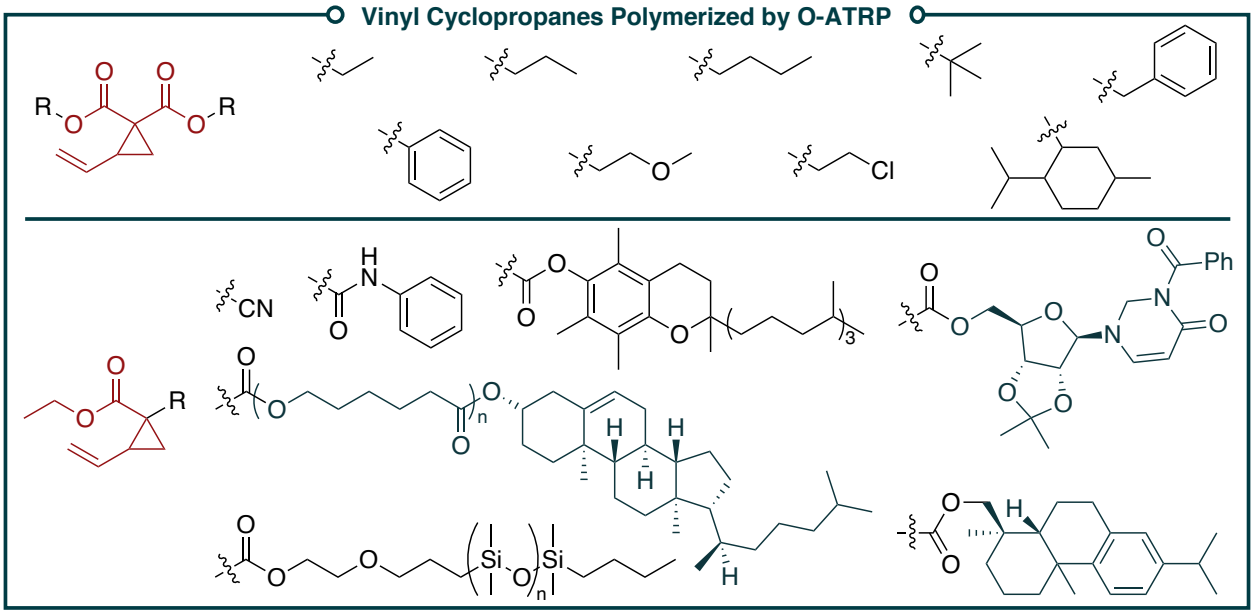

Figure 2.24. *Structures of vinyl cyclopropanes that have been polymerized by radical ring opening polymerization.*

Through variation of the ester functionalities on the vinylcyclopropane, tolerance for a wide range of functional groups was demonstrated, including alkyl chains, aromatic groups, and an alkyl chloride moiety. In general, most of the polymers synthesized showed excellent polymerization control, with M_n = ~20 kDa to 50 kDa, $Đ$ = 1.1 to 1.2, I^* ~ 80% to 110 %.[201] In

addition, later work expanded the scope of vinylcyclopropanes to include new symmetric and asymmetric monomers, which featured functionalities ranging from cyano groups to natural products, and even poly(dimethylsiloxane) polymer chains. Through polymerization of the latter monomers, brush polymers were accessed with similar control (M_n = 67.4 kDa to 309 kDa, $Đ$ = 1.1 to 1.5, I^* = 49% to 316%)[202] relative to previous vinylcyclopropane monomers.[201]

Other monomers

Finally, a handful of other monomers (Figure 2.25) have been investigated in O-ATRP, although generally as comonomers in conjunction with other monomers discussed in preceding sections. For example, when Niu and coworkers explored the polymerization of azide-containing methacrylates, they synthesized statistical copolymers with itaconic acid, ethyl vinyl ether, and butyl vinyl ether. In all three cases, polymerizations were performed with 20 mol % of the methacrylate and gave moderate polymerization control ($Đ$ ~ 1.3 to 1.4), although the methacrylate content in the product polymer ranged from 25% (ethyl vinyl ether) to 67% (itaconic acid).[173] In another example, Chen and coworkers synthesized statistical copolymers of acrylonitrile (95 mol %) and itaconic acid (5 mol %), which showed good polymerization control (M_n = 74 kDa, $Đ$ = 1.2). However, only one example of this polymerization was reported, after which this system was not investigated further.

Vieira and coworkers explored the polymerization of D-limonene using benzophenone and thioxanthene-2-one. While the resulting polymers exhibited low dispersity ($Đ$ = 1.1 to 1.2), monomer conversion was typically low (~ 6% to 12%) and seemed to plateau after several hours. As a result, polymer molecular weight was also quite low (M_n < 1 kDa),[203] suggesting initiation had occurred but that the PCs could not reactivate the dormant polymer chains after deactivation.

Given that the chain-end of the polymer should be an unactivated alkyl-bromide, it is likely that reduction potential of the polymer chain-end is too low [$E^o(P_nBr/P_nBr^{\bullet -}) < -2.0$ V vs. SCE] to be reduced by the PCs in this work. Alternatively, it is also possible that the propagating polymer in these reactions underwent rapid termination, which would result in similar polymerization kinetics and observations of limited monomer conversion. However, further investigation is necessary to understand this system.

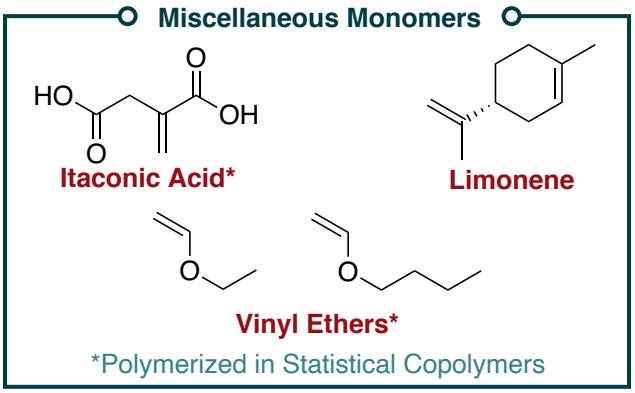

Figure 2.25. *Structures of miscellaneous monomers polymerized by O-ATRP.*

Applications of O-ATRP

One of the primary advantages of any controlled radical polymerization method is the ability to produce functional materials. In the following section, we outline the various ways in which O-ATRP has been employed in this respect, ranging from the synthesis of various polymer architectures to the surface functionalization of nanoparticles and electrodes.

Synthesis of block copolymers

The synthesis of block copolymers by O-ATRP has been achieved using several strategies.

Perhaps the simplest strategy involves the chain-extension of polymers also produced using this method, which takes advantage of their bromide chain-end functionality to initiate further O-ATRP reactions (Figure 2.26a). This strategy can be implemented in one of two ways. In the first, monomers can be added sequentially to a polymerization, such that each block of the copolymer is formed one at a time in the same pot. While operationally simple, this method requires high conversion of the first block to achieve a well-defined transition from one block to the other. However, it is also common to lose some polymerization control at high monomer conversions – a feature that is commonly seen in ATRP methods[4] – which can complicate the synthesis of well-defined copolymers by this method. As such, an alternative approach involves the synthesis and isolation of the first block – often called a macroinitiator – followed by chain-extension of the macroinitiator in a separate polymerization to generate the desired copolymer.

Since the formation of the second polymer block is dependent upon the presence of bromine chain-end groups in the first block, this method is often used to evaluate chain-end group fidelity in a given polymerization. The principle behind this experiment is depicted in Figure 2.26b. For an ideal polymer sample in which all the chain-end groups are retained, it can be expected that chain-extension by a well-controlled polymerization will result in complete conversion of the macroinitiator to the desired block copolymer. In this idealized case, analysis of the GPC trace of the copolymer should reveal a narrow, monomodal peak indicating complete chain-extension. If, instead, some portion of the first polymer block is unfunctionalized, chain-extension will primarily result in the formation of two polymer species within the sample: the unfunctionalized first polymer block and the chain-extended copolymer. The presence of this unfunctionalized polymer can sometimes be observed by GPC and is indicated by the observation of a bimodal peak in the chromatogram of the chain-extended polymer.

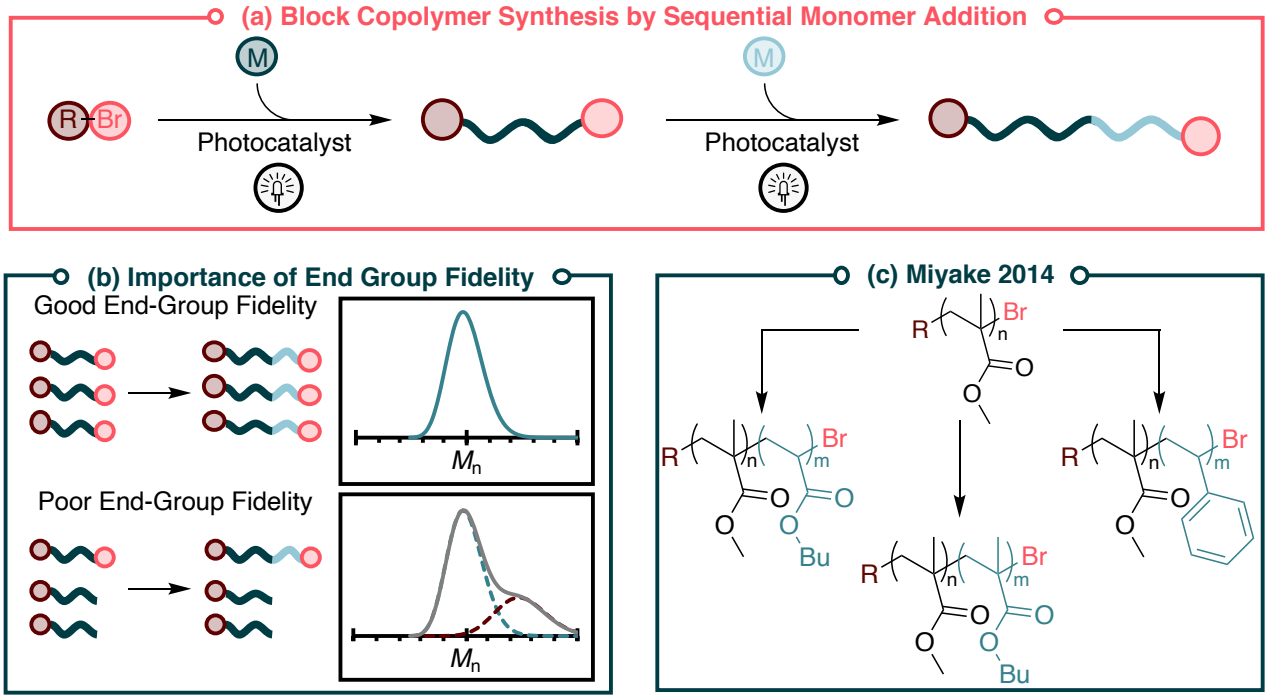

Figure 2.26 *(a) Broad depiction of block copolymer synthesis through sequential monomer (M) addition using O-ATRP. (b) The impact of end-group fidelity on Đ of the block copolymer. (c) Structures of block copolymers synthesized using perylene by Miyake and Theriot in 2014.*

Of course, other reasons may also exist for the observation of these features during GPC analysis. For example, a polymer chromatogram could be multimodal simply due to poor polymerization control. In addition, it is not uncommon for a copolymer to exhibit different hydrodynamic properties than the corresponding macroinitiator, which could lead to complications during GPC analysis. For this reason, Junkers and Michels have recommended against the use of these chromatograms alone as evidence for successful chain-extension, as they can sometimes be misleading.[204] Instead, other methods can provide more reliable evidence, such as multi angle light scattering in which absolute polymer molecular weight can be determined without interference from the polymer architecture or structure.

For examples of this block copolymer synthetic strategy being applied in O-ATRP, a number of literature reports exist. The first examples are once again found in the seminal reports

by Miyake and Theriot[32] and Hawker[33], who made copolymers from PMMA macroinitiators and a number of other comonomers. In the former report, butyl methacrylate, butyl acrylate, and styrene were used to form the second polymer block (Figure 2.26c). However, GPC analysis revealed a significant portion of unreacted PMMA, suggesting poor chain-end fidelity in O-ATRP mediated by perylene.[32] Instead, the report by Hawker showed high conversion of the PMMA macroinitiator in the copolymerization with benzyl methacrylate, suggesting better chain-end fidelity in the presence of PhenS-Ph. This conclusion was further supported with copolymerizations mediated by photoATRP and Cu catalyzed ATRP, which capitalized on the complementary strengths of these methods to form copolymers with methyl acrylate and styrene, respectively.[33]

Expanding on this work, subsequent reports showed a number of methacrylate monomers could be used to form copolymers with PMMA.[34, 35] In addition, copolymers can be synthesized with other macroinitiators, such as poly(acrylonitrile)[91], poly(*n*-butyl acrylate)[65], and poly(*N*-isopropylacrylamide)[189]. In the latter case, a copolymer of NIPAM and *t*-butyl acrylate was synthesized, after which the acrylate block was hydrolyzed to acrylic acid to achieve a copolymer that would have otherwise been challenging to synthesize.[189]

Finally, copolymers with more than two blocks have also been achieved through repetitive polymer isolation followed by chain-extension. For example, Cole *et al.* synthesized a triblock methacrylate copolymer using aryl core-substituted dihydrophenazine PCs.[81] Similarly, Buss *et al.* demonstrated the synthesis of a triblock acrylate copolymer using dihydroacridine PCs, highlighting the excellent polymerization control obtained in this method.[65]

While a number of interesting copolymers can be obtained using the strategy discussed above, it is inherently limited to the incorporation of monomers accessible through O-ATRP. For

this reason, another common strategy involves the post-polymerization modification of polymers obtained by other methods, such that they can be used as macroinitiators in O-ATRP (Figure 2.27a). For an example of this strategy, one can look to the work by Son and coworkers reported in 2018, in which copolymers of poly(ethylene glycol) (PEG) were synthesized by addition of a bromoisobutyrate group to the PEG chain-end followed by O-ATRP of glycidyl methacrylate (Figure 2.27b).[171] While polymerization control in this system was generally poor ($Đ > 1.5$), later work by the same group showed phenoxazine PCs could yield similar copolymers with greater control ($Đ < 1.5$).[96] In a similar approach, Nguyen and coworkers synthesized copolymers of poly(3-hexylthiophene) and various methacrylates with good polymerization control (Figure 2.28).[94]

In another popular strategy, multifunctional initiators are employed to perform orthogonal polymerizations of different monomers in one pot (Figure 2.29a), allowing access to a range of monomers inaccessible to a single polymerization method. These orthogonal polymerizations can either be performed separately or concurrently, depending on the desired conditions and compatibility of the chosen synthetic methods. For example, Theriot *et al.* showed dihydrophenazines could mediate PET-RAFT followed by O-ATRP to synthesize poly(acrylate-*block*-methacrylate) copolymers (Figure 2.29b).[205]

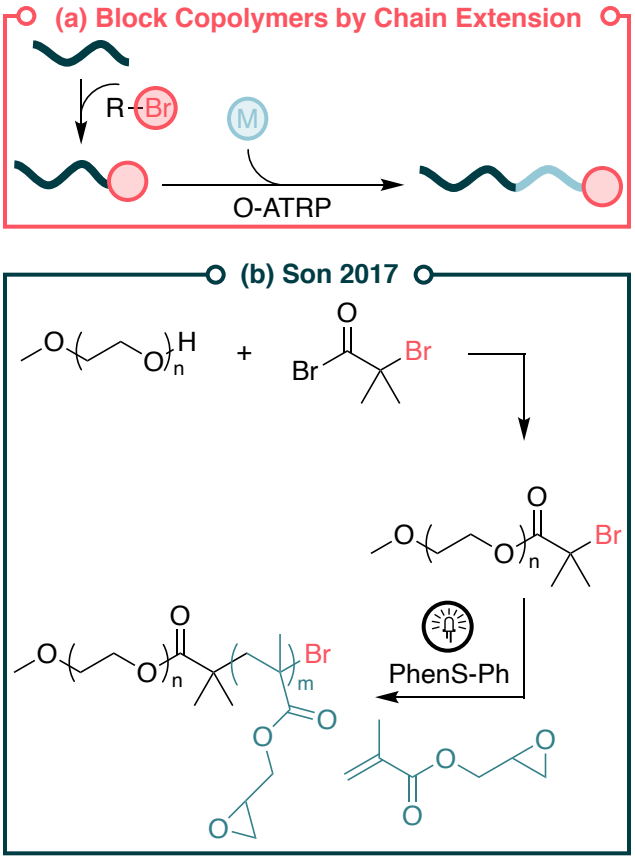

Figure 2.27. *(a) General scheme of block copolymer synthesis by functionalization of a polymer and chain-extension using O-ATRP. (b) Synthesis of amphiphilic block copolymers by functionalization and chain-extension of poly(ethylene glycol).*

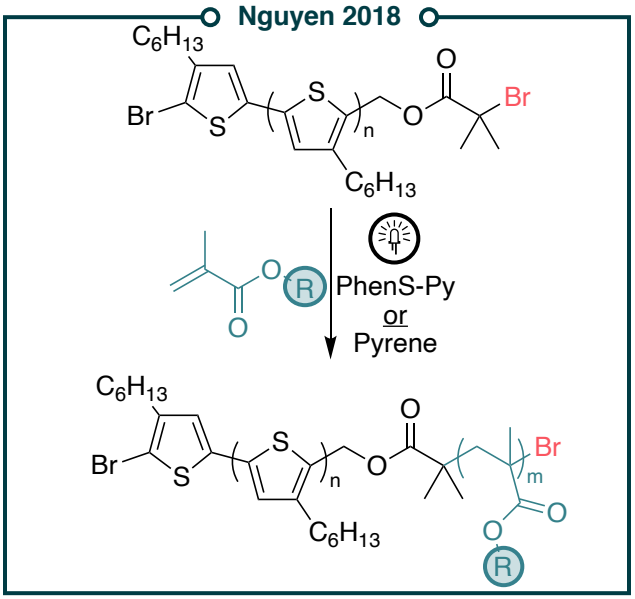

Figure 2.28. *Synthesis of P3HT-b-PMMA using O-ATRP by chain-extension of a P3HT macroinitiator.*

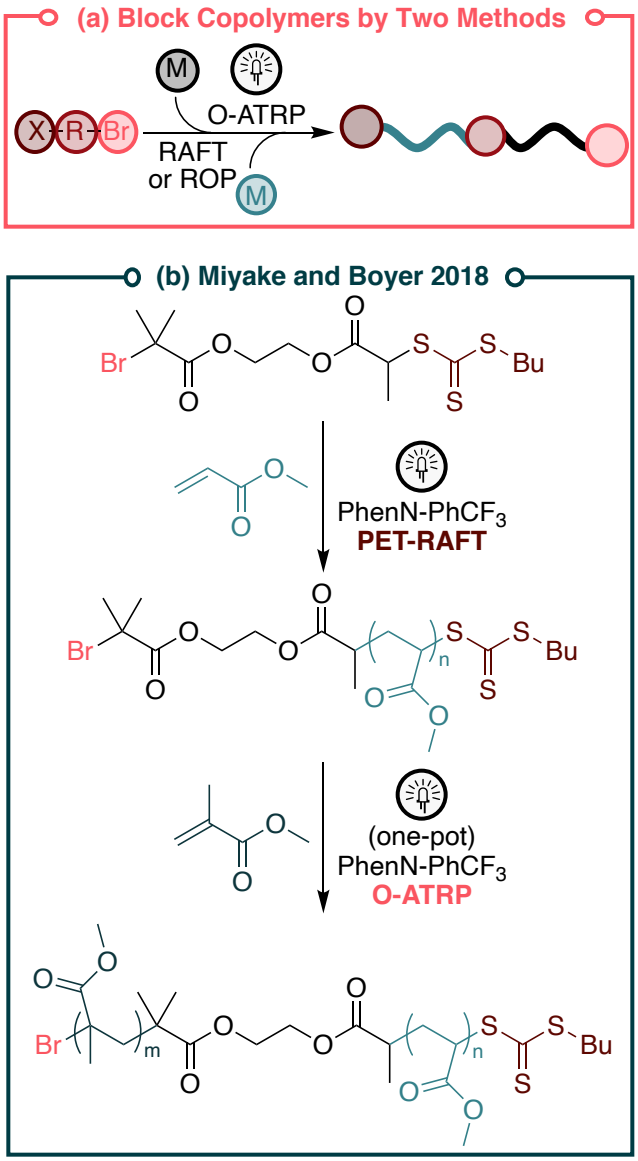

Figure 2.29. *(a) Synthesis of block copolymers through two orthogonal methods in one pot. (b) Sequential PET-RAFT and O-ATRP to synthesize PMA-b-PMMA.*

Instead, Yilmaz and Yagci used a bifunctional initiator similar to one reported by the Boyer group[206] comprised of an alcohol and a bromoisobutyrate moiety to perform concurrent ring opening polymerization and O-ATRP (Figure 2.30). Using this approach, ε-caprolactone was copolymerized with a series of vinyl monomers, including MMA, *n*-butyl acrylate, styrene, and NIPAM. A triblock copolymer was also synthesized through chain-extension of the ester block

using L-lactide, demonstrating the versatility of this method and its ability to produce highly tunable copolymers.[182] Shortly thereafter, Yilmaz extended this work to a trifunctional initiator – one bromoisobutyrate group tethered to two alcohols – allowing for the synthesis of star polymers through this same approach.[207]

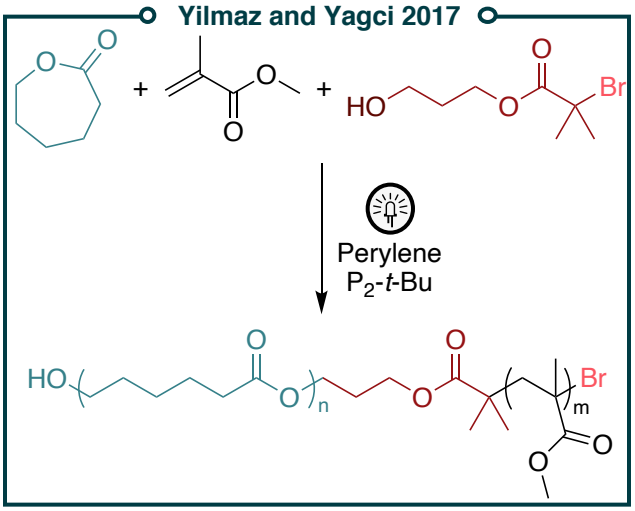

Figure 2.30. *Concurrent O-ATRP and ROP to synthesize PMMA-b-PCL.*

In work published by the Hawker and de Alaniz groups in 2018, several methods were employed to synthesize highly functionalized copolymers (Figure 2.31). First, a series of monomers and initiators suited for ATRP were synthesized bearing furan-protected maleimides. These compounds were then employed in O-ATRP to synthesize methacrylate polymers with maleimide end-groups, as well as copolymers with maleimide pendant groups. In the latter case, the versatility of O-ATRP was shown in the synthesis of a tetrablock copolymer, where polymerization of the maleimide functionalized monomers was enabled by the mild reaction conditions found in O-ATRP. Finally, polymers bearing furan protected maleimide end-groups were further modified using Diels-Alder chemistry to install a PEG block within the copolymer.[208]

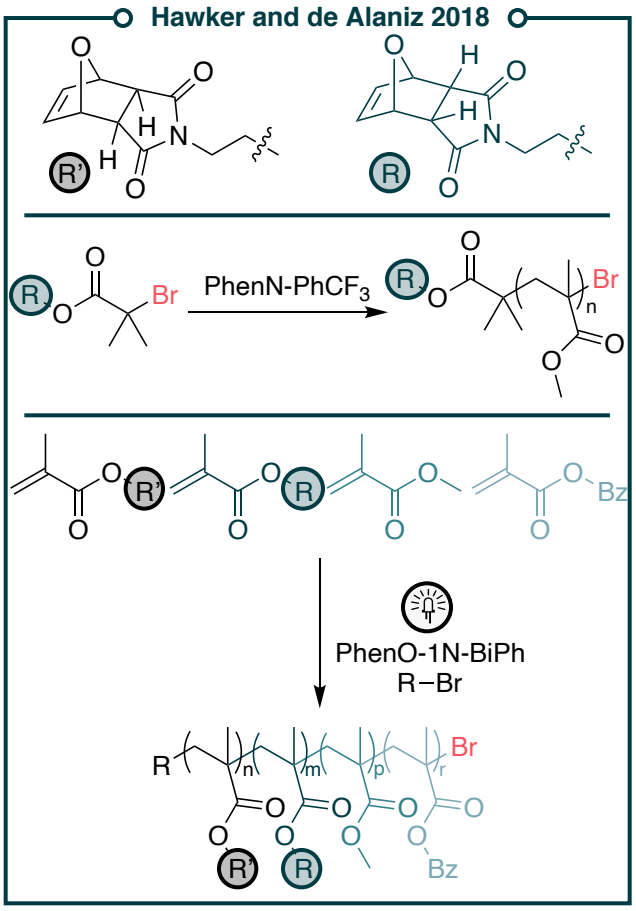

Figure 2.31. *Synthesis of initiators and block copolymers functionalized with furan-protected maleimides.*

Synthesis of graft polymers

Regarding the synthesis of polymers with higher-order architectures, O-ATRP has primarily been used for the synthesis of block copolymers. However, several examples exist of O-ATRP being used to produce more complex polymer architectures, such as graft polymers. In O-ATRP, this architecture is often achieved using a grafting-from approach, where a polymer backbone is functionalized with an alkyl halide group from which O-ATRP can be initiated. An excellent example of this approach was reported in 2018 by Chen and coworkers. In this work, the authors first developed aryl sulfonyl halides as an initiating system for O-ATRP. Once the success of this method was demonstrated using small molecule initiators, it was recognized that

poly(styrene) could be functionalized using this approach to yield sulfonyl halide initiating sites on the pendant phenyl groups of the polymer. By then performing O-ATRP from these sites, poly(styrene-*graft*-acrylate) polymers could be prepared through a grafting-from approach.[80]

In another example, the chloride functionality in the backbone of poly(vinylidene fluoride-*co*-chlorotrifluoroethylene) [P(VDF-*co*-CTFE)] was exploited for the synthesis of graft copolymers for electronic applications (Figure 2.32). Using PhenS-Ph as the catalyst, monomers such as MMA, methyl acrylate, and *n*-butyl acrylate were grafted from P(VDF-*co*-CTFE). NMR and GPC analysis demonstrated the success of the grafting process, with graft contents ranging from 5% up to 38%. However, these polymerizations showed poor control ($Đ >> 1.5$),[209] possibly due to challenges associated with the use of Cl^- in O-ATRP (see *Deactivation*). In support of this hypothesis, later work showed P(VDF-*co*-CTFE) could be dechlorinated with high yield under these conditions, suggesting activation of the polymer C-Cl bond is feasible.[210] In addition, Hu, Fang, Lu, and coworkers showed this polymerization could also be mediated by *p*-anisaldehyde, offering an inexpensive catalyst system for the synthesis of these materials.[211]

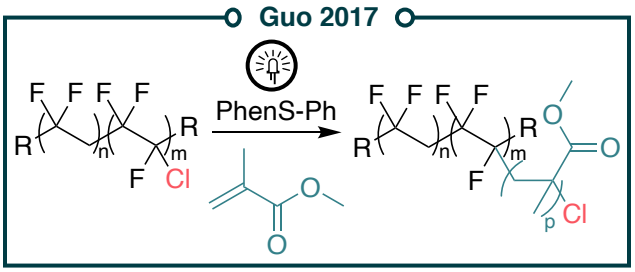

Figure 2.32. *O-ATRP initiated from the backbone of P(VDF-co-CTFE).*

Expanding on the polymeric backbones available for graft copolymer synthesis, Wang and Chu showed ethyl cellulose could be modified by installation of bromophenylacetate functionalities for use as an O-ATRP macroinitiator. After grafting various methacrylates from

this polymer backbone (Figure 2.33), a series of graft copolymers with predictable molecular weights but poor dispersities ($Đ \sim 1.7$) was obtained.[212] In later work, it was shown these polymers could be further modified to produce cellulose-based thermoset elastomers. Capitalizing on the ability to incorporate furfuryl methacrylate into the polymeric arms of the graft copolymer, the authors used Diels-Alder chemistry to create dynamic crosslinks within the polymer network. The resulting materials exhibited shape recovery, as well as self-healing properties due to the dynamic nature of the crosslinked network.[213]

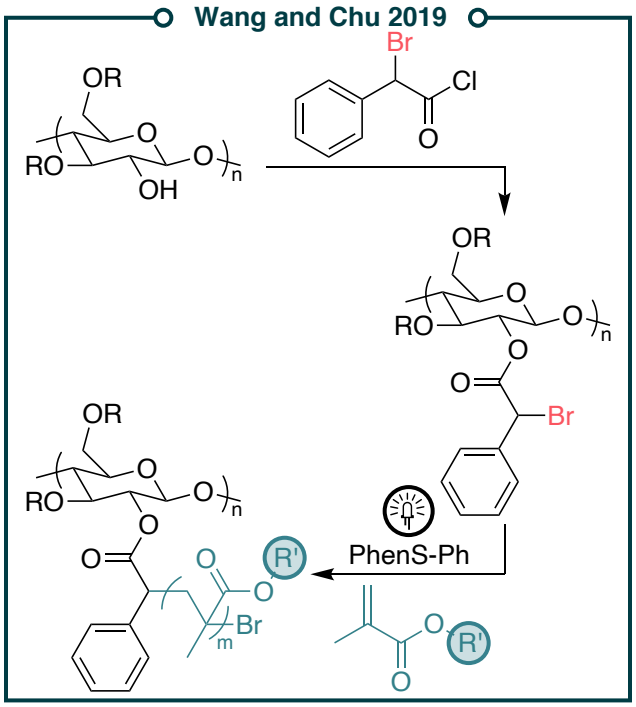

Figure 2.33. *Synthesis of graft polymers from cellulosic materials using O-ATRP.*

In addition to the grafting-from approach described above, grafting-through has also been used in the synthesis of graft polymers by O-ATRP. In this method, macromonomers – polymers bearing polymerizable end-groups – are synthesized and then polymerized to create the desired graft polymer. As such, the graft polymer backbone is formed as the macromonomers are linked

together in the polymerization. Perhaps the first example of this strategy in O-ATRP was reported by Matyjaszewski and coworkers, who synthesized poly(ethylene oxide) methacrylate lithium sulfonyl(trifluoromethylsulfonyl)imide (PEOMA-TFSI$^-$Li$^+$) – a PEG-based zwitterionic monomer for battery applications (Figure 2.34). Using O-ATRP, this monomer was polymerized with good control ($Đ$ = 1.2 to 1.4) to yield polymers with M_n tunable from 1 to 30 kDa. Through electrochemical testing, these polymers were shown to exhibit good conductivity, good electrochemical stability, and potential to suppress dendrite growth in batteries.[179]

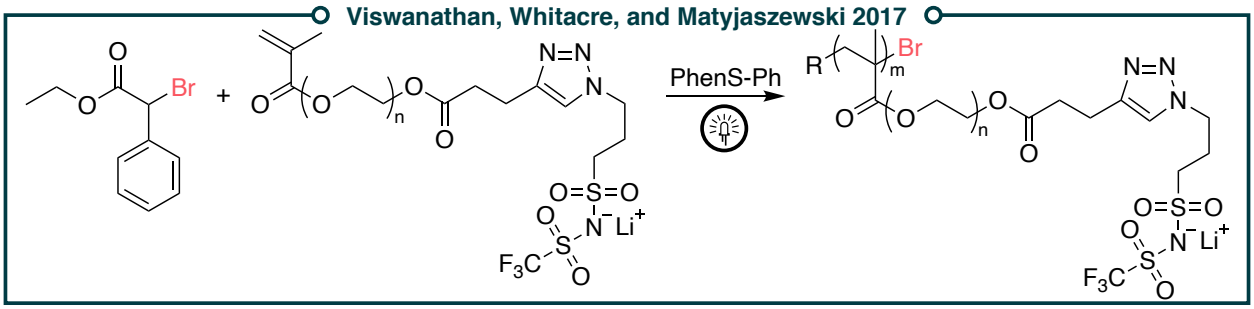

Figure 2.34. *Synthesis of polymeric electrolytes using O-ATRP.*

A similar approach to graft copolymer synthesis was later reported by Chen *et al.*, who synthesized poly(dimethylsiloxane) functionalized vinylcyclopropanes for radical ring-opening polymerization. Upon polymerization of these monomers, polymers could be obtained with $Đ$ < 1.5 and with a range of molecular weights (M_n = 67.4 kDa to 309 kDa). Further, through control of the polymerization conditions, intramolecular reorganization of the polymer backbone could be controlled to obtain a primarily linear or cyclized structure. While this feature will be discussed further in a subsequent section (see *Metal Sensitive Applications of O-ATRP*), it is worth nothing here that control over this backbone structure could enable future investigations into the impact of this structural feature on the graft polymer properties.[202]

Synthesis of hyperbranched polymers

In 2017, Yagci and coworkers showed hyperbranched polymers could be synthesized *via* O-ATRP by the simultaneous copolymerization of MMA and a methacrylate-based inimer (see *Methacrylates*). In this work, the inimer content was varied from 9% to 27%, with the resulting polymers exhibiting M_n ranging from 101 to 604 kDa and $Đ$ = 2.7 to 6.2. In addition, the resulting polymers could be chain-extended with styrene (Figure 2.35), suggesting good chain-end fidelity despite these metrics of poor polymerization control.[175] To improve upon this system, Gao and coworkers developed a similar polymerization method in microemulsion, hypothesizing that the spatial constraints created by the microemulsion would yield lower $Đ$ branched polymers. Indeed, when these polymerizations were attempted under these constraints, the resulting hyperbranched polymers exhibited much narrower molecular weight distributions ($Đ$ ~ 1.7 to 2.2), supporting the authors' hypothesis.[185] Importantly, this work also represents the only example of O-ATRP performed in microemulsion, creating opportunities for further development in this area.

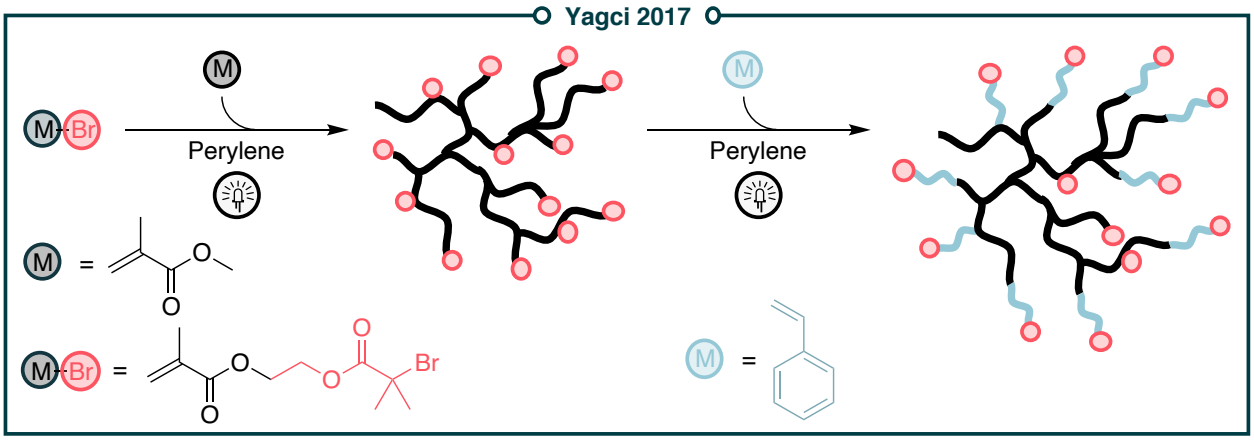

Figure 2.35. *Synthesis of hyperbranched polymers by O-ATRP through the copolymerization of MMA and a bifunctional methacrylate monomer.*

Synthesis of star polymers

First explored by Buss *et al.* in 2018[214], the synthesis of star polymers by O-ATRP has received attention from several groups in recent years. While several approaches to star-polymer synthesis exist, methods employing O-ATRP have primarily focused on the core-first approach (Figure 2.36a). In essence, this strategy involves the use of a multifunctional initiator, which during the polymerization initiates the growth of several polymer arms tethered together at the initiator center. Since the number of initiating sites on the initiator can be precisely tuned, the number of polymer arms within the star architecture can also be controlled exactly.

Highlighting the versatility of this strategy, Buss *et al.* synthesized star polymers with 2 to 8 arms using bromoisobutyrate-based multifunctional initiators (Figure 2.36b). The primary monomer chosen for these investigations was MMA, given the previous success of this monomer in O-ATRP. However, through chain-extension of PMMA star polymers, benzyl methacrylate was also incorporated into these materials. In general, polymerization control was quite good given the complexity of this architecture, with M_n = 18.3 kDa to 68.4 kDa, $Đ$ = 1.2 to 1.9, and I^* ~ 100%. As the number of polymer arms increase, polymerization control was usually lost, with $Đ$ and I^* increasing undesirably. However, this observation is not surprising and can be expected for this type of polymer architecture.[214] In later work, similar results were obtained using aryl core-substituted dihydrophenazine PCs, although at significantly reduced catalyst loadings relative to the original report above.[81]

In a similar approach, Yilmaz developed star-shaped polymers of MMA or styrene with ε-caprolactone (Figure 2.36c). In this case, the initiator had to be modified to include alcohols, which enabled the ring opening polymerization of the ester-based monomer. Nonetheless, the resulting

polymers were produced with moderate control (M_n ~ 10 to 20 kDa, $Đ$ ~ 1.3 to 1.4), highlighting the ability of O-ATRP to operate effectively in the presence of other polymerization systems.[207]

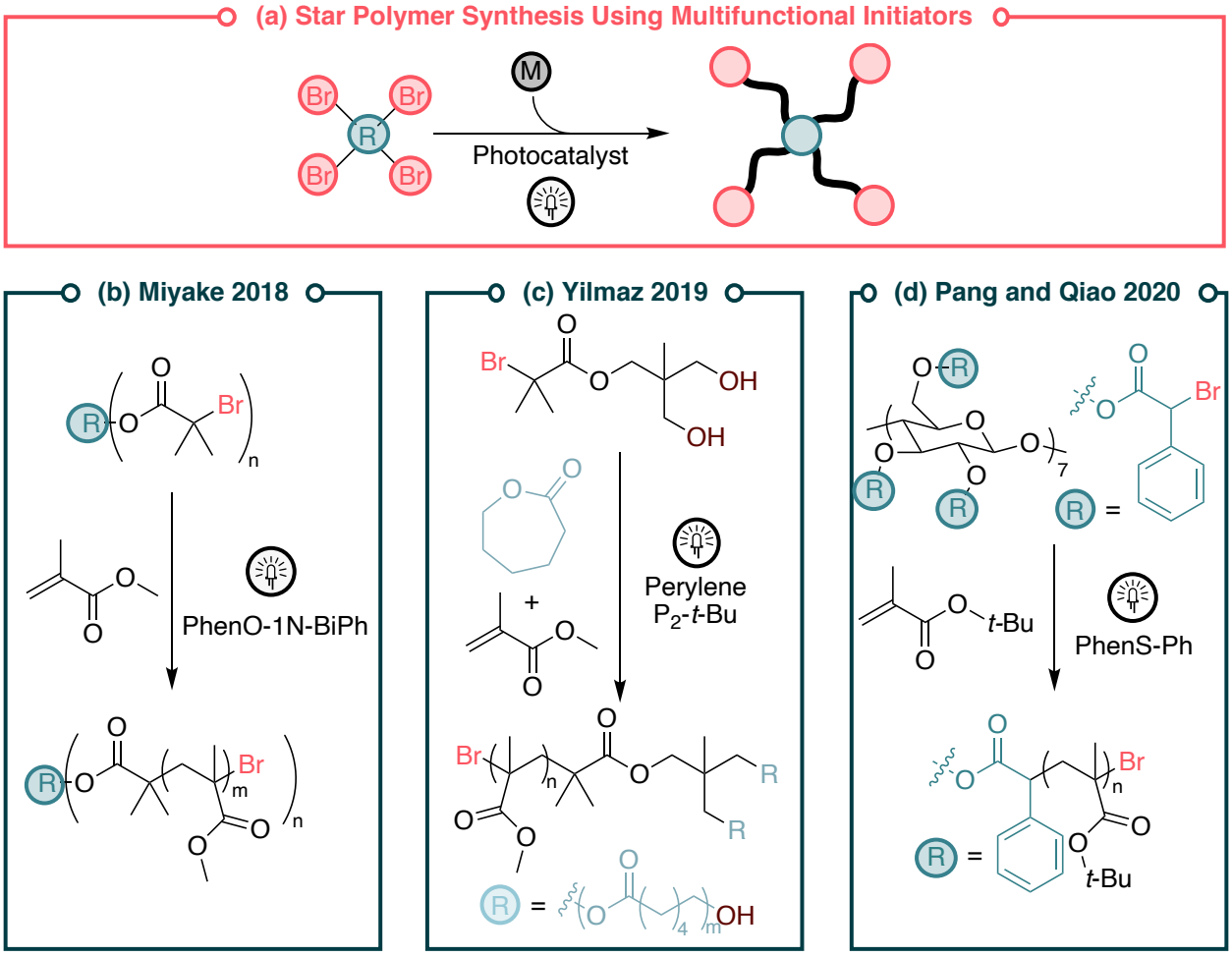

Figure 2.36. *(a) Star polymer synthesis via O-ATRP using multi-functional initiators. (b) O-ATRP from a multi-armed bromide-containing initiator. (c) Concurrent O-ATRP and ROP to produce three-armed copolymers. (d) O-ATRP from functionalized cellulosic materials to produce star polymers.*

In 2020 Pang and Qiao reported on the functionalization of β-cyclodextrin with bromophenylacetate moieties to form the core of amphiphilic star shaped polymers (Figure 2.36d). Using O-ATRP, *t*-butyl acrylate was polymerized from this core, followed by MMA to form diblock copolymer arms. The poly(*t*-butyl acrylate) block was then converted to poly(acrylic acid)

by hydrolysis, creating star polymers with hydrophilic cores and hydrophobic shells. In every case, the polymers produced showed high levels of polymerization control, including predictable molecular weights and $Đ$ typically below 1.2.[215]

Surface-initiated O-ATRP

The first example of surface-initiated O-ATRP (SI-O-ATRP) came relatively early in the development of O-ATRP. Reported by de Alaniz and Hawker in 2016, this method was first developed for the light-mediated growth of polymers tethered to silicon surfaces (Figure 2.37a,b).[216] Although this method has since been extended to a number of other materials and surfaces – such as nanoparticles (Figure 2.37c) – the principle generally remains the same: an alkyl halide initiator is tethered to a surface, after which O-ATRP is performed to generate polymer functionalities at that surface. In the report by de Alaniz and Hawker, Si wafers were functionalized with bromoisobutyrate groups, which allowed for the surface-initiated polymerization of MMA (Figure 2.38a). Unsurprisingly, this process was shown to be dependent on irradiation, where increasing the intensity of the light source increased the rate of polymer brush growth over time. In addition, the chain-end fidelity of this method was demonstrated through the synthesis of block copolymers, the success of which was determined using X-ray photoelectron spectroscopy (XPS) to identify fluoride functionalities in the second polymer block.[216]

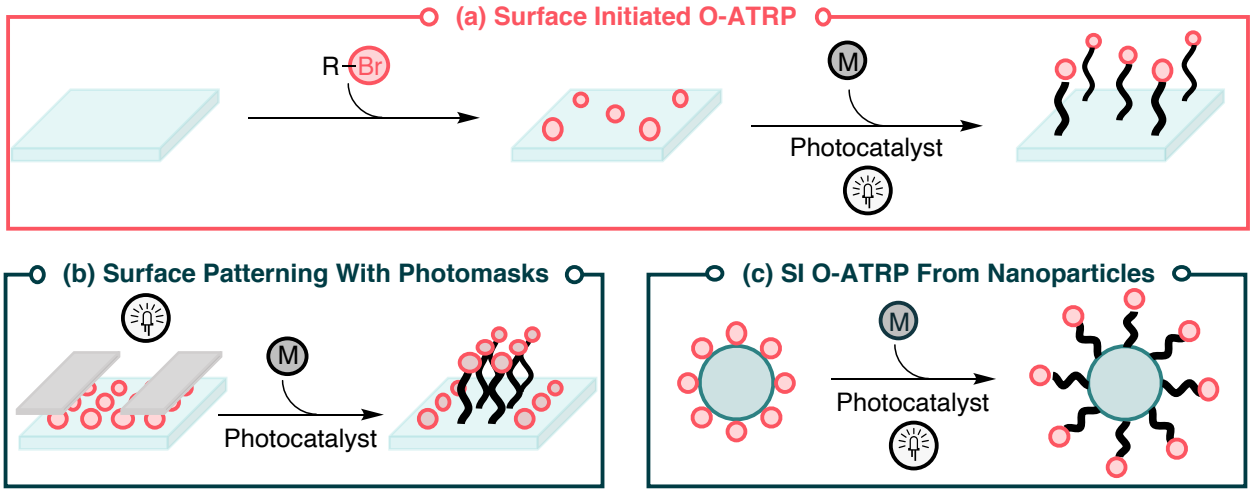

Figure 2.37. *(a) General approach to surface functionalization using O-ATRP. (b) The use of photomasks to produce patterned surfaces. (c) Functionalization of nanoparticles using SI-O-ATRP.*

Given the dependence of this polymerization on irradiation, the authors proposed surface patterning could be achieved by employing photomasks to control which parts of the surface were irradiated (Figure 2.37b). Indeed, when polymerizations were performed in the presence of a photomask, precise patterns with features on the micron scale could be achieved with excellent reliability, supporting the feasibility of this approach. In fact, this strategy could also be applied to the synthesis of block copolymers, allowing hierarchical patterns to be produced.[216]

Expanding on this method, subsequent research focused in part on the incorporation of new monomer functionalities. For example, work by Junkers and coworkers showed methacrylic acid could be grafted to Si surfaces (Figure 2.38b), the presence of which was probed using XPS and secondary ion mass spectrometry (SIMS).[170] In another case, Hawker and coworkers developed methacrylates based on emissive Ir complexes, which were polymerized through surface initiated O-ATRP to produce patterned, emissive surface coatings. This second example also showed these polymerizations could be performed under ambient conditions (i.e. under air), as long as a glass

cover slip was placed above the reaction solution to minimize the diffusion of air into the polymerization.[177]

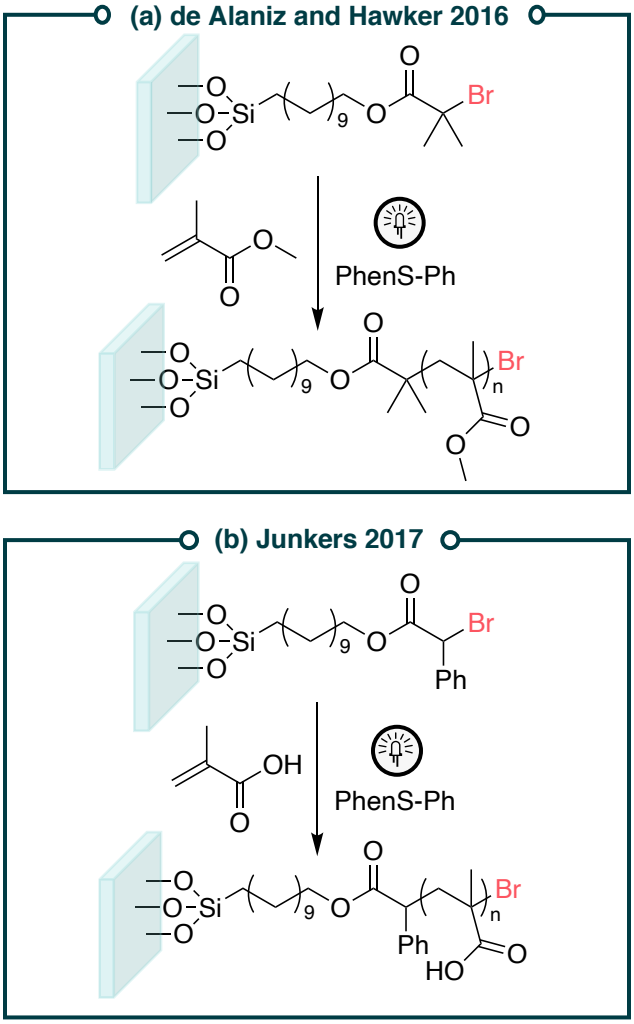

Figure 2.38. *Two approaches to SI-O-ATRP from silicon for the polymerization of MMA (a) and MAA (b).*

Of course, Si is not the only material of interest for surface functionalization, so some of the research in this field has focused on expanding surface-initiated O-ATRP to other materials. In one example, Tang, Xu, Zhou, and coworkers developed the surface-initiated polymerization of semi-fluorinated methacrylates on indium tin oxide (ITO) and fluorine doped tin oxide (FTO) glass

to improve the durability and hydrophobicity of these materials.[217] In a similar approach to that reported by Hawker,[216] the surfaces of ITO and FTO glass were functionalized with a bromoisobutyrate initiator fragment, from which O-ATRP was performed with PhenS-Ph as the catalyst. Through optical characterization of the functionalized surfaces, it was shown the polymer coating had minimal influences on the transmittance of the glass. Further, when the conductivity of the polymer functionalized ITO glass was characterized, it was discovered that films up to 1 μm in thickness had a minimal impact on the conductivity of the ITO. As such, the authors demonstrated successful functionalization of these materials with minimal impact on their desirable properties.[217]

In addition, surface-initiated O-ATRP has been used to tether polymer films to a number of electrode surfaces for electrochemical sensing applications. The first report of this type came in 2017 from the group of Yue Sun, who prepared poly(acrylamide-*block*-methacrylic acid) copolymers tethered to gold electrodes for the detection of lead ions. Like previous reports, the presence of the surface-bound polymer was probed using XPS. In addition, testing of the sensor revealed it could operate over a large linear range ($[Pb^{2+}] = 10^{-11}$ to 10^{-4} M) with a low limit of detection (2.5×10^{-12} M) and excellent selectivity for Pb^{2+} in the presence of other metal ions.[190]

Unfortunately, not all sensors exhibit high selectivity for the target analyte, and creating a selective sensor can sometimes be challenging. To address this issue, one strategy uses molecularly imprinted polymers, where polymerizations are performed in the presence molecular template to create a polymer network around the template. After the polymerization, the template is removed, leaving behind a cavity in the polymer network designed to selectively bind the template molecule during sensing applications (Figure 2.39a).[218]

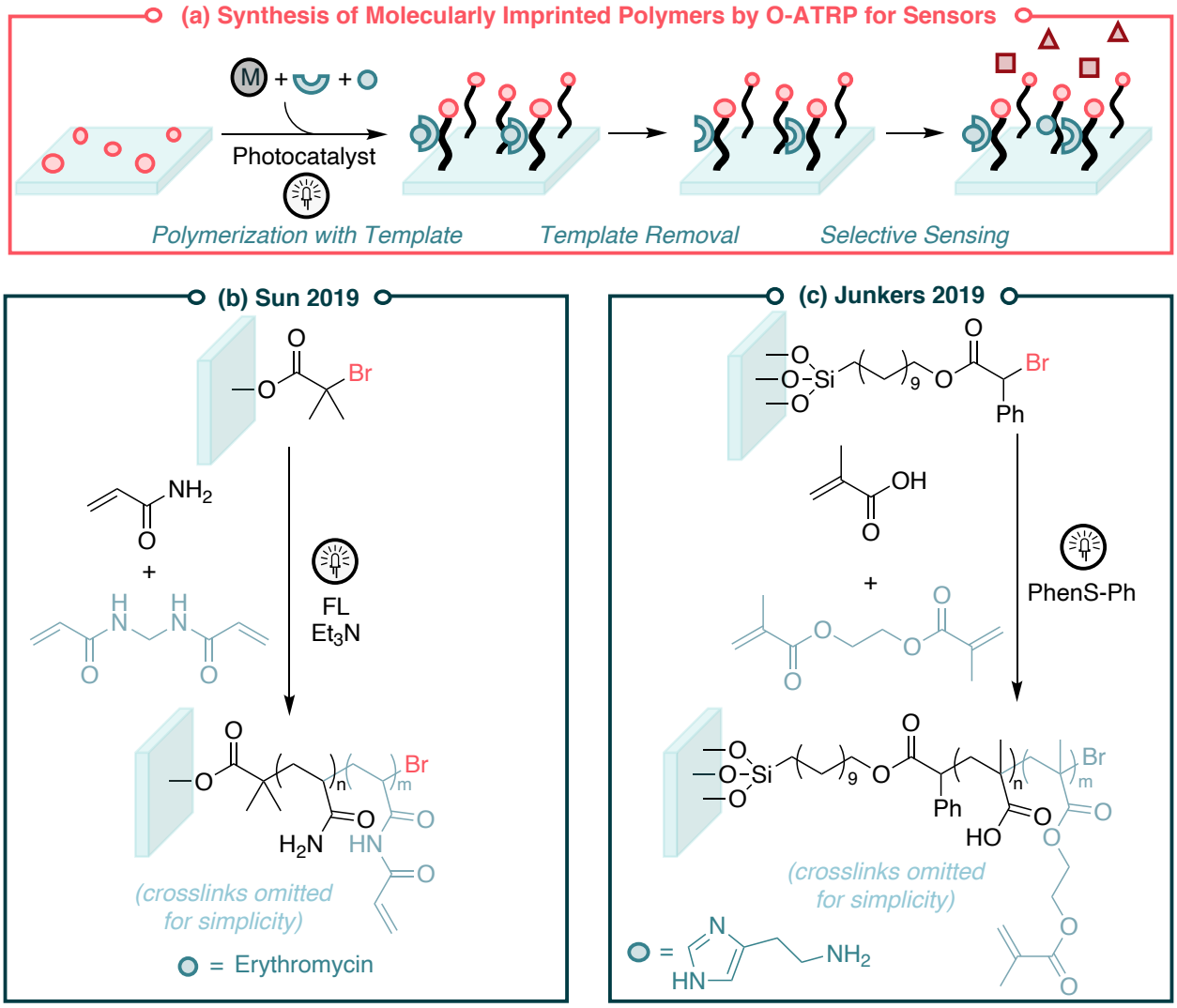

Figure 2.39. *(a) General design strategy for selective sensors by electrode functionalization using O-ATRP and molecular imprinting. (b) Copolymerization of acrylamide and a bifunctional acrylamide monomer using erythromycin as the molecular imprinting template. (c) Copolymerization of MAA and a bifunctional methacrylate using histamine as the molecular imprinting template.*

The first application of O-ATRP in molecular imprinting was reported by Sun and coworkers, who used fluorescein to copolymerize acrylamide and an acrylamide-based crosslinker on modified Au electrodes (Figure 2.39b). Erythromycin was chosen as the molecular template, as this molecule was also the target analyte the authors ultimately wanted to measure. After the polymerization and removal of the template molecule, the selectivity of the functionalized

electrode was tested by measurement of a range of analytes. Interestingly, the greatest response was obtained for erythromycin, demonstrating the success of this method. In addition, the reported sensor featured a large linear range ([Erythromycin] = 10^{-8} to 10^{-1} M) and low limit of detection (3.2×10^{-9}), suggesting the sensor is both selective and sensitive.[191]

In a similar approach, Junkers and coworkers prepared molecularly imprinted polymers for the detection of histamine using O-ATRP catalyzed by PhenS-Ph. This time, methacrylic acid was copolymerized with a methacrylate-based crosslinker from a modified titanium electrode (Figure 2.39c). When the sensitivity of the resulting electrode was compared to that of an unfunctionalized electrode, it was shown that molecular imprinting significantly increased the sensitivity of the electrode to histamine. However, when the selectivity of the sensor was investigated, it was discovered that histidine could also produce an interfering response, potentially limiting the reliability of this sensor.[176]

In addition to these reports, several other examples exist of O-ATRP being applied to generate polymeric coatings tethered to electrode surfaces. For instance, Kong and coworkers used surface initiated O-ATRP to grow ferrocenylmethyl methacrylate polymers from surface-bound DNA on Au electrodes.[178] Instead, Chen, Bain, and coworkers used surface initiated O-ATRP catalyzed by Eosin Y to polymerize glycidyl methacrylate at the surface of carbon nanotubes, which there then used as nanoprobes to improve the detection of carcinoembryonic antigen and α-ferroprotein through an electrochemical method.[219] Finally, in an example from the group of Yue Sun, immunoglobulin G imprinted polymers were prepared at the surface of a modified Au electrode using O-ATRP catalyzed by fluorescein.[220] In each of these examples, the wide range of functionalities tolerated both within monomers and other components of the sensors highlights the incredible versatility of O-ATRP.

Another common application of surface-initiated O-ATRP is in the functionalization of nanoparticles. Here, the use of a controlled polymerization is critical, as termination reactions such as radical coupling can rapidly lead to discrete nanoparticles coupling to each other and forming an interconnected network. As such, the high degree of polymerization control obtainable through O-ATRP positions this method well for use in the functionalization of discrete nanoparticles.

The first example of O-ATRP being applied in this fashion came again from de Alaniz and Hawker. In addition to functionalizing Si surfaces, these authors showed their method could be applied to SiO_2 nanoparticles, the success of which was evaluated by transition electron microscopy (TEM). Following up on this work, which primarily used a bromoisobutyrate-derived initiator,[216] Matyjaszewski showed similar results could be obtained using a bromophenylacetate-based initiator (Figure 2.40). More importantly, Matyjaszewski's report showed that greater polymerization rates and grafting densities could be obtained using bromophenylacetate initiators, enabling the density of polymer chains on the nanoparticle surface to be tuned.[221]

In an application of this method, Li and Wang demonstrated that SiO_2 nanoparticles functionalized using O-ATRP could be employed in drug delivery, where a drug is encapsulated in the polymer network and then released through exposure to a stimulus (see *Metal Sensitive Applications of O-ATRP*). In this case, a pH sensitive polymer, poly(diethylamino ethyl methacrylate), was grafted to the SiO_2 surface and loaded with Quercetin – a potential anticancer drug. When the functionalized nanoparticles were then placed in solution, drug release was controlled by increasing the pH of the solution. Through protonation of the polymer pendant groups, electrostatic repulsions caused the polymer chains to expand, leading to the release of the encapsulated drug.[222] Similar results were obtained when SBA-15 was used as the substrate for polymer grafting.[223]

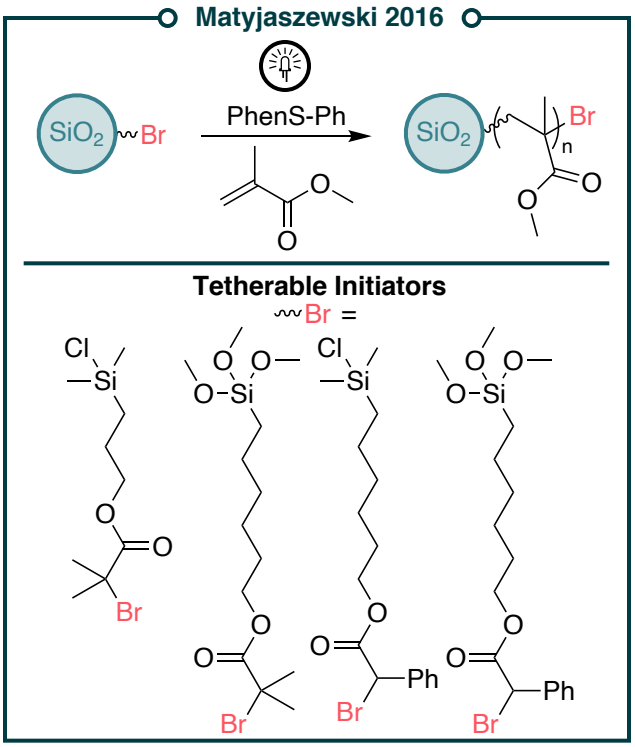

Figure 2.40. *SI-O-ATRP from silica nanoparticles using different initiators.*

In related research, other groups have applied surface-initiated O-ATRP to the functionalization of other nanoparticle materials, such as hollow SiO_2 spheres and mesoporous SiO_2. In the former example, MMA and NIPAM were polymerized from the surface of SiO_2 hollow spheres to improve their dispersibility in water.[224] In the latter case, several groups have reported on the functionalization of SBA-15,[188, 225-227] a mesoporous SiO_2 material developed by researchers at the University of California at Santa Barbara.

The first example using this material came from Li and coworkers in 2017, who showed SBA-15 functionalized with bromoisobutyrate moieties could be used to initiate the polymerization of MMA, dimethylamino ethyl methacrylate, and NIPAM. In each case, PhenS-Ph was employed as the O-ATRP catalyst. The resulting materials showed improved absorption of toluene for purification of contaminated aqueous solutions.[188] In later work, Zhang and coworkers showed similar materials could also be obtained using fluorescein as the catalyst (Figure 2.41).[225]

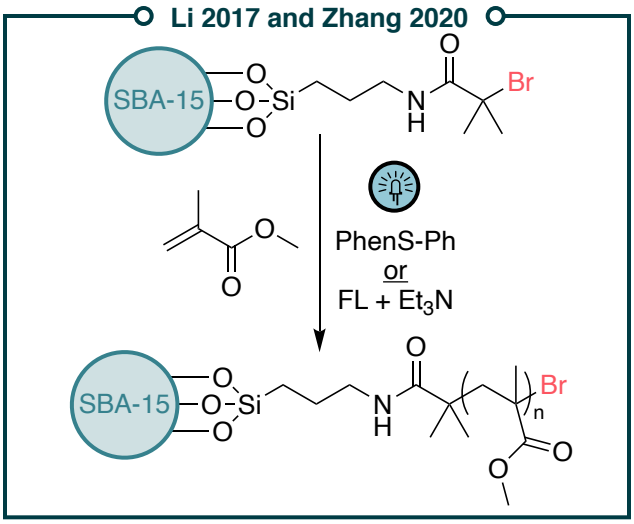

Figure 2.41. *SI-O-ATRP from SBA-15 nanoparticles.*

To understand how various reaction components impact these polymerizations, Zhang and coworkers performed a systematic investigation of the polymerization of MMA from SBA-15. To analyze polymerization control, the surface-bound PMMA was cleaved from the SBA-15 and characterized. As a result, the authors discovered the polymer $Đ$ could be lowered through increasing the solvent quantity in the polymerization, as well as increasing the amount of sacrificial amine used in conjunction with fluorescein. Interestingly, changing the quantity of added amine did not impact the molecular weight of the polymer. However, a link between the concentration of monomer and molecular weight was established, enabling predictable control over polymer molecular weight in this method.[226]

Work by Xu, Zhang, Wei, and coworkers focused on the applications of these materials, showing that they can be used for drug delivery and biological imaging when functionalized with fluorescent groups. In this case, the fluorescent moiety was a surface-bound PhenS-Ph derivative, which also served as the PC for the copolymerization of PEG methacrylate and itaconic acid. When the polymerizations were complete, cell uptake was probed using optical and fluorescence microscopy, and pH-dependent drug release was demonstrated under acidic conditions.[227]

In addition to these SiO_2 based materials, a number of other nanoparticles have been modified using surface-initiated O-ATRP. These include ceria nanoparticles[174], nanodiamond[180], rare earth doped upconversion nanoparticles[183], magnetic Fe_3O_4 nanoparticles[228, 229], ferroelectric $BaTiO_3$ nanoparticles[230], cellulose nanocrystals[231], and Eu^{3+} doped luminescent hydroxyapatite[232-234]. In particular, the functionalization of hydroxyapatite nanorods by O-ATRP has received considerable attention, with target applications including biological imaging and drug delivery. Often, surface functionalization of the nanorods is used to improve their solubility and cell-uptake properties, with the most common monomer being PEG methacrylate (Figure 2.42).[232, 234] However, other monomers have also been employed, including 2-methacryloyloxyethyl phosphorylcholine – a zwitterionic methacrylate – and itaconic acid, which were used to transport cisplatin into HeLa cells.[233]

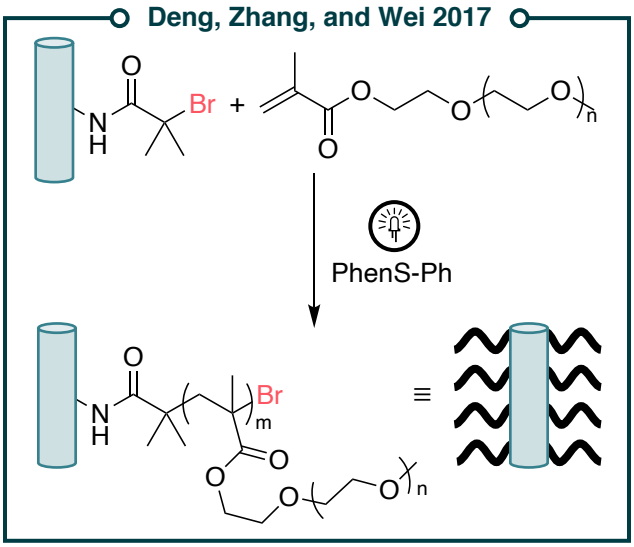

Figure 2.42. *Surface functionalization of hydroxyapatite nanoparticles for biological imaging via SI-O-ATRP.*

One final application of surface-initiated O-ATRP that has been under development is in the synthesis of self-healing hydrogels. Typically, these materials have been achieved through the

surface-initiated polymerization of 4-vinylpyridine on various nanoparticles, followed by the free radical polymerization of acrylic acid in the presence of these functionalized nanoparticles.[193-196] As a result, the pyridine moiety undergoes protonation by acrylic acid, generating ionomers that are electrostatically attracted to each other. Upon application of a force to the bulk material, these electrostatic interactions can be disrupted, leading to separation of the polymer chains and ultimately mechanical failure of the material. However, since these noncovalent interactions can be easily reestablished, self-healing properties are often observed (Figure 2.43).

In the first example of O-ATRP being used in this manner, SiO_2 nanoparticles were functionalized with poly(4-vinylpyridine) using Rhodamine B as the catalyst (Figure 2.43b).[193] Since then, various other materials have also been employed, including cellulose nanocrystals[194], porous carbon nanospheres[195], and carbon nanotubes[196]. However, regardless of the specific nanomaterial chosen, similar results are generally observed. The hydrogels produced can be broken and healed within a few hours, with up to 90% retention of the material's original tensile strength after healing.

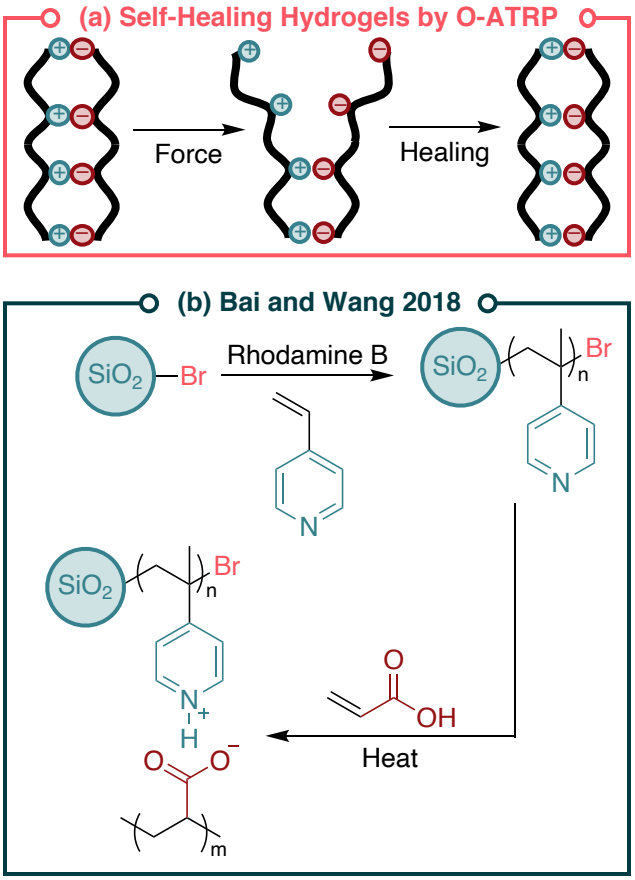

Figure 2.43. *(a) General principle behind self-healing materials produced by O-ATRP. (b) Polymerization of 4-vinyl pyridine on silica nanoparticles to produce self-healing hydrogels using O-ATRP.*

Synthesis of polymers in continuous flow

While there are several advantages to using O-ATRP over other methods, it also features several limitations. Perhaps one of its biggest limitations is one that is experienced often in photochemistry: scalability. The issue with scaling photochemical reactions is that it is often very difficult to maintain uniform irradiation of the reaction solution at large reaction volumes (i.e. more than a few mL). To address this issue, many have employed photochemical flow reactors,[107, 108, 235] where the reaction is passed through clear tubing surrounding a light source to ensure each part of the reaction is consistently and uniformly irradiated (Figure 2.44a). As a result, reactions

performed in flow can in theory be scaled limitlessly, as long as the necessary reagents and reaction components can be supplied to the reactor.

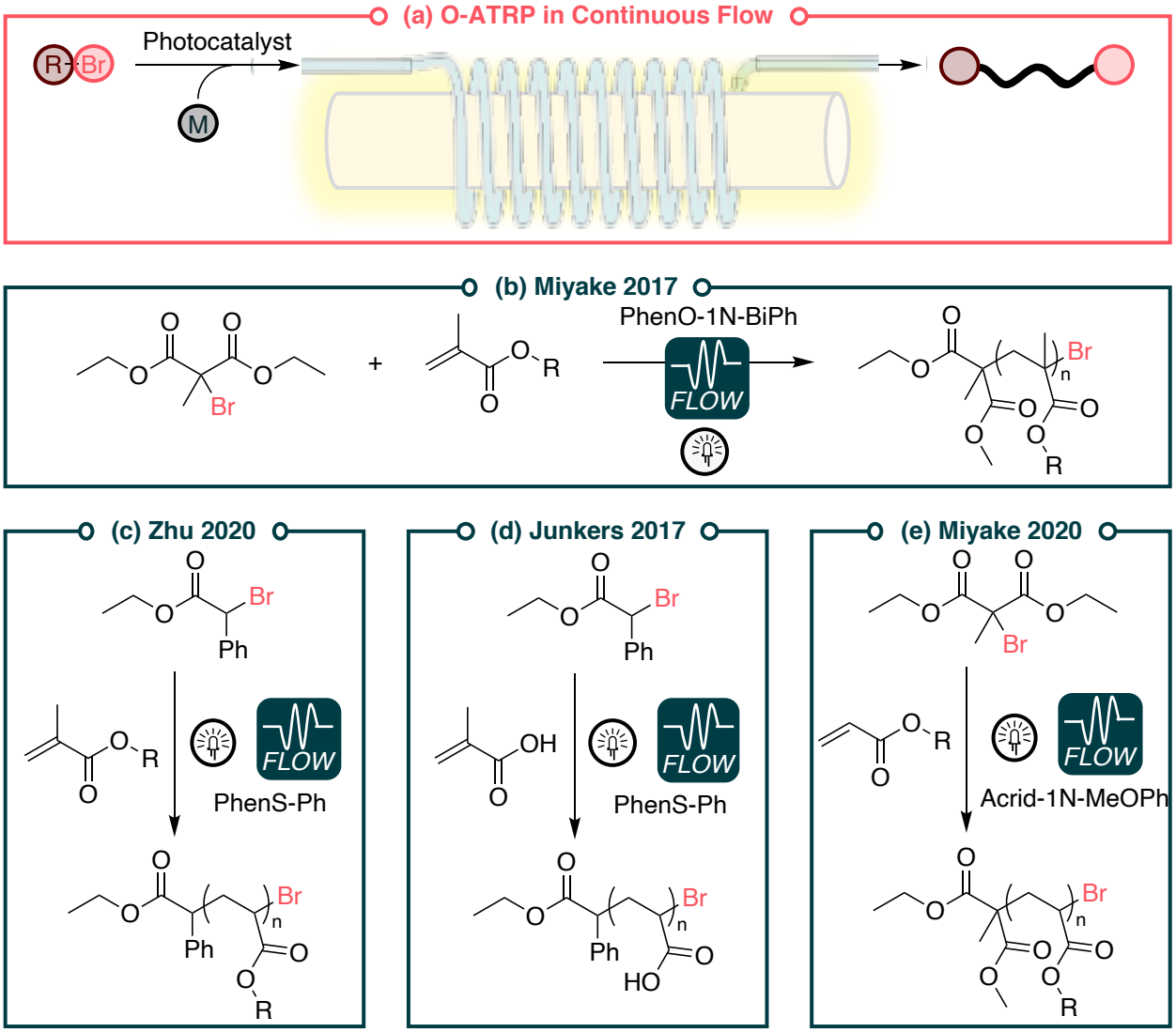

Figure 2.44. *(a) Synthesis of polymers by O-ATRP in a continuous flow reactor. (b) O-ATRP of methacrylates in flow. (c) O-ATRP of methacrylates in flow using PhenS-Ph as the PC. (d) O-ATRP of MAA in flow. (e) O-ATRP of acrylate monomers in flow.*

As such, the issue of scalability in O-ATRP has been addressed to some degree using continuous flow reactors. The first report of this type came in 2017 from Ramsey *et al.* (Figure 2.44b), who showed various methacrylates could be polymerized in the presence of phenoxazines,

phenazines, and even perylene in flow. In many cases, good polymerization control was demonstrated ($Đ \leq 1.2$, $I^* \sim 100\%$) even at reduced catalyst loadings (1000 ppm: $M_n = 6.1$ kDa, $Đ = 1.2$, I* = 95%; 100 ppm: $M_n = 7.1$ kDa, $Đ = 1.3$, I* = 90%, both with PhenO-1N-BiPh). This reduction in catalyst loading was hypothesized to be possible due to the improved irradiation conditions in a continuous flow reactor, demonstrating another advantage to this reactor design. Further, molecular weight control was demonstrated by varying the residence time of the reaction – the amount of time it takes to pass through the full length of the reactor tubing – enabling the same control over polymer structure that can be obtained under batch reaction conditions by varying reaction time.[155]

In subsequent work by Hu, Zhu, and coworkers, the application of O-ATRP using phenothiazine derivatives to a flow reactor was also investigated (Figure 2.44c). In this case, the authors investigated the effect of varying the reactor tubing diameter, as this factor could influence mixing and irradiation of the reaction solution. Ultimately, they found that the tubing diameter can significantly impact both $Đ$ and I^*, but that either too small or too large of a diameter can negatively impact polymerization control. In other words, an intermediate size exists where the best polymerization results can be achieved. In this case, a 2 mm inner diameter was optimal. In addition, the authors showed this method could be performed with a series of phenothiazine PCs, but that PhenS-Ph ultimately gave the best polymerization control in the O-ATRP of MMA.[92]

Expanding on the scope of O-ATRP in flow, Rolando and coworkers showed Eosin Y could also be employed with this reactor design. In the polymerization of MMA, this system gave moderate polymerization control, with good I^* ($I^* \sim 100\%$) and moderate dispersity ($Đ \sim 1.4$).[236] In addition, others have shown a wide range of monomers can be polymerized using O-ATRP in

flow, such as methacrylates[155], methacrylic acid (Figure 2.44d)[170], acrylates (Figure 2.44e)[65], and styrene[92].

Metal sensitive applications of O-ATRP

One of the most commonly cited metal sensitive applications of ATRP is in electronics, which is also one of the areas where the superiority of O-ATRP over traditional, metal-catalyzed ATRP has been demonstrated. In the work by Zhang and coworkers, O-ATRP was employed to synthesize graft copolymers from the backbone of P(VDF-*co*-CTFE) (see *Synthesis of Graft Polymers*). The ultimate goal of this work was to produce more efficient dielectric materials for energy storage applications, which the authors hoped to achieve by grafting insulating polymer chains to P(VDF-*co*-CTFE). In turn, it was hypothesized these insulating chains would reduce interactions between neighboring P(VDF-*co*-CTFE) domains, leading to less energy loss and improved electronic properties. However, the authors also hypothesized the use of metal catalyzed ATRP would be detrimental to the electronic properties of the product polymers, as residual metal ions remaining in the polymer matrix could migrate under an applied electric field and lead to undesirable energy loss. As such, they proposed O-ATRP would produce materials with enhanced performance relative to Cu catalyzed ATRP.[237]

To test this hypothesis, Zhang and coworkers used both O-ATRP and Cu catalyzed ATRP to grow PMMA from the C-Cl bonds in the P(VDF-*co*-CTFE) backbone. The dielectric properties of the resulting materials were then tested, which revealed undesirable ion migration in the polymers prepared by Cu catalyzed ATRP. By contrast, this issue was not observed in the polymers prepared by O-ATRP, indicating superior electronic properties as hypothesized. As such, this

report represents one of the first examples demonstrating a clear advantage of O-ATRP over traditional, metal catalyzed ATRP.[237]

In another example, Matyjaszewski and coworkers employed O-ATRP for the synthesis of graft copolymer-based electrolytes for battery applications. While it is possible that metal contamination arising from traditional ATRP methods could also be problematic in this application, this issue was not evaluated in this work.[179] Similarly, another possible application of O-ATRP in a metal sensitive system has been toward functionalizing electrode surfaces for electrochemical sensors (ex. for the detection of Pb^{2+}), although it has not be evaluated whether O-ATRP has a clear advantage over metal catalyzed ATRP.[190] Moving forward in the development of this method, further studies in these areas directly comparing materials produced by metal catalyzed ATRP and O-ATRP could be beneficial.

Another commonly cited metal-sensitive application of ATRP is in biological materials, such as those for biological imaging and drug delivery. Indeed, a number of reports exist for the application of O-ATRP in these areas,[174, 222, 223, 227, 232-234] with one notable example being that by Deng, Zhang, and Wei in 2017 (Figure 2.45). In this work, Eu^{3+} doped hydroxyapatite was functionalized using surface-initiated O-ATRP, such that the functionalized nanoparticles could be loaded with cisplatin and introduced into living cells. After HeLa cells were incubated with these materials, the fluorescent properties of the nanoparticles were exploited for cell imaging to confirm cell uptake. Further, the pH responsiveness of the polymer functionalities was employed to release cisplatin into the cell, demonstrating the potential for these nanoparticles to be used in drug delivery applications.[233]

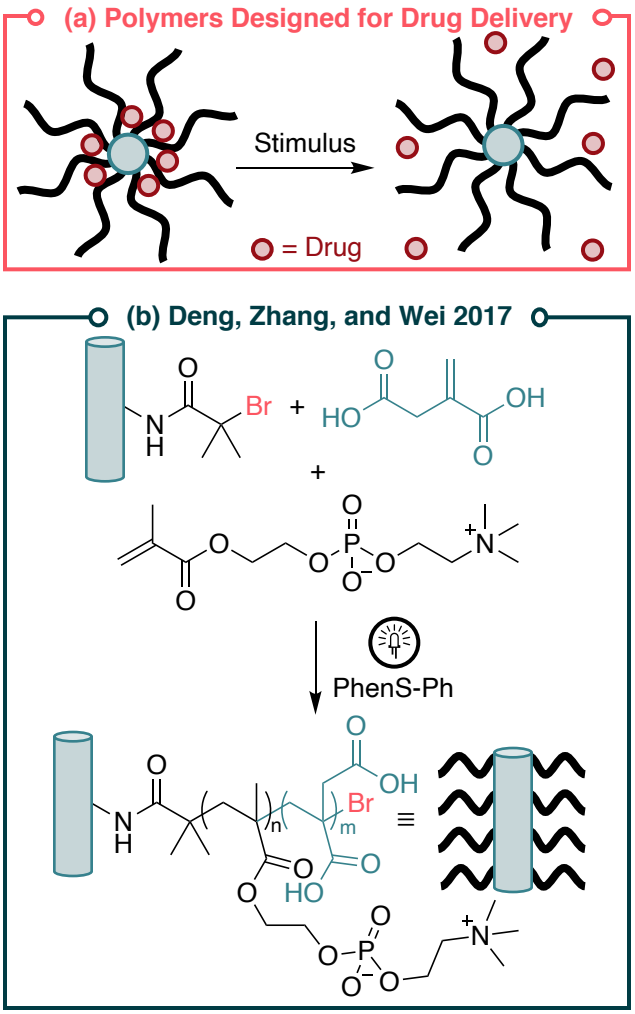

Figure 2.45. *(a) One polymeric drug delivery strategy. (b) Functionalization of hydroxyapatite for drug delivery and biological imaging.*

Although concerns of metal contamination in biological applications are often cited as a motivation for O-ATRP, it is worth noting this is a somewhat nuanced issue. For example, while some metals may pose toxicity concerns, not all metals are toxic, and this point certainly applies to the metal catalysts employed in ATRP as well. In fact, some have shown that ATRP can even be performed using nontoxic Cu dietary supplements.[238] It is also worth noting that some of the catalyst families employed in O-ATRP (ex. phenazines and phenothiazines) are known to be biologically active,[239-247] although their effect in humans is still unclear. As such, further research

is necessary to truly understand whether many of the catalysts employed in O-ATRP are biocompatible.

Another important area in which O-ATRP has a clear advantage over metal catalyzed ATRP is in the polymerization of coordinating monomers. In traditional ATRP, such monomers have typically been challenging because their coordination to the metal catalyst can alter catalytically relevant properties.[199, 200] As a result, the complex formed upon coordination may not be well suited to mediate ATRP. One way to address this issue is through the use of organic catalysts, such as in O-ATRP. The first example demonstrating this advantage was the seminal report by Hawker and coworkers, which showed PhenS-Ph could control the polymerization of dimethylamino ethyl methacrylate while a metal-based catalyst could not.[33]

In addition to this example, Chen *et al.* showed various vinylcyclopropanes could be successfully polymerized by O-ATRP with excellent control over the resulting polymer structure.[201, 202] While this monomer family was previously polymerized using Cu catalyzed ATRP, the polymerizations were limited to low monomer conversion. Further, control over the backbone configuration – which can either be linear or undergo rearrangement to a cyclic structure (Figure 2.46) – was poor in this method.[198] By contrast, the polymerization of these monomers under O-ATRP conditions (Figure 2.46) yielded high monomer conversion (> 90%) and excellent control over the backbone configuration (13% to 97% linear vs. cyclic) through modulating the reaction conditions, thus demonstrating the advantage of an organocatalyzed method with this monomer family.[201]

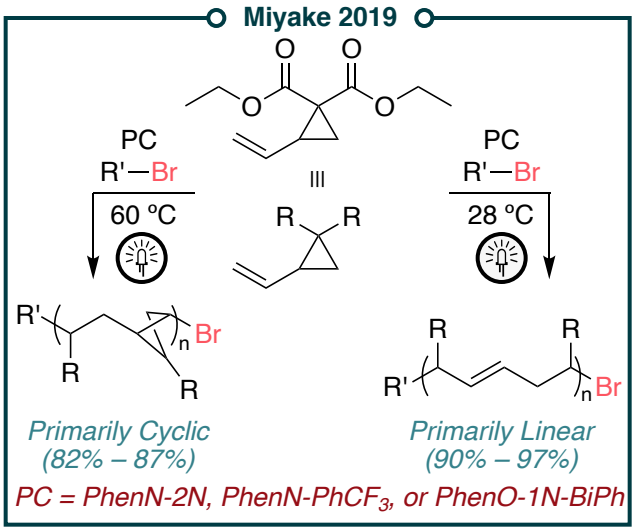

Figure 2.46. *Polymerization of a coordinating monomer by O-ATRP with control over polymer backbone composition.*

Conclusions and future directions

In this review, we have attempted to summarize developments in O-ATRP for both new practitioners and veterans in the field. In the context of other metal-free CRPs, O-ATRP is an excellent method for the precise polymerization of acrylates, methacrylates, styrene, and vinylcyclopropanes using commercially available reagents. While a limited number of strongly reducing PCs are currently available from commercial sources, continued development in the design of such PCs is beginning to address this limitation. In addition, the application of reductive quenching PCs in O-ATRP, such as eosin Y and fluorescein, will help to address this issue given the greater availability of these compounds.

We have also attempted to provide a comprehensive review of the materials produced by this method, as well as its various applications in precision polymer synthesis. In particular, the tolerance of O-ATRP to a wide range of chemical functionalities has been one of its primary advantages, especially with respect to coordinating functionalities that are poorly tolerated in traditional metal-catalyzed ATRP methods. As a result, O-ATRP has found use in a wide range of

applications, ranging from the synthesis of polymers with complex architectures through concurrent and orthogonal methods, to drug delivery and biological imaging. Indeed, we are excited to see the many new applications in which this method will be used in the coming years.

Moving forward in the development of O-ATRP, we anticipate key challenges to overcome will include:

(1) Developing a better understanding of the mechanism of O-ATRP, both in the presence of oxidative and reductive quenching PCs. In both cases, developing a detailed understanding of the activation and deactivation processes will be crucial for identifying and overcoming limitations in the mechanism of O-ATRP. While the work highlighted in this review has begun to elucidate these mechanistic details, future work should focus on investigating a wider range of PCs and developing a more generalized understanding of the O-ATRP mechanism.

(2) Developing a general understanding of solvent effects in O-ATRP. Currently, knowledge surrounding solvent effects in this method is largely focused on dihydrophenazine PCs, since these are the catalyst that have mostly been employed in solvent effect studies thus far. However, similar solvent effects have not yet been reported for other PCs, possibly due to differences in their chemical structures and photophysical properties. As such, further work is necessary in this area to understand how solvent properties impact other PC families, with the ultimate goal being a generalized model to understand and predict solvent effects across a range of O-ATRP catalysts.

(3) Identifying important characteristics for successful initiators in O-ATRP. Aside from limited initiator screens and work investigating the impact of the halide identity (i.e. alkyl bromides vs. chlorides), little is known about the initiator in O-ATRP. In the coming years, systematic investigations of O-ATRP initiators would be beneficial to understand how this reaction

variable impacts control over the product polymer structure. In particular, if there are any special requirements for O-ATRP that are not present in other ATRP methods, identifying them would be of significant interest. In addition, since O-ATRP catalysts operate through outer sphere electron transfer (as opposed to inner sphere electron transfer as observed with many traditional ATRP catalysts), perhaps the use of new initiators may be possible in O-ATRP that cannot be employed in traditional ATRP methods.

(4) Expanding the monomer scope of O-ATRP, especially to monomers that are inaccessible by metal-catalyzed methods. While any advancements in the monomer scope of O-ATRP will certainly be useful to the field, it is our hope that future work will expand beyond applications that are already accessible through other methods to those that are currently inaccessible using ATRP. One example of such monomers could be α-olefins, which can be difficult to polymerize by ATRP due to the strong C-Br bond that forms at the end of the polymer chain during polymerization. Due to the strength of this bond, activation of the chain-end can be extremely challenging using traditional ATRP catalysts. However, it may be possible for some O-ATRP catalysts to reduce this bond, enabling the polymerization of this elusive class of monomers. As such, further investigation in this area is warranted.

(5) Developing new catalysts that are effective, easy to synthesize, and inexpensive. Currently, few catalysts exist that meet all three of these criteria. For example, many reductive quenching PCs (ex. xanthenes) are inexpensive and readily available for purchase, but the level of control they offer in O-ATRP is often lower than that available using oxidative quenching PCs (see *Oxidative and Reductive Quenching Mechanisms*). However, many oxidative quenching PCs (ex. phenoxazines) require multiple-step syntheses that can increase the barrier to using O-

ATRP as a non-expert. As such, the development of PCs that are highly effective, easy to synthesize or purchase, and inexpensive will have a significant impact on the field.

(6) Understanding the toxicity of O-ATRP catalysts, such that they can be employed in biological applications without the need for polymer purification. Since many of the catalysts employed in O-ATRP have only recently been developed, little information is known regarding their effects on biological organisms. Despite this fact, one of the most cited potential applications of O-ATRP is in biological applications. As such, research is critically needed to understand the biological effects of common O-ATRP PCs to ensure the compatibility of this method with sensitive biological systems.

(7) Expanding the range of irradiation wavelengths that can be employed in O-ATRP to longer wavelengths that can penetrate biological tissue, enabling *in-vivo* applications of O-ATRP. Since longer wavelengths of light possess less energy than shorter wavelengths, thermodynamic restrictions may arise in which a single photon of light cannot impart enough energy to a PC for reduction of a C-Br bond. However, new photochemical processes employing two-photon excitations may be beneficial in this area, allowing a PC to harness the energy of multiple photons to access higher-energy excited states capable of activation in O-ATRP.

(8) The ability to synthesize high molecular weight polymers. Current O-ATRP methods typically produce polymers with $M_n \sim 1$ to 50 kDa, but polymers with $M_n > 100$ kDa are not uncommon using other polymerization techniques. Future work should seek to elucidate why this limit exists, as well as how it can be overcome.

(9) The ability to achieve high or quantitative monomer conversion. Especially with regards to the synthesis of block-copolymers, achieving this property will be crucial for increasing the accessibility of this method.

By continuing to address these challenges, O-ATRP will continue to be established as a powerful metal-free strategy for the synthesis of precision polymers in a variety of advanced applications and fields.

REFERENCES

(1) Matyjaszewski, K.; Xia, J. H. Atom transfer radical polymerization. *Chem. Rev.* **2001,** *101*, 2921–2990.

(2)Braunecker, W. A.; Matyjaszewski, K. Controlled/living radical polymerization: features, developments, and perspectives. *Prog. Polym. Sci.* **2007,** *32*, 93–146.

(3) Matyjaszewski, K., Atom transfer radical polymerization (ATRP): current status and future perspectives. *Macromolecules* **2012,** *45*, 4015–4039.

(4) Krys, P.; Matyjaszewski, K., Kinetics of atom transfer radical polymerization. *Eur. Polym. J.* **2017,** *89*, 482–523.

(5) Matyjaszewski, K., Advanced materials by atom transfer radical polymerization. *Adv. Mater.* **2018,** *30*, 1706441.

(6) Corrigan, N.; Jung, K.; Moad, G.; Hawker, C. J.; Matyjaszewski, K.; Boyer, C., Reversible-deactivation radical polymerization (controlled/living radical polymerization): from discovery to materials design and applications. *Prog. Polym. Sci.* **2020,** *111*, 101311.

(7) Odian, G. G. *Principles of polymerization*. 4th ed.; Wiley: Hoboken, N.J, 2004.

(8) Wang, J. S.; Matyjaszewski, K. Controlled/"living" radical polymerization. Atom-transfer radical polymerization in the presence of transition-metal complexes. *J. Am. Chem. Soc.* **1995,** *117*, 5614–5615.

(9) Kato, M.; Kamigaito, M.; Sawamoto, M.; Higashimura, T. Polymerization of methyl-methacrylate with the carbon tetrachloride/dichlorotris(triphenylphosphine)ruthenium(II)/methylaluminum bis(2,6-di-tert-

butylphenoxide) initiating system: possibility of living radical polymerization. *Macromolecules* **1995,** *28*, 1721–1723.

(10) Jakubowski, W.; Min, K.; Matyjaszewski, K. Activators regenerated by electron transfer for atom transfer radical polymerization of styrene. *Macromolecules* **2006,** *39*, 39–45.

(11) Matyjaszewski, K.; Jakubowski, W.; Min, K.; Tang, W.; Huang, J. Y.; Braunecker, W. A.; Tsarevsky, N. V. Diminishing catalyst concentration in atom transfer radical polymerization with reducing agents. *P. Natl. Acad. Sci. U.S.A.* **2006,** *103*, 15309–15314.

(12) Tasdelen, M. A.; Uygun, M.; Yagci, Y. Photoinduced controlled radical polymerization in methanol. *Macromol. Chem. Phys.* **2010,** *211*, 2271–2275.

(13) Tasdelen, M. A.; Uygun, M.; Yagci, Y. Photoinduced controlled radical polymerization. *Macromol. Rapid Commun.* **2011,** *32*, 58–62.

(14) Zhang, T.; Gieseler, D.; Jordan, R. Lights on! A significant photoenhancement effect on ATRP by ambient laboratory light. *Polym. Chem.* **2016,** *7*, 775–779.

(15) Fors, B. P.; Hawker, C. J. Control of a living radical polymerization of methacrylates by light. *Angew. Chem. Int. Ed.* **2012,** *51*, 8850–8853.

(16) Magenau, A. J. D.; Strandwitz, N. C.; Gennaro, A.; Matyjaszewski, K. Electrochemically mediated atom transfer radical polymerization. *Science* **2011,** *332*, 81–84.

(17) Zhang, G.; Song, I. Y.; Ahn, K. H.; Park, T.; Choi, W. Free radical polymerization initiated and controlled by visible light photocatalysis at ambient temperature. *Macromolecules* **2011,** *44*, 7594–7599.

(18) Pan, X.; Tasdelen, M. A.; Laun, J.; Junkers, T.; Yagci, Y.; Matyjaszewski, K. Photomediated controlled radical polymerization. *Prog. Polym. Sci.* **2016,** *62*, 73–125.

(19) Chen, M.; Zhong, M. J.; Johnson, J. A. Light-controlled radical polymerization: mechanisms, methods, and applications. *Chem. Rev.* **2016,** *116*, 10167–10211.

(20) Dadashi-Silab, S.; Doran, S.; Yagci, Y. Photoinduced electron transfer reactions for macromolecular syntheses. *Chem. Rev.* **2016,** *116*, 10212–10275.

(21) Shanmugam, S.; Xu, J. T.; Boyer, C. Photocontrolled living polymerization systems with reversible deactivations through electron and energy transfer. *Macromol. Rapid Commun.* **2017,** *38*, 1700143.

(22) Pan, X. C.; Fantin, M.; Yuan, F.; Matyjaszewski, K. Externally controlled atom transfer radical polymerization. *Chem. Soc. Rev.* **2018,** *47*, 5457–5490.

(23) Ludwig, J. R.; Schindler, C. S. Catalyst: sustainable catalysis. *Chem* **2017,** *2*, 313–316.

(24) Ravelli, D.; Fagnoni, M.; Albini, A. Photoorganocatalysis. What for? *Chem. Soc. Rev.* **2013,** *42*, 97–113.

(25) Romero, N. A.; Nicewicz, D. A. Organic photoredox catalysis. *Chem. Rev.* **2016,** *116*, 10075–10166.

(26) Shanmugam, S.; Boyer, C. Organic photocatalysts for cleaner polymer synthesis. *Science* **2016,** *352*, 1053–1054.

(27) Trotta, J. T.; Fors, B. P. Organic catalysts for photocontrolled polymerizations. *Synlett* **2016,** *27*, 702–713.

(28) Pitre, S. P.; McTiernan, C. D.; Scaiano, J. C. Understanding the kinetics and spectroscopy of photoredox catalysis and transition-metal-free alternatives. *Acc. Chem. Res.* **2016,** *49*, 1320–1330.

(29) Bonardi, A. H.; Dumur, F.; Noirbent, G.; Lalevee, J.; Gigmes, D. Organometallic vs organic photoredox catalysts for photocuring reactions in the visible region. *Beilstein J. Org. Chem.* **2018,** *14*, 3025–3046.

(30) Bogdos, M. K.; Pinard, E.; Murphy, J. A. Applications of organocatalysed visible-light photoredox reactions for medicinal chemistry. *Beilstein J. Org. Chem.* **2018,** *14*, 2035–2064.

(31) Corbin, D. A.; Lim, C. H.; Miyake, G. M., Phenothiazines, dihydrophenazines, and phenoxazines: sustainable alternatives to precious-metal-based photoredox catalysts. *Aldrichim. Acta* **2019,** *52*, 7-21.

(32) Miyake, G. M.; Theriot, J. C. Perylene as an organic photocatalyst for the radical polymerization of functionalized vinyl monomers through oxidative quenching with alkyl bromides and visible light. *Macromolecules* **2014,** *47*, 8255–8261.

(33) Treat, N. J.; Sprafke, H.; Kramer, J. W.; Clark, P. G.; Barton, B. E.; de Alaniz, J. R.; Fors, B. P.; Hawker, C. J. Metal-free atom transfer radical polymerization. *J. Am. Chem. Soc.* **2014,** *136*, 16096–16101.

(34) Theriot, J. C.; Lim, C. H.; Yang, H.; Ryan, M. D.; Musgrave, C. B.; Miyake, G. M. Organocatalyzed atom transfer radical polymerization driven by visible light. *Science* **2016,** *352*, 1082–1086.

(35) Pearson, R. M.; Lim, C. H.; McCarthy, B. G.; Musgrave, C. B.; Miyake, G. M. Organocatalyzed atom transfer radical polymerization using *N*-aryl phenoxazines as photoredox catalysts. *J. Am. Chem. Soc.* **2016,** *138*, 11399–11407.

(36) Liu, X. D.; Zhang, L. F.; Cheng, Z. P.; Zhu, X. L. Metal-free photoinduced electron transfer-atom transfer radical polymerization (PET-ATRP) via a visible light organic photocatalyst. *Polym. Chem.* **2016,** *7*, 689–700.

(37) Theriot, J. C.; McCarthy, B. G.; Lim, C. H.; Miyake, G. M. Organocatalyzed atom transfer radical polymerization: perspectives on catalyst design and performance. *Macromol. Rapid Commun.* **2017,** *38*, 1700040.

(38) Discekici, E. H.; Anastasaki, A.; de Alaniz, J. R.; Hawker, C. J. Evolution and future directions of metal-free atom transfer radical polymerization. *Macromolecules* **2018,** *51*, 7421–7434.

(39) Yilmaz, G.; Yagci, Y. Photoinduced metal-free atom transfer radical polymerizations: state-of-the-art, mechanistic aspects and applications. *Polym. Chem.* **2018,** *9*, 1757–1762.

(40) Yilmaz, G.; Kutahya, C.; Allushi, A.; Aydogan, C.; Aykac, S.; Yagci, Y. Photoinduced metal free strategies for atom transfer radical polymerization. In *Reversible Deactivation Radical Polymerization: Mechanisms and Synthetic Methodologies*; ACS Symposium Series, Vol. 1284; American Chemical Society, 2018; pp 263-271. DOI: 10.1021/bk-2018-1284.ch011.

(41) Kreutzer, J.; Yagci, Y. Metal free reversible-deactivation radical polymerizations: advances, challenges, and opportunities. *Polymers* **2018,** *10*, 35.

(42) Zhu, N.; Hu, X.; Fang, Z.; Guo, K., Continuous flow photoinduced reversible deactivation radical polymerization. *Chemphotochem* **2018,** *2*, 831–838.

(43) Gong, H. H.; Gu, Y.; Chen, M. Controlled/living radical polymerization of semifluorinated (meth)acrylates. *Synlett* **2018,** *29*, 1543–1551.

(44) Hu, X.; Zhu, N.; Guo, K. Advances in organocatalyzed atom transfer radical polymerization. *Adv. Polym. Technol.* **2019,** *2019*, 7971683.

(45) Li, N.; Hu, X.; Fang, L.; Kou, J. H.; Ni, Y. R.; Lu, C. H. Organocatalyzed atom transfer radical polymerization. *Prog. in Chem.* **2019,** *31*, 791–799.

(46) Aklujkar, P. S.; Rao, A. R. Developments in the components of metal-free photoinitiated organocatalyzed-atom transfer radical polymerization (O-ATRP). *Chemistryselect* **2020,** *5*, 14884–14899.

(47) Chiefari, J.; Chong, Y. K.; Ercole, F.; Krstina, J.; Jeffery, J.; Le, T. P. T.; Mayadunne, R. T. A.; Meijs, G. F.; Moad, C. L.; Moad, G. *et al.* Living free-radical polymerization by reversible addition-fragmentation chain transfer: The RAFT process. *Macromolecules* **1998,** *31*, 5559–5562.

(48) Xu, J. T.; Jung, K.; Atme, A.; Shanmugam, S.; Boyer, C. A robust and versatile photoinduced living polymerization of conjugated and unconjugated monomers and its oxygen tolerance. *J. Am. Chem. Soc.* **2014,** *136*, 5508–5519.

(49) Xu, J. T.; Jung, K.; Boyer, C. Oxygen tolerance study of photoinduced electron transfer-reversible addition-fragmentation chain transfer (PET-RAFT) polymerization mediated by $Ru(bpy)_3Cl_2$. *Macromolecules* **2014,** *47*, 4217–4229.

(50) Xu, J. T.; Shanmugam, S.; Boyer, C. Organic electron donor-acceptor photoredox catalysts: enhanced catalytic efficiency toward controlled radical polymerization. *AACS Macro Lett.* **2015,** *4*, 926–932.

(51) Xu, J. T.; Shanmugam, S.; Duong, H. T.; Boyer, C. Organo-photocatalysts for photoinduced electron transfer-reversible addition-fragmentation chain transfer (PET-RAFT) polymerization. *Polym. Chem.* **2015,** *6*, 5615–5624.

(52) Phommalysack-Lovan, J.; Chu, Y. Y.; Boyer, C.; Xu, J. T. PET-RAFT polymerisation: towards green and precision polymer manufacturing. *Chem. Commun.* **2018,** *54*, 6591–6606.

(53) Otsu, T.; Yoshida, M. Role of initiator-transfer agent-terminator (iniferter) in radical polymerizations: polymer design by organic disulfides as iniferters. *Makromol. Chem. Rapid Commun.* **1982,** *3*, 127–132.

(54) Otsu, T. Iniferter concept and living radical polymerization. *J. Polym. Sci. Part A Polym. Chem.* **2000,** *38*, 2121–2136.

(55) Quinn, J. F.; Barner, L.; Barner-Kowollik, C.; Rizzardo, E.; Davis, T. P. Reversible addition-fragmentation chain transfer polymerization initiated with ultraviolet radiation. *Macromolecules* **2002,** *35*, 7620–7627.

(56) Grubbs, R. B. Nitroxide-mediated radical polymerization: limitations and versatility. *Polym. Rev.* **2011,** *51*, 104–137.

(57) Nicolas, J.; Guillaneuf, Y.; Lefay, C.; Bertin, D.; Gigmes, D.; Charleux, B. Nitroxide-mediated polymerization. *Prog. Polym. Sci.* **2013,** *38*, 63–235.

(58) Audran, G.; Bagryanskaya, E. G.; Marque, S. R. A.; Postnikov, P. New variants of nitroxide mediated polymerization. *Polymers* **2020,** *12*, 1481.

(59) Yoshida, E. Photo-living radical polymerization of methyl methacrylate by a nitroxide mediator. *Colloid Polym. Sci.* **2008,** *286*, 1663–1666.

(60) Guillaneuf, Y.; Bertin, D.; Gigmes, D.; Versace, D. L.; Lalevee, J.; Fouassier, J. P. Toward nitroxide-medlated photopolymerization. *Macromolecules* **2010,** *43*, 2204–2212.

(61) Ni, Y. Y.; Zhang, L. F.; Cheng, Z. P.; Zhu, X. L. Iodine-mediated reversible-deactivation radical polymerization: a powerful strategy for polymer synthesis. *Polym. Chem.* **2019,** *10*, 2504–2515.

(62) Tatemoto, M.; Yutani, Y.; Fujiwara, K. Novel Iodine-Containing Compound and Preparation Thereof. European Patent EP 0272698 A2, 1988.

(63) Matyjaszewski, K.; Gaynor, S.; Wang, J. S. Controlled radical polymerizations: the use of alkyl iodides in degenerative transfer. *Macromolecules* **1995,** *28*, 2093–2095.

(64) Isse, A. A.; Lin, C. Y.; Coote, M. L.; Gennaro, A. Estimation of standard reduction potentials of halogen atoms and alkyl halides. *J. Phys. Chem. B* **2011,** *115*, 678–684.

(65) Buss, B. L.; Lim, C.-H.; Miyake, G. M. Dimethyl dihydroacridines as photocatalysts in organocatalyzed atom transfer radical polymerization of acrylate monomers. *Angew. Chem. Int. Ed.* **2020,** *59*, 3209–3217.

(66) Liu, Y. M.; Chen, Q.; Tong, Y. J.; Ma, Y. G. 9,9-Dimethyl dihydroacridine-based organic photocatalyst for atom transfer radical polymerization from modifying "unstable" electron donor. *Macromolecules* **2020,** *53*, 7053–7062.

(67) Shaw, M. H.; Twilton, J.; MacMillan, D. W. C. Photoredox catalysis in organic chemistry. *J. Org. Chem.* **2016,** *81*, 6898–6926.

(68) Prier, C. K.; Rankic, D. A.; MacMillan, D. W. C. Visible light photoredox catalysis with transition metal complexes: applications in organic synthesis. *Chem. Rev.* **2013,** *113*, 5322–5363.

(69) 10-Phenylphenothiazine. https://www.sigmaaldrich.com/catalog/product/aldrich/903167?lang=en&region=US&cm_sp=Insite-_-caSrpResults_srpRecs_srpModel_phenyl%20phenothiazine-_-srpRecs3-1 (accessed February 15).

(70) Dihydrophenazine PC B0301. https://www.sigmaaldrich.com/catalog/product/aldrich/901112?lang=en&region=US&cm_sp=Insite-_-caSrpResults_srpRecs_srpModel_dihydrophenazine-_-srpRecs3-1 (accessed February 15).

(71) Phenoxazine PC A0202. https://www.sigmaaldrich.com/catalog/product/aldrich/901111?lang=en&region=US (accessed February 15).

(72) Phenyl-(benzo)phenothiazine. https://www.sigmaaldrich.com/catalog/product/aldrich/916722?lang=en&region=US (accessed February 15).

(73) Furst, L.; Matsuura, B. S.; Narayanam, J. M. R.; Tucker, J. W.; Stephenson, C. R. J. Visible light-mediated intermolecular c-h functionalization of electron-rich heterocycles with malonates. *Org. Lett.* **2010**, *12*, 3104–3107.

(74) Bachman, J. C.; Kavian, R.; Graham, D. J.; Kim, D. Y.; Noda, S.; Nocera, D. G.; Shao-Horn, Y.; Lee, S. W. Electrochemical polymerization of pyrene derivatives on functionalized carbon nanotubes for pseudocapacitive electrodes. *Nat. Commun.* **2015,** *6*, 7040.

(75) Singh-Rachford, T. N.; Castellano, F. N. Triplet sensitized red-to-blue photon upconversion. *J. Phys. Chem. Lett.* **2010,** *1*, 195–200.

(76) Grimme, S.; Parac, M. Substantial errors from time-dependent density functional theory for the calculation of excited states of large pi systems. *Chemphyschem* **2003,** *4* (3), 292–295.

(77) Kikuchi, K.; Niwa, T.; Takahashi, Y.; Ikeda, H.; Miyashi, T. Quenching mechanism in a highly exothermic region of the rehm-weller relationship for electron-transfer fluorescence quenching. *J. Phys. Chem.* **1993,** *97*, 5070–5073.

(78) Theriot, J. C.; McCarthy, B. G.; Lim, C. H.; Miyake, G. M. Organocatalyzed atom transfer radical polymerization: perspectives on catalyst design and performance. *Macromol. Rapid Commun.* **2017,** *38*, 1700040.

(79) Pan, X. C.; Fang, C.; Fantin, M.; Malhotra, N.; So, W. Y.; Peteanu, L. A.; Isse, A. A.; Gennaro, A.; Liu, P.; Matyjaszewskit, K. Mechanism of photoinduced metal-free atom transfer radical polymerization: experimental and computational studies. *J. Am. Chem. Soc.* **2016,** *138*, 2411–2425.

(80) Zhao, Y. C.; Gong, H. H.; Jiang, K. M.; Yan, S. J.; Lin, J.; Chen, M. Organocatalyzed photoredox polymerization from aromatic sulfonyl halides: facilitating graft from aromatic C-H bonds. *Macromolecules* **2018,** *51*, 938–946.

(81) Cole, J. P.; Federico, C. R.; Lim, C. H.; Miyake, G. M. Photoinduced organocatalyzed atom transfer radical polymerization using low ppm catalyst loading. *Macromolecules* **2019,** *52*, 747–754.

(82) Luo, J.; Zhang, J., Donor–acceptor fluorophores for visible-light-promoted organic synthesis: photoredox/Ni dual catalytic $C(sp^3)$–$C(sp^2)$ cross-coupling. *ACS Catal.* **2016,** *6*, 873–877.

(83) Shen, T.; Zhao, Z. G.; Yu, Q.; Xu, H. J. Photosensitized reduction of benzil by heteroatom-containing anthracene dyes. *J. Photochem. Photobiol. A Chem.* **1989,** *47*, 203–212.

(84) Timpe, H. J.; Kronfeld, K. P. Light-induced polymer and polymerization reactions .33. direct photoinitiation of methyl-methacrylate polymerization by excited-states of ketones. *J. Photochem. Photobiol. A Chem.* **1989,** *46*, 253–267.

(85) Timpe, H. J.; Kronfeld, K. P.; Lammel, U.; Fouassier, J. P.; Lougnot D. J. Excited-states of ketones as electron-donors ketone iodonium salt systems as photoinitiators for radical polymerization. *Journal of J. Photochem. Photobiol. A Chem.* **1990,** *52*, 111–122.

(86) Arias-Rotondo, D. M.; McCusker, J. K. The photophysics of photoredox catalysis: a roadmap for catalyst design. *Chem. Soc. Rev.* **2016,** *45*, 5803–5820.

(87) Su, X.; Jessop, P. G.; Cunningham, M. F. Versatility of organocatalyzed atom transfer radical polymerization and CO_2-switching for preparing both hydrophobic and hydrophilic polymers with the recycling of a photocatalyst. *Macromolecules* **2019,** *52*, 6725–6733.

(88) McCarthy, B.; Sartor, S.; Cole, J.; Damrauer, N.; Miyake, G. M. Solvent effects and side reactions in organocatalyzed atom transfer radical polymerization for enabling the controlled polymerization of acrylates catalyzed by diaryl dihydrophenazines. *Macromolecules* **2020,** *53*, 9208–9219.

(89) Corbin, D. A.; Puffer, K. O.; Chism, K. A.; Cole, J. P.; Theriot, J. C.; McCarthy, B. G.; Buss, B. L.; Lim, C.-H.; Lincoln, S. R.; Newell, B. S. *et al.* Radical addition to *N,N*-diaryl dihydrophenazine photoredox catalysts and implications in photoinduced organocatalyzed atom transfer radical polymerization. *Macromolecules* **2021,** *54*, 4507–4516.

(90) Zhang, Y.; Jiang, D.; Fang, Z.; Zhu, N.; Sun, N.; He, W.; Liu, C.; Zhao, L.; Guo, K. Photomediated core modification of organic photoredox catalysts in radical addition: mechanism and applications. *Chem. Sci.* **2021**, DOI: 10.1039/D1SC02258J.

(91) Pan, X. C.; Lamson, M.; Yan, J. J.; Matyjaszewski, K. Photoinduced metal-free atom transfer radical polymerization of acrylonitrile. *ACS Macro Lett.* **2015,** *4*, 192–196.

(92) Huang, W. J.; Zhai, J. L.; Hu, X.; Duan, J. D.; Fang, Z.; Zhu, N.; Guo, K. Continuous flow photoinduced phenothiazine derivatives catalyzed atom transfer radical polymerization. *Eur. Polym. J.* **2020,** *126*, 109565.

(93) Tran, H. M.; Phan, L. N. T.; Le, T. V.; Truong, T. T.; Nguyen, T. H.; Truong, K. T.; Nguyen, L. T. T.; Phong, M. T.; Nguyen, H. T., Phenothiazine derivative as organic photocatalyst for metal free atom transfer radical polymerization. *Polym. Korea* **2019,** *43*, 496–502.

(94) Nguyen, T. H.; Nguyen, L. T. T.; Nguyen, V. Q.; Phan, L. N. T.; Zhang, G.; Yokozawa, T.; Phung, D. T. T.; Nguyen, H. T. Synthesis of poly(3-hexylthiophene) based rod-coil conjugated block copolymers via photoinduced metal-free atom transfer radical polymerization. *Polym. Chem.* **2018,** *9*, 2484–2493.

(95) McCarthy, B. G.; Pearson, R. M.; Lim, C. H.; Sartor, S. M.; Damrauer, N. H.; Miyake, G. M. Structure-property relationships for tailoring phenoxazines as reducing photoredox catalysts. *J. Am. Chem. Soc.* **2018,** *140*, 5088–5101.

(96) Park, G. S.; Back, J.; Choi, E. M.; Lee, E.; Son, K. S., Visible light-mediated metal-free atom transfer radical polymerization with *N*-trifluoromethylphenyl phenoxazines. *Eur. Polym. J.* **2019,** *117*, 347–352.

(97) Bian, C.; Zhou, Y. N.; Deetz, J. D.; Luo, Z. H. Experimental and computational investigation of oxidative quenching governed aqueous organocatalyzed atom transfer radical polymerization. *Chem. Eng. J.* **2019,** *362*, 721–730.

(98) Zhang, Z.; Chen, W.; Zhang, Y.; Wang, Y.; Tian, Y.; Fang, L.; Ba, X. Photoredox organocatalysts with thermally activated delayed fluorescence for visible-light-driven atom transfer radical polymerization. *Macromolecules* **2021,** *54*, 4633–4640.

(99) McCarthy, B.; Miyake, G. M. Organocatalyzed Atom transfer radical polymerization catalyzed by core modified *N*-aryl phenoxazines performed under air. *ACS Macro Lett.* **2018,** *7*, 1016–1021.

(100) Flory, P. J. *Principles of Polymer Chemistry*. Cornell University Press: New York, 1995.

(101) Turro, N. J.; Ramamurthy, V.; Scaiano, J. C. *Modern Molecular Photochemistry of Organic Molecules*. University Science Books: Mill Valley, CA, 2010.

(102) Beuermann, S.; Buback, M. Rate coefficients of free-radical polymerization deduced from pulsed laser experiments. *Prog. Polym. Sci.* **2002,** *27*, 191–254.

(103) Gillies, M. B.; Matyjaszewski, K.; Norrby, P. O.; Pintauer, T.; Poli, R.; Richard, P. A DFT study of R-X bond dissociation enthalpies of relevance to the initiation process of atom transfer radical polymerization. *Macromolecules* **2003,** *36*, 8551–8559.

(104) Tang, W.; Matyjaszewski, K. Effects of initiator structure on activation rate constants in ATRP. *Macromolecules* **2007,** *40*, 1858–1863.

(105) Hartman, R. L.; McMullen, J. P.; Jensen, K. F. Deciding whether to go with the flow: evaluating the merits of flow reactors for synthesis. *Ange. Chem. Int. Ed.* **2011,** *50*, 7502–7519.

(106) Tucker, J. W.; Zhang, Y.; Jamison, T. F.; Stephenson, C. R. J. Visible-light photoredox catalysis in flow. *Angew. Chem. Int. Ed.* **2012,** *51*, 4144–4147.

(107) Junkers, T.; Wenn, B. Continuous photoflow synthesis of precision polymers. *React. Chem. Eng.* **2016,** *1*, 60–64.

(108) Buss, B. L.; Miyake, G. M. Photoinduced controlled radical polymerizations performed in flow: methods, products, and opportunities. *Chem. Mater.* **2018,** *30*, 3931–3942.

(109) Allushi, A.; Jockusch, S.; Yilmaz, G.; Yagci, Y. Photoinitiated metal-free controlled/living radical polymerization using polynuclear aromatic hydrocarbons. *Macromolecules* **2016,** *49*, 7785–7792.

(110) Wang, G. X.; Lu, M.; Zhou, M. J.; Liang, E. X.; He, B. H. Photo-induced ATRP of MMA under blue light irradiation in the presence of 3,4,9,10-tetra-(12-alkoxycarbonyl)-perylene as a photocatalyst. *Iran. Polym. J.* **2018,** *27*, 43–48.

(111) Zeng, L. L.; Xie, W. Y.; Yang, C. X.; Liang, E. X.; Wang, G. X. Photomediated atom transfer radical polymerization of MMA under long-wavelength light irradiation. *Iran. Polym. J.* **2018,** *27*, 881–887.

(112) Ma, Q.; Song, J. S.; Zhang, X.; Jiang, Y.; Ji, L.; Liao, S. H., Metal-free atom transfer radical polymerization with ppm catalyst loading under sunlight. *Nat. Commun.* **2021,** *12*, 429.

(113) Kutahya, C.; Allushi, A.; Isci, R.; Kreutzer, J.; Ozturk, T.; Yilmaz, G.; Yagci, Y. Photoinduced metal-free atom transfer radical polymerization using highly conjugated thienothiophene derivatives. *Macromolecules* **2017,** *50*, 6903–6910.

(114) Huang, Z. C.; Gu, Y.; Liu, X. D.; Zhang, L. F.; Cheng, Z. P.; Zhu, X. L. Metal-free atom transfer radical polymerization of methyl methacrylate with ppm level of organic photocatalyst. *Macromol. Rapid. Commun.* **2017,** *38*, 1600461.

(115) Singh, V. K.; Yu, C.; Badgujar, S.; Kim, Y.; Kwon, Y.; Kim, D.; Lee, J.; Akhter, T.; Thangavel, G.; Park, L. S. *et al.* Highly efficient organic photocatalysts discovered via a computer-aided-design strategy for visible-light-driven atom transfer radical polymerization. *Nat. Catal.* **2018,** *1*, 794–804.

(116) Wang, G. X.; Lu, M.; Zhou, M. J. Photo-induced metal-free ATRP of MMA with 2,7-bi-(*N*-penothiazinyl)fluorenone as photocatalyst. *J. Macromol. Sci. Part A Pure Appl. Chem.* **2018,** *55*, 85–89.

(117) Wang, L.; Li, R.; Zhang, K. A. I. Atom transfer radical polymerization (ATRP) catalyzed by visible light-absorbed small molecule organic semiconductors. *Macromol. Rapid Commun.* **2018,** *39*, 1800466.

(118) Ma, Q.; Zhang, X.; Ji, L.; Liao, S. H. BINOLs as visible light photocatalysts for metal-free atom transfer radical polymerization. *Polym. Chem.* **2019,** *10*, 6662–6668.

(119) Jia, T.; Huang, S.; Bohra, H.; Wang, M. F., Examining derivatives of quinacridone, diketopyrrolopyrrole and indigo as the visible-light organic photocatalysts for metal-free atom transfer radical polymerization. *Dyes Pigments* **2019,** *165*, 223–230.

(120) Yang, L.; Huang, Y. J.; Peng, Y. T.; Liu, F.; Zhang, C.; He, H. C.; Wang, J.; Jiang, L.; Zhou, Y. Pyridine-diketopyrrolopyrrole-based novel metal-free visible-light organophotoredox catalyst for atom-transfer radical polymerization. *J. Phys. Chem. A* **2020,** *124*, 1068–1075.

(121) Li, M. M.; Wang, S. X.; Li, F. F.; Zhou, L.; Lei, L. Organocatalyzed atom transfer radical polymerization (ATRP) using triarylsulfonium hexafluorophosphate salt (THS) as a photocatalyst. *Polym. Chem.* **2020,** *11*, 2222–2229.

(122) Ma, W.; Zhang, X.; Ma, Y.; Chen, D.; Wang, L.; Zhao, C.; Yang, W. Photoinduced controlled radical polymerization of methacrylates with benzaldehyde derivatives as organic catalysts. *Polym. Chem.* **2017,** *8*, 3574–3585.

(123) Zaborniak, I.; Chmielarz, P.; Wolski, K. Riboflavin-induced metal-free ATRP of (meth)acrylates. *Eur. Polym. J.* **2020,** *140*, 110055.

(124) Kutahya, C.; Aykac, F. S.; Yilmaz, G.; Yagci, Y. LED and visible light-induced metal free ATRP using reducible dyes in the presence of amines. *Polym. Chem.* **2016,** *7*, 6094–6098.

(125) Wang, Y. A.; Li, H. L.; Dong, J. H.; Hu, L. J.; Wei, D. L.; Bai, L. J.; Yang, H. W.; Chen, H. Recyclable bio-based photoredox catalyst in metal-free atom transfer radical polymerization. *Macromol. Chem. Phys.* **2021,** *222*, 8.

(126) Xu, X. M.; Xu, X.; Zeng, Y. N.; Zhang, F. A. Oxygen-tolerant photo-induced metal-free atom transfer radical polymerization. *J. Photochem. Photobiol. A Chem.* **2021,** *411*, 113191.

(127) Allushi, A.; Kutahya, C.; Aydogan, C.; Kreutzer, J.; Yilmaz, G.; Yagci, Y. Conventional type II photoinitiators as activators for photoinduced metal-free atom transfer radical polymerization. *Polym. Chem.* **2017,** *8*, 1972–1977.

(128) Liu, L. C.; Yi, Y. S. Photo-mediated metal free atom transfer radical polymerization of acrylamide in water. *J. Appl. Polym. Sci.* **2018,** *135*, 46567.

(129) Zaborniak, I.; Macior, A.; Chmielarz, P.; Najarro, M. C.; Iruthayaraj, J. Lignin-based thermoresponsive macromolecules via vitamin-induced metal-free ATRP. *Polymer* **2021,** *219*, 11.

(130) Anslyn, E. V.; Dougherty, D. A. *Modern physical organic chemistry.* University Science: Mill Valley, California, 2006.

(131) Lakowicz, J. R., *Principles of Fluorescence Spectroscopy*, 3rd ed.; Springer US: New York, NY, 2006.

(132) Turro, N. J., *Modern Molecular Photochemistry*. University Science Books, 1991.

(133) Kasha, M. Characterization of electronic transitions in complex molecules. *Discuss. Faraday Soc.* **1950,** *9*, 14–19.

(134) Arnaut, L. G.; Formosinho, S. J.; Burrows, H. *Chemical kinetics: from molecular structure to chemical reactivity*, 1st ed.; Elsevier: Amsterdam, 2007.

(135) Lim, C. H.; Ryan, M. D.; McCarthy, B. G.; Theriot, J. C.; Sartor, S. M.; Damrauer, N. H.; Musgrave, C. B.; Miyake, G. M. Intramolecular charge transfer and ion pairing in *N,N*-diaryl dihydrophenazine photoredox catalysts for efficient organocatalyzed atom transfer radical polymerization. *J. Am. Chem. Soc.* **2017,** *139*, 348–355.

(136) Sartor, S. M.; McCarthy, B. G.; Pearson, R. M.; Miyake, G. M.; Damrauer, N. H. Exploiting charge-transfer states for maximizing intersystem crossing yields in organic photoredox catalysts. *J. Am. Chem. Soc.* **2018,** *140*, 4778–4781.

(137) Sartor, S. M.; Lattke, Y. M.; McCarthy, B. G.; Miyake, G. M.; Damrauer, N. H. Effects of naphthyl connectivity on the photophysics of compact organic charge-transfer photoredox catalysts. *J. Phys. Chem. A* **2019,** *123*, 4727–4736.

(138) Sartor, S. M.; Chrisman, C. H.; Pearson, R. M.; Miyake, G. M.; Damrauer, N. H. Designing high-triplet-yield phenothiazine donor-acceptor complexes for photoredox catalysis. *J. Phys. Chem. A* **2020,** *124*, 817–823.

(139) Ryan, M. D.; Pearson, R. M.; French, T. A.; Miyake, G. M. Impact of light intensity on control in photoinduced organocatalyzed atom transfer radical polymerization. *Macromolecules* **2017,** *50*, 4616–4622.

(140) Dolinski, N. D.; Page, Z. A.; Discekici, E. H.; Meis, D.; Lee, I. H.; Jones, G. R.; Whitfield, R.; Pan, X. C.; McCarthy, B. G.; Shanmugam, S. *et al.* What happens in the dark? Assessing the temporal control of photo-mediated controlled radical polymerizations. *J. Polym. Sci. Part A Polym. Chem.* **2019,** *57*, 268–273.

(141) Guo, J. K.; Luo, Z. H. How the catalyst circulates and works in organocatalyzed atom transfer radical polymerization. *AIChE J.* **2018,** *64*, 2581–2591.

(142) Jockusch, S.; Yagci, Y. The active role of excited states of phenothiazines in photoinduced metal free atom transfer radical polymerization: singlet or triplet excited states? *Polym. Chem.* **2016,** *7*, 6039–6043.

(143) Koyama, D.; Dale, H. J. A.; Orr-Ewing, A. J., Ultrafast observation of a photoredox reaction mechanism: photoinitiation in organocatalyzed atom-transfer radical polymerization. *J. Am. Chem. Soc.* **2018,** *140*, 1285–1293.

(144) Lewis-Borrell, L.; Sneha, M.; Bhattacherjee, A.; Clark, I. P.; Orr-Ewing, A. J. Mapping the multi-step mechanism of a photoredox catalyzed atom-transfer radical polymerization reaction by direct observation of the reactive intermediates. *Chem. Sci.* **2020,** *11*, 4475–4481.

(145) Bhattacherjee, A.; Sneha, M.; Lewis-Borrell, L.; Amoruso, G.; Oliver, T. A. A.; Tyler, J.; Clark, I. P.; Orr-Ewing, A. J. Singlet and triplet contributions to the excited-state activities of dihydrophenazine, phenoxazine, and phenothiazine organocatalysts used in atom transfer radical polymerization. *J. Am. Chem. Soc.* **2021,** *143*, 3613–3627.

(146) Lattke, Y. M.; Corbin, D. A.; Sartor, S. M.; McCarthy, B. G.; Miyake, G. M.; Damrauer, N. H. Interrogation of O-ATRP activation conducted by singlet and triplet excited states of phenoxazine photocatalysts. *J. Phys. Chem. A* **2021**, *125*, 3109–3121.

(147) Du, Y.; Pearson, R. M.; Lim, C. H.; Sartor, S. M.; Ryan, M. D.; Yang, H. S.; Damrauer, N. H.; Miyake, G. M. Strongly reducing, visible-light organic photoredox catalysts as sustainable alternatives to precious metals. *Chem. Eur. J.* **2017,** *23*, 10962–10968.

(148) Ryan, M. D.; Theriot, J. C.; Lim, C. H.; Yang, H. S.; Lockwood, A. G.; Garrison, N. G.; Lincoln, S. R.; Musgrave, C. B.; Miyake, G. M. Solvent effects on the intramolecular charge transfer character of *N,N*-diaryl dihydrophenazine catalysts for organocatalyzed atom transfer radical polymerization. *J. Polym. Sci. Part A Polym. Chem.* **2017,** *55*, 3017–3027.

(149) Krzysztof, M.; Thomas, P. D. *Handbook of Radical Polymerization*. Wiley-Interscience: Hoboken, N.J., 2002.

(150) Moad, G.; Solomon, D. H. 5 - Termination. In *The Chemistry of Radical Polymerization,* 2nd ed., Moad, G.; Solomon, D. H.; Elsevier Science Ltd: Amsterdam, 2005; pp 233-278.

(151) Corbin, D. A.; McCarthy, B. G.; van de Lindt, Z.; Miyake, G. M. Radical cations of phenoxazine and dihydrophenazine photoredox catalysts and their role as deactivators in organocatalyzed atom transfer radical polymerization. *Macromolecules* **2021,** *54*, 4726–4738.

(152) Kotsinaris, A.; Kyriacou, G.; Lambrou, C. Electrochemical reduction of dichloromethane to higher hydrocarbons. *J. Appl. Electrochem.* **1998**, *28*, 613–616.

(153) Bian, C.; Zhou, Y. N.; Guo, J. K.; Luo, Z. H. Aqueous metal-free atom transfer radical polymerization: experiments and model-based approach for mechanistic understanding. *Macromolecules* **2018,** *51*, 2367–2376.

(154) Dadashi-Silab, S.; Pan, X. C.; Matyjaszewski, K., Phenyl benzo-[b]-phenothiazine as a visible light photoredox catalyst for metal-free atom transfer radical polymerization. *Chem. Eur. J.* **2017,** *23*, 5972–5977.

(155) Ramsey, B. L.; Pearson, R. M.; Beck, L. R.; Miyake, G. M. Photoinduced organocatalyzed atom transfer radical polymerization using continuous flow. *Macromolecules* **2017,** *50*, 2668–2674.

(156) Beuermann, S.; Buback, M.; Hesse, P.; Lacik, I. Free-radical propagation rate coefficient of nonionized methacrylic acid in aqueous solution from low monomer concentrations to bulk polymerization. *Macromolecules* **2006,** *39*, 184–193.

(157) Beuermann, S.; Buback, M.; Davis, T. P.; Gilbert, R. G.; Hutchinson, R. A.; Olaj, O. F.; Russell, G. T.; Schweer, J.; vanHerk, A. M. Critically evaluated rate coefficients for free-radical polymerization .2. propagation rate coefficients for methyl methacrylate. *Macromol. Chem. Phys.* **1997,** *198*, 1545–1560.

(158) Beuermann, S.; Buback, M.; Davis, T. P.; Gilbert, R. G.; Hutchinson, R. A.; Kajiwara, A.; Klumperman, B.; Russell, G. T. Critically evaluated rate coefficients for free-radical polymerization .3. propagation rate coefficients for alkyl methacrylates. *Macromol. Chem. Phys.* **2000,** *201*, 1355–1364.

(159) Hutchinson, R. A.; Beuermann, S.; Paquet, D. A.; McMinn, J. H. Determination of free-radical propagation rate coefficients for alkyl methacrylates by pulsed-laser polymerization. *Macromolecules* **1997,** *30*, 3490–3493.

(160) Buback, M.; Kruz, C. H. Free-radical propagation rate coefficients for cyclohexyl methacrylate, glycidyl methacrylate and 2-hydroxyethyl methacrylate homopolymerizations. *Macromol. Chem. Phys.* **1998,** *199*, 2301–2310.

(161) Hutchinson, R. A.; Beuermann, S.; Paquet, D. A.; McMinn, J. H.; Jackson, C., Determination of free-radical propagation rate coefficients for cycloalkyl and functional methacrylates by pulsed-laser polymerization. *Macromolecules* **1998,** *31*, 1542–1547.

(162) Zammit, M. D.; Coote, M. L.; Davis, T. P.; Willett, G. D. Effect of the ester side-chain on the propagation kinetics of alkyl methacrylates: an entropic or enthalpic effect? *Macromolecules* **1998,** *31*, 955–963.

(163) Manders, L. G. *Pulsed initiation polymerization: applications in homogeneous and heterogeneous radical systems.* Technische Universiteit Eindhoven, Eindhoven, 1997.

(164) Lyons, R. A.; Hutovic, J.; Piton, M. C.; Christie, D. I.; Clay, P. A.; Manders, B. G.; Kable, S. H.; Gilbert, R. G. Pulsed-laser polymerization measurements of the propagation rate coefficient for butyl acrylate. *Macromolecules* **1996,** *29*, 1918–1927.

(165) Buback, M.; Kurz, C. H.; Schmaltz, C. Pressure dependence of propagation rate coefficients in free-radical homopolymerizations of methyl acrylate and dodecyl acrylate. *Macromol. Chem. Phys.* **1998,** *199*, 1721–1727.

(166) Buback, M.; Gilbert, R. G.; Hutchinson, R. A.; Klumperman, B.; Kuchta, F. D.; Manders, B. G.; Odriscoll, K. F.; Russell, G. T.; Schweer, J. Critically evaluated rate coefficients for free-radical polymerization .1. propagation rate coefficient for styrene. *Macromol. Chem. Phys.* **1995,** *196*, 3267–3280.

(167) International Workshop on Polymer Reaction, E.; Reichert, K. H.; Moritz, H. U.; Dechema In *5th International Workshop on Polymer Reaction Engineering: papers of the 5th International Workshop on Polymer Reaction Engineering, Berlin, 9-11 October, 1995*; VCH Publishers: Frankfurt am Main; New York, 1995

(168) Deibert, S.; Bandermann, F.; Schweer, J.; Sarnecki, J. Propagation rate coefficient of free-radical polymerization of 1,3-butadiene. *Makromol. Chem. Rapid Commun.* **1992,** *13*, 351–355.

(169) Hutchinson, R. A.; Aronson, M. T.; Richards, J. R. Analysis of pulsed-laser-generated molecular-weight distributions for the determination of propagation rate coefficients. *Macromolecules* **1993,** *26*, 6410–6415.

(170) Ramakers, G.; Krivcov, A.; Trouillet, V.; Welle, A.; Mobius, H.; Junkers, T. Organocatalyzed photo-atom transfer radical polymerization of methacrylic acid in continuous flow and surface grafting. *Macromol. Chem. Phys.* **2017,** *38*, 1700423.

(171) Kim, Y. A.; Park, G. S.; Son, K. S. Amphiphilic diblock and crosslinked copolymers synthesized via metal-free atom transfer radical polymerization. *Polym. Int.* **2018,** *67*, 127–131.

(172) Wang, J. F.; Yuan, L.; Wang, Z. K.; Rahman, M. A.; Huang, Y. C.; Zhu, T. Y.; Wang, R. B.; Cheng, J. J.; Wang, C. P.; Chu, F. X. *et al.* Photoinduced metal-free atom transfer radical polymerization of biomass-based monomers. *Macromolecules* **2016,** *49*, 7709–7717.

(173) Ni, B. Q.; Wang, D. K.; Zhang, H.; Li, P. Q.; Niu, T. F. Visible light controlled polymerization of azide-derived monomers: a facile, metal-free PET-ATRP route to construct azide polymers. *Macromol. Chem. Phys.* **2019,** *220*, 1800529.

(174) Mehmood, R.; Mofarah, S. S.; Rawal, A.; Tomasetig, F.; Wang, X. C.; Yang, J. L.; Koshy, P.; Sorrell, C. C. Green synthesis of zwitterion-functionalized nano-octahedral ceria for enhanced intracellular delivery and cancer therapy. *ACS Sustain. Chem. Eng.* **2019,** *7*, 9189–9201.

(175) Aydogan, C.; Yilmaz, G.; Yagci, Y. Synthesis of hyperbranched polymers by photoinduced metal-free ATRP. *Macromolecules* **2017,** *50*, 9115–9120.

(176) Ramakers, G.; Wackers, G.; Trouillet, V.; Welle, A.; Wagner, P.; Junkers, T. Laser-grafted molecularly imprinted polymers for the detection of histamine from organocatalyzed atom transfer radical polymerization. *Macromolecules* **2019,** *52*, 2304–2313.

(177) Narupai, B.; Page, Z. A.; Treat, N. J.; McGrath, A. J.; Pester, C. W.; Discekici, E. H.; Dolinski, N. D.; Meyers, G. F.; de Alaniz, J. R.; Hawker, C. J. Simultaneous preparation of multiple polymer brushes under ambient conditions using microliter volumes. *Angew. Chem. Int. Ed.* **2018,** *57*, 13433–13438.

(178) Liu, Q. R.; Jian, L. H.; Liu, R. Q.; Yang, H. X.; Kong, J. M.; Zhang, X. J. Metal-free photoinduced atom transfer radical polymerization for highly sensitive detection of lung cancer DNA. *Chem. Eur. J.* **2020,** *26*, 1633–1639.

(179) Li, S. P.; Mohamed, A. I.; Pande, V.; Wang, H.; Cuthbert, J.; Pan, X. C.; He, H. K.; Wang, Z. Y.; Viswanathan, V.; Whitacre, J. F. *et al.* Single-ion homopolymer electrolytes with high transference number prepared by click chemistry and photoinduced metal-free atom-transfer radical polymerization. *ACS Energy Lett.* **2018,** *3*, 20–27.

(180) Zeng, G. J.; Liu, M. Y.; Shi, K. X.; Heng, C. N.; Mao, L. C.; Wan, Q.; Huang, H. Y.; Deng, F. J.; Zhang, X. Y.; Wei, Y. Surface modification of nanodiamond through metal free atom transfer radical polymerization. *Appl. Surf. Sci.* **2016,** *390*, 710–717.

(181) Luo, Y. R., *Handbook of Bond Dissociation Energies in Organic Compounds*. CRC Press: 2002.

(182) Aydogan, C.; Kutahya, C.; Allushi, A.; Yilmaz, G.; Yagci, Y. Block copolymer synthesis in one shot: concurrent metal-free ATRP and ROP processes under sunlight. *Polym. Chem.* **2017,** *8*, 2899–2903.

(183) Chen, R. Y.; Zhang, W. J.; Dai, T. Z.; He, J. H.; Ye, H. M.; Wang, Y. D. Facile fabrication of water-soluble polyacrylic acid encapsulated core@shell upconversion nanoparticles via metal-free light induced surface initiated atom transfer radical polymerization. *Mater. Lett.* **2020,** *273*, 127874.

(184) Qian, Y. Q.; Han, N.; Gao, X. F.; Gao, X. Y.; Li, W.; Zhang, X. X. Cellulose-based phase change fibres for thermal energy storage and management applications. *Chem. Eng. J.* **2021,** *412*, 128596.

(185) Cuneo, T.; Wang, X. F.; Shi, Y.; Gao, H. F. Synthesis of hyperbranched polymers via metal-free atrp in solution and microemulsion. *Macromol. Chem. Phys.* **2020,** *221*, 2000008.

(186) Niu, T. F.; Jiang, J. Y.; Li, S. Y.; Ni, B. Q.; Liu, X. M.; Chen, M. Q. Well-defined high-molecular-weight polyacrylonitrile formation via visible-light-induced metal-free radical polymerization. *Macromol. Chem. Phys.* **2017,** *218*, 1700169.

(187) Wei, D. L.; Xu, Y. G.; Liu, C. R.; Zhai, Y. X.; Chen, H.; Bai, L. J.; Yang, H. W.; Yang, L. X.; Wang, W. X.; Niu, Y. Z. Visible light-induced metal-free atom transfer radical polymerization: An efficient approach to polyacrylonitrile. *J. Polym. Sci. Part A Polym. Chem.* **2019,** *57*, 1265–1269.

(188) Ma, L.; Li, N.; Zhu, J.; Chen, X. D. Visible light-induced metal free surface initiated atom transfer radical polymerization of methyl methacrylate on SBA-15. *Polymers* **2017,** *9*, 58.

(189) Xu, Y. Y.; Li, G. C.; Hu, Y. F.; Wang, Y. B. Synthesis of poly(*N*-isopropylacrylamide)-block-poly(tert-butyl methacrylate) block copolymer by visible light-induced metal-free atom transfer polymerization. *Macromol. Chem. Phys.* **2018,** *219*, 1800192.

(190) Sun, Y.; Li, J.; Zhao, M. Y.; Liu, Y. T.; Zhang, J. M.; Lv, C. W. Preparation of block copolymers via metal-free visible-light-induced ATRP for the detection of lead ions. *J. Appl. Polym. Sci.* **2018,** *135*, 45863.

(191) Sun, Y.; Zhao, M. Y.; Liu, Y. T.; Fu, L. Y.; Li, S. Y.; Yang, Y. F. Preparation of erythromycin imprinted polymer by metal-free visible-light-induced ATRP and its application in sensor. *J. Solid State Chem.* **2019,** *23*, 583–590.

(192) Swisher, N. A.; Corbin, D. A.; Miyake, G. M. Synthesis, characterization, and reactivity of *N*-alkyl phenoxazines in organocatalyzed atom transfer radical polymerization. *ACS Macro Lett.* **2021**, *10*, 453–459.

(193) Ma, A. Y.; Zhang, J. K.; Wang, N.; Bai, L. J.; Chen, H.; Wang, W. X.; Yang, H. W.; Yang, L. X.; Niu, Y. Z.; Wei, D. L. Surface-initiated metal-free photoinduced ATRP of 4-vinylpyridine from SiO_2 via visible light photocatalysis for self-healing hydrogels. *Ind. Eng. Chem. Res.* **2018,** *57*, 17417–17429.

(194) Bai, L. J.; Jiang, X. Y.; Sun, Z. X.; Pei, Z. X.; Ma, A. Y.; Wang, W. X.; Chen, H.; Yang, H. W.; Yang, L. X.; Wei, D. L. Self-healing nanocomposite hydrogels based on modified cellulose nanocrystals by surface-initiated photoinduced electron transfer ATRP. *Cellulose* **2019,** *26*, 5305–5319.

(195) Fan, D. C.; Wang, G. L.; Ma, A. Y.; Wang, W. X.; Chen, H.; Bai, L. J.; Yang, H. W.; Wei, D. L.; Yang, L. X. Surface engineering of porous carbon for self-healing nanocomposite hydrogels by mussel-inspired chemistry and PET-ATRP. *ACS Appl. Mater. Interfac.* **2019,** *11*, 38126–38135.

(196) Jiang, X. Y.; Xi, M. Z.; Bai, L. J.; Wang, W. X.; Yang, L. X.; Chen, H.; Niu, Y. Z.; Cui, Y. M.; Yang, H. W.; Wei, D. L. Surface-initiated PET-ATRP and mussel-inspired chemistry for

surface engineering of MWCNTs and application in self-healing nanocomposite hydrogels. *Mater. Sci. Eng. C. Mater. Biol. Appl.* **2020,** *109*, 110553.

(197) Nguyen, L. T.; Pham, H. Q.; Nguyen, D. A. S.; Huynh, K. P. H.; Tran, H. L.; Mai, P. T.; Nguyen, H.; Nguyen, L. T. T.; Truong, T. T. 10-(pyren-1-yl)-10h-phenothiazine and pyrene as organic catalysts for photoinitiated ATRP of 4-vinylpyridine. *Polimeros* **2021,** *31*, 7.

(198) Singha, N. K.; Kavitha, A.; Sarker, P.; Rimmer, S. Copper-mediated controlled radical ring-opening polymerization (RROP) of a vinylcycloalkane. *Chem. Commun.* **2008,** 3049–3051.

(199) Lad, J.; Harrisson, S.; Mantovani, G.; Haddleton, D. M. Copper mediated living radical polymerisation: interactions between monomer and catalyst. *Dalton Trans.* **2003,** 4175–4180.

(200) Mittal, A.; Sivaram, S.; Baskaran, D. Unfavorable coordination of copper with methyl vinyl ketone in atom transfer radical polymerization. *Macromolecules* **2006,** *39*, 5555–5558.

(201) Chen, D. F.; Boyle, B. M.; McCarthy, B. G.; Lim, C. H.; Miyake, G. M. Controlling polymer composition in organocatalyzed photoredox radical ring-opening polymerization of vinylcyclopropanes. *J. Am. Chem. Soc.* **2019,** *141*, 13268–13277.

(202) Chen, D. F.; Bernsten, S.; Miyake, G. M. Organocatalyzed photoredox radical ring-opening polymerization of functionalized vinylcyclopropanes. *Macromolecules* **2020,** *53*, 8352–8359.

(203) de Oliveira, E. R. M.; Vieira, R. P. Synthesis and characterization of poly(limonene) by photoinduced controlled radical polymerization. *J. Polym. Environ.* **2020**, *28*, 2931–2938.

(204) Philipps, K.; Junkers, T.; Michels, J. J. The block copolymer shuffle in size exclusion chromatography: the intrinsic problem with using elugrams to determine chain extension success. *Polym. Chem.* **2021**, *12*, 2522–2531.

(205) Theriot, J. C.; Miyake, G. M.; Boyer, C. A. *N,N*-Diaryl dihydrophenazines as photoredox catalysts for PET-RAFT and sequential PET-RAFT/O-ATRP. *ACS Macro Lett.* **2018,** *7*, 662–666.

(206) Fu, C.; Xu, F.; Boyer, C. Photoacid-mediated ring opening polymerization driven by visible light. *Chem. Commun.* **2016**, *52*, 7126–7129.

(207) Yilmaz, G. One-pot synthesis of star copolymers by the combination of metal-free ATRP and ROP processes. *Polymers* **2019,** *11*, 1577.

(208) Discekici, E. H.; St Amant, A. H.; Nguyen, S. N.; Lee, I.-H.; Hawker, C. J.; de Alaniz, J. R. Endo and exo diels-alder adducts: temperature-tunable building blocks for selective chemical functionalization. *J. Am. Chem. Soc.* **2018,** *140*, 5009–5013.

(209) Hu, X.; Zhang, Y. J.; Cui, G. P.; Zhu, N.; Guo, K. Poly(vinylidene fluoride-co-chlorotrifluoroethylene) modification via organocatalyzed atom transfer radical polymerization. *Macromol. Rapid Commun.* **2017,** *38*, 1700399.

(210) Tan, S. B.; Zhao, Y. F.; Zhang, W. W.; Gao, P.; Zhu, W. W.; Zhang, Z. C. A light-mediated metal-free atom transfer radical chain transfer reaction for the controlled hydrogenation of poly(vinylidene fluoride-chlorotrifluoroethylene). *Polym. Chem.* **2018,** *9*, 221–227.

(211) Hu, X.; Li, N.; Heng, T. T.; Fang, L.; Lu, C. H. Functionalization of PVDF-based copolymer via photo-induced p-anisaldehyde catalyzed atom transfer radical polymerization. *React. Funct. Polym.* **2020,** *150*, 104541.

(212) Lu, C. W.; Wang, C. P.; Yu, J.; Wang, J. F.; Chu, F. X. Metal- free ATRP "grafting from" technique for renewable cellulose graft copolymers. *Green Chem.* **2019,** *21*, 2759–2770.

(213) Lu, C. W.; Guo, X. L.; Wang, C. P.; Wang, J. F.; Chu, F. X. Integration of metal-free ATRP and Diels-Alder reaction toward sustainable and recyclable cellulose-based thermoset elastomers. *Carbohyd. Polym.* **2020,** *242*, 116404.

(214) Buss, B. L.; Beck, L. R.; Miyake, G. M., Synthesis of star polymers using organocatalyzed atom transfer radical polymerization through a core-first approach. *Polym. Chem.* **2018,** *9*, 1658–1665.

(215) Yin, X. Z.; Wang, L. N.; Zhang, X. M.; Zhao, H. T.; Cui, Z.; Fu, P.; Liu, M. Y.; Pang, X. C.; Qiao, X. G. Synthesis of amphiphilic star-shaped block copolymers through photo-induced metal free atom transfer radical polymerization. *Eur. Polym. J.* **2020,** *126*, 109557.

(216) Discekici, E. H.; Pester, C. W.; Treat, N. J.; Lawrence, I.; Mattson, K. M.; Narupai, B.; Toumayan, E. P.; Luo, Y. D.; McGrath, A. J.; Clark, P. G. *et al.* Simple benchtop approach to polymer brush nanostructures using visible-light-mediated metal-free atom transfer radical polymerization. *ACS Macro Lett.* **2016,** *5*, 258–262.

(217) Xu, Z. F.; Tang, B.; Zhou, H.; Li, H.; Wang, Y.; Xu, X. Z.; Zhou, G. F. Metal-free and photo-controlled fabrication of fluorinated anti-fouling film. *Polymer* **2020,** *186*, 122073.

(218) BelBruno, J. J. Molecularly imprinted polymers. *Chem. Rev.* **2019,** *119*, 94–119.

(219) Wang, N.; Zhao, X. Q.; Chen, H.; Bai, L. J.; Xu, H.; Wang, W. X.; Yang, H. W.; Wei, D. L.; Yang, L. X. Fabrication of novel electrochemical immunosensor by mussel-inspired chemistry and surface-initiated PET-ATRP for the simultaneous detection of CEA and AFP. *React. Funct. Polym.* **2020,** *154*, 104632.

(220) Bai, R.; Sun, Y.; Zhao, M.; Han, Z.; Zhang, J.; Sun, Y.; Dong, W.; Li, S. Preparation of IgG imprinted polymers by metal-free visible-light-induced ATRP and its application in biosensor. *Talanta* **2021,** *226*, 122160.

(221) Yan, J. J.; Pan, X. C.; Schmitt, M.; Wang, Z. Y.; Bockstaller, M. R.; Matyjaszewski, K. Enhancing initiation efficiency in metal-free surface-initiated atom transfer radical polymerization (SI-ATRP). *ACS Macro Lett.* **2016,** *5*, 661–665.

(222) Xu, L.; Li, H. L.; Wang, L. P. pH-Sensitive, polymer functionalized, nonporous silica nanoparticles for quercetin controlled release. *Polymers* **2019,** *11*, 2026.

(223) Su, H. L.; Xu, L.; Hu, X. J.; Chen, F. F.; Li, G.; Yang, Z. K.; Wang, L. P.; Li, H. L. Polymer grafted mesoporous SBA-15 material synthesized via metal-free ATRP as pH-sensitive drug carrier for quercetin. *Eur. Polym. J.* **2021,** *148*, 110354.

(224) Yan, C. N.; Liu, Q.; Xu, L.; Bai, L. P.; Wang, L. P.; Li, G. Photoinduced metal-free surface initiated ATRP from hollow spheres surface. *Polymers* **2019,** *11*, 599.

(225) Xu, X.; He, J. J.; Zeng, Y. N.; Yu, C. L.; Zhang, F. Controllable surface-initiated metal-free atom transfer radical polymerization of methyl methacrylate on mesoporous SBA-15 via reductive quenching. *Eur. Polym. J.* **2020,** *131*, 109724.

(226) Xu, X.; Zou, Y.; He, J. J.; Zeng, Y. N.; Yu, C. L.; Zhang, F. A. Insight into the effects of reaction conditions on metal-free surface-initiated atom-transfer radical polymerization of methyl methacrylate from SBA-15. *J. Appl. Phys.* **2020,** *127*, 115102.

(227) Huang, L.; Yu, S. X.; Long, W.; Huang, H. Y.; Wen, Y. Q.; Deng, F. J.; Liu, M. Y.; Xu, W. Y.; Zhang, X. Y.; Wei, Y. The utilization of multifunctional organic dye with aggregation-induced emission feature to fabricate luminescent mesoporous silica nanoparticles based polymeric composites for controlled drug delivery. *Micropor. Mesopor. Mat.* **2020,** *308*, 110520.

(228) Yang, Y.; Liu, X. G.; Ye, G.; Zhu, S.; Wang, Z.; Huo, X. M.; Matyjaszewski, K.; Lu, Y. X.; Chen, J. Metal-free photoinduced electron transfer-atom transfer radical polymerization integrated with bioinspired polydopamine chemistry as a green strategy for surface engineering of magnetic nanoparticles. *ACS Appl. Mater. Interfac.* **2017,** *9*, 13637–13646.

(229) Wang, X. B.; You, N.; Lan, F. Q.; Fu, P.; Cui, Z.; Pang, X. C.; Liu, M. Y.; Zhao, Q. X. Facile synthesis of size-tunable superparamagnetic/polymeric core/shell nanoparticles by metal-free atom transfer radical polymerization at ambient temperature. *RSC Adv.* **2017,** *7*, 7789–7792.

(230) You, N.; Zhang, C. X.; Liang, Y. C.; Zhang, Q.; Fu, P.; Liu, M. Y.; Zhao, Q. X.; Cui, Z.; Pang, X. C. Facile fabrication of size-tunable core/shell ferroelectric/polymeric nanoparticles with tailorable dielectric properties via organocatalyzed atom transfer radical polymerization driven by visible light. *Scientific Reports* **2019,** *9*, 1869.

(231) Chen, J. Y.; Mao, L. C.; Qi, H. X.; Xu, D. Z.; Huang, H. Y.; Liu, M. Y.; Wen, Y. Q.; Deng, F. J.; Zhang, X. Y.; Wei, Y. Preparation of fluorescent cellulose nanocrystal polymer composites with thermo-responsiveness through light-induced ATRP. *Cellulose* **2020,** *27*, 743–753.

(232) Zeng, G. J.; Liu, M. Y.; Heng, C. N.; Huang, Q.; Mao, L. C.; Huang, H. Y.; Hui, J. F.; Deng, F. J.; Zhang, X. Y.; Wei, Y. Surface polyPEGylation of Eu^{3+} doped luminescent hydroxyapatite nanorods through the combination of ligand exchange and metal free surface initiated atom transfer radical polymerization. *Appl. Surf. Sci.* **2017,** *399*, 499–505.

(233) Zeng, G. J.; Liu, M. Y.; Jiang, R. M.; Heng, C. N.; Huang, Q.; Mao, L. C.; Hui, J. F.; Deng, F. J.; Zhang, X. Y.; Wei, Y. Surface grafting of Eu^{3+} doped luminescent hydroxyapatite nanomaterials through metal free light initiated atom transfer radical polymerization for theranostic applications. Mat*er. Sci. Eng. C Mater. Biol. Appl.* **2017,** *77*, 420–426.

(234) Jiang, R. M.; Liu, M. Y.; Huang, H. Y.; Huang, L.; Huang, Q.; Wen, Y. Q.; Cao, Q. Y.; Tian, J. W.; Zhang, X. Y.; Wei, Y. A novel self-catalyzed photoATRP strategy for preparation of fluorescent hydroxyapatite nanoparticles and their biological imaging. *Appl. Surf. Sci.* **2018,** *434*, 1129–1136.

(235) Garlets, Z. J.; Nguyen, J. D.; Stephenson, C. R. J., The development of visible-light photoredox catalysis in flow. *Israel J. Chem.* **2014,** *54*, 351–360.

(236) El Achi, N.; Bakkour, Y.; Adhami, W.; Molina, J.; Penhoat, M.; Azaroual, N.; Chausset-Boissarie, L.; Rolando, C. Metal-free ATRP catalyzed by visible light in continuous flow. *Front. Chem.* **2020,** *8*, DOI: 10.3389/fchem.2020.00740.

(237) Tan, S. B.; Xiong, J.; Zhao, Y. F.; Liu, J. J.; Zhang, Z. C. Synthesis of poly(vinylidene fluoride-cochlorotrifluoroethylene)-g-poly(methyl methacrylate) with low dielectric loss by photo-induced metal-free ATRP. *J. Mater. Chem. C* **2018,** *6*, 4131–4139.

(238) Nikolaou, V.; Anastasaki, A.; Alsubaie, F.; Simula, A.; Fox, D. J.; Haddleton, D. M. Copper(II) gluconate (a non-toxic food supplement/dietary aid) as a precursor catalyst for effective photo-induced living radical polymerisation of acrylates. *Polym. Chem.* **2015,** *6*, 3581–3585.

(239) Gilman, H.; Shirley, D. A. Some derivatives of phenothiazine. *J. Am. Chem. Soc.* **1944,** *66*, 888–893.

(240) Massie, S. P. The chemistry of phenothiazine. *Chem. Rev.* **1954,** *54*, 797–883.

(241) Shirley, D. A.; Lehto, E. A. The metalation of 4-t-butyldiphenyl sulfone with n-butyllithium *J. Am. Chem. Soc.* **1957,** *79*, 3481–3485.

(242) Dietrich, L. E. P.; Teal, T. K.; Price-Whelan, A.; Newman, D. K. Redox-active antibiotics control gene expression and community behavior in divergent bacteria. *Science* **2008,** *321*, 1203–1206.

(243) Price-Whelan, A.; Dietrich, L. E. P.; Newman, D. K. Rethinking 'secondary' metabolism: physiological roles for phenazine antibiotics. *Nat. Chem. Biol.* **2006,** *2*, 71–78.

(244) Palmer, B. D.; Rewcastle, G. W.; Atwell, G. J.; Baguley, B. C.; Denny, W. A. Potential antitumor agents. 54. Chromophore requirements for in vivo antitumor activity among the general class of linear tricyclic carboxamides. *J. Med. Chem.* **1988,** *31*, 707–712.

(245) Laursen, J. B.; Nielsen, J. Phenazine natural products: biosynthesis, synthetic analogues, and biological activity. *Chem. Rev.* **2004,** *104*, 1663–1685.

(246) Mavrodi, D. V.; Blankenfeldt, W.; Thomashow, L. S. Phenazine compounds in fluorescent Pseudomonas spp. Biosynthesis and regulation. *Annual Rev. Phytopath.* **2006,** *44*, 417–445.

(247) McRose, D. L.; Newman, D. K. Redox-active antibiotics enhance phosphorus bioavailability. *Science* **2021,** *371*, 1033–1037

CHAPTER 3.

FUNDAMENTALS OF PHOTOCHEMICAL REDOX REACTIONS

Overview

The extensive development of photoredox catalysis in the past decade has enabled both old and new reactions to be performed under mild, light-driven conditions. In this chapter, and overview of photoredox reactions is provided, starting with a brief history of photoredox catalysis and electron donor-acceptor (EDA) chemistry. Fundamental concepts, common instrumental techniques, and general considerations for photoredox reactions are broadly discussed, as well as specific details related to photoredox catalysis and EDA chemistry. Examples demonstrating the application of these chemistries in organic synthesis and polymer chemistry are highlighted. Finally, as this chapter aims to serve as a broad introduction to photoredox reactions, additional reading is suggested at the end of the chapter where readers can delve into the concepts presented herein in greater detail.

Introduction: A Brief History of Photochemistry

For centuries, scientists have sought to understand how light impacts chemical reactions. In 1790 Joseph Priestley reported the photochemical conversion of nitric acid to nitrogen dioxide, and around the same time he formed hypotheses on the basic nature of photosynthesis.[1] Serendipitously, in the late nineteenth century, the German chemist Heinrich Klinger observed photochemical reductions of various quinones to hydroquinones using sunlight (Figure 3.1). In what are considered the first examples of synthetic organic photochemistry, Klinger established that sunlight drove the intermolecular reaction of quinones and aldehydes or ketones to yield

interesting new products, although the mechanistic basis for these transformations was not understood at the time.

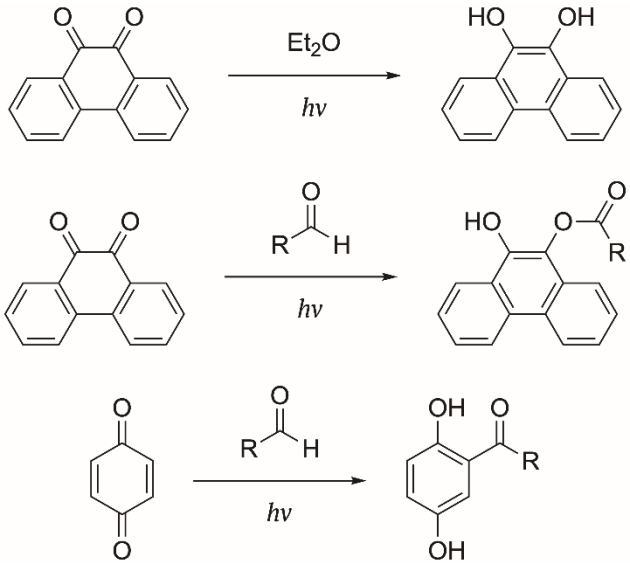

Figure 3.1. *Early photochemical quinone reductions studied by Klinger.*

Many further developments in early solar photochemistry arose from the collaboration of Giacomo Ciamician and Paul Silber at the University of Bologna.[2] Over the course of many years, the pair discovered several fascinating reactions that were frequently conducted on their rooftop laboratory. Photochemical olefin isomerizations, pinacol-type couplings, and cycloadditions are just some of the reaction categories explored thoroughly. Both the reduction of nitrobenzene in ethanol to 2-methylquinoline and the coupling of acetone and methanol made apparent the potential of natural light in the synthesis of organic compounds (Figure 3.2).

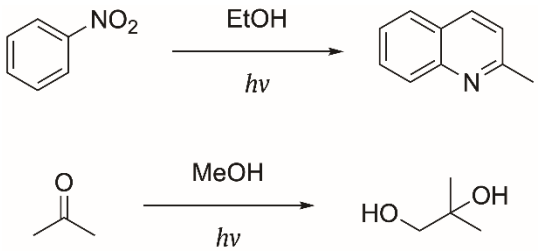

Figure 3.2. *Condensation of nitrobenzene and ethanol to form 2-methylquinoline and coupling reaction of acetone and methanol studied by Ciamician and Silber in Bologna.*

Two key advances that spurred progress in synthetic photochemistry in the following decades were the development of modern light sources and transition metal photocatalysts, namely ruthenium and iridium polypyridyl complexes. The 1978 reduction of sulfonium salts with Hantzsch esters in the presence of visible light and catalytic amounts of the complex $[Ru(bpy)_3]Cl_2$ by Kellogg highlights the power of these innovations (Figure 3.3).[3] This reaction is considered one of the earliest examples of photoredox catalysis, or catalysis using light energy to initiate single electron transfer (SET) processes.

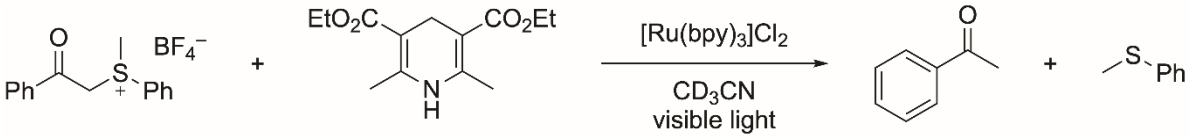

Figure 3.3. *First catalytic photoredox reaction for the reduction of sulfonium salts reported by Kellogg in 1978.*

Other early instances of reductive photoredox catalysis also utilized $[Ru(bpy)_3]Cl_2$ as a photocatalyst and nitrogen-containing heterocyclic compounds as stoichiometric reductants. In 1981, Pac disclosed an electron-poor olefin reduction with 1-benzyl-1,4-dihydronicotinamide as a reductant under visible light to model biological redox reactions (Figure 3.4).[4] Further, Fukuzumi and coworkers described the dehalogenation of phenacyl bromides with 10-methyl-9,10-dihydroacridine as an electron and H-atom donor in 1990.[5]

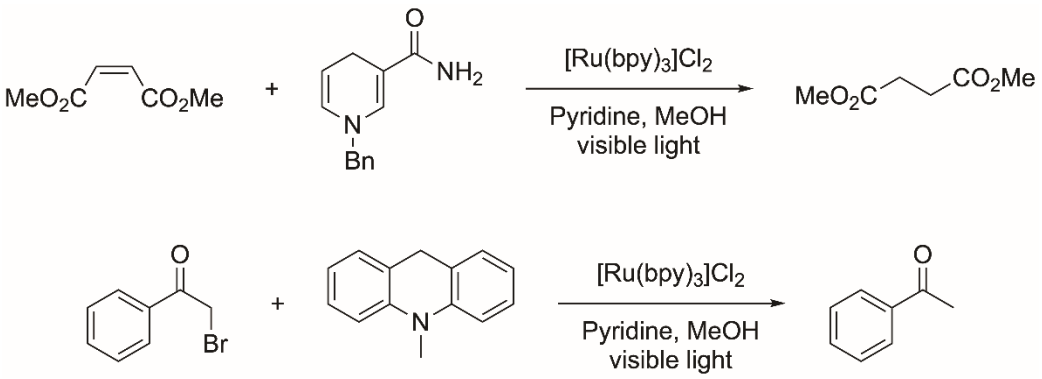

Figure 3.4. *Early photoredox reductions detailed by Pac and Fukuzumi.*

Net oxidative reactions in early photoredox catalysis include the conversion of benzyl alcohols to aldehydes mediated by aryl diazonium salts observed in 1984 by Cano-Yelo and Deronzier (Figure 3.5).[6] Similarly, an intramolecular Pschorr cyclization of an aryl diazonium salt from the same authors represents the first catalytic, redox-neutral organic photoredox reaction in the literature.[7]

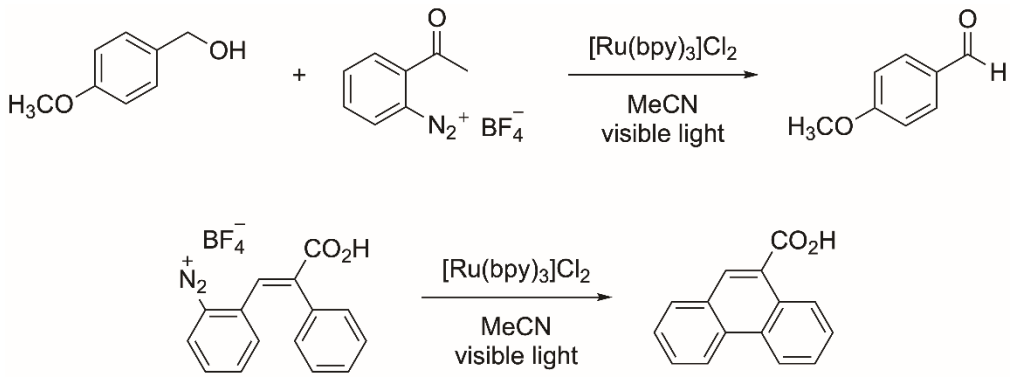

Figure 3.5. *Photoredox reactions of aryl diazonium salts developed by Cano-Yelo and Deronzier.*

The modern resurgence of photoredox catalysis began in 2008 with reports by Yoon and MacMillan on stereoselective visible light mediated reactions. Yoon's group communicated diastereoselective [2+2] photocycloadditions of bis(enones) to give bicyclic cyclobutane-containing diones, again using $[Ru(bpy)_3]Cl_2$ as a photocatalyst (Figure 3.6).[8] While the use of

high-intensity flood lights enabled efficient cycloaddition reactions, sunlight from a laboratory window also promoted the reaction with high yield and stereoselectivity. By virtue of the milder reaction conditions employed as compared to conventional transition metal or electrochemical catalysis, Yoon's method enjoyed a wide substrate scope including both electron-deficient and rich enones.

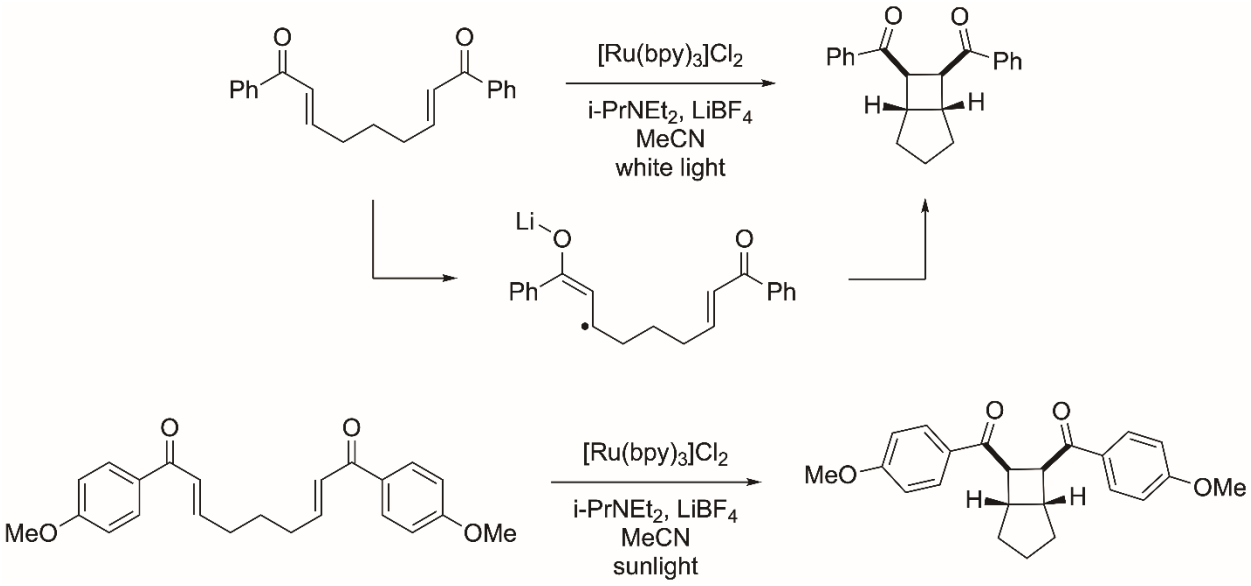

Figure 3.6. *Photoredox [2+2] enone cycloadditions reported by Yoon.*

The simultaneous publication by Nicewicz and MacMillan on the enantioselective α-alkylations of aldehydes using a combination of photoredox and organocatalysis was another seminal milestone in the field (Figure 3.7).[9] Using simple household 15W compact fluorescent lightbulbs (CFLs), they found that alkyl bromides could serve as suitable coupling partners to aldehydes in the presence of chiral imidazolidinone catalysts and $[Ru(bpy)_3]Cl_2$ as the photocatalyst. Prior to this disclosure, the direct enantioselective functionalization of aldehydes with simple alkyl groups was considered a fundamental challenge in organic synthesis,

demonstrating the synergistic power of photoredox catalysis when merged with other forms of catalysis.

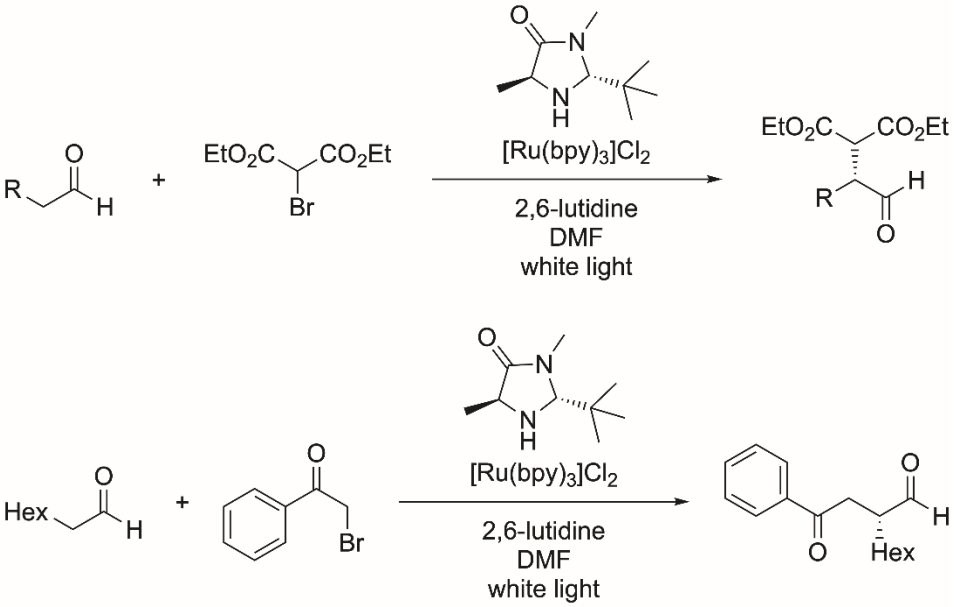

Figure 3.7. *MacMillan's report on the enantioselective alkylation of aldehydes with simple alkyl halide coupling partners.*

In 2009 Stephenson further expanded the possibilities of photoredox catalysis in the dehalogenation of a diverse array of Csp^3-X (X = Br, Cl) bonds (Figure 3.8).[10] With a simple alkylamine base as a terminal reductant, this synthetic method provided an excellent alternative to the toxicity and product separation issues that plague classical tin-mediated dehalogenations. Thus, improvements in photoredox catalysis can be attractive from the perspective of substituting relatively benign reagents for inconvenient and hazardous compounds in interesting redox reactions.

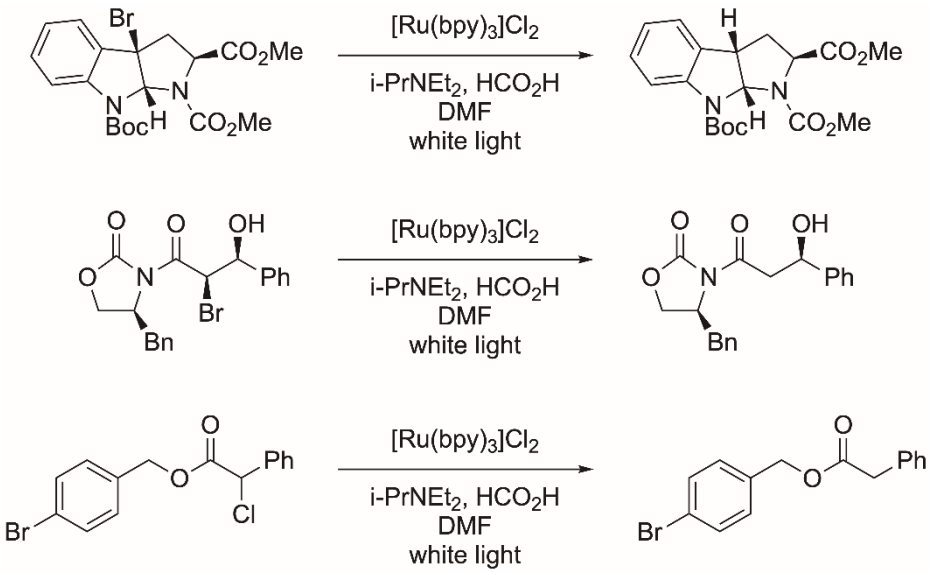

Figure 3.8. *Photoredox dehalogenation reactions developed by Stephenson.*

In the years following these landmark discoveries, applications of photoredox catalysis have expanded to a very broad array of transformations, including those once thought to be the domain of transition metal catalysis. Photoredox carbon-sulfur cross-coupling reactions between aryl halides and thiols have been performed by dual-catalysis employing both transition metal and organic photoredox catalysts.[11] Further, through control experiments, investigations have revealed some photoredox reactions can proceed in the absence of a photocatalyst (see *Rediscovering EDA complexes through photoredox catalysis* section).[12–14] For example, Miyake and coworkers revealed that certain C-S cross-coupling reactions could be conducted under visible light irradiation without any photocatalyst at all (Figure 3.9).[15,16] Mechanistic studies supported that such reactions can proceed through the formation of electron donor-acceptor (EDA) complexes, which when irradiated undergo electron transfer to initiate redox reactions.[13–15] In the example reported by Miyake and coworkers, this intermolecular electron transfer generates aryl and thiyl radicals, which subsequently combine to yield the C-S coupling products.[15] In photochemical transformations, the formation of such EDA complexes, also referred to as charge transfer (CT)

complexes, between electron-rich donor molecules and electron-poor acceptor molecules must always be considered a possibility for conducting electron transfer without catalysts.

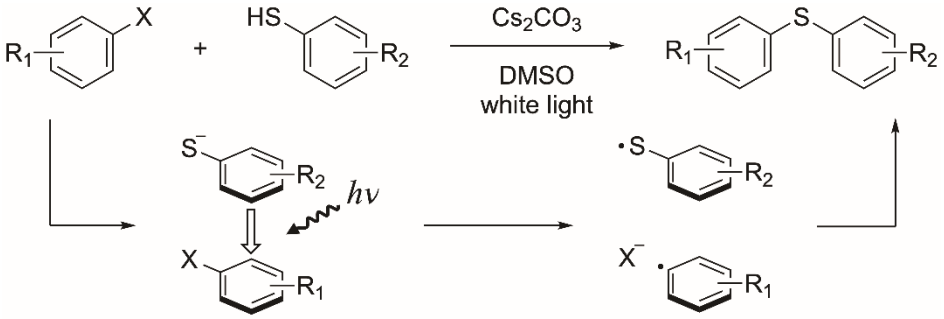

Figure 3.9. *Carbon-sulfur bond formation as a result of EDA complex formation and photoinduced intermolecular electron transfer.*

The remainder of this chapter begins with an overview of the fundamental concepts required to understand photoredox reactions. The theory behind common instrumental techniques and their application to the characterization of photoredox processes is also presented. With this foundation, the basic mechanisms of different classes of photoredox catalysis are then discussed, followed by a survey of the many different families of transition metal and organic photoredox catalysts reported in the literature. Finally, the recent development and application of EDA complexes in synthetic organic transformations is briefly reviewed.

Photochemistry: Background and Theory

The electromagnetic spectrum

Light is all around us. Even when we cannot see it, light, or electromagnetic radiation, warms our food, allows us to communicate with each other over vast distances, and offers a glimpse into the human body through medical imaging. Just as light is at the center of numerous technologies we use in our everyday lives, it also plays a role in a variety of chemical processes.

Figure 3.10 shows a common depiction of the electromagnetic spectrum broken into seven categories: γ-ray, x-ray, ultra-violet (UV), visible, infrared, microwaves, and radio waves. Each category is defined by a range of wavelengths or frequencies, which correspond to the energy of that light (Equation 3.1). Often, different units of energy are used for light, so some helpful conversions have been provided in Figure 3.10 and in Equations 3.2 – 3.4.

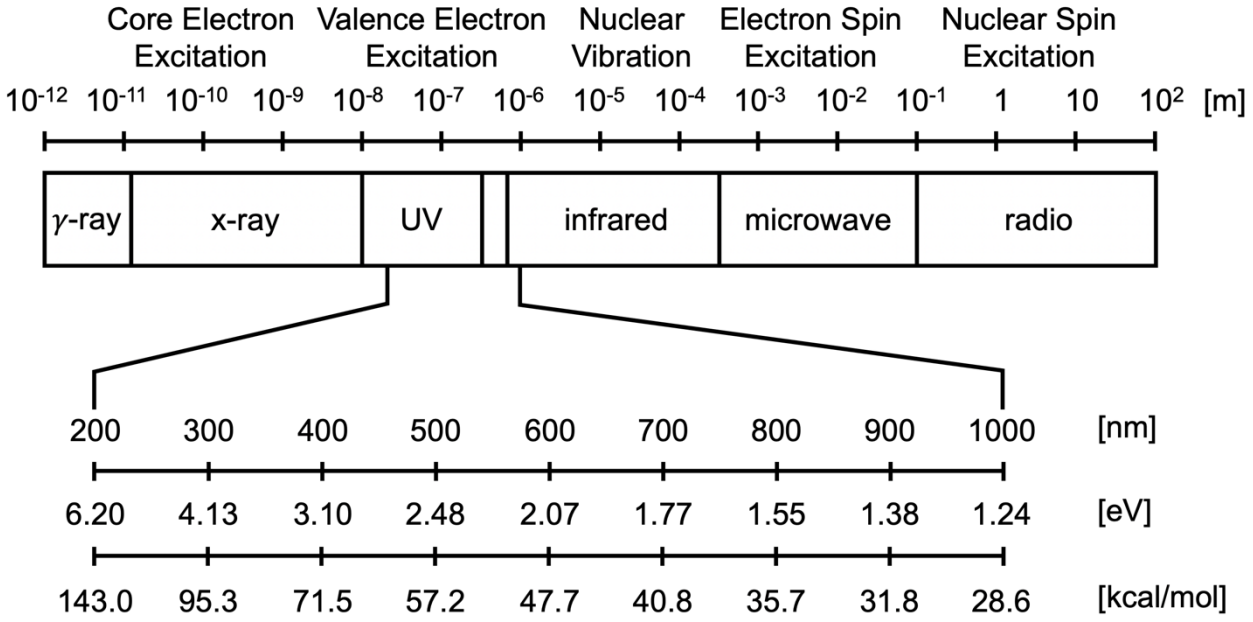

Figure 3.10. *Electromagnetic spectrum, with a focus on regions associated with electronic transitions. On the top, labels indicate the approximate regions in which different transitions and excitations occur. On the bottom, wavelengths often associated with electronic transitions are converted into other useful units.*

Importantly, the energy of light can sometimes correspond to chemical transitions (Figure 3.10), giving rise to a myriad of photochemical processes. For example, in nuclear magnetic resonance spectroscopy, radio waves are used to cause transitions between different nuclear spin states and probe the chemical environment around those nuclei. Since the difference in energy between nuclear spin states is quite small, very low energy light is necessary to probe these processes. On the other end of the spectrum, x-rays can be found at the heart of x-ray photoelectron

spectroscopy, where they are used to promote high energy transitions and ionize core electrons of various elements. One application of light in chemistry that has recently garnered significant attention is the use of light to promote valence electronic transitions that lead to interesting redox reactions. Since such reactions usually involve breaking bonds, a process that generally requires 20-100 kcal/mol of energy, it is unsurprising that ultraviolet (UV) and visible light have been explored extensively for this application.

$$E = h\nu = \frac{hc}{\lambda} \quad \text{(Eq. 3.1)}$$

$$E = \frac{1240\ eV \cdot nm}{\lambda} \quad \text{(Eq. 3.2)}$$

$$E = \frac{2.86 \cdot 10^4\ kcal \cdot nm \cdot mol^{-1}}{\lambda} \quad \text{(Eq. 3.3)}$$

$$1\ eV = 23.06\ kcal \cdot mol^{-1} \quad \text{(Eq. 3.4)}$$

Allowed and forbidden transitions

Within an atom or molecule, one can imagine a number of different electronic transitions from one state to another. Broadly, we can classify transitions that are theoretically predicted to occur as quantum mechanically allowed, whereas those that are not predicted to occur are forbidden. It is important to note that the origin of allowed and forbidden transitions is quantum mechanical, meaning one can use theory to predict whether certain transitions will be allowed based on changes in quantum numbers and symmetry. These predictions regarding what transitions allowed or forbidden are often referred to as selection rules.

Curiously, although some transitions are considered forbidden, they can still occur to some degree through various processes. For example, in centrosymmetric metal complexes (those containing inversion center symmetry), transitions between two d-orbitals are considered forbidden based on the Laporte selection rule, yet d to d transitions are still observed for many metal complexes. This phenomenon arises because the Laporte selection rule applies only to symmetric molecules. Therefore, if a vibration within a molecule breaks its symmetry, this selection rule no longer applies and d to d transitions can become allowed. This specific process is referred to as vibronic coupling. Another process through which forbidden transitions might occur is called spin orbit coupling and this phenomenon will be discussed later in the text (see *Intersystem crossing* section). Importantly, while forbidden transitions can occur under the appropriate conditions, they typically occur to only a small degree, making them relatively weak or infrequent transitions.

Photophysical processes

Jablonski diagrams. When discussing photophysical processes, it is common to depict them on a Jablonski diagram. First proposed by Aleksander Jabłoński in 1933,[17] this diagram depicts different electronic states and the possible transitions between them (Figure 3.11). Sometimes, electronic states may be depicted as potential wells, but they are often simplified into lines representing the lowest energy vibrational state for each electronic state. Within each electronic level, one can also find several vibrational states. Since vibrational transitions are usually lower in energy than electronic transitions, the spacing between different vibrational states is smaller than that between electronic states.

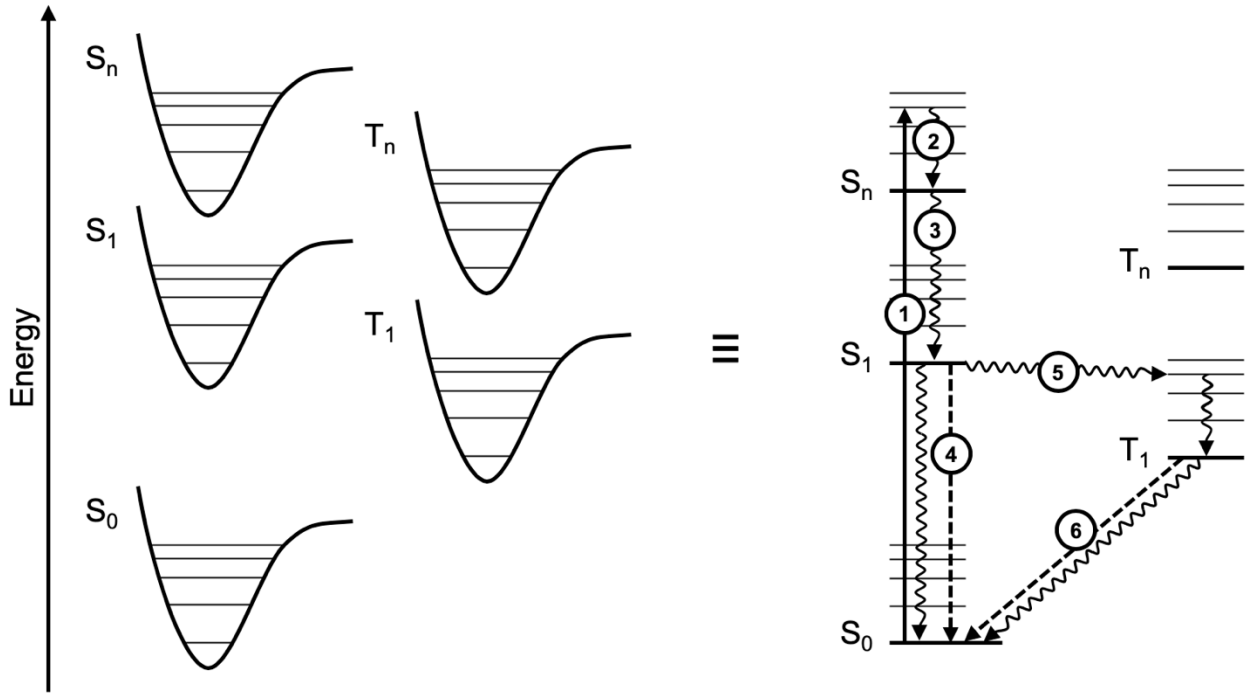

Figure 3.11. *A Jablonski diagram depicted in two ways. On the left, electronic states are represented by potential wells, within which each energy level represents a different vibrational state. For ease of viewing, the diagram on the right is often used, which simplifies each electronic state to a line rather than a potential well. Transitions between different states can occur through absorption of light (1), vibrational relaxation (2), internal conversion (3), fluorescence (4), intersystem crossing (5), or phosphorescence (6). S = singlet state; T = triplet state.*

In addition, the electronic states can be labeled according to their multiplicity and relative energies. Multiplicity (M) refers to the number of unpaired electrons in a given state and is defined as $M = 2S + 1$, where S is the total spin angular momentum quantum number for a multielectron system. Put simply, each unpaired electron has a value of $S = ½$. Therefore, a state with no unpaired electrons has $M = 1$ and is termed a singlet state. Instead, a system with one unpaired electron has $M = 2$ and is termed a doublet state, whereas a system with two unpaired electrons has $M = 3$ and is termed a triplet state. States of even higher multiplicity are certainly possible and have been identified, especially in inorganic and organometallic systems where it is common to find molecules with a number of unpaired d-electrons. However, the three states outlined here are most common for organic molecules and their excited states and will be the focus of this discussion. Of

course, multiple electronic states may exist with the same multiplicity, so it is common to label them based on their relative energies. For example, S_0 corresponds to the lowest energy singlet state, often the ground state of many organic molecules, while S_1 corresponds to an electronic excited state with singlet character.

Finally, since we are interested in the processes for moving from one state to another on the Jablonski diagram, we can label these transitions with one of several different arrows. Typically, absorption (Figure 3.11: 1) is represented by a solid arrow, whereas emission (Figure 3.11: 3 and 6) is depicted using a dashed arrow. In addition, a number of nonradiative relaxation processes can occur (Figure 3.11: 2, 3, and 5), which are commonly represented by wavy arrows. Importantly, transitions between states occur when their potential energy surfaces cross at one or more points, although these crossing points are often not depicted in Jablonski diagrams for simplicity. In the following sections, we will delve deeper into each of these photophysical processes and important related concepts.

Absorption. Absorption is the process by which energy from light is taken-in by electrons to promote transitions from lower energy electronic states to ones of higher energy. This process is quite fast, generally occurring on the time scale of 10^{-16} – 10^{-14} s. As a result, very few processes can compete with the absorption of light, since these electronic transitions tend to be much faster than anything else. For example, even nuclear motion is relatively slow compared to this process, occurring over 10^{-13} – 10^{-12} s. In fact, one can consider nuclei to be effectively motionless during an electronic transition, a concept known as the Frank-Condon principle. As a consequence of this principle, the geometries of two interconverting states must be identical prior to an electronic transition, since the geometry of the molecule does not change during the transition.

Table 3.1. *Typical time scales of photophysical processes for organic molecules.*

Process	Time Scale (s)
Absorption	$10^{-16} – 10^{-14}$
Vibrational Relaxation	$10^{-12} – 10^{-10}$
Internal Conversion	$10^{-11} – 10^{-9}$
Fluorescence	$10^{-8} – 10^{-5}$
Intersystem Crossing	$10^{-8} – 10^{-3}$
Phosphorescence	$10^{-3} – 10^{2}$

For a photon of light to be absorbed by a molecule, the energy of the photon must exactly match the difference in energy between two states. Further, only one photon can be absorbed to promote a transition (although two photons can be absorbed consecutively to access higher energy excited states). Together, these principles are known as the Stark-Einstein Law, and they have important implications in chemistry. For instance, since the energy of light absorbed must correspond to the energy of a transition, we can measure what light is absorbed or emitted by a molecule (or atom) to learn about the relative energies of its electronic states. Further, considering the use of light in chemical synthesis, if we desire to use certain wavelengths of light – such as those in the visible spectrum – we must design the system appropriately to absorb those wavelengths of light.

With these thoughts in mind, it can be useful when performing photochemistry to investigate what wavelengths of light a molecule absorbs when irradiated. Often this technique, called absorption spectroscopy, is performed using UV and visible light to probe electronic transitions, but it is certainly not limited to just these wavelength ranges. While a more detailed description of this technique will be provided in a later section (see *UV-visible spectroscopy*

section), here it will suffice to understand that absorption spectroscopy quantifies how much light is absorbed at a specific wavelength. This quantity is often given as the unitless value of absorbance (A), often used interchangeably with optical density (OD), which corresponds to the logarithm of the intensity of light entering the sample (I_o) over the intensity of light exiting the sample and reaching the detector (I).

$$A = OD = log_{10}\left(\frac{I_o}{I}\right) \quad \text{(Eq. 3.5)}$$

When the absorption of an atom or molecule is measured across a range of wavelengths, the resulting spectrum is called an absorption spectrum. In the simplest case, one can imagine a molecule with a single electronic transition, which would absorb a single wavelength of light. The absorption spectrum of this molecule would have a vertical line corresponding to the wavelength of light absorbed. In reality, molecules often have numerous possible transitions between different electronic and vibrational states that are close in energy, resulting in absorption spectra with broad features rather than lines corresponding to single transitions.

Of course, not all electronic transitions are equally probable, and some occur to a greater degree than others. As a result, one often sees that the intensities of peaks in an absorption spectrum vary from one to the next, corresponding to different amounts of light being absorbed to promote certain transitions. The propensity of a molecule to absorb a certain wavelength of light can be described using molar absorptivity (ε), which is also referred to as the extinction coefficient. However, other factors can also impact the amount of light absorbed, such as the concentration of the absorbing molecule (c) as well as the path length (b) of the sample through which light must travel. These concepts are summarized as Beer's Law (Equation 3.6), which relates the amount of light absorbed at a particular wavelength to each factor above:

$$A = \epsilon bc \qquad \text{(Eq. 3.6)}$$

Finally, when employing light as a reagent in chemical synthesis, it is important to consider how that light will interact with different compounds in the reaction. Table 3.2 lists the approximate wavelength of maximum absorption (λ_{max}), approximate molar absorptivity at λ_{max} (ε_{max}), and the type of transition observed for common organic functional groups. As can be seen, many organic functionalities tend to absorb light in the UV range, meaning that irradiation with light in this range of the spectrum could give rise to a number of different reactions. While this reactivity can be useful in certain situations, it is often undesirable as it can be difficult to control. Therefore, synthetic strategies employing visible light are often desirable, since under these conditions, reactions can be targeted without unwanted excitation of other molecules in solution.

Vibrational relaxation. When light is absorbed by a molecule, it promotes the formation of a number of different electronic and vibrational excited states. For simplicity, this discussion will focus on a generic organic system, in which excitation occurs from a singlet ground state (S_0) to a generic singlet excited state (S_n, $n > 0$). From these excited states, a number of possible relaxation processes can occur, including radiative – ones involving the emission of light – and nonradiative processes. The first that will be considered is vibrational relaxation, by which a molecule relaxes from a vibrational excited state to the vibrational ground state within a given S_n (Figure 3.11: 2). During this nonradiative process, excess energy is converted to kinetic energy and distributed throughout the molecule and surrounding environment through vibrations. As a result, vibrational relaxation is generally quite fast, occurring on the time scale of 10^{-12} – 10^{-10} s.

Table 3.2. *Absorption characteristics of common organic functional groups.*

Functional Group	Approximate λ_{max} (nm)	Approximate ε_{max} (L mol^{-1} cm^{-1})	Transition
Alkane	< 180	10^3	$\sigma \rightarrow \sigma^*$
Alcohol	180	10^2	$n \rightarrow \sigma^*$
Alkene	180	10^4	$\pi \rightarrow \pi^*$
Alkyne	180	10^4	$\pi \rightarrow \pi^*$
Carboxylic Acid	200	10^1	$n \rightarrow \pi^*$
Conjugated Alkene	> 200	10^4	$\pi \rightarrow \pi^*$
Amide	210	10^1	$n \rightarrow \pi^*$
Bromo	210	10^2	$n \rightarrow \sigma^*$
Iodo	260	10^2	$n \rightarrow \sigma^*$
Benzene	280	10^2	$\pi \rightarrow \pi^*$
Carbonyl	280	10^1	$n \rightarrow \pi^*$
Naphthalene	310	10^2	$\pi \rightarrow \pi^*$
Anthracene	380	10^4	$\pi \rightarrow \pi^*$

Internal conversion. Once a molecule has relaxed to the lowest vibrational state within an electronic excited state, it can then relax to lower energy electronic excited states through a nonradiative process known as internal conversion (Figure 3.11: 3). Practically, this process is very similar to vibrational relaxation, although it can be slower due to the greater energy difference between electronic states relative to vibrational states. A typical time scale for internal conversion is 10^{-11} – 10^{-9} s, though this process can be slower for transitions between states of significantly different energies (ex. $S_1 \rightarrow S_0$).

In most cases, a molecule in the condensed phase will rapidly relax through internal conversion and vibrational relaxation to the lowest energy excited state, in this case S_1 (Kasha's

rule).[18] Practically, this means that most photochemistry in condensed phases occurs from the lowest energy excited state,[19] a phenomenon that has been extensively observed for a variety of different systems. As a result, many of the processes that follow, as well as most photochemical processes that are of interest to the synthetic chemist, occur from either S_1 or T_1, the latter of which will be discussed further in subsequent sections (see *Intersystem crossing* and *Phosphorescence* sections). Of course, several exceptions to Kasha's rule have been observed,[20] with one notable example being azulene, in which fluorescence occurs primarily from S_2 rather than S_1. In addition, Kasha's rule is less applicable in the gas phase, where internal conversion and vibrational relaxation are much slower due to decreased intermolecular interactions.

Fluorescence. Once a molecule has relaxed to S_1 (with a few exceptions as discussed above), it can undergo a radiative relaxation process to S_0 called fluorescence (Figure 3.11: 4), typically within 10^{-8} – 10^{-5} s. Importantly, while fluorescence is often observed from S_1 to S_0, it is relevant for any two states of the same multiplicity. Sometimes, this process may also be referred to as emission or luminescence, but one should note that these latter terms are more general and can also refer to emission from a triplet state (see *Phosphorescence* section). Fluorescence may occur to any vibrational state within S_0, leading to emission over a range of wavelengths.

Much useful information can be obtained by monitoring the fluorescence of a compound, some of which will be discussed further in a later section (see *Emission Spectroscopy* section). One example is the S_1 excited state energy, since the energy of the photon emitted during relaxation is equal to the energy difference between S_0 and S_1. Although the same relationship also holds true for absorption, fluorescence has the advantage of operating primarily from a single excited state due to Kasha's rule. By contrast, absorption may promote formation of a number of different excited states, making it difficult to measure the energy of just one.

In addition, since some energy is lost to various relaxation processes prior to fluorescence, it is common that the λ_{max} of fluorescence is red-shifted (shifted to lower energies of light, also known as a bathochromic shift) relative to the λ_{max} of absorption. This shift in the λ_{max} is known as a Stokes shift. On rare occasions, a molecule may exhibit an anti-Stokes shift, where the λ_{max} of fluorescence is blue-shifted (shifted to higher energies of light, also known as a hypsochromic shift) relative to the λ_{max} of absorption. This phenomenon is made possible when absorption occurs from a vibrational excited state of S_0, such that the energy absorbed is less than the energy emitted during the transition from S_1 to the vibrational ground state of S_0.

Finally, the fluorescence of a molecule can sometimes be sensitive to environmental factors, providing another opportunity to investigate the properties of the excited state. One example of such a property is solvatochromism, where the fluorescence of the molecule changes as a function of solvent polarity. By measuring this solvatochromic effect, one can gain insight into the relative stability of the excited state, as well as charge transfer effects that might give rise to a polar excited state. Solvatochromism is not unique to emission and can even be observed in absorption, although this phenomenon is less common.

Intersystem crossing. An alternative process that may occur is intersystem crossing, although this process is generally slower (10^{-8} – 10^{-3}) and cannot always compete with faster relaxation processes. Specifically, intersystem crossing (ISC) is the process by which the spin – an intrinsic form of angular momentum exhibited by elementary particles – of the excited electron is inverted, converting a singlet excited state to a triplet excited state. For ISC to occur, the corresponding singlet and triplet states must share a common geometry (the Frank-Condon principle, see *Absorption* section), which corresponds to a crossing point of their potential energy surfaces. Since the inversion of spin is considered a forbidden transition, it is unsurprising that this

process is generally slower than other relaxation events. Regardless, ISC from S_n produces a triplet excited state (T_n), which then rapidly relaxes to T_1 in accordance with Kasha's rule (see *Internal conversion* section). Importantly, the reader should remember that this discussion focuses on singlet and triplet states for simplicity, but ISC is certainly not limited to these states. For example, it is also feasible for intersystem crossing to convert a doublet to a quartet state.[21]

When considering ISC, the question arises: how does a spin-flip occur if it is quantum mechanically forbidden? The answer is through spin-orbit coupling. To understand this phenomenon, it is important to first understand why a spin-flip is forbidden. Typically, spin-flips are considered forbidden because it is thought that the spin angular momentum of an electron must remain constant. However, a more accurate statement is that the total angular momentum of the electron must remain constant, which is a sum of the spin angular momentum and the orbital angular momentum. As a consequence, while a spin-flip does change spin angular momentum, this change can be compensated by an equal but opposite change in orbital angular momentum. Hence, spin-orbit coupling combines a spin-flip with an orbital change to conserve the total angular momentum of the electron, making ISC allowed under the appropriate conditions.

As a result of spin-orbit coupling, atoms or molecules with a greater number of orbitals are more likely to undergo intersystem crossing. This concept is known as the heavy atom effect, since heavier atoms tend to also have a greater number of atomic orbitals (ex. iodine vs. fluorine), leading to a greater probability that an orbital change can be coupled to a spin flip. Therefore, ISC is generally more common for inorganic or organometallic molecules than for organic molecules, although several strategies exist for increasing the triplet yield of organic molecules. For example, incorporating heavy atoms such as bromine or iodine can increase intersystem crossing in a molecule. In addition, the presence of carbonyls can be advantageous, as

spin-orbit coupling can be achieved by converting between an (n,π*) S_1 state to a (π,π*) T_1 state (El Sayed's rules), providing the necessary orbital change. Finally, twisted intramolecular charge transfer (TICT) states can also be advantageous for promoting ISC. TICT refers to charge transfer between an electron donor and acceptor that are connected by a single bond, which gives rise to a twisted charge-separated state. The product of TICT is a molecule that closely resembles a radical ion pair, where an electron from a donor-centered orbital is transferred to an acceptor-centered orbital. As such, this orbital change can also serve to promote intersystem crossing.

Phosphorescence. After ISC produces a triplet excited state, several possible relaxation pathways analogous to those previously discussed for S_1 exist. For instance, the molecule may relax to S_0 *via* nonradiative decay processes, such as vibrational relaxation or internal conversion. For organic molecules, these nonradiative processes are generally predominant, leading to limited phosphorescence (Figure 3.11: 6), or emission from T_1. Similar to fluorescence, phosphorescence can occur between any two states that involve and inversion of spin, but T_1 to S_0 is most common in organic molecules. Often, organic molecules must be cooled to low temperatures in a glassing solvent, such as 2-methyl tetrahydrofuran, to reduce nonradiative relaxation, allowing phosphorescence to be observed. Further, compared to other relaxation processes, the time scale of phosphorescence is generally quite slow – on the order of 10^{-3} – 10 s or even longer. As a consequence, triplet excited states tend to be long lived – on the order of tens of nanoseconds up to microseconds, milliseconds, seconds, and even minutes – making them well suited to engage in bimolecular reactions.

Electron transfers

Up to this point, we have mainly discussed photophysical processes that occur when a

molecule interacts with light. In this section, we will briefly discuss theories of electron transfer and how they can be applied to photoredox reactions.

Photoinduced electron transfer. When applying photoredox chemistry to chemical synthesis, we are interested in harnessing energy from light to enable interesting transformations under mild conditions that might not otherwise be possible. As such, it is important to understand how that light is converted to chemical energy, and how this strategy is unique to others.

When light is absorbed by a compatible molecule, that light promotes an electron into an excited state with different properties relative to the molecule's electronic ground state. In some cases, the excited state may have drastically different redox properties than the ground state, leading to electron transfer events that would otherwise be challenging. When electron transfer (ET) is promoted by absorption of light, it is termed photoinduced electron transfer (PET). Such ETs will be the basis of much of the chemistry discussed in the coming sections (see *Photoredox catalysis* and *Photochemistry of electron donor-acceptor complexes* sections).

The Gibbs free energy of PET (ΔG^o_{ET}) in units of [J mol^{-1}] can be calculated according to Equation 3.7:

$$\Delta G^o_{ET} = N_A \{e[E^o(D^+/D) - E^o(A/A^-)] + w(D^+A^-) - w(DA)\} - \Delta E_{0-0} \qquad \text{(Eq. 3.7)}$$

where N_A is Avogadro's number (6.022 x 10^{23} mol^{-1}), e is the elementary charge (1.602 x 10^{-19} C), D is a generic donor, A is a generic acceptor, E^o is a standard potential [V], w is an electrostatic work function [J], and $\Delta E_{0\text{-}0}$ is the energy difference between the lowest vibrational level of the ground state and relevant excited state [J/mol]. The electrostatic work function is given by Equation 3.8:

$$w(XY) = \frac{z_x z_y e^2}{4\pi\epsilon_o\epsilon_r a} \qquad \text{(Eq. 3.8)}$$

where *x* and *y* are two generic components (ex. D and A), *z* is the signed magnitude of the charge [unitless], ε_o is the vacuum permittivity (8.854 x 10^{-12} C^2 J^{-1} m^{-1}), ε_r is the relative medium static permittivity (also referred to as the solvent dielectric constant) [unitless], and *a* is the distance between the charged species after electron transfer [m]. Equation 3.7 is sometimes referred to as the Rehm-Weller equation, although IUPAC has recommended against doing so as this name is inaccurate.[22]

Data for use in Equation 3.7 can be obtained using two techniques. The standard potentials can be approximated by the $E_{1/2}$ for the relevant redox couple obtained using cyclic voltammetry (see *Cyclic voltammetry* section). $\Delta E_{0\text{-}0}$ corresponds to the excited state energy, which can be measured using emission spectroscopy (see *Emission spectroscopy* section). Further, while electrostatic work can be more challenging to determine, it can often be omitted during photoredox reaction development, as the magnitude of *w* is generally negligible.[23]

Mechanisms of electron transfer. Broadly, ETs can be broken into two categories: inner sphere electron transfer (ISET) and outer sphere electron transfer (OSET). In each case, electron transfer occurs between an electron donor (D) and an electron acceptor (A), but the mechanism of ET is different. In ISET, the D and A are connected *via* a covalent bond through which the electron is transferred. During this process, it is common that bonds may be broken and new ones formed to facilitate the ET. In addition, ISET is often associated with adiabatic electron transfer, where electronic coupling (V_{el}) between the D and A is significant. Schematically, this property can be visualized by considering a reaction coordinate diagram where a smooth transition connects the reactant (R) and product (P) energy surfaces (Figure 3.12, right).

By contrast, in OSET the D and A do not necessarily need to be covalently bound. Electron transfer occurs through space, so it is sufficient for the D and A to associate through intermolecular interactions prior to ET and form an encounter complex. Due to the Frank-Condon principle (see *Absorption* section), preassociation to form the encounter complex must occur *prior* to OSET. Further, electronic coupling of the D and A is minimal, meaning the electron must "jump" from one energy surface to the other at a crossing point (Figure 3.12, left). This crossing point is a key feature of the non-adiabatic regime.

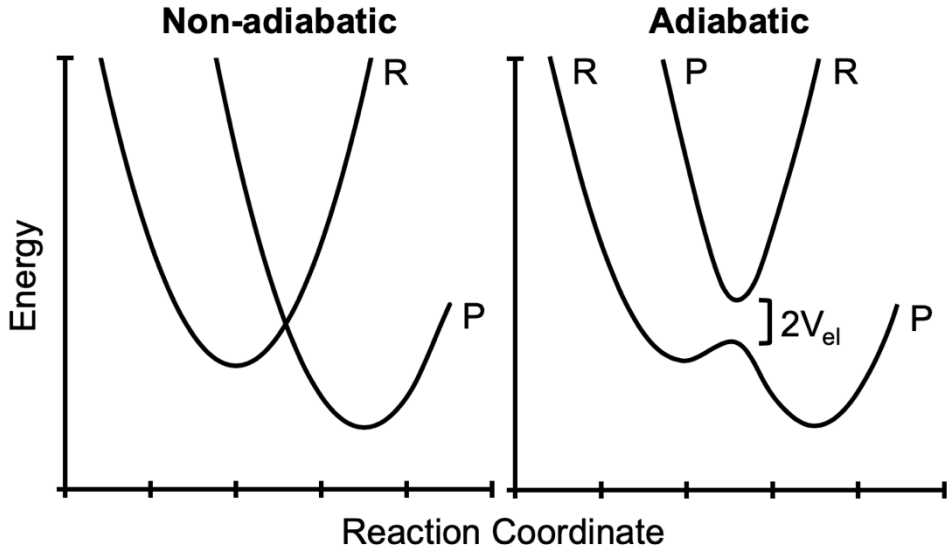

Figure 3.12. *Potential energy surfaces for electron transfer in the non-adiabatic (left) and adiabatic (right) regimes. R and P refer to the reactant and product energy surfaces, respectively.*

<u>*Marcus theory.*</u> Photoinduced electron transfer often occurs through an OSET mechanism. This section will provide a brief introduction to Marcus Theory, which is the predominant theory used to understand OSET. Marcus theory begins by considering the ET between D and A. If one restricts this process to an outer sphere mechanism, the D and A must associate to form the encounter complex [D-A]. Considering the electron transfer as a chemical reaction, [D-A] is the reactant. After the ET occurs, the product is the complex $[D^{+}A^{-}]$, which can then dissociate or

undergo back-electron transfer (BET) to regenerate [D-A]. To visualize this process, Marcus Theory considers a simplified reaction coordinate diagram, where the R and P energy surfaces are represented by simple parabolas. Figure 3.13 shows reaction coordinates for the three most common cases.

In the normal region (Figure 3.13, left side), ET occurs generally as one might expect. Considering an exergonic ET, where the free energy change of the reaction (ΔG^o) is negative, one can anticipate finding a barrier to the reaction ($\Delta G^‡$) associated with the formation of a transition state. However, once this barrier is overcome, ET occurs to form the desired product [D^+A^-]. One term that is often referred to in Marcus theory is the reorganization energy (λ_r). This term represents the energy that would be required to achieve the product ground state geometry within the reactant, and it is a sum of inner sphere (within the [D-A] complex) and outer sphere (solvent molecules around the encounter complex) components (i.e. $\lambda_r = \lambda_i + \lambda_o$).

If the magnitude of ΔG^o is increased (i.e. making it more negative), this process can be visualized on a reaction coordinate diagram as a gradual lowering of the product energy surface in the y-direction. As ΔG^o becomes more negative, one notices that $\Delta G^‡$ becomes smaller and smaller until eventually $\Delta G^‡ = 0$. Practically, this statement has several important consequences. The first is that in Marcus theory, thermodynamics and kinetics are intertwined. That is, as the reaction becomes more thermodynamically favorable (i.e. more negative ΔG^o), the rate of the reaction increases due to a lowering of the barrier to the reaction. Second, when $\Delta G^‡ = 0$, the reaction becomes barrierless such that ET occurs almost instantaneously.

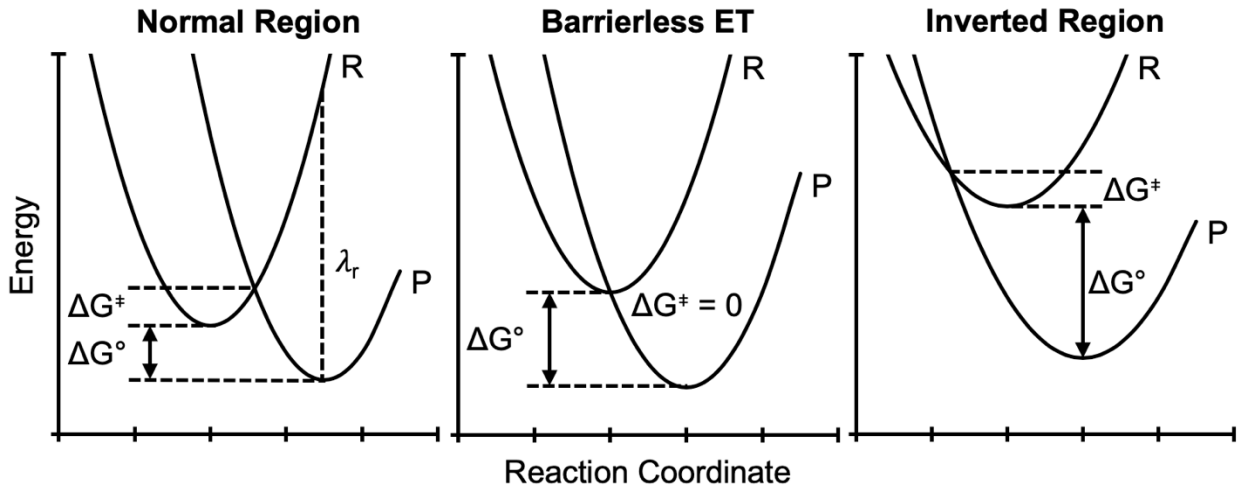

Figure 3.13. *Simplified reaction coordinate diagrams used to describe Marcus theory in the Marcus normal region (left), for barrierless electron transfer (middle), and in the Marcus inverted region (right). $\Delta G^{\ddagger}$ = free energy of the transition; ΔG^{o} = free energy of the reaction; λ_r = reorganization energy.*

Interestingly, Marcus theory predicts a limit to which this phenomenon holds true, as one will eventually enter the Marcus inverted region (Figure 3.13, right side). To understand what this means, consider the case where the reaction becomes more and more thermodynamically favorable. As one continues to lower ΔG^{o} past the point where the reaction becomes barrierless, the crossing point between the R and P energy surfaces begins to rise again, resulting in an increase in $\Delta G^{\ddagger}$. In other words, as the reaction becomes more exergonic, the barrier to ET increases, resulting in a decrease in the rate of ET. While this phenomenon may seem counter-intuitive, it has been observed experimentally.[24]

Laboratory techniques for studying photoredox processes

The following section will provide a general overview of techniques commonly used to study photochemical and photophysical processes. While this list is certainly not exhaustive, it serves an introduction to relevant techniques and aims to point the reader to further useful reading where possible.

UV-Visible Spectroscopy. UV-Visible spectroscopy (UV-vis) is a form of absorption spectroscopy focused on the UV and visible regions of the electromagnetic spectrum. In its most basic form, instrument design for this measurement is quite simple, involving a light source that shines through a sample and a detector on the other side to measure the light transmitted through the sample (Figure 3.14, left). Of course, modern instruments can be more complicated as well, allowing for more accurate and precise measurements on a range of different samples (ex. solutions, solids, films, reactions *in-situ*, etc.).

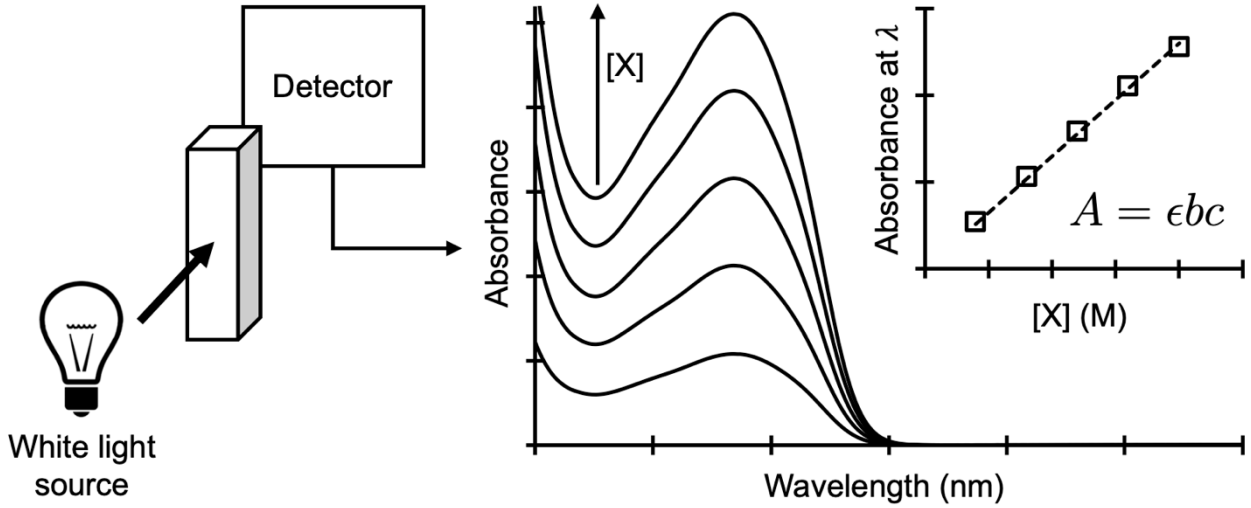

Figure 3.14. *General instrument layout for absorption spectroscopy (left) and examples of data obtained by this technique (right). Once an absorption spectrum has been obtained, the molar absorptivity of a compound at a wavelength can be determined by measuring absorbance as a function of concentration (inset).*

When the measurement is performed, the instrument collects transmittance data as it measures light that passes through the sample without being absorbed. However, a more useful quantity for spectroscopy is absorbance (used interchangeably with optical density, see *Absorption* section), as absorbance can be related to other important quantities using Beer's law. Equation 3.9 shows the conversion of transmittance (T) to absorbance.

$$A = OD = log_{10}\left(\frac{1}{T}\right) \quad \text{(Eq. 3.9)}$$

It's worth noting that scattering, reflection, and refraction of light that results in loss of detected transmittance is treated as absorption when applying Eq. 3.9, as is commonly done automatically in modern spectrometers. Typically, the use of optically transparent cuvettes positioned at a right angle to the incoming light minimizes these effects as long as the sample consists of a homogeneous solution, such that absorption and optical density can be used interchangeably.

Perhaps the simplest use of UV-vis is to examine the absorbance of different reaction components. In photoredox chemistry, such a study can be an important control experiment to ensure irradiation does not cause background reactivity through direct excitation of a substrate. In addition to measuring the absorbance of each reaction component, it can also be useful to measure the absorbance of different substrates in combination. As will be discussed later in the chapter (see *Photochemistry of electron donor-acceptor complexes* section), EDA complexes can form unique absorption bands relative to their individual components. As such, measurement of the components alone would yield little insight into the possibility of such a reactive complex.

In addition, it is often useful to know the molar absorptivity of a molecule, as this property can yield insight into the efficiency with which it absorbs a certain wavelength of light. In particular, this value can be important in photoredox catalysis, where the molar absorptivity of the catalyst directly impacts the penetration depth of the light into the reaction vessel. To measure this quantity, one can take advantage of Beer's Law (Equation 3.6) which states that absorbance is directly proportional to the concentration of the absorbing species. Since the molar absorptivity of a molecule is constant at a certain wavelength, and one can maintain a constant path length, plotting

absorbance at a wavelength vs. concentration for a molecule of interest gives a straight line with the slope corresponding to the molar absorptivity at that wavelength (Figure 3.14, inset). Importantly, since the percent of light transmitted, and therefore detected, above $A = 1$ is quite small, molar absorptivity measurements should be conducted on solutions with $A < 1$ when possible to ensure the highest accuracy.

Emission spectroscopy. Using emission spectroscopy, one can probe the nature of an excited state as well as its reactivity. The instrument used to measure emission is called a fluorimeter, although most fluorimeters can also measure phosphorescence. In its simplest form, a fluorimeter has many of the same components as an absorption spectrometer. However, since the intensity of emission is generally quite weak compared to the light source, the detector is placed at a 90º angle to the light source, allowing most of the source light to go undetected (Figure 3.15, left).

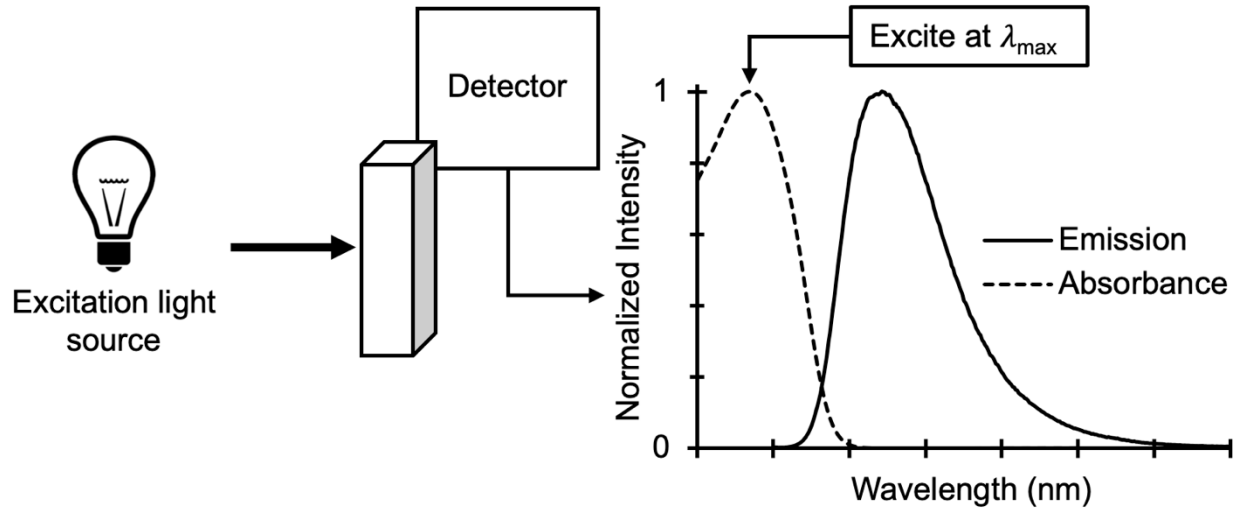

Figure 3.15. *General instrument layout for emission spectroscopy (left) and an example of data obtained by this technique (right). Once an absorption spectrum has been obtained, a sample is typically excited at its λ_{max} to obtain an emission spectrum.*

In a simple emission measurement, one chooses an excitation wavelength – determined from the absorption spectrum of the molecule being probed – and monitors for emission at longer wavelengths of light (Figure 3.15, right). Since most molecules exhibit a Stokes shift (see *Fluorescence* section), it is often not necessary to monitor areas blue-shifted to the excitation wavelength. Once an emission spectrum has been collected, it can be used to estimate the energy of the excited state ($E_{0,0}$) based on the energy of light emitted. In theory, since the highest-energy transition should be between the vibrational ground state of S_1 and that of S_0, the maximum wavelength of emission should correspond to this transition. However, several conventions exist for estimating $E_{0,0}$, including the use of the emission maximum, the onset of emission, and the crossing point between the emission and absorption spectra.

Of course, which excited state one investigates depends on the emission being measured. By monitoring fluorescence, one can determine the energy of the S_1 state, whereas monitoring phosphorescence will give the energy of the T_1 state. For the latter measurement, it might be necessary to cool the sample in a glassing solvent to slow down nonradiative decay pathways from T_1. In addition, to isolate phosphorescence from fluorescence, one may need to use a time-delay between excitation and measurement of the sample, since phosphorescence is generally longer lived than fluorescence.

Closely related to an emission spectrum is an excitation spectrum, in which emission intensity at a single wavelength is monitored as the excitation wavelength is varied. Since the amount of light emitted by a fluorophore, or a fluorescent molecule, is proportional to the amount of light absorbed (i.e. Beer's law), a fluorophore's excitation spectrum should be identical to its absorption spectrum as long as Kasha's rule is obeyed. When this relationship is not true, the excitation spectrum can yield insight into the presence of anti-Kasha behavior (emission from a

higher state or vibrational mode), or more commonly the presence of an impurity or aggregate species in solution.

Emission spectroscopy can also be used to probe the quantum yield of different states. Quantum yield (ϕ) is the ratio of the quantity of emission (or states formed) relative to the quantity of light absorbed by a system. Typically, quantum yield is reported as a value between 0 and 1 or as a percentage, where 1 (or 100%) corresponds to every photon absorbed leading to the desired outcome. Quantum yield can be used to describe various processes, such as fluorescence, phosphorescence, intersystem crossing, or nonradiative decay. In addition, ϕ is commonly used to report the degree to which a certain state forms, such as T_1. However, since both the light absorbed and the light emitted must be quantified precisely, the measurement of ϕ is more complicated than a standard emission measurement, requiring comparison to a standard or use of an integrating sphere.

The final technique employing emission spectroscopy that will be discussed is Stern-Volmer quenching. In this technique, the emission of a molecule is compared in the absence and in the presence of a potential quencher to determine if electron or energy transfer (see *General mechanisms of photocatalysis* section) can occur from the excited state to a substrate. In theory, if no electron or energy transfer occurs, the emission of the molecule should be unchanged in the presence of another molecule. By contrast, if one of these processes is operative, it will lower the concentration of the excited state, thereby reducing the intensity of emission. Equation 3.10 relates the intensity of emission in the absence (I_f^o) and presence (I_f) of a quencher (Q) to the rate constant for quenching (k_q) and the lifetime of the excited state in the absence of quencher (τ_o). Importantly, since emission quenching would be observed both in the case of electron transfer and energy transfer, this technique cannot provide insight into which mechanism is operative in a reaction.

$$\frac{I_f^o}{I_f} = 1 + k_q \tau_o \cdot [Q] \qquad \text{(Eq. 3.10)}$$

While this technique can be quite powerful, one must be wary of other processes that might reduce emission as well, such as the ground state (or excited state) association of the quencher with the emitting molecule to form a non-emissive complex. In addition, one must be careful to avoid the inner-filter effect, which is the absorption of light used for excitation or the emission of the fluorophore by either the fluorophore or the quencher. For this reason, emission spectroscopy is often performed at low concentrations of the fluorophore ($A < 0.1$), even though mathematical and experimental corrections for the inner-filter effect have been devised.[25]

Transient absorption Spectroscopy. While many common spectroscopic techniques perform measurements under steady state conditions on relatively long time scales, transient techniques make measurements on very short time scales to gain insights into chemical dynamics. In this section, we will focus our discussion to transient absorption spectroscopy, as this is perhaps the most common transient technique used in the investigation of photochemical systems.

Broadly, transient absorption spectroscopy (TA), also called pump-probe spectroscopy, is very similar to standard absorption spectroscopy. Commonly, the UV and visible regions of the electromagnetic spectrum are probed, so this discussion will focus on those regions, although the technique can certainly be applied to other regions as well. In the case of UV-visible absorption, a white light source is used to irradiate a cuvette containing the sample, and the light transmitted is monitored by a detector (Figure 3.16, left side). Under such conditions, one would observe a spectrum corresponding to the ground state molecule, as one would observe in a standard UV-visible absorption measurement. To probe the characteristics of an excited state, a laser pulse (or pump) is applied to the sample orthogonal to the probe pulse – so as to not interfere with the

detector – generating a small region of excited state molecules for observation. Since the cross-section of the laser is often quite small, the probe light will still interact with a significant amount of ground state molecules, making it difficult to observe the excited state species. As such, data is often reported with units of ΔA (or ΔOD, Figure 3.16, right side), such that absorption from the ground state can be subtracted from the overall signal and the absorption of excited state species can be isolated. Related to this technique is transient emission spectroscopy or time-resolved emission spectroscopy, where a sample is simply excited with a laser pulse and its emission monitored in the absence of a probe light.

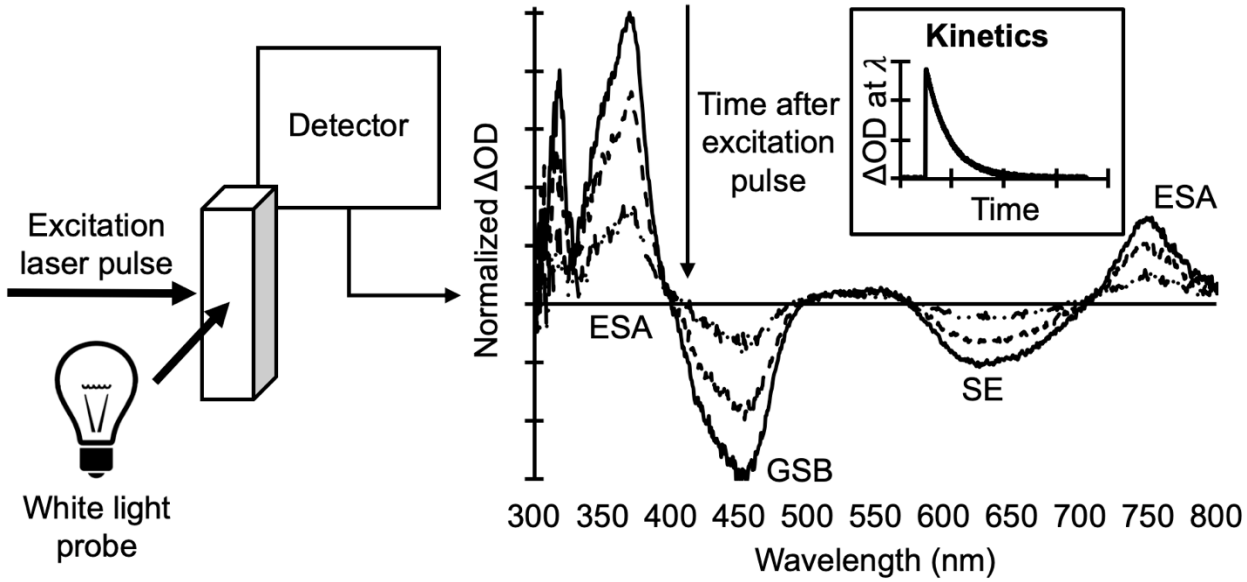

Figure 3.16. *General instrument layout for transient absorption (left) and examples of data obtained by this technique (right). Excited state spectra can be observed using absorption spectroscopy at different time delays after an excitation pulse with a laser. By then selecting a wavelength corresponding to an excited state and monitoring absorbance at that wavelength as a function of time (inset), excited state lifetimes can be determined. Abbreviations: ESA = excited state absorption; GSB = ground state bleach; SE = stimulated emission.*

Using modern instruments, measurements on the picosecond and femtosecond time scale can be achieved, providing information about even the fastest photophysical processes. As such,

these techniques have been used to monitor the fast relaxation processes that occur after the absorption of light by a molecule, allowing chemists to probe the formation and characteristics of excited states within photoactive molecules. In particular, two measurements are common in such studies.

In the first, the absorption spectrum of an excited sample is collected at different time delays after the excitation pulse (Figure 3.16, right side), allowing one to monitor changes in the excited state identity after absorption. Several common features may be observed in such a measurement, including a ground state bleach (GCB), corresponding to a negative ΔOD where ground state molecules have been converted to an excited state in a region of the spectrum where the excited state does not absorb; an excited state absorption (ESA), where newly formed excited state species absorb the probe light and are promoted to higher energy excited states; and stimulated emission (SE), where excited state molecules are forced to emit light through an interaction with the probe light. Second, once a feature has been identified, the lifetime of this species can be determined by monitoring the change in absorbance at a relevant wavelength over time. This measurement is sometimes called single wavelength kinetics (Figure 3.16, right side inset) and requires fitting the data to an exponential function to determine the excited state lifetime. If multiple features are identified that belong to the same excited state, monitoring any feature should give the same single wavelength kinetics (within error). If significant differences are observed, it may indicate the presence of another species.

In addition, these measurements can be employed in a number of other important studies probing the reactivity of certain excited states. For instance, in photocatalysis, kinetics measurements are often used to probe whether a reaction occurs through an electron transfer or energy transfer mechanism (see *General mechanisms of photocatalysis* section), as the products

of these mechanisms can be differentiated spectroscopically. Further, Stern-volmer quenching can be performed by monitoring how different quenchers impact the lifetimes (or decay rate constants k_1 and k_2) of different excited state species (Equation 3.11), allowing one to determine which excited state is responsible for an observed reaction.

$$\frac{k_2}{k_1} = 1 + \frac{k_q}{k_1}[Q] \qquad \text{(Eq. 3.11)}$$

Cyclic voltammetry. To investigate the reduction and oxidation of molecules, cyclic voltammetry is commonly used. Broadly, cyclic voltammetry (CV) involves applying an electrochemical potential to a sample, which is changed (or swept) at a constant rate, and then measuring the current that flows in and out of the sample at each applied potential (Figure 3.17). In essence, by changing the applied potential, one is altering the thermodynamic driving force for electron transfer, and by monitoring the current response of the sample, one is measuring the kinetics of electron transfer between the sample and the electrode. By doing so, one can determine the ground state reduction and oxidation potentials of a molecule, which correspond to the average of the peak potentials ($E_{1/2}$) as observed in Figure 3.17 (solid line).

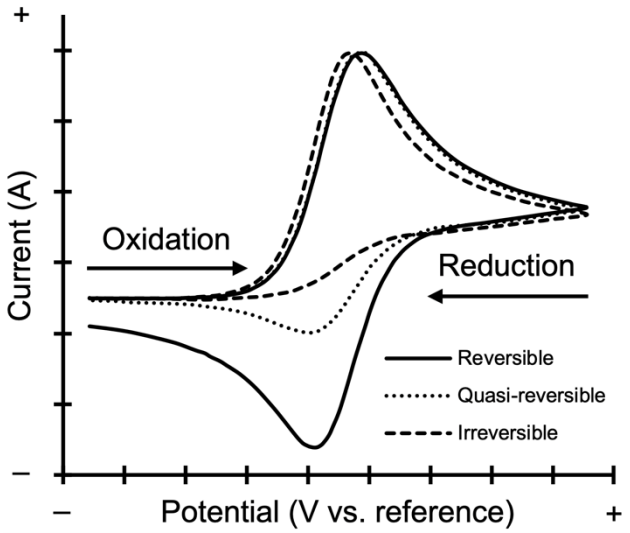

Figure 3.17. *Examples of cyclic voltammograms for reversible, quasi-reversible, and irreversible systems.*

In addition, one can determine from the shape of the current response whether an electron transfer is reversible, where a perfectly reversible one-electron transfer has an oxidation and reduction peak of equal magnitude that are separated by 57 mV (Equation 3.12), where ΔE_p is the peak separation [V], R is the ideal gas constant (8.314 J mol^{-1} K^{-1}), T is the absolute temperature [K], n is the number of electrons being transferred, and F is Faraday's constant (96485 C mol^{-1}).

$$\Delta E_p = 2.22\frac{RT}{nF} \qquad \text{(Eq. 3.12)}$$

By contrast, a completely irreversible ET would only exhibit an oxidation or reduction peak (Figure 3.17, dashed line), as the oxidized or reduced compound disappears prior to the return scan and is not regenerated in the original oxidation state. A system can appear irreversible for both chemical and electrochemical reasons, although it is not always simple to determine which is the case. Sometimes, a system may appear to exist somewhere between totally reversible or irreversible (Figure 3.17, dotted line) and can be referred to as quasi-reversible.

With regard to photoredox chemistry, several useful pieces of information can be obtained using CV. In photoredox catalysis, determination of a photoredox catalyst's ground state oxidation and reduction potentials can provide insight into possible catalytic mechanisms, as well as compatibility with certain substrates when the redox properties of the substrates are also known or measured. In addition, by combining CV with emission spectroscopy, it is possible to estimate the redox properties of a photocatalyst's excited state, providing insight into the reactivity of this key catalytic species (see *Design principles for effective photoredox catalysis* section). Finally, CV can also be used to guide the development of reactions employing EDA complexes, as the reduction and oxidation potentials of molecules can serve as estimates of their electron donating and accepting abilities.

Practical considerations for performing photochemical reactions

Factors influencing bimolecular reactions. The rate of a bimolecular reaction in solution is limited by the rate of diffusion. While the rate of a reaction may be slower than diffusion, the fastest two molecules can react is only as quickly as they can diffuse to each other. As such, it is important to keep this consideration in mind when designing a photochemical reaction, as the relevant photoexcited species must be long enough lived to interact with the other molecules in solution. For a bimolecular system, the lower limit for this excited state lifetime is generally on the order of a few nanoseconds, although some exceptions certainly exist. Sometimes, a short excited state lifetime can be overcome by increasing the concentration of the reagents in solution, although this can come at the cost of increased catalyst loadings or waste generation.

Photoreactor design. Another important consideration that is often overlooked is the design of the photoreactor. In fact, reactor design in photochemistry has drawn significant criticism

over the years, as few standardized designs exist, leading to significant variability among different research groups, though several different commercially available photoreactors are currently available. As such, careful reactor design and reporting are necessary to ensure the reproducibility of photochemical reactions.

Broadly, two different reactor designs can be considered, each with its own set of design parameters that can be tuned. A batch reactor (Figure 3.18, left) is perhaps the simplest and involves surrounding a reaction flask with light source. In its most basic form, this reactor design can be achieved by placing a light source next to a reaction flask, although this design can introduce significant variability from one reaction to the next if care is not taken. Another simple but more reproducible design involves wrapping LED strips on the inside of a beaker or recrystallization dish, such that the average distance of the light source from the reaction vessel can be easily controlled. In addition, the beaker itself can be wrapped with a reflective coating, directing more of the light into the reaction vessel rather than the surroundings. Regardless of the design employed, it is important to remember that the intensity of light entering the reaction is inversely proportional to the distance squared ($1/d^2$) between the reaction and the light source. Therefore, it is advantageous to keep the reaction as close as possible to the light source.

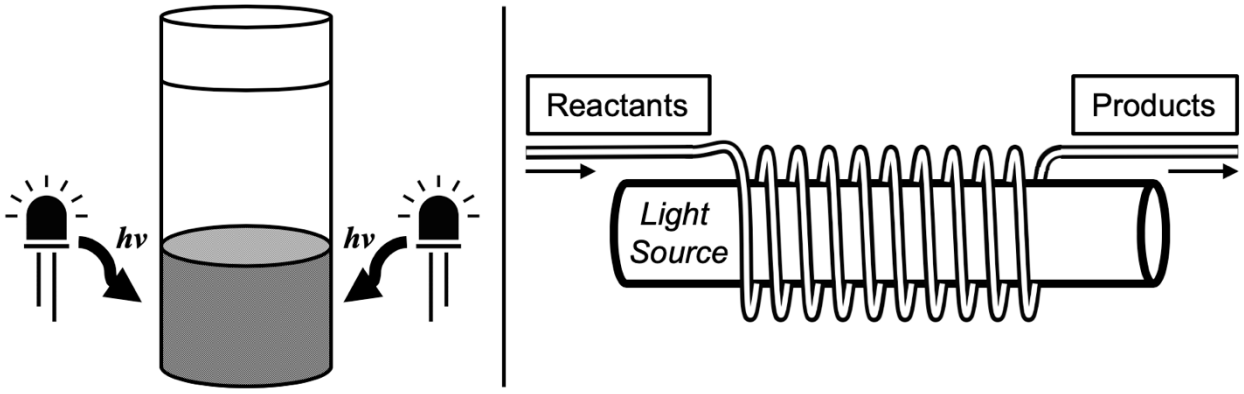

Figure 3.18. *General design of a batch reactor (left) and a flow reactor (right).*

Toward this end, continuous flow reactors (Figure 3.18, right) can be advantageous, as they achieve very uniform and consistent irradiation conditions by passing the reagents through a transparent tube and around a light source. In addition, flow reactors have the advantage of being scalable, as they are not limited by reaction volume, whereas batch photochemistry is typically challenging to scale-up. The primary disadvantage of a flow reactor design is that it introduces added complexity and new factors such as fluid dynamics and mixing that must be considered, requiring some degree of experience to optimize reaction conditions. In addition, reaction screening can be slow with this reactor design, although it is not impossible. However, a number of resources exist to introduce the interested reader to this apparatus.[26,27]

Regardless of the reactor design, temperature control of the reactor is an important consideration as that heat produced by the light source could give rise to thermal background reactivity. In most cases, cooling can easily be achieved through the use of cooling fans.

Choice of light source. Of course, one of the most important reactor components is the light source. In modern photochemistry, a number of different light sources are available for use, including multicolor and white LEDs, monochromatic LEDs, fluorescent lights, incandescent bulbs, arc lamps, lasers, sunlight, and more. While each may have different advantages and disadvantages, white and monochromatic LEDs are among the most popular due to their ease of operation, generally low cost, compact size, and easy incorporation into a variety of reactor designs.

Photoredox Catalysis

General mechanisms of photocatalysis

Photoredox catalysis is generally divided into two mechanisms based on whether the

photoredox catalyst (PC) behaves as an excited state oxidant or reductant. When the PC is an excited state oxidant, it accepts an electron from the substrate or a sacrificial electron donor and is itself reduced (Figure 3.19). As such, this mechanism is referred to as reductive quenching, since the excited state is quenched by reduction of the PC. To regenerate the ground state catalyst, the reduced PC must then donate an electron to a substrate or sacrificial electron acceptor. By contrast, an oxidative quenching mechanism involves reduction of a substrate or sacrificial electron acceptor to generate the oxidized form of the PC, which then accepts an electron to regenerate the ground state. Typically, the mechanism that dominates depends on the excited state redox properties of the PC, as well as the redox properties of the other molecules in solution.

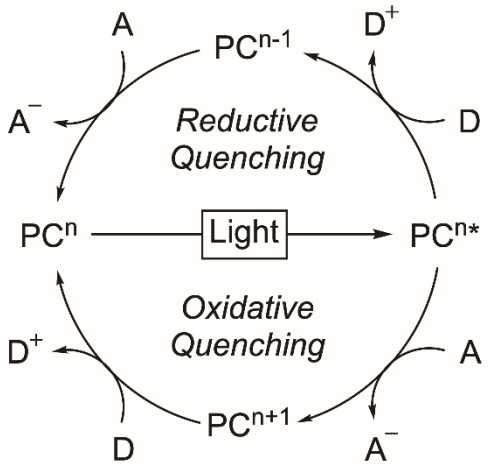

Figure 3.19. *Generalized photoredox catalytic cycles proceeding through oxidative (bottom) and reductive (top) quenching mechanisms. D = electron donor, A = electron acceptor.*

In addition, some photocatalytic transformations can proceed through an energy transfer pathway, where energy from the excited state PC is transferred to a substrate, generating the PC ground state and the substrate excited state. The substrate excited state can then participate in electron transfer reactions that are inaccessible to the substrate ground state. Energy transfer is quite common in photocatalysis and can proceed through different mechanisms. However, since

this pathway is not a redox process and has been discussed by others [23,28], it will not be covered in this chapter.

Design principles for effective photoredox catalysts

The following section outlines several important properties commonly exhibited by effective photoredox catalysts. While this list is not universal and each reaction might have its own additional requirements, the properties listed below are generally considered desirable and can serve as a useful starting point for developing a photoredox catalyzed reaction.

Effective absorption of light. Since the energy to generate the excited state PC is derived from light, effective absorption of light is necessary; this statement means two things. First, the PC must absorb light in a desirable region of the electromagnetic spectrum. For organic synthesis, near-IR, visible, and low energy UV light ($\lambda > 350$ nm) are most often used, since these wavelengths of light have sufficient energy to promote reactivity but are not absorbed by most organic molecules (see *Absorption* section). Second, the PC should have a sufficient molar absorptivity in the spectral region corresponding to the light source. Importantly, while a high molar absorptivity could allow for more efficient absorption of light and therefore lower catalyst loadings, it also decreases the penetration depth of the incident light. As such, one has to consider the requirements of a given reaction system to determine what value of molar absorptivity is most desirable. For example, a reaction performed in a flow reactor might benefit from a strongly absorbing catalyst, whereas one performed in a batch reactor might benefit from a weaker absorbing PC due to the greater depth of the reactor.

High quantum yield of desired excited state. Quantum yield refers to the ratio of a state formed relative to the number of photons absorbed by the system. For a PC to maximize the utility

of each photon, it is desirable for the quantum yield of the catalytic state to be as close to 1 as possible. For example, if a reaction is mediated by a PC triplet excited state, then a PC with a high triplet yield would be most desirable. Generally, the specific state desired may vary depending on the reaction, the reaction conditions, and the specific PC being employed.

Long lived excited state. In photoredox catalysis, reactions commonly proceed through a bimolecular mechanism, where the excited state PC must collide with a substrate in solution prior to electron transfer taking place. As such, the excited state of the PC must be long enough lived to undergo bimolecular collisions – a process that generally occurs on the order of a few nanoseconds. In many cases, triplet excited states can exhibit sufficient lifetimes to participate in bimolecular reactivity because of the forbidden nature of a spin flip, which makes relaxation to the ground state a relatively slow process. However, they also have some drawbacks. Due to photophysical relaxation processes, triplet states tend to be less energetic than singlet states. In addition, triplet excited states can be quenched by oxygen, often necessitating that reactions be performed under an inert atmosphere. This reactivity arises because oxygen has a triplet ground state, which can undergo energy transfer with many triplet excited state PCs to produce the ground state PC and singlet oxygen.

Singlet excited states can be advantageous because they are not as easily quenched by oxygen. However, the lifetimes of these states are generally much shorter than those for triplet excited states. As a consequence, many singlet excited states may not exhibit long enough lifetimes to participate in bimolecular electron transfer, sometimes limiting their utility in synthesis. With regard to doublet excited states, which have only recently begun to be employed in synthesis through photoexcitation of radical species (see *Open shell photoredox catalysis* section), the lifetimes of these states are generally quite short, often in the picosecond timescale.[29,30]

Favorable thermodynamics. Like all redox reactions, one must consider whether a reaction of interest is thermodynamically feasible based on the reduction and oxidation potentials of the substrates and the catalyst. For a photoredox catalyst, the excited state redox properties can be estimated using modified Rehm-Weller equations (Equations 3.13 and 3.14):

$$E^*(PC^{n+1}/PC^{n*}) = E^o(PC^{n+1}/PC^n) - E_{0,0} \quad \text{(Eq. 3.13)}$$

$$E^*(PC^{n*}/PC^{n-1}) = E^o(PC^n/PC^{n-1}) + E_{0,0} \quad \text{(Eq. 3.14)}$$

where E^o is approximated using the $E_{1/2}$ obtained from cyclic voltammetry, and $E_{0,0}$ is the excited state energy in eV obtained from the emission spectrum of the molecule.

The redox properties of the oxidized or reduced catalyst (i.e. PC^{n+1} or PC^{n-1}) are also important to consider, since electron transfer to or from these species is necessary to regenerate the ground state catalyst. These redox properties can be determined by cyclic voltammetry and are also necessary for calculation of the excited state redox properties above.

Redox reversibility. Finally, to ensure catalyst turnover, redox reversibility of the PC is important. Put simply, it is crucial that PC^{n+1} or PC^{n-1} does not undergo side reactivity, otherwise catalyst degradation can occur. Using cyclic voltammetry, the reversibility of a catalyst can be evaluated based on the reversibility of the relevant redox couple.

Inorganic photocatalysts

Transition metal catalyzed photoredox synthesis has been historically dominated by the use of d^6 polypyridyl Ru(II) and Ir(III) catalysts. The complex $[Ru(bpy)_3]Cl_2$ (Figure 3.20, bpy = 2,2'-bipyridine) in particular has been employed across a wide range of catalytic reactions, aided by thorough study of its photophysical properties.[31] The complex strongly absorbs visible light

(λ_{max} = 452 nm, ε = 14,600 M^{-1} cm^{-1} in H_2O) to access long lived (τ ~ 1 μs) triplet excited states which can be assigned as metal-to-ligand charge-transfer (MLCT).[32] As a result of relatively low-lying π* orbitals of the bipyridyl ligands, excitation of a d electron from the Ru(II) center results in a rich excited state topology for $[Ru(bpy)_3]^{2+}$*. The widespread use of $[Ru(bpy)_3]Cl_2$ in photoredox catalysis also stems from its versatile redox properties. While the ground state reduction potential of the catalyst is modest [$E^o(Ru^{II}/Ru^{III})$ ~ 1.26 V vs. SCE], in the excited state the PC becomes significantly more reducing [$E^o(Ru^{II}*/Ru^{III})$ ~ −0.81 V vs. SCE] and oxidizing [$E^o(Ru^{I}*/Ru^{II})$ ~ 0.77 V vs. SCE].[33] Furthermore, reductive quenching of the PC excited state with sacrificial donors such as amines to form $[Ru(bpy)_3]^+$ results in significantly more reducing species [$E^o(Ru^{I}/Ru^{II})$ ~ −1.33 V vs. SCE]. Modifications to the complex's ancillary ligand are also useful for tuning PC redox properties, as in the case of substituting 2,2'-bipyrazine (bpz) for bipyridine where [$E^o(Ru^{II}/Ru^{III})$ ~ 1.86 V vs. SCE] for $[Ru(bpz)_3]Cl_2$. As the π-accepting character of the ancillary ligand increases, the decreased electron density at the metal makes oxidation less favorable.

In modern photoredox catalysis, Ir(III) PCs with 2-phenylpyridine (ppy) ligands are ubiquitous (Figure 3.20). As compared to 2,2-bipyridine, use of the strongly donating 2-phenylpyridine ligand such as in *fac*-$[Ir(ppy)_3]$ helps to stabilize the resulting Ir(IV) complex after oxidative quenching, as evidenced by the very negative excited state reduction potential observed [$E^o(Ir^{III}*/Ir^{IV})$ ~ −1.73 V vs SCE].[33] Stephenson showed that *fac*-$[Ir(ppy)_3]$ catalyzes the reduction of unactivated alkyl and aryl iodides, while dehalogenation by $[Ru(bpy)_3]Cl_2$ is mainly limited to activated bromides (Figure 3.21).[34]

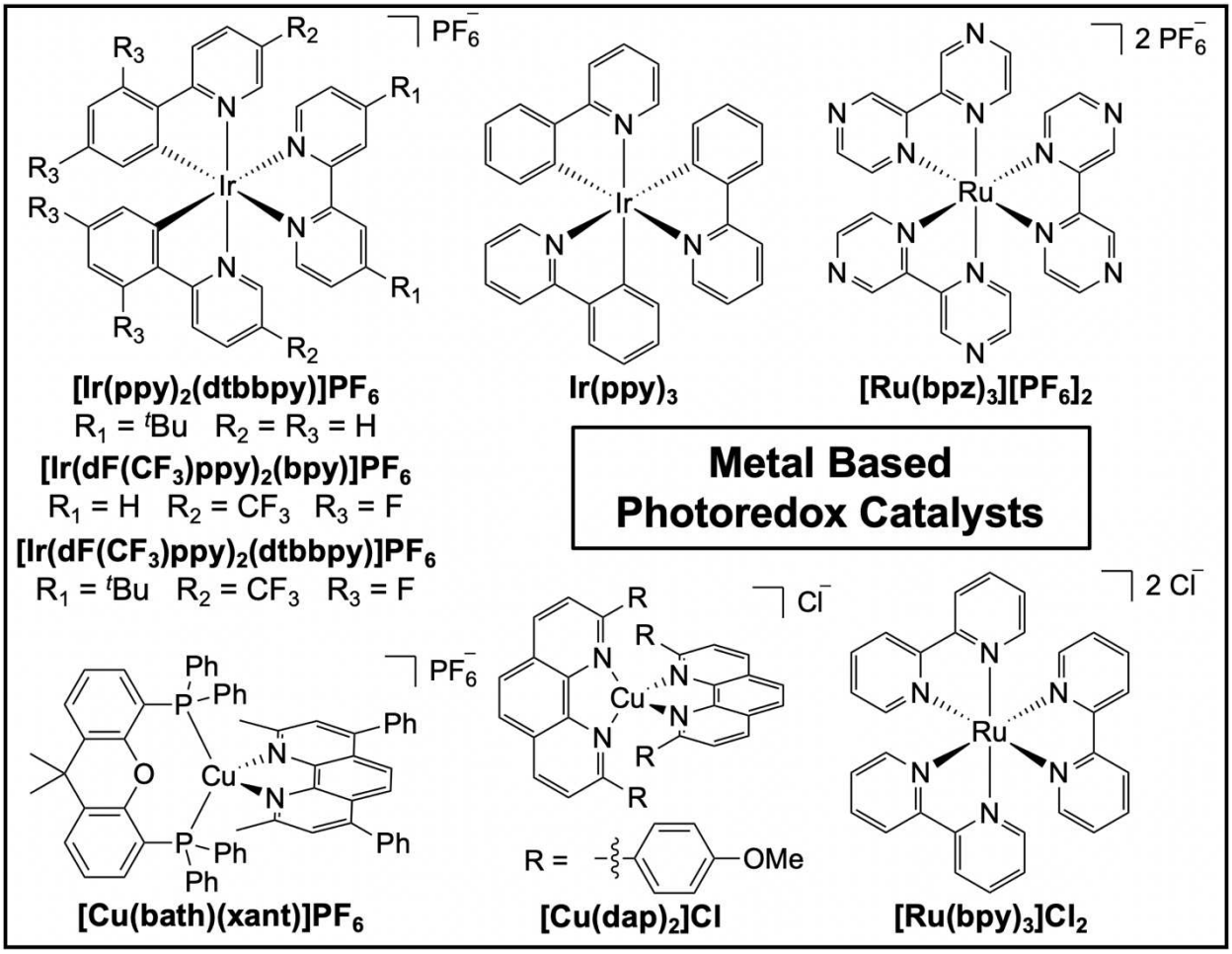

Figure 3.20. *Common photoredox catalysts based on Ru, Ir, and Cu complexes.*

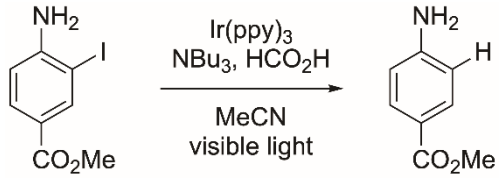

Figure 3.21. *Ir(III) photocatalyzed hydrodehalogenation of an aryl iodide.*

Heteroleptic Ir(III) PCs with combinations of substituted 2-phenylpyridine and bipyridine ligands are able to access a wide range of redox potentials and thus are very attractive in terms of broad applicability in photoredox catalysis for organic synthesis. This versatility is evident in their ability to affect tertiary amine functionalization through reductive quenching pathways. Stephenson reported that under visible light irradiation, $[Ir(ppy)_2(dtbbpy)]PF_6$ catalyzes an aza-

Henry reaction between *N*-aryl tetrahydroisoquinolines and nitromethane, likely proceeding through iminium ion intermediates (Figure 3.22).[35]

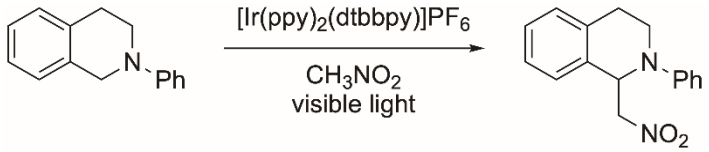

Figure 3.22. *Visible light mediated aza-Henry reaction of a N-aryl tetrahydroisoquinoline.*

In an example of an overall redox-netural reaction, Koike and Akita demonstrated the *fac*-$Ir(ppy)_3$ catalyzed atom transfer radical addition (ATRA) of trifluoromethyl radicals derived from Umemoto's reagent to styrenes.[36] The authors hypothesized that oxidation of intermediate benzylic radicals followed by trapping with oxygen nucleophiles led to the observed oxytrifluoromethylation products (Figure 3.23).

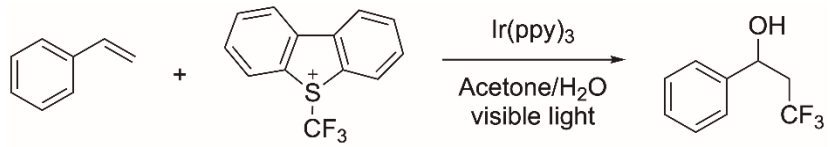

Figure 3.23. *Oxytrifluoromethylation of styrene using an Ir(III) photocatalyst.*

A particular strength of photoredox catalysis has been the mild generation of carbon radicals from carboxylic acid precursors. MacMillan disclosed a method for decarboxylation of a wide scope of aliphatic carboxylic acids and subsequent trapping of the formed carbon radicals with Selectfluor (Figure 3.24).[37] The reaction could be catalyzed by either Ru or Ir PCs.

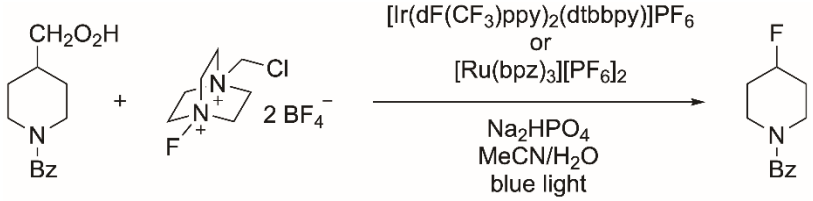

Figure 3.24. *Decarboxylative fluorination with metal photocatalysts.*

Unfortunately, noble metal PCs suffer from fundamental drawbacks such as their low natural abundance and potential toxicity. First-row transition metal complexes offer attractive alternatives as more sustainable PCs, but the photophysical properties of first-row metal complexes often differ greatly from their second and third-row analogs. For example, photoexcited Fe(II) polypyridyl complexes are typically unable to operate via MLCT excited states because of deactivation from relatively low lying metal centered states, a consequence of smaller ligand field splitting for 3d metal complexes.[38] Ultimately, metal centered excited states in potential first-row PCs provide undesirable nonradiative decay pathways, typically resulting in short (ps) excited state lifetimes. However, increasing ligand field strength by replacing pyridyl ligands with strongly donating N-heterocyclic carbene ligands has shown promise to mitigate the issue of short excited state lifetimes in Fe(II) PCs.[39]

A more successful family of non-noble metal PCs is that of Cu(I) photocatalysts. Because of their d^{10} configuration, Cu(I) complexes do not possess metal centered excited states and do exhibit MLCT. Cu(I) complexes like $[Cu(dap)_2]Cl$ (Figure 3.20) have been shown to be highly reducing in their excited state [$E^o(Cu^{I*}/Cu^{II}) = -1.43$ V vs. SCE] and have found use in selective ATRA reactions under green light irradiation (Figure 3.25).[40] Thus, PCs based on earth abundant metals are promising candidates to rival the redox power and synthetic utility of their more venerable precious metal counterparts.

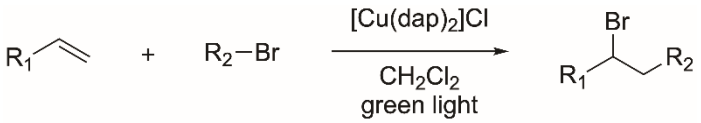

Figure 3.25. *ATRA catalyzed by a Cu(I) photocatalyst.*

Organic excited state oxidants

Fully organic photoredox catalysts are inherently attractive from the perspective of sustainability as compared to rare noble metal complexes. Xanthene dyes are well-established in photoredox catalysis, with PCs such as Rose Bengal (Figure 3.26) capable of promoting the same transformations as precious metal photocatalysts such as the oxidative functionalization of tertiary amines under visible light irradiation (Figure 3.27).[41]

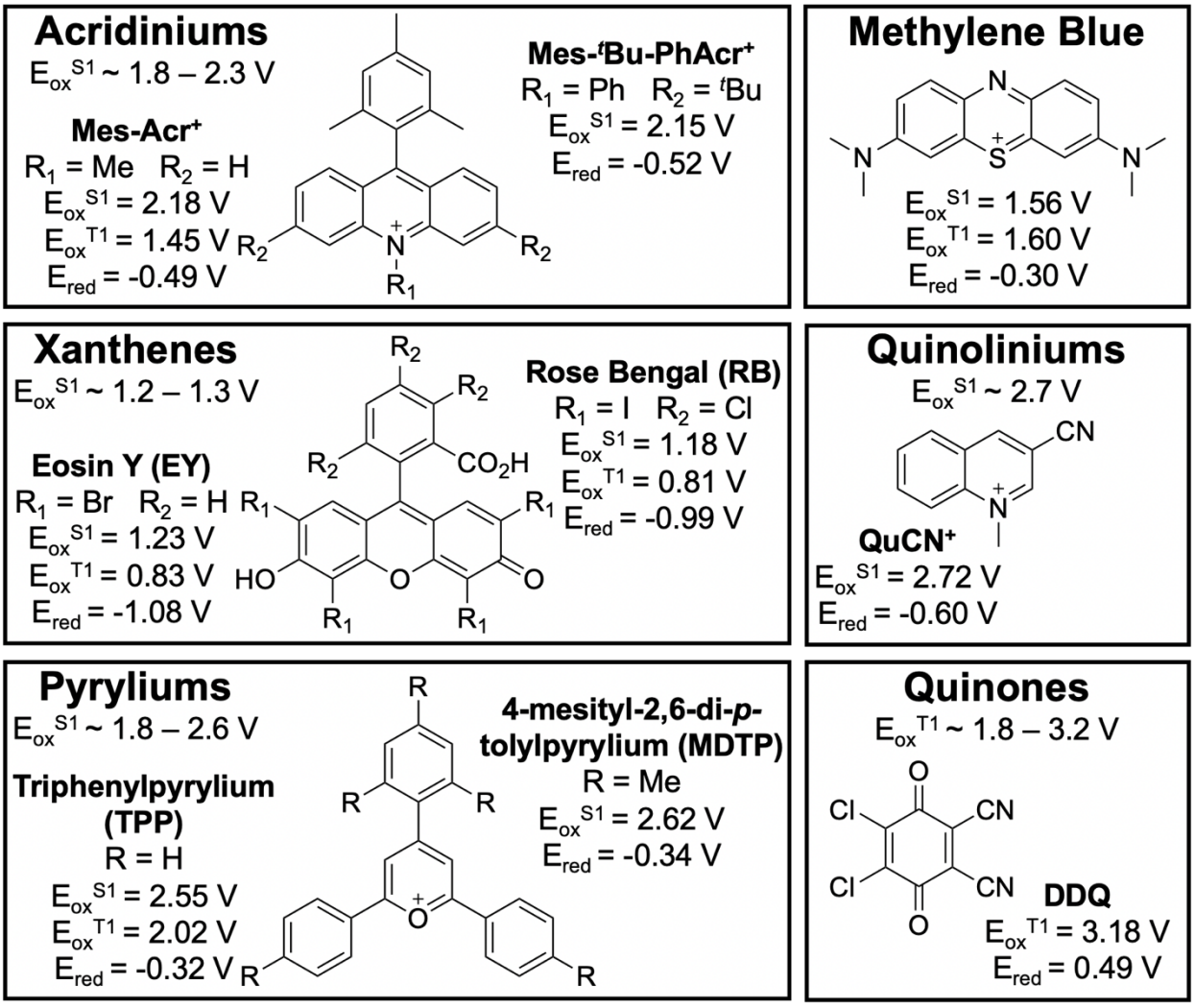

Figure 3.26. *Redox properties of organic excited state oxidants. Since many of these families are tunable through structural modification, key examples of commonly used PCs are shown, as well as the redox properties specific to those molecules.* $E_{ox}^{S1} = E^o(PC^{\bullet-}/{}^1PC^*)$; $E_{ox}^{T1} = E^o(PC^{\bullet-}/{}^3PC^*)$; $E_{red} = E^o(PC^{\bullet-}/PC)$. *All potentials are shown in V vs. saturated calomel electrode (SCE). For conditions under which redox properties were measured, see references* [23,43,44,47–53].

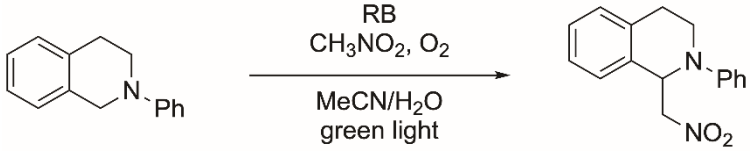

Figure 3.27. *Oxidative amine functionalization by an organic photocatalyst.*

Additionally, certain organic PCs have been found to exhibit excited state redox potentials that exceed typical ranges found in transition metal catalysts. Acridinium salts (Figure 3.26) have

been fascinating subjects of study since early controversy over the precise dynamics of their photoexcited states.[42–44] The existence of highly oxidizing [$E^o(PC^{\bullet-}/PC^*) > 2.00$ V vs. SCE] excited singlet states in 9-mesitylacridinium dyes, however, is widely agreed upon and key to their exceptional oxidative reactivity with organic compounds. In depth mechanistic studies by Nicewicz have revealed the importance of these states in anti-Markovnikov alkene functionalization reactions.[45] In combination with redox-active hydrogen donors, acridinium dyes have been reported to catalyze the anti-Markovnikov addition of a range of nucleophiles such as amines to putative alkene cation radical intermediates (Figure 3.28).[46]

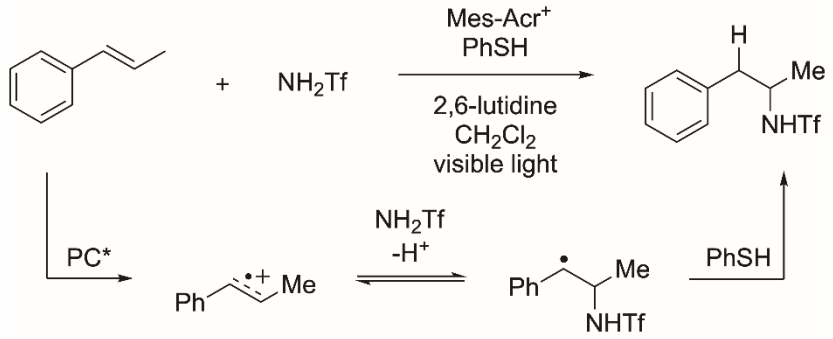

Figure 3.28. *Anti-Markovnikov hydroamination of olefins via radical cation intermediates.*

Acridinium PCs have also been employed for the C-H functionalization of aromatic substrates. Under aerobic conditions, Nicewicz reported the C-H amination of substituted arenes with nitrogen heterocycles such as pyrazole, again via likely cation radical intermediates (Figure 3.29).[54] One drawback to this approach to aromatic functionalization with acridinium catalysts is its limited utility in the oxidation of unactivated arenes, whose oxidation potentials exceed the power of visible light excited acridinium PCs.

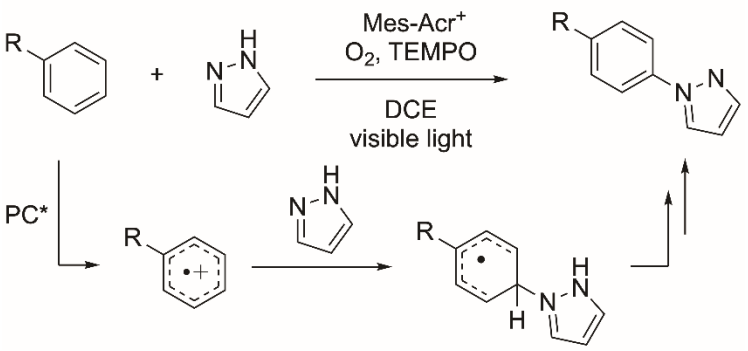

Figure 3.29. *Photoredox catalyzed C-H amination reported by Nicewicz.*

In contrast, Fukuzumi and coworkers have exploited high energy UV light to generate excited 3-cyanoquinolinium ions [$QuCN^+$, $E^o(PC/PC^{+}*)$ = 2.72 V vs. SCE] for the direct aerobic oxidation of benzene to phenol with water.[55] As an alternative method, the same group later disclosed the use of stoichiometric, visible light excited DDQ (Figure 3.26) [$E^o(PC^{\bullet-}/PC*)$ = 3.18 V vs. SCE] to affect the same transformation.[49] Catalytic amounts of *tert*-butyl nitrite ($^tBuNO_2$) were used to turn over reduced DDQ, but oxygen remained the terminal oxidant for the overall reaction (Figure 3.30).

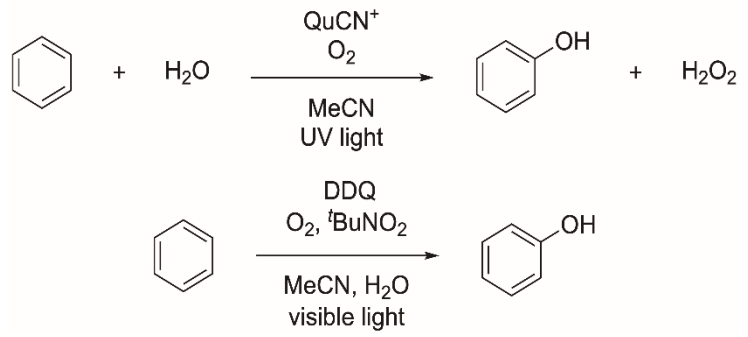

Figure 3.30. *Photocatalytic oxygenation of benzene to form phenol.*

Triarylpyrylium ions are another class of visible light absorbing PCs which possess highly oxidizing excited states. In order to overcome issues of PC degradation by nucleophilic species in catalysis, Beeler designed a relatively sterically hindered catalyst 4-mesityl-2,6-di-*p*-tolylpyrylium

(MDTP, Figure 3.26) capable of promoting oxidation of benzylic epoxides to carbonyl ylides.[56] The generated carbonyl ylides were subsequently trapped by dimethyl acetylenedicarboxylate (DMAD) in [3+2] dipolar cycloadditions to give diverse dihydrofuran products (Figure 3.31). Introduction of a mesityl group to increase catalyst durability was inspired by similar effects seen for acridinium compounds, illustrating the importance of catalyst development across multiple families of PCs.[57]

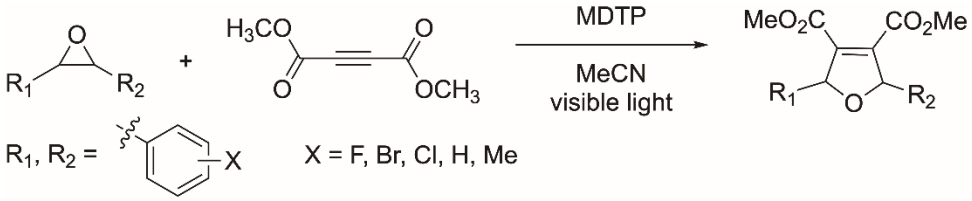

Figure 3.31. *Oxidation of benzylic epoxides and cycloaddition with DMAD to form dihydrofurans.*

Organic excited state reductants

Until about 2016, the range of redox properties accessible by excited state reductants was limited compared to excited state oxidants. Early examples of common excited state reductants include α-sexithiophene[58,59] and benzophenones such as Michler's ketone (MK)[23,53,60–62] (Figure 3.32). However, both systems have associated disadvantages, such as the limited tunability of α-sexithiophene and the necessity of a UV light source for MK.

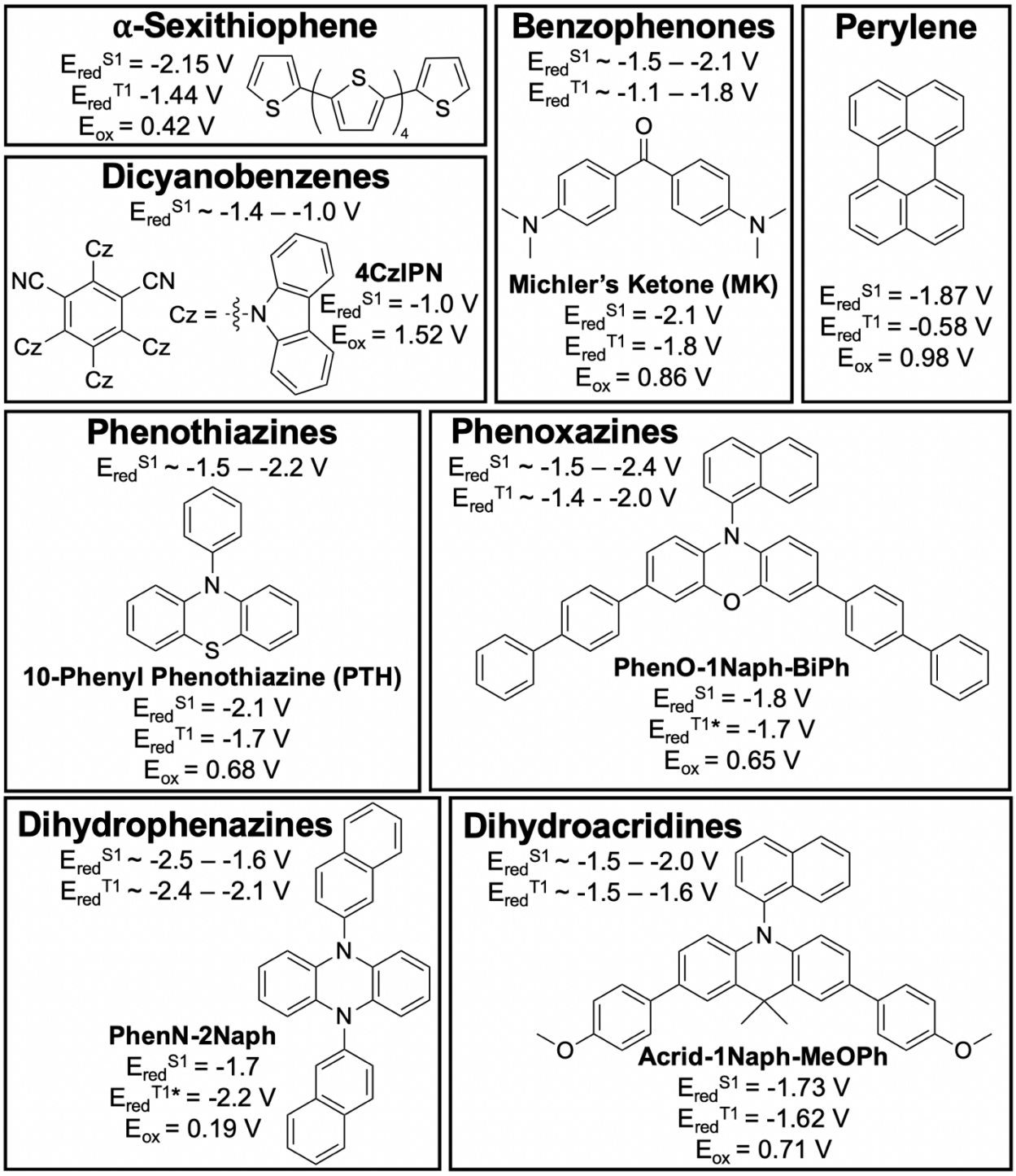

Figure 3.32. *Redox properties of organic excited state reductants. Since many of these families are tunable through structural modification, key examples of commonly used PCs are shown, as well as the redox properties specific to those molecules.* $E_{red}^{S1} = E^o(PC^{\bullet+}/^1PC^*)$; $E_{red}^{T1} = E^o(PC^{\bullet+}/^3PC^*)$; $E_{ox} = E^o(PC^{\bullet+}/PC)$. *All potentials are shown in V vs. saturated calomel electrode (SCE). For conditions under which redox properties were measured, see references* [23,53,59–62,64–66,68–77]. *Computed redox potentials indicated by * (ex.* E_{red}^{T1}*), see references for details.*[66,75]

In 2014, motivation for the development of strongly reducing organic PCs grew after two concurrent reports from the Miyake [63] and Hawker [64] groups detailing the first organocatalyzed atom transfer radical polymerization (O-ATRP). Analogous to atom transfer radical addition, ATRP involves reversibly breaking and forming carbon-halide bonds at the end of polymer chains to synthesize polymers with well-defined structures from vinyl monomers (Figure 3.33). In O-ATRP, a strongly reducing organic PC mediates this process, where PC* reduces polymer C-Br bonds to "activate" the polymer growth, after which the oxidized catalyst species reforms the C-Br bond to "deactivate" the polymer and prevent radical-based side reactions.

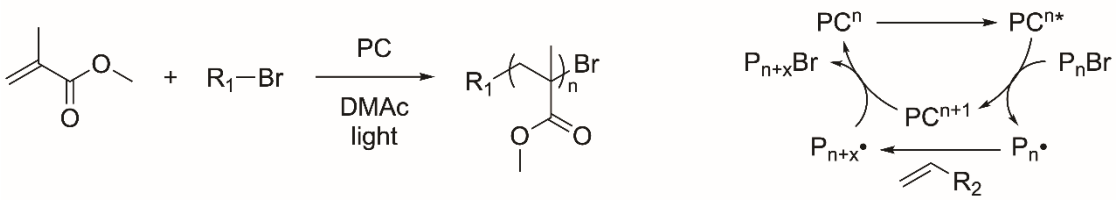

Figure 3.33. *General scheme (left) and mechanism (right) of O-ATRP.*

In early reports, both perylene [63] and 10-phenyl phenothiazine (PTH) [64] were demonstrated as PCs for O-ATRP, although each had associated advantages and disadvantages. Using perylene, O-ATRP could be performed under visible light irradiation with moderate control over polymer structure.[63] By contrast, the use of PTH provided better control over polymer structure while requiring UV light,[64] increasing the risk of photoinduced side reactions. Since the reduction potential [E^o(C-Br/C-Br$^{\bullet-}$)] of a typical C-Br bond in ATRP is about −0.8 – −0.6 V vs SCE,[65] the superior ability of PTH to mediate a controlled polymerization was attributed to its stronger excited state reduction potential (Figure 3.32), motivating the development of more powerful excited state reductants that could operate under visible light.

Early advances in catalyst design came through the development of dihydrophenazine and phenoxazine PCs. Dihydrophenazines (Figure 3.32) were the first organic catalyst family capable of mediating the synthesis of well-defined polymers by O-ATRP under visible light. Through deeper investigation of catalysts in this family, researchers discovered important design principles for effective catalysis. For example, using density functional theory (DFT), it was found that the best catalysts for O-ATRP exhibited intramolecular charge transfer (CT) in the triplet excited state from the phenazine core to the *N*-aryl substituent (Figure 3.32).[66] In later studies, it was shown that this improvement in catalysis is likely due to increased intersystem crossing enabled by the charge transfer state,[67] which produces a long-lived triplet excited state.

Formation of the CT state could be encouraged through installation of electron withdrawing groups (EWGs) or substituents bearing extended conjugation at the *N*-aryl position. In addition, through both computational and experimental studies, it was found that EWGs at the *N*-aryl position decreased the excited state reduction potential (i.e. made it less reducing) and increased the oxidation potential of the PC radical cation, whereas electron donating groups (EDGs) had the opposite effect.[66] In turn, these discoveries formed the basis for tuning the photophysical and redox properties of these and similar PCs in future investigations (*vide infra.*).

Shortly thereafter, phenoxazines (Figure 3.32) were introduced as organic PCs that could also mediate O-ATRP under visible light. Computational and crystallographic investigations compared the phenoxazine and phenothiazine cores to understand the impact of the PC core on catalysis. Ultimately, this work showed that although the redox properties of analogous phenoxazines and phenothiazines are similar, the core geometries of key catalytic intermediates varied significantly. In the case of phenoxazines, the core is predicted to remain relatively planar transitioning from the triplet excited state (^{3}PC*) to the radical cation (PC$^{\bullet+}$) to the PC ground

state. By contrast, the phenothiazine core transitions from a twisted geometry in ^{3}PC* to planar in PC$^{\bullet+}$ and finally to a bent geometry in the ground state. As a result, phenothiazines are predicted to have higher reorganization energies during electron transfer, resulting in a lower rate of ET (see *Marcus theory* section).[75]

In the studies that followed, the scope and tunability of these and similar PCs was greatly widened through several strategies. For example, a number of researchers have reported on methods to tune phenoxazines[65,78] and phenothiazines[79–83] by installation of different substituents at the *N*-aryl position and on the catalyst core – usually at the 3 and 7 positions for these families. Similarly, a number of new dihydrophenazine PCs have been reported through variation of the *N*-aryl substituent[84,85] as well as substitution of the phenazine core, the latter of which produced PCs that can operate at extremely low catalyst loadings in O-ATRP.[76] More recently, dihydroacridines were introduced as organic PCs for O-ATRP, featuring strong excited state reduction potentials [E^o(PC$^{\bullet+}$/^{3}PC*) < −1.5 V vs. SCE] and even more oxidizing radical cations than phenoxazines or phenothiazines (Figure 3.32).[77]

Given the impressive photophysical and redox properties of these molecules, it is not surprising that they have found numerous applications in small molecule and polymer synthesis.[86] For example, the Hawker group demonstrated the utility of phenothiazines in aryl-halide dehalogenation reactions, first in hydrogenation reactions [87] and later in C-C coupling reactions.[79] Notably, the later report demonstrated that selectivity for different carbon halide bonds could be achieved through modulation of the PC's excited state reduction potential (Figure 3.34),[79] emphasizing motivation for the development of highly tunable catalyst systems.

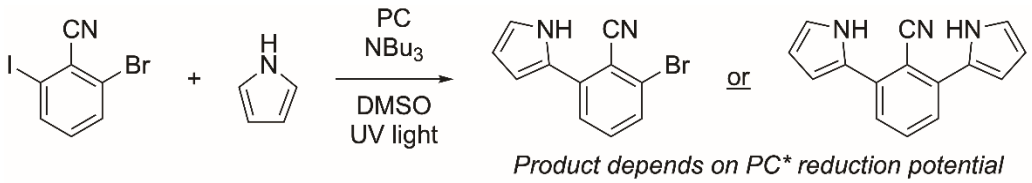

Figure 3.34. *Selective functionalization of aryl-halides using phenothiazine PCs.*

In another example highlighting the capabilities of these PCs, the Jui group reported on the ability of PTH to activate aryl trifluoromethyl C-F bonds for catalytic defluoroalkylations in the presence of cyclohexanethiol as a cocatalyst (Figure 3.35). While direct reduction of the C-F bond was not proposed, the strong excited state reduction potentials of these PCs were nonetheless critical to the success of this transformation, which began through reduction of the aromatic substrate [E^o(sub/sub$^{\bullet-}$) ~ −2.0 V vs. SCE] followed by mesolytic cleavage of a C-F bond to generate the desired radical intermediate.[88]

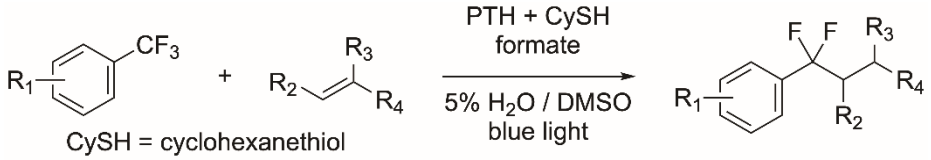

Figure 3.35. *Alkylation of trifluoromethyl arenes through defluorination using an organic excited state reductant.*

Finally, the ability of phenoxazines and dihydrophenazines to act as precious-metal-free alternatives to Ru and Ir based PCs was demonstrated through several transformations. Using a 2-naphthyl substituted dihydrophenazine (PhenN-2Naphth, Figure 3.32), trifluoromethylations were carried out under visible light to afford a variety of substituted alkenes (Figure 3.36). In addition, through the use of phenoxazine and dihydrophenazine PCs with a Ni cocatalyst, both aryl C-N (Figure 3.37) and aryl C-S (Figure 3.38) couplings were successful, providing a more sustainable approach to these transformations that reduces dependence on precious metals.[11]

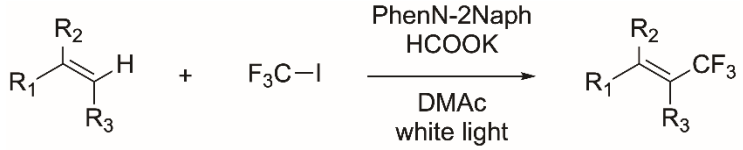

Figure 3.36. *Trifluoromethylation of alkenes using a dihydrophenazine PC.*

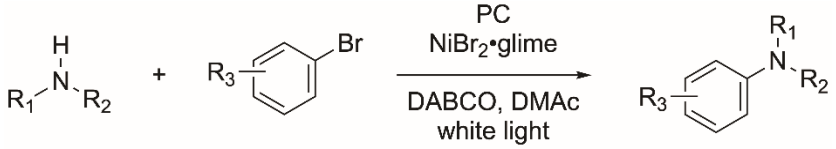

Figure 3.37. *Aryl C-N coupling reactions employing dihydrophenazine and phenoxazine PCs.*

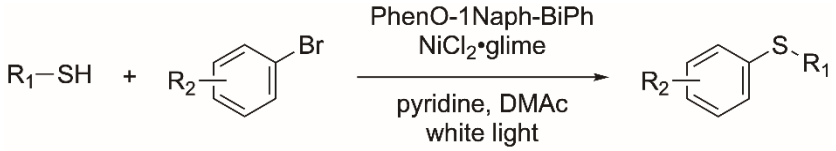

Figure 3.38. *Aryl C-S couplings using a phenoxazine PC.*

While these PCs have been used in a number of other transformations and continue to find new applications, they are too numerous to discuss in great detail here and have been discussed elsewhere.[86] In addition, a number of other strong excited state reductants have been explored, such as dicyanobenzenes (Figure 3.32) [72,85,89,90], naphthochromenones [91], coumarin dyes [92], diketopyrrolopyrroles [93,94], dihydropyridines [95], anthracenes [96], naphthalenes [97], carbazoles [98,99], and more.

Open shell photoredox catalysts

In order to expand the energies accessible to excited PCs beyond those of visible light photons, one strategy described in the literature involves consecutive photoinduced electron transfer (ConPET). A single photon of blue light (440 nm) possesses 2.8 eV of energy which could theoretically be employed by an excited PC, but ISC and nonradiative decay pathways diminish

the energy available for bimolecular PET with substrate compounds. Wasielewski studied the photophysical properties of electrochemically generated radical anions of a series of aromatic diimides and found that they were highly reducing upon photoexcitation.[100] In 2014 König reported multiphoton visible light excitation of one such perylene diimide (PDI) photocatalyst capable of reducing aryl chlorides (ScFigure 3.39), a substrate class for which typical reduction potentials [$E^o(ArCl^{\bullet-}/ArCl) < -2.0$ V vs. SCE] exceed the reducing power of conventional PCs excited by a single photon of visible light.[101]

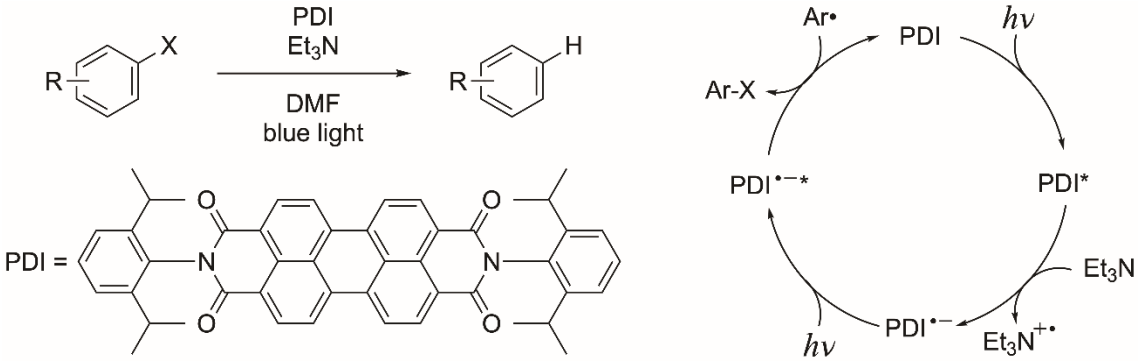

Figure 3.39. *Hydrodehalogenation of aryl halides with PDI photocatalysts.*

The reaction likely proceeds first through initial visible light excitation of the PDI to generate the excited state PDI*. Reductive quenching with Et_3N generates the radical anion $PDI^{\bullet-}$, which after excitation by a second photon yields an excited radical anion $PDI^{\bullet-}$*. This species is a potent reductant capable of electron transfer to an aryl halide acceptor and subsequent regeneration of the ground state catalyst.[102] In addition to organic radical anion photoexcitation, Nicewicz has shown that the neutral acridine radicals produced by reductive quenching of excited acridinium PCs with simple amines can also undergo excitation to generate a powerful reductant [$E^o(PC^+/PC^{\bullet}*) \sim -3.36$ V vs. SCE].[30] Although these examples demonstrate the power of

photoredox catalysis via ConPET, drawbacks include possible side reactions from radical cation byproducts of the sacrificial reductant.

Electrochemistry provides an alternative approach to generating open shell intermediates for subsequent photoexcitation. The groups of Wickens and Lin have disclosed photoexcitation of cathodically generated organic radical anions followed by selective catalytic reductive couplings of aryl halides.[103,104] In the latter case, electrochemical reduction of 1,9-dicyanoanthracene (DCA) to form a radical anion $DCA^{\bullet-}$ and subsequent irradiation with visible light was proposed to form the excited species $DCA^{\bullet-}$* with an extreme estimated reduction potential [$E^o(PC/PC^{\bullet-}*) \sim -3.20$ V vs. SCE]. Importantly, under these conditions, aryl halides could be selectively reduced and borylated even in the presence of potentially sensitive substrate functional groups (Figure 3.40). The authors propose that the observed chemoselectivity is a result of the controlled generation of low concentrations of the highly reactive excited state species $DCA^{\bullet-}$*.

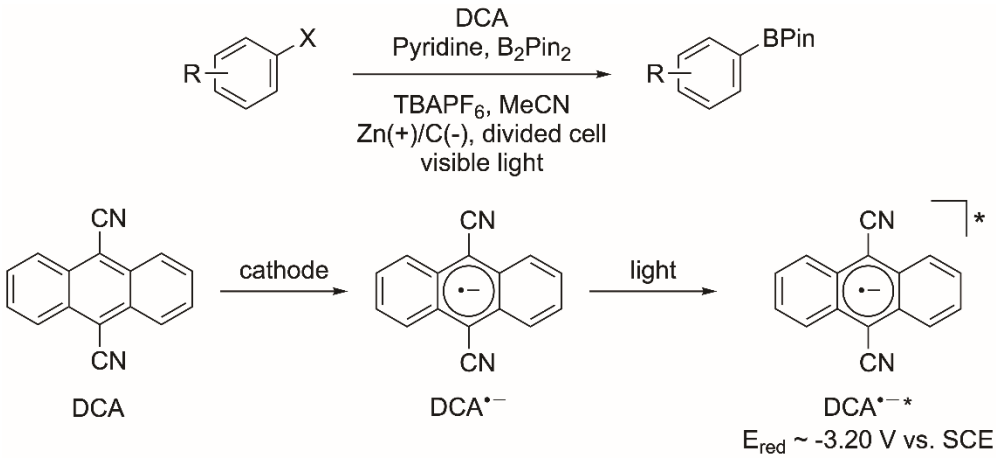

Figure 3.40. *Reductive coupling of aryl halides with an excited radical anion electrophotocatalyst.* $E_{red} = E^o(PC/PC^{\bullet-}*)$.

As an example of an aromatic reduction not involving aryl halides, Miyake and coworkers have developed a visible light mediated photoredox Birch reduction using benzo[ghi]perylene

imide PCs (Figure 3.41). In this system, basic reductants like OH^- are proposed to form an anionic adduct with the PC, which after photolytic fragmentation yields a radical anion which can absorb a second photon of visible light. It is proposed that the subsequent excited radical anion species can ionize to form solvated electrons, which might be responsible for the observed conversion of arene substrates to unconjugated cyclohexadienes.[105]

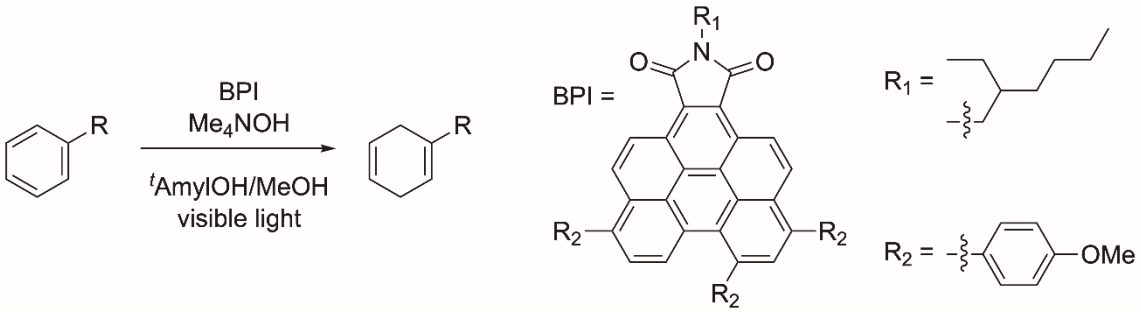

Figure 3.41. *Organocatalyzed visible light mediated photoredox Birch reduction.*

In contrast to reports of photoredox catalysis via reduced open shell species, photoexcitation of oxidized open shell species is less common. Wasilewski discovered that phenothiazine radical cations can be excited by visible light to access doublet excited states with oxidation potentials upwards of $E^o(PC/PC^{\bullet+*}) \sim 2.1$ V vs. SCE (Figure 3.42).[106] Lambert and coworkers found that visible light irradiation of an anodically generated trisaminocyclopropenium radical dication (Figure 3.42) yielded a highly oxidizing species [$E^o(PC^+/PC^{2+*}) \sim 3.33$ V vs. SCE] which could be applied to the oxidation of benzene and subsequent C-N coupling.[107]

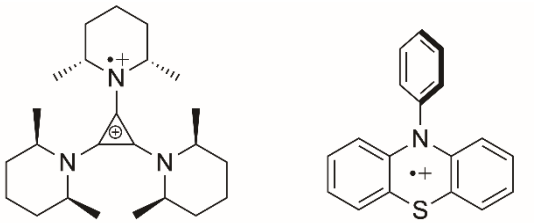

E_{ox} ~ 3.33 V vs. SCE E_{ox} ~ 2.1 V vs. SCE

Figure 3.42. *Highly oxidizing excited organic radical cations.* E_{ox} = $E^o(PC^+/PC^{2+}*)$ *or* $E^o(PC/PC^{\bullet+}*)$.

Finally, Kerzig and Wenger demonstrated how multiple excitation events can be combined to produce higher-energy reactants, which in their case led to the formation of solvated electrons that could perform otherwise challenging reductions. In this example, a collimating lens was used to focus light from a 1 W laser into a small reaction volume, creating a region of very high light intensity. As a result, the PC employed in these reactions was able to undergo two consecutive photoexcitation events, ultimately leading to ionization of the PC to form a solvated electron.[108] In later work, the synthetic utility of this approach was demonstrated in comparison to traditional photoexcitation of the same PC. While irradiation with lower intensity light only allowed for reduction of aryl C-Br bonds (due to the lower excited state reduction potential of PC*), the use of high intensity light to produce solvated electrons allowed for the reduction of aryl C-Cl bonds that would otherwise be inaccessible to the PC.[109]

Photochemistry of Electron Donor-Acceptor Complexes

Background and Theory

What is an EDA complex? An EDA complex, also referred to as a charge transfer complex, is composed of an electron-rich molecule (donor) and an electron-poor molecule (acceptor) that reversibly associate in the ground state through intermolecular forces. Due to the generally weak nature of these interactions (ex. Van der Waals forces), EDA complexes are quite sensitive to

environmental factors, such as temperature, solvent, and D/A concentrations. These complexes have been studied extensively since the 1950s and were observed even earlier, such as in the interaction of iodine with various solvents to give rise to different colored solutions.[110]

Early work in this area was carried out by Mulliken, who first proposed the existence of EDA complexes in his charge transfer theory in 1952.[111–113] It was here that Mulliken first defined an EDA complex and proposed that the donor should be electron rich and have a low ionization potential, whereas the electron acceptor should be electron poor and have a high electron affinity. Based on these definitions, one can estimate the electron donating or accepting ability of a molecule according to its redox properties, as the ionization potential of a donor can be approximated by its oxidation potential in solution, and the electron affinity of an acceptor can be approximated by its reduction potential. Importantly, using this data in combination with Equation 3.7 (see *Photoinduced electron transfer* section), the likelihood of reactivity between an electron donor and acceptor pair can be predicted. Even when the excited state energy ($\Delta E_{0\text{-}0}$) of the EDA complex is unavailable, comparison of the D and A redox properties can serve as a guide for reaction design. For examples of common donors and acceptors that form EDA complexes, the reader can refer to reviews by Kochi [114] and Paixaõ [115]. In addition, work by Nicewicz and coworkers has tabulated the reduction and oxidation potentials of numerous common organic molecules that could be relevant to this chemistry.[116]

How do EDA complexes interact with light? Upon formation of an EDA complex, new molecular orbitals (MOs) form through mixing of the D and A highest occupied and lowest unoccupied molecular orbitals (HOMO and LUMO, respectively). The formation of this new MO gives rise to a charge transfer band in the absorption spectrum of the EDA complex, which is typically red-shifted relative to the absorption bands of the D and A alone. Often, this CT band

can appear in the visible spectrum, allowing the EDA complex to absorb visible light even when the D and A cannot. As a result, irradiation of the EDA complex can give rise to photoinduced electron transfer (Figure 3.43), creating the opportunity for reactivity in these complexes.

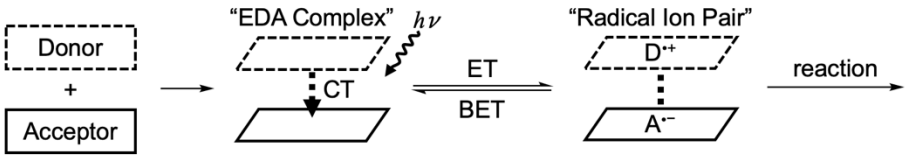

Figure 3.43. *General diagram showing the association of a donor and acceptor to form an EDA complex, which through irradiation undergoes electron transfer and subsequent reactions.*

Broadly, EDA complexes can also be considered an absorption complex, which refers to two molecules that cooperatively absorb a single photon of light. Closely related to this concept is an exciplex, or an excited state complex, as well as an excimer, which is an excited state dimer, both of which form from excited states associating with other molecules.

Electron transfer in EDA complexes. Electron transfer in an EDA complex can be considered as either ISET (adiabatic) or OSET (non-adiabatic, see *Electron transfers* section). While ISET is most often observed,[115] the specific mechanism of ET depends on both the structural and electronic characteristics of the EDA complex. For example, EDA complexes that operate through ISET typically have a D-A distance of about 3 Å, strong electronic coupling (V_{el} ~ 1000 – 3000 cm^{-1}), and moderate equilibrium association constants (K_{EDA} ~ 0.1 – 1 M^{-1}). By contrast, EDA complexes that undergo OSET have larger D-A distances (5 – 6 Å), weaker electronic coupling (V_{el} ~ 100 – 300 cm^{-1}), and small association constants that are often too small to measure (Table 3.3).[114,115]

An important consideration in the chemistry of EDA complexes is back electron transfer (BET), where the radical anion of the acceptor formed after ET can donate an electron back to the

radical cation of the donor and regenerate the ground state EDA complex (Figure 3.43). Practically, this process can lead to limited product formation if BET is not minimized. A strategy to address this issue includes designing the acceptor molecule to contain a leaving group, which rapidly and irreversibly cleaves after ET to prevent BET.

Table 3.3. *Typical properties of EDA complexes that undergo ISET and OSET.*

	ISET	**OSET**
D-A Distance (Å)	3.0 – 3.3	5 – 6
V_{el} (cm^{-1})	1000 – 3000	100 – 300
K_{EDA} (M^{-1})	0.1 – 1	n/a

Environmental factors affecting EDA complexes. As mentioned previously, the weak intermolecular interactions that lead to D-A association also make an EDA complex sensitive to several environmental factors. For example, since the D, A, and EDA complex are in equilibrium, the EDA complex will be sensitive to typical equilibrium perturbations such as temperature and the concentration of the reactants (D and A). Further, given the charged nature of the products (a radical anion and cation), solvents can have a significant impact on EDA complex reactivity. Generally, polar solvents stabilize the radical anion and cation formed after ET, favoring dissociation of the ion pair over BET.[114]

Early examples of EDA photochemistry

Photoredox chemistry in EDA complexes was observed as early as the 1970s and 1980s by several researchers, although examples of such reactivity were limited for a number of reasons. Melchiorre and coworkers have proposed that early examples of EDA complex photochemistry

might have been limited by challenges in overcoming BET.[117] In addition, until about 2008, photochemistry in organic synthesis remained relatively underexplored. Therefore, the number of researchers investigating EDA complex photochemistry prior to this time was likely limited, further slowing the development of this chemistry.

Cantacuzene reported an early example of this chemistry in 1977, which involved the condensation of enamines with perfluoroalkyl iodides to yield α-substituted ketones.[118] Similar products were obtained by Bunnett in the same year through the reaction of ketones with potassium alkoxides, which upon irradiation gave α-substituted ketones.[119] In 1983, Fox showed that this reaction likely proceeds through formation and photoexcitation of an EDA complex, ultimately leading to electron transfer.[120]

Another researcher who contributed several early examples of EDA complex photochemistry is Kochi. For example, in 1979, Kochi's group studied the addition of a tetraalkyltin compounds to tetracyanoethylene, which was found to proceed through photoexcitation of an EDA complex.[121] In addition, his group also reported aromatic nitration reactions proceeding through irradiation of an EDA complex in 1987.[122]

In the same year, Kornblum disclosed a reaction between p-nitrobenzylchloride and sodium azide, which he proposed proceeded through EDA complex photochemistry.[123] Similar reactivity was observed in 1991 by Russell and coworkers with other nitrogen containing donors.[124] Finally, in 1991, Hall's group reported on the cycloaddition of vinyl carbazole to a substituted dicyanoethylene, which were proposed to form an EDA complex prior to the cycloaddition.[125]

Recent examples of EDA photochemistry

Rediscovering EDA complexes through photoredox catalysis. The renaissance of EDA complex photochemistry arguably began in 2013 as a result of two concurrent reports from the Chatani [14] and Melchiorre [13] groups. An even earlier example of this chemistry might have been observed in 2011 by the MacMillan group during work on photoredox catalyzed trifluoromethylations, which in some cases was observed to proceed to high yields in the absence of a PC. While photoexcitation of an EDA complex was proposed, this mechanism was not confirmed at the time.[12]

The example by Chatani in 2013 was also discovered serendipitously through investigations focused on photoredox catalysis, which revealed that arylations of pyrrole using diaryliodonium salts could proceed efficiently in the absence of a photocatalyst (Figure 3.44).[14] In the same year, Melchiorre reported a stereoselective approach to synthesizing α-alkylated aldehydes, which was found to proceed through photoexcitation of an EDA complex. This interesting example, which will be referred to several times throughout this section, combines a number of strategies to catalytically generate an EDA complex and then stereoselectively substitute aldehydes to produce the desired products (Figure 3.45).[13]

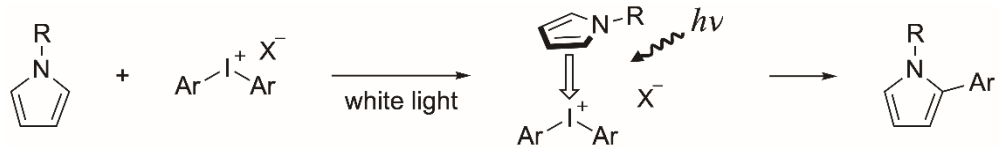

Figure 3.44. *An example of EDA complex reactivity for coupling pyrroles and aryl-iodonium salts reported by Chatani in 2013.*

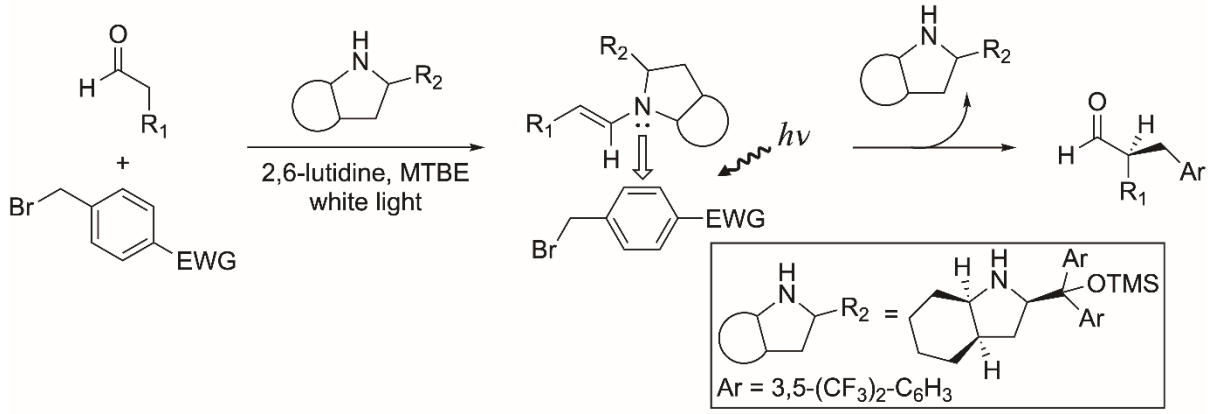

Figure 3.45. *An example of EDA complex reactivity for enantioselective coupling reactions reported by Melchiorre in 2013.*

<u>*Stoichiometric EDA reactions.*</u> The simplest reactions involving EDA complexes are stoichiometric, where the donor and acceptor ultimately couple to each other to generate the product. An excellent example of a stoichiometric EDA reaction was reported by Melchiorre in 2015 for coupling electron deficient benzyl bromides to indoles (Figure 3.46). In this reaction, indole acts as an electron donor with the electron deficient arene to generate the EDA complex, which upon absorption of visible light generates a radical ion pair. The C-Br bond of the radical anion then rapidly cleaves to form a radical at the benzylic position, which is trapped to yield various substituted indoles. Excitingly, Melchiorre and coworkers were able to obtain a crystal structure of the EDA complex formed during this reaction, which is typically challenging given the weak association inherent to these complexes.[126]

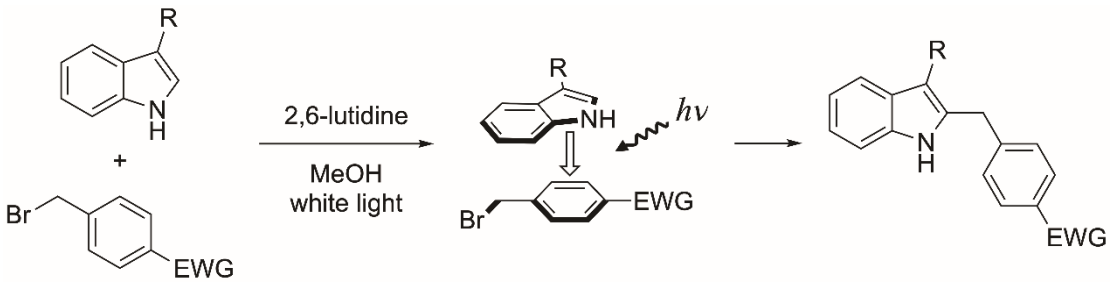

Figure 3.46. *A reaction reported by Melchiorre in 2015 that proceeds through photoexcitation of an EDA complex to couple benzyl-bromides to indoles.*

A similar strategy is seen in the aryl-thiol couplings reported by Miyake and coworkers in 2017, which generates an EDA complex from aryl halides and aryl thiolates (Figure 3.47). Although neither compound alone absorbs light in the visible region, the EDA complex is colored, allowing these C-S couplings to be performed selectively under mild conditions.[15,16] Closely related to this reaction, Wang and coworkers reported a strategy for coupling aryl halides and phenols, which was proposed to undergo a similar mechanism to the aryl halide–thiol coupling.[127]

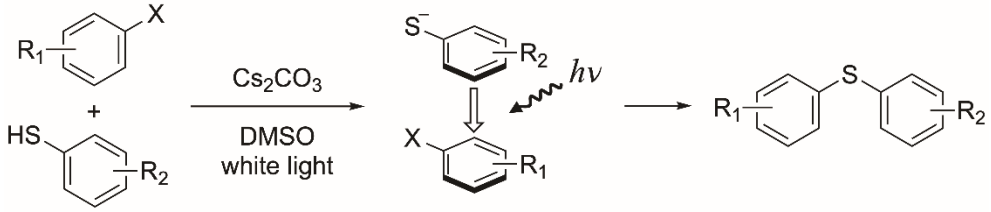

Figure 3.47. *A C-S coupling reaction enabled by EDA complex reactivity reported in 2017 by Miyake and coworkers.*

<u>*Use of sacrificial donors and acceptors.*</u> In some cases, couplings between moieties that are poor electron donors or acceptors have been achieved through the use of sacrificial donors or acceptors, which enable formation of the EDA complex but are not incorporated into the final product. An example from Paixão in 2015 exhibits this strategy, where intramolecular cyclizations to form indoles were performed utilizing tris(TMS)silane (TMS = trimethylsilyl) as a sacrificial electron donor to generate the EDA complex and perform electron transfer to the substrate (Figure

3.48). Upon generation of the acceptor radical anion, the aryl C-X bond (X = halide) cleaves to generate an aryl radical, enabling an intramolecular cyclization with the alkyne to yield substituted indoles. The same approach was also demonstrated to synthesize oxindoles when the appropriate amide was employed as the acceptor rather than an amine.[128]

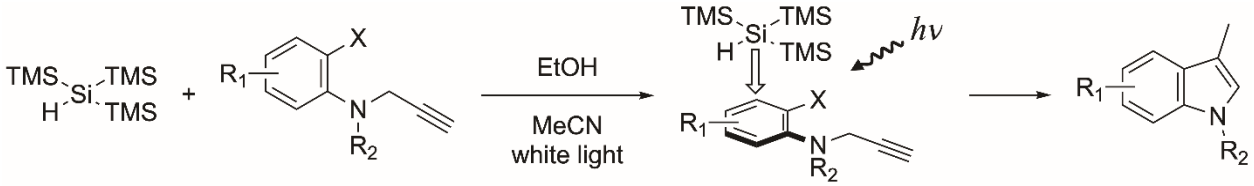

Figure 3.48. *An example from Paixão in 2015 employing a sacrificial donor to form an EDA complex, which upon photoexcitation generates substituted indoles.*

Along these lines, in 2017 Chen reported the alkylation of alkenes using photoexcited EDA complexes that employed both a sacrificial electron donor and a redox auxiliary electron acceptor. The redox auxiliary moiety can be thought of as a sacrificial electron acceptor, which upon electron transfer generates a reactive species for use in the reaction. In Chen's example, an *N*-substituted phthalimide is used as the redox auxiliary, whereas Hantzsch ester is used as the sacrificial donor. Upon irradiation of the EDA complex with blue light, an alkyl radical is generated and then trapped to yield the product (Figure 3.49).[129]

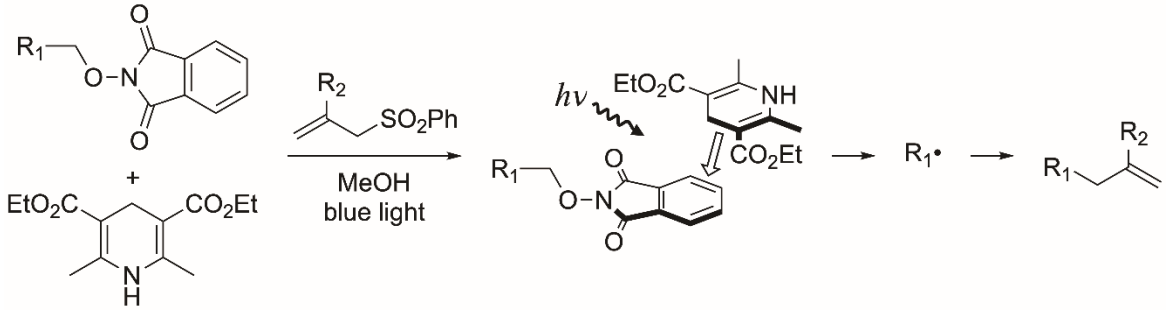

Figure 3.49. *Reaction reported in 2017 by Chen that employs both a sacrificial donor and a redox auxiliary to yield substituted alkenes.*

Redox auxiliaries to expand donor and acceptor scope. Expanding on the use of redox auxiliaries, Leonori disclosed a reaction employing an electron deficient aryl moiety as an acceptor to yield substituted pyrrolines through intramolecular cyclizations. Interestingly, hydrogenation or hydroxylation could be selectively achieved in the last step of the reaction through addition or exclusion of 1,4-cyclohexadiene, respectively (Figure 3.50).[130]

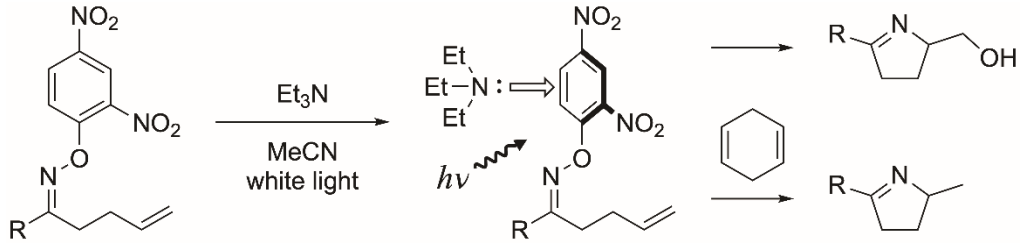

Figure 3.50. *Reported by Leonori in 2015, this reaction employs an auxiliary redox moiety to generate substituted pyrrolines.*

Further, Aggarwal developed a series of borylation reactions employing redox auxiliaries.[131–133] Notably, his report in 2017 demonstrates how a substituted phthalimide can undergo PET with bis(catecholato)diboron to generate an alkyl radical and a catecholboryl radical. While this reaction was originally proposed to proceed through formation of a ternary complex,[131] it has since been suggested this reaction might proceed through the formation of an EDA complex (Figure 3.51).[117] Regardless, upon coupling of the radicals produced and addition of pinacol, the desired pinacolborane can be obtained under mild conditions (Figure 3.51).[131]

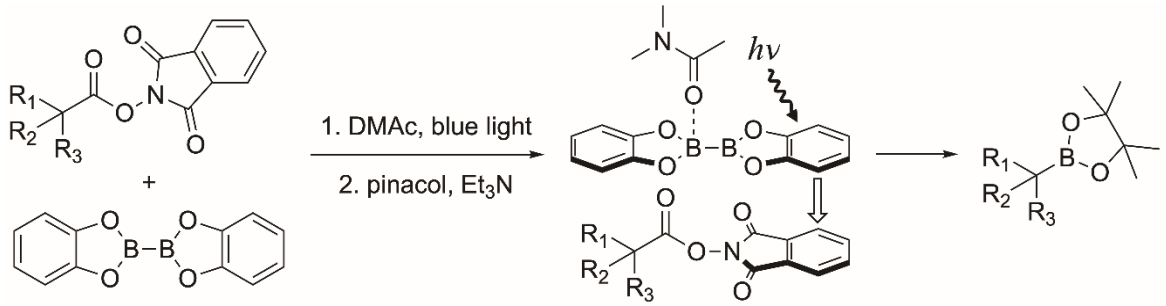

Figure 3.51. *This reaction, reported by Aggarwal in 2017, employs an auxiliary redox moiety to enable C-B couplings through photoexcitation of an EDA complex.*

<u>*Catalytic EDA reactions.*</u> In contrast to stoichiometric EDA reactions, catalytic reactions employ acceptors or donors that are regenerated during the course of the reaction and then subsequently reused. An early example of such reactivity is evident in Melchiorre's seminal 2013 report, where an amine reacts with an aldehyde to form the donor species and is later regenerated upon product formation (Figure 3.45).[13] Similarly, Bosque and Bach reported a reaction employing a catalytic donor in 2019, where a substituted quinuclidine served as a sacrificial donor and was regenerated later in the reaction to perform a series of decarboxylations (Figure 3.52).[134]

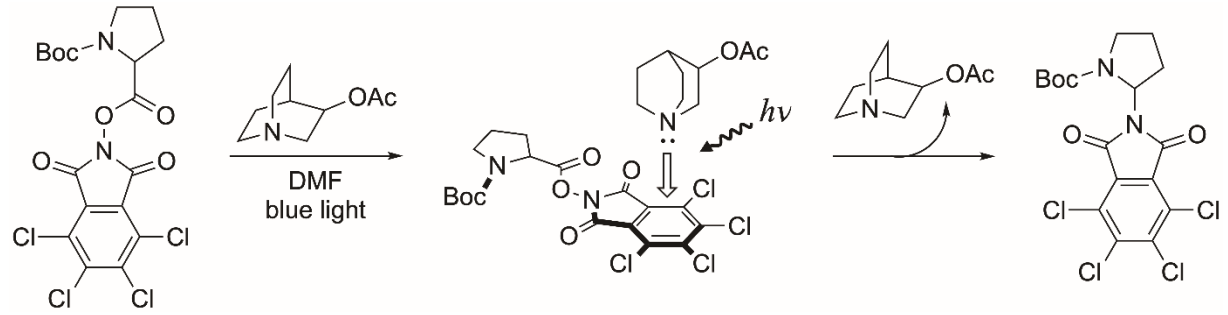

Figure 3.52. *An example from Bosque and Bach in 2019 of an EDA complex reaction in which a catalytic donor is employed.*

<u>*Enantioselective reactions of EDA complexes.*</u> Several strategies have been reported for performing enantioselective reactions using EDA complexes. Again, the seminal example by

Melchiorre demonstrates this reactivity, where a chiral amine catalyst was used to direct the formation of the final product (Figure 3.45).[13]

In 2016, Hyster reported the use of ketoreductase enzymes to perform enantioselective hydrogenations of halolactones, where the enantiomer produced could be precisely controlled through selection of the appropriate ketoreductase (Figure 3.53). Further, through investigation of the reaction mechanism, evidence was found suggesting formation of an EDA complex between the substrate and dihydronicotinamide-adenine dinucleotide phosphate (NADPH), which only occurred in the presence of a ketoreductase enzyme.[135]

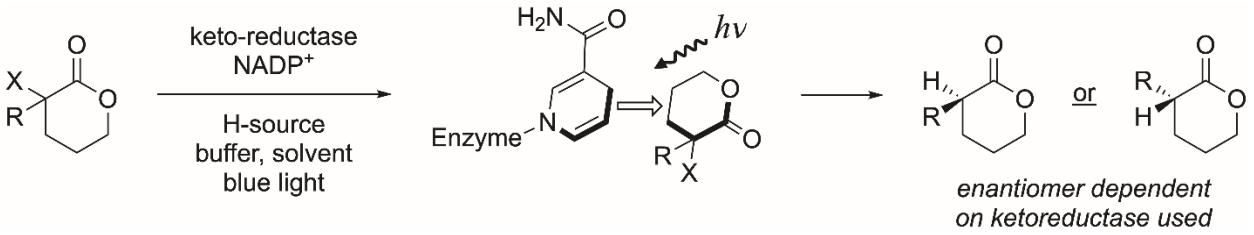

Figure 3.53. *Enantioselective reductive dehalogenation reported by Hyster in 2016.*

Conclusion

In this chapter, the fundamentals of photoredox chemistry were discussed, including photophysical processes and theories of electron transfer relevant to photochemistry. While much of this fundamental knowledge was uncovered over the last century, it has provided the foundation for the recent renaissance of photochemistry for organic synthesis that began around 2008. Enabled by these previous discoveries and advances in lighting technology, recent work in photochemistry has led to the wide-spread implementation of photoredox catalysis in organic synthesis. As a result, countless reactions can now be performed under mild reaction conditions that were previously inaccessible or required harsh reagents or forcing conditions. In addition, studies focused on photocatalysis have revealed that some reactions can proceed in the absence of a catalyst, reviving

interest in EDA complex photochemistry. Combined, these photoredox strategies offer many unique and exciting opportunities to perform challenging reactions in a more sustainable manner that are becoming a pillar of synthetic chemistry.

Additional Reading

Photochemistry and photophysical processes

- Anslyn, E. V. and Dougherty, D. A. (2006). Chapter 16: Photochemistry. In *Modern Physical Organic Chemistry*, University Science Books.
- Turro, N. J. (1991). *Modern Molecular Photochemistry*, University Science Books.
- Turro, N. J. (2010). *Modern Molecular Photochemistry of Organic Molecules*, University Science Books.
- Lakowicz, J. R. (2006). *Principles of Fluorescence Spectroscopy*, Springer.

Electrochemical methods

- Elgrishi, N., Rountree, K. J., McCarthy, B. D., Rountree, E. S., Eisenhart, T. T., Dempsey, J. L. (2018). A Practical Beginner's Guide to Cyclic Voltammetry. *J. Chem. Educ.* 95: 197.
- Bard, A. J. and Faulkner, L. R. (2001). *Electrochemical Methods: Fundamentals and Applications,* Wiley.

Photoredox catalysis

- Arias-Rotondo, D. M. and McCusker, J. K. (2016). The Photophysics of Photoredox Catalysis: A Roadmap for Catalyst Design. *Chem. Soc. Rev.* 45: 5803.

- Romero, N. A. and Nicewicz, D. A. (2016). Organic Photoredox Catalysis. *Chem. Rev.* 116: 10075.
- Gesmundo, N. J., Shaw, M. H., Twilton, J., Tellis, J. C., MacMillan, D. W. C., Nicewicz, D. A. (2019). Photoredox Catalysis Desk Reference and User's Guide. *Sigma-Aldrich*.
- Prier, C. K., Rankic, D. A., MacMillan, D. W. C. (2013). Visible Light Photoredox Catalysis with Transition Metal Complexes: Applications in Organic Synthesis. *Chem. Rev.* 113: 5322.
- Corrigan, N., Shanmugam, S., Xu, J., Boyer, C. (2016). Photocatalysis in Organic and Polymer Synthesis. *Chem. Soc. Rev.* 45: 6165.

Earth abundant metal photoredox catalysis

- Hockin, B.M., Li, C., Robertson, N., Zysman-Colman, E. (2019). Photoredox Catalysts Based on Earth Abundant Metal Complexes. *Catal. Sci. Technol.* 9: 889.
- Wenger, O.S. (2018). Photoactive Complexes with Earth-Abundant Metals. *J. Am. Chem. Soc.* 140: 13522.
- McCusker, J. K. (2019). Electronic Structure in the Transition Metal Block and Its Implications for Light Harvesting. *Science* 363: 484.

EDA complexes

- Lima, C. G. S., Lima, T. de M., Duarte, M., Jurberg, I. D., Paixão, M. W. (2016). Organic Synthesis Enabled by Light-Irradiation of EDA Complexes: Theoretical Background and Synthetic Applications. *ACS Catal.* 6: 1389.

- Rosokha, S. V. and Kochi, J. K. (2008). Fresh Look at Electron-Transfer Mechanisms via the Donor/Acceptor Bindings in the Critical Encounter Complex. *Acc. Chem. Res.* 41: 641.
- Crisenza, G. E. M., Mazzarella, D., Melchiorre, P. (2020). Synthetic Methods Driven by Photoactivity of Electron Donor-Acceptor Complexes. *J. Am. Chem. Soc.* 142: 5461.

REFERENCES

(1) Roth, H. D. The beginnings of organic photochemistry. *Angew. Chem. Int. Ed. Engl.***1989**, *28*, 1193–1207.

(2) Heindel, N. D.; and Pfau, M. A. A profitable partnership: Giacomo Ciamician and Paul Silber. *J. Chem. Educ.***1965**, *42*, 383.

(3) Hedstrand, D. M.; Kruizinga, W. H.; Kellogg, R. M. Light induced and dye accelerated reductions of phenacyl onium salts by 1,4-dihydropyridines. *Tetrahedron Lett.* **1978**, *19*, 1255–1258.

(4) Pac, C.; Ihama, M.; Yasuda, M.; Miyauchi, Y.; Sakurai, H. $Ru(bpy)_3^{2+}$-mediated photoreduction of olefins with 1-benzyl-1,4-dihydronicotinamide: a mechanistic probe for electron-transfer reactions of NAD(P)H-model compounds. *J. Am. Chem. Soc.* **1981**, *103*, 6495–6497.

(5) Fukuzumi; S; Mochizuki, S.; Tanaka, T. Photocatalytic reduction of phenacyl halides by 9,10-dihydro-10-methylacridine: control between the reductive and oxidative quenching pathways of tris(bipyridine)ruthenium complex utilizing an acid catalysis. *J. Phys. Chem.* **1990**, *94*, 722–726.

(6) Deronzier, A. Photo-oxidation of some carbinols by the Ru(II) polypyridyl complex-aryl diazonium salt system. *Tetrahedron Lett.* **1984**, *25*, 5517–5520.

(7) Cano-Yelo, H.; Deronzier, A. Photocatalysis of the pschorr reaction by $Ru(bpy)_3^{2+}$. *J. Photochem.* **1987**, *37*, 315–321.

(8) Ischay, M. A.; Anzovino, M. E.; Du, J.; Yoon, T. P.; Efficient visible light photocatalysis of [2+2] enone cycloadditions. *J. Am. Chem. Soc.* **2008**, *130*, 12886–12887.

(9) Nicewicz, D. A.; MacMillan, D. W. C. Merging photoredox catalysis with organocatalysis: the direct asymmetric alkylation of aldehydes. *Science* **2008**, *322*, 77–80.

(10) Narayanam, J. M. R.; Tucker, J. W.; Stephenson, C. R. J. Electron-transfer photoredox catalysis: development of a tin-free reductive dehalogenation reaction. *J. Am. Chem. Soc.* **2009**, *131*, 8756–8757.

(11) Du, Y.; Pearson, R. M.; Lim, C.-H.; Sartor, S. M.; Ryan, M. D.; Yang, H.; Damrauer, N. H.; Miyake, G. M. Strongly reducing, visible-light organic photoredox catalysts as sustainable alternatives to precious metals. *Chem. - Eur. J.* **2017**, *23*, 10962–10968.

(12) Pham, P. V.; Nagib, D. A.; MacMillan, D. W. C. Photoredox catalysis: a mild, operationally simple approach to the synthesis of α-trifluoromethyl carbonyl compounds. *Angew. Chem. Int. Ed.* **2011**, *50*, 6119–6122.

(13) Arceo, E.; Jurberg, I. D.; Álvarez-Fernández, A.; Melchiorre, P. Photochemical activity of a key donor–acceptor complex can drive stereoselective catalytic α-alkylation of aldehydes. *Nat. Chem.* **2013**, *5*, 750–756.

(14) Tobisu, M.; Furukawa, T.; Chatani, N. Visible light-mediated direct arylation of arenes and heteroarenes using diaryliodonium salts in the presence and absence of a photocatalyst. *Chem. Lett.* **2013**, *42*, 1203–1205.

(15) Liu, B.; Lim, C.-H.; Miyake, G. M. Visible-light-promoted C–S cross-coupling via intermolecular charge transfer. *J. Am. Chem. Soc.* **2017**, *139*, 13616–13619.

(16) Liu, B.; Lim, C.-H.; Miyake, G. M. Transition-metal-free, visible-light-promoted C–S cross-coupling through intermolecular charge transfer. *Synlett,* **2018**, *29*, 2449–2455.

(17) Jablonski, A. Efficiency of anti-stokes fluorescence in dyes. *Nature* **1933**, *131*, 839.

(18) Kasha, M. Characterization of electronic transitions in complex molecules. *Discuss. Faraday Soc.* **1950**, *9*, 14–19.

(19) Demchenko, A. P.; Heldt, J.; Waluk, J.; Chou, P.-T.; Sengupta, P. K.; Brizhik, L.; del Valle, J. C. (2014) Michael Kasha: From Photochemistry and Flowers to Spectroscopy and Music. *Angew. Chem. Int. Ed.* **2014**, *53*, 14316–14324.

(20) Demchenko, A. P.; Tomin, V. I.; Chou, P.-T. Breaking the Kasha rule for more efficient photochemistry. *Chem. Rev.* **2017**, *117*, 13353–13381.

(21) Okamura, T.; Sancar, A.; Heelis, P. F.; Hirata, Y.; Mataga, N. Doublet-quartet intersystem crossing of flavin radical in DNA photolyase. *J. Am. Chem. Soc.* **1989**, *111*, 5967–5969.

(22) International Union of Pure and Applied Chemistry. The Gold Book: Gibbs energy of photoinduced electron transfer. https://goldbook.iupac.org/terms/view/GT07388 (accessed 13 July 2020)

(23) Romero, N. A.; Nicewicz, D. A. Organic photoredox catalysis. *Chem. Rev.* **2016**, *116*, 10075–10166.

(24) Miller, J. R.; Calcaterra, L. T.; Closs, G. L. Intramolecular long-distance electron transfer in radical anions. The effects of free energy and solvent on the reaction rates. *J. Am. Chem. Soc.* **1984**, *106*, 3047–3049.

(25) Lakowicz, J. R. *Principles of fluorescence spectroscopy*, Springer, 2006.

(26) Garlets, Z. J.; Nguyen, J. D.; Stephenson, C. R. J. The development of visible-light photoredox catalysis in flow. *Isr. J. Chem.* **2014**, *54*, 351–360.

(27) Buss, B. L.; Miyake, G. M. Photoinduced controlled radical polymerizations performed in flow: methods, products, and opportunities. *Chem. Mater.* **2018**, *30*, 3931–3942.

(28) Arias-Rotondo, D. M.; McCusker, J. K. The photophysics of photoredox catalysis: a roadmap for catalyst design. *Chem. Soc. Rev.* **2016**, *45*, 5803–5820.

(29) Weir, D.; Scaiano, J. C. Substituent effects on the lifetime and fluorescence of excited diphenylmethyl radicals in solution. *Chem. Phys. Lett.* **1986**, *128*, 156–159.

(30) MacKenzie, I. A.; Wang, L.; Onuska, N. P. R.; Williams, O. F.; Begam, K.; Moran, A. M.; Dunietz, B. D.; Nicewicz, D. A. Discovery and characterization of an acridine radical photoreductant. *Nature* **2020**, *580*, 76–80.

(31) Kalyanasundaram, K. Photophysics, photochemistry and solar energy conversion with tris(bipyridyl)ruthenium(II) and its analogues. *Coord. Chem. Rev.* **1982**, *46*, 159–244.

(32) Thompson, D. W.; Ito, A.; Meyer, T. J. $[Ru(bpy)_3]^{2+*}$ and other remarkable metal-to-ligand charge transfer (MLCT) excited states. *Pure Appl. Chem.* **2013**, *85*, 1257–1305.

(33) Tucker, J. W.; Stephenson, C. R. J. Shining light on photoredox catalysis: theory and synthetic applications. *J. Org. Chem.* **2012**, *77*, 1617–1622.

(34) Nguyen, J. D.; D'Amato, E. M.; Narayanam, J. M. R.; Stephenson, C. R. J. Engaging unactivated alkyl, alkenyl and aryl iodides in visible-light-mediated free radical reactions. *Nat. Chem.* **2012**, *4*, 854–859.

(35) Condie, A. G.; González-Gómez, J. C.; Stephenson, C. R. J. Visible-light photoredox catalysis: aza-Henry reactions via C−H functionalization. *J. Am. Chem. Soc.* **2010**, *132*, 1464–1465.

(36) Yasu, Y.; Koike, T.; Akita, M. Three-component oxytrifluoromethylation of alkenes: highly efficient and regioselective difunctionalization of C–C bonds mediated by photoredox catalysts. *Angew. Chem. Int. Ed.* **2012**, *51*, 9567–9571.

(37) Ventre, S.; Petronijevic, F. R.; MacMillan, D. W. C. Decarboxylative fluorination of aliphatic carboxylic acids via photoredox catalysis. *J. Am. Chem. Soc.* **2015**, *137*, 5654–5657.

(38) Liu, Y.; Persson, P.; Sundström, V.; Wärnmark, K. (2016). Fe N-heterocyclic carbene complexes as promising photosensitizers. *Acc. Chem. Res.* **2016**, *49*, 1477–1485.

(39) Kjær, K. S.; Kaul, N.; Prakash, O.; Chábera, P.; Rosemann, N. W.; Honarfar, A.; Gordivska, O. Fredin, L. A.; Bergquist, K.-E.; Häggström, L.; Ericsson, T.; Lindh, L.; Yartsev, A.; Styring, S.; Huang, P.; Uhlig, J.; Bendix, J.; Strand, D.; Sundström, V.; Persson, P.; Lomoth, R.; Wärnmark, K. Luminescence and reactivity of a charge-transfer excited iron complex with nanosecond lifetime. *Science* **2019**, *363*, 249–253.

(40) Pirtsch, M.; Paria, S.; Matsuno, T.; Isobe, H.; Reiser, O. [Cu(dap)$_2$Cl] as an efficient visible-light-driven photoredox catalyst in carbon-carbon bond-forming reactions. *Chem. - Eur. J.* **2012**, *18*, 7336–7340.

(41) Pan, Y.; Kee, C. W.; Chen, L.; Tan, C.-H. Dehydrogenative coupling reactions catalysed by Rose Bengal using visible light irradiation. *Green Chem.* **2011**, *13*, 2682.

(42) Wang, Y.; Haze, O.; Dinnocenzo, J. P.; Farid, S.; Farid, R. S.; Gould, I. R. Bonded exciplexes. A new concept in photochemical reactions. *J. Org. Chem.* **2007**, *72*, 6970–6981.

(43) Yamago, S.; Miyazoe, H.; Iida, K.; Yoshida, J. Highly efficient and chemoselective reductive bis-silylation of quinones by silyltellurides. *Org. Lett.* **2000**, *2*, 3671–3673.

(44) Ohkubo, K.; Fujimoto, A.; Fukuzumi, S. Visible-light-induced oxygenation of benzene by the triplet excited state of 2,3-dichloro-5,6-dicyano-p-benzoquinone. *J. Am. Chem. Soc.* **2013**, *135*, 5368–5371.

(45) Fukuzumi, S.; Kitano, T. Mechanisms of reductive methylation of NAD + analogues by a trans-dimethylcobalt(III) complex. *J. Chem. Soc. Perkin Trans. 2* **1991**, 41.

(46) Searle, R.; Williams, J. L. R.; DeMeyer, D. E.; Doty, J. C. The sensitization of stilbene isomerization. *Chem. Commun. Lond.* **1967**, 1165.

(47) Kitaguchi, H.; Ohkubo, K.; Ogo, S.; Fukuzumi, S. Electron-transfer oxidation properties of unsaturated fatty acids and mechanistic insight into lipoxygenases. *J. Phys. Chem. A* **2006**, *110*, 1718–1725.

(48) Benniston, A. C.; Harriman, A.; Li, P.; Rostron, J. P.; Verhoeven, J. W. Illumination of the 9-mesityl-10-methylacridinium ion does not give a long-lived photoredox state. *Chem. Commun.* **2005**, 2701.

(49) Benniston, A. C.; Harriman, A.; Li, P.; Rostron, J. P.; van Ramesdonk, H. J.; Groeneveld, M. M.; Zhang, H.; Verhoeven, J. W. Charge shift and triplet state formation in the 9-mesityl-10-methylacridinium cation. *J. Am. Chem. Soc.* **2005**, *127*, 16054–16064.

(50) Shen, T.; Zhao, Z.-G.; Yu, Q.; Xu, H.-J. Photosensitized reduction of benzil by heteroatom-containing anthracene dyes. *J. Photochem. Photobiol. Chem.* **1989**, *47*, 203–212.

(51) Fukuzumi, S.; Kotani, H.; Ohkubo, K.; Ogo, S.; Tkachenko, N. V.; Lemmetyinen, H. Electron-transfer state of 9-mesityl-10-methylacridinium ion with a much longer lifetime and higher energy than that of the natural photosynthetic reaction center. *J. Am. Chem. Soc.* **2004**, *126*, 1600–1601.

(52) Romero, N. A.; Nicewicz, D. A. Mechanistic insight into the photoredox catalysis of anti-Markovnikov alkene hydrofunctionalization reactions. *J. Am. Chem. Soc.* **2004**, *136*, 17024–17035.

(53) Nguyen, T. M.; Manohar, N. Nicewicz, D. A. Anti-Markovnikov hydroamination of alkenes catalyzed by a two-component organic photoredox system: direct access to phenethylamine derivatives. *Angew. Chem. Int. Ed.* **2014**, *53*, 6198–6201.

(54) Romero, N. A.; Margrey, K. A.; Tay, N. E.; Nicewicz, D. A. Site-selective arene C–H amination via photoredox catalysis. *Science* **2015**, *349*, 1326–1330.

(55) Ohkubo, K.; Kobayashi, T.; Fukuzumi, S. Direct oxygenation of benzene to phenol using quinolinium ions as homogeneous photocatalysts. *Angew. Chem. Int. Ed.* **2011**, *50*, 8652–8655.

(56) Alfonzo, E.; Alfonso, F. S.; Beeler, A. B. Redesign of a pyrylium photoredox catalyst and its application to the generation of carbonyl ylides. *Org. Lett.* **2017**, *19*, 2989–2992.

(57) Lin, Y.-C.; Chen, C.-T. Acridinium salt-based fluoride and acetate chromofluorescent probes: molecular insights into anion selectivity switching. *Org. Lett.* **2009**, *11*, 4858–4861.

(58) McTiernan, C. D.; Pitre, S. P.; Scaiano, J. C. Photocatalytic dehalogenation of vicinal dibromo compounds utilizing sexithiophene and visible-light irradiation. *ACS Catal.* **2014**, *4*, 4034–4039.

(59) Pitre, S. P.; McTiernan, C. D.; Scaiano, J. C. Understanding the kinetics and spectroscopy of photoredox catalysis and transition-metal-free alternatives. *Acc. Chem. Res.* **2016**, *49*, 1320–1330.

(60) Suppan, P. Photoreactivity of Michler's ketone in solution. *J. Chem. Soc. Faraday Trans. 1 Phys. Chem. Condens. Phases,* **1975**, *71*, 539–547.

(61) Timpe, H.-J.; Kronfeld, K.-P.; Lammel, U.; Fouassier, J.-P.; Lougnot, D.-J. Excited states of ketones as electron donors-ketone-iodonium salt systems as photoinitiators for radical polymerization. *J. Photochem. Photobiol. Chem.* **1990**, *52*, 111–122.

(62) Schweitzer, C.; Mehrdad, Z.; Noll, A.; Grabner, E.-W.; Schmidt, R. Oxygen Quenching of nπ* Triplet Phenyl Ketones: Local Excitation and Local Deactivation. *Helv. Chim. Acta* **2001**, 15.

(63) Bachman, J. C.; Kavian, R.; Graham, D. J.; Kim, D. Y.; Noda, S.; Nocera, D. G.; Shao-Horn, Y.; Lee, S. W. Electrochemical polymerization of pyrene derivatives on functionalized carbon nanotubes for pseudocapacitive electrodes. *Nat. Commun.* **2015**, *6*, 7040.

(64) Singh-Rachford, T. N.; Castellano, F. N. Triplet sensitized red-to-blue photon upconversion. *J. Phys. Chem. Lett.* **2010**, *1*, 195–200.

(65) Parac, M.; Grimme, S. A TDDFT study of the lowest excitation energies of polycyclic aromatic hydrocarbons. *Chem. Phys.* **2003**, *292*, 11–21.

(66) Kikuchi, K.; Niwa, T.; Takahashi, Y.; Ikeda, H.; Miyashi, T. Quenching mechanism in a highly exothermic region of the Rehm-Weller relationship for electron-transfer fluorescence quenching. *J. Phys. Chem.* **1993**, *97*, 5070–5073.

(67) Luo, J.; Zhang, J. Donor–acceptor fluorophores for visible-light-promoted organic synthesis: photoredox/Ni dual catalytic $C(sp^3)$–$C(sp^2)$ cross-coupling. *ACS Catal.* **2016**, *6*, 873–877.

(68) Treat, N. J.; Sprafke, H.; Kramer, J. W.; Clark, P. G.; Barton, B. E.; Read de Alaniz, J.; Fors, B. P.; Hawker, C. J. Metal-free atom transfer radical polymerization. *J. Am. Chem. Soc.* **2014**, *136*, 16096–16101.

(69) Korobov, V. E.; Shubin, V. V.; Chibisov, A.-K. Triplet state of rhodamine dyes and its role in production of intermediates. *Chem. Phys. Lett.* **1977**, *45*, 4.

(70) Yasui, S.; Tsujimoto, M.; Itoh, K.; Ohno, A. Quenching of a photosensitized dye through single-electron transfer from trivalent phosphorus compounds. *J. Org. Chem.* **2000**, *65*, 4715–4720.

(71) Theriot, J. C.; Lim, C.-H.; Yang, H.; Ryan, M. D.; Musgrave, C. B.; Miyake, G. M. Organocatalyzed atom transfer radical polymerization driven by visible light. *Science* **2016**, *352*, 1082–1086.

(72) Pearson, R. M.; Lim, C.-H.; McCarthy, B. G.; Musgrave, C. B.; Miyake, G. M. Organocatalyzed atom transfer radical polymerization using N-aryl phenoxazines as photoredox catalysts. *J. Am. Chem. Soc.* **2016**, *138*, 11399–11407.

(73) McCarthy, B. G.; Pearson, R. M.; Lim, C.-H.; Sartor, S. M.; Damrauer, N. H.; Miyake, G. M. Structure–property relationships for tailoring phenoxazines as reducing photoredox catalysts. *J. Am. Chem. Soc.* **2018**, *140*, 5088–5101.

(74) Cole, J. P.; Federico, C. R.; Lim, C.-H.; Miyake, G. M. Photoinduced organocatalyzed atom transfer radical polymerization using low ppm catalyst loading. *Macromolecules* **2019**, *52*, 747–754.

(75) Buss, B. L.; Lim, C.-H.; Miyake, G. M. Dimethyl dihydroacridines as photocatalysts in organocatalyzed atom transfer radical polymerization of acrylate monomers. *Angew. Chem. Int. Ed.* **2020**, *59*, 3209–3217.

(76) Miyake, G. M.; Theriot, J. C. Perylene as an organic photocatalyst for the radical polymerization of functionalized vinyl monomers through oxidative quenching with alkyl bromides and visible light. *Macromolecules* **2014**, *47*, 8255–8261.

(77) Sartor, S. M.; McCarthy, B. G.; Pearson, R. M.; Miyake, G. M.; Damrauer, N. H. Exploiting charge-transfer states for maximizing intersystem crossing yields in organic photoredox catalysts. *J. Am. Chem. Soc.* **2018**, *140*, 4778–4781.

(78) Park, G. S.; Back, J.; Choi, E. M.; Lee, E.; Son, K. (2019). Visible light-mediated metal-free atom transfer radical polymerization with N-trifluoromethylphenyl phenoxazines. *Eur. Polym. J.* **2019**, *117*, 347–352.

(79) Poelma, S. O.; Burnett, G. L.; Discekici, E. H.; Mattson, K. M.; Treat, N. J.; Luo, Y.; Hudson, Z. M.; Shankel, S. L.; Clark, P. G.; Kramer, J. W.; Hawker, C. J.; Read de Alaniz, J. Chemoselective radical dehalogenation and C–C bond formation on aryl halide substrates using organic photoredox catalysts. *J. Org. Chem.* **2016**, *81*, 7155–7160.

(80) Dadashi-Silab, S.; Pan, X.; Matyjaszewski, K. Phenyl benzo[b]phenothiazine as a visible light photoredox catalyst for metal-free atom transfer radical polymerization. *Chem. - Eur. J.* **2017**, *23*, 5972–5977.

(81) Gong, H.; Zhao, Y.; Shen, X.; Lin, J.; Chen, M. Organocatalyzed photocontrolled radical polymerization of semifluorinated (meth)acrylates driven by visible light. *Angew. Chem. Int. Ed.* **2018**, *57*, 333–337.

(82) Zhao, Y.; Gong, H.; Jiang, K.; Yan, S.; Lin, J.; Chen, M. Organocatalyzed photoredox polymerization from aromatic sulfonyl halides: facilitating graft from aromatic C–H bonds. *Macromolecules* **2018**, *51*, 938–946.

(83) Sartor, S. M.; Chrisman, C. H.; Pearson, R. M.; Miyake, G. M.; Damrauer, N. H. Designing high-triplet-yield phenothiazine donor–acceptor complexes for photoredox catalysis. *J. Phys. Chem. A* **2020**, *124*, 817–823.

(84) Ryan, M. D.; Theriot, J. C.; Lim, C.-H.; Yang, H.; G. Lockwood, A.; Garrison, N. G.; Lincoln, S. R.; Musgrave, C. B.; Miyake, G. M. Solvent effects on the intramolecular charge transfer character of N,N-diaryl dihydrophenazine catalysts for organocatalyzed atom transfer radical polymerization. *J. Polym. Sci. Part A: Polym. Chem.* **2017**, *55*, 3017–3027.

(85) Singh, V. K.; Yu, C.; Badgujar, S.; Kim, Y.; Kwon, Y.; Kim, D.; Lee, J.; Akhter, T.; Thangavel, G.; Park, L. S.; Lee, J.; Nandajan, P. C.; Wannemacher, R.; Milián-Medina, B.; Lüer, L.; Kim, K. S.; Gierschner, J.; Kwon, M.S. Highly efficient organic photocatalysts discovered via a computer-aided-design strategy for visible-light-driven atom transfer radical polymerization. *Nat. Catal.* **2018**, *1*, 794–804.

(86) Corbin, D. A.; Lim, C.-H.; Miyake, G. M. Phenothiazines, dihydrophenazines, and phenoxazines: sustainable alternatives to precious-metal-based photoredox catalysts. *Aldrichimica Acta* **2019**, *52*, 15.

(87) Discekici, E. H.; Treat, N. J.; Poelma, S. O.; Mattson, K. M.; Hudson, Z. M.; Luo, Y.; Hawker, C. J.; de Alaniz, J. R. A highly reducing metal-free photoredox catalyst: design and application in radical dehalogenations. *Chem. Commun.* **2015**, *51*, 11705–11708.

(88) Wang, H.; Jui, N. T. Catalytic defluoroalkylation of trifluoromethylaromatics with unactivated alkenes. *J. Am. Chem. Soc.* **2018**, *140*, 163–166.

(89) Uoyama, H.; Goushi, K.; Shizu, K.; Nomura, H.; Adachi, C. Highly efficient organic light-emitting diodes from delayed fluorescence. *Nature* **2012**, *492*, 234–238.

(90) Ishimatsu, R.; Matsunami, S.; Kasahara, T.; Mizuno, J.; Edura, T.; Adachi, C.; Nakano, K.; Imato, T. Electrogenerated chemiluminescence of donor-acceptor molecules with thermally activated delayed fluorescence. *Angew. Chem. Int. Ed.* **2014**, *53*, 6993–6996.

(91) Mateos, J.; Rigodanza, F.; Vega-Peñaloza, A.; Sartorel, A.; Natali, M.; Bortolato, T.; Pelosi, G.; Companyó, X.; Bonchio, M.; Dell'Amico, L. Naphthochromenones: organic bimodal photocatalysts engaging in both oxidative and reductive quenching processes. *Angew. Chem. Int. Ed.* **2020**, *59*, 1302–1312.

(92) Gualandi, A.; Rodeghiero, G.; Della Rocca, E.; Bertoni, F.; Marchini, M.; Perciaccante, R.; Jansen, T.P.; Ceroni, P.; Cozzi, P. G. Application of coumarin dyes for organic photoredox catalysis. *Chem. Commun.* **2018**, *54*, 10044–10047.

(93) Jia, T.; Huang, S.; Bohra, H.; Wang, M. Examining derivatives of quinacridone, diketopyrrolopyrrole and indigo as the visible-light organic photocatalysts for metal-free atom transfer radical polymerization. *Dyes Pigments,* **2019**, *165*, 223–230.

(94) Yang, L.; Huang, Y.; Peng, Y.; Liu, F.; Zhang, Q.; He, H.; Wang, J.; Jiang, L.; Zhou, Y. Pyridine-diketopyrrolopyrrole-based novel metal-free visible-light organophotoredox catalyst for atom-transfer radical polymerization. *J. Phys. Chem. A* **2020**, *124*, 1068–1075.

(95) Buzzetti, L.; Prieto, A.; Roy, S. R.; Melchiorre, P. Radical-based C−C bond-forming processes enabled by the photoexcitation of 4-alkyl-1,4-dihydropyridines. *Angew. Chem. Int. Ed.* **2017**, *56*, 15039–15043.

(96) Noto, N.; Tanaka, Y.; Koike, T.; Akita, M. Strongly reducing (diarylamino)anthracene catalyst for metal-free visible-light photocatalytic fluoroalkylation. *ACS Catal.* **2018**, *8*, 9408–9419.

(97) Noto, N.; Koike, T.; Akita, M. Visible-light-triggered monofluoromethylation of alkenes by strongly reducing 1,4-bis(diphenylamino)naphthalene photoredox catalysis. *ACS Catal.* **2019**, *9*, 4382–4387.

(98) Matsubara, R.; Shimada, T.; Kobori, Y.; Yabuta, T.; Osakai, T.; Hayashi, M. Photoinduced charge-transfer state of 4-carbazolyl-3-(trifluoromethyl)benzoic acid: photophysical property and application to reduction of carbon−halogen bonds as a sensitizer. *Chem. – Asian J.* **2016**, *11*, 2006–2010.

(99) Matsubara, R.; Yabuta, T.; Md Idros, U.; Hayashi, M.; Ema, F.; Kobori, Y.; Sakata, K. UVA- and visible-light-mediated generation of carbon radicals from organochlorides using nonmetal photocatalyst. *J. Org. Chem.* **2018**, *83*, 9381–9390.

(100) Gosztola, D.; Niemczyk, M. P.; Svec, W.; Lukas, A. S.; Wasielewski, M. R. Excited doublet states of electrochemically generated aromatic imide and diimide radical anions. *J. Phys. Chem. A* **2000**, *104*, 6545–6551.

(101) Ghosh, I.; Ghosh, T.; Bardagi, J. I.; Konig, B. Reduction of aryl halides by consecutive visible light-induced electron transfer processes. *Science* **2014**, *346*, 725–728.

(102) Zeman, C. J.; Kim, S.; Zhang, F.; Schanze, K. S. Direct Observation of the Reduction of Aryl Halides by a Photoexcited Perylene Diimide Radical Anion. *J. Am. Chem. Soc.* **2020**, *142*, 2204–2207.

(103) Cowper, N. G. W.; Chernowsky, C. P.; Williams, O. P.; Wickens, Z. K. Potent reductants via electron-primed photoredox catalysis: unlocking aryl chlorides for radical coupling. *J. Am. Chem. Soc.* **2020**, *142*, 2093–2099.

(104) Kim, H.; Kim, H.; Lambert, T. H.; Lin, S. Reductive electrophotocatalysis: merging electricity and light to achieve extreme reduction potentials. *J. Am. Chem. Soc.* **2020**, *142*, 2087–2092.

(105) Cole, J. P.; Chen, D.-F.; Kudisch, M.; Pearson, R. M.; Lim, C.-H.; Miyake, G. M. Organocatalyzed birch reduction driven by visible light. *J. Am. Chem. Soc.* ***2020****, 142*, 13573–13581.

(106) Christensen, J. A.; Phelan, B. T.; Chaudhuri, S.; Acharya, A.; Batista, V. S.; Wasielewski, M. R. Phenothiazine radical cation excited states as super-oxidants for energy-demanding reactions. *J. Am. Chem. Soc.* **2018**, *140*, 5290–5299.

(107) Huang, H.; Strater, Z. M.; Rauch, M.; Shee, J.; Sisto, T. J.; Nuckolls, C.; Lambert, T. H. Electrophotocatalysis with a trisaminocyclopropenium radical dication. *Angew. Chem. Int. Ed.* **2019**, *58*, 13318–13322.

(108) Kerzig, C.; Guo, X.; Wenger, O. S. Unexpected hydrated electron source for preparative visible-light driven photoredox catalysis. *J. Am. Chem. Soc.* **2019**, *141*, 2122–2127.

(109) Kerzig, C.; Wenger, O. S. Reactivity control of a photocatalytic system by changing the light intensity. *Chem. Sci.* **2019**, *10*, 11023–11029.

(110) Hildebrand, J. H.; Glascock, B. L. The color of iodine solutions. *J. Am. Chem. Soc.* **1909**, *31*, 26–31.

(111) Mulliken, R. S. Structures of complexes formed by halogen molecules with aromatic and with oxygenated solvents. *J. Am. Chem. Soc.* **1950**, *72*, 600–608.

(112) Mulliken, R. S. Molecular compounds and their spectra. II. *J. Am. Chem. Soc.* **1952**, *74*, 811–824.

(113) Mulliken, R. S. Molecular compounds and their spectra. III. The interaction of electron donors and acceptors. *J. Phys. Chem.* **1952**, *56*, 801–822.

(114) Rosokha, S. V.; Kochi, J. K. Fresh look at electron-transfer mechanisms via the donor/acceptor bindings in the critical encounter complex. *Acc. Chem. Res.* **2008**, *41*, 641–653.

(115) Lima, C. G. S.; de M. Lima, T.; Duarte, M.; Jurberg, I. D.; Paixão, M. W. Organic synthesis enabled by light-irradiation of EDA complexes: theoretical background and synthetic applications. *ACS Catal.* **2016**, *6*, 1389–1407.

(116) Roth, H.; Romero, N.; Nicewicz, D. Experimental and calculated electrochemical potentials of common organic molecules for applications to single-electron redox chemistry. *Synlett* **2015**, *27*, 714–723.

(117) Crisenza, G. E. M.; Mazzarella, D.; Melchiorre, P. Synthetic methods driven by the photoactivity of electron donor–acceptor complexes. *J. Am. Chem. Soc.* **2020**, *142*, 5461–5476.

(118) Cantacuzène, D.; Wakselman, C.; Dorme, R. Condensation of perfluoroalkyl iodides with unsaturated nitrogen compounds. *J Chem Soc Perkin Trans 1* **1977**, 1365–1371.

(119) Hoz, S.; Bunnett, J. F. A quantitative study of the photostimulated reaction of iodobenzene with diethyl phosphite ion. *J. Am. Chem. Soc.* **1977**, *99*, 4690–4699.

(120) Fox, M. A.; Younathan, J.; Fryxell, G. E. Photoinitiation of the $S_{RN}1$ reaction by excitation of charge-transfer complexes. *J. Org. Chem.* **1983**, *48*, 3109–3112.

(121) Fukuzumi, S.; Mochida, K.; Kochi, J. K. A unified mechanism for thermal and photochemical activation of charge-transfer processes with organometals. Steric effects in the insertion of tetracyanoethylene. *J. Am. Chem. Soc.* **1979**, *101*, 5961–5972.

(122) Sankararaman, S.; Haney, W. A.; Kochi, J. K. Annihilation of aromatic cation radicals by ion-pair and radical pair collapse. Unusual solvent and salt effects in the competition for aromatic substitution. *J. Am. Chem. Soc.* **1987**, *109*, 7824–7838.

(123) Wade, P. A.; Morrison, H. A.; Kornblum, N. The effect of light on electron transfer substitution at a saturated carbon atom. *J. Org. Chem.* **1987**, *52*, 3102–3107.

(124) Russell, G. A.; Wang, K. Homolytic alkylation of enamines by electrophilic radicals. *J. Org. Chem.* **1991**, *56*, 3475–3479.

(125) Gotoh, T.; Padias, A. B.; Hall, H. K. An electron donor-acceptor complex and thermal triplex as intermediates in the cycloaddition reaction of N-vinylcarbazole with dimethyl 2,2-dicyanoethylene-1,1-dicarboxylate. *J. Am. Chem. Soc.* **1991**, *113*, 1308–1312.

(126) Kandukuri, S. R.; Bahamonde, A.; Chatterjee, I.; Jurberg, I. D.; Escudero-Adán, E. C.; Melchiorre, P. X-Ray characterization of an electron donor-acceptor complex that drives the photochemical alkylation of indoles. *Angew. Chem. Int. Ed.* **2015**, *54*, 1485–1489.

(127) Yang, Q.-Q.; Liu, N.; Yan, J.-Y.; Ren, Z.-L.; Wang, L. Visible light- and heat-promoted C-O coupling reaction of phenols and aryl halides. *Asian J. Org. Chem.* **2020**, *9*, 116–120.

(128) da Silva, G. P.; Ali, A.; da Silva, R. C.; Jiang, H.; Paixão, M. W. Tris(trimethylsilyl)silane and visible-light irradiation: a new metal- and additive-free photochemical process for the synthesis of indoles and oxindoles. *Chem. Commun.* **2015**, *51*, 15110–15113.

(129) Zhang, J.; Li, Y.; Xu, R.; Chen, Y. Donor-acceptor complex enables alkoxyl radical generation for metal-free $C(sp^3)$-$C(sp^3)$ cleavage and allylation/alkenylation. *Angew. Chem. Int. Ed.* **2017**, *56*, 12619–12623.

(130) Davies, J.; Booth, S. G.; Essafi, S.; Dryfe, R. A. W.; Leonori, D. Visible-light-mediated generation of nitrogen-centered radicals: metal-free hydroimination and iminohydroxylation cyclization reactions. *Angew. Chem. Int. Ed.* **2015**, *54*, 14017–14021.

(131) Fawcett, A.; Pradeilles, J.; Wang, Y.; Mutsuga, T.; Myers, E. L.; Aggarwal, V. K. Photoinduced decarboxylative borylation of carboxylic acids. *Science* **2017**, *357*, 283–286.

(132) Wu, J.; He, L.; Noble, A.; Aggarwal, V. K. Photoinduced deaminative borylation of alkylamines. *J. Am. Chem. Soc.* **2018**, *140*, 10700–10704.

(133) Wu, J.; Bär, R. M.; Guo, L.; Noble, A.; Aggarwal, V. K. Photoinduced deoxygenative borylations of aliphatic alcohols. *Angew. Chem. Int. Ed.* **2019**, *58*, 18830–18834.

(134) Bosque, I.; Bach, T. 3-Acetoxyquinuclidine as catalyst in electron donor–acceptor complex-mediated reactions triggered by visible light. *ACS Catal.* **2019**, *9*, 9103–9109.

(135) Emmanuel, M. A.; Greenberg, N. R.; Oblinsky, D. G.; Hyster, T. K. Accessing non-natural reactivity by irradiating nicotinamide-dependent enzymes with light. *Nature* **2016**, *540*, 414–417.

CHAPTER 4.

IMPACTS OF PERFORMING ELECTROLYSIS DURING ORGANOCATALYZED ATOM TRANSFER RADICAL POLYMERIZATION

Overview

An electrochemical variant of organocatalyzed atom transfer radical polymerization (O-ATRP) is developed and investigated. Inspired by electrochemically mediated atom transfer radical polymerization (eATRP), potentiostatic electrolysis is used to manipulate the catalyst's redox states in O-ATRP to understand whether deactivation in O-ATRP can be enhanced to improve polymerization control. During the course of this work, several possible side reactions are investigated, and the electrochemical apparatus is optimized to reduce side reactions at the counter electrode. This electrochemically modified O-ATRP method (eO-ATRP) is then studied at different applied potentials, under different irradiation conditions, and with two photoredox catalysts to understand the impact of electrolysis on polymerization control. Ultimately, although electrolysis was successfully used to improve polymerization control in O-ATRP, some additional challenges have been identified. Several key questions are postulated to guide future work in this area.

Introduction

First reported in 2014, organocatalyzed atom transfer radical polymerization (O-ATRP) is a controlled radical polymerization method employing organic photoredox catalysts (PCs) for the production of polymers with targeted molecular weights and architectures.[1,2] The proposed mechanism of O-ATRP proceeds through absorption of light by a PC to access an excited state

(PC*). This excited state then reduces the alkyl-halide bond of an initiator or polymer chain-end to generate the PC radical cation ($PC^{\bullet+}$), Br^-, and 'active' radicals capable of polymerization propagation with vinyl monomers (Figure 4.1). Importantly, the $PC^{\bullet+}$ that forms mediates deactivation in O-ATRP, during which bromine is reinstalled on the chain-end of a polymer to generate a 'dormant' species and the ground state PC.[1-4] It has been proposed that deactivation in O-ATRP could proceed through a termolecular reaction, in which $PC^{\bullet+}$, Br^-, and the radical chain-end react simultaneously to form the dormant polymer and ground state PC.[5] While computational results support that this termolecular reaction is thermodynamically feasible, our working hypothesis is that deactivation proceeds through a bimolecular reaction, in which $PC^{\bullet+}$ and Br^- preassociate to form the $PC^{\bullet+}Br^-$ ion pair that then reacts with the propagating radical. Regardless of the exact mechanism of this process, the effect is the same: deactivation reduces the concentration of radicals in solution and thereby suppresses radical-based termination reactions, which would otherwise hinder control over polymer structure.[6-10]

Since the inception of this method, much work has focused on expanding the utility of O-ATRP through various approaches. Some strategies have focused on the development of new photoredox catalysts[3,4,11-17] as a means to access the polymerization of new monomers, such as acrylonitrile[11] and acrylates[17]. Alternatively, other advancements have come through the application of O-ATRP for the synthesis of materials with advanced architectures[18,19] and applications[20,21], while some investigations have focused on understanding the mechanism of O-ATRP[5,22] and the structure-property relationships of the PCs[3,4,15,23-25] employed therein. Despite these advancements, the monomer scope of O-ATRP and its ability to produce polymers of high molecular weight[26-31] remains limited, especially in comparison to metal catalyzed ATRP.[32]

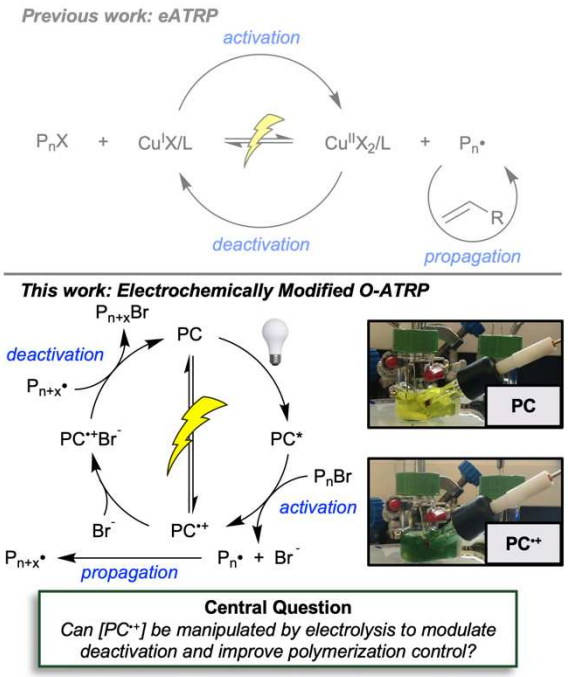

Figure 4.1. *Previous work demonstrated the ability to mediate ATRP using electrochemistry (top). In this work (bottom), we ask whether this principle can be applied to O-ATRP to control the concentration of $PC^{\bullet+}$ and thereby control deactivation in this polymerization method. Figure inset (bottom right) demonstrates the conversion of PC to $PC^{\bullet+}$ using potentiostatic bulk electrolysis.*

To overcome these limitations and further advance the O-ATRP method, more detailed investigation of the deactivation mechanism and methods to control this process are desirable. In some sense, modulation of deactivation has been attempted through the development of new PCs with more oxidizing radical cations,[17] which might mediate a faster deactivation process than less oxidizing radical cations. However, we envisioned a more direct approach to study the deactivation process would be to manipulate the concentration of deactivator present rather than the oxidation potential of the species. To achieve this effect, we drew inspiration from electrochemically mediated ATRP (eATRP, Figure 4.1), wherein electrochemistry has been used to control activator and deactivator concentrations in metal catalyzed ATRP and mediate controlled polymerizations under a range of different conditions.[33-37] Analogously, one can envision manipulating the concentration of $PC^{\bullet+}$ in solution by potentiostatic electrolysis of the PC (Figure 4.1, inset)

according to the Nernst equation (Eq. 4.1). By performing this process to generate a higher [$PC^{\bullet+}$] *in-situ*, it might be possible to increase the rate of deactivation to afford enhanced polymerization control in challenging systems. As such, this work probes whether electrolysis of the PC can be used during O-ATRP to increase the [$PC^{\bullet+}$] to improve deactivation, as well as the impact of performing electrolysis on the polymerization solution.

$$\frac{[PC^{\cdot+}]}{[PC]} = e^{\frac{F(E_{app}-E_{1/2})}{RT}} \quad \text{(Eq. 4.1)}$$

The Nernst equation relates the applied electrochemical potential (E_{app}) to the ratio of PC to $PC^{\bullet+}$ at the electrode surface where F is Faraday's constant [C mol^{-1}], E_{app} is the applied electrochemical potential [V], $E_{1/2} \sim E^o(PC^{\bullet+}/PC)$ determined by cyclic voltammetry [V], R is the ideal gas constant [J mol^{-1} K^{-1}], and T is the absolute temperature [K]. Using rapid stirring, this ratio can be manipulated in the bulk solution.

Results and Discussion

Initial Conditions and Polymerization Results

The central hypothesis of this work is that by applying an appropriate electrochemical potential (E_{app}), the concentration of $PC^{\bullet+}$ (the deactivator) in O-ATRP can be manipulated to improve polymerization control. Polymerization control in this work was determined by four criteria: (1) linear first-order kinetics of monomer conversion, (1) linear and increasing molecular weight (M_n) as a function of monomer conversion, (3) decreasing and low dispersity ($Đ < 1.5$) during the course of polymerization, and (4) achieving initiator efficiency near 100% ($I^* = M_{n,\,theo} / M_{n,\,exp}$).

To investigate the effects of increasing the concentration of $PC^{\bullet+}$ in O-ATRP using electrolysis, a degree of polymerization (DP) of 200 was targeted since previous reports at this DP

exhibited only moderate control relative to lower targeted DPs.[3,4,16] Moreover, to minimize the possibility for introducing redox side reactions, dihydrophenazine PCs were employed, since this family of PCs would require application of the least oxidizing potential to achieve a higher concentration of $PC^{\bullet+}$ relative to other PC families. However, within the dihydrophenazine family, radical addition to the phenazine core has been proposed as a possible side reaction leading to poor initiator efficiency in O-ATRP. As such, PC **1** was chosen because the core-positions of this PC are blocked by naphthyl substituents (Figure 4.2), reducing the risk of this PC reacting undesirably with radicals in solution.[16] With this PC chosen, all other polymerization conditions (Figure 4.2) were selected based on published conditions for O-ATRP using PC **1**.[16]

For the supporting electrolyte (SE), a 0.1 M mixture of tetra-*n*-butylammonium hexafluorophosphate (Bu_4NPF_6, 94%) and tetra-*n*-butylammonium bromide (Bu_4NBr, 6%) was initially chosen based on conditions reported for eATRP[33] and altered later. A lower E_{app} was used relative to eATRP [$E_{app} = E_{1/2} - 120$ mV vs. $E_{app} \sim E_{1/2}(Cu^{II}/Cu^{I})$]. In eATRP, both the concentrations of Cu^{I} and Cu^{II} can be manipulated by electrolysis, directly impacting both activation and deactivation. However, in O-ATRP activation is mediated by PC* (Figure 4.1), the concentration of which is likely dependent on the intensity of the light source. In fact, based on published data[38] for common PCs in O-ATRP, estimates indicate that only up to about 1% of the PC exists as PC* under steady state conditions (see *Estimation of Excited State PC Concentration* in SI). As such, electrolysis conditions were chosen to produce roughly 1% $PC^{\bullet+}$ based on Equation 1. Finally, to prevent side reactions from occurring at the counter electrode, a U-cell was chosen with a very-fine glass frit separating the counter electrode from the polymerization solution (see *Experimental Equipment* in SI).

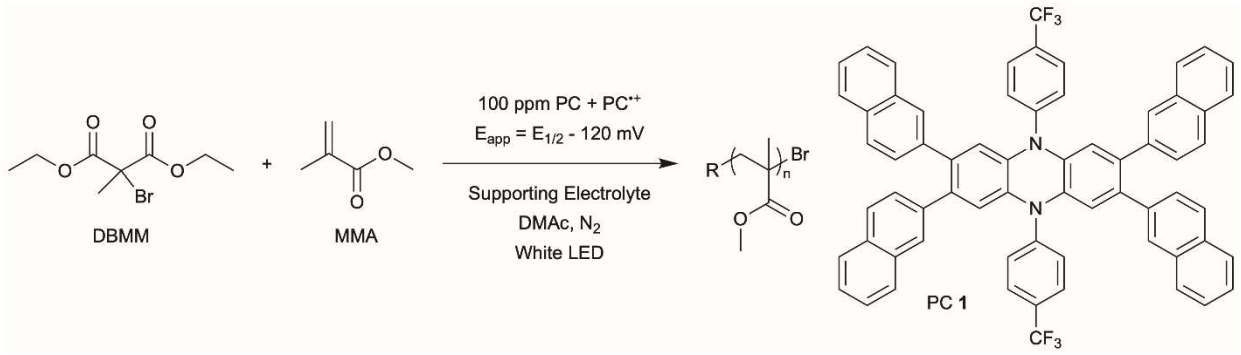

Figure 4.2. *General scheme for the eO-ATRP of MMA using DBMM as the initiator and 100 ppm of PC **1**.*

To evaluate the impact of electrolysis on polymerization control, eO-ATRP was conducted in the presence of an oxidizing applied potential (E_{app} = $E_{1/2}$ – 120 mV) (Figure 4.3). It was hypothesized that these eO-ATRP conditions would lead to a slower overall rate of polymerization and the synthesis of PMMA with lower *Đ,* yet neither effect was observed. The observed rate constants of the polymerizations (O-ATRP = 0.17 h^{-1}, eO-ATRP = 0.14 h^{-1}) and *Đ* of the PMMA synthesized (*Đ* = 1.23 for O-ATRP, *Đ* = 1.19 for eO-ATRP) were similar. Unexpectedly, eO-ATRP exhibited some loss of control, with *I** values deviating significantly from 100%, especially at higher monomer conversions (*I** = 72% at 66% conversion and *I** = 61% at 94% conversion).

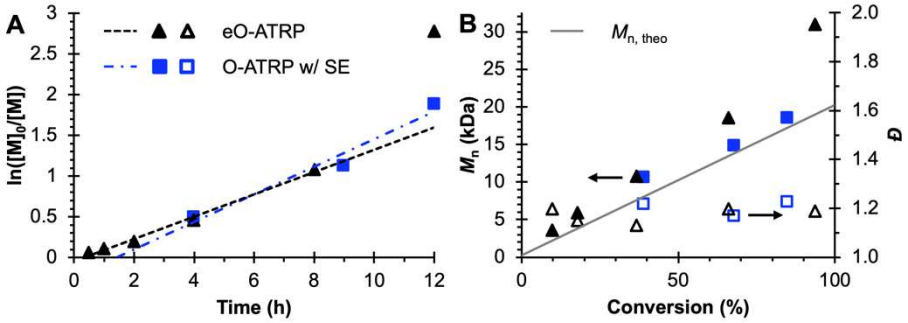

Figure 4.3. *Plot of the natural logarithm of monomer (M) consumption over time (A). Molecular weight (filled markers) and Đ (hollow markers) evolution (B) for eO-ATRP (black triangles) and O-ATRP with supporting electrolyte (blue squares). Conditions: [MMA]:[DBMM]:[**1**] = [1000]:[5]:[0.1], 2 mL MMA, 2 mL DMAc, SE = 0.094 M Bu_4NPF_6 and 0.006 M Bu_4NBr. Reactions performed in a U-cell and irradiated with a high-power white LED (see Experimental Equipment in SI). For eO-ATRP, working electrode = glassy carbon, counter electrode = Pt wire, reference electrode = Ag wire quasi-reference electrode, and E_{app} = $E_{1/2}$ – 120 mV.*

Hypotheses for Poor Control

In total, nine hypotheses to explain the observed data were formulated. While all nine hypotheses are stated below, hypotheses 1 – 8 are also depicted schematically in Table 4.1.

1. Due to the highly reducing nature of PC* [$E^o(\mathbf{1}^{\bullet+}/\mathbf{1}^*) \sim$ -1.8 V vs. SCE],[16] tetra-*n*-butylammonium cation (Bu_4N^+) is reduced to form a reactive species that hinders polymerization control. This process likely occurs through formation of $Bu_4N^{\bullet}$, which rapidly decomposes to tributylamine and butyl radical.[39] The amine may act as an electron donor to quench $PC^{\bullet+}$, leading to poor deactivation. Further, butyl radical formation could lead to unwanted initiation and termination events in the polymerization.
2. MMA is oxidized at the surface of the working electrode to generate a reactive species, which either reacts with the PC or interrupts the polymerization.
3. DBMM is oxidized at the surface of the working electrode to generate a reactive species, which either reacts with the PC or interrupts the polymerization. Consumption of the initiator through this side reaction would also lower I^*.
4. Bromide ion, either from the supporting electrolyte or the activation of an alkyl-bromide bond, is oxidized at the working electrode, generating a bromine radical capable of initiating polymer chains.
5. Photoexcitation of $PC^{\bullet+}$ generates a strongly oxidizing excited-state species, which oxidizes DMAc to generate a reactive radical capable of performing initiation and termination reactions.
6. Photoexcited $PC^{\bullet+}$ oxidizes the radical chain-end of a propagating polymer, generating a reactive carbocation that rapidly and irreversibly terminates under O-ATRP conditions.

7. Photoexcited $PC^{\bullet+}$ oxidizes Br^-, either from the supporting electrolyte or from the activation of an alkyl-bromide bond, generating a bromine radical capable of initiating new polymer chains.
8. Hexafluorophosphate from the supporting electrolyte competitively ion-pairs with $PC^{\bullet+}$ to form $PC^{\bullet+}PF_6^-$, leading to poor polymerization control. If this process occurs to a significant extent, it would limit the formation of $PC^{\bullet+}Br^-$ and thereby reduce the rate of deactivation.
9. Under current conditions, the counter electrode is insufficiently separated from the polymerization. As such, control is lost either as the PC and $PC^{\bullet+}$ diffuse to the counter electrode and undergo degradation, or as reactive species produced at the counter electrode diffuse into the polymerization and cause side reactions.

Table 4.1. *Schematic representations of hypotheses 1 – 8 for the investigation of potential side reactions that can occur during eO-ATRP. See Experimental section for Figures 4.39 – 4.44.*

Hypothesis	Scheme	Key Data
1	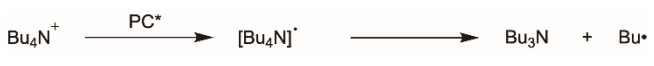	Table 4.2, entry 1 Figure 4.39
2	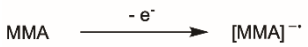	Figure 4.40
3	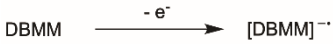	Figure 4.41
4	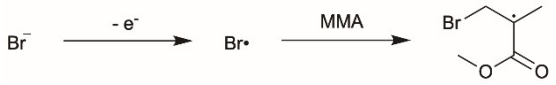	Table 4.2, entry 2 Figure 4.42
5	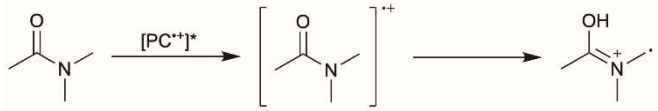	Hypothesis not disproved
6	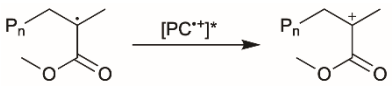	Kinetically unlikely (see text)
7	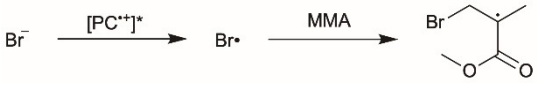	Hypothesis not disproved (see text)

8		Table 4.2, entry 3 Figure 4.44

With these hypotheses in hand, experiments were then devised to test and support or disprove each one. For example, in hypothesis 1, it is proposed that the reduction of Bu_4N^+ (hypothesis 1) could be responsible for side reactivity in eO-ATRP leading to poor control. If this hypothesis is true, changing the supporting electrolyte to $LiPF_6$ (Table 4.2, entry 1; also see SI) should eliminate reduction of the cation and thereby improve the polymerization outcome, as **1*** should not be able to reduce Li^+. Of course, this experiment is based on the assumption that no other significant side reactivity would occur with $LiPF_6$, but this assumption is supported by later experiments with this supporting electrolyte (*vide infra*). However, no improvement in polymerization control was observed in this experiment ($Đ$ = 2.08, I* = 82%), disproving hypothesis 1.

Table 4.2. *Polymerization results related to tests of hypotheses 1, 4, and 8. For full experimental details, please see the Control Experiments section of the Experimental.*

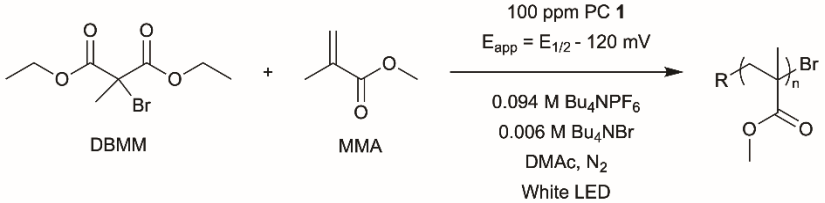

Entry	Deviation from Scheme	Hypothesis Tested	Conv. (%)	$M_{n,\,theo}$ (kDa)	$M_{n,\,GPC}$ (kDa)	$Đ^a$	I* (%)[b]
1	SE = 0.1 M $LiPF_6$	1	77	15.7	19.2	2.08	82
2	no PC or light	4	0	-	-	-	-
3	no electrolysis, SE = 0.1 M $LIPF_6$	8	68	13.8	12.1	1.17	114

[a]*Calculated by* M_w / M_n. [b]*Calculated by* $M_{n,\,theo} / M_{n,\,GPC}$.

To test hypotheses 2 – 4, cyclic voltammetry (CV) was performed to examine the redox behavior of each component of the polymerization solution. Since the CV of **1** in DMAc with 0.1 M Bu_4NPF_6 has previously been reported elsewhere,[16] the redox stability of the solvent and this supporting electrolyte were not examined. To test the redox stability of MMA (hypothesis 2), CV was used to examine a mixture of MMA and DMAc in a ratio corresponding to that used in eO-ATRP (Figure 4.40 of the *Experimental* section). No current response was observed in the relevant potential range (-0.1 – 0.1 V vs $Ag/AgNO_3$), disproving hypothesis 2. Next, DBMM was added to the solution and its redox stability (hypothesis 3) examined by CV, which revealed only a reduction peak around -1.2 V vs. $Ag/AgNO_3$ (Figure 4.41 of the *Experimental* section). Since no response was observed in the range relevant to eO-ATRP, these data disprove hypothesis 3.

A similar experiment was performed to test for Br^- oxidation at the working electrode (hypothesis 4), where CV was used to examine a solution of 0.1 M Bu_4NPF_6 (94%) and Bu_4NBr (6%) in MMA and DMAc. This time, an irreversible oxidation followed by a quasi-reversible redox couple was observed (Figure 4.42 of the *Experimental* section), presumably corresponding to Br^- oxidation to form Br_3^-, followed by oxidation of Br_3^- to form Br_2.[39-43] However, no current response was seen in the appropriate potential range for eO-ATRP, indicating this redox reaction is unlikely to interfere in these polymerizations. Further evidence to disprove this hypothesis was found in a control reaction excluding **1** and light (see *Control Experiments* section in SI). If Br^- oxidation at the working electrode could lead to unwanted polymerization of MMA, it should be observable under these conditions. However, proton NMR analysis of the reaction solution after 24 h of electrolysis showed no polymer formation (Table 4.2, entry 2), disproving hypothesis 4.

Since no evidence could be found for deleterious side reactivity at the working electrode, hypotheses 5 – 7 for possible side reactions involving photoexcited $PC^{\bullet+}$ were considered next.

Each hypothesis is based on the concept that $PC^{\bullet+}$ might be able to access a strongly oxidizing excited state by absorption of visible light. In turn, photoexcitation of this species might lead to the oxidation of DMAc (hypothesis 5), the radical chain-end of a propagating polymer (hypothesis 6), or Br^- (hypothesis 7). Currently, no evidence exists to disprove the oxidation of DMAc by this species (hypothesis 5), so this hypothesis will be revisited later in the text (*vide infra*).

With regard to the oxidation of the chain-end radical (hypotheses 6), the ground state of $PC^{\bullet+}$ is not sufficiently oxidizing to directly cause this side reaction, necessitating photoexcitation to make the oxidation thermodynamically feasible. However, it seems unlikely that this reaction would occur to a significant extent considering that the components of this reaction should both be in low concentrations. Due to deactivation in O-ATRP, the formation of chain-end radicals should be suppressed to prevent radical-coupling reactions. In addition, it seems unlikely that the concentration of photoexcited $PC^{\bullet+}$ would be sufficient to react with this species to a significant degree, since the lifetimes of photoexcited species are generally quite short 10^{-9} – 10^{-6} s) and most of the $PC^{\bullet+}$ should exist in the ground state. Of course, this argument does not necessarily mean that this side reaction does not take place in eO-ATRP. However, based on these kinetics considerations as well as experiments related to hypothesis 9 (*vide infra*), this side reaction does not appear sufficient to explain the current issues observed in eO-ATRP.

With regard to the oxidation of Br^- by photoexcited $PC^{\bullet+}$ (hypothesis 7), while a bimolecular reaction between Br^- and photoexcited $PC^{\bullet+}$ could be considered unlikely based on the same kinetic argument that is presented above (at least in the absence of a bromide-containing supporting electrolyte), it is also possible that $PC^{\bullet+}$ and Br^- could associate prior to photoexcitation. If photoexcitation of the $PC^{\bullet+}Br^-$ ion pair occurred, the oxidation of Br^- would be more feasible given the close proximity of these species, which would reduce the necessity for a long-lived $PC^{\bullet+}$

excited state. Currently, no evidence exists rule out the photoexcitation of $PC^{\bullet+}Br^-$. However, to our knowledge, no evidence for this side reaction in O-ATRP has yet been found, as the prevalence of this reaction would hinder the production of well-defined polymers by O-ATRP. Further, since an improvement in polymerization control was observed in experiments related to hypothesis 9 (*vide infra*), where this side reaction would have still been present, this reaction does not appear to be a significant contributor to poor control in eO-ATRP.

Another possibility that was considered is competitive ion pairing between $PC^{\bullet+}$ and either Br^- or PF_6^- (hypothesis 8). Depending on the relative strengths of ion pairing in $PC^{\bullet+}Br^-$ and $PC^{\bullet+}PF_6^-$, it is possible that the formation of $PC^{\bullet+}PF_6^-$ might prevent the formation of $PC^{\bullet+}Br^-$ and thereby lower the rate of deactivation. To test this hypothesis, O-ATRP was carried out in the presence of 0.1 M $LiPF_6$ (Table 4.2, entry 3; also see Figure 4.44 of the *Experimental* section), yielding PMMA with low $Đ$ ($Đ$ = 1.17) and good molecular weight control (I^* = 114%). While this experiment does not indicate whether competitive ion pairing is present in eO-ATRP, it does suggest this interaction does not limit polymerization control, disproving hypothesis 8.

Therefore, the remaining hypotheses that were considered are the oxidation of DMAc by photoexcited $PC^{\bullet+}$ (hypothesis 5) and insufficient separation of the counter electrode from the reaction solution (hypothesis 9). To test hypothesis 9, a new apparatus (Figure 4.4) was employed featuring a vycor-glass frit (pore size ~ 4 nm[44]) to separate the counter electrode instead of the previously used U-cells with very-fine glass frits (pore size ~ 2 μm[45]). Excitingly, eO-ATRP with 0.1 M $LiPF_6$ as the supporting electrolyte exhibited excellent control (Table 4.3, entry 4: $Đ$ = 1.17, I^* = 110%), with I^* near 100% and $Đ$ below 1.2 for nearly the entire polymerization (Figure 4.5). Further, while this experiment does not directly test hypothesis 5 for DMAc oxidation by photoexcited $PC^{\bullet+}$, it does suggest this side reaction is less significant, as its effects should have

been observable even under these new experimental conditions. Based on this result and complying with Ockham's Razor,[46] hypothesis 9 appears to be the simplest explanation for why eO-ATRP initially showed limited improvement over O-ATRP under similar conditions. As such, all future experiments were performed with this new apparatus using vycor-glass separators for the counter and reference electrodes.

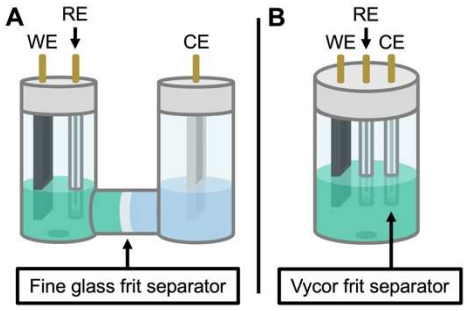

Figure 4.4. *Diagram of the apparatus used in this work. Originally, a modified U-cell was employed to separate the working and counter electrode compartments (A). When this separator was found to be ineffective on the time scale of eO-ATRP, a new apparatus was developed using a 5-neck electrochemical flask (see Experimental Equipment in SI) and vycor frit separators to isolate the counter electrode (B). WE = working electrode, RE = reference electrode, and CE = counter electrode.*

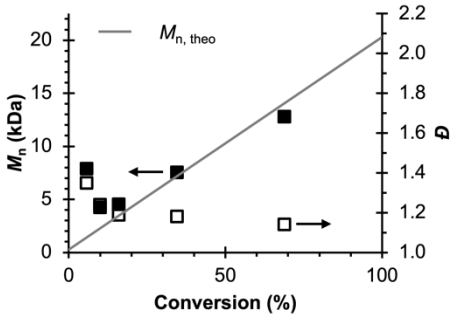

Figure 4.5. *Evolution of molecular weight (filled squares) and Đ (hollow squares) for eO-ATRP using a vycor-glass frit to separate the counter electrode from the polymerization solution. Conditions: [MMA]:[DBMM]:[**1**] = [1000]:[5]:[0.1], 2 mL MMA, 2 mL DMAc, SE = 0.1 M $LiPF_6$. Reaction performed in a 5-neck pear flask and irradiated with an 80 mm x 40 mm white LED well (9 LED segments, see Experimental Equipment in SI). Working electrode = glassy carbon, counter electrode = Pt wire, reference electrode = $Ag/AgNO_3$, and $E_{app} = E_{1/2} - 120$ mV.*

Impact of Reaction Parameters on Control

To evaluate how each reaction component contributes to eO-ATRP, control polymerizations were performed (Table 4.3). In the absence of electrolysis (entry 5) or supporting electrolyte (entry 6), a controlled polymerization was still observed, but $Đ$ and I^* both rose ($Đ$ = 1.33 and 1.27, I^* = 127% and 126%, respectively) relative to eO-ATRP ($Đ$ = 1.17, I^* = 110%). These data demonstrate that improvement in polymerization control can be obtained by the application of an electrochemical potential. Reactions performed in the absence of PC (entry 7) or initiator (entry 8) exhibited characteristics of a free radical polymerization ($Đ$ = 2.23 and 1.94, respectively), whereas reactions in the dark – with or without PC, entries 9 and 10, respectively – showed no conversion by ^{1}H NMR after 24 hours.

Table 4.3. *Results for the eO-ATRP of MMA using the electrochemical cell in Figure 4.4B.*

Entry	Control[a]	Conv. (%)	$M_{n,\,theo}$ (kDa)	$M_{n,\,GPC}$ (kDa)	$Đ$[b]	I^*[c] (%)
4	none	69	14.0	12.8	1.17	110
5	no electrolysis	52	10.7	8.47	1.33	127
6	no SE	68	13.8	11.0	1.27	126
7	no PC	7	1.56	52.7	2.23	3.0
8	no initiator	63	-	239	1.94	-
9	no light	0	-	-	-	-
10	no PC or light	0	-	-	-	-

*[a]General conditions unless otherwise stated: [MMA]:[DBMM]:[**1**] = [1000]:[5]:[0.1], 2 mL MMA, 2 mL DMAc, SE = 0.1 M $LiPF_6$. Reactions performed in a 5-neck pear flask and irradiated with an 80 mm x 40 mm white LED well (9 LED segments, see Experimental Equipment in SI). Where applicable, working electrode = glassy carbon, counter electrode = Pt wire, reference electrode = $Ag/AgNO_3$, and $E_{app} = E_{1/2} – 120$ mV. [b]Calculated by M_w / M_n. [c]Calculated by $M_{n,\,theo} / M_{n,\,GPC}$.*

Further influences on polymerization control were studied by variation of the light source, application of a more oxidizing electrochemical potential, and use of a different PC (see

Supplemental Polymerization Data in SI). Similar to previous O-ATRP systems,[47] it was found that intensity of the light source had a significant impact on polymerization control. Lowering the intensity of the light caused a decrease in polymerization control, as observed by a gradual increase in $Đ$ and deviation of I^* from 100% (Figures 4.48 and 4.49 of the *Experimental* section). Interestingly, while a small increase in light intensity afforded similar control (Figure 4.50 of the *Experimental* section), large increases in light intensity from use of high-power LEDs resulted in a decrease in control (Figures 4.53 and 4.54 of the *Experimental* section). When a more oxidizing electrochemical potential was applied to this system ($E_{app} = E_{1/2} - 60$ mV) to compensate for a possible increase in the rate of activation, further loss of control was observed (Figure 4.55 of the *Experimental* section). While this result is consistent with the possibility of a side reaction stemming from photoexcitation of $PC^{\bullet+}$, further investigation of this possible reactivity is necessary. Finally, eO-ATRP was attempted with 3,7-di(4-biphenyl)-1-naphthyl-10-phenoxazine (**2**) as the PC. However, no improvement in polymerization control was observed, as electrolysis led to a significant increase in $Đ$ and complete loss of molecular weight control (Figures 4.57 and 4.58 of the *Experimental* section).

Conclusion

In summary, through a number of control experiments, we have investigated the impact of performing electrolysis during O-ATRP to manipulate the concentration of deactivator in solution. Using cyclic voltammetry, several background reactions at the working electrode were evaluated and ruled out. The formation of bromine radical at the working electrode to initiate undesired polymerizations was further probed through a control polymerization, although this reaction did not appear operative under the conditions used in this work. Further, the impact of competitive ion

pairing between the PC radical cation and PF_6^- from the supporting electrolyte was studied but found to be insignificant under these conditions. While the possibility of side reactivity originating from photoexcitation of the PC radical cation was also proposed, ultimately it was discovered that optimization of the electrochemical apparatus to prevent side reactions at the counter electrode was most important for establishing a controlled polymerization.

Although some improvement in polymerization control was observed in eO-ATRP relative to O-ATRP, this work has revealed the complexity of performing electrolysis during O-ATRP. Based on these results, several questions arise that are the focus of our ongoing work and that we believe will further improve the results of eO-ATRP. These questions include:

1. What is the effect of the supporting electrolyte on PC redox and photophysical properties?
2. Is the PF_6^- anion truly inert, or does competitive ion-pairing occur to any degree that might impact polymerization control?
3. If competitive ion-pairing occurs, is this effect more prominent for certain PCs or PC families than others?
4. Are there any side reactions through which $PC^{\bullet+}$ is consumed during O-ATRP, such that increasing the concentration of $PC^{\bullet+}$ in eO-ATRP increases the occurrence of these degradation pathways?
5. Is $PC^{\bullet+}Br^-$ truly the deactivator in O-ATRP, or is another species responsible for this process?

Experimental

Materials and Methods

Purchased Chemicals

For the Synthesis of Photocatalysts

Phenazine Reduction. Phenazine and sodium hydrosulfite were purchased from Alfa Aesar. Reagent grade alcohol was purchased from Fisher.

Buchwald Couplings. 4-Bromobenzotrifluoride, bis(dibenzylideneacetone)palladium(0), the 1 M tri-*tert*-butylphosphine solution in toluene, and sodium *tert*-butoxide were purchased from Sigma Aldrich. 1-Bromonaphthalene was purchased from VWR. Toluene was purified using an mBraun MB-SPS-800 solvent purification system and kept under nitrogen atmosphere.

Bromination using Molecular Bromine. Bromine was purchased from Beantown Chemical, while benzene was purchased from Sigma Aldrich. Copper wire was purchased from Fisher.

Bromination using *N*-bromosuccinimide. *N*-Bromosuccinimide was purchased from VWR. Unstabilized tetrahydrofuran (THF) was purchased from Millipore Sigma.

Suzuki Coupling. Potassium carbonate, 2-naphthylboronic acid, and tetrakis(triphenylphosphine)palladium(0) were purchased form Sigma Aldrich. 4-Biphenylboronic acid was purchased from TCI America. Unstabilized THF was purchased from Millipore Sigma.

For Polymerizations

N,N-Dimethylacetamide (DMAc), methyl methacrylate (MMA), and diethyl-2-bromo-2-methylmalonate (DBMM) were purchased form Sigma Aldrich.

For Electrochemical Experiments

Tetra-n-butylammonium hexafluorophosphate (Bu_4NPF_6), tetra-n-butylammonium bromide (Bu_4NBr), and lithium hexafluorophosphate were purchased from TCI America. Ferrocene, silver nitrate, tetra-n-butylammonium chloride (Bu_4NCl), acetonitrile, and *N,N*-dimethylacetamide were purchased from Sigma Aldrich.

Chemical Preparation and Storage

Toluene was purified using an mBraun MB-SPS-800 solvent purification system and kept under nitrogen atmosphere until it was used. MMA and DBMM dried overnight using calcium hydride, vacuum distilled, and degassed by freeze-pump-thaw. They were then stored under nitrogen atmosphere until their use in polymerizations. For electrochemical experiments, MMA was purified to remove inhibitors by passing it through an alumina column. It was then stored in an amber glass bottle in a -25 ºC freezer until its use. Bis(dibenzylideneacetone)palladium(0), tetrakis(triphenylphosphine)palladium(0), DMAc for polymerizations, and lithium hexafluorophosphate were received and stored under inert atmosphere until their use.

Experimental Equipment

Electrodes

All cyclic voltammetry (CV) was performed using a glassy carbon working electrode and a platinum wire counter electrode. Prior to use, the working electrode was polished using a 0.05-micron alumina slurry on a polishing pad, followed by 5 minutes of sonication in DI water and then 5 minutes of sonication in ethanol. In every case, the reference electrode was either 0.01 M $AgNO_3$/Ag in MeCN with 0.1 M Bu_4NPF_6, or a silver wire quasi-reference electrode (QRE).

For electrolysis, a glassy carbon rod was used as the working electrode and prepared in the same fashion as described above (see working electrode preparation for CV). For the counter electrode, a platinum wire was used. In experiments employing a U-cell, a coiled wire was used to maximize the electrode surface area in contact with the solution. Instead, in experiments employing a 5-neck pear flask (Gamry Dr. Bob's cell), a platinum wire was placed in a Teflon tube with a vycor frit separator on one end and filled with the supporting electrolyte solution.

Again, the reference electrode was either 0.01 M $AgNO_3$/Ag in MeCN with 0.1 M Bu_4NPF_6, or a silver wire QRE.

For calibration of the silver wire QRE in 50/50 (*v/v*) DMAc/MMA with 0.1 M Bu_4NPF_6 (94%) and Bu_4NBr (6%), cyclic voltammetry of ferrocene (Fc) was performed to obtain an $E_{1/2}$ (Fc/Fc^+) = 0.903 V.

Electrolysis Cells

For work employing a U-cell for electrolysis, a custom cell was designed and built by scientific glassblower Michael Olsen at Colorado State University. The cell features a working and counter electrode compartment, separated by an extra-fine glass frit (Figure 4.6). Both compartments were fitted with ground glass joints, allowing for further customization as needed, and the working compartment was designed to include a side-arm for the reference electrode to be inserted to the solution.

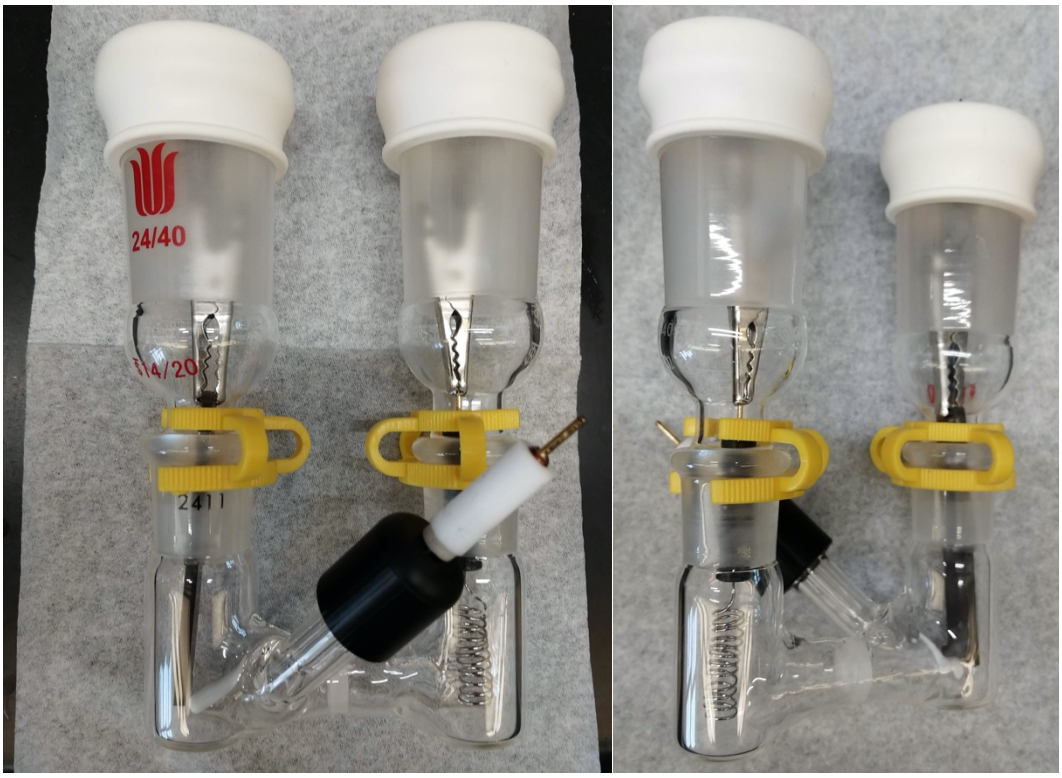

Figure 4.6. *Photographs of the U-cell used in this work. (Left) Front side of the cell, showing the working electrode compartment on the left side, with a glassy carbon working electrode and reference electrode inserted in the side-arm. In the center, an extra-fine glass frit acts as a separator to prevent reaction solution from contacting the counter electrode, which is displayed in the right-side compartment. (Right) View of the U-cell from the back-side.*

For work employing a 5-neck pear flask, a Gamry Dr. Bob's cell was used (part number: 990-00193). To achieve separation of the counter electrode in this cell, a teflon tube was fitted with a vycor glass frit (Gamry Porous Glass Frit, part number: 955-00003) and inserted into the cell. In addition, the working and counter electrodes were inserted through separate ports, and a ground glass nitrogen adapter was used to maintain the cell under inert atmosphere (Figure 4.7).

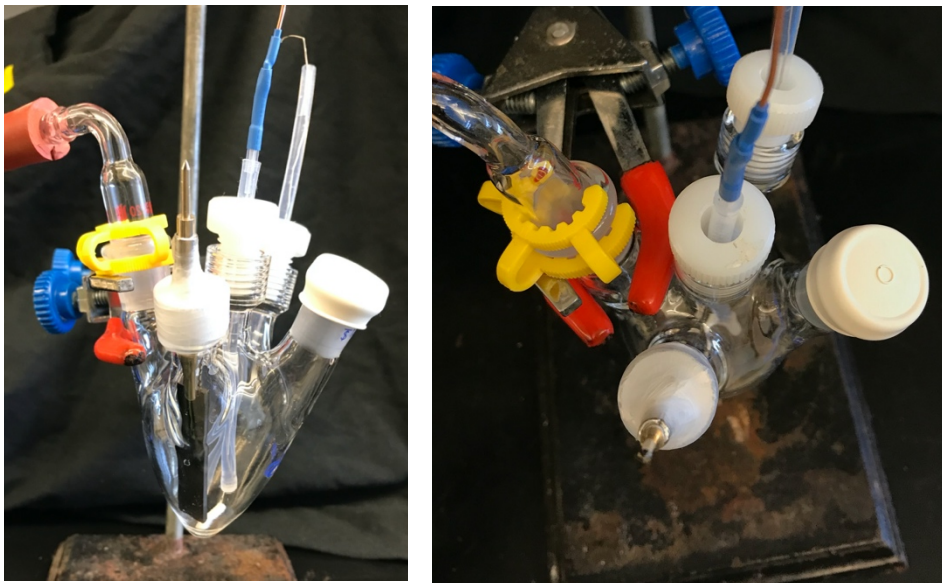

Figure 4.7. *Photographs of the 5-neck electrochemical cell used in this work. (Left) A side view of the cell, showing (from left to right) the nitrogen gas inlet, working electrode, reference electrode, counter electrode (with separator), and sampling port. (Right) A top-down view of the cell showing the various ports.*

Light Reactors

The following LEDs were used in the construction of light reactors for this work. For light beakers, strips of water-resistant white LEDs were purchased from Creative Lighting Solutions (item no. CL-FRS5050WPDD-5M-12V-WH). For LED wells, strips of white LEDs were purchased from Creative Lighting Solutions (item no. CL-FRS1210-5M-12V-WH). For high-power light reactors, cool white LED emitters were purchased from LED Engin (item no. LZ4-00CW08). For LED dimming, a Dragonpad 12V12A inline mini LED dimmer control for single color LED strip lights with 7 dimmer settings was installed between the power supply and LED strip. Correlation between dimmer settings and percent LED intensity was obtained from previously published measurements.[47]

Below, the various light reactors used in this work are pictured and described:

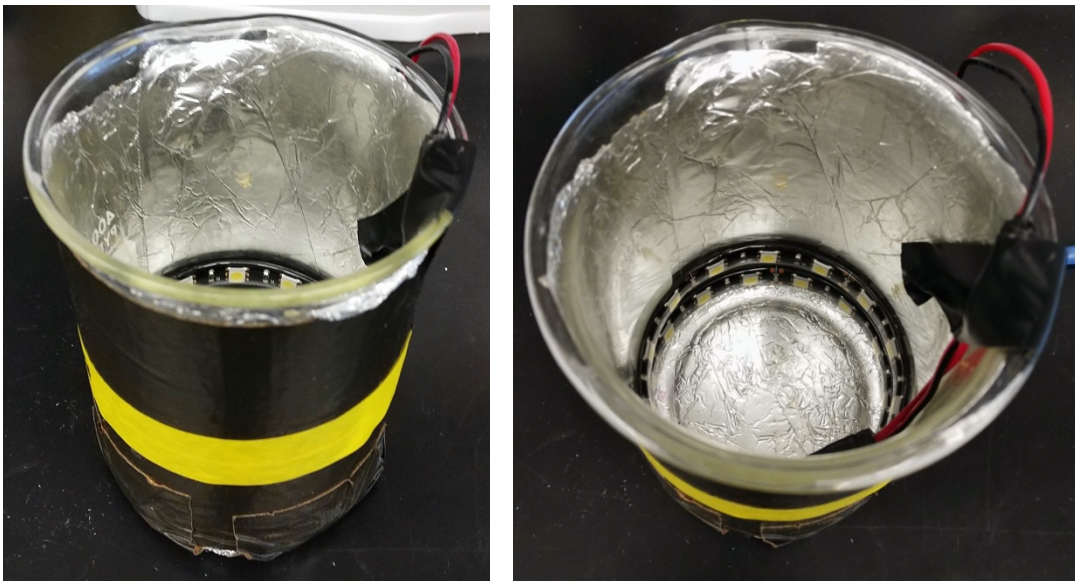

Figure 4.8. *Photographs of the LED beaker used in this work from the front (left) and top (right). The reactor was constructed by wrapping a 400 mL beaker (10.0 cm tall, 8.5 cm diameter) with aluminum foil and wrapping a coated white LED strip (9 LED segments, 16" total) inside the bottom of the beaker.*

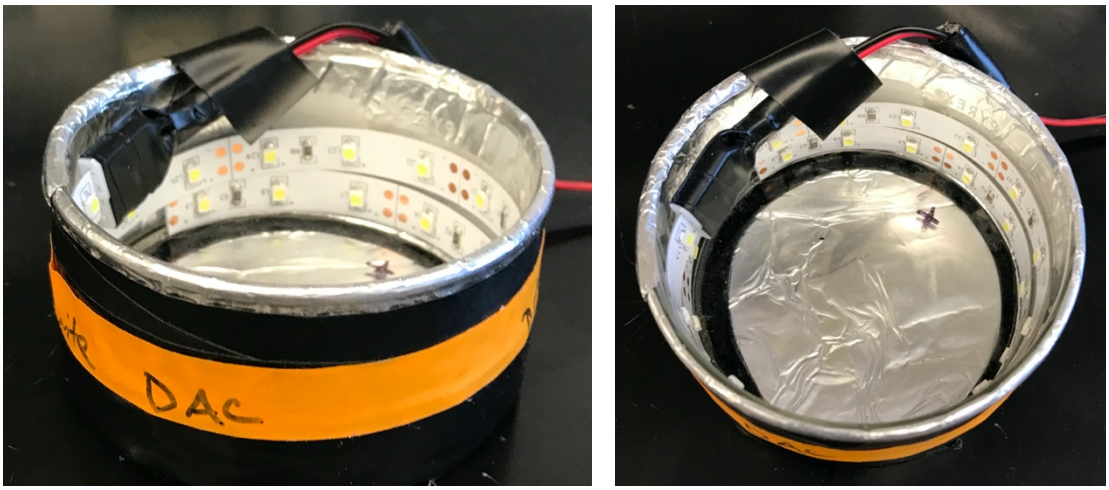

Figure 4.9. *Photographs of the LED wells used in the majority of this work. These reactors were built by wrapping an 80 mm x 40 mm recrystallization dish with aluminum foil and wrapping uncoated white LED strips (9 LED segments) around the inside of the disk. The photographs provide a side view (left) and top view (right).*

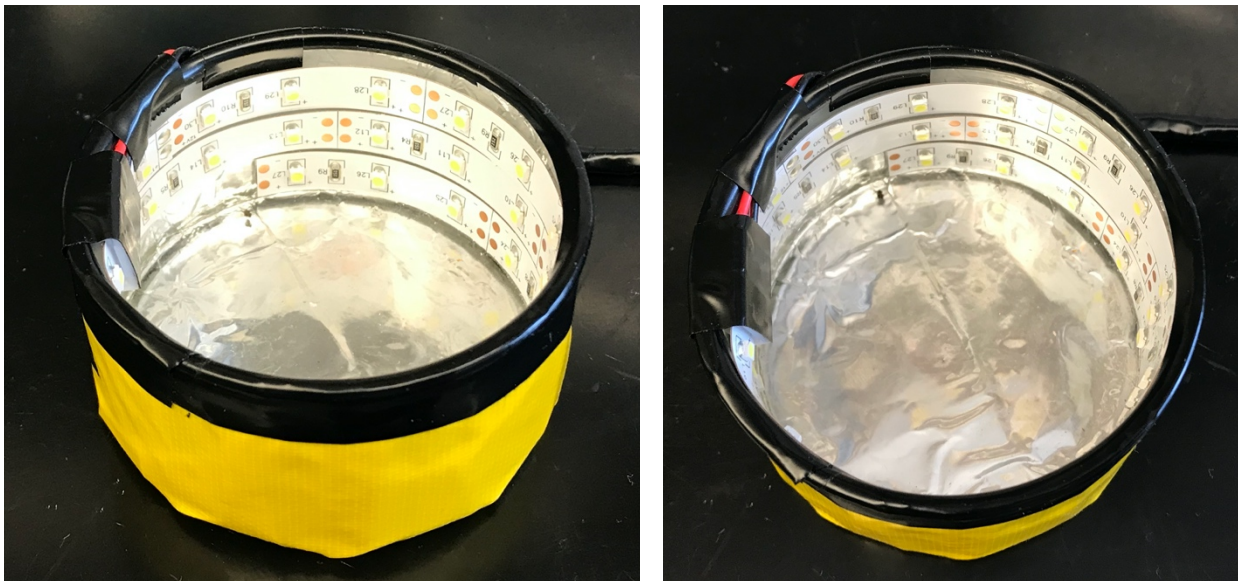

Figure 4.10. *Photographs of the LED wells constructed with more light strips. These reactors were built by wrapping an 80 mm x 40 mm recrystallization dish with aluminum foil and wrapping uncoated white LED strips (15 LED segments) around the inside of the disk. The photographs provide a side view (left) and top view (right).*

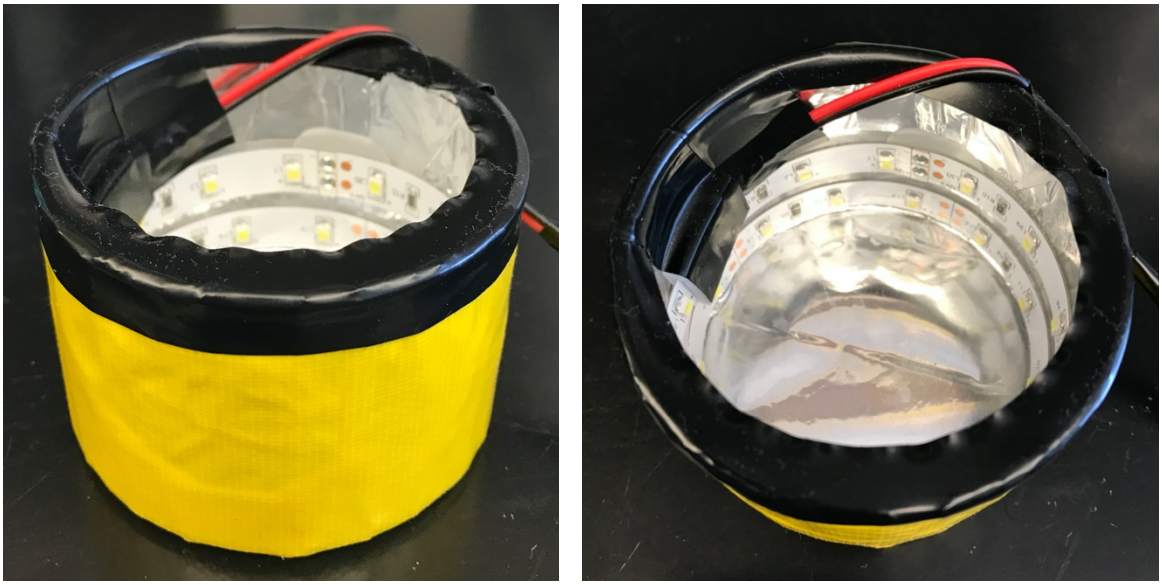

Figure 4.11. *Photographs of the LED wells constructed to move the LEDs closer to the reaction vessel. These reactors were built by wrapping a 70 mm x 50 mm recrystallization dish with aluminum foil and wrapping uncoated white LED strips (9 LED segments) around the inside of the disk. The photographs provide a side view (left) and top view (right).*

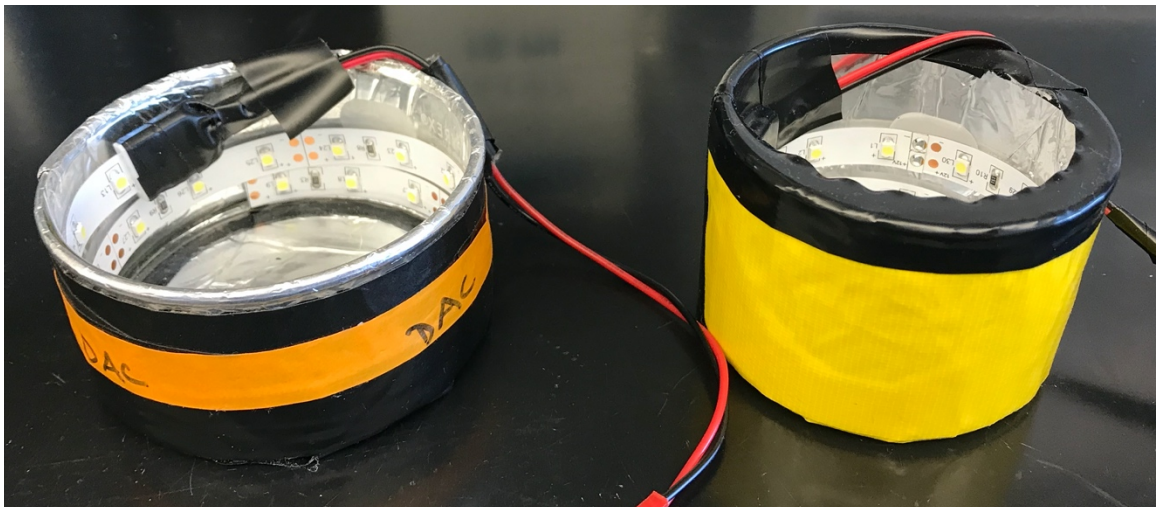

Figure 4.12. *Photograph comparing the original light well used in this work (left, dimensions: 80 x 40 with 9 LED segments) and that constructed to move the LEDs closer to the reaction vessel (right, dimensions: 70 x 50 with 9 LED segments).*

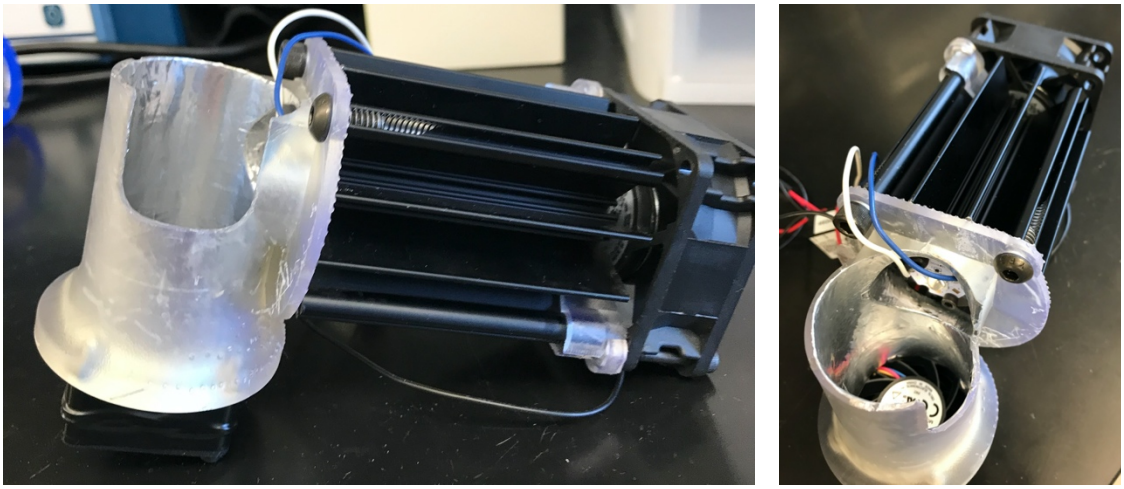

Figure 4.13. *Photographs of the high-power LED reactor[48] designed for use with the U-cell. (Left) A side view of the reactor, showing the 3D-printed reactor body, which can be designed and exchanged depending on the flask being used. Attached to this reactor body is a cooling fan (bottom) used to maintain the temperature of the reaction vessel, as well as a cooling fin connected to the LED and another cooling fan used to regulate the temperature of the LED. (Right) Top view of the reactor body, showing the LED attached to the cooling fin and the LED that points inside of the reactor body.*

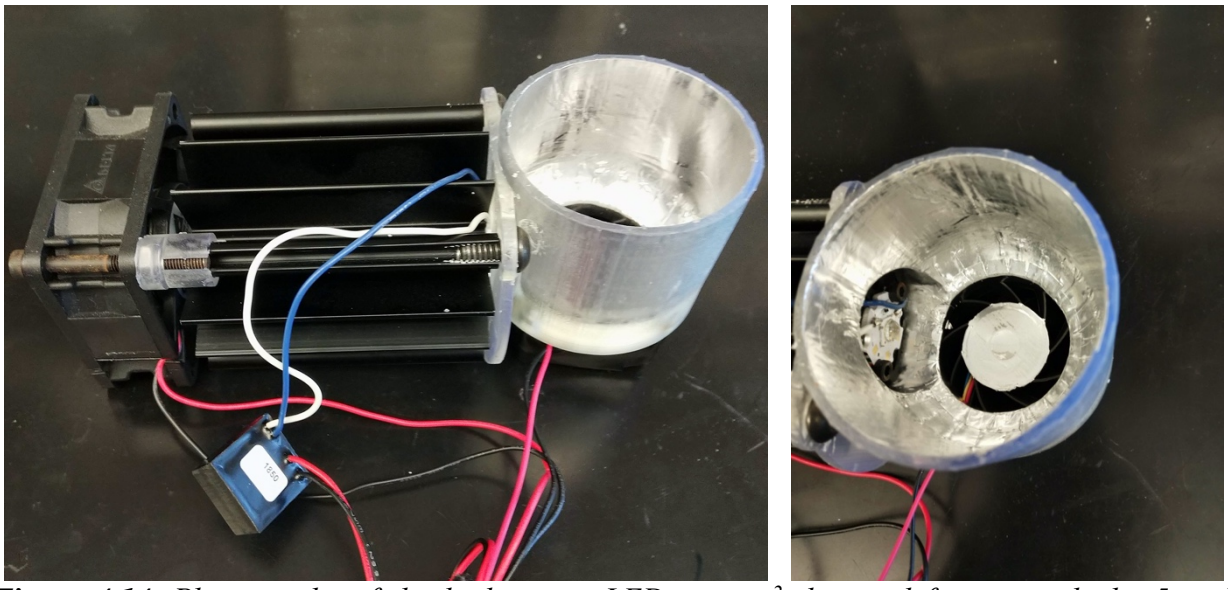

Figure 4.14. *Photographs of the high-power LED reactor[2] designed for use with the 5-neck electrochemical cell. (Left) A side view of the reactor, showing a cooling fan (left) connected to cooling fins (center) that maintain the temperature of the LED. On the right side of the cooling fin is a 3D-printed reactor body, which can be designed and exchanged depending on the flask being used. (Right) Top view of the reactor body, showing the LED attached to the cooling fin and another cooling fan on the bottom of the reactor body used to control the temperature of the reaction vessel.*

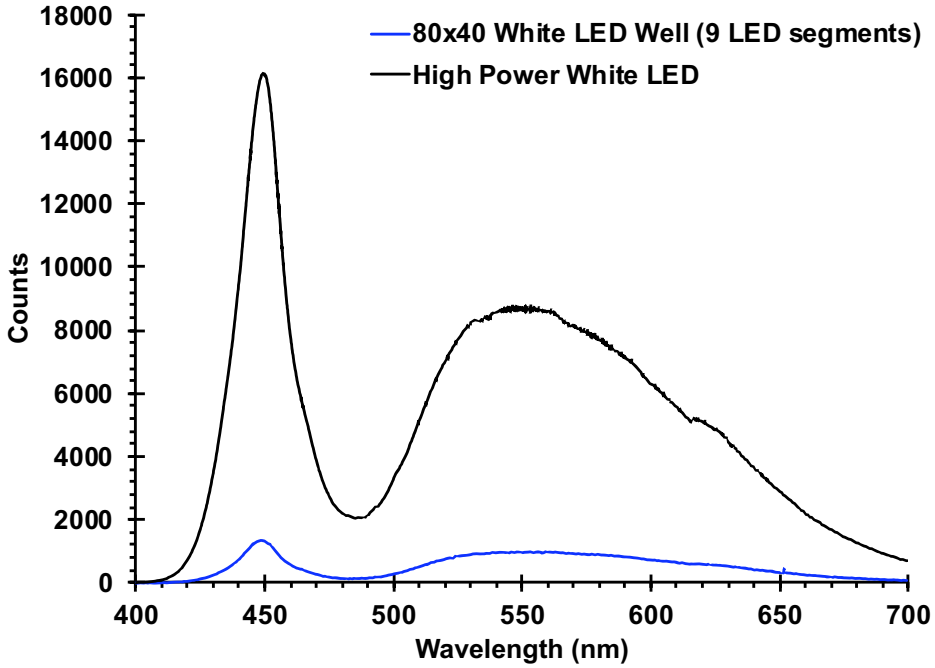

FigureSAV-4.15. *Qualitative emission spectra of white LEDs used in this work: white LEDs used in light wells (blue) and high-power light reactors (black).*

Instrumentation

Nuclear magnetic resonance (NMR) spectroscopy was performed using either a Bruker US 400 MHZ spectrometer or a Bruker Ascend 400 MHZ spectrometer. All ^{1}H NMR spectra are reported in **δ** units, parts per million (ppm), and are referenced to residual chloroform (7.26 ppm) or benzene (7.15) signals. Analysis of polymer molecular weights were performed via gel permeation chromatography (GPC) coupled with multi-angle light scattering (MALS), using an Agilent HPLC fitted with one guard column, three PLgel 5 μm MIXED-C gel permeation columns, a Wyatt Technology TrEX differential refractometer, and a Wyatt Technology miniDAWN TREOS light scattering detector, using THF as the eluent at a flow rate of 1.0 mL/min and a dn/dc value of 0.084. Electrochemical measurements were performed using either a Gamry Interface 1010B or 1010E potentiostat. UV-Visible spectroscopy was performed using an Agilent Cary 5000 UV-Vis-NIR spectrometer. Measurements of LED emission were made using an Olympus IX73 inverted microscope connected to a Horiba iHR 550 spectrometer with a Horiba Synapse back-illuminated CCD camera and a 1200 blaze/mm grating. For qualitative measurements of LED emission intensity, light sources were placed in the same configuration and the light directed into an opening in the microscope.

Procedures

Photocatalyst Synthesis

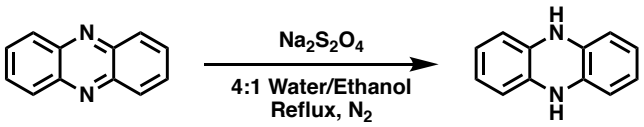

Figure 4.16. *Scheme for the synthesis of 5,10-dihydrophenazine by reduction of phenazine.*

Synthesis of 5,10-dihydrophenazine. Dihydrophenazine used in this work was synthesized using a published literature procedure.[3]

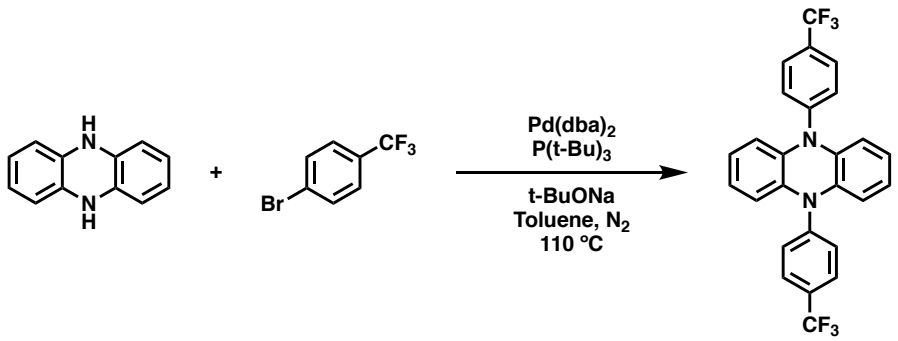

Figure 4.17. *Scheme for the synthesis of 5,10-di(4-trifluorobenzo)-5,10-dihydrophenazine via Buchwald coupling.*

Synthesis of 5,10-di(4-trifluorobenzo)-5,10-dihydrophenazine. A modified literature procedure as used.[15] A Schlenk flask was charged with sodium *tert*-butoxide (3.173 g, 33.02 mmol, 3 eq) and degassed. Using standard Schlenk techniques, 4-bromobenzotrifluoride (3.84 mL, 27.5 mmol, 2.5 eq), which had been degassed by nitrogen bubbling, was added to the flask. The reaction flask was then brought into a nitrogen filled glovebox, where dihydrophenazine (1.9997 g, 10.974 mmol, 1 eq), bis(dibenzylideneacetone)palladium(0) (130.4 mg, 0.2268 mmol, 0.02 eq), tri-*tert*-butylphosphine (1 M solution in toluene, 0.68 mL, 0.66 mmol, 0.06 eq), and toluene (40 mL) were added to the flask. The reaction was then refluxed at 110 ºC for 44 h, after which it was cooled to room temperature. The reaction mixture was then combined with dichloromethane (DCM, 200 mL), causing a yellow precipitate to form. The solid was collected by vacuum filtration and washed with cold DCM. Further purification was achieved by sublimation (190 ºC, 50 mtorr) to yield 3.4470 g of product (66.7%). NMR characterization (^{1}H and ^{19}F in C_6D_6) matched previously published data.[3]

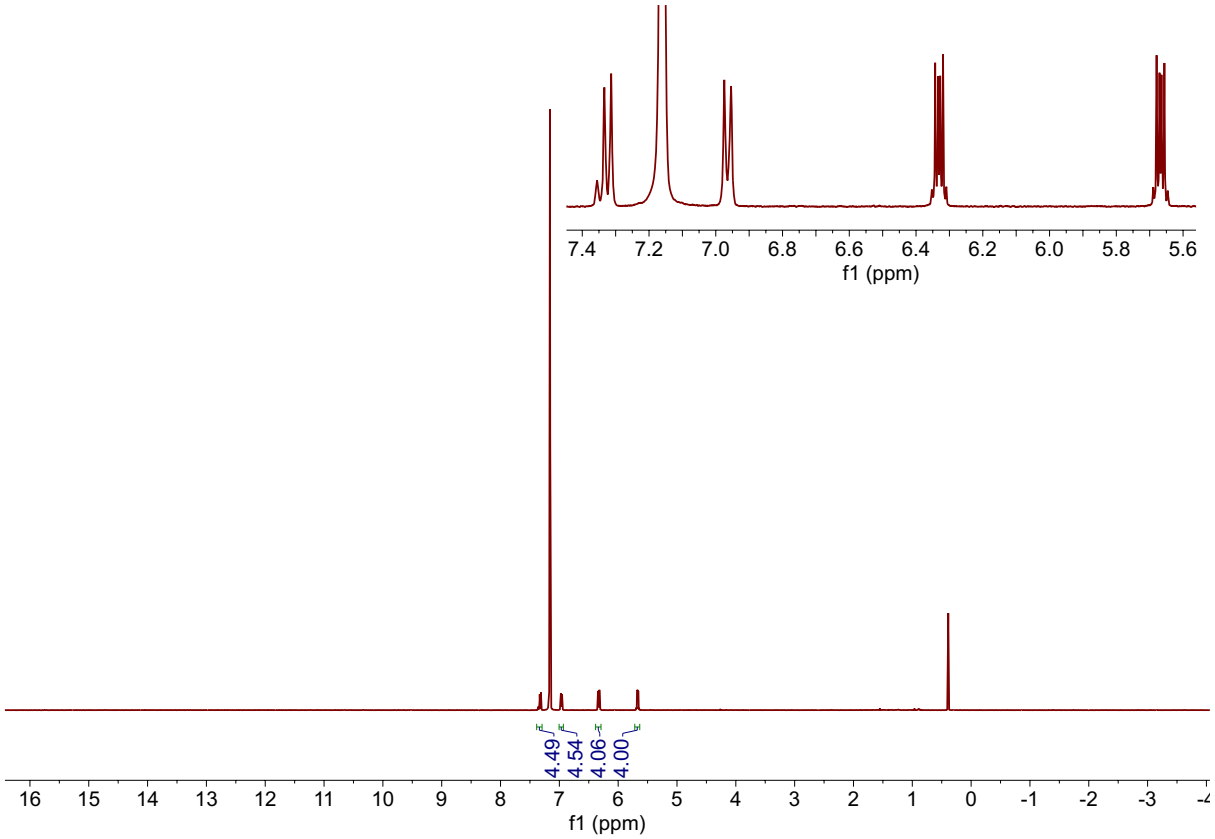

Figure 4.18. *^{1}H NMR spectrum of 5,10-di(4-trifluorobenzo)-5,10-dihydrophenazine in C_6D_6.*

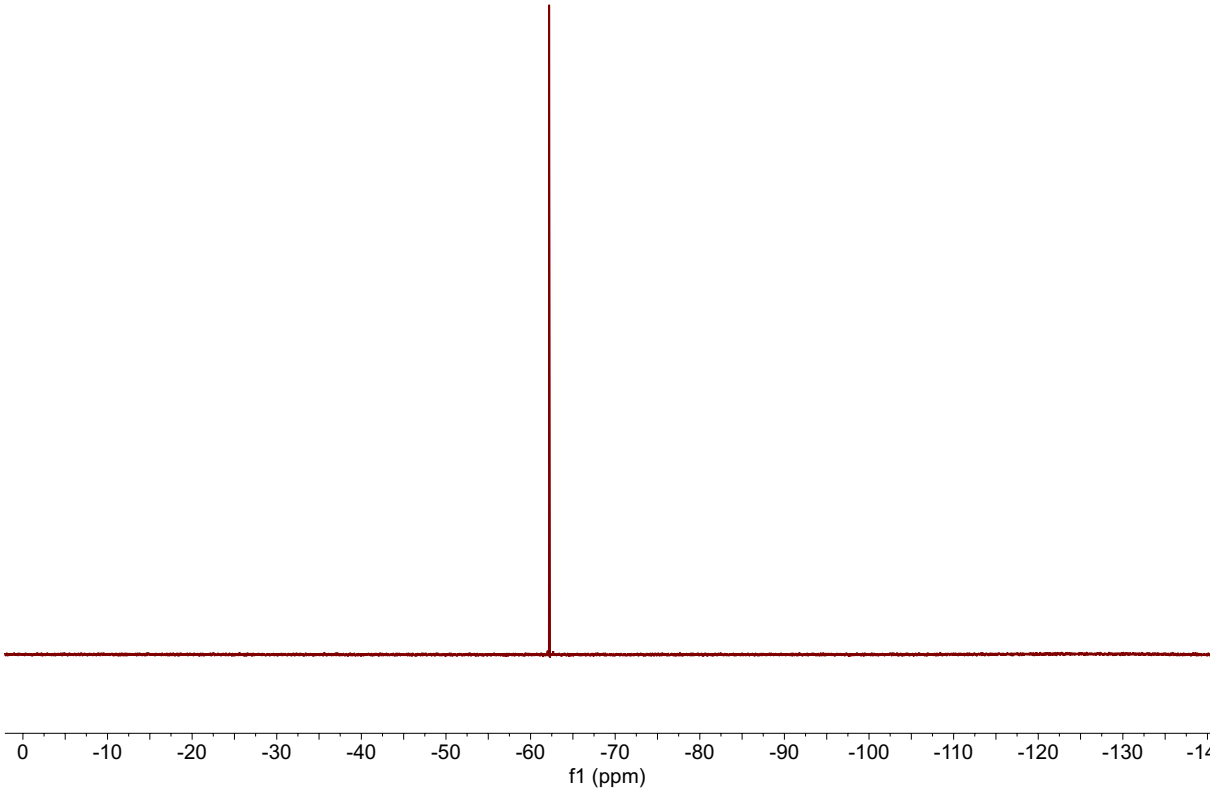

Figure 4.19. *^{19}F NMR spectrum of 5,10-di(4-trifluorobenzo)-5,10-dihydrophenazine in C_6D_6.*

Substitution of the dihydrophenazine core with aryl-functional groups was achieved by following a published literature procedure.[16]

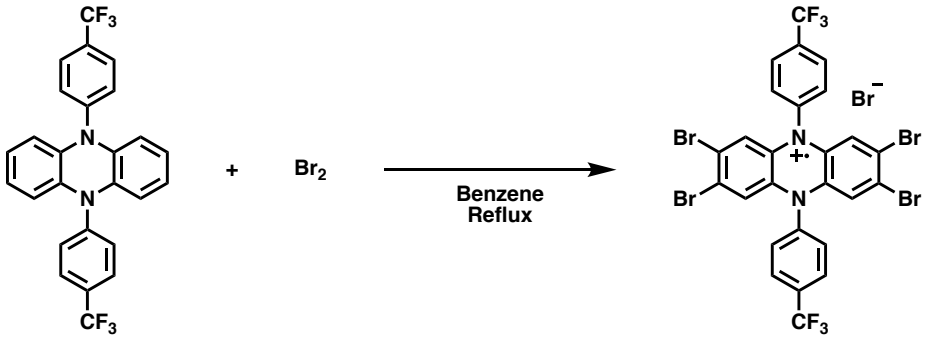

Figure 4.20. *Scheme for the bromination of 5,10-di(4-trifluorobenzo)-5,10-dihydrophenazine using molecular bromine.*

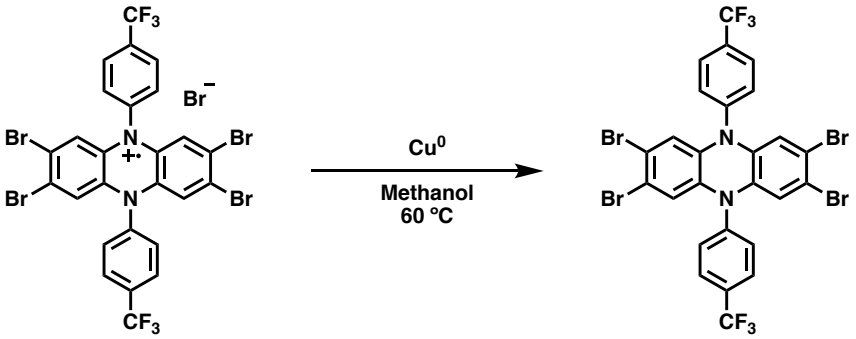

Figure 4.21. *Scheme for the reduction of the radical cation resulting from the bromination of 5,10-di(4-trifluorobenzo)-5,10-dihydrophenazine.*

Synthesis of 2,3,7,8-tetrabromo-5,10-di(4-trifluorobenzo)-5,10-dihydrophenazine.

Bromination of 5,10-di(4-trifluorobenzo)-5,10-dihydrophenazine and reduction of the subsequent radical cation was carried out according to a published literature procedure.[16]

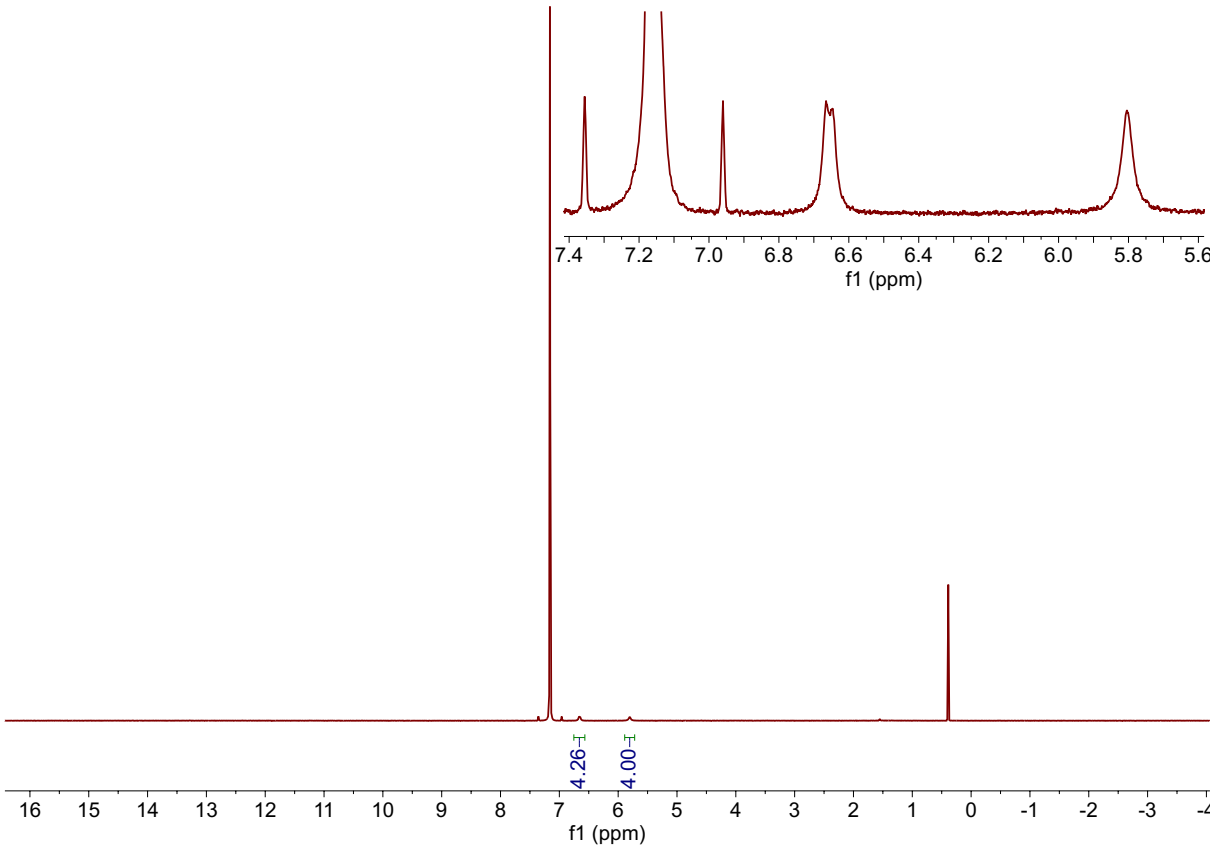

Figure 4.22. *^1H NMR spectrum of 2,3,7,8-tetrabromo-5,10-di(4-trifluorobenzo)-5,10-dihydrophenazine in C_6D_6.*

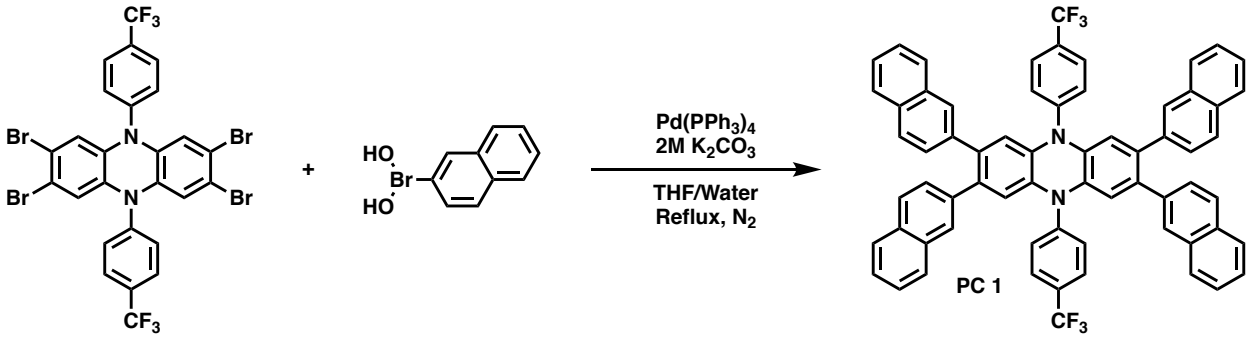

Figure 4.23. *Scheme for the synthesis of 2,3,7,8-tetra(2-naphthyl)-5,10-di(4-trifluorobenzo)-5,10-dihydrophenazine (**1**) via Suzuki coupling.*

*Synthesis of 2,3,7,8-tetra(2-naphthyl)-5,10-di(4-trifluorobenzo)-5,10-dihydrophenazine (**1**).* Synthesis of PC **1** was performed according to a published literature procedure and purified by a modified procedure.[16] A Schlenk flask was charged with 2,3,7,8-tetrabromo-5,10-di(4-trifluorobenzo)-5,10-dihydrophenazine (1.996 g, 2.533 mmol, 1 eq) and 2-naphthylboronic acid (3.504 g, 20.37 mmol, 8 eq). The flask was degassed and brought into a nitrogen filled glovebox, where tetrakis(triphenylphosphine)palladium(0) (299.3 mg, 0.2590 mmol, 0.1 eq) was added to the reaction. The flask was then removed from the glovebox, and THF (200 mL) and potassium carbonate (2M in degassed DI water, 25.4 mL, 50.8 mmol, 20 eq) were added to the reaction. The solution was then heated at 100 ºC for 48 h, after which it was cooled to room temperature and 200 mL DCM was added to the flask. The yellow precipitate that formed was collected by vacuum filtration and further purified by recrystallization from hot DCM and methanol at 0 ºC, yielding 0.8143 g of product (32.9%). NMR characterization (^{1}H in C_6D_6) matched that previously reported for this compound.[16]

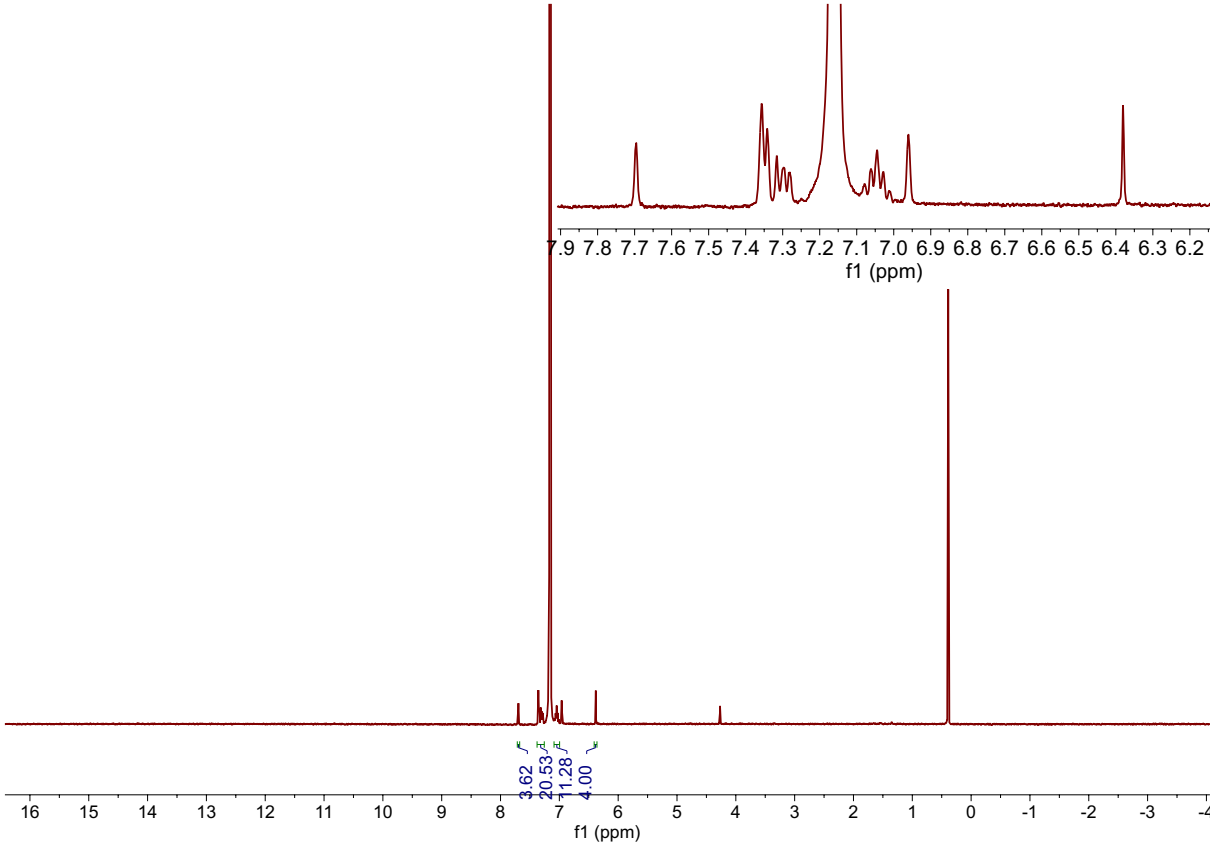

Figure 4.24. *^{1}H NMR spectrum of **1** in C_6D_6.*

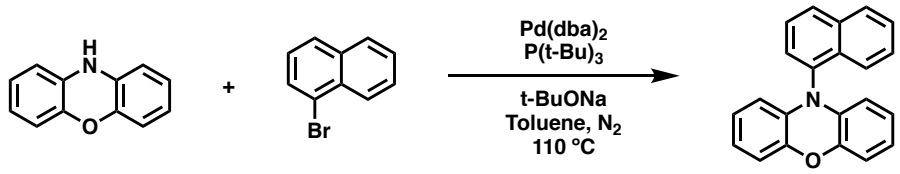

Figure 4.25. *Scheme for the synthesis of 1-naphthyl-10-phenoxazine via Buchwald coupling.*

Synthesis of 1-naphthyl-10-phenoxazine. Synthesis of 1-naphthyl-10-phenoxazine was performed according to a published literature procedure.[4]

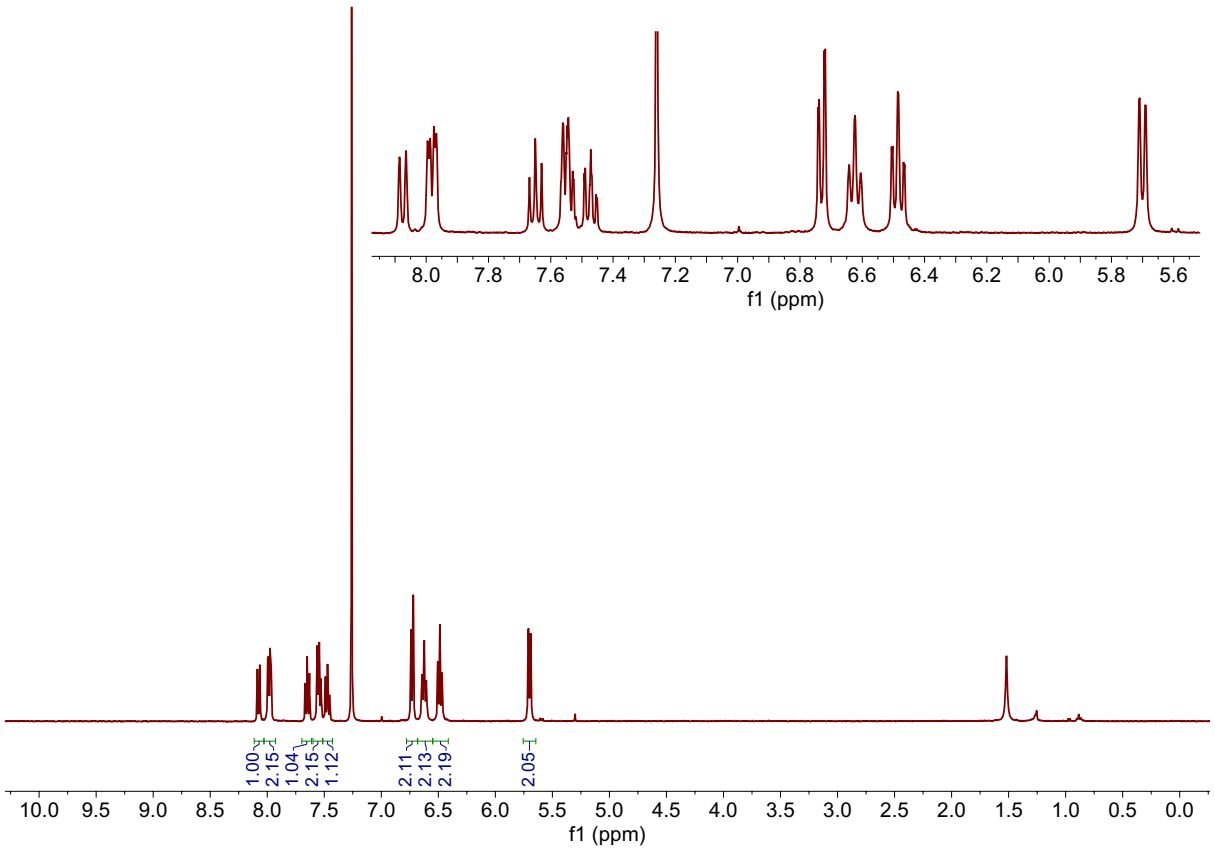

Figure 4.26. *^{1}H NMR spectrum of 1-naphthyl-10-phenoxazine in $CDCl_3$.*

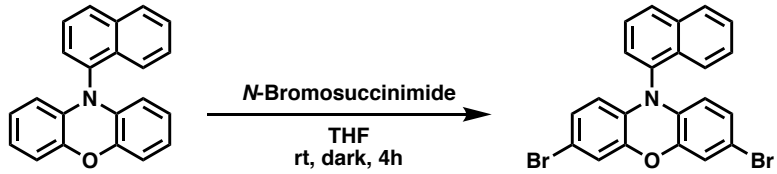

Figure 4.27. *Scheme for the bromination of 1-naphthyl-10-phenoxazine.*

Synthesis of 3,7-dibromo-1-naphthyl-10-phenoxazine. Bromination of 1-naphthyl-10-phenoxazine was performed according to a published literature procedure.[4]

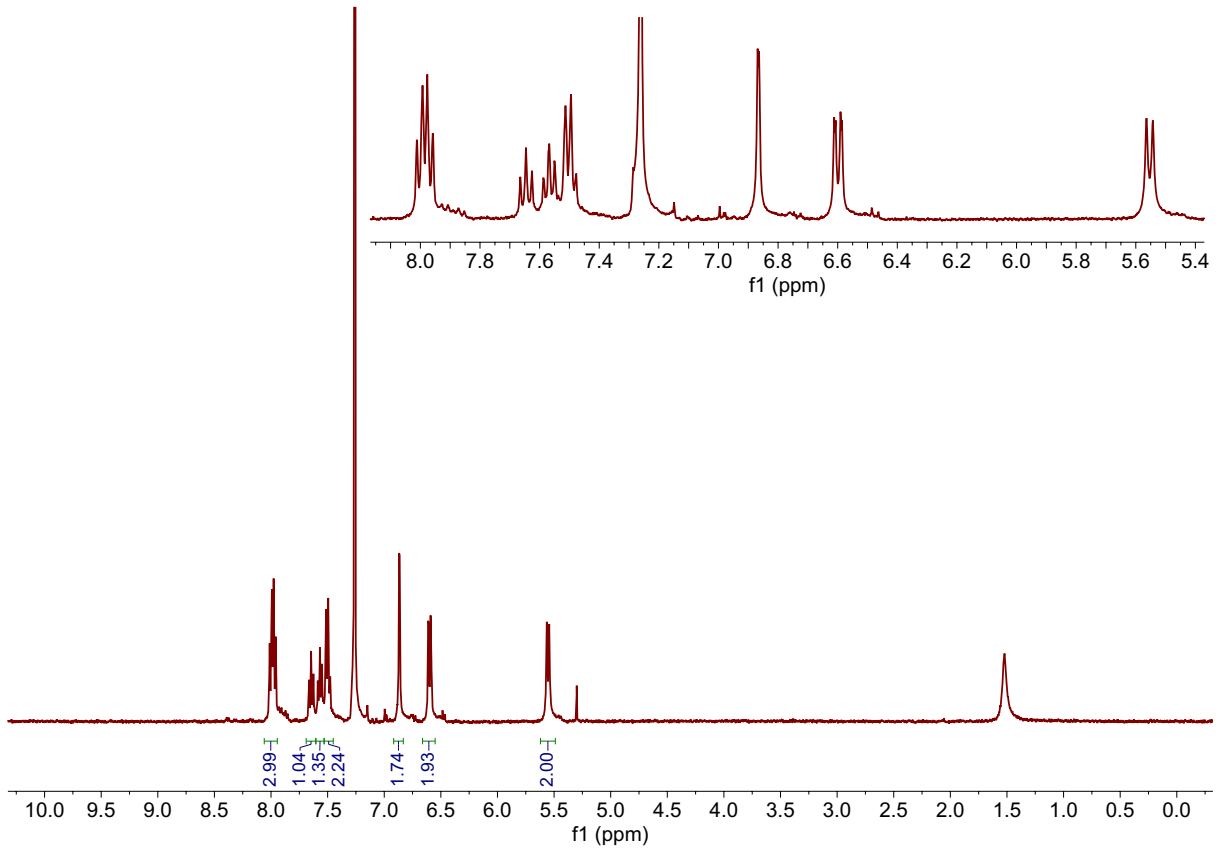

Figure 4.28. *^{1}H NMR spectrum of 3,7-dibromo-1-naphthyl-10-phenoxazine in $CDCl_3$.*

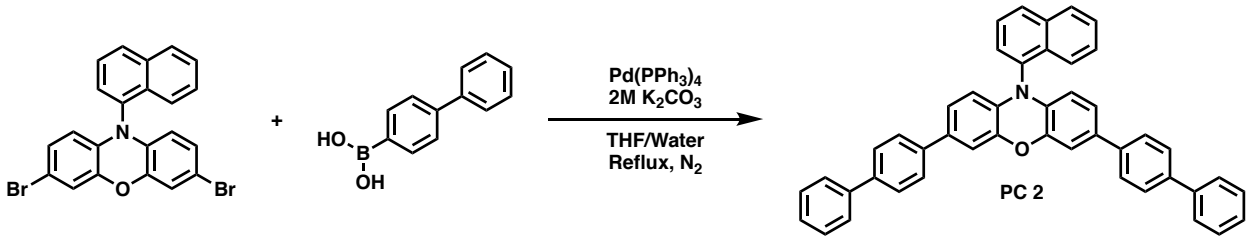

Figure 4.29. *Scheme for the synthesis of 3,7-di(4-biphenyl)-1-naphthyl-10-phenoxazine (**2**) via Suzuki coupling.*

*Synthesis of 3,7-di(4-biphenyl)-1-naphthyl-10-phenoxazine (**2**).* Synthesis of PC **2** was carried out according to a published literature procedure.[4]

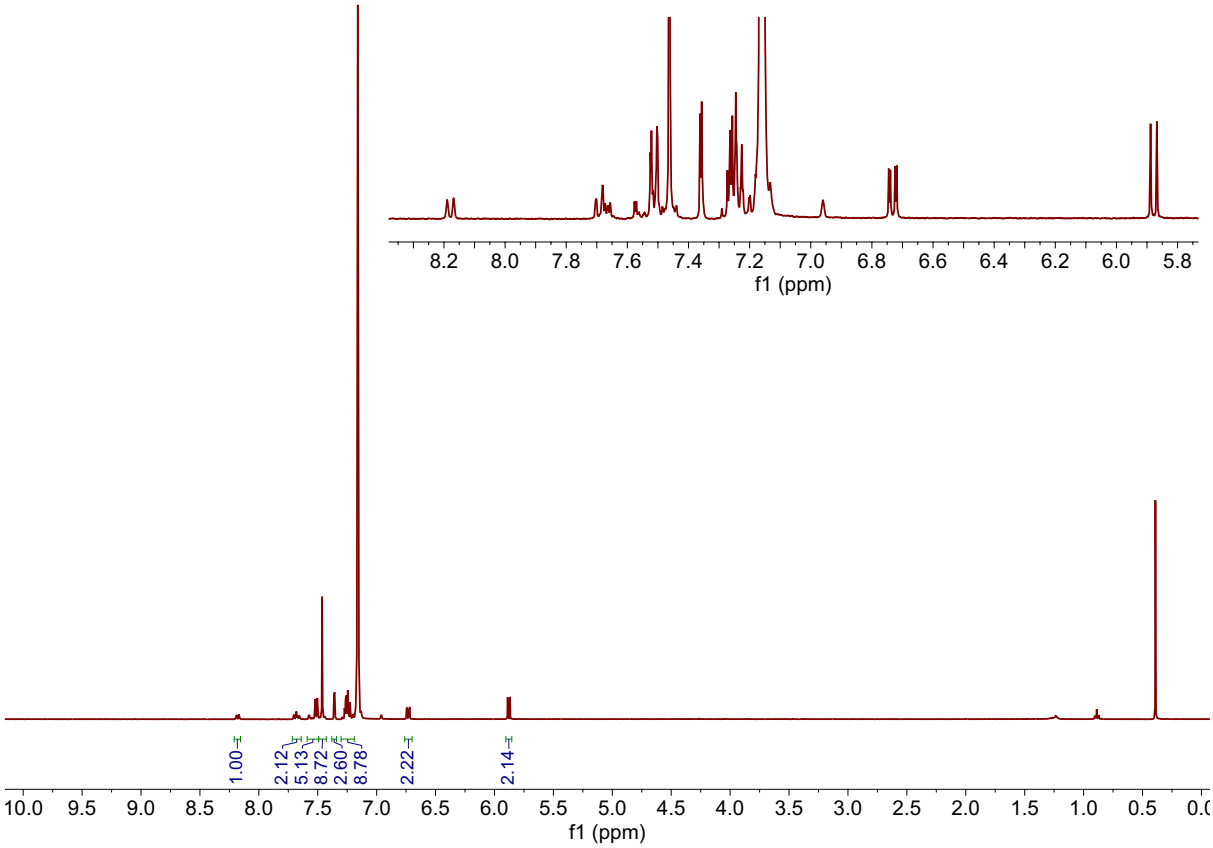

Figure 4.30. *^{1}H NMR spectrum of 3,7-di(4-biphenyl)-1-naphthyl-10-phenoxazine in C_6D_6.*

Cyclic Voltammetry of PCs 1 and 2

To determine the appropriate electrochemical potentials to apply during eO-ATRP, catalysts were characterized by cyclic voltammetry (CV) in 50/50 (*v/v*) DMAc/MMA to mimic polymerization conditions. From the resulting cyclic voltammogram, the $E_{1/2}$ of the PC was determined to approximate the standard reduction potential (E^o). For all measurements reported, the solution was sparged with N_2 for 5 minutes prior to measurement, the working electrode was a glassy carbon disk, and the counter electrode was composed of Pt. Reference electrodes and supporting electrolytes used are stated in the respective figure captions.

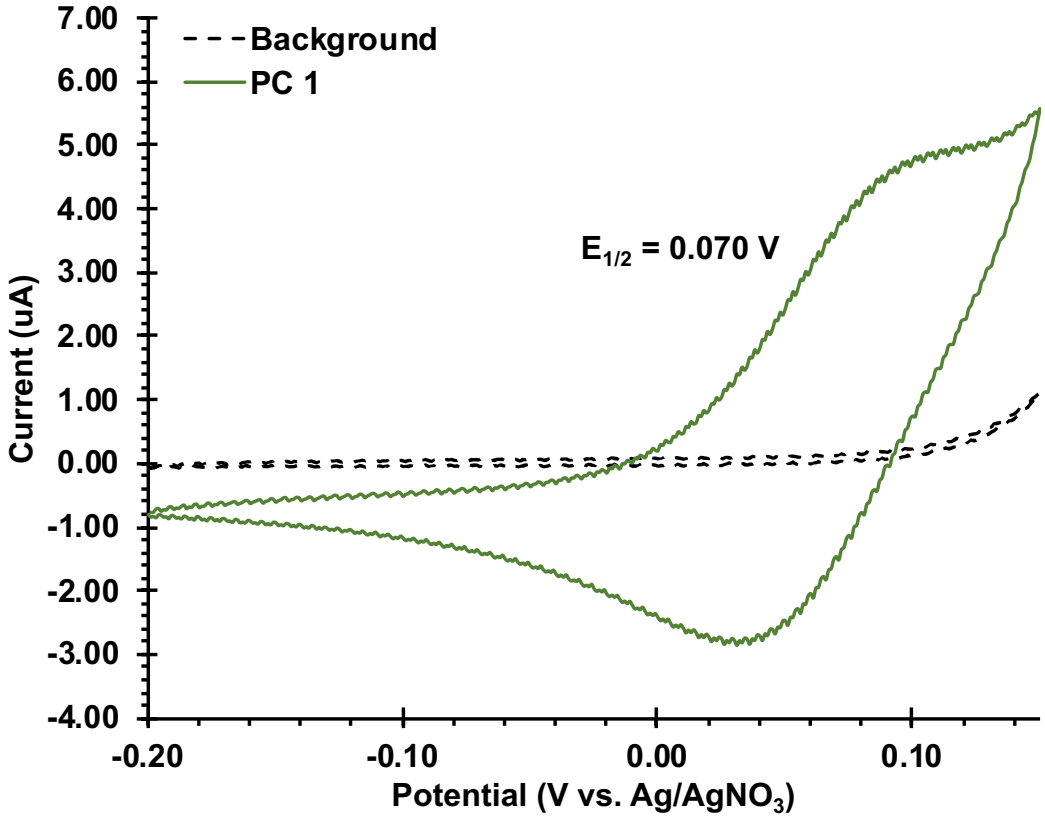

Figure 4.31. *Cyclic voltammogram of PC **1** with supporting electrolyte = 0.094 M Bu_4NPF_6 and 0.006 M Bu_4NBr. Reference electrode = $Ag/AgNO_3$.*

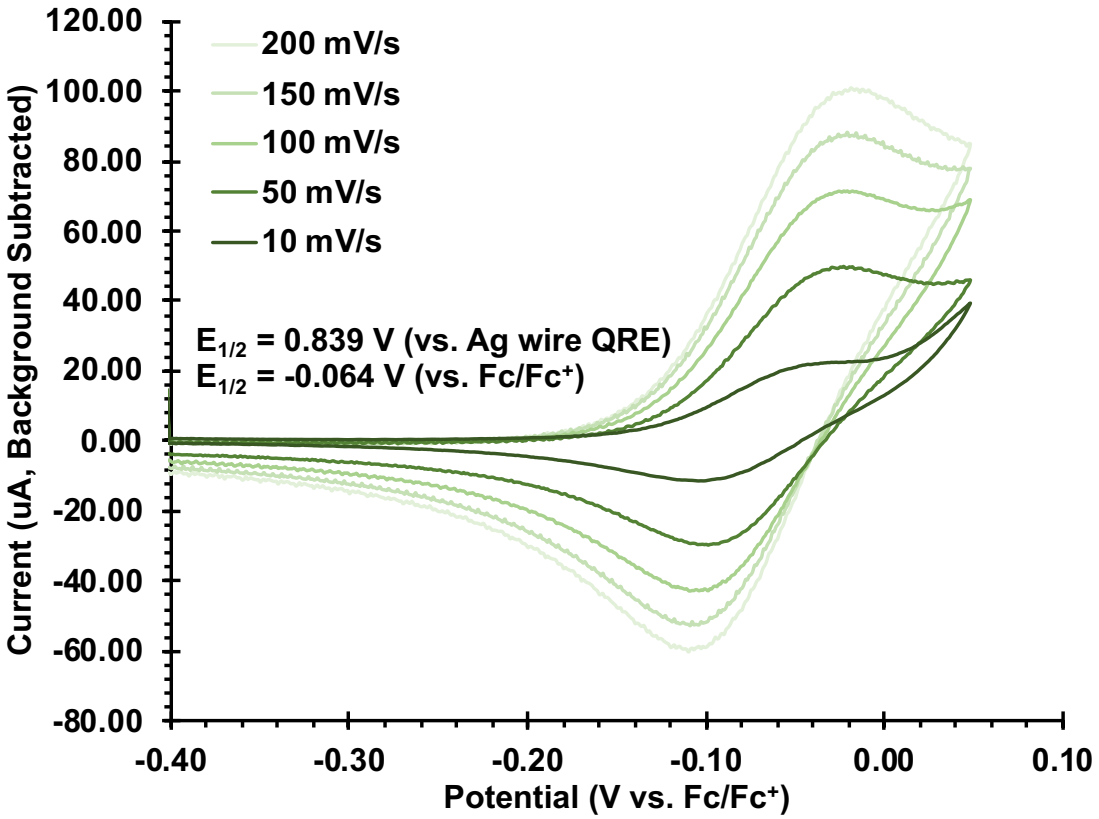

Figure 4.32. *Cyclic voltammogram of PC **1** with supporting electrolyte = 0.094 M Bu_4NPF_6 and 0.006 M Bu_4NBr. Reference electrode = Ag wire quasi-reference electrode. Background subtraction to improve peak resolution was performed by measuring the background CV at each scan rate and subtracting it from each collected voltammogram of PC **1**.*

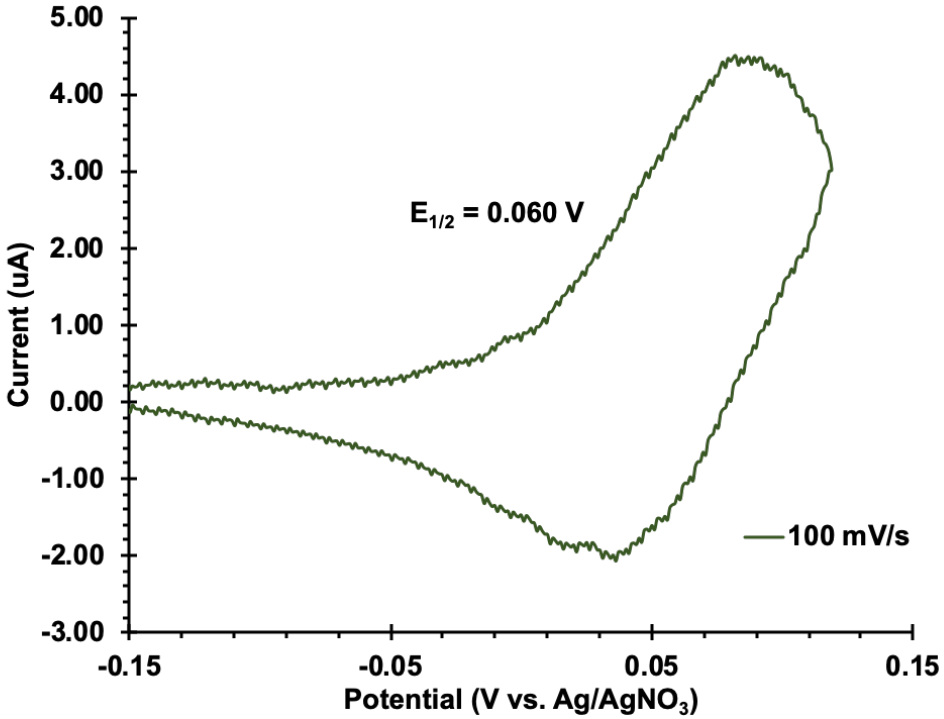

Figure 4.33. *Cyclic voltammogram of PC **1** with supporting electrolyte = 0.094 M $LiPF_6$ and 0.006 M LiBr. Reference electrode = $Ag/AgNO_3$. Due to overlap of the $PC^{\bullet+}$/PC redox couple with the onset of bromide oxidation, background subtraction and curve smoothing were used to resolve the desired redox couple.*

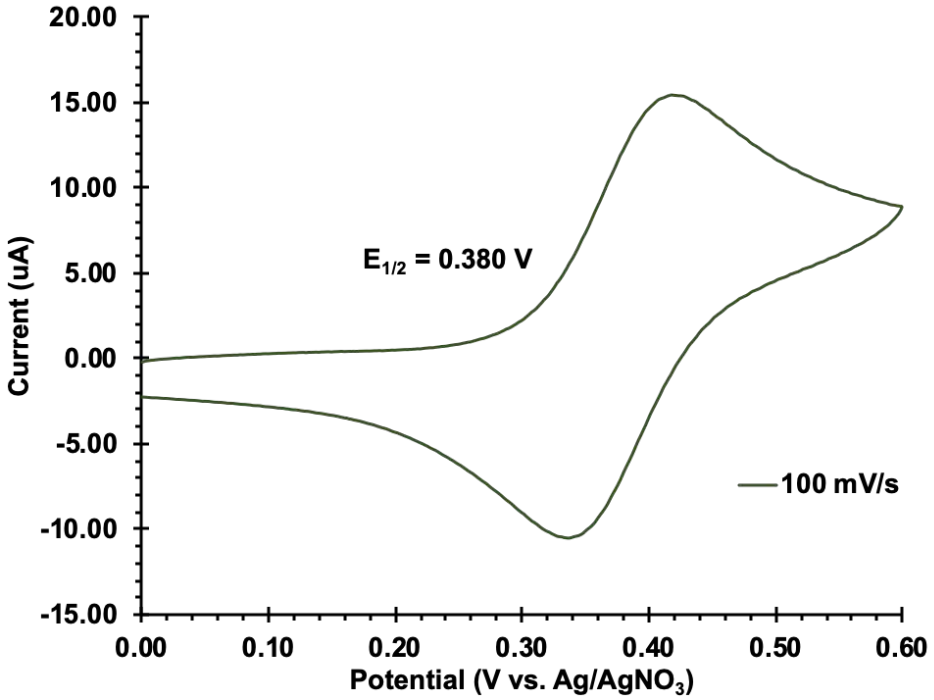

Figure 4.34. *Cyclic voltammogram of PC **2** with supporting electrolyte = 0.1 M $LiPF_6$. Reference electrode = $Ag/AgNO_3$.*

General Methods for Electrochemically Mediated O-ATRP (eO-ATRP)

eO-ATRP in U-Cells

The working electrode compartment of a U-cell – an electrochemical cell with two compartments separated by a fine or extra-fine glass frit – was charged with **1** (1.8 mg, 1.87 μmol, 0.1 eq) and a magnetic stir-bar. The cell was assembled with a working and reference electrode in the same compartment as **1**, and counter-electrode in the other compartment. After purging the cell for 15 minutes with N_2, a supporting electrolyte solution in DMAc (2 mL, 0.2 M, either 94% Bu_4NPF_6 and 6% Bu_4NBr, or $LiPF_6$) was added to both compartments of the cell, followed by addition of MMA (2 mL, 18.7 mmol, 1000 eq) to both compartments using standard Schlenk techniques to make the final concentration of supporting electrolyte 0.1 M. After addition of diethyl-2-bromo-2-methylmalonante (DBMM, 17.9 μL, 9.35 x 10^{-2} mmol, 5 eq), bulk electrolysis

was performed overnight in the dark to generate the desired ratio of **1** to $\mathbf{1}^{\bullet+}$ prior to irradiation, and then irradiation was commenced.

eO-ATRP in 5-neck pear flasks

A 5-neck pear flask (Gamry Dr. Bob's cell) was charged with **1** (1.8 mg, 1.87 μmol, 0.1 eq) and a magnetic stir-bar. The cell was assembled with a glassy carbon working electrode, a platinum wire counter electrode – separated by a vycor frit – and a $Ag/AgNO_3$ reference electrode. After purging the cell for 15 minutes under a positive pressure of N_2, a solution in DMAc (2 mL), MMA (2 mL, 1000 eq, 18.7 mmol), DBMM (17.9 μL, 9.35 x 10^{-2} mmol, 5 eq), and $LiPF_6$ (60.8 mg, 0.1 M final concentration) was added to the cell using standard Schlenk techniques. Bulk electrolysis was performed overnight in the dark to generate the desired ratio of **1** to $\mathbf{1}^{\bullet+}$ prior to irradiation, and then irradiation was commenced.

General Method for Analysis of Kinetics and Molecular Weight Growth

To monitor polymerizations, 0.1 mL aliquots were removed periodically using a nitrogen purged syringe and needle. Aliquots were quenched in a deuterated chloroform containing 250 ppm butylated hydroxytoluene (BHT). These solutions were then transferred to an NMR tube for ^1H NMR analysis to determine the extent of monomer conversion. Afterwards, solutions were dried under compressed air and dissolved in unstabilized THF for GPC analysis to obtain number average molecular weight and dispersity.

Estimation of Excited State PC Concentration

The following calculations were performed to obtain a rough estimate of how much PC*

forms upon irradiation of a solution of PC under conditions similar to those used in this work. First, to simplify the system, a solution without initiator or polymer was considered. In addition, the PC was considered to operate from a generic excited state (PC*), such that the singlet and triplet excited states – and the processes converting between them – did not have to be considered separately. Under these conditions, the concentration of PC* is impacted by (1) photoexcitation and (2) relaxation to the ground state.

Table 4.4. *Reactions considered in the estimation of PC* concentrations.*

Reaction	Scheme	Process
1	PC + hν ⟶ PC*	Photoexcitation
2	PC* $\xrightarrow{k_{relax}}$ PC + hν	Relaxation

Assuming PC* reaches a steady state, the following equation can be written:

$$\frac{d[PC^*]}{dt} = I^o[PC] - k_{relax}[PC^*] = 0 \qquad \text{(Eq. 4.2)}$$

However, this equation can be further simplified considering that the reaction rate will likely be limited by either the concentration of catalyst or the photon flux into the reaction vessel. Data published for PC **1** suggests that this O-ATRP system lies in the flux limited regime, as changes in catalyst loading showed no impact on the observed rate of polymerization.[16] Further, in an investigation of the impact of light intensity in O-ATRP with PC **2**, it was shown that the observed rate of polymerization with this PC is dependent on light intensity.[47] Together, these data provide a strong indication that O-ATRP under these conditions is flux limited, allowing Eq. 4.2 to be simplified.

$$\frac{d[PC^*]}{dt} = I^o - k_{relax}[PC^*] = 0 \qquad \text{(Eq. 4.3)}$$

Where I^o is the concentration of photons entering the reaction vessel in a given unit of time [mol $L^{-1}s^{-1}$]. Solving Eq. 4.3 for the concentration of PC*, one gets:

$$[PC^*] = \frac{I^o}{k_{relax}} \qquad \text{(Eq. 4.4)}$$

Here, k_{relax} can be related to the lifetime of the excited state. Since O-ATRP catalysts likely operate from the triplet excited state, this value can be written as:

$$k_{relax} = \frac{1}{\tau_t} \qquad \text{(Eq. 4.5)}$$

Thus, plugging Eq. 4.5 into Eq. 4.4, one gets:

$$[PC^*] = I^o \cdot \tau_t \qquad \text{(Eq. 4.6)}$$

Where τ_t is the triplet excited state lifetime. Since the triplet excited state lifetime for PC **1** has not been reported, those for two common O-ATRP PCs were considered instead (Figure 4.35). For PC **2**, τ_t = 480 μs, whereas τ_t = 4.3 μs for PC **3**.[38]

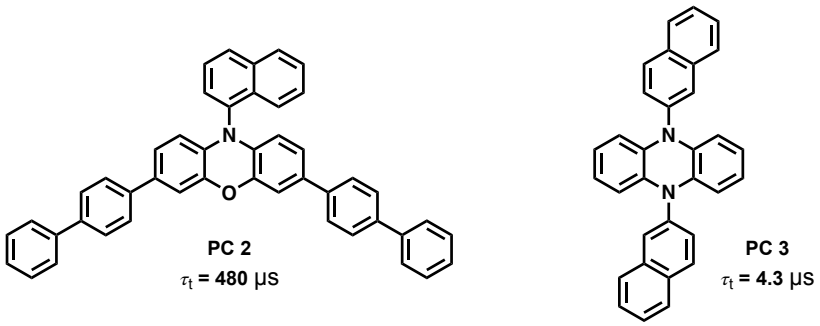

Figure 4.35. *Structures and triplet excited state lifetimes of PCs used in the estimation of [PC*].*

With these values known, we now need to know the photon flux for the LEDs used in this work. Since this value is challenging to obtain for a white light source and most of the light absorbed by the PC is under 500 nm, only the blue emission feature of the LEDs was considered

for this calculation. Further, this blue feature was approximated by the emission of a similar blue LED (Figure 4.36), for which photon flux could be determined (14.5 μmol s^{-1}).[49] Since the blue portion of the white LED emission is about 2.5 times more intense than for the blue LED, the photon flux for this feature can be approximated as 36.3 μmol s^{-1}. Accounting for the reaction volume used in this work (4.0 mL), I^o is calculated from this value of photon flux to be 9.0 x 10^{-3} M s^{-1}.

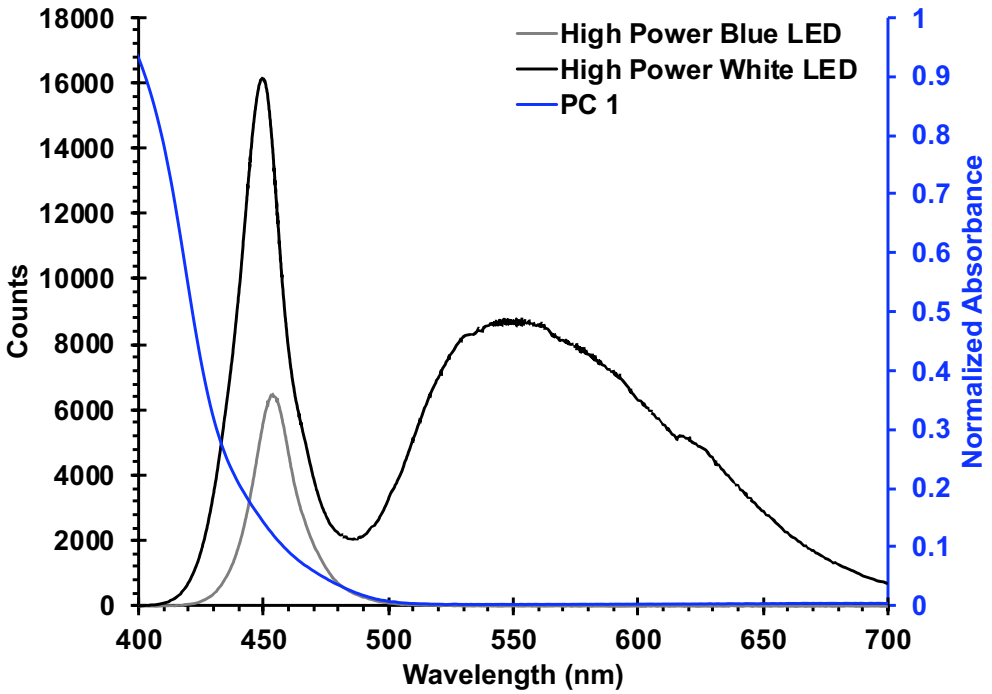

Figure 4.36. *Qualitative emission spectra of the high-power white LEDs used in this work (black) and a similar model blue LED (grey). Overlay of the absorption spectrum of* ***1*** *in the polymerization solution (blue) shows the blue portion of the LED emission (peak around 450 nm) makes up the majority of the light absorbed by the PC. Solution composed of 0.04 mM* ***1*** *in 50/50 (v/v) DMAc/MMA with 0.094 M* Bu_4NPF_6 *and 0.006 M* Bu_4NBr.

Finally, we can use these values of photon flux and triplet excited state lifetime to estimate the concentration of PC* under irradiation with a high-power white LED, which for **2** is about 4.3 x 10^{-6} M and for **3** is 4.0 x 10^{-8} M. Under the conditions used in this work (100 ppm PC), the

concentration of PC is 4.6 x 10^{-4} M. Therefore, when PC **2** is used, about 0.9% of the total PC in solution is PC*, whereas when PC **3** is used, roughly 0.008% is in the form of PC*. Since the excited state lifetime of **1** is unknown and we therefore cannot know how much of **1** exists in solution as PC*, an electrochemical potential was chosen to generate 0.9% $PC^{\bullet+}$ ($E_{app} = E_{1/2} - 120$ mV) to ensure a sufficiently high concentration of $PC^{\bullet+}$ to effectively mediate deactivation.

Control Experiments

Hypothesis 1: Reduction of Tetra-n-butylammonium Cation

Hypothesis: Photoexcited **1** reduces the tetrabutylammonium cation by single electron transfer to generate a reactive species that leads to undesirable side reactivity.

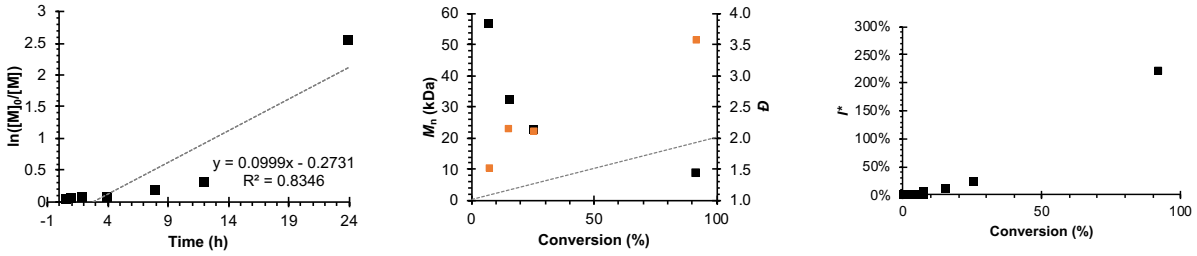

Figure 4.37. *eO-ATRP performed in a U-cell with 0.094 M $LiPF_6$ and 0.006 M LiBr supporting electrolyte. Conditions: 2 mL DMAc, 2 mL MMA, 17.9 µL DBMM, 1.8 mg **1**. Working electrode = glassy carbon rod, counter electrode = Pt wire, reference electrode = 0.01 M $AgNO_3$/Ag in MeCN with 0.1 M Bu_4NPF_6, $E_{app} = E_{1/2} - 120$ mV (~1% $PC^{\bullet+}$). Polymerization irradiated with a high-power white LED. Key: First order kinetics plot (left), molecular weight (black) and dispersity (orange) as a function of monomer conversion (center), and initiator efficiency as a function of monomer conversion (right).*

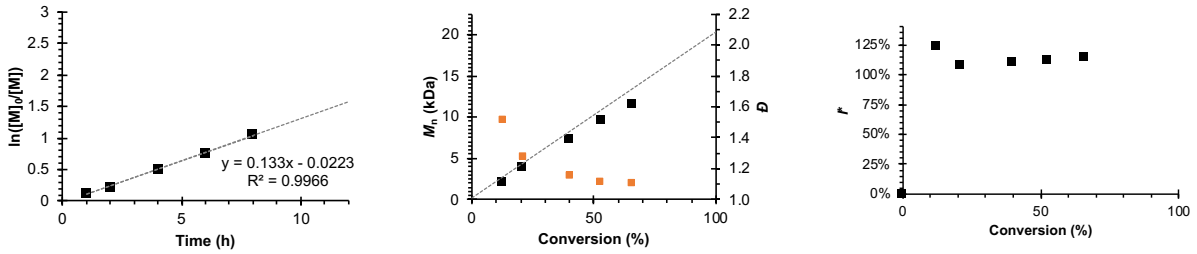

Figure 4.38. *O-ATRP performed in a 20 mL scintillation vial with 0.094 M $LiPF_6$ and 0.006 M LiBr supporting electrolyte. Conditions: 2 mL DMAc, 2 mL MMA, 17.9 µL DBMM, 1.8 mg* ***1****. Polymerization irradiated in a white LED beaker. Key: First order kinetics plot (left), molecular weight (black) and dispersity (orange) as a function of monomer conversion (center), and initiator efficiency as a function of monomer conversion (right).*

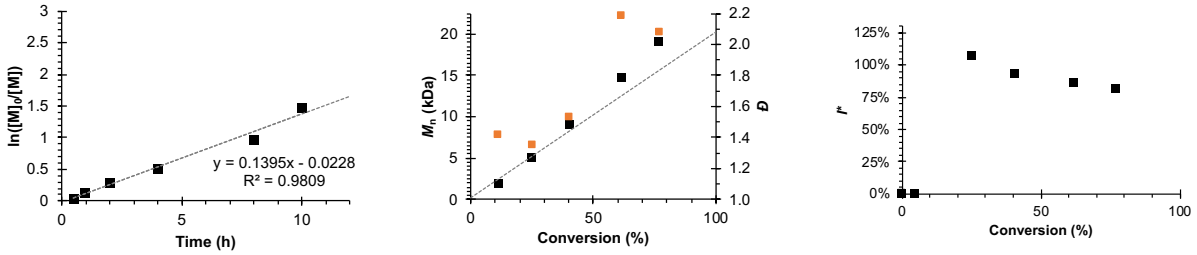

Figure 4.39. *eO-ATRP performed in a U-cell with 0.1 M $LiPF_6$ supporting electrolyte. Conditions: 2 mL DMAc, 2 mL MMA, 17.9 µL DBMM, 1.8 mg* ***1****. Working electrode = glassy carbon rod, counter electrode = Pt wire, reference electrode = 0.01 M $AgNO_3$/Ag in MeCN with 0.1 M Bu_4NPF_6, $E_{app} = E_{1/2} - 120$ mV (~1% $PC^{\bullet+}$). Polymerization irradiated with a high-power white LED. Key: First order kinetics plot (left), molecular weight (black) and dispersity (orange) as a function of monomer conversion (center), and initiator efficiency as a function of monomer conversion (right).*

Hypothesis 2: Oxidation of MMA at the Working Electrode

Hypothesis: MMA is oxidized at the working electrode to produce a reactive species that initiates undesired side reactions, leading to poor polymerization control.

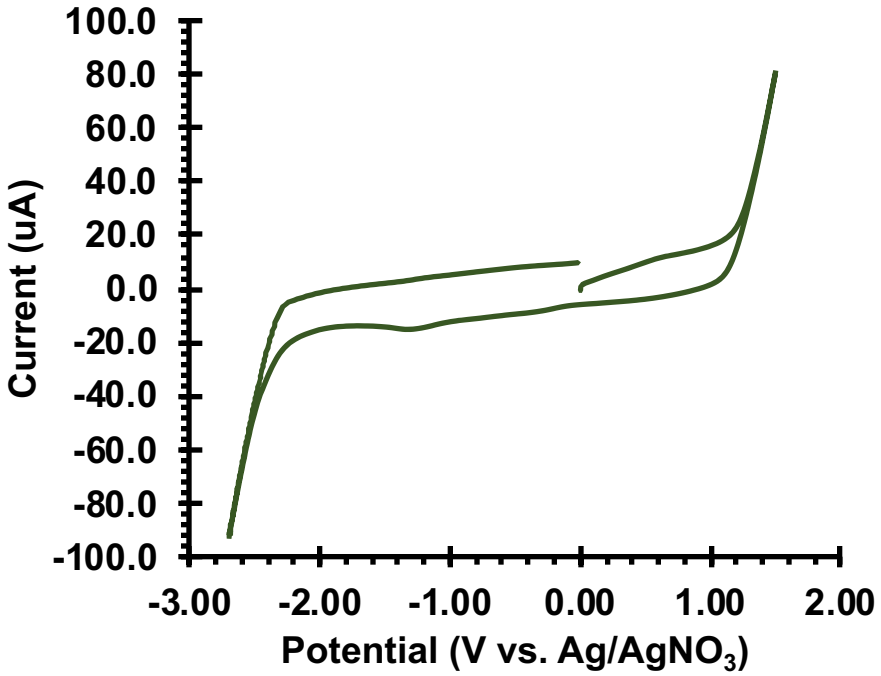

Figure 4.40. *Cyclic voltammogram of 50/50 (v/v) DMAc and MMA with 0.1 M Bu_4NPF_6 at a glassy carbon working electrode.*

Hypothesis 3: Oxidation of DBMM at the Working Electrode

Hypothesis: DBMM is oxidized at the working electrode to produce a reactive species that initiates undesired side reactions, leading to poor polymerization control.

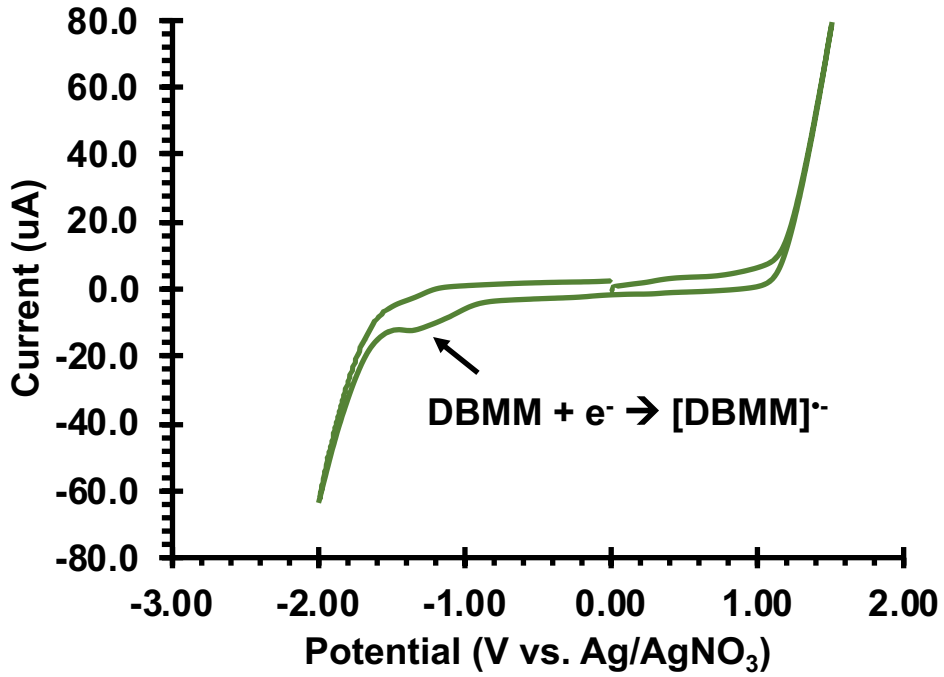

Figure 4.41. *Cyclic voltammogram of 13 mM DBMM in 50/50 (v/v) DMAc and MMA with 0.1 M* Bu_4NPF_6 *at a glassy carbon working electrode.*

Hypothesis 4: Bromide Oxidation at the Working Electrode

Hypothesis: Bromide is oxidized at the working electrode to produce a reactive species that initiates undesired side reactions, leading to poor polymerization control.

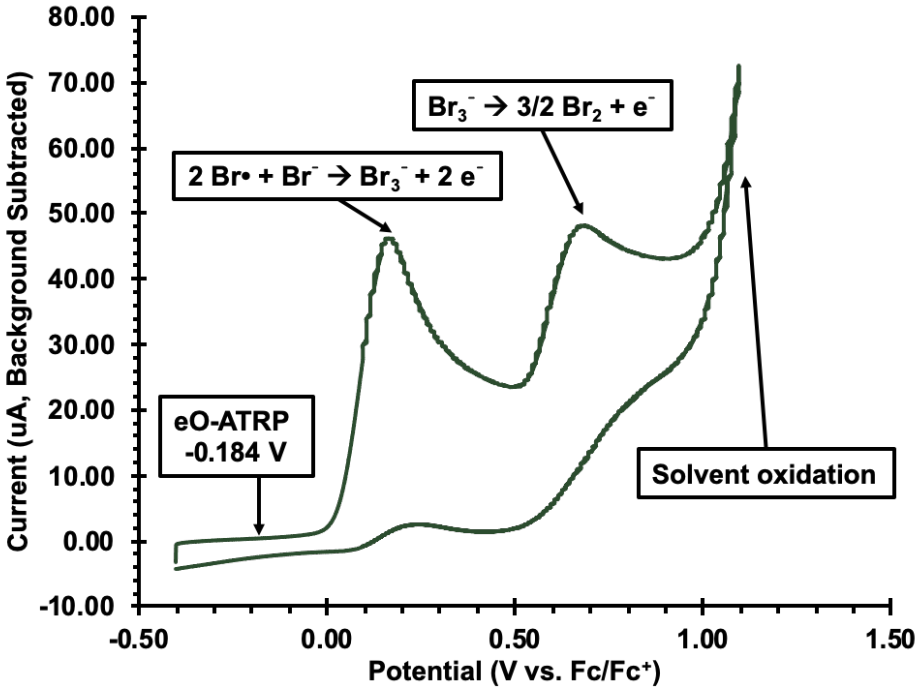

Figure 4.42. *Cyclic voltammogram bromide ion in 50/50 (v/v) DMAc and MMA with 0.1 M Bu_4NPF_6 (94%) and Bu_4NBr (6%) at a glassy carbon working electrode. Since the refence electrode used was a silver wire QRE, potentials are reported vs. the ferrocene/ferrocenium couple (Fc/Fc^+). For reference, eO-ATRP under these conditions is performed at -0.184 V, corresponding to $E_{1/2}(\mathbf{1}^{\bullet+}/\mathbf{1})$ – 120 mV.*

In addition to the electrochemical control shown above, a control reaction was performed to test whether bromide oxidation might cause an undesired polymerization at the relevant electrochemical potential for eO-ATRP. For this experiment, a typical polymerization solution was prepared in a U-cell with DMAc (2 mL), MMA (2 mL, 1000 eq, 18.7 mmol), DBMM (17.9 µL, 9.35 x 10^{-2} mmol, 5 eq), and supporting electrolyte (0.1 M Bu_4NPF_6 (94%) and Bu_4NBr (6%)). To prevent any undesired reactivity due to stray light entering the flask, no **1** was added to this solution. The cell was then kept in the dark and electrolysis (E_{app} = $E_{1/2}(\mathbf{1}^{\bullet+}/\mathbf{1})$ – 120 mV) commenced. After 24h, an aliquot of the reaction mixture was removed for ^{1}H NMR analysis. No monomer conversion was observed.

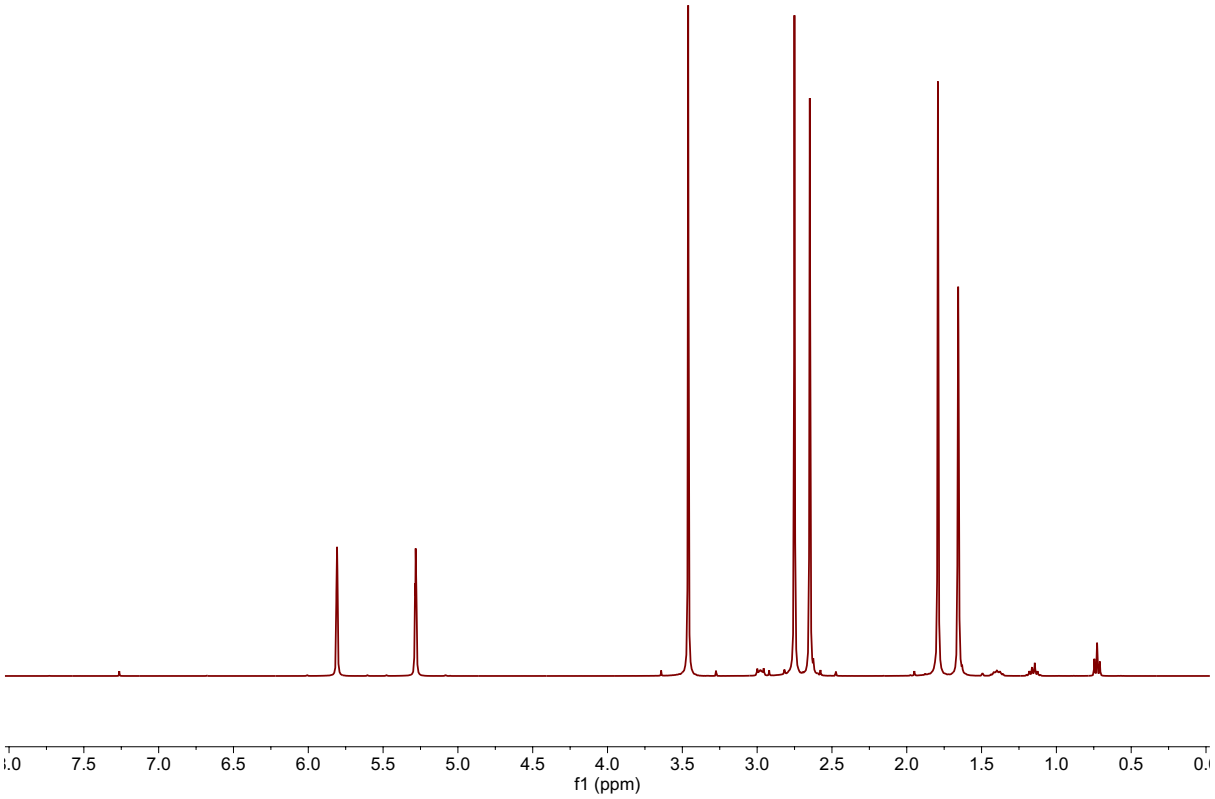

Figure 4.43. *^{1}H NMR of the control polymerization testing for the impact of bromide oxidation at 24 h of electrolysis.*

Hypotheses 5 – 7: Photoexcitation of the Radical Cation

Hypothesis: The radical cation of **1** is photoexcited to generate a strongly oxidizing state, which causes side reactivity by oxidizing either DMAc (hypothesis 5), the radical chain end (hypothesis 6), or bromide ion (hypothesis 7).

- Currently, no evidence exists to disprove the oxidation of DMAc or the radical chain end, though a kinetic argument can be used to eliminate oxidation of the chain end as a viable hypothesis (see main text).
- To test whether the oxidation of bromide could be problematic, the following experiment was devised (note that this experiment is not intended to shed light on what would cause

the bromide oxidation; it is simply meant to test whether the resulting bromine radical would initiate a polymer chain under relevant conditions):

For this experiment, a typical polymerization solution was prepared in a U-cell with DMAc (2 mL), MMA (2 mL, 1000 eq, 18.7 mmol), and supporting electrolyte (0.1 M Bu_4NPF_6 (94%) and Bu_4NBr (6%)). To prevent any undesired reactivity due to stray light entering the flask, no **1** was added to this solution. The cell was then kept in the dark and electrolysis (E_{app} = 1 V vs Ag wire QRE, ~ 0.1 V vs Fc/Fc^+) commenced. After 48h, an aliquot of the reaction mixture was removed for ^1H NMR analysis and the cell inspected. A white film was observed on the surface of the working electrode, and NMR analysis showed about 2% monomer conversion. Both samples were dried, dissolved in THF, and analyzed by GPC; the results are below.

Table 4.5. *Results from the control polymerization of MMA by electrolysis of bromide to make bromine radical.*

Sample	Time	Conv. (%)	M_n (kDa)	$Đ$
Aliquot[a]	48 h	2	24.4 47.7	1.23 1.39
Film	48 h	N/A	53.9	1.99

[a]*GPC results for this sample were multimodal, so analysis of all relevant peaks is reported.*

Hypothesis 8: Competitive Ion-Pairing

Hypothesis: Competitive ion pairing between Br^- and PF_6^- hinders formation of the proposed deactivating species $PC^{\bullet+}Br^-$. As a result, the rate of deactivation decreases, resulting in poor polymerization control.

To investigate the impact of the $LiPF_6$ supporting electrolyte on O-ATRP, a polymerization was carried out in the following manner. A 20 mL scintillation vial was charged with **1** (1.8 mg,

1.87 µmol, 0.1 eq) and a magnetic stir-bar. In a nitrogen filled glovebox, $LiPF_6$ (60.8 mg, 0.4 mmol, 0.1 M final concentration) was weighed into the vial, followed by the addition of DMAc (2 mL), MMA (2 mL, 18.7 mmol, 1000 eq), and DBMM (17.9 µL, 9.35 x 10^{-2} mmol, 5 eq). The reaction was then irradiated using a white LED beaker and aliquots removed periodically to monitor the progression of the polymerization.

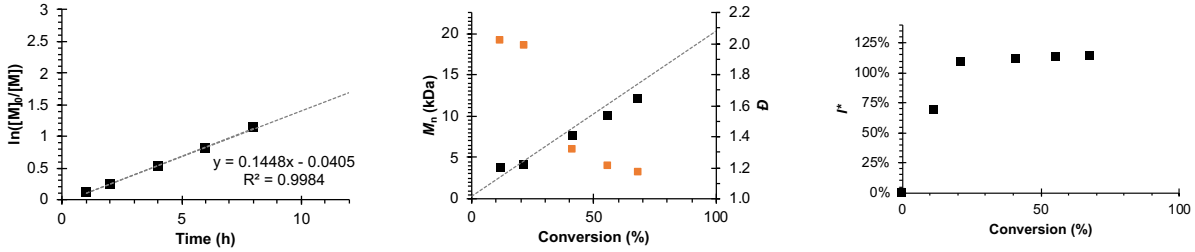

Figure 4.44. *Results of the O-ATRP of MMA in the presence of 0.1 M $LIPF_6$. Key: First order kinetics plot (left), molecular weight (black) and dispersity (orange) as a function of monomer conversion (center), and initiator efficiency as a function of monomer conversion (right).*

Hypothesis 9: Insufficient Separation of the Counter Electrode

Hypothesis: The glass frit separator in the U-cell is an insufficient barrier to prevent diffusion of reaction components towards the counter electrode on the timescale of a polymerization (~24h – 48h). As a result, key components, such as the PC or $PC^{\bullet+}$, undergo degradation at the counter electrode, resulting in poor control over the polymerization.

For reaction setup, see previous section - General Methods for Electrochemically Mediated O-ATRP (eO ATRP). In this experiment, a $Ag/AgNO_3$ reference electrode was used, and E_{app} = $E_{1/2}$ – 120 mV. Irradiation was carried out using an 80x40 light beaker with 9 LED segments.

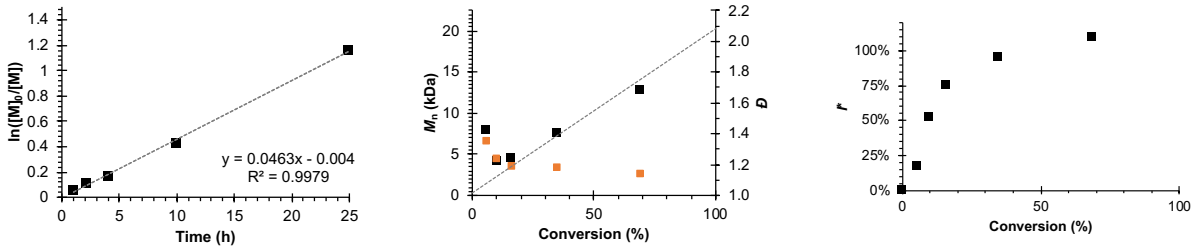

Figure 4.45. *Results of eO-ATRP of MMA using a new apparatus featuring separation of the counter electrode using a vycor glass frit. Key: First order kinetics plot (left), molecular weight (black) and dispersity (orange) as a function of monomer conversion (center), and initiator efficiency as a function of monomer conversion (right).*

Control Polymerizations

The following polymerizations were performed systematically eliminating one reaction component from eO-ATRP at a time to test the effect of each component on the overall reaction. For reaction setup, see previous section - General Methods for Electrochemically Mediated O-ATRP (eO ATRP). In each experiment below, a $Ag/AgNO_3$ reference electrode was used, and $E_{app} = E_{1/2} - 120$ mV. Irradiation was carried out using a white LED well (80 mm x 40 mm) with 9 LED segments.

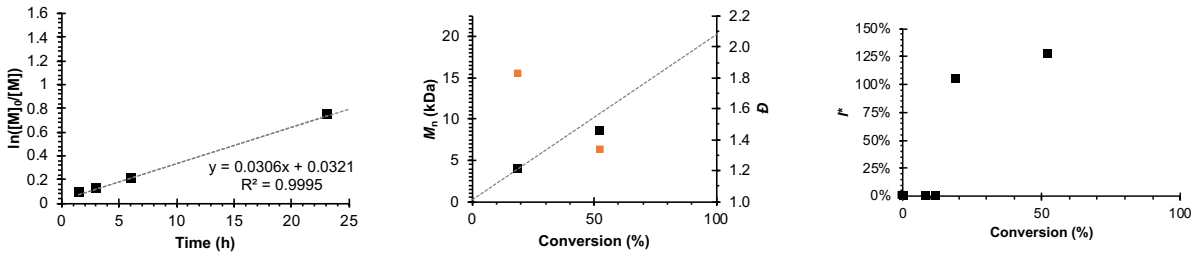

Figure 4.46. *Results of O-ATRP in the presence of 0.1 M $LiPF_6$ without electrolysis. Key: First order kinetics plot (left), molecular weight (black) and dispersity (orange) as a function of monomer conversion (center), and initiator efficiency as a function of monomer conversion (right).*

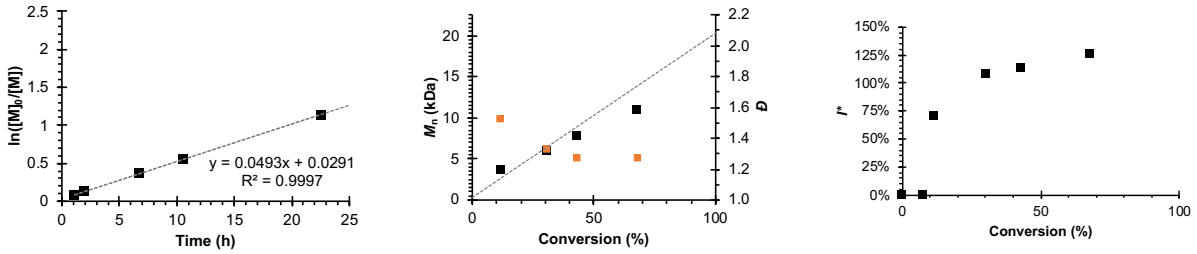

Figure 4.47. *Results of O-ATRP in a 5-neck pear flask without supporting electrolyte or electrolysis. Key: First order kinetics plot (left), molecular weight (black) and dispersity (orange) as a function of monomer conversion (center), and initiator efficiency as a function of monomer conversion (right).*

In addition to the experiments above, control reactions eliminating the PC, DBMM, light, and PC and light were carried out. The results of these experiments are provided in the main text.

Supplemental Polymerization Data

eO-ATRP Lighting Screen

For reaction setup, see previous section - General Methods for Electrochemically Mediated O-ATRP (eO ATRP). In each experiment below, a $Ag/AgNO_3$ reference electrode was used, and $E_{app} = E_{1/2} - 120$ mV. Irradiation was carried out using the setup described in the respective figure caption.

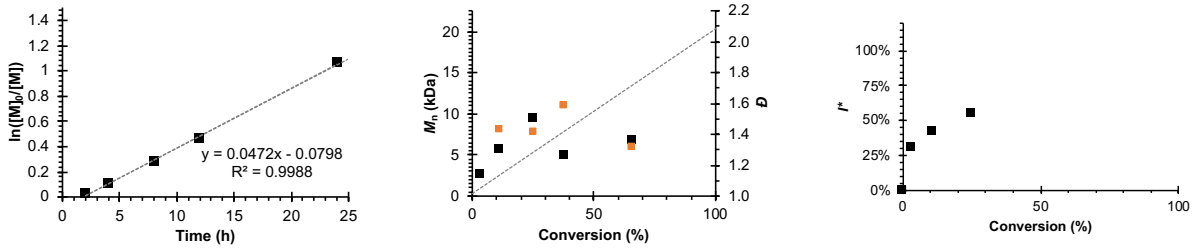

Figure 4.48. *Polymerization results from eO-ATRP of MMA using a 80x40 light well (9 LED segments) at 50% irradiation intensity, which was achieved by use of an in-line LED dimmer.[1] Key: First order kinetics plot (left), molecular weight (black) and dispersity (orange) as a function of monomer conversion (center), and initiator efficiency as a function of monomer conversion (right).*

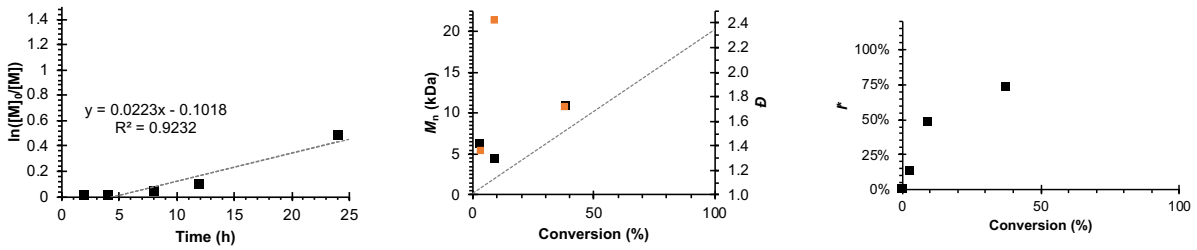

Figure 4.49. *Polymerization results from eO-ATRP of MMA using a 80x40 light well (9 LED segments) at 5% irradiation intensity, which was achieved by use of an in-line LED dimmer.[1] Key: First order kinetics plot (left), molecular weight (black) and dispersity (orange) as a function of monomer conversion (center), and initiator efficiency as a function of monomer conversion (right).*

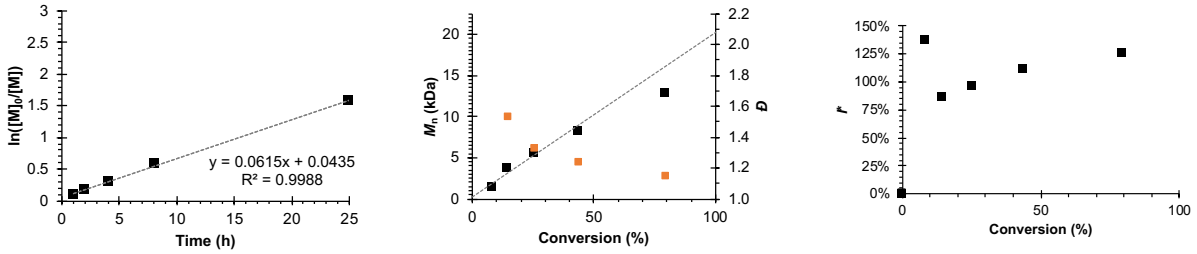

Figure 4.50. *Polymerization results from eO-ATRP of MMA using a 80x40 light well with a larger concentration of LEDs than used previously (15 LED segments) to test the impact of increased irradiation intensity. Key: First order kinetics plot (left), molecular weight (black) and dispersity (orange) as a function of monomer conversion (center), and initiator efficiency as a function of monomer conversion (right).*

Data from the three figures above is replotted below for more facile comparison of the data.

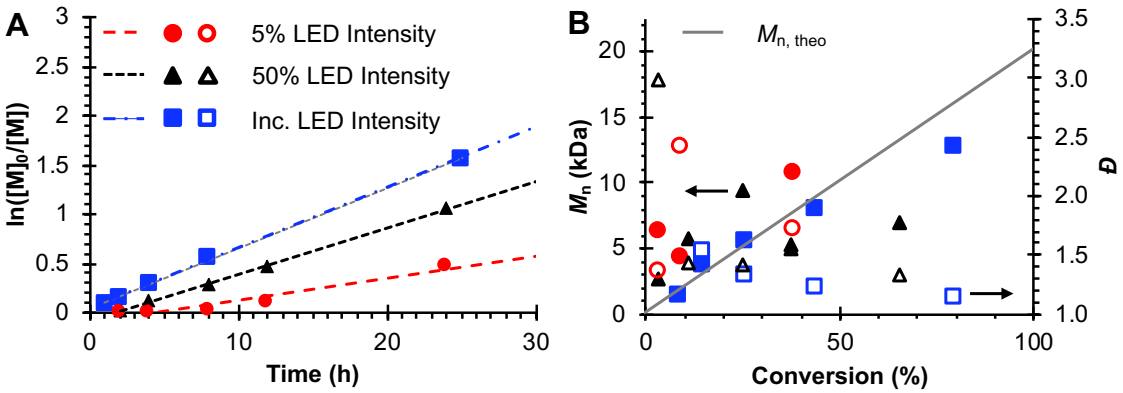

Figure 4.51. *Comparison of kinetics (A) as well as molecular weight (filled markers) and Đ (hollow markers) evolution (B) for eO-ATRP under irradiation of varying intensity (blue squares: increased intensity, black triangles: 50% intensity, red circles: 5% intensity). Conditions: [MMA]:[DBMM]:[**1**] = 1000:5:0.1, 2 mL MMA, 2 mL DMAc, supporting electrolyte = 0.1 M $LiPF_6$. Reactions performed in a 5-neck pear flask with working electrode = glassy carbon, counter electrode = Pt wire, reference electrode = $Ag/AgNO_3$, and $E_{app} = E_{1/2} - 120$ mV. See Experimental for irradiation conditions (section: eO-ATRP lighting screen).*

Table 4.6. *Results for eO-ATRP[a] performed under various light intensities. Entry 4 from Table C provided for comparison to eO-ATRP under normal irradiation conditions.*

Entry	LED Intensity[b]	Time (h)	Conv. (%)	$M_{n,\,theo}$ (kDa)	$M_{n,\,GPC}$ (kDa)	Đ[c]	I* (%)[d]
4	unchanged	25	69	14.0	12.8	1.17	110
S1	increased[e]	25	79	16.1	12.8	1.14	126
S2	50%[f]	24	66	13.4	6.88	1.32	194
S3	5%[f]	24	38	7.84	10.8	1.72	73

*[a]General conditions unless otherwise stated: [MMA]:[DBMM]:[**1**] = 1000:5:0.1, 2 mL MMA, 2 mL DMAc, SE = 0.1 M $LiPF_6$. Reactions performed in a 5-neck pear flask with working electrode = glassy carbon, counter electrode = Pt wire, reference electrode = $Ag/AgNO_3$, and $E_{app} = E_{1/2} - 120$ mV. [b]LED intensity relative to an 80mm x 40mm white LED well with 9 LED segments. [c]Calculated by M_w / M_n. [d]Calculated by $M_{n,\,theo} / M_{n,\,GPC}$. [e]Increased LED intensity achieved by lining an 80mm x 40mm white LED well with 15 LED segments. [f]Decreased LED intensity achieved by used of an in-line dimmer with an 80mm x 40mm white LED well (9 LED segments, see Experimental Equipment in Experimental).*

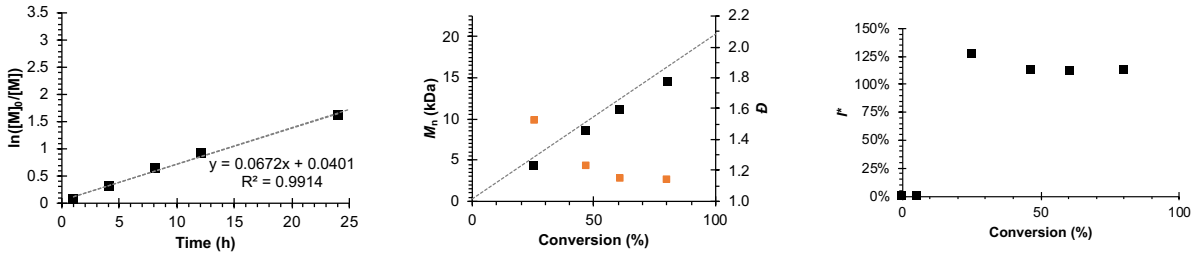

Figure 4.52. *Polymerization results from eO-ATRP of MMA using a 70x50 light well with the same number of LED segments (9 LED segments) to test the impact of having the LEDs closer to the reaction. Key: First order kinetics plot (left), molecular weight (black) and dispersity (orange) as a function of monomer conversion (center), and initiator efficiency as a function of monomer conversion (right).*

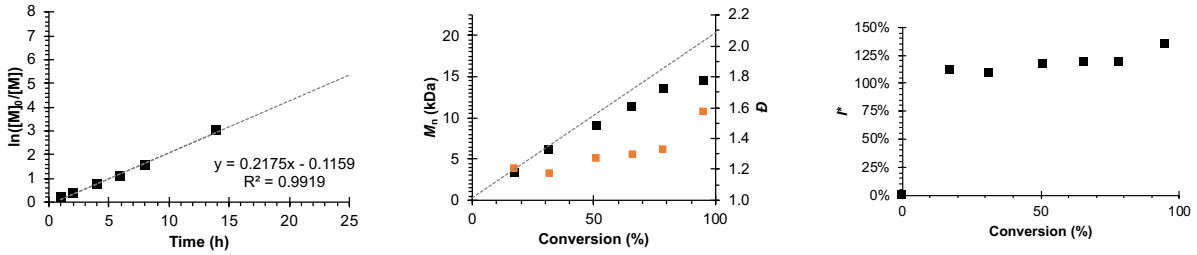

Figure 4.53. *Polymerization results from eO-ATRP of MMA using a high-power white LED reactor (see Experimental Equipment section) to test the impact of further increased irradiation intensity. Key: First order kinetics plot (left), molecular weight (black) and dispersity (orange) as a function of monomer conversion (center), and initiator efficiency as a function of monomer conversion (right).*

To investigate the impact of this new irradiation apparatus on O-ATRP in the absence of electrolysis, a control polymerization was carried out under the same conditions – in a 5-neck flask, using the same light reactor – but in the absence of the electrodes and applied electrochemical potential. To account for any effects that could be attributed to the supporting electrolyte, $LIPF_6$ (0.1 M) was added to this polymerization.

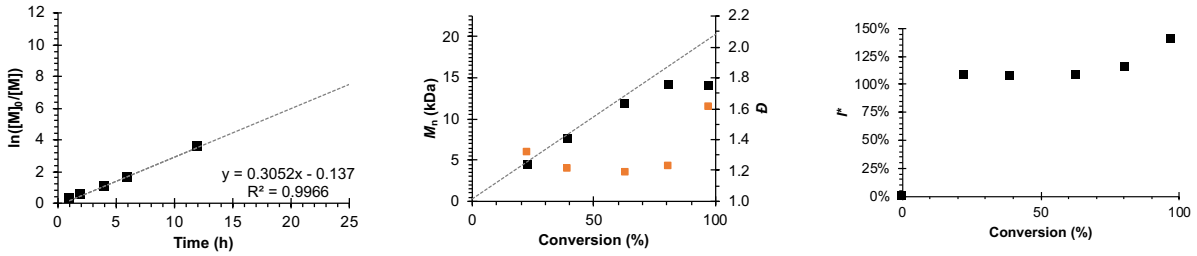

Figure 4.54. *Polymerization result from a control reaction (O-ATRP with 0.1 M $LIPF_6$) in the high-power LED reactor. Key: First order kinetics plot (left), molecular weight (black) and dispersity (orange) as a function of monomer conversion (center), and initiator efficiency as a function of monomer conversion (right).*

eO-ATRP At a More Oxidizing Potential

To investigate whether increasing the concentration of $PC^{\bullet+}$ improves polymerization control, eO-ATRP was performed at a more oxidizing potential: $E_{app} = E_{1/2} - 60$ mV, corresponding to ~10% radical cation relative to the total concertation of **1**. Irradiation was carried out using the high-power white LED apparatus.

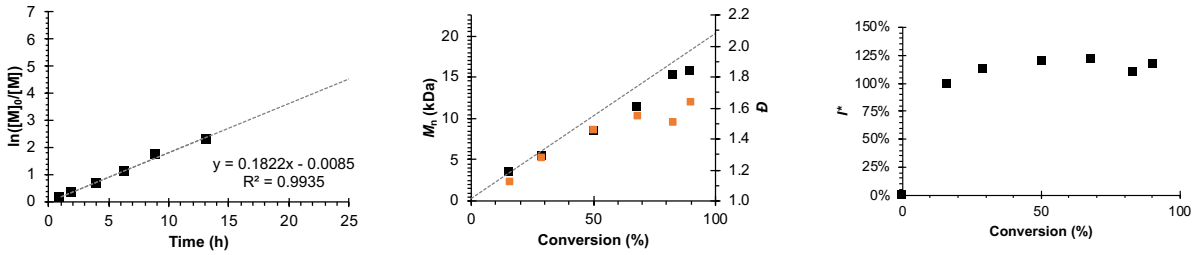

Figure 4.55. *Polymerization results for eO-ATRP of MMA carried out at a more oxidizing potential to further increase [$PC^{\bullet+}$]. Key: First order kinetics plot (left), molecular weight (black) and dispersity (orange) as a function of monomer conversion (center), and initiator efficiency as a function of monomer conversion (right).*

For facile comparison, the data in Figure 4.55 is replotted below with data for polymerizations under the same conditions but at a less oxidizing E_{app} and without electrolysis.

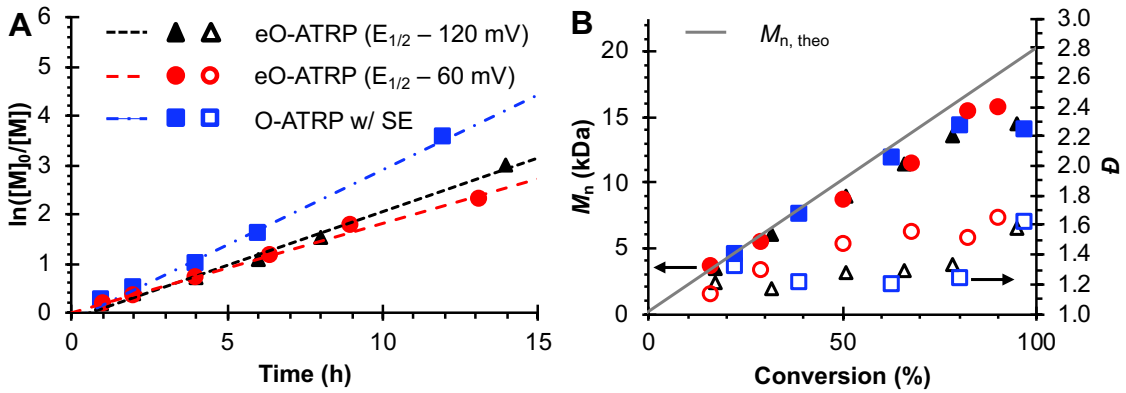

Figure 4.56. *Plot of the natural logarithm of monomer (M) consumption over time (A). Molecular weight (filled markers) and Đ (hollow markers) evolution (B) for eO-ATRP at two applied potentials (black triangles: $E_{app} = E_{1/2} - 120$ mV, red circles: $E_{app} = E_{1/2} - 60$ mV) and O-ATRP with supporting electrolyte (blue squares), all in a high-power light reactor. Conditions: [MMA]:[DBMM]:[**1**] = 1000:5:0.1, 2 mL MMA, 2 mL DMAc, SE = 0.1 M $LiPF_6$. Reactions performed in a 5-neck pear flask and irradiated with a high-power white LED (see Experimental Equipment in SI). For eO-ATRP, working electrode = glassy carbon, counter electrode = Pt wire, and reference electrode = $Ag/AgNO_3$.*

*Polymerizations with PC **2***

To understand if observations related to eO-ATRP are applicable to other PC families, eO-ATRP was performed with PC **2**. For general reaction setup, see previous section - General Methods for Electrochemically Mediated O-ATRP (eO ATRP). For eO-ATRP, a 5-neck pear flask apparatus was employed with a $Ag/AgNO_3$ reference electrode, and $E_{app} = E_{1/2} - 60$ mV. For O-ATRP in the presence of supporting electrolyte, a 5-neck pear flask was used without electrodes or an applied potential. Irradiation in both cases was carried out using an 80 mm x 40 mm white LED well with 9 LED segments. [MMA]:[DBMM]:[**2**] = 1000:5:1.

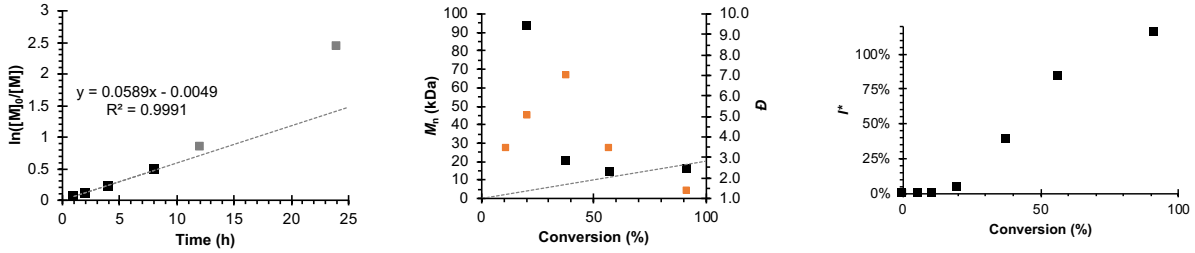

Figure 4.57. *Polymerization results from eO-ATRP of MMA using PC* ***6*** *with* $E_{app} = E_{1/2} - 60$ *mV. Key: First order kinetics plot (left), molecular weight (black) and dispersity (orange) as a function of monomer conversion (center), and initiator efficiency as a function of monomer conversion (right).*

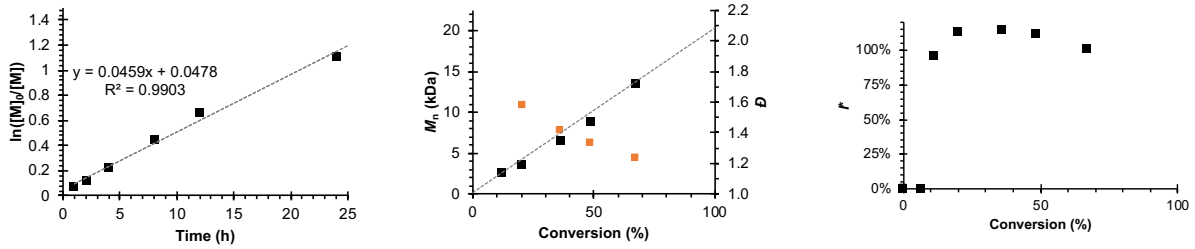

Figure 4.58. *Polymerization results from O-ATRP of MMA using PC* ***2*** *in the presence of 0.1 M* $LiPF_6$*. Key: First order kinetics plot (left), molecular weight (black) and dispersity (orange) as a function of monomer conversion (center), and initiator efficiency as a function of monomer conversion (right).*

eO-ATRP with a Chloride Supporting Electrolyte

To investigate the compatibility of eO-ATRP with a chloride supporting electrolyte, eO-ATRP was performed in the presence of 0.1 M tetra-n-butylammonium chloride (Bu_4NCl). For reaction setup, see previous section - General Methods for Electrochemically Mediated O-ATRP (eO ATRP). In this experiment, a 5-neck pear flask apparatus was employed, a $Ag/AgNO_3$ reference electrode was used, and $E_{app} = E_{1/2} - 120$ mV. Irradiation was carried out using an 80 mm x 40 mm white LED well with 9 LED segments.

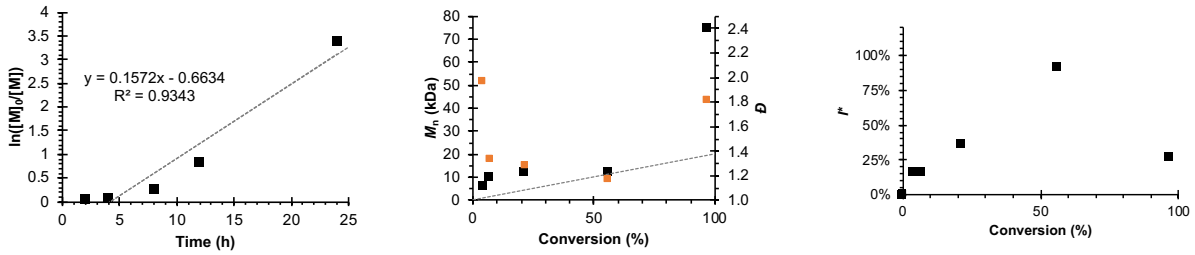

Figure 4.59. *Polymerization results from eO-ATRP of MMA where the supporting electrolyte is 0.1 M Bu_4NCl. Key: First order kinetics plot (left), molecular weight (black) and dispersity (orange) as a function of monomer conversion (center), and initiator efficiency as a function of monomer conversion (right).*

REFERENCES

(1) Miyake, G. M.; Theriot, J. C. *Macromolecules*, **2014**, *47*, 8255 – 8261.

(2) Treat, N. J.; Sprafke, H.; Kramer, J. W.; Clark, P. G.; Barton, B. E.; de Alaniz, J. R.; Fors, B. P.; Hawker, C. J. *J. Am. Chem. Soc.*, **2014**, *136*, 16096 – 16101.

(3) Theriot, J. C.; Lim, C.-H.; Yang, H.; Ryan, M. D.; Musgrave, C. B.; Miyake, G. M. *Science*, **2016**, *352*, 1082 – 1086.

(4) Pearson, R. M.; Lim, C.-H.; McCarthy, B. G.; Musgrave, C. B.; Miyake, G. M. *J. Am. Chem. Soc.*, **2016**, *138*, 11399 – 11407.

(5) Pan, X. C.; Fang, C.; Fantin, M.; Malhotra, N.; So, W. Y.; Peteanu, L. A.; Isse, A. A.; Gennaro, A.; Liu, P.; Matyjaszewskit, K. *J. Am. Chem. Soc.*, **2016**, *138*, 2411 – 2425.

(6) Theriot, J. C.; McCarthy, B. G.; Lim, C.-H.; Miyake,G. M. *Macromol. Rapid Commun.*, **2017**, *38*, 1700040.

(7) Discekici, E. H.; Anastasaki, A.; de Alaniz, J. R.; Hawker, C. J. *Macromolecules*, **2018**, *51*, 7421 – 7434.

(8) G. Yilmaz, G.; Yagci, Y. *Polym. Chem.,* **2018**, *9*, 1757 – 1762.

(9) Corrigan, N.; Shanmugam, S.; Xu, J. T.; Boyer, C. *Chem. Soc. Rev.*, **2016**, *45*, 6165 – 6212.

(10) Chen, M.; Zhong, M. J.; Johnson, J. A. *Chem. Rev.*, **2016**, *116*, 10167 – 10211.

(11) Pan, X. C.; Lamson, M.; Yan, J. J.; Matyjaszewski, K. *ACS Macro Lett.*, **2015**, *4*, 192 – 196.

(12) Dadashi-Silab, S.; Pan, X. C.; Matyjaszewski, K. *Chem. Eur. J.*, **2017**, *23*, 5972 – 5977.

(13) Ryan, M. D.; Theriot, J. C.; Lim, C.-H.; Yang, H. S.; Lockwood, A. G.; Garrison, N. G.; Lincoln, S. R.; Musgrave, C. B.; Miyake, G. M. *J. Polym. Sci., Part A: Polym. Chem.*, **2017**, *55*, 3017 – 3027.

(14) Singh, V. K.; Yu, C.; Badgujar, S.; Kim, Y.; Kwon, Y.; Kim, D.; Lee, J.; Akhter, T.; Thangavel, G.; Park, L. S.; Nandajan, P. C.; Wannemacher, R.; Milian-Medina, B.; Luer, L.; Kim, K. S.; Gierschner, J.; Kwon, M. S. *Nat. Catal.*, **2018**, *1*, 794 – 804.

(15) McCarthy, B. G.; Pearson, R. M.; Lim, C.-H.; Sartor, S. M.; Damrauer, N. H.; Miyake, G. M. *J. Am. Chem. Soc.*, **2018**, *140*, 5088 – 5101.

(16) Cole, J. P.; Federico, C. R.; Lim, C.-H.; Miyake, G. M. *Macromolecules*, **2019**, *52*, 747 – 754.

(17) Buss, B. L.; Lim, C.-H.; Miyake, G. M. *Angew. Chem. Int. Ed.*, **2020**, *59*, 3209.

(18) Buss, B. L.; Beck, L. R.; Miyake, G. M. *Polym. Chem.*, **2018**, *9*, 1658 – 1665.

(19) Zhao, Y. C.; Gong, H. H.; Jiang, K. M.; Yan, S. J.; Lin, J.; Chen, M. *Macromolecules*, **2018**, *51*, 938 – 946.

(20) Discekici, E. H.; Pester, C. W.; Treat, N. J.; Lawrence, I.; Mattson, K. M.; Narupai, B.; Toumayan, E. P.; Luo, Y. D.; McGrath, A. J.; Clark, P. G.; de Alaniz, J. R.; Hawker, C. J. *ACS Macro Lett.*, **2016**, *5*, 258 – 262.

(21) Tan, S. B.; Xiong, J.; Zhao, Y. F.; Liu, J. J.; Zhang, Z. C. *J. Mater. Chem. C*, **2018**, *6*, 4131 – 4139.

(22) Lim, C.-H.; Ryan, M. D.; McCarthy, B. G.; Theriot, J. C.; Sartor, S. M.; Damrauer, N. H.; Musgrave, C. B.; Miyake, G. M. *J. Am. Chem. Soc.*, **2017**, *139*, 348 – 355.

(23) Sartor, S. M.; Lattke, Y. M.; McCarthy, B. G.; Miyake, G. M.; Damrauer, N. H. *J. Phys. Chem. A*, **2019**, *123*, 4727 – 4736.

(24) Koyama, D.; Dale, H. J. A.; Orr-Ewing, A. J. *J. Am. Chem. Soc.*, **2018**, *140*, 1285 – 1293.

(25) Jockusch, S.; Yagci, Y. *Polym. Chem.*, **2016**, *7*, 6039 – 6043.

(26) Carmean, R. N.; Becker, T. E.; Sims, M. B.; Sumerlin, B. S. *Chem*, **2017**, *2*, 93 – 101.

(27) Xu, J. T.; Jung, K.; Atme, A.; Shanmugam, S.; Boyer, C. *J. Am. Chem. Soc.*, **2014**, *136*, 5508 – 5519.

(28) Gong, H. H.; Gu, Y.; Zhao, Y. C.; Quan, Q. Z.; Han, S. T.; Chen, M. *Angew. Chem. Int. Ed.*, **2020**, *59*, 919 – 927.

(29) Mueller, L.; Jakubowski, W.; Matyjaszewski, K.; Pietrasik, J.; Kwiatkowski, P.; Chaladaj, W.; Jurczak, J. *Eur. Polym. J.*, **2011**, *47*, 730 – 734.

(30) Percec, V.; Guliashvili, T.; Ladislaw, J. S.; Wistrand, A.; Stjerndahl, A.; Sienkowska, M. J.; Monteiro, M. J.; Sahoo, S. *J. Am. Chem. Soc.*, **2006**, *128*, 14156 – 14165.

(31) Rzayev, J.; Penelle, J. *Angew. Chem. Int. Ed.*, **2004**, *43*, 1691 – 1694.

(32) Matyjaszewski, K. *Adv. Mater.*, **2018**, *30*, 22.

(33) Magenau, A. J. D.; Strandwitz, N. C.; Gennaro, A.; Matyjaszewski, K. *Science*, **2011**, *332*, 81 – 84.

(34) Park, S.; Chmielarz, P.; Gennaro, A.; Matyjaszewski, K. *Angew. Chem. Int. Ed.*, **2015**, *54*, 2388 – 2392.

(35) Li, B.; Yu, B.; Huck, W. T. S.; Liu, W. M.; Zhou, F. *J. Am. Chem. Soc.*, **2013**, *135*, 1708 – 1710.

(36) Fantin, M.; Isse, A. A.; Venzo, A.; Gennaro, A.; Matyjaszewski, K. *J. Am. Chem. Soc.*, **2016**, *138*, 7216 – 7219.

(37) Wang, J. R.; Tian, M. Y.; Li, S. Q.; Wang, R.; Du, F. P.; Xue, Z. G. *Polym. Chem.*, **2018**, *9*, 10.

(38) Du, Y.; Pearson, R. M.; Lim, C.-H.; Sartor, S. M.; Ryan, M. D.; Yang, H. S.; Damrauer, N. H.; Miyake, G. M. *Chem. Eur. J.*, **2017**, *23*, 10962.

(39) Dahm, C. E.; Peters, D. G. *J. Electroanal. Chem.*, **1996**, *402*, 91 – 96.

(40) Popov, A. I.; Geske, D. H. *J. Am. Chem. Soc.*, **1958**, *80*, 1340 – 1352.

(41) Zittel, H. E.; Miller, F. J. *Anal. Chim. Acta*, **1967**, *37*, 141 – 150.

(42) Iwasita, T.; Giordano, M. C. *Electrochim. Acta*, **1969**, *14*, 1045 – 1059.

(43) Allen, G. D.; Buzzeo, M. C.; Villagran, C.; Hardacre, C.; Compton, R. G. *J. Electroanal. Chem.*, **2005**, *575*, 311 – 320.

(44) Mousavi, M. P. S.; Saba, S. A.; Anderson, E. L.; Hillmyer, M. A.; Buhlmann, P. *Anal. Chem.*, **2016**, *88*, 8706 – 8713.

(45) Frit Porosity and Sizes, https://adamschittenden.com/technical/frits/frit-size#EuroPorosities, (accessed April 2020).

(46) Hoffman, R.; Minkin, V. I.; Carpenter, B. K. *International Journal for Philosophy of Chemistry*, **1997**, *3*, 3 – 28.

(47) Ryan, M. D.; Pearson, R. M.; French, T. A.; Miyake, G. M. *Macromolecules*, **2017**, *50*, 4616 – 4622.

(48) Kudisch, M.; Lim, C.-H.; Thordarson, P.; Miyake, G. M. *J. Am. Chem. Soc.* **2019**, *141*, 19479.

(49) Specifications Sheet for LZ4-00B208 457 nm LED, https://www.osram.us/ledengin/products/luxigen/lz4.jsp, (Accessed April 2020).

CHAPTER 5.

RADICAL CATIONS OF PHENOXAZINE AND DIHYDROPHENAZINE PHOTOREDOX CATALYSTS AND THEIR ROLE AS DEACTIVATORS IN ORGANOCATALYZED ATOM TRANSFER RADICAL POLYMERIZATION

Overview

Radical cations of photoredox catalysts used in organocatalyzed atom transfer radical polymerization (O-ATRP) have been synthesized and investigated to gain insight into deactivation in O-ATRP. The stability and reactivity of these compounds were studied in two solvents, *N,N*-dimethylacetamide and ethyl acetate, to identify possible side reactions in O-ATRP and to investigate the ability of these radical cations to deactivate alkyl radicals. A number of other factors that could influence deactivation in O-ATRP were also probed, such as ion pairing with the radical cations, radical cation oxidation potential, and halide oxidation potential. Ultimately, these studies enabled radical cations to be employed as reagents during O-ATRP to demonstrate improvements in polymerization control with increasing radical cation concentration. In the polymerization of acrylates, this approach enabled superior molecular weight control, a decrease in polymer dispersity from 1.90 to 1.44, and an increase in initiator efficiency from 78% to 102%. This work highlights the importance of understanding the mechanism and side reactions of O-ATRP, as well as the importance of catalyst radical cations for successful O-ATRP.

Introduction

The development of polymerization methods that exhibit precise control over polymer molecular weight, dispersity ($Đ$), and structure has long been a focus of polymer chemistry.[1-4]

Early examples of controlled polymerizations – also referred to as "living" polymerizations – were technically challenging to execute and required demanding reaction conditions,[5] limiting their broad utility. However, with the advent of controlled radical polymerization (CRP) methods,[6-9] precision polymer synthesis has become more powerful and accessible. One recently developed CRP is organocatalyzed atom transfer radical polymerization (O-ATRP), which employs organic photoredox catalysts (PCs) to synthesize well defined polymers under mild, metal-free conditions.[10, 11]

Similar to traditional atom transfer radical polymerization (ATRP) methods,[12-14] O-ATRP controls polymer growth through a reversible deactivation mechanism (Figure 5.1a). During this process, the PC activates a "dormant" polymer possessing a terminal C-Br bond by reduction of the polymer chain-end, generating a carbon centered radical capable of propagation as well as Br^- and the PC radical cation ($PC^{\bullet+}$). As with all radical polymerizations, the propagating radical is susceptible to irreversible termination by reaction with other radicals in solution. As such, a key feature of O-ATRP is reversible deactivation, wherein the $PC^{\bullet+}$ mediates reinstallation of Br on the polymer chain-end to lower the concentration of radicals in solution. Macroscopically, this process minimizes irreversible termination reactions while allowing the polymer chain to be reactivated for subsequent chain growth, enabling control over the polymer structure.

While O-ATRP retains many of the advantages of traditional ATRP as well as some added benefits, such as mild and metal-free reaction conditions, it remains relatively limited in monomer scope and mechanistic understanding. Previously, limitations in monomer scope have generally been addressed through the development of new catalysts. For example, Matyjaszewski extended the scope of O-ATRP from methacrylates to acrylonitrile by developing new phenothiazine

catalysts,[15] although phenyl phenothiazine – first reported by Hawker for the O-ATRP of methacrylates[11] – exhibited the best performance.[15] The development of dihydrophenazine[16] and

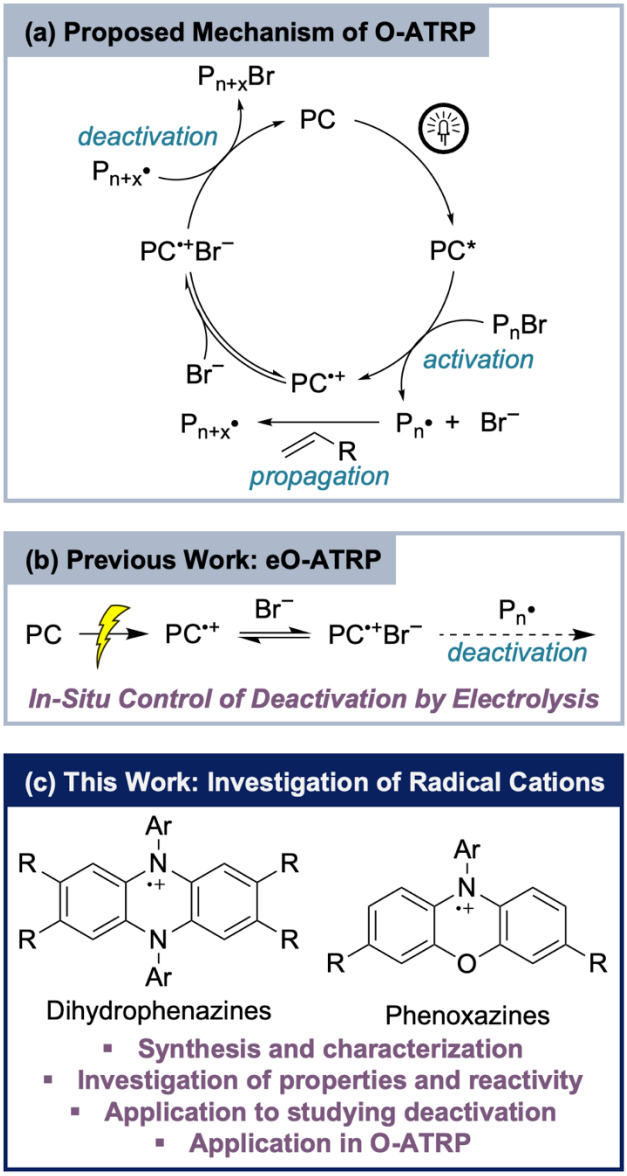

Figure 5.1. *A proposed mechanism of O-ATRP (a) and previous work to improve deactivation during O-ATRP (b). This work (c) aims to develop a better understanding of deactivation, the species involved in this step, and how they can be used to improve polymerization control in O-ATRP.*

phenoxazine[17] catalysts ultimately led to the controlled polymerization of vinylcyclopropanes with tunable polymer backbone composition.[18] Through further development of the dihydrophenazine

family, the controlled polymerizations of styrene[19] and various acrylates[20] were achieved. Finally, the first example of the controlled polymerization of acrylate monomers *via* O-ATRP came through the introduction of dihydroacridine catalysts in 2020, which feature strongly oxidizing radical cations [$E^o(PC^{\bullet+}/PC)$] capable of controlling the fast propagation of acrylates through deactivation.[21]

In an alternative approach, we recently reported the first application of electrolysis in O-ATRP in an attempt to gain external control of deactivation during a polymerization.[22] We reasoned that applying an oxidizing electrochemical potential to a polymerization solution would increase the concentration of the PC radical cation ($PC^{\bullet+}$), which would in turn lead to improved deactivation and polymerization control during O-ATRP (Figure 5.1b). While this hypothesis was ultimately supported, this work highlighted limitations in our understanding of the mechanism of this method, and it inspired new questions to guide future experimentation. Namely, is $PC^{\bullet+}$ the deactivator in O-ATRP, does $PC^{\bullet+}$ engage in side-reactions that inhibit deactivation, and what factors influence the ability of a $PC^{\bullet+}$ to effectively mediate deactivation?[22] In other words, this work highlighted the necessity of furthering our mechanistic understanding of O-ATRP.

Although several investigations of the O-ATRP mechanism have been previously reported, the majority of these reports focus on activation[23-26] and the impact of PC photophysics on this step.[27-29] With regards to deactivation, only a handful of reports exist,[26, 30] despite this step being critical to polymerization control. Further, these investigations relied primarily on computational methods rather than experimental evidence to probe the mechanism of deactivation[26] and impact of ion pairing[30] in this process. While the results of these studies were certainly informative and served as useful guides for future development, experimental investigation of the deactivation process and methods to manipulate this process are still needed.

In the present work (Figure 5.1c), we attempt to address these limits in our understanding of deactivation in O-ATRP through investigation PC radical cations – the key catalytic species we propose mediate this process. To do so, several radical cations of O-ATRP PCs are synthesized and characterized for the first time. Through investigation of the reactivity of these compounds, new side reactions are identified that can inhibit deactivation in O-ATRP. Further, through development of a deactivation model reaction, evidence is found supporting the role of $PC^{\bullet+}Br^-$ as the deactivator, and factors influencing this process are identified. The most notable factors include the radical cation oxidation potential [$E^o(PC^{\bullet+}/PC)$] and the oxidation potential of the halide [$E^o(X\bullet/X^-)$], both of which can directly impact the rate of deactivation. By investigating ion pairing with $PC^{\bullet+}$, it is found that the choice of reaction solvent is far more influential than $PC^{\bullet+}$ structure for the formation of a $PC^{\bullet+}$ ion pair. Finally, by employing an isolated radical cation in O-ATRP, it is demonstrated that these compounds can be used to improve polymerization control, further supporting their role in deactivation. Altogether, this work highlights the utility of PC radical cations in O-ATRP, as well as the importance of mechanistic understanding for the continued development of O-ATRP.

Results and Discussion

Synthesis and characterization of radical cations.

Synthesis. Radical cations of **1** – **11** (Figure 5.2a) were synthesized using nitrosonium hexafluorophosphate, as the oxidation potential of NO^+ is more than sufficient to oxidize **1** – **11** [$E^o(NO^+/NO)$ = 1.25 V,[31] $E_{1/2} \sim E^o(PC^{\bullet+}/PC)$ = 0.14 to 0.73 V, both vs saturated calomel electrode (SCE) in MeCN]. Since the byproduct of this reaction is $NO_{(g)}$, the product can be easily isolated by precipitation and washing with hexanes. For PCs **1** – **5**, it should be noted that the cyclic

voltammograms in MeCN exhibit two reversible oxidations that could be accessible using $NOPF_6$ (see Section 3 of *Experimental*). As such, precise stoichiometry is necessary to avoid

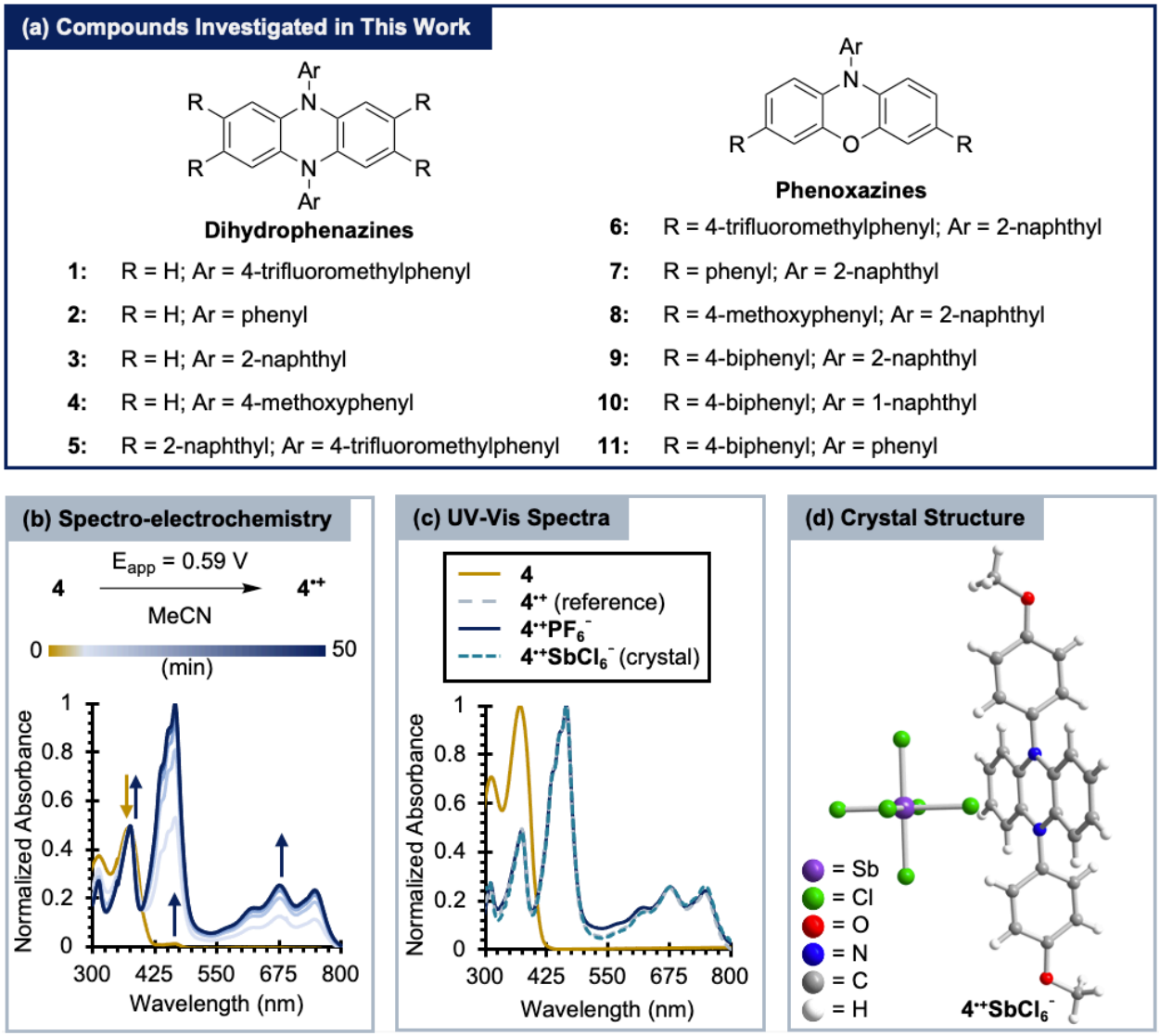

Figure 5.2. *(a) Structures of photoredox catalysts studied in this work. (b) Representative example of radical cation spectra obtained by spectro-electrochemistry in acetonitrile. (c) Representative comparison of UV-Vis spectra for a PC (solid, yellow), the $PC^{\bullet+}$ obtained by spectro-electrochemistry (dashed, light blue), $PC^{\bullet+}PF_6^-$ (solid, dark blue), and a redissolved $PC^{\bullet+}SbCl_6^-$ crystal (dashed, teal). (d) Crystal structure of a phenazine radical cation (solvent molecule removed for clarity).*

overoxidation of these compounds to the dicationic species. For crystallography, crystal growth was attempted using various methods with a range of $PC^{\bullet+}PF_6^-$ salts. However, crystals of these

compounds suitable for single crystal x-ray diffractometry (SCXRD) could not be obtained. Given the large size of the radical cations, we envisioned the PF_6^- anion might be too small to enable effective crystal packing and that a larger counter ion might be beneficial. As such, radical cations for SCXRD analysis were synthesized using tris(4-bromophenyl)ammoniumyl hexachloroantimonate, yielding $\mathbf{4^{\bullet+}SbCl_6^-}$ and $\mathbf{9^{\bullet+}SbCl_6^-}$. In both cases, crystallization by vapor diffusion (see Section 2 of *Experimental* for details) gave needles of suitable quality for x-ray diffraction studies.

Spectroscopic Characterization. To verify the identity of each $PC^{\bullet+}$, absorption spectra of the isolated compounds were compared to $PC^{\bullet+}$ spectra obtained using spectro-electrochemistry (Figure 5.2b). The spectra of the isolated compounds were found to agree well with the reference spectra (Figure 5.2c), supporting the successful synthesis of each $PC^{\bullet+}$. In addition, the spectra of $\mathbf{4^{\bullet+}PF_6^-}$ and $\mathbf{4^{\bullet+}SbCl_6^-}$ were nearly identical, suggesting the identity of the counter anion has a negligible impact on the spectroscopic properties of the radical cation.

Since crystals of $\mathbf{4^{\bullet+}SbCl_6^-}$ and $\mathbf{9^{\bullet+}SbCl_6^-}$ were obtained and analyzed by SCXRD to determine their crystal structures (see *Crystallography* below), we wondered if the solid-state spectra of these compounds would match their solution spectra. Unfortunately, the crystals obtained were insufficiently transparent to obtain well resolved absorption spectra in the solid state, so this comparison could not be made. Instead, the crystals were redissolved in MeCN and their spectra measured in solution (Figure 5.2c). The agreement of these spectra and the $PC^{\bullet+}PF_6^-$ spectra further support the identity of the $PC^{\bullet+}$ salts.

Electrochemical Characterization. For each of the radical cations synthesized, estimates of their purities were obtained by measurement of their open circuit potentials (E_{ocp}) in MeCN.

According to the Nernst Equation (Eq. 5.1), the E_{ocp} of a $PC^{\bullet+}$ solution is dependent on the $E_{1/2}$ of the redox couple and the relative quantities of PC and $PC^{\bullet+}$.

$$E_{ocp} = E_{1/2} + \frac{RT}{F} ln \left(\frac{[PC^{\cdot+}]}{[PC]} \right) \quad \text{(Eq. 5.1)}$$

Where R is the ideal gas constant, T is the absolute temperature, and F is Faraday's constant. Rearranging this equation, an expression giving the ratio of $PC^{\bullet+}$ to PC based on the E_{ocp} and $E_{1/2}$ can be written (Eq. 5.2). Using Eq. 5.2, the purity of each $PC^{\bullet+}PF_6^-$ salt was estimated to be ~ 97% or greater. To verify the accuracy of this method, elemental analysis was also performed for $\mathbf{11^{\bullet+}PF_6^-}$, which agreed well with the calculated elemental composition of this compound (see *Experimental*).

$$\frac{[PC^{\cdot+}]}{[PC]} = e^{\frac{F(E_{ocp} - E_{1/2})}{RT}} \quad \text{(Eq. 5.2)}$$

<u>*Crystallography.*</u> Single crystal x-ray diffractometry was performed using crystals obtained for $\mathbf{4^{\bullet+}SbCl_6^-}$ (Figure 5.2d) and $\mathbf{9^{\bullet+}SbCl_6^-}$. In each case, the $\mathbf{SbCl_6^-}$ anion was found centered above the aromatic core of the $PC^{\bullet+}$, and the $PC^{\bullet+}$ was found to co-crystallize with one equivalent of solvent molecule (Figures 5.65 and 5.66 in *Experimental* section). While $\mathbf{4^{\bullet+}SbCl_6^-}$ exhibited minimal disorder and was easily refined, $\mathbf{9^{\bullet+}SbCl_6^-}$ exhibited significant disorder that had to be modeled during refinement. Namely, the 2-naphthyl ring at the *N*-aryl position was disordered over two positions, presumably because the substituent can rotate about the C-N bond. In both cases, the refined crystal structures matched the structures anticipated for the radical cations. Combined with the spectroscopic data presented above, these data provide further support for the identities of these $PC^{\bullet+}$ salts.

<u>*Stability of radical cations in solution.*</u> During initial work with these compounds, it was noticed that the stability of $PC^{\bullet+}$ in solution was strongly dependent on solvent. To understand the

factors influencing the stability of $PC^{\bullet+}$, a series of experiments was performed to follow the decomposition of $PC^{\bullet+}$ using UV-Vis spectroscopy in solvents relevant to O-ATRP. Since it was previously observed that dihydrophenazine PCs can undergo side reactions to be substituted at the PC core,[20] $\mathbf{5}^{\bullet+}$ was primarily used for these investigations as its core positions are protected by 2-naphthyl substituents.

In *N,N*-dimethylacetamide (DMAc), decomposition of $\mathbf{5}^{\bullet+}$ was observed with and without irradiation (Figure 5.3). Following the kinetics of these reactions by UV-Vis revealed the decomposition reaction is accelerated by irradiation with white light (Figures 5.67 – 5.69 in *Experimental* section) and exhibits pseudo-first-order kinetics in the dark (k_{obs} = 0.00064 M^{-1} s^{-1}) and under irradiation (k_{obs} = 0.39 M^{-1} s^{-1}). The observed increase in the rate of $\mathbf{5}^{\bullet+}$ disappearance with light suggests the possibility of excited state reactivity, which has previously been observed for similar radical cations with electron rich substrates tethered at the *N*-aryl position.[32] By contrast, $\mathbf{5}^{\bullet+}$ exhibited excellent stability in ethyl acetate (EtAc) regardless of irradiation (Figures 5.76 – 5.78 in *Experimental* section).

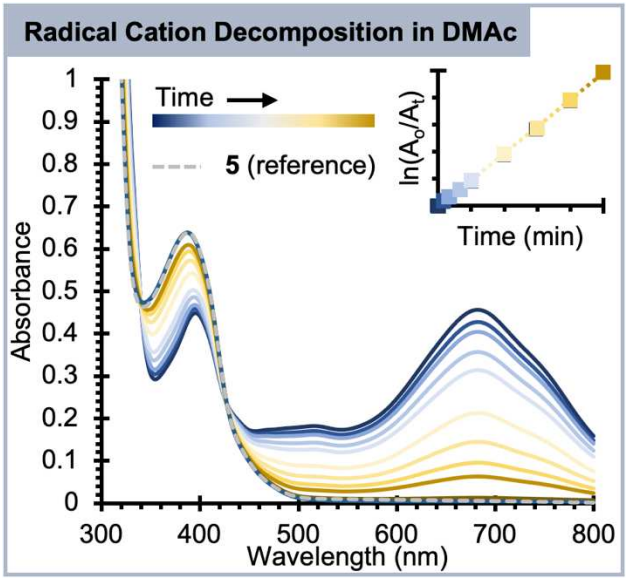

Figure 5.3. *Representative example of UV-Vis spectra following the disappearance of* ***5***$^{\bullet+}$ *in DMAc under irradiation with a white LED. Figure inset shows linear pseudo-first-order kinetics following the absorption at the* λ_{max} *= 682 nm.*

To investigate whether this behavior is unique to **5**$^{\bullet+}$, the same study was performed with a non-core substituted phenazine (**3**$^{\bullet+}$, Figures 5.70 – 5.72 in *Experimental* section) and a phenoxazine radical cation (**10**$^{\bullet+}$, Figures 5.73 – 5.75 in *Experimental* section). The same behavior was found, but with a greater rate for the disappearance of **10**$^{\bullet+}$ relative to **5**$^{\bullet+}$ and **3**$^{\bullet+}$. As **10**$^{\bullet+}$ is significantly more oxidizing in the ground state [$E_{1/2} \sim E^o$(**10**$^{\bullet+}$/**10**) = 0.66 V vs. SCE in MeCN], its greater reactivity may be due to its stronger oxidation potential.

In every case, an isosbestic point was observed during the disappearance of PC$^{\bullet+}$, indicating conversion to a single product. Further, when the reaction was carried out to high conversion (as indicated by complete loss of the PC$^{\bullet+}$ signal), the product spectrum closely resembled that of the PC. These data, combined with the observation of pseudo-first-order kinetics, led us to hypothesize that decomposition of PC$^{\bullet+}$ occurs by single electron transfer from DMAc to generate the neutral PC. Under irradiation, this reaction might proceed through a more oxidizing PC$^{\bullet+}$ excited state,

which would explain why the rate of the reaction increases. However, this possibility will be discussed further in a later section (see *Investigation of Radical Cation Reactivity*).

While the oxidation of DMAc by $PC^{\bullet+}$ is consistent with the data presented above, it is surprising given that the oxidation potential of DMAc [$E^{o}_{calc}(DMAc^{+}/DMAc)$ = 1.98 V vs. SCE] is significantly more positive than that of any $PC^{\bullet+}$ in this work [$E_{1/2} \sim E^{o}(PC^{\bullet+}/PC)$ = 0.14 to 0.73 V vs. SCE]. To probe this reaction further, a kinetic isotope study was performed using DMF and deuterated DMF (d_7-DMF), assuming similar reactivity would be observed as with DMAc (see *Radical Cation Stability Studies* in *Experimental*). A normal kinetic isotope effect was observed in the dark (k_H/k_D = 5.9), and an inverse isotope effect was observed under irradiation (k_H/k_D = 0.18 ± 0.04). As inverse equilibrium isotope effects are more common than inverse kinetic isotope effects,[33] this result led us to believe an equilibrium might be involved in the excited state oxidation of DMAc and DMF. We hypothesize that $PC^{\bullet+}$ pre-associates with a solvent molecule prior to photoinduced electron transfer. However, regardless of the mechanism of this reaction, the observation of this isotope effect supports a direct reaction between DMF and $\mathbf{5}^{\bullet+}$.

Several alternative hypotheses explaining the decomposition of $\mathbf{5}^{\bullet+}$ were also investigated, including the oxidation of the PF_6^- anion and the possibility of solvent impurities. To rule out a reaction with PF_6^-, a solution of $\mathbf{5}^{\bullet+}\mathbf{PF_6}^-$ was prepared in deuterated DMF and irradiated with white LEDs. After the solution turned from dark blue to yellow, indicating conversion of $\mathbf{5}^{\bullet+}$ to **5**, the reaction products were analyzed by ^{19}F NMR (Figure 5.79 in *Experimental* section). The resulting spectrum was consistent with preservation of the PF_6^- anion. To test for solvent impurities, DMF and d_7-DMF were analyzed by gas chromatography (Figures 5.81 and 5.82 in *Experimental* section). Neither analysis revealed volatile impurities that could account for the observed reactivity, supporting a direct reaction between $\mathbf{5}^{\bullet+}$ and DMF.

Investigation of Radical Cation Side Reactions

Impact of irradiation on radical cation reactivity. To further investigate possible reactivity from the excited state of $\mathbf{5}^{\bullet+}$, a series of reactions were performed in the presence of substrates with increasing oxidation potentials. For substrates with lower oxidation potentials [$E^o(S^+/S) \leq 1$ V vs. SCE], the slow disappearance of $\mathbf{5}^{\bullet+}$ was observed with equal kinetics under irradiation and in the dark (Table 5.10). Since irradiation did not impact this reaction, a ground state mechanism is proposed to be most likely with these substrates. Instead, for substrates with greater oxidation potentials, no reactivity was observed either in the dark or under irradiation, with DMAc being the only exception at high concentrations. This observation may be linked to the excited state lifetime of $\mathbf{5}^{\bullet+}$, which could be too short to engage in bimolecular reactions in solution unless the substrate is present in high enough concentration (i.e. solvent quantities) to overcome the lifetime of this species.

In the presence of bromide. The reactivity of $\mathbf{5}^{\bullet+}$ was also investigated in the presence of halides (Figure 5.4a), given the relevance of these ions to O-ATRP. Although some experiments were performed in ethyl acetate (Figures 5.115 – 5.117 in *Experimental* section), the reaction of $\mathbf{5}^{\bullet+}$ with halides proved challenging to track due to the rate of the reaction. As such, DMAc was used instead for these investigations.

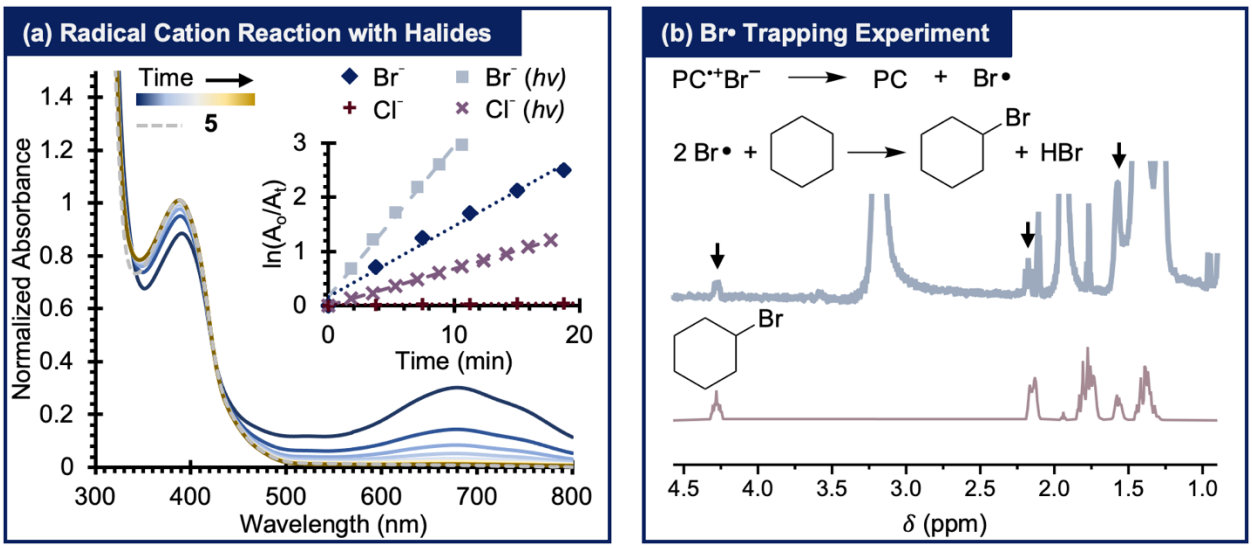

Figure 5.4. *(a) Representative example of UV-Vis spectra following the disappearance of* $\mathbf{5}^{\bullet+}$ *in the presence of LiBr. Figure inset shows a comparison of pseudo-first-order kinetics demonstrating the impact of irradiation and the halide identity. (b) Identification by* ^{1}H *NMR of bromocyclohexane formed from Br• after oxidation of* Br^- *by* $\mathbf{5}^{\bullet+}$*.*

In the presence of 0.1 M LiBr in the dark, $\mathbf{5}^{\bullet+}$ exhibited reactivity ($k_{Br\text{-}dark} = 0.14 \pm 0.02$ $M^{-1}s^{-1}$) that was distinguishable from the background reaction with DMAc ($k_{DMAc\text{-}dark} = 0.00064$ M^{-1} s^{-1}), suggesting a possible ground state reaction between $\mathbf{5}^{\bullet+}$ and Br^-. An increase in the rate of disappearance for $\mathbf{5}^{\bullet+}$ was observed under irradiation ($k_{Br\text{-}light} = 0.31 \pm 0.06$ $M^{-1}s^{-1}$), although it is difficult to distinguish whether this change in rate was due to a reaction with Br^- or simply with DMAc ($k_{DMAc\text{-}light} = 0.39$ M^{-1} s^{-1}). Regardless of irradiation, the formation of **5** was observed by UV-Vis in each case (Figures 5.111 and 5.113 in *Experimental* section), suggesting a single electron transfer mechanism between $\mathbf{5}^{\bullet+}$ and Br^-.

Since such a reaction would be expected to generate bromine radical (Br•), an experiment was devised to probe for the presence of Br• in this reaction. To do so, the radical halogenation of alkanes was employed, wherein a halogen radical performs hydrogen atom abstraction from an alkane to generate an alkyl radical, followed by radical coupling of the alkyl radical with another halogen radical to give the halogenated alkane. The reaction of $\mathbf{5}^{\bullet+}$ and Br^- was performed in the

presence of cyclohexane and monitored by ^{1}H NMR for the formation of bromocyclohexane. Excitingly, a small quantity of bromocyclohexane was observed (Figure 5.4b), supporting the hypothesized oxidation of Br^- by $\mathbf{5}^{\bullet+}$.

Finally, the kinetics of this reaction were investigated with two other radical cations. When the reaction of $\mathbf{3}^{\bullet+}$ and Br^- was followed, similar results were observed as with $\mathbf{5}^{\bullet+}$, although at a reduced rate ($k_{\mathbf{3}\text{-dark}} = 0.02\ M^{-1}\ s^{-1}$, $k_{\mathbf{3}\text{-light}} = 0.08\ M^{-1}\ s^{-1}$). Instead, the reaction between $\mathbf{10}^{\bullet+}$ and Br^- was too rapid to follow by UV-Vis (Figure 5.121 in *Experimental* section), even in the absence of light. These results broadly correlate with the oxidation potentials of these compounds [$E_{1/2}(\mathbf{3}^{\bullet+}/\mathbf{3})$ = 0.18 V; $E_{1/2}(\mathbf{5}^{\bullet+}/\mathbf{5})$ = 0.32 V; $E_{1/2}(\mathbf{10}^{\bullet+}/\mathbf{10})$ = 0.66 V, all vs. SCE in MeCN], possibly yielding insight into their capabilities as deactivators in O-ATRP. This possibility will be discussed in greater detail later in the text (see *Factors Influencing the Deactivation of Alkyl Radicals*).

In the presence of chloride. While metal catalyzed ATRP is often performed in the presence of bromide and chloride (either by using alkyl bromide or chloride initiators, or through the addition of halide salts),[12] O-ATRP in the presence of chloride has remained challenging. One difference between these halides is that alkyl chloride bond strengths are typically greater than alkyl bromides, which would make activation more challenging with alkyl chlorides. However, previous investigations by Matyjaszewski and coworkers have suggested the issue with chloride may be ineffective deactivation,[26] though the origin of this issue remains a mystery. To investigate this limitation of O-ATRP further, the reactivity of $\mathbf{5}^{\bullet+}$ was studied in the presence of LiCl. Unlike the reaction with Br^-, that with Cl^- in the dark exhibited only a minor increase in the rate of disappearance of $\mathbf{5}^{\bullet+}$ ($k_{\text{Cl-dark}} = 0.0020 \pm 0.0007\ M^{-1}s^{-1}$) relative to the background reaction in DMAc ($k_{\text{DMAc-dark}} = 0.00064\ M^{-1}\ s^{-1}$). Irradiation with white LEDs again increased the rate of $\mathbf{5}^{\bullet+}$

disappearance ($k_{Cl\text{-}light}$ = 0.074 ± 0.013 $M^{-1}s^{-1}$), though this reaction was still slower than with Br^- both in the dark ($k_{Br\text{-}dark}$ = 0.14 ± 0.02 $M^{-1}s^{-1}$) and under irradiation ($k_{Br\text{-}light}$ = 0.31 ± 0.06 $M^{-1}s^{-1}$).

Under both irradiation conditions, the oxidation of Cl^- appears to be significantly slower than the oxidation of Br^-. This observation is consistent with the oxidation potentials of these ions [$E^o(Br_3^-/Br^-)$ = 0.7 V, $E^o(Cl_3^-/Cl^-)$ = 1.1 V, both vs. SCE in MeCN[34]]. As such, a possible explanation for poor deactivation in O-ATRP using Cl^- could be that it is more challenging to oxidize this ion, which leads to an overall slower rate of deactivation with Cl^- relative to Br^-. This hypothesis is further supported by experiments measuring the rate of deactivation in the presence of Br^- versus Cl^-, although these data will be discussed later (see *Factors Influencing the Deactivation of Alkyl Radicals*).

Despite the kinetic differences observed between Cl^- and Br^-, irradiation of $\mathbf{5}^{\bullet+}$ in the presence of Cl^- again led to the recovery of the ground state UV-vis spectrum of **5** (Figure 5.126 in *Experimental* section), indicating a similar redox mechanism leading to the formation of **5** and Cl•. A trapping experiment was attempted to provide evidence for the formation of Cl•, but this experiment was unsuccessful. While this result does not rule out the formation of Cl•, it further highlights the inefficiency of Cl^- oxidation by $\mathbf{5}^{\bullet+}$.

Proposed Mechanism of Substrate Oxidation. Considering the reactivity studies discussed thus far, we propose the following mechanisms for substrate oxidation by $PC^{\bullet+}$. In the ground state, substrate oxidation appears to proceed through a bimolecular electron transfer reaction, which results in the formation of neutral **5** and the oxidized substrate. Instead, in the excited state, association of the substrate with $\mathbf{5}^{\bullet+}$ prior to photoexcitation may facilitate electron transfer (Figure 5.5). After pre-association, irradiation of $\mathbf{5}^{\bullet+}$ could lead to photoinduced electron transfer, which is likely followed by dissociation of the product complex to yield free **5** and oxidized substrate.

While such an association with $\mathbf{5}^{\bullet+}$ is not surprising for Cl^- or Br^-, it is perhaps less anticipated for a neutral substrate such as DMAc. However, DMAc contains a lone pair of electrons at the nitrogen position as well as significant electron density around the carbonyl oxygen, which might be susceptible to a weak interaction with the positively charged $PC^{\bullet+}$. While this weak interaction might be negligible at low concentrations, higher concentrations may enable a small degree of association between DMAc and $\mathbf{5}^{\bullet+}$, enabling excited state reactivity. Alternatively, a bimolecular reaction between the excited state of $\mathbf{5}^{\bullet+}$ and the substrate may also be feasible, depending on the lifetime of this excited state and the concentration of the substrate in solution. However, deeper investigation of the photophysical properties of these radical cations is necessary to probe this possible reactivity further.

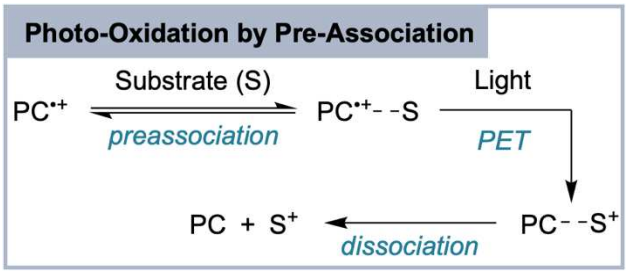

Figure 5.5. *One proposed mechanism for substrate oxidation by photoexcited $PC^{\bullet+}$ facilitated by pre-association of the $PC^{\bullet+}$ and substrate.*

Factors Influencing the Deactivation of Alkyl Radicals

Deactivation of alkyl radicals. To better understand these radical cations in the context of deactivation, their reactions with alkyl radicals were investigated. A reaction to model deactivation in O-ATRP was devised using $\mathbf{5}^{\bullet+}$ in the presence of Br^- to deactivate thermally generated radicals from azobisisobutyronitrile (AIBN) (Figure 5.7a). To first determine whether $\mathbf{5}^{\bullet+}$ could operate as a radical deactivator, the formation of the brominated deactivation product was monitored by ^1H NMR (Figures 5.129 and 5.130 in *Experimental* section). The NMR spectrum of the model

reaction showed a peak matching the expected chemical shift of the deactivation product (δ = 2.07 ppm in CD_3CN), suggesting $\mathbf{5}^{\bullet+}$ can indeed deactivate alkyl radicals.

Previous computational investigations have attempted to determine the mechanism of deactivation using density functional theory and Marcus theory to predict the rate of deactivation *via* various mechanisms.[26] This work concluded that a termolecular mechanism was most favorable with phenyl phenothiazine as the catalyst.[35] Instead, we hypothesize a bimolecular deactivation mechanism is operative, wherein $PC^{\bullet+}$ and Br^- form an ion pair ($PC^{\bullet+}Br^-$) prior to reaction with the propagating radical (Figure 5.6, "concerted mechanism"). Based on the observed reactivity between $\mathbf{5}^{\bullet+}$ and Br^-, it was also envisioned that deactivation could occur through a stepwise mechanism. In this case, formation of the $PC^{\bullet+}Br^-$ ion pair might lead to the oxidation of Br^-, generating a free equivalent of Br• that could then undergo radical coupling with the radical on the polymer chain-end in a subsequent step (Figure 5.6, "stepwise mechanism"). In either case, the products of deactivation would be the same. It should be noted that in this work, the primary catalyst family investigated was dihydrophenazines, which differ structurally from the previously investigated phenothiazines by a second *N*-aryl substituent. In addition, the radical cations of dihydrophenazines are typically much less oxidizing than those of phenothiazines. Both these properties could ultimately impact the mechanism of deactivation, leading to differences between various catalyst families.

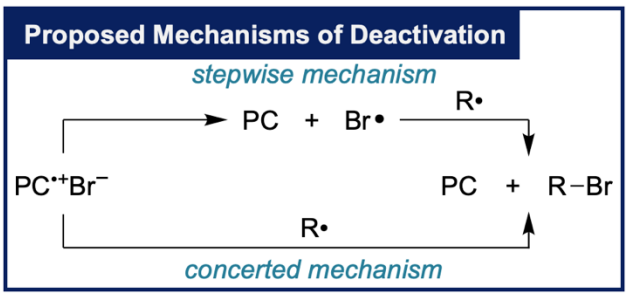

Figure 5.6. *Hypothesized mechanisms of deactivation investigated in this work.*

To investigate which of these mechanisms might predominate, another model reaction employing AIBN was employed. Cyclohexane was also added to the reaction in an attempt to trap Br• *during* deactivation. It was reasoned that the formation of bromocyclohexane should only be observed if free Br• forms during deactivation through a stepwise mechanism. Instead, if deactivation proceeds through a concerted mechanism, a reaction between Br• and cyclohexane should be sufficiently challenging to prevent the formation of bromocyclohexane. Indeed, when this experiment was carried out using $\mathbf{5}^{\bullet+}$, the primary product of the reaction was found to be that from deactivation (2-bromo-2-methylpropanenitrile), with little-to-no bromocyclohexane detectable by ^{1}H NMR (Figures 5.131 and 5.132 in *Experimental* section). This experiment suggests a concerted mechanism may be most likely

Bromide vs. Chloride. As was discussed briefly above, O-ATRP in the presence of chloride has remained challenging, presumably due to an issue during deactivation with Cl^-.[26] Based on our investigations of radical cation reactivity in the presence of Br^- and Cl^-, one possible explanation for why deactivation is successful with Br^- but not Cl^- is based on their difference in oxidation potentials. Since Cl^- is more challenging to oxidize, the deactivation reaction with Cl^- is likely slower, leading to ineffective deactivation and poor polymerization control in O-ATRP.

To test this hypothesis more directly, the deactivation model reaction employed above was followed *in-situ* using UV-Vis spectroscopy (Figure 5.7a). By doing so, the disappearance of $\mathbf{5}^{\bullet+}$

during deactivation could be monitored to measure the kinetics of deactivation, yielding direct insight into factors that might influence the rate of deactivation. Unsurprisingly, when the reaction was performed in the presence of Cl^-, the disappearance of $\mathbf{5}^{\bullet+}$ was much slower than with Br^- (Figure 5.7b), indicating less efficient deactivation. In the absence of halide, the disappearance of $\mathbf{5}^{\bullet+}$ was only slightly slower than in the presence of Cl^-. Therefore, while deactivation still appears to occur in the presence of Cl^-, it is very slow. In O-ATRP, slow deactivation would promote a higher concentration of radicals during the reaction, ultimately increasing termination reactions and inhibiting polymerization control.

In addition to the difference in oxidation potentials of the halides, we hypothesized the propensity of Br• and Cl• to undergo side reactions might also be important. Cl• could be more prone to H-atom abstraction than Br• based on the greater bond strength of H-Cl than H-Br,[36] which makes H-Cl formation more thermodynamically favorable. In turn, this greater driving force might lead to more side reactions in O-ATRP. To probe this possibility, a collector-generator experiment was performed using a rotating ring-disk electrode with LiBr or LiCl in a mixture of DMAc and MMA to mimic O-ATRP conditions (Figure 5.140 in *Experimental* section). The results of these experiments revealed that 0.7% of Br• was collected, whereas 5.9% of Cl• was collected. In other words, Cl• underwent fewer side reactions than Br•. Further, if the mechanism of deactivation is in fact concerted as previous experiments suggested, the possibility of side reactions from free Br• or Cl• is likely reduced. Therefore, such side reactions may not be responsible for poor control in O-ATRP using Cl^-.

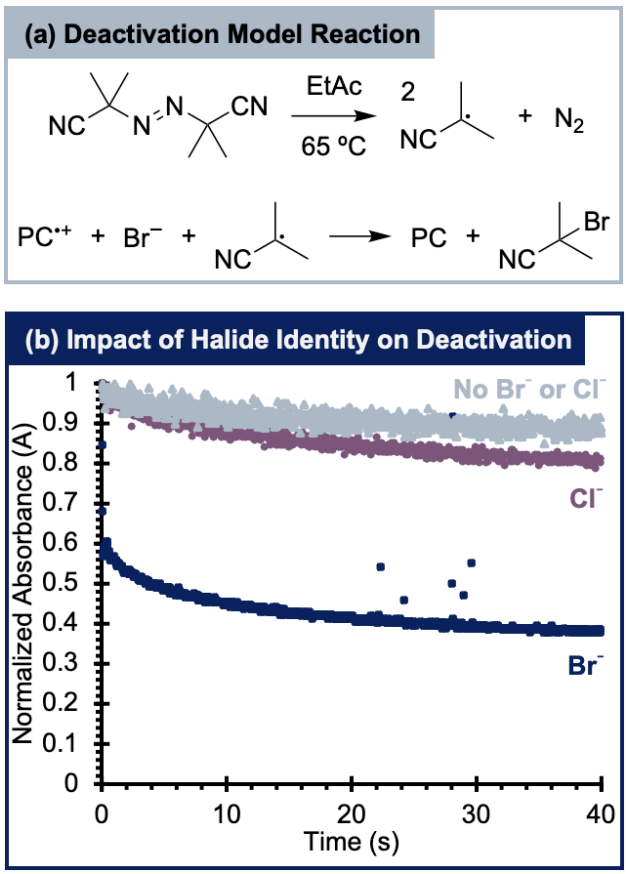

Figure 5.7. *(a) Model reaction used in this work to investigate deactivation in O-ATRP. (b) In-situ kinetics of deactivation with* ***5***$^{\bullet+}$ *(monitored at 677 nm) in the presence of halides (*Br^-*, dark blue;* Cl^-*, purple) and in their absence. Data normalized to maximum absorbance at time of* $PC^{\bullet+}$ *addition (t = 0).*

<u>*Radical Cation Structure.*</u> One long standing hypothesis in the design of O-ATRP PCs is that increasing the oxidation potential of $PC^{\bullet+}$ increases the rate of deactivation.[21, 37] While this hypothesis has motivated the development of new PCs with strongly oxidizing radical cations,[17, 21] it has never been tested. As such, another series of model reactions was performed using $\mathbf{4}^{\bullet+}$ [$E_{1/2}(\mathbf{4}^{\bullet+}/\mathbf{4})$ = 0.14 V vs. SCE], $\mathbf{3}^{\bullet+}$ [$E_{1/2}(\mathbf{3}^{\bullet+}/\mathbf{3})$ = 0.18 V vs. SCE], and $\mathbf{1}^{\bullet+}$ [$E_{1/2}(\mathbf{1}^{\bullet+}/\mathbf{1})$ = 0.33 V vs. SCE], which feature increasing oxidation potentials (Figure 5.8). A correlation was observed between the oxidation potential of $PC^{\bullet+}$ and the rate of deactivation, supporting the validity of this hypothesis.

Since core substitution of dihydrophenazine PCs by alkyl radicals has been reported as a possible side reaction,[20] control experiments were performed in the absence of LiBr to rule out interference from these reactions (Figures 5.136 – 5.138 in *Experimental* section). Further, this experiment was also attempted with radical cations of phenoxazines **6** – **8**, although these reactions proceeded too rapidly to be measured quantitatively (Figure 5.139 in *Experimental* section).

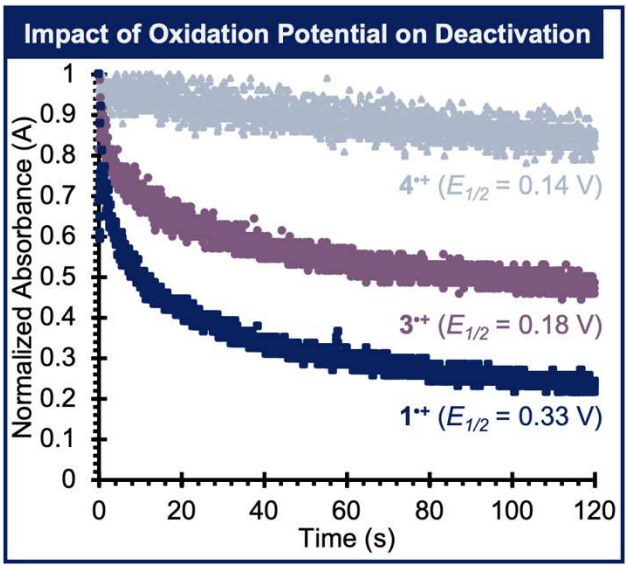

Figure 5.8. *In-situ kinetics of deactivation with three dihydrophenazine radical cations demonstrating the impact of PC oxidation potential [$E_{1/2}$ ~ $E°(PC^{•+}/PC)$, all in V vs. SCE] on the rate of deactivation. Kinetics monitored at 682 nm (**1**$^{•+}$), 680 nm (**3**$^{•+}$), and 677 nm (**4**$^{•+}$). Data normalized to maximum absorbance at time of $PC^{•+}$ addition (t = 0).*

<u>*Ion Pairing in Radical Cations.*</u> Given that the $PC^{•+}Br^-$ ion pair is the hypothesized deactivator in O-ATRP, the susceptibility of $PC^{•+}$ to form this ion pair could be important for effective deactivation during a polymerization. To probe the variables impacting ion pairing with $PC^{•+}$, the equilibrium association constants (K_{assoc}) of various $PC^{•+}PF_6^-$ salts were measured using conductometry. While $PC^{•+}PF_6^-$ is not the true deactivator in O-ATRP, we hypothesized these salts would exhibit similar trends in ion pairing as $PC^{•+}Br^-$, allowing broad conclusions to be drawn.

To understand how the radical cation structure impacts ion pairing, K_{assoc} was measured for each $PC^{\bullet+}PF_6^-$ synthesized (Table 5.12). To our surprise, all the radical cations investigated showed K_{assoc} values within roughly one order of magnitude of each other ($\Delta\Delta G_{assoc} \sim 1$ kcal mol^{-1}), which is only slightly outside of the error of the measurement (Table 5.14). Coupled with the fact that no trends in the conductometry data were observed, these results suggest that the impact of $PC^{\bullet+}$ structure on ion pairing in $PC^{\bullet+}PF_6^-$ is minimal at best. By contrast, the solvent appears to have a much greater impact on ion pairing in $PC^{\bullet+}PF_6^-$. When conductometry was performed with $\mathbf{1}^{\bullet+}\mathbf{PF_6}^-$ in four different solvent systems – from DMAc to THF (Table 5.13) – K_{assoc} varied over several orders of magnitude ($10^2 – 10^6$ M^{-1}, $\Delta\Delta G_{assoc} \sim 5$ kcal mol^{-1}). Further, K_{assoc} varied predictably as a function of the solvent dielectric constant as suggested by theory (Figure 5.158 in *Experimental* section).[38] Thus, while the structure of $PC^{\bullet+}$ appears to have only a minor influence on ion pairing, the choice of solvent can be very impactful.

Impact of Radical Cations in O-ATRP

Polymerization of Methyl Methacrylate. To better understand the role of radical cations in O-ATRP, polymerizations were conducted in the presence of increasing quantities of $PC^{\bullet+}$. In each case, the kinetics of the polymerizations and the resulting polymers were characterized to understand how the addition of $PC^{\bullet+}$ impacted the reaction. Since $PC^{\bullet+}$ is the hypothesized deactivator in O-ATRP, we anticipated adding supplemental $PC^{\bullet+}$ to O-ATRP would result in: (1) a lower observed rate of the polymerization; (2) more linear molecular weight growth; (3) lower $Đ$ ($1 < Đ \leq 1.5$) throughout the polymerization, especially at low monomer conversions; and (4) improved initiator efficiency ($I^* \sim 100\%$).

For initial investigations, the polymerization of MMA using **5** under published conditions[39] was targeted. While DMAc has typically been the solvent of choice for O-ATRP, ethyl acetate was chosen given the greater stability of $\mathbf{5}^{\bullet+}\mathbf{PF_6}^-$ in ethyl acetate relative to DMAc. In addition, LiBr was added to these polymerization ([LiBr] = [**5**] + [$\mathbf{5}^{\bullet+}$]) to facilitate formation of the $PC^{\bullet+}Br^-$ ion pair. Since the addition of Br^- salts alone has been shown to improve deactivation,[26] we first investigated the impact of this reagent on polymerization control (Table 5.1, Entries 1 and 2). Unsurprisingly, adding LiBr resulted in a slight decrease in $Đ$ ($Đ$ = 1.14 with LiBr vs. 1.19 without), although otherwise similar polymerization results.

To then understand the impact of adding $\mathbf{5}^{\bullet+}\mathbf{PF_6}^-$ to this polymerization, the ratio of [**5**]:[$\mathbf{5}^{\bullet+}$] was varied while maintaining the overall catalyst loading ([**5**] + [$\mathbf{5}^{\bullet+}$] = 100 ppm) constant (Table 5.1, Entries 2 – 6) in the presence of 100 ppm LiBr. Overall, no significant improvements in polymerization control were observed upon increasing [$\mathbf{5}^{\bullet+}$] (ex. $Đ$ = 1.14 for [**5**]:[$\mathbf{5}^{\bullet+}$] = 1:0 vs. $Đ$ = 1.10 for [**5**]:[$\mathbf{5}^{\bullet+}$] = 0:1), presumably because the polymerization with **5** already exhibits excellent polymerization control. However, a decrease in the rate of the polymerizations was observed, especially during the first several hours (k_{obs} = 0.053 M^{-1} s^{-1} for [**5**]:[$\mathbf{5}^{\bullet+}$] = 1:0 vs. k_{obs} = 0.037 M^{-1} s^{-1} for [**5**]:[$\mathbf{5}^{\bullet+}$] = 0:1), consistent with improved deactivation.

Table 5.1. *Initial polymerization results for the O-ATRP of MMA with increasing quantities of supplemental deactivator.*

Entry	[5]:[5$^{\bullet+}$]	Time (h)	Conv. (%)[a]	k_{obs} ($M^{-1}h^{-1}$)[b]	$M_{n,\,theo}$ (kDa)	$M_{n,\,exp}$ (kDa)[c]	$Đ$[c]	I^* (%)[d]
1[e]	1:0	24	67.5	0.046	7.01	6.19	1.19	113
2	1:0	24	71.3	0.053	7.40	6.71	1.14	110
3	3:1	24	64.8	0.046	6.74	6.38	1.16	106
4	1:1	24	68.1	0.044	7.07	6.87	1.12	103
5	1:3	24	55.4	0.039	5.80	5.60	1.16	103
6	0:1	24	75.8	0.037	7.84	7.36	1.10	107

*Unless stated otherwise, [MMA]:[DBMM]:[**5**/**5**$^{\bullet+}$]:[LiBr] = [1000]:[10]:[0.1]:[0.1] (see Section 11 of Experimental for full experiment details).* [a]*Determined by* ^{1}*H NMR.* [b]*Determined from the first three time-points (1h, 2h, and 4h).* [c]*Determined by GPC.* [d]*Initiator efficienty (I*) =* $(M_{n,\,theo} / M_{n,\,exp})\bullet 100\%$. [e]*Reaction run without LiBr.*

For polymerizations started with only **5**$^{\bullet+}$**PF$_6^-$**, one might expect activation to be inaccessible due to the lack of **5**. However, we hypothesized the reaction between **5**$^{\bullet+}$ and Br^- would generate a small quantity of **5**, allowing the polymerization to begin upon irradiation. Support for this hypothesis was found when control reactions were performed (Table 5.15), which showed significantly reduced conversion in the absence of LiBr (8.3% versus 75.8%). Further, visual inspection of this polymerization revealed the reaction remained dark blue even after 8h of irradiation with white LEDs, indicating persistence of **5**$^{\bullet+}$ in solution. By contrast, when the same polymerization was performed with LiBr present, the dark blue solution gradually turned light green (Figure 5.168 in *Experimental* section), indicating a mixture of **5**$^{\bullet+}$ (blue) to **5** (yellow).

In an effort to improve polymerization control in a more challenging system, the synthesis of high molecular weight PMMA was undertaken. Although high molecular weight polymers have been synthesized by a number of other controlled radical polymerization methods,[40-45] they have remained elusive in O-ATRP. In part, this issue may be because the concentration of initiator must be reduced to target higher molecular weights, but the percentage of terminated chains in ATRP

is predicted to vary inversely with initiator concentration.[46] As such, to target higher molecular weight polymers, better deactivation may be necessary to control termination reactions.[47]

To this end, a series of polymerizations was performed increasing the target molecular weight ($M_{n,target}$) of the polymer by varying the ratio of monomer to initiator. When these polymerizations were performed starting with **5**, polymers with low $Đ$ were consistently obtained, although I^* increased undesirably over 100% with $M_{n,target}$ (Table 5.16). Further, the number average molecular weight (M_n) measured for the polymers produced was limited to about 45 kDa, after which molecular weight growth began to plateau (Figures 5.169 – 5.174 in *Experimental* section). We anticipated performing these polymerizations using $\mathbf{5}^{\bullet+}$ instead of **5** would improve these results, but no significant improvements were observed (Table 5.16). Even after varying the [LiBr] (Table 5.17) and $\mathbf{5}^{\bullet+}$ loading (Table 5.18), the M_n of the product polymers remained limited to about 45 kDa. Further work is ongoing to determine the mechanistic cause of this limitation.

Polymerization of Acrylates. Another limitation of O-ATRP is its monomer scope, which remains narrow in comparison to traditional ATRP.[12] While different monomers present different challenges, acrylate monomers have been difficult to access in O-ATRP because of their large propagation rate constants. In order to compensate for an increase in the rate of propagation with acrylates relative to methacrylates, faster deactivation is necessary. Previously, our group reported two strategies to access the O-ATRP of acrylates. In the first, a new class of organic PCs – dihydroacridines – was developed, which featured strongly oxidizing radical cations to increase the thermodynamic driving force for deactivation.[21] More recently, a second strategy was reported, in which a dihydrophenazine PC was first reacted with DBMM to generate a new substituted catalyst, followed by O-ATRP using this new PC. It was discovered that the reaction of the PC and DBMM not only led to the formation of a more oxidizing catalyst, but it also generated an

excess of $PC^{\bullet+}$ prior to O-ATRP which likely improved deactivation during the polymerization of acrylates.[20] In the present work, we hypothesized that the addition of isolated radical cations in the O-ATRP of acrylates would also improve polymerization control.

To first probe the impact of adding $PC^{\bullet+}$ to the polymerization of an acrylate (methyl acrylate, MA), a series of polymerizations were performed in which [$\mathbf{5}^{\bullet+}$] was increased while keeping the overall catalyst loading ([**5**] + [$\mathbf{5}^{\bullet+}$] = 100 ppm) constant (Table 5.2). With regards to the polymerization kinetics, increasing [$\mathbf{5}^{\bullet+}$] resulted in increasingly linear pseudo-first-order kinetics (Figure 5.9a) and a lower rate of the polymerization (k_{obs} = 0.89 M^{-1} s^{-1} for [**5**]:[$\mathbf{5}^{\bullet+}$] = 1:0 vs. k_{obs} = 0.17 M^{-1} s^{-1} for [**5**]:[$\mathbf{5}^{\bullet+}$] = 0:1). In particular, it is interesting that polymerizations with low [$\mathbf{5}^{\bullet+}$] exhibited downward sloping pseudo-first-order kinetics, as this feature is consistent with a prevalence of termination reactions due to poor deactivation.[12] The disappearance of this feature and the lowering of k_{obs} with increasing [$\mathbf{5}^{\bullet+}$] are consistent with improved deactivation.

Table 5.2. *Initial polymerization results for the O-ATRP of MA with increasing quantities of supplemental deactivator.*

Entry	[5]:[$5^{\bullet+}$]	Time (h)	Conv. (%)[a]	k_{obs} ($M^{-1}h^{-1}$)[b]	$M_{n,\,theo}$ (kDa)	$M_{n,\,exp}$ (kDa)[c]	$Đ$[c]	I^* (%)[d]
7[e]	1:0	6	80.7	0.40	7.20	8.59	2.21	84
8	1:0	6	91.6	0.89	8.14	11.6	1.77	70
9	3:1	6	84.2	0.58	7.50	8.09	1.88	93
10	1:1	6	70.6	0.29	6.33	8.40	1.67	75
11	1:3	6	73.3	0.28	6.57	6.98	1.65	94
12	0:1	6	61.4	0.17	5.54	6.45	1.55	86

*Unless stated otherwise, [MA]:[DBMM]:[**5**/$\mathbf{5}^{\bullet+}$]:[LiBr] = [1000]:[10]:[0.1]:[0.1] (see Section 12 of Experimental for full experiment details).* [a]*Determined by* ^{1}*H NMR.* [b]*Determined from the first three time-points (0.5h, 1h, and 1.5h).* [c]*Determined by GPC.* [d]*Initiator efficienty (I*) =* $(M_{n,\,theo} / M_{n,\,exp}) \bullet 100\%$. [e]*Reaction run without LiBr.*

Increasing [**5**$^{\bullet+}$] also improved control during these polymerizations (Table 5.2). As [**5**$^{\bullet+}$] increased, $Đ$ decreased ($Đ$ = 1.77 for [**5**]:[**5**$^{\bullet+}$] = 1:0 vs. $Đ$ = 1.55 for [**5**]:[**5**$^{\bullet+}$] = 0:1) and I* approached 100% (I* = 70% for [**5**]:[**5**$^{\bullet+}$] = 1:0 vs. I* = 86% for [**5**]:[**5**$^{\bullet+}$] = 0:1). However, the most significant improvement was in the evolution of molecular weight during the polymerization, which decreased with only **5** – indicating no molecular weight control – but increased with **5**$^{\bullet+}$ (Figure 5.9b). Together, these results represent a significant improvement in the polymerization of MA using O-ATRP, although there are still several indicators of poor control in these results. For example, while $Đ$ was reduced through the use of **5**$^{\bullet+}$, a controlled polymerization should exhibit $Đ \leq 1.5$. In addition, I* = 86% for the O-ATRP of MA using **5**$^{\bullet+}$, but I* = 100% is most desirable.

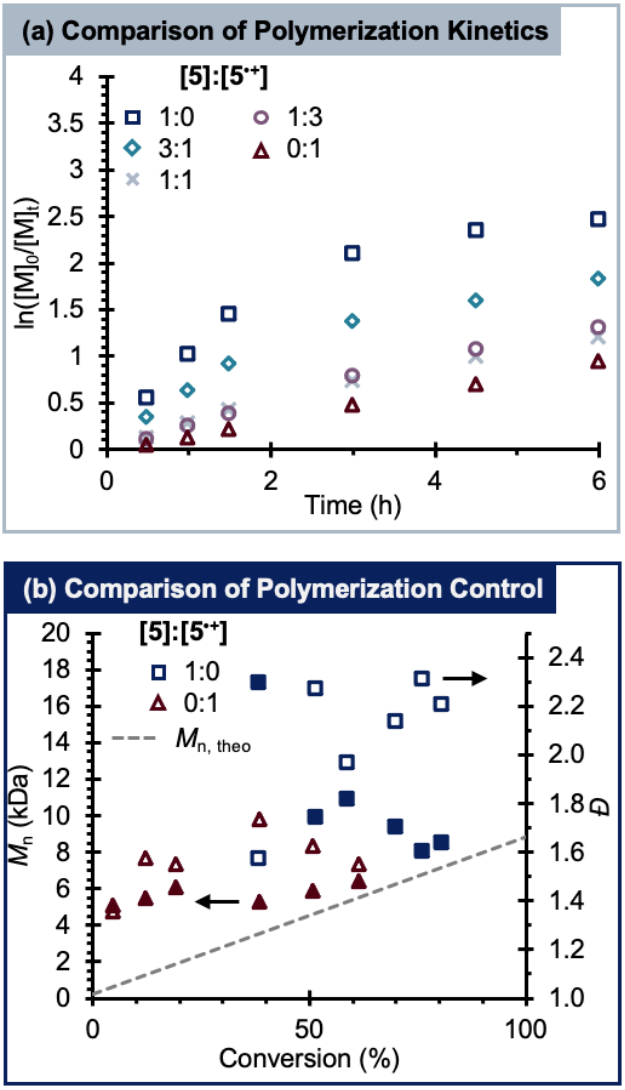

Figure 5.9. *(a) Polymerization kinetics for the O-ATRP of MA catalyzed by* ***5*** *demonstrating increasingly linear pseudo-first-order kinetics with increasing quantities of* $\mathbf{5}^{\bullet+}$*. (b) Evolution of polymer molecular weight (*M_n*, filled shapes) and Đ (hollow shapes) for the polymerization of MA by O-ATRP with* ***5*** *(blue) and* $\mathbf{5}^{\bullet+}$ *(red).*

In an effort to further improve these results, an experiment was performed increasing [$\mathbf{5}^{\bullet+}$] along with [LiBr] such that [LiBr] = [$\mathbf{5}^{\bullet+}$]. Again, increasing the concentration of the radical cation resulted in a decrease in the rate of the polymerization (Figure 5.10), indicating improved deactivation with more $\mathbf{5}^{\bullet+}$. In addition, improvements in polymerization control were observed up to 200 ppm $\mathbf{5}^{\bullet+}$, resulting in $Đ$ = 1.44 and I^* = 102% (Table 5.3) versus $Đ$ = 1.90 and I^* = 78%

with 200 ppm **5** and LiBr. Importantly, polymerizations performed by O-ATRP with 200 ppm **5** remained completely uncontrolled (Figure 5.183 in *Experimental* section), indicating these improvements are directly attributable to the presence of $PC^{\bullet+}$.

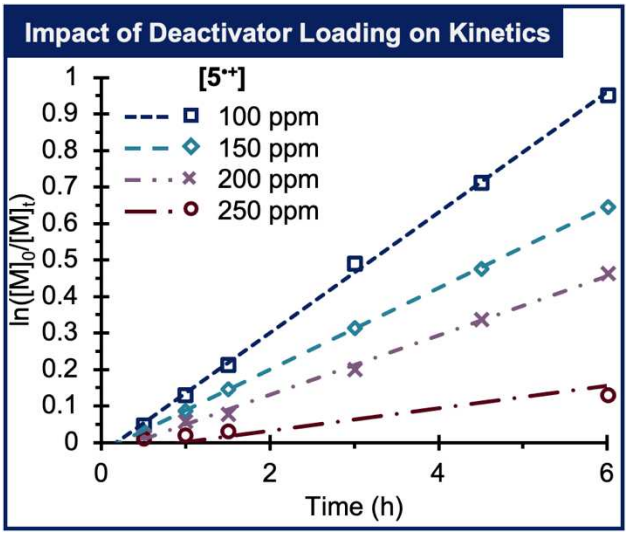

Figure 5.10. *Polymerization kinetics for the O-ATRP of MA catalyzed by* ***5*** *demonstrating a decrease in polymerization rate with increasing quantities of* $\mathbf{5}^{\bullet+}$.

Table 5.3. *Polymerization results for the O-ATRP of MA with increasing quantities of* $\mathbf{5}^{\bullet+}$.

Entry	$[\mathbf{5}^{\bullet+}]$ (ppm)	Time (h)	Conv. (%)[a]	k_{obs} ($M^{-1}h^{-1}$)[b]	$M_{n,\,theo}$ (kDa)	$M_{n,\,exp}$ (kDa)[c]	$Đ$[c]	I^* (%)[d]
13	100	6	61.4	0.16	5.54	6.45	1.55	86
14	150	10	69.3	0.11	6.22	6.97	1.44	89
15	200	14	71.3	0.08	6.39	6.25	1.44	102
16	250	24	53.5	0.02	4.86	4.26	1.83	114

For all polymerizations, [MMA]:[DBMM] = [1000]:[10], and [LiBr] = $[\mathbf{5}^{\bullet+}]$ *(see Section 12 of Experimental for full experiment details).* [a]*Determined by* ^1H *NMR.* [b]*Determined from the first 6 hours.* [c]*Determined by GPC.* [d]*Initiator efficienty (I*) =* $(M_{n,\,theo} / M_{n,\,exp})\bullet 100\%$.

Unfortunately, further increasing $[\mathbf{5}^{\bullet+}]$ above 200 ppm did not provide better control in the polymerization of MA; instead, it decreased control (Table 5.3, Entry 16). We hypothesized this decrease in control might be due to a background polymerization of MA, which is insignificant

over shorter reaction times (6h – 14h) but becomes competitive at longer reaction times (24h). Control reactions support this hypothesis. When both $\mathbf{5}^{\bullet+}$ and LiBr were removed (Table 5.19, Entry S22), significant conversion of the monomer to polymer was still observed (57.1% at 14h), and a high molecular weight polymer was recovered (M_n = 467 kDa). Significant gelling of the reaction mixture was also observed (Figure 5.187 in *Experimental* section), which is consistent with the free radical polymerization of MA. For comparison, when the same control experiment was performed using MMA, only 2% conversion and no gelling of the reaction mixture were observed.

To balance improvements in polymerization control but suppress this background reaction, all remaining acrylate polymerizations were performed using 200 ppm $\mathbf{5}^{\bullet+}$. Under these conditions, reaction variables were tuned in an effort to further improve polymerization control. For example, the choice of solvent can have significant effects in O-ATRP,[20, 30, 48] presumably by impacting the photophysics of the PC and ion pairing in $PC^{\bullet+}Br^-$. However, no improvements in O-ATRP using $\mathbf{5}^{\bullet+}$ were obtained by changing the solvent. Using THF, similar results were obtained as with ethyl acetate (Table 5.20). By contrast, using DMAc led to a complete loss of control (Table 5.20, Entry S31), likely because $\mathbf{5}^{\bullet+}$ reacts with DMAc and decomposes to **5**. As a result, polymerizations in this solvent are more analogous to traditional O-ATRP using **5**.

In addition, the quantity of LiBr was varied while maintaining a constant [$\mathbf{5}^{\bullet+}$]. We hypothesized increasing [LiBr] would improve polymerization control by further encouraging deactivation. However, it is also possible that adding more LiBr to the polymerization might increase the rate of the side reaction between $\mathbf{5}^{\bullet+}$ and Br^-, leading to faster decomposition of $\mathbf{5}^{\bullet+}$ to **5**. In this case, decreasing [LiBr] might be more advantageous, as it might increase the lifetime of $\mathbf{5}^{\bullet+}$ and improve deactivation during later reaction times. To test these hypotheses, polymerizations

were performed varying the ratio of [**5**$^{\bullet+}$]:[LiBr] from [1]:[0.1] to [1]:[10] (Table 5.21), but no improvements in polymerization control were observed.

We next sought to understand whether **5**$^{\bullet+}$ could be applied to the O-ATRP of other acrylate monomers. In total, five other acrylates were polymerized in this manner (Table 5.4). For monomers with shorter alkyl chains – ethyl acrylate (EA) and *n*-butyl acrylate (*n*Ba) – similar polymerization results were obtained as with MA. However, increasing the length of the alkyl chain led to a decrease in polymerization control (Entry 20). In part, this observation can be attributed to the increase in the rate of propagation of acrylate monomers with longer alkyl chains.[49] In addition, increasing the length of the monomer alkyl substituent likely lowers the overall polarity of the polymerization solution, which might impact PC photophysics and ion pairing in PC$^{\bullet+}$Br^{-}.

Table 5.4. *Results from the polymerization of various acrylate monomers by O-ATRP using* ***5***$^{\bullet+}$.

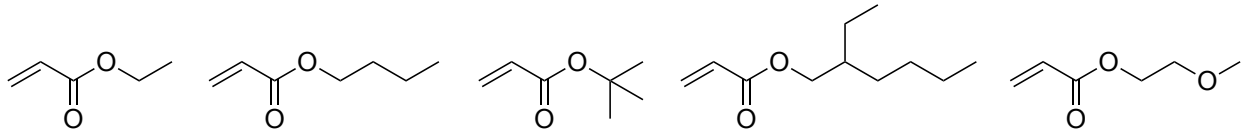

EA *n*BA *t*BA EHA EGMEA

Entry	Monomer	Time (h)	Conv. (%)[a]	$M_{n,\,theo}$ (kDa)	$M_{n,\,exp}$ (kDa)[b]	$Đ$[b]	I^* (%)[c]
17	EA	14	64.2	6.68	6.72	1.47	99
18	*n*BA	14	64.4	8.51	8.89	1.47	96
19	*t*BA	14	84.1	11.0	9.36	1.74	118
20	EHA	14	87.1	16.3	17.6	1.85	93
21	EGMEA	14	87.0	11.6	13.5	1.60	86

*In all cases, [monomer]:[DBMM]:[**5**$^{\bullet+}$]:[LiBr] = [1000]:[10]:[0.2]:[0.2] (see Section 12 of Experimental for full experiment details).* [a]*Determined by* ^{1}*H NMR.* [b]*Determined by GPC.* [c]*Initiator efficienty* $(I^* = (M_{n,\,theo} / M_{n,\,exp}) \bullet 100\%$.

Finally, one important feature of all ATRP methods is the retention of the C-Br bonds at the ends of the polymer chains. This feature – termed chain-end group fidelity – is key for

subsequent functionalization of the polymers produced by ATRP, such as by chain-extension or block copolymer synthesis. As such, the chain-end fidelity of poly(methyl acrylate) (pMA) synthesized using $\mathbf{5}^{\bullet+}$ was characterized and compared to pMA synthesized with **5**. We anticipated the use of $\mathbf{5}^{\bullet+}$ would yield superior chain-end fidelity, since improving deactivation suppresses the termination reactions that cause loss of the Br functionality.

To investigate this property, we first synthesized pMA under optimized conditions using both **5** and $\mathbf{5}^{\bullet+}$ (Table 5.22). The resulting polymers were characterized by ^{1}H NMR (Figures 5.199 and 5.200 in *Experimental* section), which was consistent with the expected spectrum for pMA. To identify the chain-ends present arising from each set of polymerization conditions, the polymers were characterized using matrix assisted laser desorption ionization time of flight mass spectrometry (MALDI-TOF MS). For pMA synthesized using **5**, two peak distributions were observed, corresponding to two sets of end-groups. The first distribution corresponded to polymers capped by the DBMM-derived malonate moiety and a Br end group. Instead, the second set of peaks was consistent with polymers containing the same malonate group and an H end group. Together, these results indicate that while some of the Br chain-end groups are retained, some loss of the Br functionality is also present. For pMA synthesized with $\mathbf{5}^{\bullet+}$, two distinct peak distributions were also observed. One set corresponded to the DBMM-derived malonate group on one end and Br on the other – the expected end groups. The other peak distribution corresponded to H and Br end groups, which can be explained by the proposed background polymerization – a free radical polymerization that is ultimately suppressed by deactivation. Alternatively, the same end groups could also arise from polymers initiated by Br• that ultimately undergo irreversible termination.

To further investigate chain-end fidelity in the absence and presence of $\mathbf{5}^{\bullet+}$, the synthesis of block copolymers was attempted using previously isolated pMA as a macroinitiator in place of DBMM. When pMA synthesized using **5** was resubjected to polymerization conditions in the presence of MA, the resulting polymer was nearly identical to the pMA macroinitiator (Figure 5.11a, blue). Similarly, when MA was replaced by *t*-butyl acrylate (*t*BA), only a minor shift in the chromatogram of the block copolymer was observed relative to the macroinitiator (Figure 5.11a, red). These results indicate significant loss of the Br chain-ends during the O-ATRP of MA.

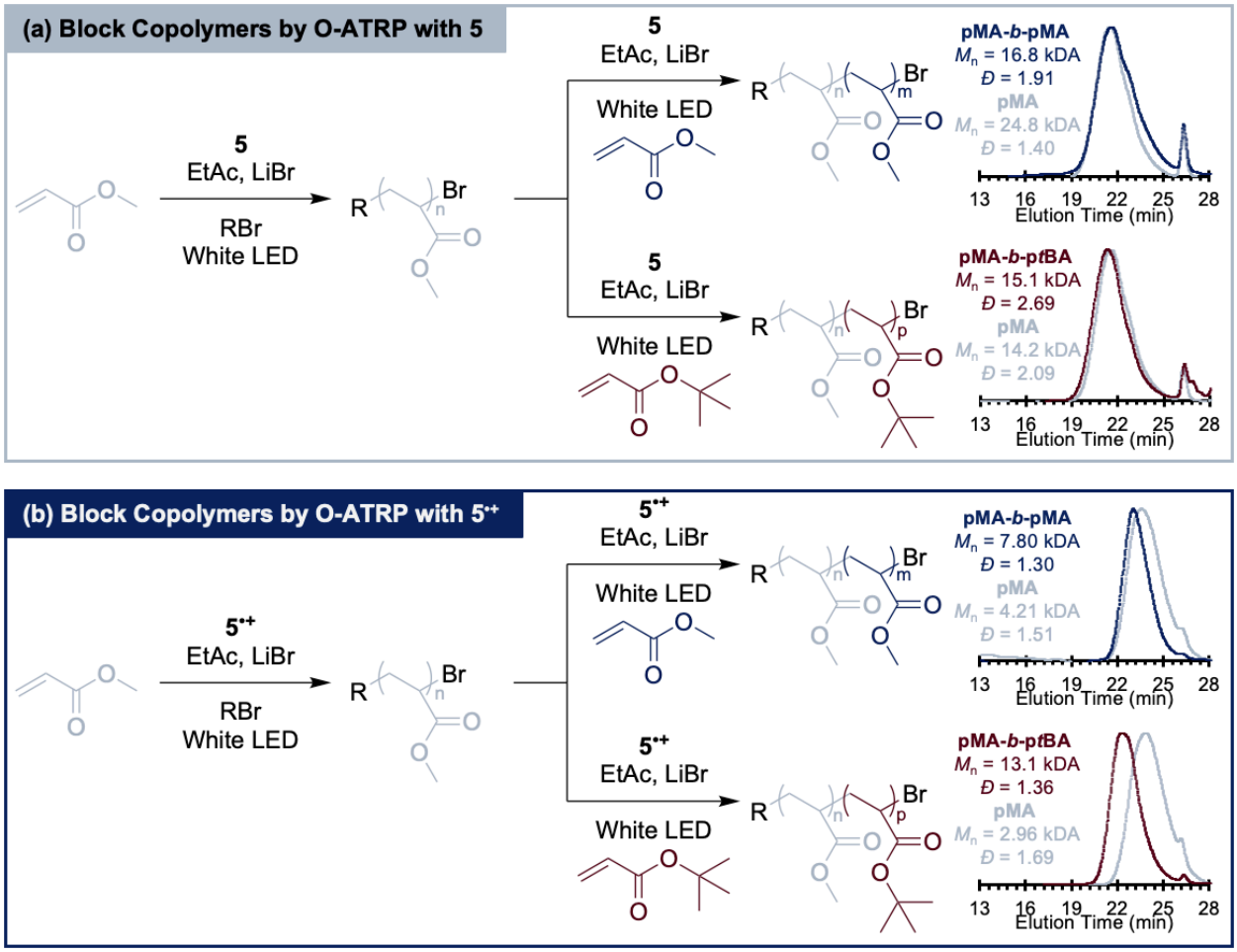

Figure 5.11. *Synthesis of acrylate block copolymers by O-ATRP with* ***5*** *(a) and* $\mathbf{5}^{\bullet+}$ *(b). GPC traces correspond to isolated and dried polymers as measured using a differential refractive index detector (see Section 12 of Experimental for full experiment details).*

By contrast, when pMA synthesized with $\mathbf{5}^{\bullet+}$ was resubjected to polymerization conditions in the presence of MA and *t*BA, clear evidence was found supporting the chain-extension of this macroinitiator. In the case of pMA-*block*-pMA, a small shift in the chromatogram was observed (Figure 5.11b, blue) and the polymer molecular weight (M_n = 7.80 kDa) increased relative to the macroinitiator (M_n = 4.21 kDa). For pMA-*b*-p*t*BA, a more significant shift in the chromatogram (Figure 5.11b, red) and an increase in the copolymer molecular weight (M_n = 13.1 kDa vs. 2.96 kDa for pMA) were observed, providing evidence for improved chain-end fidelity for the polymerization using $\mathbf{5}^{\bullet+}$.

Conclusion

Radical cations of O-ATRP catalysts were synthesized and characterized using a combination of spectroscopic, electrochemical, and x-ray diffraction techniques. To understand their role and possible side reactions in O-ATRP, the reactivity of these compounds was investigated in solution, in deactivation model reactions, and in O-ATRP. Under the appropriate conditions, we discovered these compounds can exhibit reactivity from both the ground state and a photoexcited state. However, the mechanism of this excited state reactivity remains unclear, and deeper investigation of radical cation photophysics is necessary to understand this interesting phenomenon.

Using a deactivation model reaction, the ability of one $PC^{\bullet+}$ to deactivate alkyl radicals was demonstrated by identification of the expected deactivation product. This model reaction was further used to investigate the impact of various factors on deactivation kinetics, such as the identity of the halide or the structure of $PC^{\bullet+}$. Ultimately, four main conclusions were drawn from these experiments: (1) $PC^{\bullet+}Br^-$ is likely the deactivator in O-ATRP; (2) the mechanism of

deactivation appears to be concerted, where $PC^{\bullet+}Br^-$ undergoes a bimolecular reaction with the propagating radical; (3) deactivation with Br^- is faster than with Cl^-, likely because Cl^- is more challenging to oxidize; and (4) the oxidation potential of $PC^{\bullet+}$ correlates with the rate of deactivation, such that more oxidizing radical cations exhibit faster deactivation.

When ion pairing in $PC^{\bullet+}PF_6^-$ was investigated by conductometry, the structure of $PC^{\bullet+}$ was found to have only a minor impact on the strength of ion pairing. However, the polarity of the solvent significantly influences ion pairing, supporting the importance of solvent choice in O-ATRP.

Finally, the impact of radical cations on polymerization control in O-ATRP was investigated with two different monomers. While only limited improvements in polymerization control were observed with MMA – presumably because this system is already well controlled in the absence of added $PC^{\bullet+}$ – significant improvements in the polymerization of MA were achieved by performing O-ATRP with $PC^{\bullet+}$ instead of PC. Ultimately, this work demonstrates the importance of radical cations for deactivation in O-ATRP and shows how limitations in this polymerization method can be overcome by understanding their reactivity.

Experimental

Materials and Methods

Purchased Chemicals

Phenazine Reduction. Phenazine and sodium hydrosulfite were purchased from Alfa Aesar. Reagent grade alcohol was purchased from Fisher.

Buchwald Couplings. Bis(dibenzylideneacetone)palladium(0), sodium t-butoxide, 4-bromobenzotrifluoride, and 4-bromoanisole were purchased from Sigma Aldrich. Bromobenzene,

2-bromonaphthylene, and 1-bromonaphthylene were purchased from Oakwood Chemical. Phenoxazine was purchased from Oxchem, and toluene was obtained and purified using an mBraun MB-SPS-800 solvent purification system and kept under nitrogen atmosphere.

Bromination using N-Bromosuccinimide. *N*-Bromosuccinimide was purchased from VWR, while unstabilized tetrahydrofuran (THF) was purchased from Millipore Sigma.

Bromination using Molecular Bromine. Molecular bromine was purchased from Beantown Chemical, benzene was obtained from Sigma Aldrich, and methanol was purchased from Fisher Scientific.

Suzuki Couplings. Potassium carbonate, 2-naphthylboronic acid, tetrakis(triphenylphosphine)palladium(0), phenylboronic acid, and 4-methoxyphenylboronic acid were purchased from Sigma Aldrich. 4-Biphenylboronic acid was obtained from TCI, 4-trifluoromethylphenylboronic acid was purchased from Matrix Scientific, and THF was obtained and purified using an mBraun MB-SPS-800 solvent purification system and kept under nitrogen atmosphere until use.

$PC^{\bullet+}PF_6^-$ Synthesis. Nitrosonium hexafluorophosphate was purchased from Alfa Aesar, and dichloromethane (DCM) was purchased from Millipore Sigma.

$PC^{\bullet+}SbCl_6^-$ Synthesis. Tris(4-bromophenyl)ammoniumyl hexachloroantimonate was obtained from Sigma Aldrich, whereas DCM was purchased from Millipore Sigma.

For Electrochemistry. Acetonitrile (MeCN), ferrocene, silver nitrate, lithium bromide, lithium chloride, methyl methacrylate, and iron (III) chloride were purchased from Sigma Aldrich. Tetra-n-butylammonium hexafluorophosphate (Bu_4NPF_6) was obtained from TCI America, and hydrochloric acid was purchased from Fisher Scientific.

For Stability Studies. *N,N*-Dimethylacetamide (DMAc), ethyl acetate (EtAc), deuterated (d_7) *N,N*-dimethylformamide (d_7-DMF), lithium bromide, and lithium chloride were purchased from Sigma Aldrich. *N,N*-Dimethylformamide (DMF) was purchased from Alfa Aesar.

For Radical Cation Excited State Studies. Ethyl acetate, o-phenylenediamine, *N,N*-dimethylaniline, aniline, 3-methylindole, 1-methylindole, indole, 1,4-dimethoxybenzene, *N*-methylacetanilide, and *N,N*-dimethylacetamide were purchased from Sigma Aldrich. *N*-Methylaniline was purchased from Alpha Aesar, while *N,N*-dimethyltrifluoroacetamide was purchased from TCI.

For Bromine Radical Trapping Experiments. Bromocyclohexane, chlorocyclohexane, deuterated acetonitrile, and deuterated (d_7) *N,N*-dimethylformamide were purchased from Sigma Aldrich. Cyclohexane was purchased from Acros Organics, and deuterated dimethylsulfoxide (DMSO) was purchased from Cambridge Isotopes.

For Deactivation Model Reactions. Azobisisobutyronitrile (AIBN), lithium bromide, lithium chloride, ethyl acetate, and 2-bromo-2-methylpropanenitrile were purchased from Sigma Aldrich.

For Ion Pairing Measurements. *N,N*-Dimethylacetamide, ethyl acetate, and tetrahydrofuran were purchased from Sigma Aldrich. Acetone was purchased from Fisher Scientific, while tetra-n-butylammonium bromide was purchased from TCI.

For Polymerizations. *N,N*-Dimethylacetamide, ethyl acetate, tetrahydrofuran, methyl methacrylate (MMA), ethyl acrylate (EA), n-butyl acrylate (nBA), 2-ethylhexyl acrylate (EHA), ethylene glycol methyl ether acrylate (EGMEA), diethyl-2-bromo-2-methylmalonate (DBMM), and lithium bromide were purchased from Sigma Aldrich. Methyl acrylate (MA) was purchased from Alfa Aesar, while t-butyl acrylate was purchased from Millipore Sigma.

For Matrix Assisted Laser Desorption Ionization Time of Flight Mass Spectrometry. Sodium trifluoroacetate was purchased from TCI, 4-hydroxybenzilidenemalononitrile was purchased from Alfa Aesar, and unstabilized tetrahydrofuran was purchased from Millipore Sigma.

Chemical Preparation and Storage

Unless otherwise stated, chemicals and reagents were used as received from the manufacturer. Dihydrophenazine, bis(dibenzylideneacetone)palladium(0), and tris(4-bromophenyl)ammoniumyl hexachloroantimonate were stored in a nitrogen filled glovebox until their use. Tetrakis(triphenylphosphine)palladium(0) and nitrosonium hexafluorophosphate were stored in a nitrogen filled glovebox at -40 ºC. Toluene and THF (for Suzuki couplings) were purified using an mBraun MB-SPS-800 solvent purification system and kept under nitrogen atmosphere until they were used. Solvents for radical cation syntheses (DCM), stability studies (DMAc, EtAc, DMF, d_7-DMF), radical cation excited state studies (EtAc), and polymerizations (DMAc, EtAc, THF) were stored in a nitrogen filled glovebox prior to use.

For Radical Cation Excited State Studies. o-Phenylenediamine and 3-methylindole were purified by sublimation and stored under nitrogen prior to use. Aniline, *N*-methylaniline, *N,N*-dimethylaniline, and 1-methylindole were purified by distillation, degassed by nitrogen bubbling, and then stored under nitrogen prior to being used. All other substrates were used as received and stored under nitrogen prior to use.

For Polymerizations. Methyl methacrylate, methyl acrylate, ethyl acrylate, n-butyl acrylate, t-butyl acrylate, 2-ethylhexyl acrylate, ethylene glycol methyl ether acrylate, and diethyl-2-bromo-2-methymalonate were dried overnight using calcium hydride, distilled under reduced

pressure, and freeze-pump-thawed prior to being stored in a nitrogen glovebox at -40 ºC. All reagents were allowed to warm to room temperature prior to their use in polymerizations.

For Electrochemistry. Methyl methacrylate was purified to remove inhibitor by passing it through an alumina plug. It was then stored at -25 ºC until it was used.

Experimental Equipment

Electrochemistry. For all electrochemistry performed in this work, 0.1 M Bu_4NPF_6 was used as the supporting electrolyte. Cyclic voltammetry and spectro-electrochemistry were performed using a three-electrode cell, with a glassy carbon working electrode, platinum counter electrode, and a silver/silver nitrate (0.01 M $AgNO_3$ in MeCN with 0.1 M Bu_4NPF_6) reference electrode. For spectro-electrochemistry, the counter electrode was separated from the PC solution using a vycor glass frit. As appropriate, potentials were referenced to a saturated calomel electrode (SCE) by adding 0.29 V to the potential vs. $AgNO_3$, or referenced to the ferrocene/ferrocenium redox couple by measurement of ferrocene under identical conditions. Open circuit potential measurements were performed using the same experimental apparatus used for cyclic voltammetry. Instead, conductometry measurements were made using a two-electrode conductivity probe with a cell constant of 1.

For measurements using a rotating ring disk electrode (RRDE), a Gamry RDE710 Rotating Electrode was used along with two Gamry potentiostats (see *Instrumentation Section*). For the working electrode, a Gamry E7HT HotSpot RRDE tip (glassy carbon disk, platinum disk, part number: AFE7R2GCPT) was used. The counter electrode was a platinum wire, and a silver/silver nitrate reference electrode was used in the same solvent system.

Light Reactors. The following LEDs were used in the construction of light reactors for this work. For light beakers and LED wells, strips of white LEDs were purchased from Creative Lighting Solutions (item no. CL-FRS1210-5M-12V-WH). Reactors were constructed by wrapping a 400 mL beaker (10.0 cm tall, 8.5 cm diameter) or a recrystallization disk (5.0 cm tall, 7.0 cm diameter) with aluminum foil and wrapping LED strips (9 LED segments, 16” total) around the inside of the reactor. Figure 5.14 shows the qualitative emission spectrum of the LEDs used in this work.

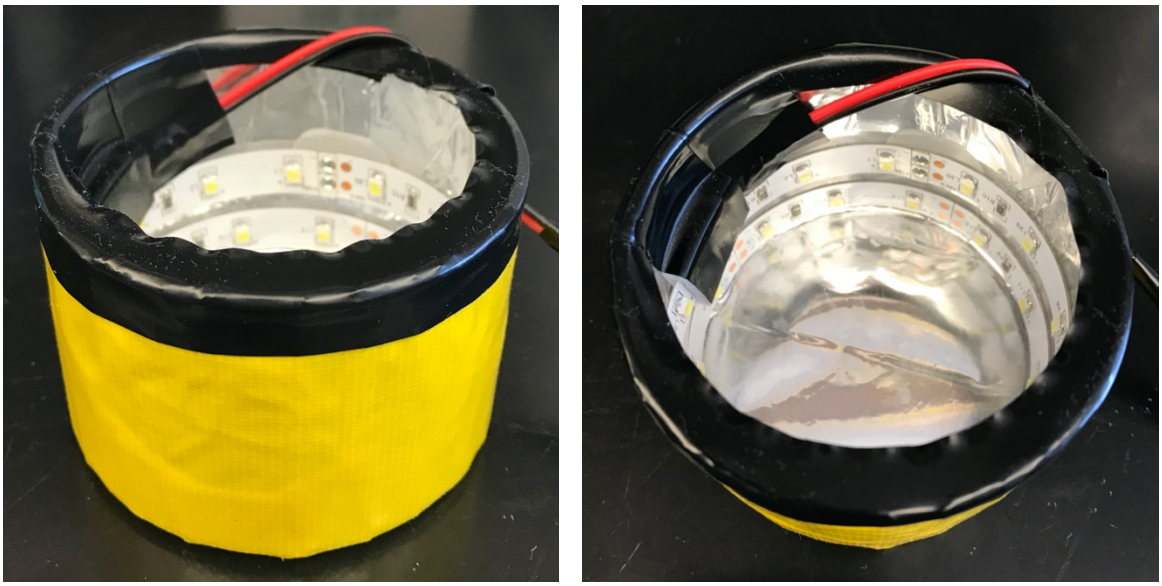

Figure 5.12. *Photographs of the LED wells used in this work.*

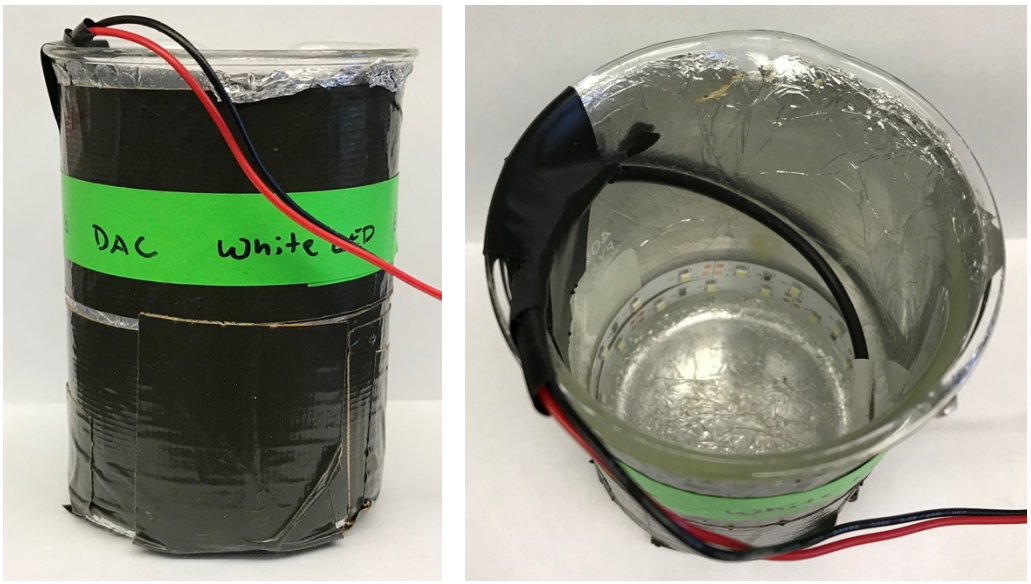

Figure 5.13. *Photographs of the LED beakers used in this work.*

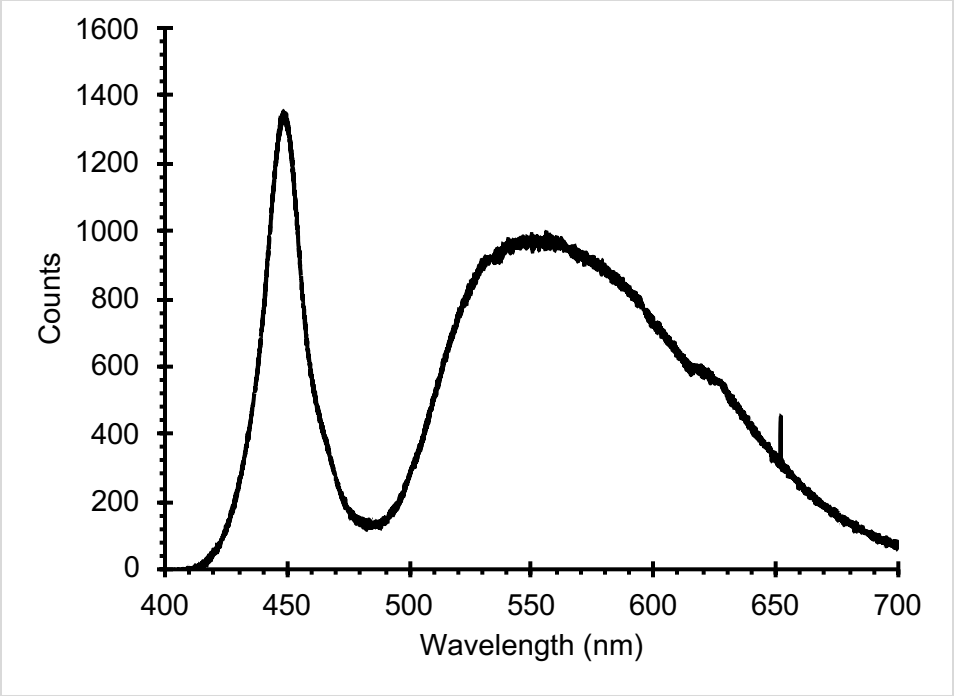

Figure 5.14. *Emission spectrum of the LEDs used in this work.*

Instrumentation

Nuclear magnetic resonance (NMR) spectroscopy was performed using either a Bruker US 400 MHZ spectrometer or a Bruker Ascend 400 MHZ spectrometer. All ^{1}H NMR spectra are

reported in **δ** units, parts per million (ppm), and are referenced to residual chloroform (7.26 ppm), benzene (7.15), or acetonitrile (1.94) signals. Analysis of polymer molecular weights were performed via gel permeation chromatography (GPC) coupled with multi-angle light scattering (MALS), using an Agilent HPLC fitted with one guard column, three PLgel 5 μm MIXED-C gel permeation columns, a Wyatt Technology TrEX differential refractometer, and a Wyatt Technology miniDAWN TREOS light scattering detector, using THF as the eluent at a flow rate of 1.0 mL/min. The following dn/dc values were used for analysis of polymer molecular weight (Table 5.5):

Table 5.5. *Values of dn/dc used to determine the molecular weight of homopolymers in this work.*

Homopolymer	dn/dc	Reference
poly(methyl methacrylate)	0.084	-
poly(methyl acrylate)	0.068	50
poly(ethyl acrylate)	0.061	50
poly(n-butyl acrylate)	0.063	50
poly(t-butyl acrylate)	0.064	50
poly(2-ethylhexyl acrylate)	0.068	50
poly(ethylene glycol methyl ether acrylate)	0.060	51

For block copolymers, dn/dc values were measured *on-line* by measurement of a sample at known concentration. Electrochemical measurements were performed using either a Gamry Interface 1010B or 1010E potentiostat. UV-Visible spectroscopy was performed using an Agilent Cary 5000 UV-Vis-NIR spectrometer. For *in-situ* UV-Vis measurements, an ocean-optics FLAME-S-VIS-NIR-ES spectrometer was used with an Agilent SS replaceable tip, 10 mm path length, Cary 100/300 fiber optic probe. Measurements of LED emission were made using an Olympus IX73 inverted microscope connected to a Horiba iHR 550 spectrometer with a Horiba Synapse back-illuminated CCD camera and a 1200 blaze/mm grating. For qualitative measurements of LED emission intensity, light sources were placed in the same configuration and

the light directed into an opening in the microscope. Single crystal X-ray diffractometry was performed using a Bruker D8 Quest ECO single-crystal X-ray diffractometer equipped with Mo Kα (λ = 0.71073 Å). Data was collected and integrated using the Bruker APEX 3 software. Absorption correction were applied using SADABS.[52] Crystal structures were solved using SHELXT and refined with the aid of successive difference Fourier maps by SHELXL operated in conjunction with OLEX2 software.[53-55] Hydrogen atoms were placed in ideal positions and refined using a riding model for all structures. Gas chromatography was performed using a Varian CP-3800 gas chromatograph equipped with a flame ionization detector. Conductometry was performed using a Yellow Springs Instruments model 31 conductivity bridge with a Topac S216T conductivity probe. Matrix assisted laser desorption ionization time of flight mass spectrometry was performed using a Bruker Microflex LRF.

Procedures

Photocatalyst (PC) Synthesis

Catalysts **1 – 11** were synthesized according to previously published literature procedures (Figure 5.15).[16,17,39,56] ^{1}H NMR characterization matched that reported for the original syntheses.

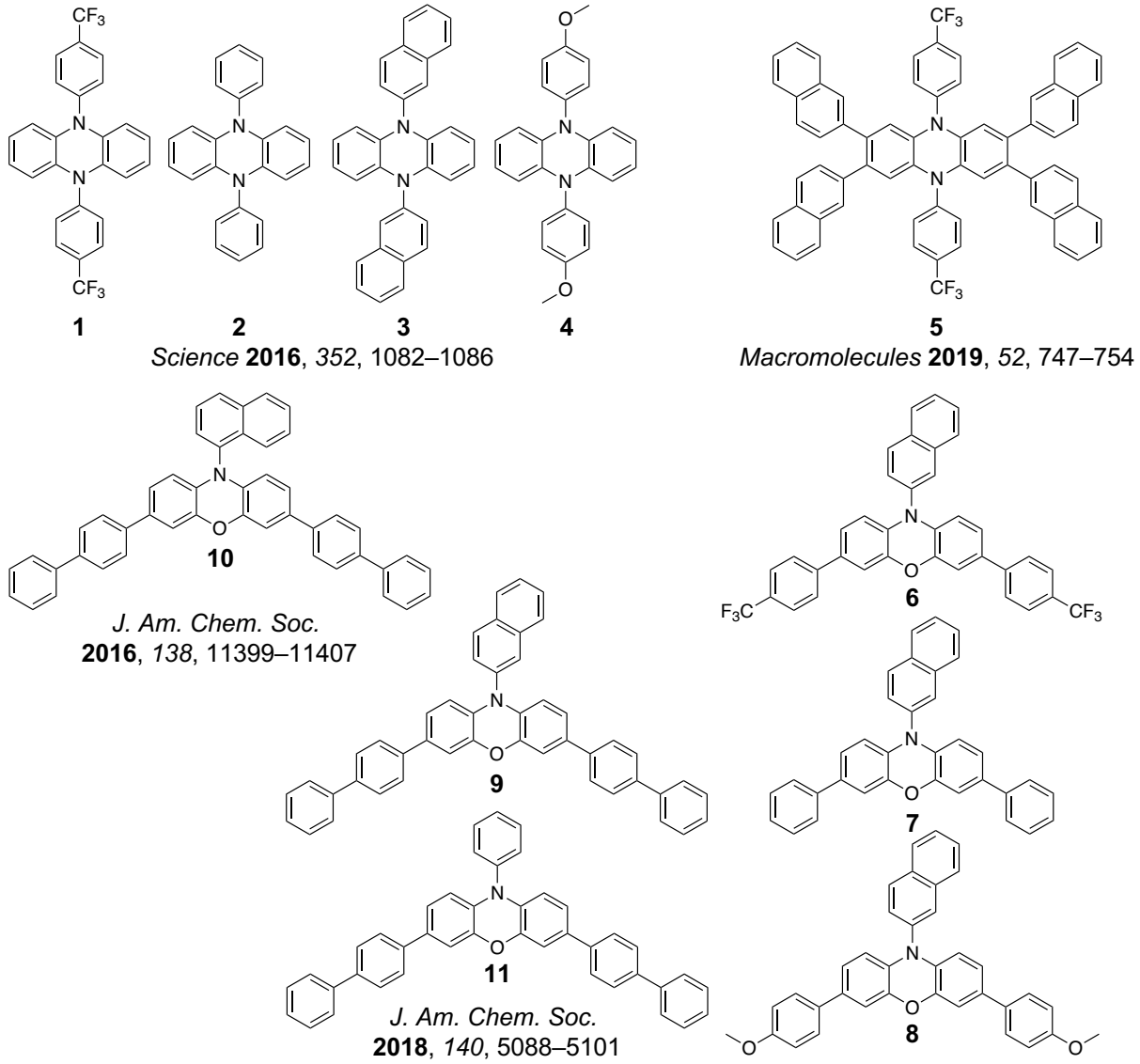

Figure 5.15. *Structures of catalysts investigated in this work and references for their syntheses.*

Radical Cation Syntheses Using Nitrosonium Hexafluorophosphate

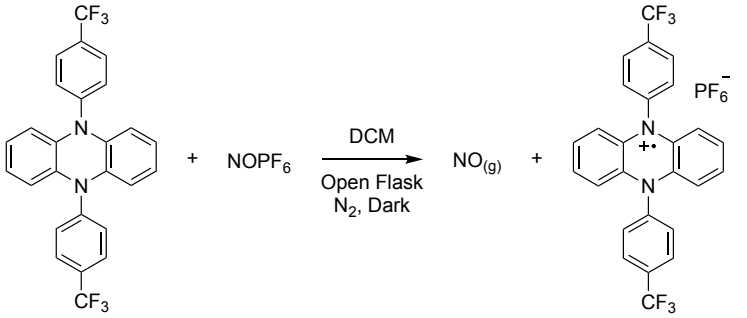

Figure 5.16. *Scheme for the synthesis of* $\boldsymbol{1^{\bullet+}PF_6^-}$.

*Synthesis of 5,10-di(4-trifluorobenzo)-5,10-dihydrophenazinium hexafluorophosphate (**1**$^{\bullet+}$**PF**$_6^-$).* A flask was charged with **1** (198.4 mg, 0.4218 mmol, 1 eq) and a magnetic stir bar before being pumped into a nitrogen glovebox. DCM (20 mL) was added to the flask. Under constant purge, nitrosonium hexafluorophosphate (73.9 mg, 0.422 mmol, 1 eq) was weighed out using a plastic spatula and added to the flask. The reaction was then covered with aluminum foil and left to stir in the dark, open to the glovebox atmosphere with constant purging, for 30 min. *Caution: the $NO_{(g)}$ that forms as a byproduct of this reaction is toxic.* After the reaction was complete, the reaction solution was crashed out into hexanes (200 mL), resulting in the formation of a green precipitate. The solid was collected by vacuum filtration and washed with additional hexanes prior to being dried overnight under high vacuum. Yield = 0.1725 g (66.47%).

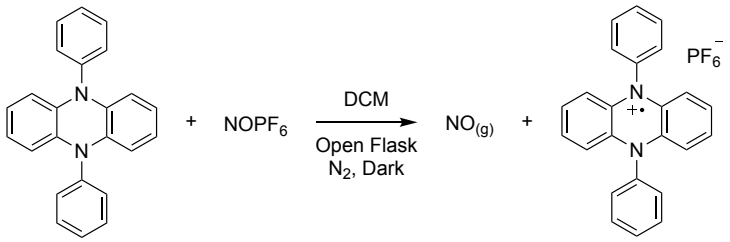

Figure 5.17. *Scheme for the synthesis of **2**$^{\bullet+}$**PF**$_6^-$.*

*Synthesis of 5,10-diphenyl-5,10-dihydrophenazinium hexafluorophosphate (**2**$^{\bullet+}$**PF**$_6^-$).* A flask was charged with **2** (200.8 mg, 0.6004 mmol, 1 eq) and a magnetic stir bar before being pumped into a nitrogen glovebox. DCM (20 mL) was added to the flask. Under constant purge, nitrosonium hexafluorophosphate (105.0 mg, 0.6001 mmol, 1 eq) was weighed out using a plastic spatula and added to the flask. The reaction was then covered with aluminum foil and left to stir in the dark, open to the glovebox atmosphere with constant purging, for 30 min. *Caution: the $NO_{(g)}$ that forms as a byproduct of this reaction is toxic.* After the reaction was complete, the reaction

solution was crashed out into hexanes (200 mL), resulting in the formation of a green precipitate. The solid was collected by vacuum filtration and washed with additional hexanes prior to being dried overnight under high vacuum. Yield = 275.7 mg (95.86%).

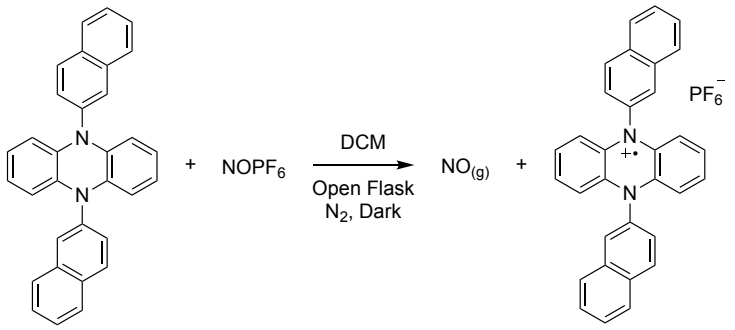

Figure 5.18. *Scheme for the synthesis of* ***3•+PF6-****.*

Synthesis of 5,10-di(2-naphthyl)-5,10-dihydrophenazinium hexafluorophosphate ***(3•+PF6-).*** A flask was charged with **3** (123.8 mg, 0.2849 mmol, 1 eq) and a magnetic stir bar before being pumped into a nitrogen glovebox. DCM (20 mL) was added to the flask. Under constant purge, nitrosonium hexafluorophosphate (49.9 mg, 285 mmol, 1 eq) was weighed out using a plastic spatula and added to the flask. The reaction was then covered with aluminum foil and left to stir in the dark, open to the glovebox atmosphere with constant purging, for 30 min. *Caution: the $NO_{(g)}$ that forms as a byproduct of this reaction is toxic.* After the reaction was complete, the reaction solution was crashed out into hexanes (200 mL), resulting in the formation of a green precipitate. The solid was collected by vacuum filtration and washed with additional hexanes prior to being dried overnight under high vacuum. Yield = 137.4 mg (83.17%).

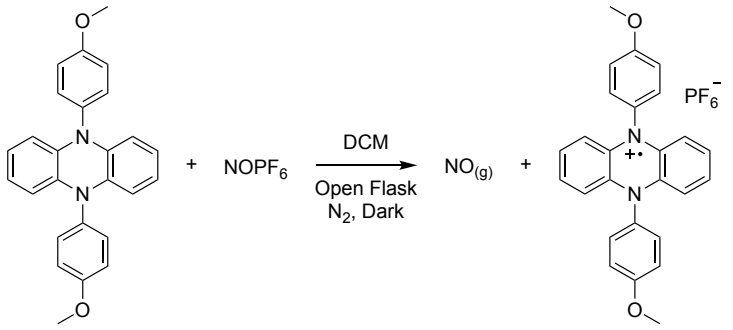

Figure 5.19. *Scheme for the synthesis of* ***4•+PF6-****.*

*Synthesis of 5,10-di(4-methoxyphenyl)-5,10-dihydrophenazinium hexafluorophosphate (**4•+PF6-**).* A flask was charged with **4** (196.6 mg, 0.4984 mmol, 1 eq) and a magnetic stir bar before being pumped into a nitrogen glovebox. DCM (20 mL) was added to the flask. Under constant purge, nitrosonium hexafluorophosphate (86.9 mg, 0.497 mmol, 1 eq) was weighed out using a plastic spatula and added to the flask. The reaction was then covered with aluminum foil and left to stir in the dark, open to the glovebox atmosphere with constant purging, for 30 min. *Caution: the $NO_{(g)}$ that forms as a byproduct of this reaction is toxic.* After the reaction was complete, the reaction solution was crashed out into hexanes (200 mL), resulting in the formation of a green precipitate. The solid was collected by vacuum filtration and washed with additional hexanes prior to being dried overnight under high vacuum. Yield = 0.2114 g (78.62%). Anal. Calcd. For $C_{26}H_{22}F_6N_2O_2P$: C, 57.89; H, 4.11; N, 5.19; P, 5.74. Found: C, 56.99; H, 4.31; N, 4.86; P, 5.78.

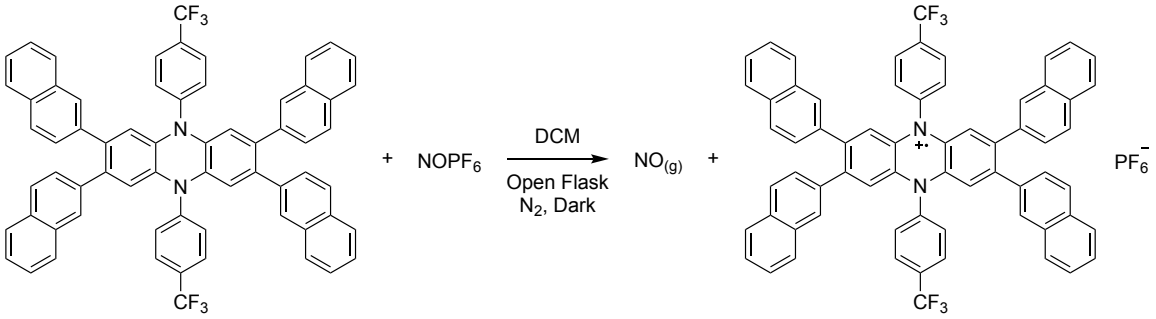

Figure 5.20. *Scheme for the synthesis of* ***5•+PF6-****.*

*Synthesis of 2,3,7,8-tetra(2-naphthyl)-5,10-di(4-trifluorobenzo)-5,10-dihydrophenazinium hexafluorophosphate (**5**$^{\bullet+}$**PF**$_6^-$).* A flask was charged with **5** (196.4 mg, 0.2014 mmol, 1 eq) and a magnetic stir bar before being pumped into a nitrogen glovebox. DCM (20 mL) was added to the flask. Under constant purge, nitrosonium hexafluorophosphate (36.0 mg, 0.206 mmol, 1 eq) was weighed out using a plastic spatula and added to the flask. The reaction was then covered with aluminum foil and left to stir in the dark, open to the glovebox atmosphere with constant purging, for 30 min. *Caution: the $NO_{(g)}$ that forms as a byproduct of this reaction is toxic.* After the reaction was complete, the reaction solution was crashed out into hexanes (200 mL), resulting in the formation of a blue precipitate. The solid was collected by vacuum filtration and washed with additional hexanes prior to being dried overnight under high vacuum. Yield = 179.8 mg (79.70%).

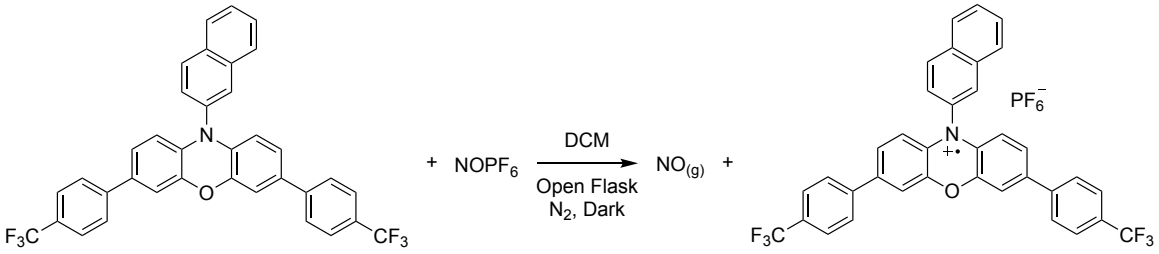

Figure 5.21. *Scheme for the synthesis of **6**$^{\bullet+}$**PF**$_6^-$.*

*Synthesis of 3,7-di(4-trifluorobenzo)-10-(2-naphthyl)-phenoxazinium hexafluorophosphate (**6**$^{\bullet+}$**PF**$_6^-$).* A flask was charged with **6** (203.5 mg, 0.3406 mmol, 1 eq) and a magnetic stir bar before being pumped into a nitrogen glovebox. DCM (20 mL) was added to the flask. Under constant purge, nitrosonium hexafluorophosphate (59.6 mg, 0.341 mmol, 1 eq) was weighed out using a plastic spatula and added to the flask. The reaction was then covered with aluminum foil and left to stir in the dark, open to the glovebox atmosphere with constant purging,

for 30 min. *Caution: the $NO_{(g)}$ that forms as a byproduct of this reaction is toxic.* After the reaction was complete, the reaction solution was crashed out into hexanes (200 mL), resulting in the formation of a green precipitate. The solid was collected by vacuum filtration and washed with additional hexanes prior to being dried overnight under high vacuum. Yield = 0.2083 g (82.36%).

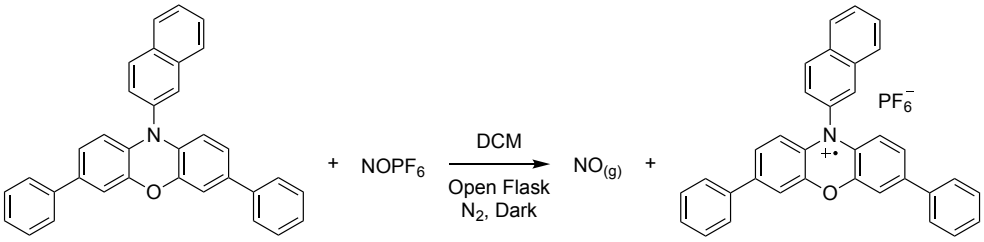

Figure 5.22. *Scheme for the synthesis of* ***$7^{\bullet+}PF_6^-$***.

*Synthesis of 3,7-diphenyl-10-(2-naphthyl)-phenoxazinium hexafluorophosphate (**$7^{\bullet+}PF_6^-$**).*

A flask was charged with **7** (200.6 mg, 0.4346 mmol, 1 eq) and a magnetic stir bar before being pumped into a nitrogen glovebox. DCM (20 mL) was added to the flask. Under constant purge, nitrosonium hexafluorophosphate (76.0 mg, 434 mmol, 1 eq) was weighed out using a plastic spatula and added to the flask. The reaction was then covered with aluminum foil and left to stir in the dark, open to the glovebox atmosphere with constant purging, for 30 min. *Caution: the $NO_{(g)}$ that forms as a byproduct of this reaction is toxic.* After the reaction was complete, the reaction solution was crashed out into hexanes (200 mL), resulting in the formation of a green precipitate. The solid was collected by vacuum filtration and washed with additional hexanes prior to being dried overnight under high vacuum. Yield = 0.2388 g (90.59%).

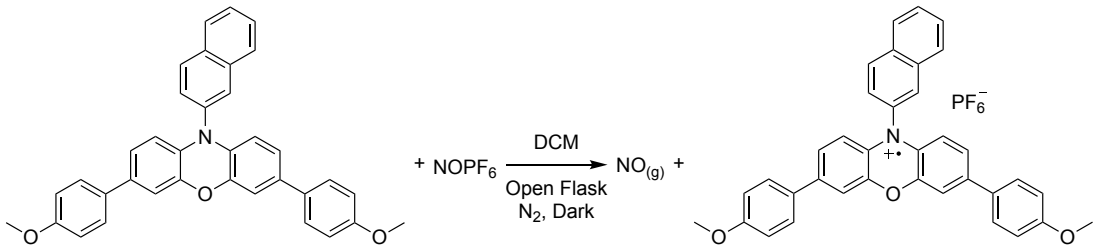

Figure 5.23. *Scheme for the synthesis of* ***8•+PF6-***.

*Synthesis of 3,7-di(4-methoxyphenyl)-10-(2-naphthyl)-phenoxazinium hexafluorophosphate (**8•+PF6-**).* A flask was charged with **8** (208.5 mg, 0.3997 mmol, 1 eq) and a magnetic stir bar before being pumped into a nitrogen glovebox. DCM (10 mL) was added to the flask. Under constant purge, nitrosonium hexafluorophosphate (70.2 mg, 0.400 mmol, 1 eq) was weighed out using a plastic spatula and added to the flask. The reaction was then covered with aluminum foil and left to stir in the dark, open to the glovebox atmosphere with constant purging, for 30 min. *Caution: the $NO_{(g)}$ that forms as a byproduct of this reaction is toxic.* After the reaction was complete, the reaction solution was crashed out into hexanes (200 mL), resulting in the formation of a green precipitate. The solid was collected by vacuum filtration and washed with additional hexanes prior to being dried overnight under high vacuum. Yield = 244.7 mg (82.45%).

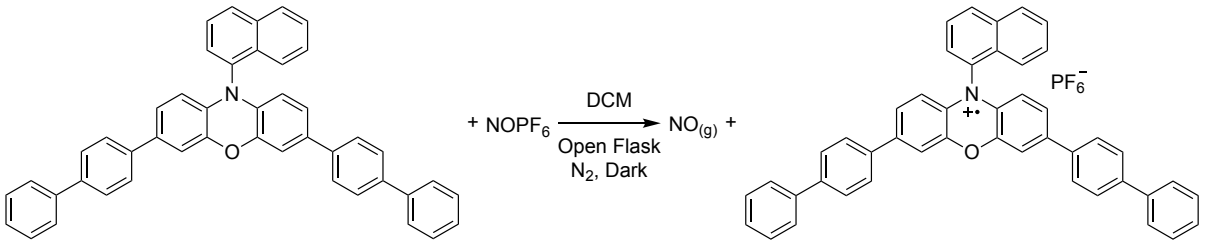

Figure 5.24. *Scheme for the synthesis of* ***10•+PF6-***.

*Synthesis of 3,7-di(4-biphenyl)-10-(1-naphthyl)-phenoxazinium hexafluorophosphate (**10•+PF6-**).* A flask was charged with **10** (204.1 mg, 0.3325 mmol, 1 eq) and a magnetic stir bar

before being pumped into a nitrogen glovebox. DCM (20 mL) was added to the flask. Under constant purge, nitrosonium hexafluorophosphate (58.6 mg, 0.335 mmol, 1 eq) was weighed out using a plastic spatula and added to the flask. The reaction was then covered with aluminum foil and left to stir in the dark, open to the glovebox atmosphere with constant purging, for 30 min. *Caution: the $NO_{(g)}$ that forms as a byproduct of this reaction is toxic.* After the reaction was complete, the reaction solution was crashed out into hexanes (200 mL), resulting in the formation of a green precipitate. The solid was collected by vacuum filtration and washed with additional hexanes prior to being dried overnight under high vacuum. After the product of this reaction was characterized, it was determined that a significant portion of neutral **10** remained in the mixture. As such, a portion of the mixture (95.7 mg) was subjected to further oxidation with nitrosonium hexafluorophosphate (24.4 mg) in DCM (10 mL), yielding the product in greater purity (*see Estimation of Radical Cation Purity by Open Circuit Potential for details*).

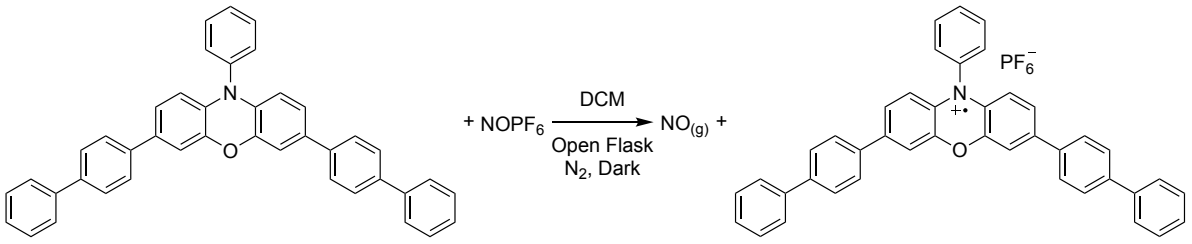

Figure 5.25. *Scheme for the synthesis of* ***11$^{\bullet+}$PF$_6^-$***.

*Synthesis of 3,7-di(4-biphenyl)-10-phenylphenoxazinium hexafluorophosphate (**11$^{\bullet+}$PF$_6^-$**).*

A flask was charged with **11** (193.1 mg, 0.3426 mmol, 1 eq) and a magnetic stir bar before being pumped into a nitrogen glovebox. DCM (20 mL) was added to the flask. Under constant purge, nitrosonium hexafluorophosphate (60.0 mg, 0.343 mmol, 1 eq) was weighed out using a plastic spatula and added to the flask. The reaction was then covered with aluminum foil and left to stir

in the dark, open to the glovebox atmosphere with constant purging, for 30 min. *Caution: the $NO_{(g)}$ that forms as a byproduct of this reaction is toxic.* After the reaction was complete, the reaction solution was crashed out into hexanes (200 mL), resulting in the formation of a green precipitate. The solid was collected by vacuum filtration and washed with additional hexanes prior to being dried overnight under high vacuum. After the product of this reaction was characterized, it was determined that a significant portion of neutral **11** remained in the mixture. As such, a portion of the mixture (97.8 mg) was subjected to further oxidation with nitrosonium hexafluorophosphate (26.9 mg) in DCM (10 mL), yielding the product in greater purity (*see Estimation of Radical Cation Purity by Open Circuit Potential for details*). Anal. Calcd. For $C_{42}H_{29}F_6NOP$: C, 71.18; H, 4.12; N, 1.98; P, 4.37. Found: C, 69.92; H, 4.54; N, 2.03; P, 4.66.

Radical Cation Synthesis Using Tris(4-bromophenyl)ammoniumyl Hexachloroantimonate

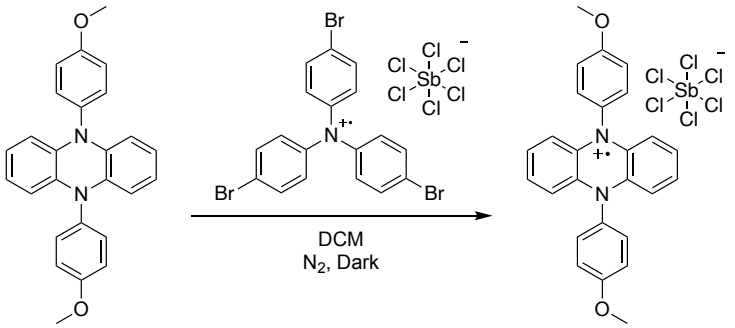

Figure 5.26. *Scheme for the synthesis of* ***$4^{\bullet+}SbCl_6^-$***.

*Synthesis of 5,10-di(4-methoxyphenyl)-5,10-dihydrophenazinium hexachloroantimonate (**$4^{\bullet+}SbCl_6^-$**).* A flask was charged with **4** (104.9 mg, 0.2535 mmol, 1 eq) and a magnetic stir bar before being pumped into a nitrogen glovebox. DCM (20 mL) was added to the flask. Tris(4-bromophenyl)ammoniumyl hexachloroantimonate (217.9 mg, 0.2669 mmol, 1 eq) was weighed

out using a plastic spatula and added to the flask. The reaction was then covered with aluminum foil and left to stir in the dark for 30 min. After the reaction was complete, the reaction solution was crashed out into hexanes (200 mL), resulting in the formation of a green precipitate. The solid was collected by vacuum filtration and washed with additional hexanes prior to being dried overnight under high vacuum. Yield = 173.5 mg (89.53%). Crystals for single crystal x-ray diffraction were obtained by dissolving $\mathbf{4^{\bullet+}SbCl_6^-}$ in hot MeCN followed by vapor diffusion of benzene into the solution over several days, which yielded dark green needles.

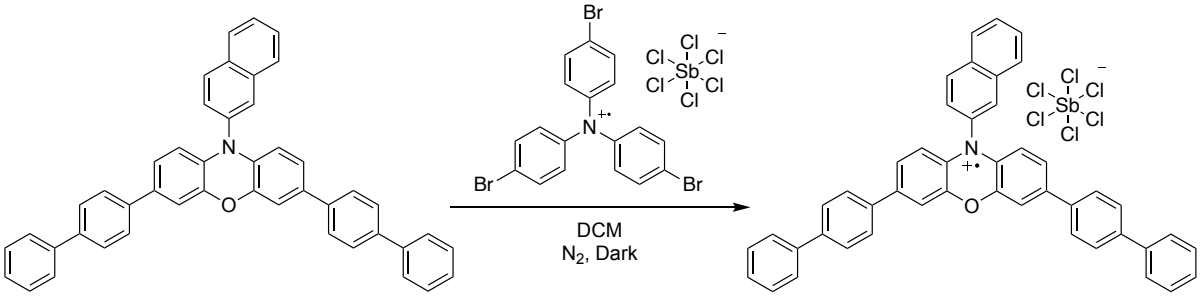

Figure 5.27. *Scheme for the synthesis of* $\mathbf{9^{\bullet+}SbCl_6^-}$.

Synthesis of 3,7-di(4-biphenyl)-10-(2-naphthyl)-phenoxazinium hexafluorophosphate ($\mathbf{9^{\bullet+}SbCl_6^-}$). A flask was charged with **9** (96.4 mg, 0.1571 mmol, 1 eq) and a magnetic stir bar before being pumped into a nitrogen glovebox. DCM (20 mL) was added to the flask. Tris(4-bromophenyl)ammoniumyl hexachloroantimonate (153.0 mg, 0.1874 mmol, 1 eq) was weighed out using a plastic spatula and added to the flask. The reaction was then covered with aluminum foil and left to stir in the dark for 30 min. After the reaction was complete, the reaction solution was crashed out into hexanes (200 mL), resulting in the formation of a green precipitate. The solid was collected by vacuum filtration and washed with additional hexanes prior to being dried overnight under high vacuum. Yield = 153.1 mg (96.78%). Crystals for single crystal x-ray diffraction were obtained by dissolving $\mathbf{9^{\bullet+}SbCl_6^-}$ in hot DCM followed by vapor diffusion of

hexanes into the solution over several days, which yielded dark green needles.

Characterization of Photocatalysts and Radical Cations

Cyclic Voltammetry of Photocatalysts in Acetonitrile

For details regarding the electrochemical apparatus, see *Experimental Equipment* section of this document. For PCs **1** – **11**, cyclic voltammetry was previously performed and reported to evaluate redox reversibility and utility as a catalyst.[16,17,39,56] However, these molecules are often measured in DMAc, both for solubility reasons and applicability to O-ATRP. As the electrochemistry in this work (spectro-electrochemistry and open circuit potential measurements) was performed in MeCN, the following cyclic voltammograms were collected to determine the $E_{1/2} \sim E^o(PC^{\bullet+}/PC)$ in this solvent system.

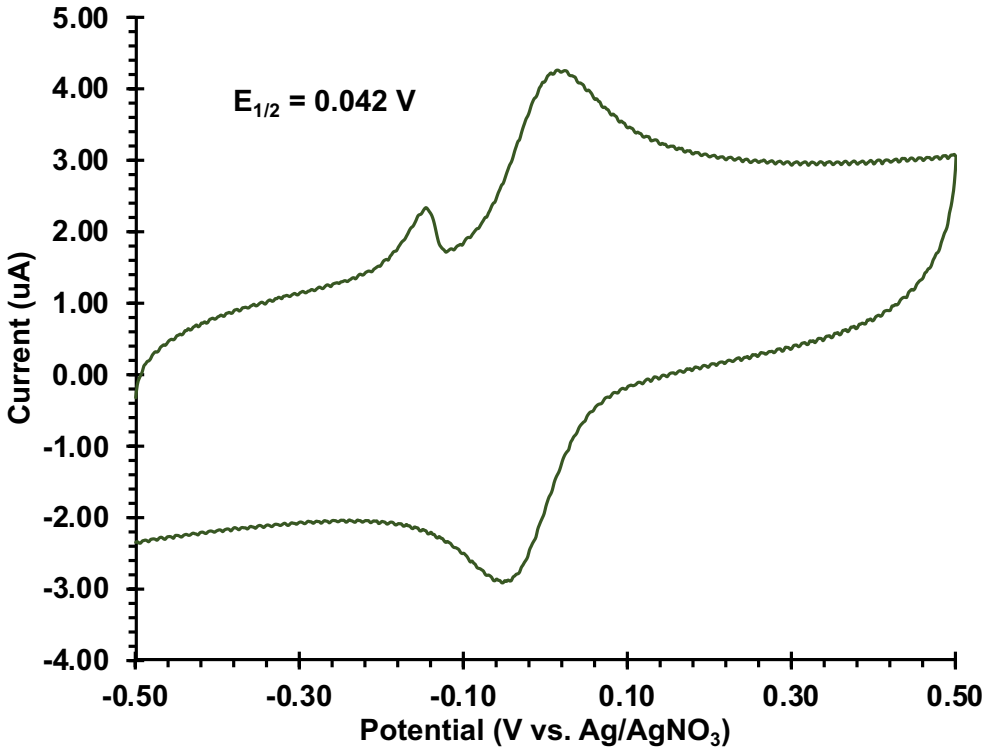

Figure 5.28. *Cyclic voltammogram of **1** in MeCN (scan rate = 100 mV s^{-1}).*

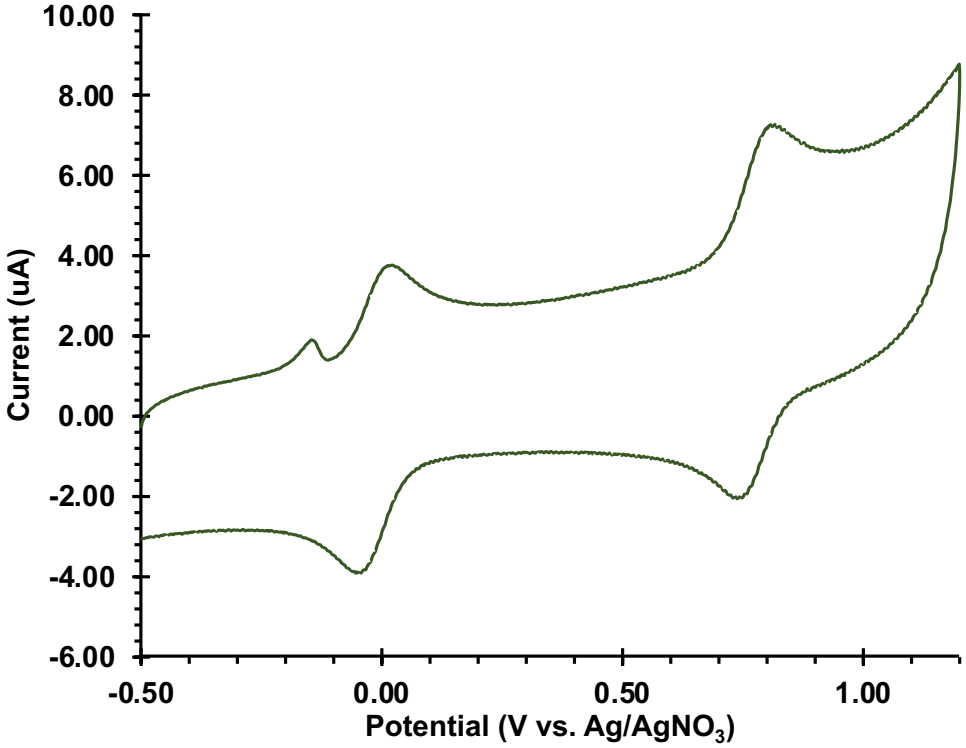

Figure 5.29. *Cyclic voltammogram showing the double oxidation of* ***1*** *in MeCN (scan rate = 100 mV* s^{-1}*).*

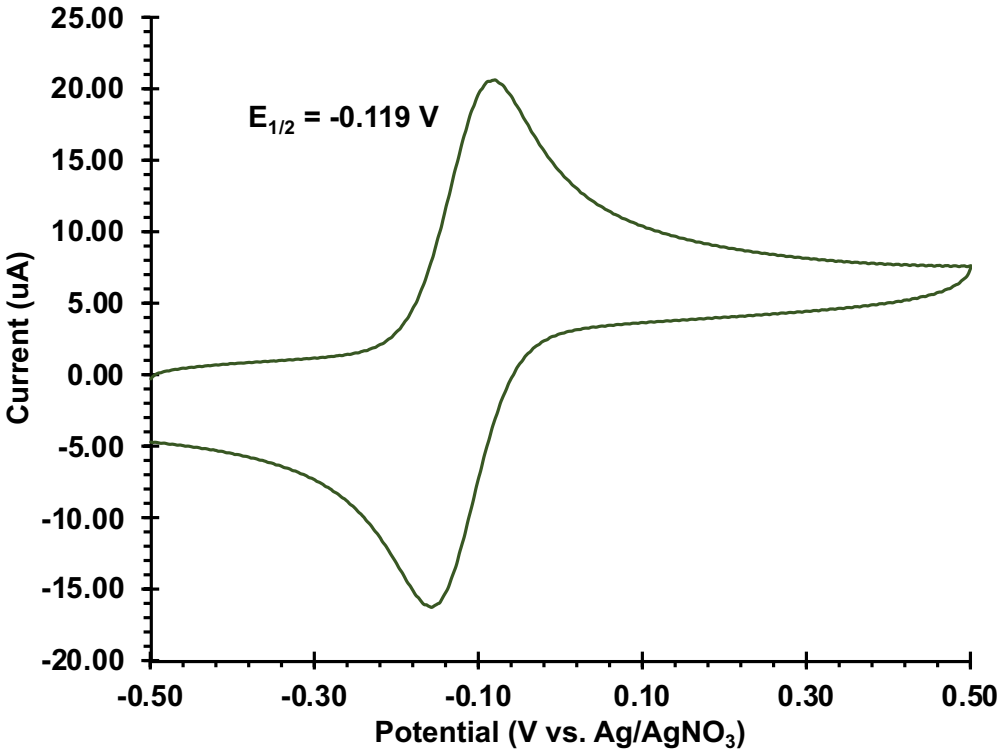

Figure 5.30. *Cyclic voltammogram of* ***2*** *in MeCN (scan rate = 100 mV s^{-1}).*

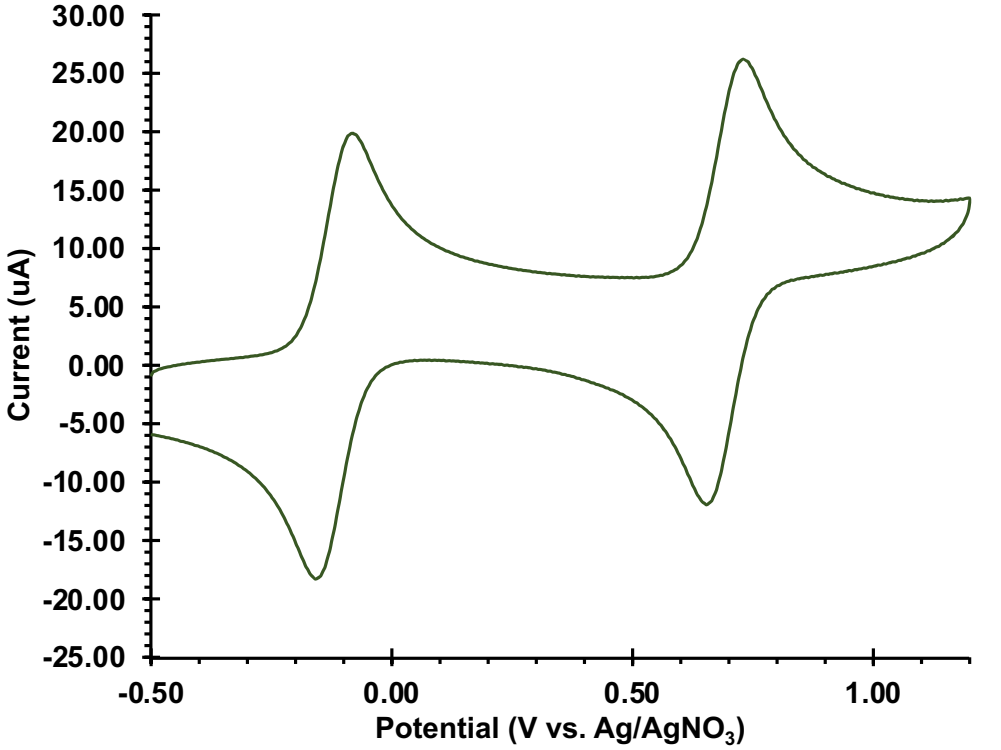

Figure 5.31. *Cyclic voltammogram showing the double oxidation of* ***2*** *in MeCN (scan rate = 100 mV s^{-1}).*

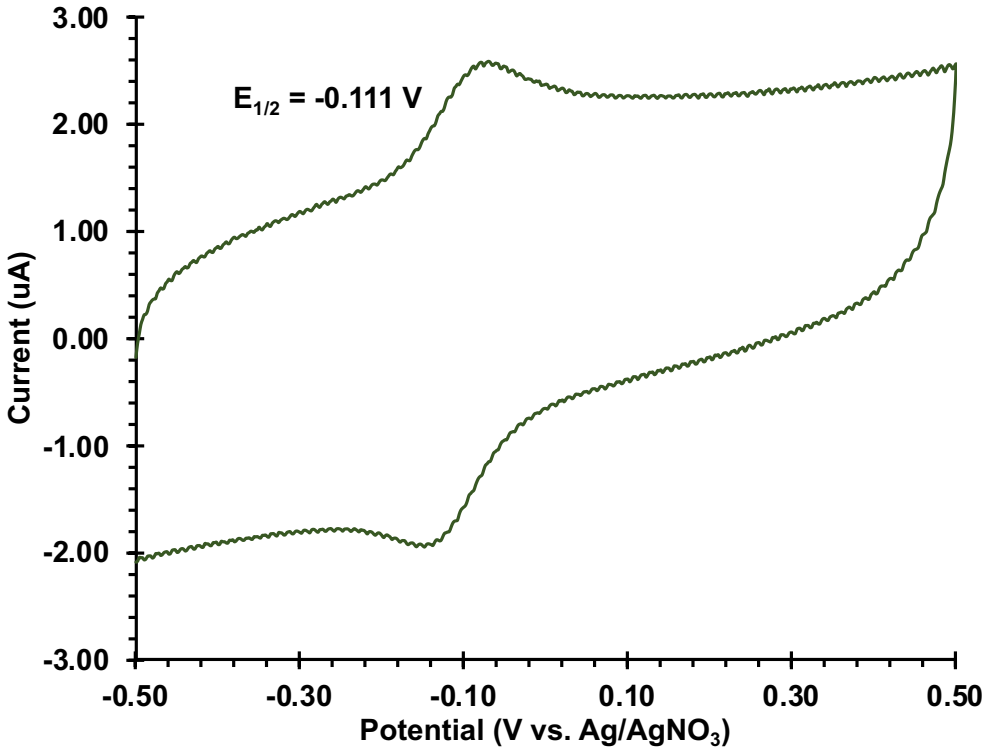

Figure 5.32. *Cyclic voltammogram of **3** in MeCN (scan rate = 100 mV s^{-1}).*

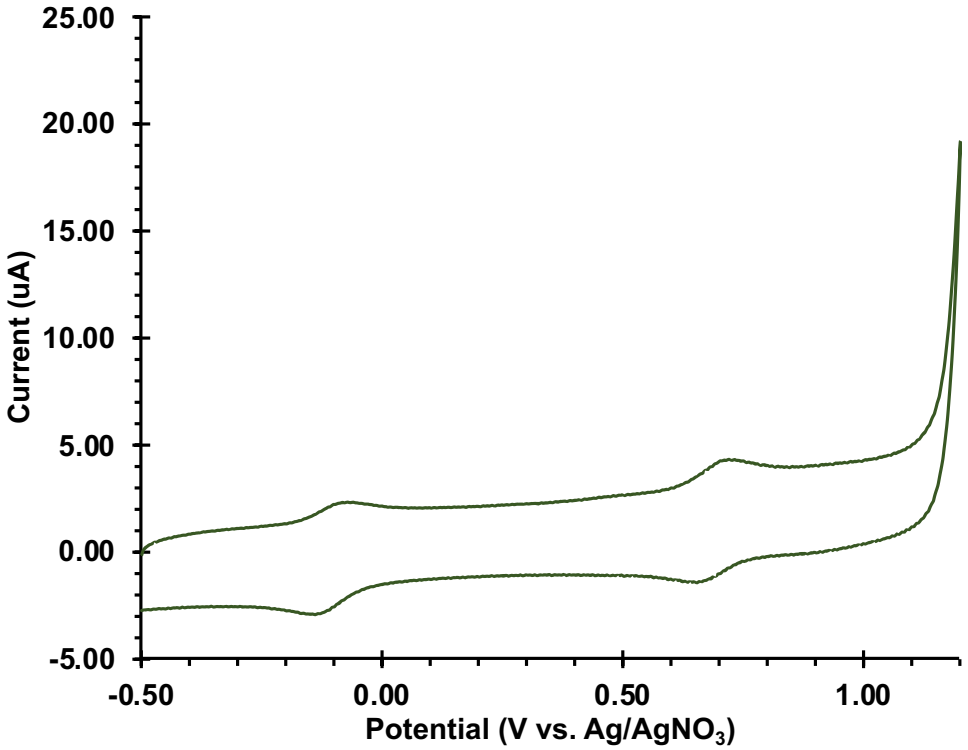

Figure 5.33. *Cyclic voltammogram showing the double oxidation of **3** in MeCN (scan rate = 100 mV s^{-1}).*

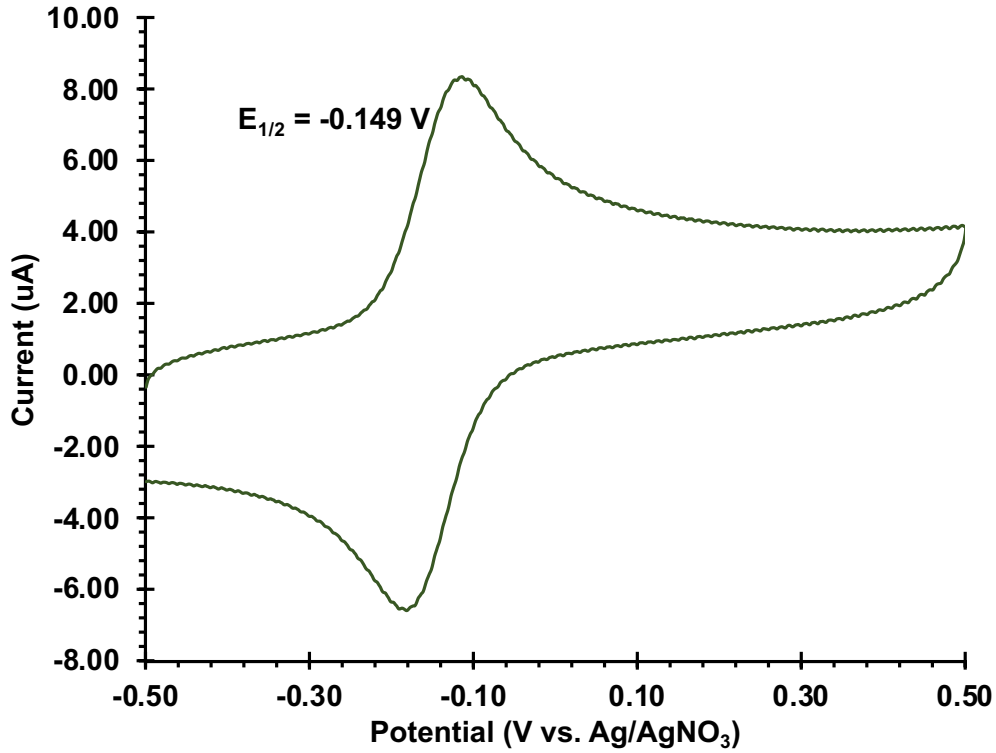

Figure 5.34. *Cyclic voltammogram of* ***4*** *in MeCN (scan rate = 100 mV s^{-1}).*

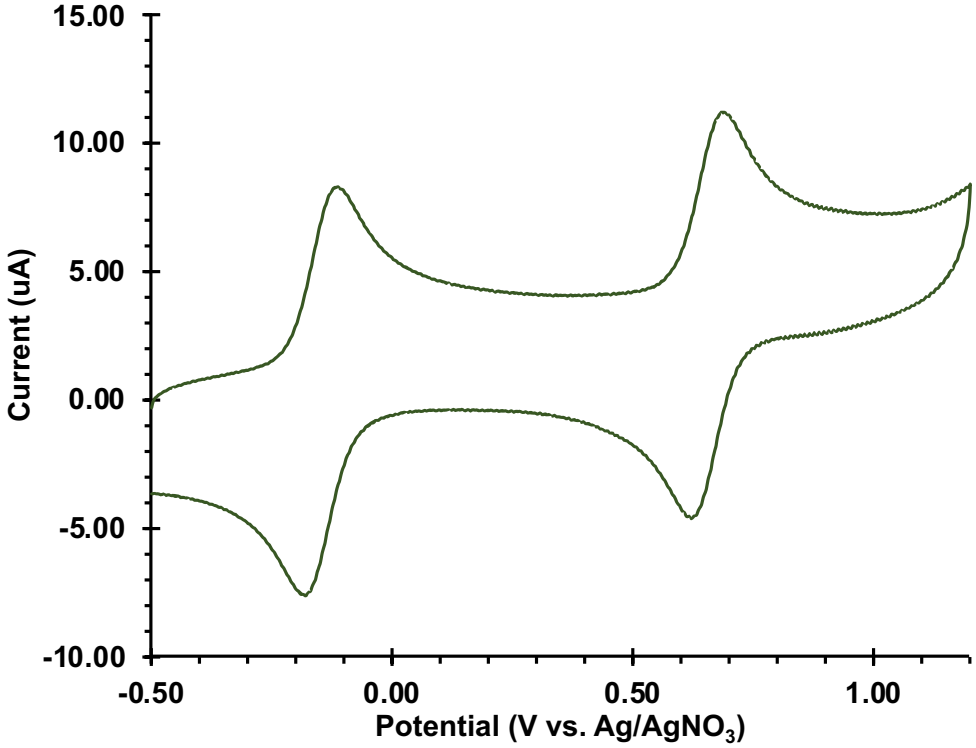

Figure 5.35. *Cyclic voltammogram showing the double oxidation of* ***4*** *in MeCN (scan rate = 100 mV s^{-1}).*

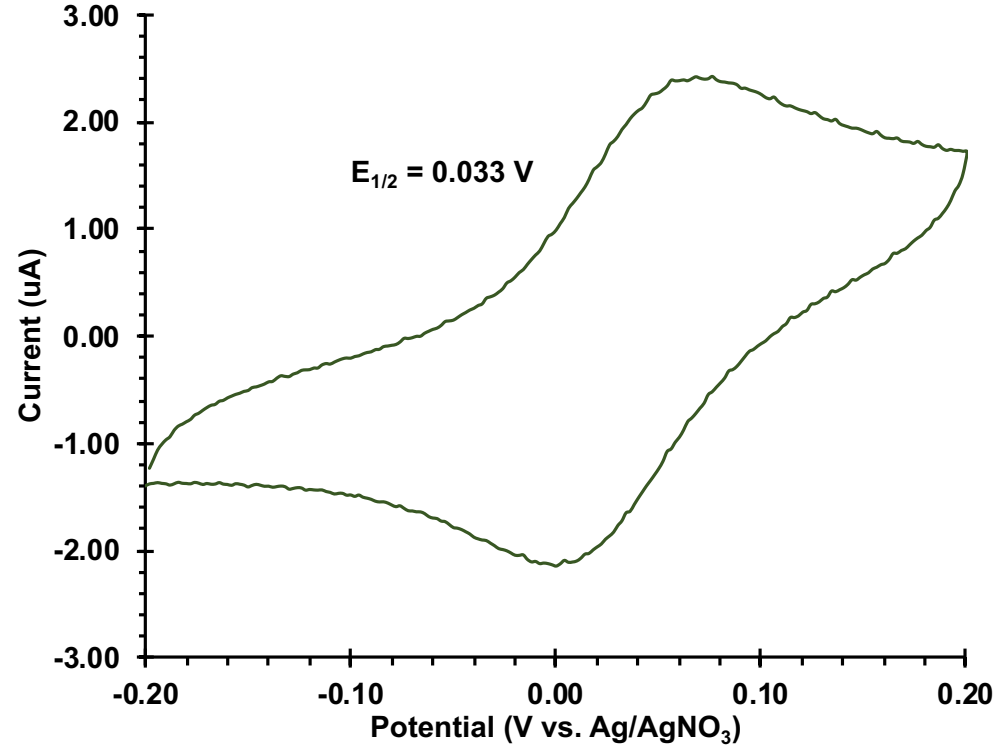

Figure 5.36. *Cyclic voltammogram of* ***5*** *in MeCN (scan rate = 100 mV* s^{-1}*).*

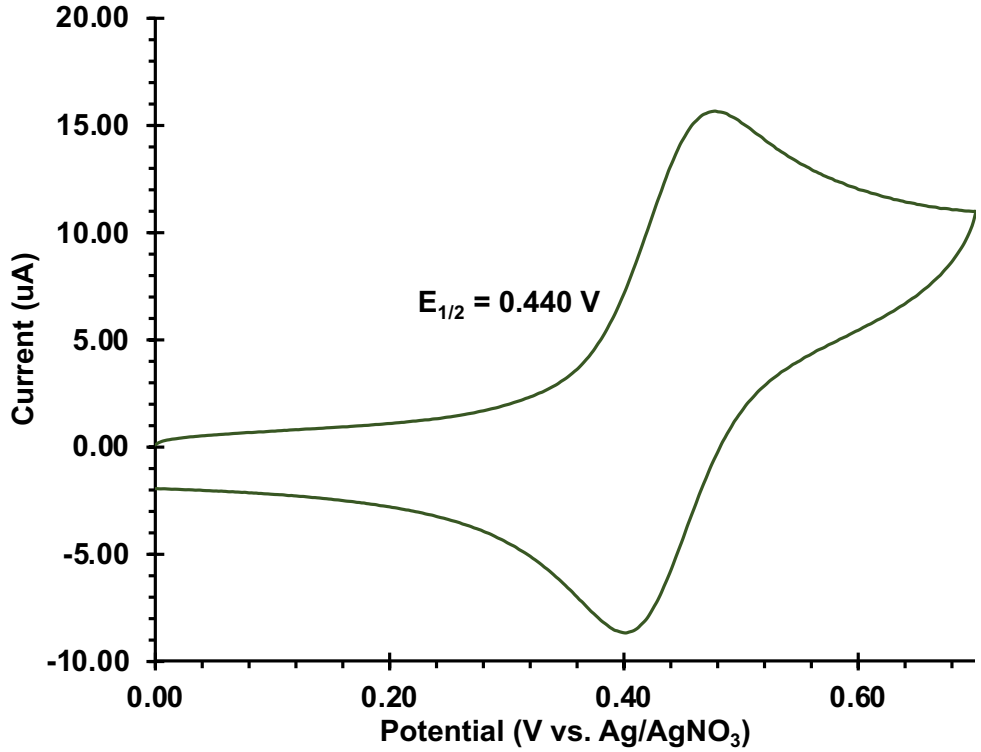

Figure 5.37. *Cyclic voltammogram of* ***6*** *in MeCN (scan rate = 100 mV* s^{-1}*).*

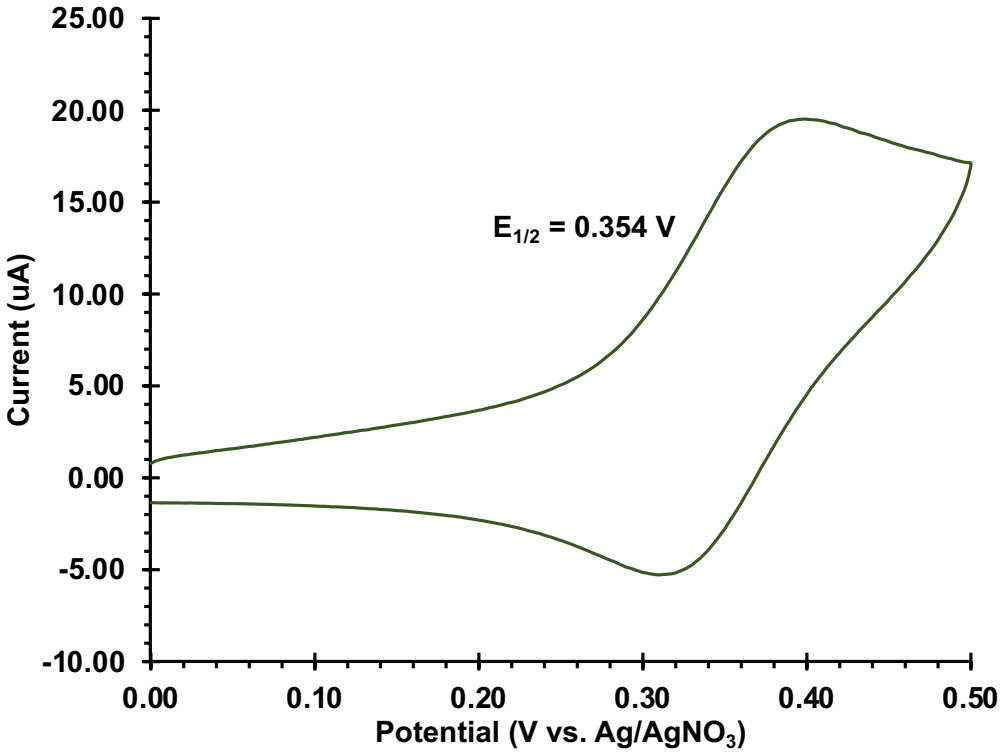

Figure 5.38. *Cyclic voltammogram of **7** in MeCN (scan rate = 100 mV s^{-1}).*

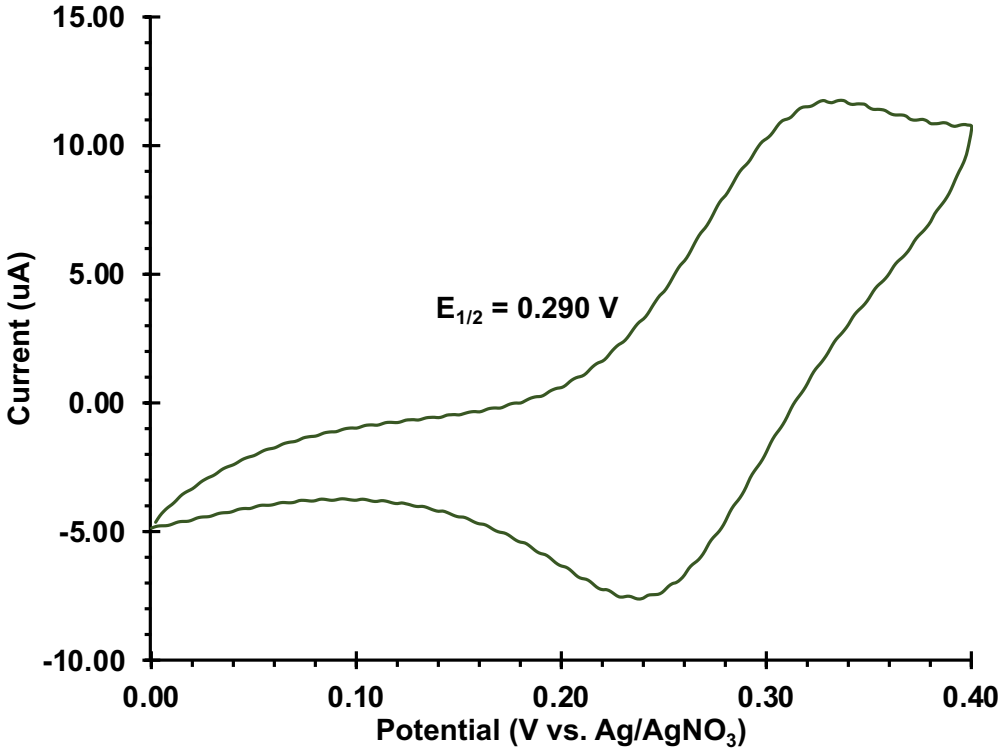

Figure 5.39. *Cyclic voltammogram of **8** in MeCN (scan rate = 100 mV s^{-1}).*

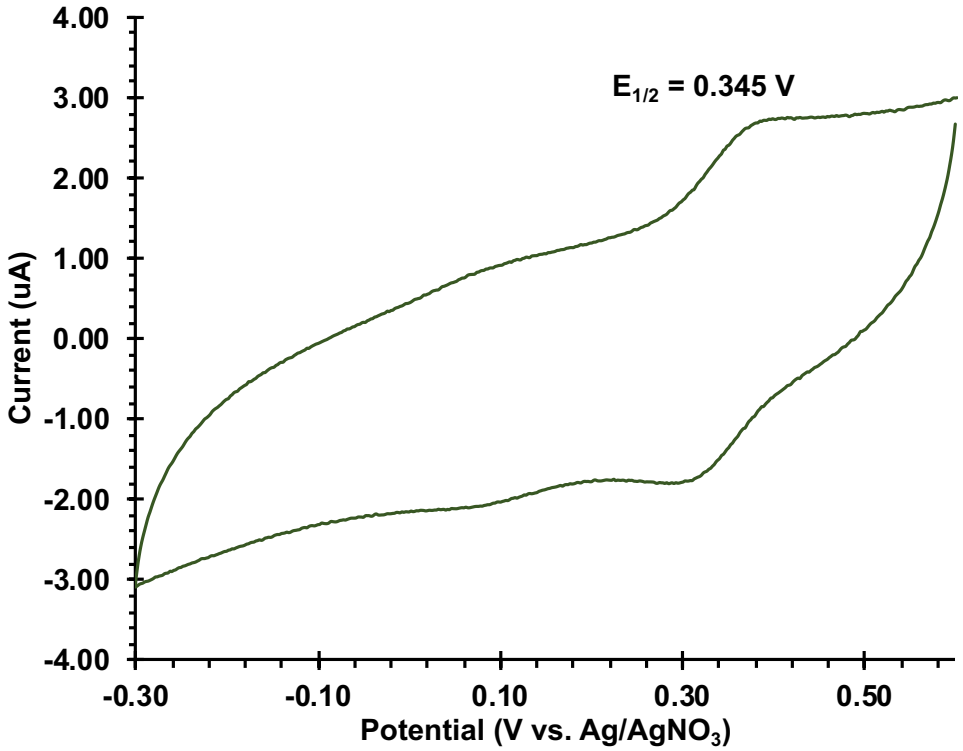

Figure 5.40. *Cyclic voltammogram of* ***9*** *in MeCN (scan rate = 100 mV s^{-1}).*

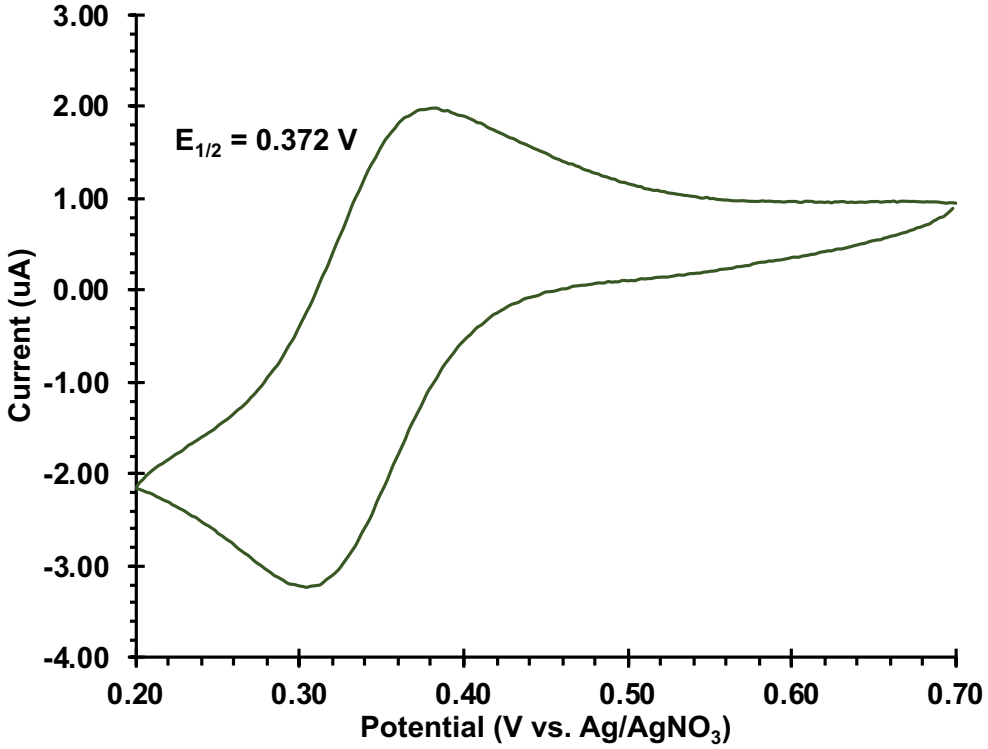

Figure 5.41. *Cyclic voltammogram of* ***10*** *in MeCN (scan rate = 100 mV s^{-1}).*

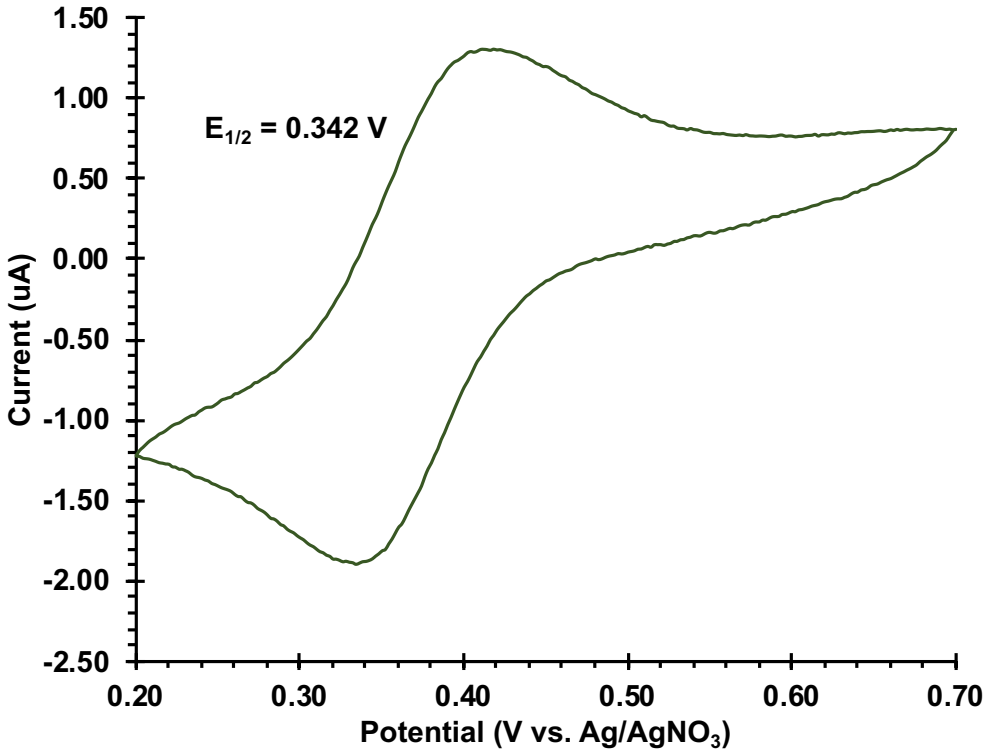

Figure 5.42. *Cyclic voltammogram of* ***11*** *in MeCN (scan rate = 100 mV* s^{-1}*).*

Spectro-Electrochemistry

For all spectro-electrochemistry experiments, the working electrode was held at a potential at least 200 mV greater than the $E_{1/2}$ of the catalyst under investigation. Each solution was stirred continuously, and changes in the solution spectra were monitored *in-situ* using a fiber optic probe connected to a Cary 5000 UV-Vis-NIR spectrometer.

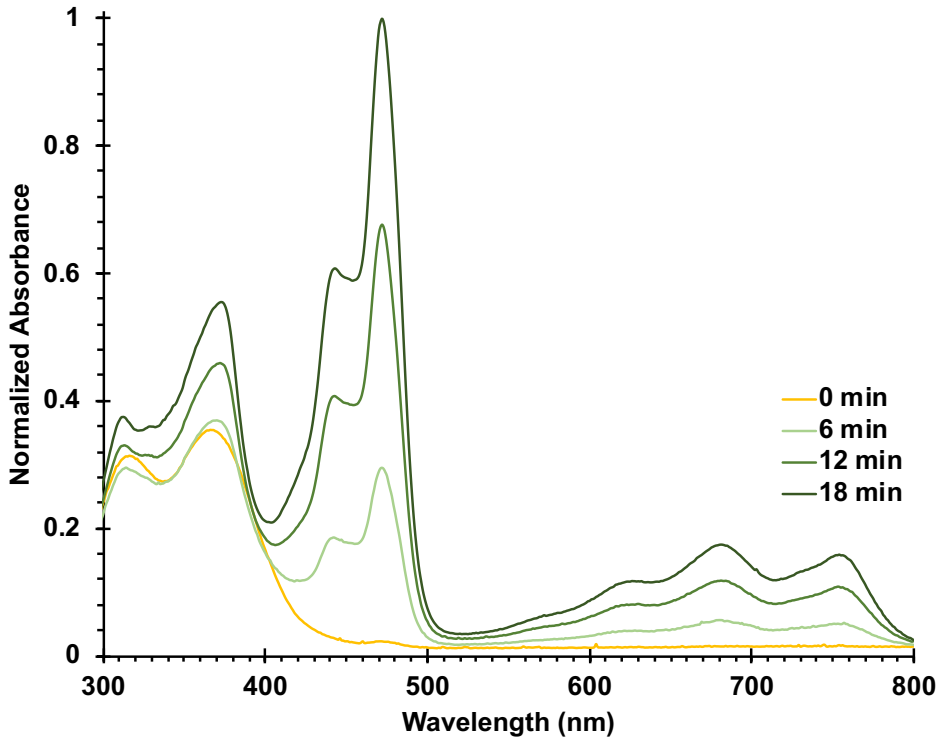

Figure 5.43. *Spectro-electrochemistry showing the conversion of* ***1*** *to* $\mathbf{1}^{\bullet+}$ *(E_{app} = 300 mV vs. Ag/AgNO₃).*

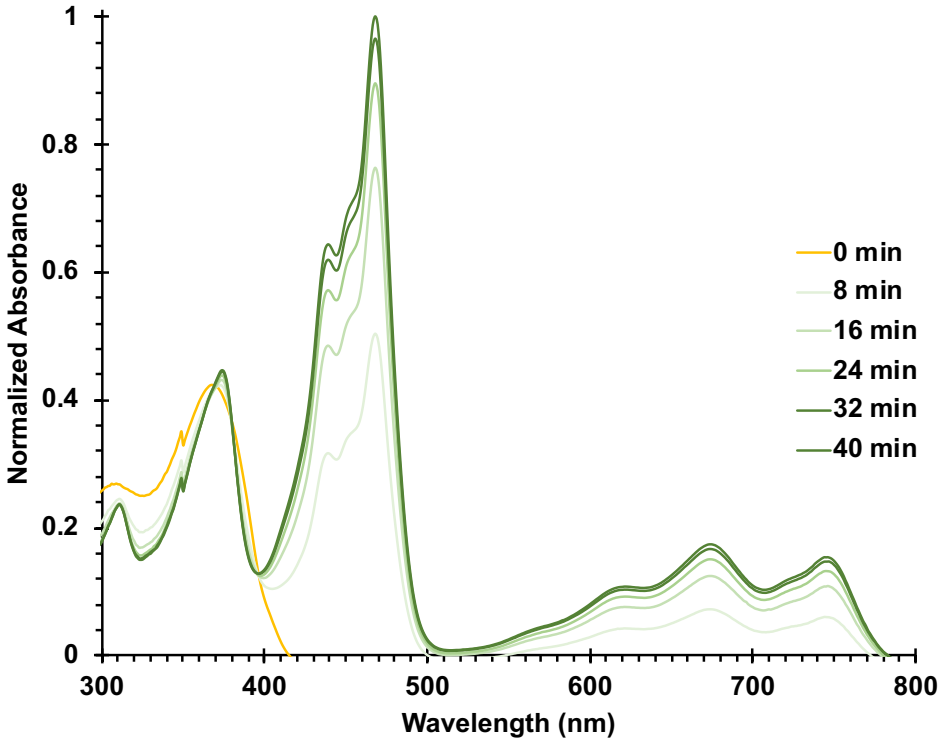

Figure 5.44. *Spectro-electrochemistry showing the conversion of* ***2*** *to* $\mathbf{2}^{\bullet+}$ *(E_{app} = 300 mV vs. Ag/AgNO₃).*

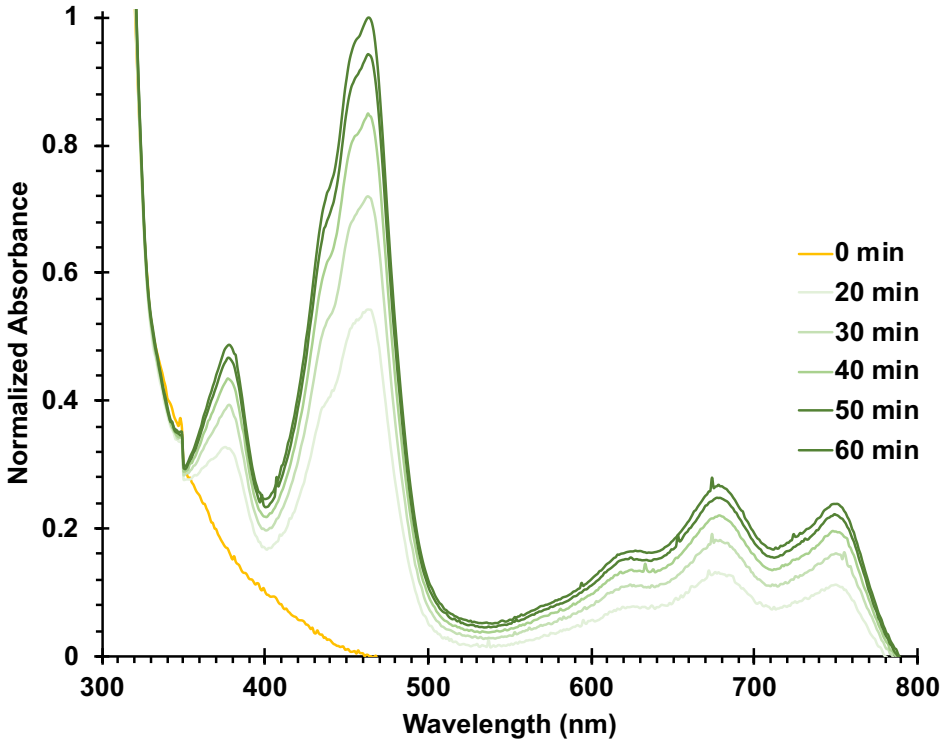

Figure 5.45. *Spectro-electrochemistry showing the conversion of* ***3*** *to* $\mathbf{3}^{\bullet+}$ *(E_{app} = 300 mV vs. Ag/AgNO₃).*

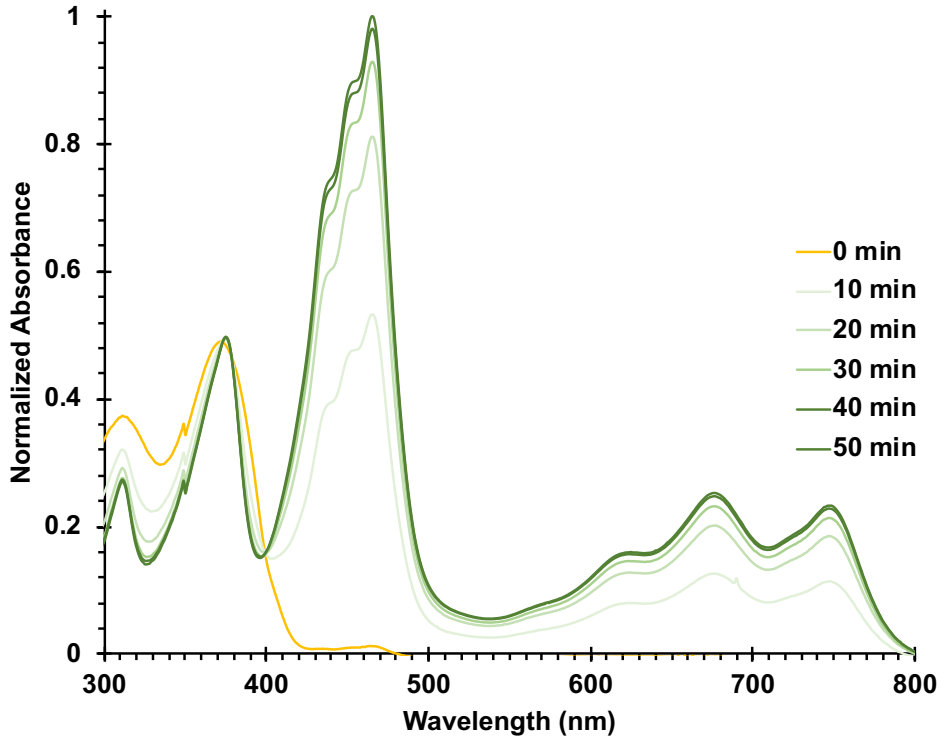

Figure 5.46. *Spectro-electrochemistry showing the conversion of* ***4*** *to* $\mathbf{4}^{\bullet+}$ *(E_{app} = 300 mV vs. Ag/AgNO₃).*

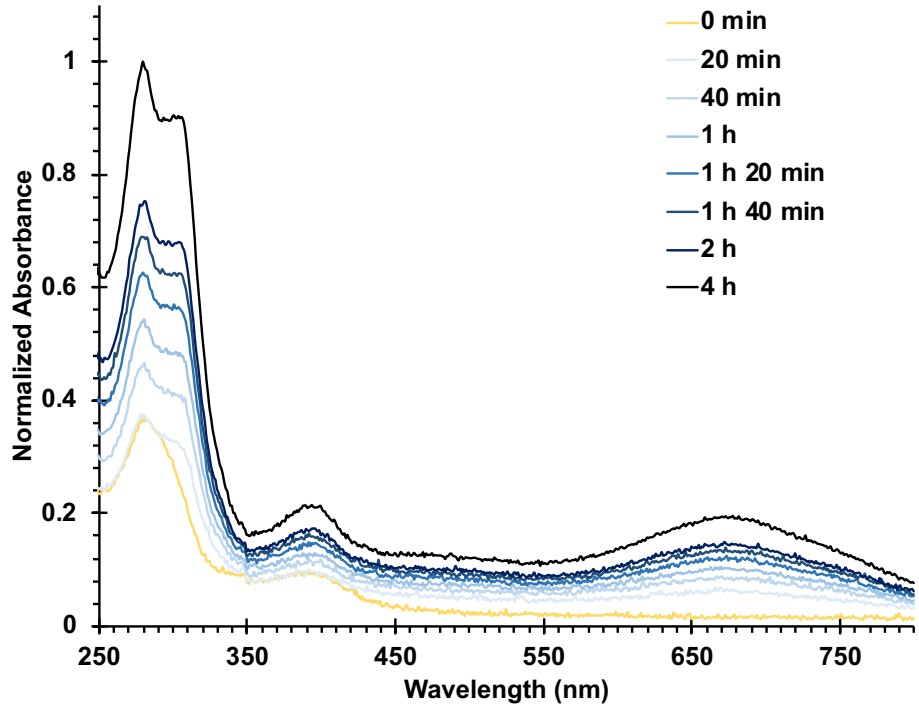

Figure 5.47. *Spectro-electrochemistry showing the conversion of* ***5*** *to* $\mathbf{5}^{\bullet+}$ *(E_{app} = 230 mV for 2 h, then 430 mV, both vs. Ag/AgNO₃).*

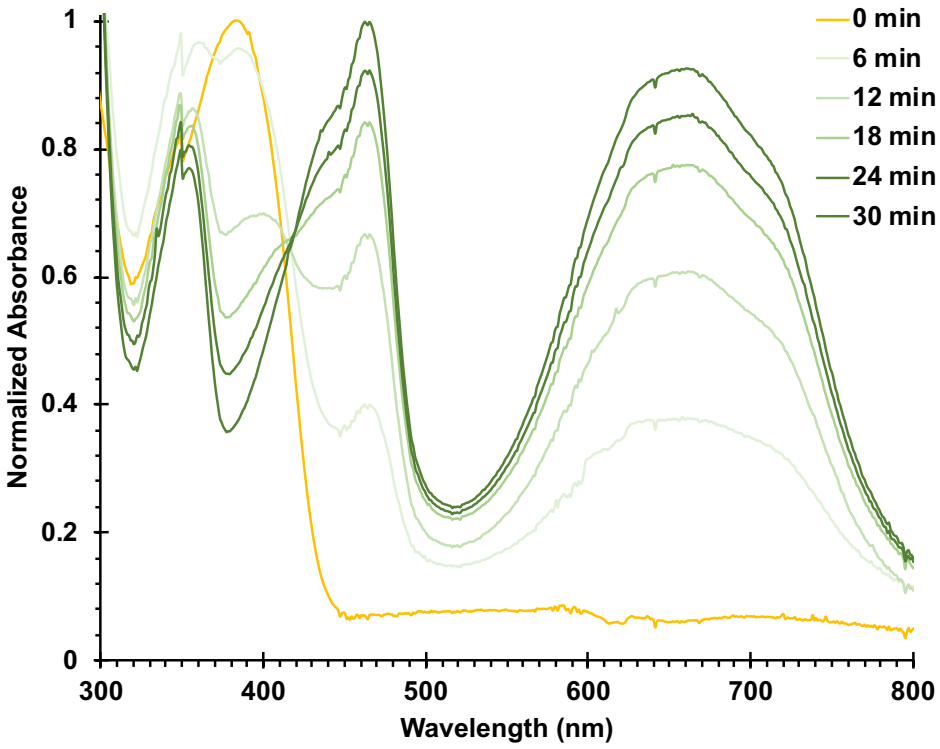

Figure 5.48. *Spectro-electrochemistry showing the conversion of* ***6*** *to* $\mathbf{6}^{\bullet+}$ *(E_{app} = 700 mV vs. Ag/AgNO₃).*

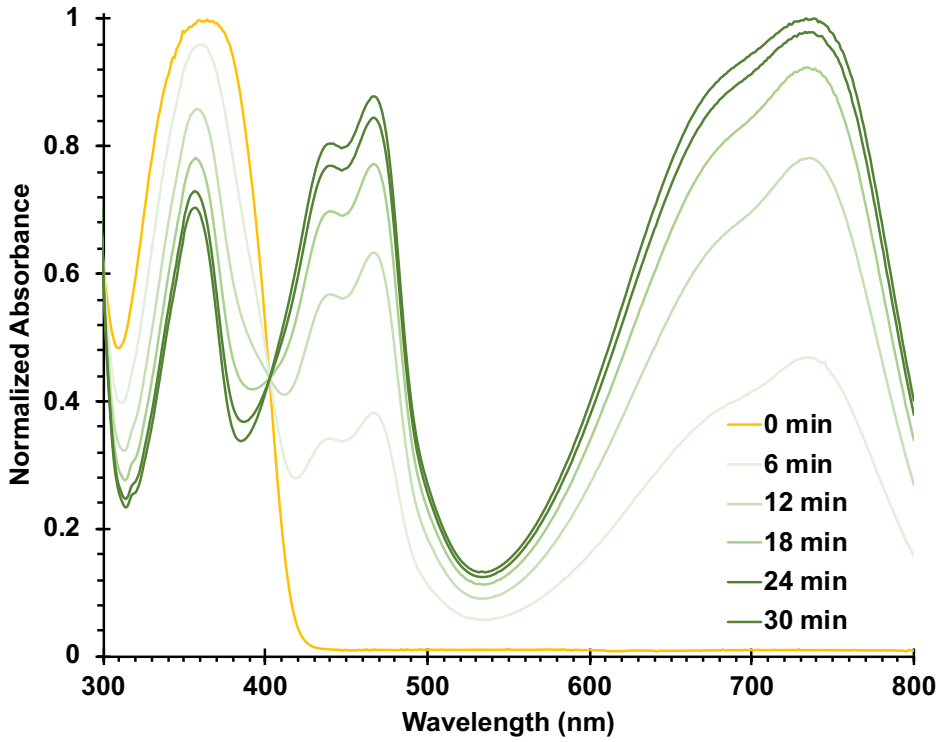

Figure 5.49. *Spectro-electrochemistry showing the conversion of* ***7*** *to* $\mathbf{7}^{\bullet+}$ *(E_{app} = 600 mV vs. Ag/AgNO₃).*

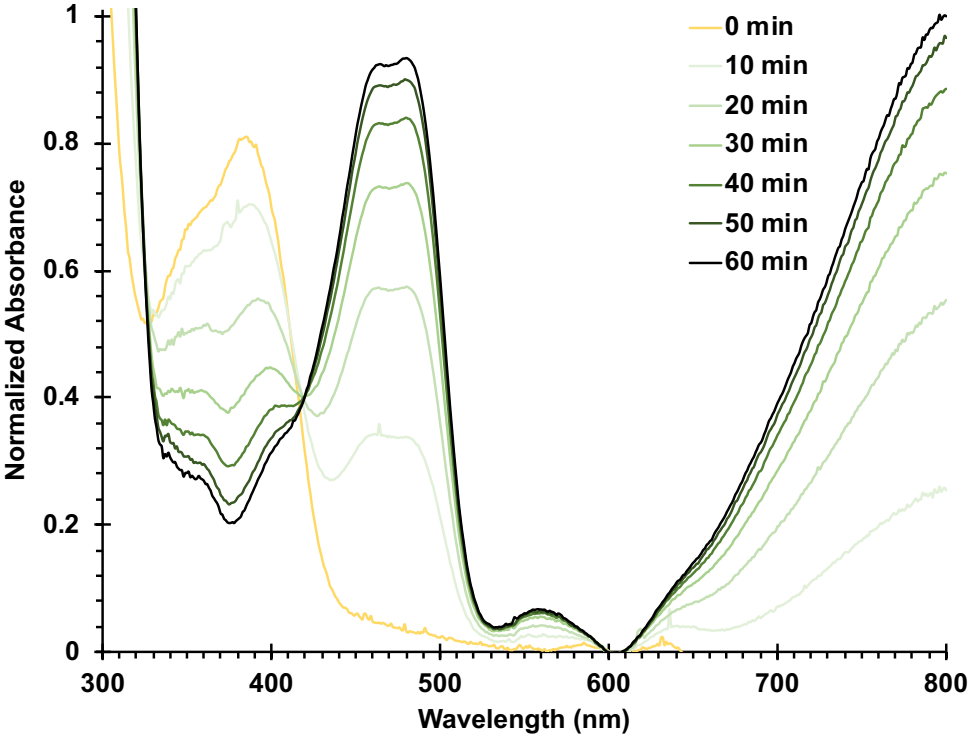

Figure 5.50. *Spectro-electrochemistry showing the conversion of* ***8*** *to* $\mathbf{8}^{\bullet+}$ *(E_{app} = 600 mV vs. Ag/AgNO₃).*

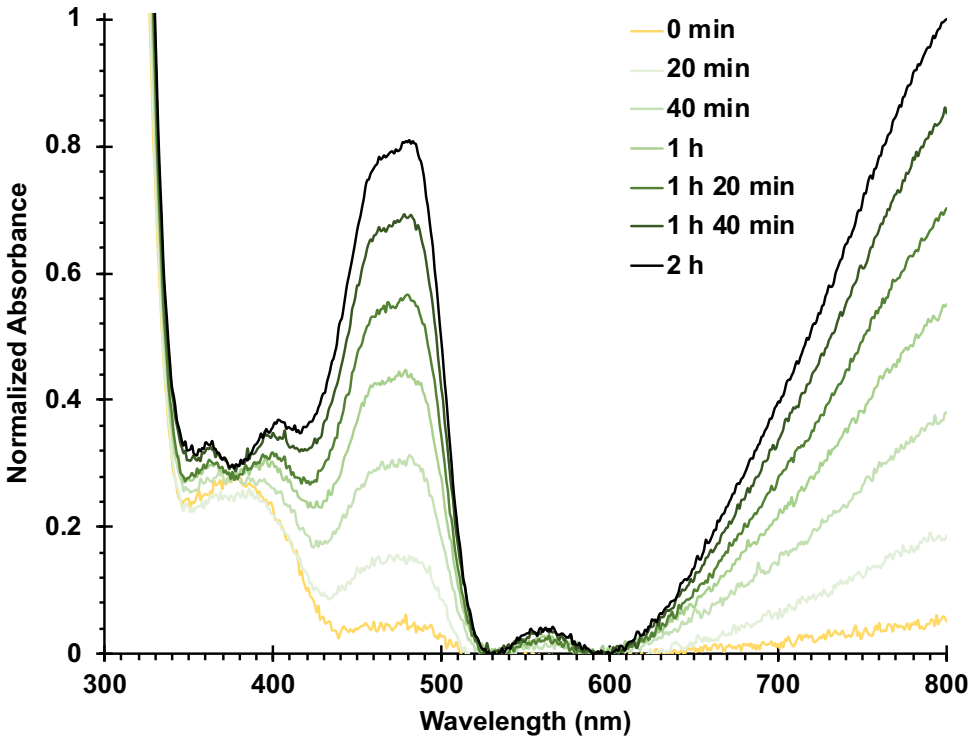

Figure 5.51. *Spectro-electrochemistry showing the conversion of* ***9*** *to* $\mathbf{9}^{\bullet+}$ *(E_{app} = 750 mV vs. Ag/AgNO₃).*

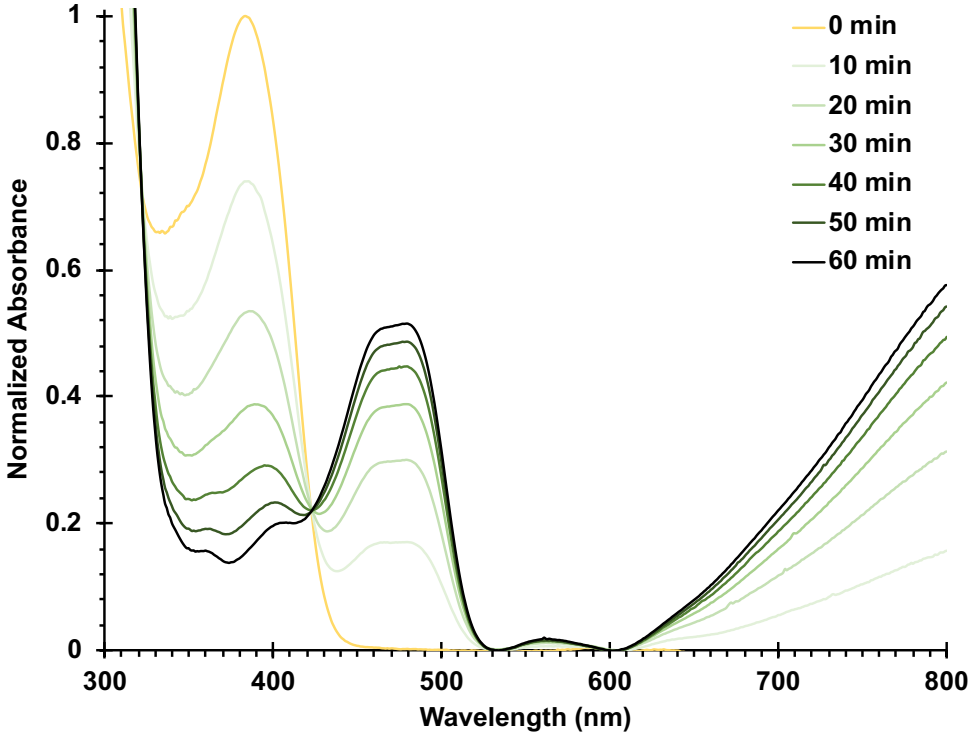

Figure 5.52. *Spectro-electrochemistry showing the conversion of* ***10*** *to* $\mathbf{10}^{\bullet+}$ *(E_{app} = 600 mV vs. Ag/AgNO₃).*

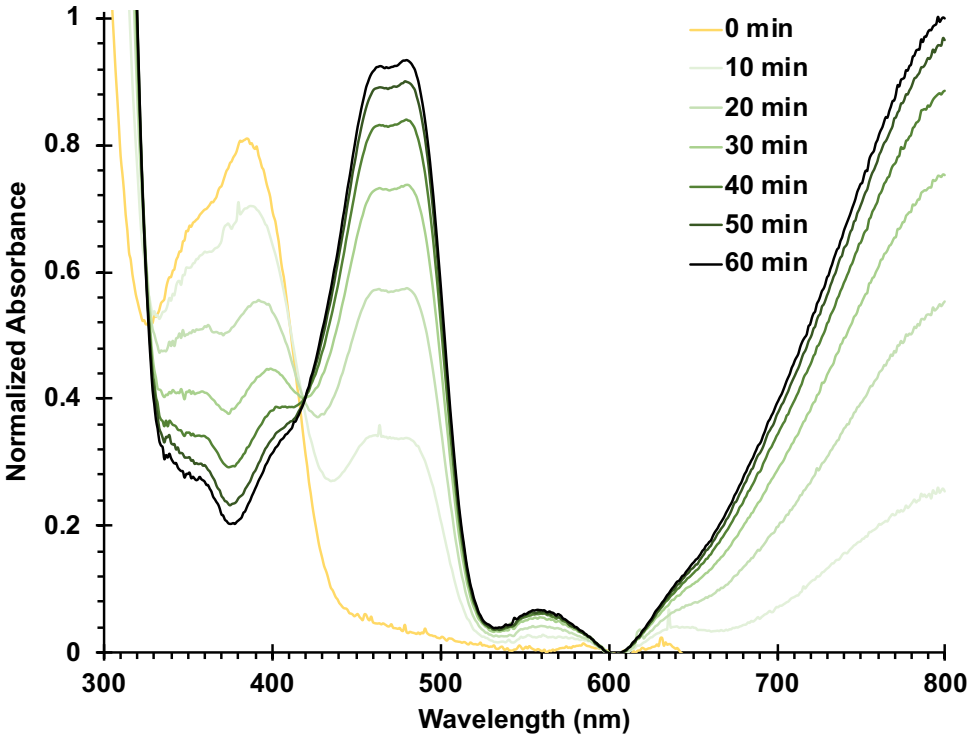

Figure 5.53. *Spectro-electrochemistry showing the conversion of* ***11*** *to* ***11***$^{\bullet+}$ *(E_{app} = 600 mV vs. $Ag/AgNO_3$).*
UV-Vis Spectra

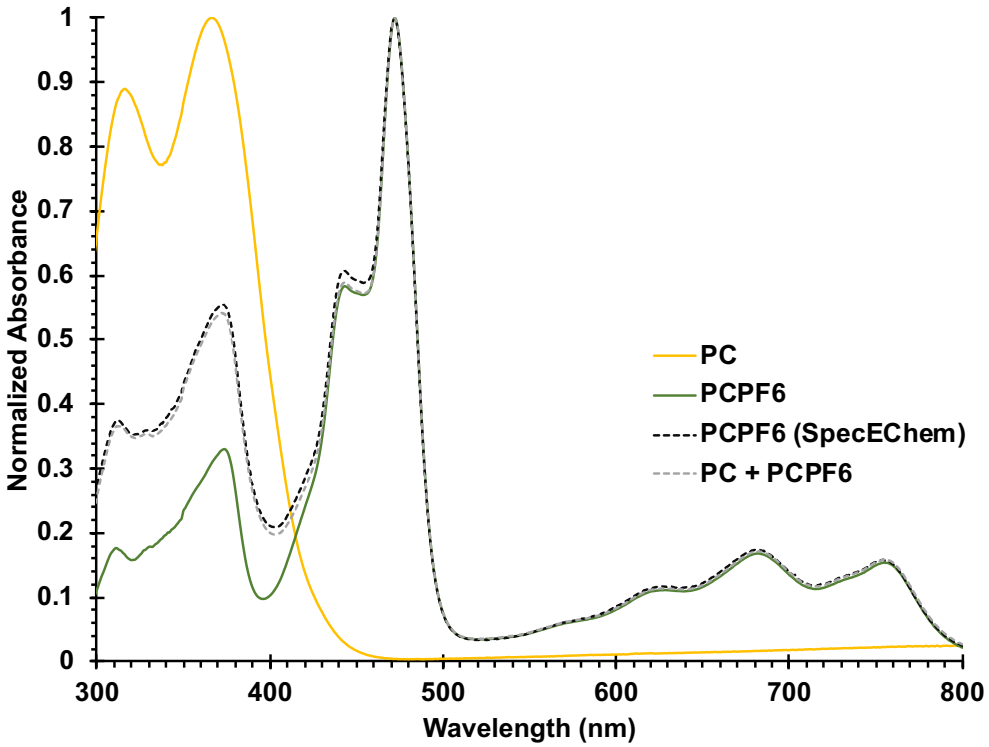

Figure 5.54. *Overlaid UV-Vis spectra of* ***1*** *(solid, yellow),* $\mathbf{1}^{\bullet+}\mathbf{PF_6}^-$ *(solid, green),* $\mathbf{1}^{\bullet+}$ *obtained by spectro-electrochemistry (dashed, black), and the addition spectrum of* ***1*** *and* $\mathbf{1}^{\bullet+}\mathbf{PF_6}^-$ *showing that disagreement between the spectra of isolated* $\mathbf{1}^{\bullet+}$ *and that from spectro-electrochemistry stems from incomplete conversion during spectro-electrochemistry.*

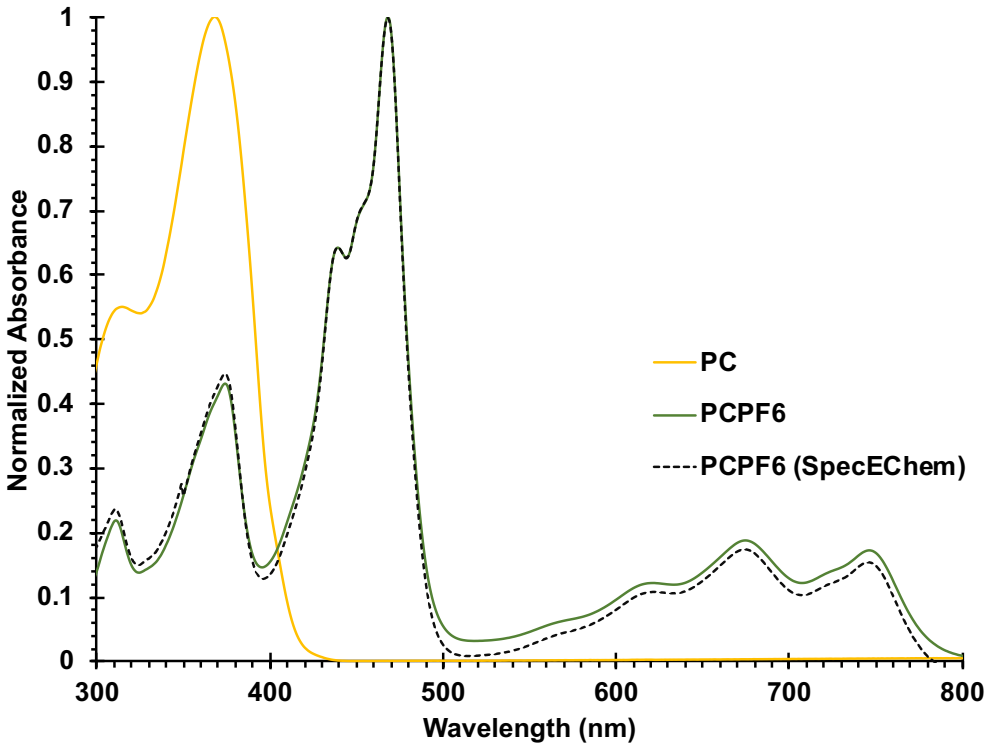

Figure 5.55. *Overlaid UV-Vis spectra of* ***2*** *(solid, yellow),* $\mathbf{2}^{\bullet+}\mathbf{PF_6}^-$ *(solid, green), and* $\mathbf{2}^{\bullet+}$ *obtained by spectro-electrochemistry (dashed, black).*

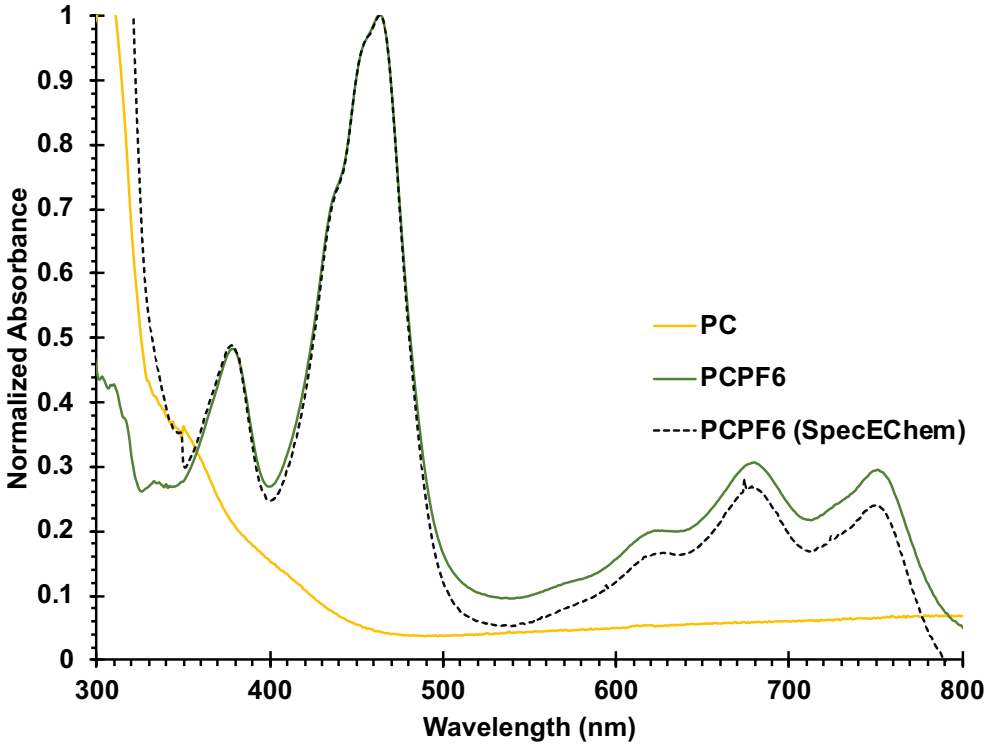

Figure 5.56. *Overlaid UV-Vis spectra of* ***3*** *(solid, yellow),* $\mathbf{3}^{\bullet+}\mathbf{PF_6}^-$ *(solid, green), and* $\mathbf{3}^{\bullet+}$ *obtained by spectro-electrochemistry (dashed, black).*

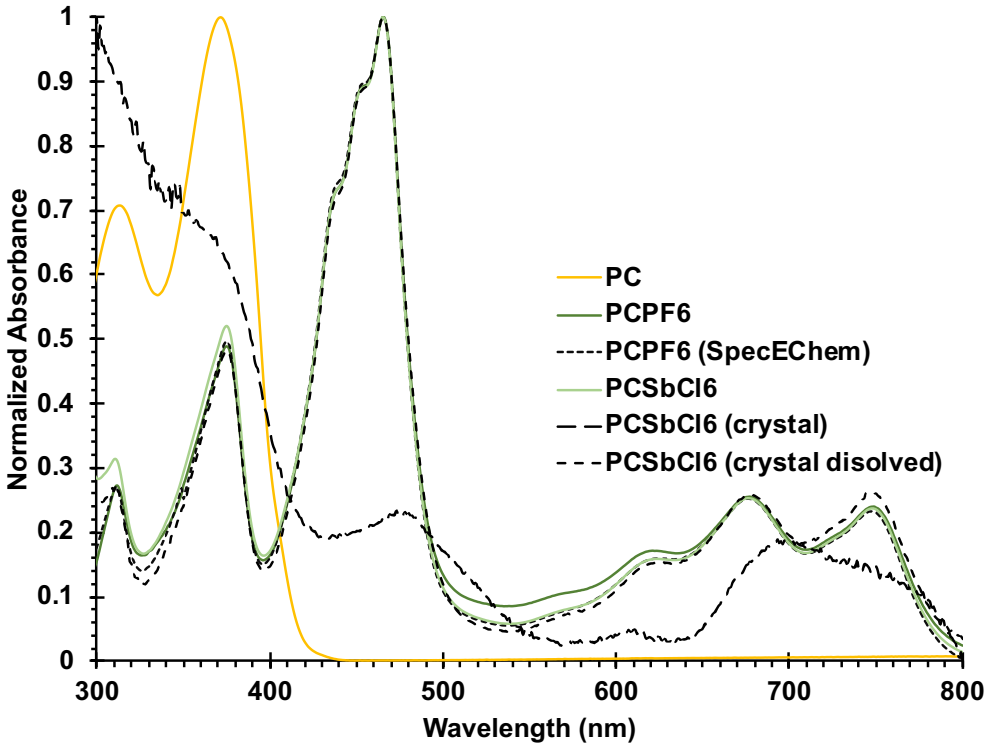

Figure 5.57. *Overlaid UV-Vis spectra of* ***4*** *(solid, yellow),* $\mathbf{4}^{\bullet+}\mathbf{PF_6}^-$ *(solid, dark green),* $\mathbf{4}^{\bullet+}$ *obtained by spectro-electrochemistry (small dash, black),* $\mathbf{4}^{\bullet+}\mathbf{SbCl_6}^-$ *(solid, light green),* $\mathbf{4}^{\bullet+}\mathbf{SbCl_6}^-$ *solid crystals (large dash, black), and* $\mathbf{4}^{\bullet+}\mathbf{SbCl_6}^-$ *crystals dissolved again in MeCN (medium dash, black).*

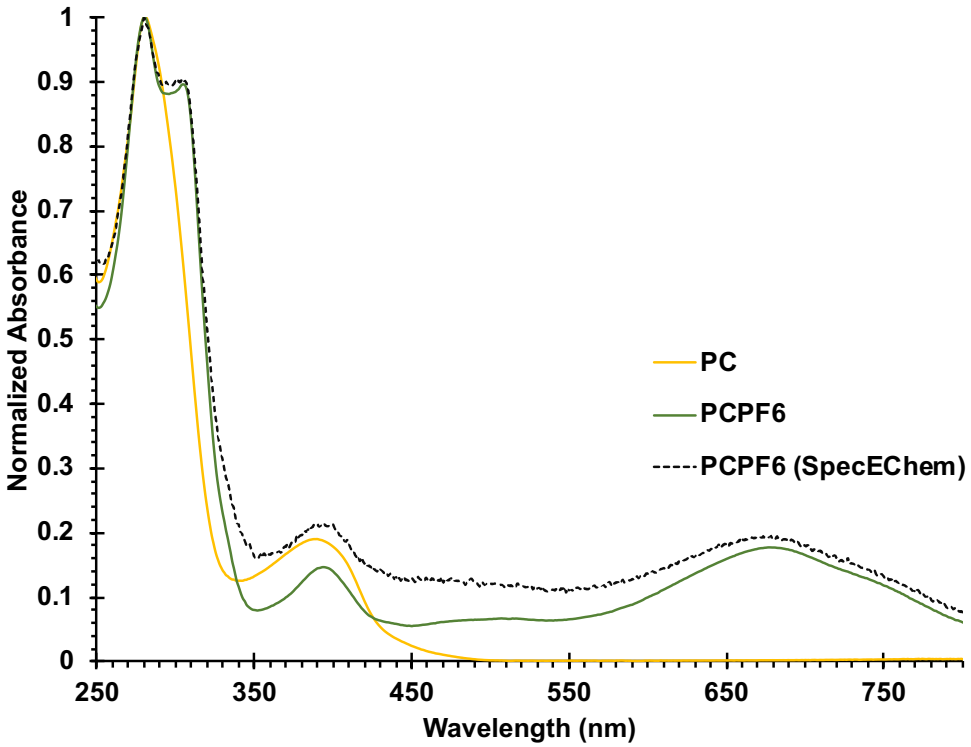

Figure 5.58. *Overlaid UV-Vis spectra of* ***5*** *(solid, yellow),* ***5***$^{\bullet+}$***PF***$_6^-$ *(solid, green), and* ***5***$^{\bullet+}$ *obtained by spectro-electrochemistry (dashed, black).*

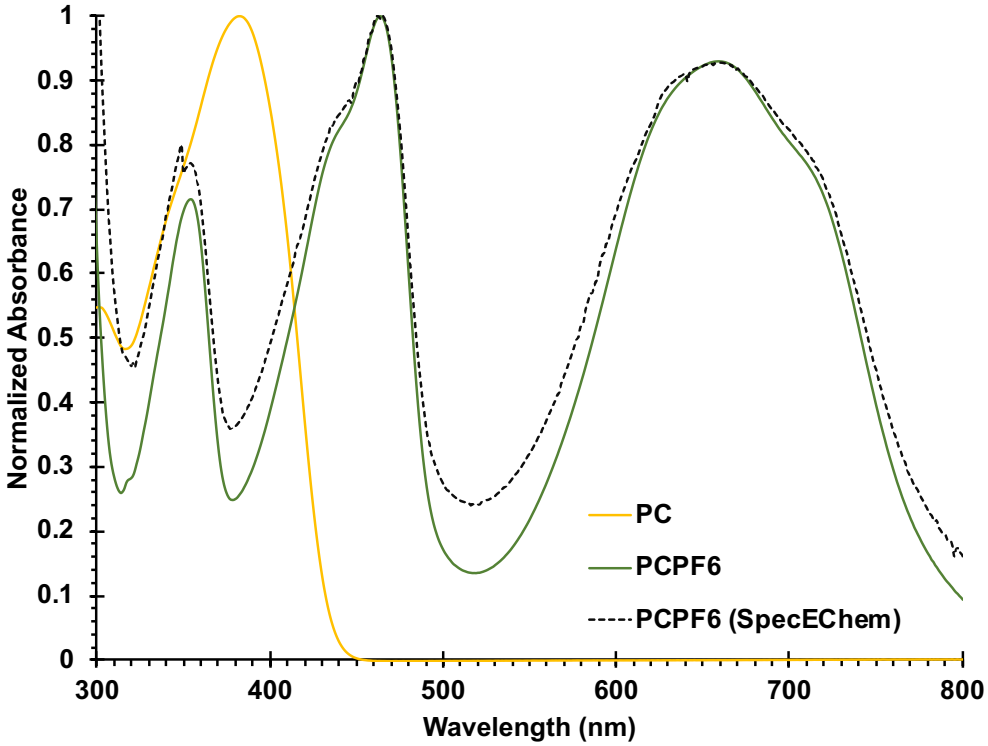

Figure 5.59. *Overlaid UV-Vis spectra of* ***6*** *(solid, yellow),* ***6***$^{\bullet+}$***PF***$_6^-$ *(solid, green), and* ***6***$^{\bullet+}$ *obtained by spectro-electrochemistry (dashed, black).*

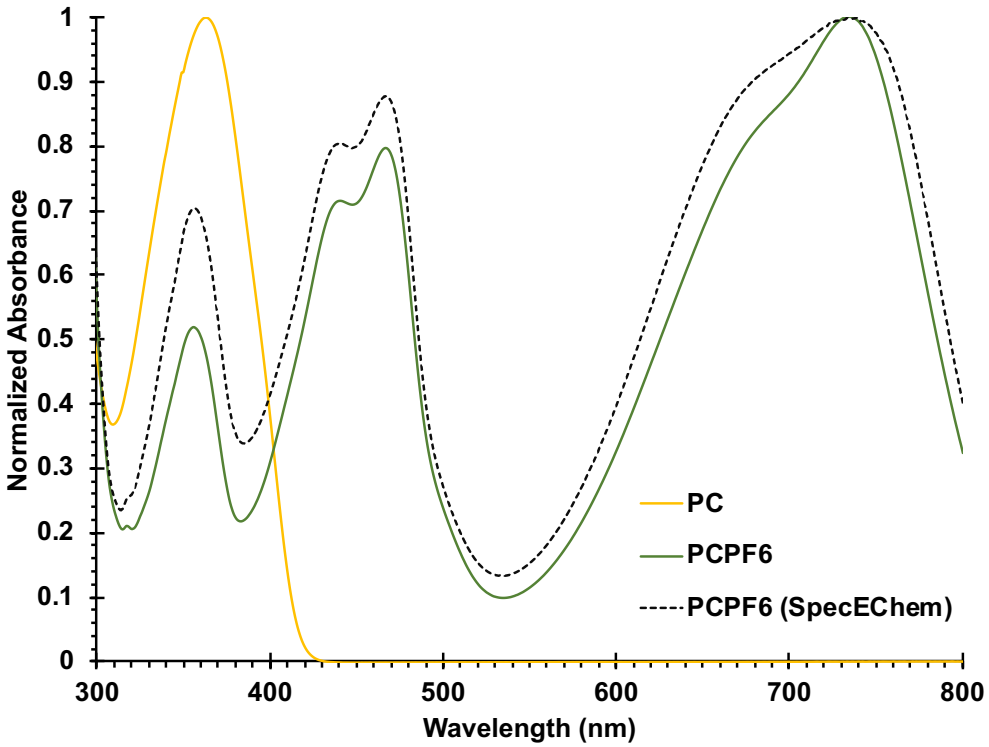

Figure 5.60. *Overlaid UV-Vis spectra of* ***7*** *(solid, yellow),* ***7***$^{\bullet+}$***PF***$_6^-$ *(solid, green), and* ***7***$^{\bullet+}$ *obtained by spectro-electrochemistry (dashed, black).*

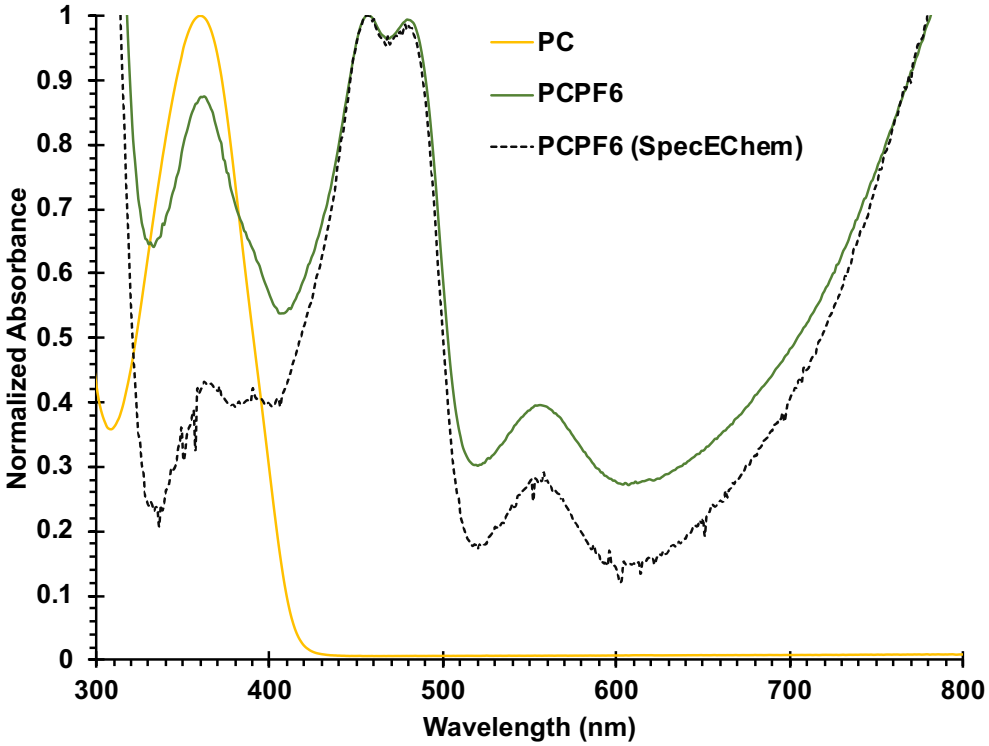

Figure 5.61. *Overlaid UV-Vis spectra of* ***8*** *(solid, yellow),* ***8***$^{\bullet+}$***PF***$_6^-$ *(solid, green), and* ***8***$^{\bullet+}$ *obtained by spectro-electrochemistry (dashed, black).*

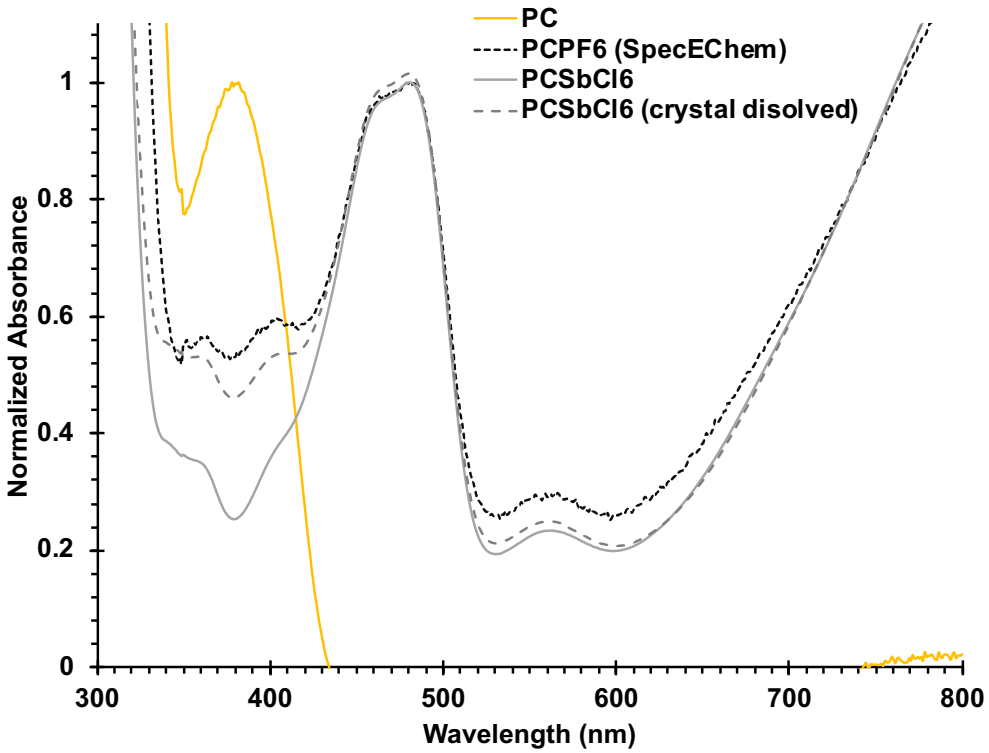

Figure 5.62. *Overlaid UV-Vis spectra of* ***9*** *(solid, yellow),* ***9***$^{\bullet+}$ *obtained by spectro-electrochemistry (small dash, black),* ***9***$^{\bullet+}$***SbCl***$_6^-$ *(solid, light grey), and* ***9***$^{\bullet+}$***SbCl***$_6^-$ *crystals dissolved again in MeCN (medium dash, grey).*

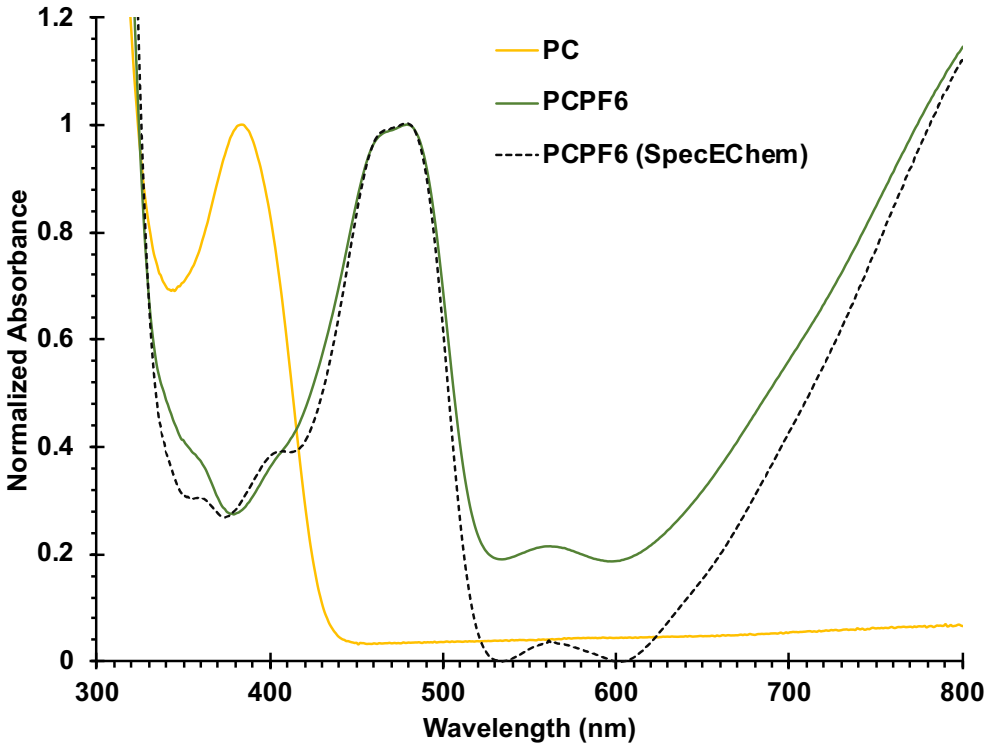

Figure 5.63. *Overlaid UV-Vis spectra of* ***10*** *(solid, yellow),* ***10$^{\bullet+}$PF$_6^-$*** *(solid, green), and* ***10$^{\bullet+}$*** *obtained by spectro-electrochemistry (dashed, black, baseline corrected).*

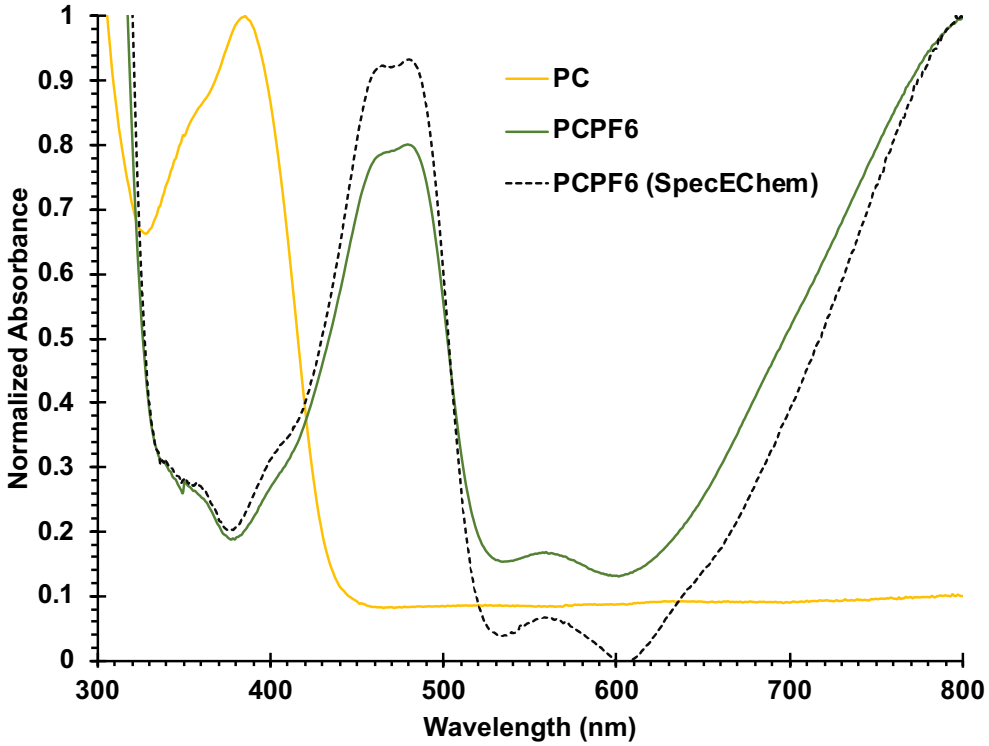

Figure 5.64. *Overlaid UV-Vis spectra of* ***11*** *(solid, yellow),* ***11$^{\bullet+}$PF$_6^-$*** *(solid, green), and* ***11$^{\bullet+}$*** *obtained by spectro-electrochemistry (dashed, black, baseline corrected).*

Estimation of Radical Cation Purity by Open Circuit Potential

This method was based on an experiment previously described by Dempsey *et al.*.[57] Based on the Nernst Equation (Eq. 5.3), the open circuit potential of a solution of radical cation should be dependent on the ratio of $PC^{\bullet+}$ to PC present in solution. As a consequence, measurement of the open circuit potential of a solution can serve as an estimate of the relative quantities of $PC^{\bullet+}$ and PC present in a given sample.

$$\frac{[PC^{\cdot+}]}{[PC]} = e^{\frac{F(E_{ocp}-E_{1/2})}{RT}} \qquad \text{(Eq. 5.3)}$$

With the ratio of $PC^{\bullet+}$ to PC determined, the percentage of $PC^{\bullet+}$ can be calculated according to Eq. 5.4:

$$percent\ PC^{\cdot+} = \left(\frac{\frac{[PC^{\cdot+}]}{[PC]}}{\frac{[PC^{\cdot+}]}{[PC]} + 1} \right) \cdot 100\% \qquad \text{(Eq. 5.4)}$$

Table 5.6 shows the results of these measurements and calculations for each $PC^{\bullet+}PF_6^-$ synthesized in this work.

Table 5.6. *Computed purities of* ***1•+PF6- – 11•+PF6-*** *as determined by open circuit potential measurements.*

$PC^{\bullet+}$	$E_{1/2}$[a] (V vs. SCE)	E_{ocp}[a] (V vs. SCE)	$[PC^{\bullet+}]/[PC]$	% $PC^{\bullet+}$
$1^{\bullet+}$	0.33	0.48	320	99.7%
$2^{\bullet+}$	0.17	0.39	5100	100%
$3^{\bullet+}$	0.18	0.74	3.1×10^9	100%
$4^{\bullet+}$	0.14	0.42	5.2×10^4	100%
$5^{\bullet+}$	0.32	0.50	980	99.9%
$6^{\bullet+}$	0.73	0.83	49	98.1%
$7^{\bullet+}$	0.64	0.78	200	99.5%
$8^{\bullet+}$	0.58	0.73	340	99.7%
$9^{\bullet+}$[b]	0.64	-	-	-
$10^{\bullet+}$	0.66	0.75	31	96.9%
$11^{\bullet+}$	0.63	1.01	2.5×10^6	100%

[a]*Measured in MeCN with 0.1 M* Bu_4NPF_6 *as the supporting electrolyte.* [b]***9•+PF6-*** *not synthesized.*

Crystallographic Information for ***4***$^{\bullet+}$***SbCl***$_6^-$

See the attached .CIF file for the full crystal structure and experiment details.

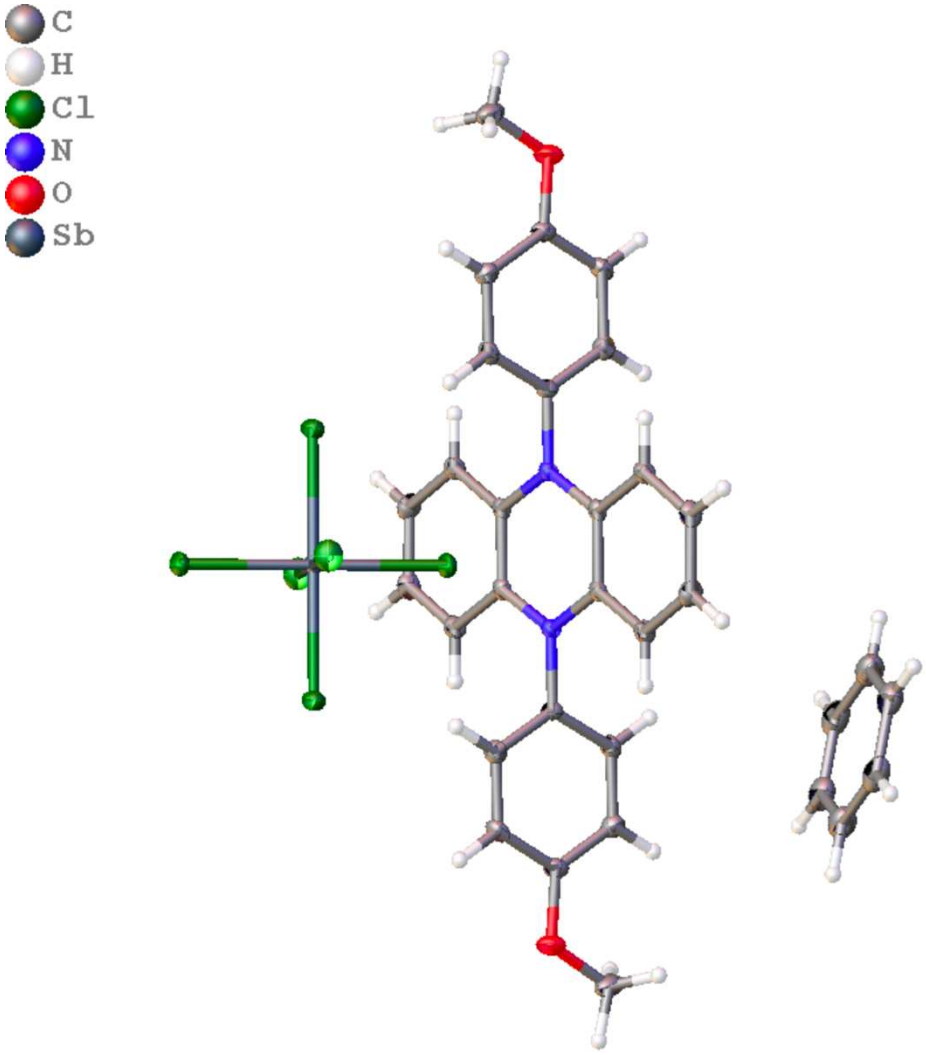

Figure 5.65. *Crystal structure of* ***4***$^{\bullet+}$***SbCl***$_6^-$ *shown as an ORTEP plot.*

Table 5.7. *Crystallographic information for the structural refinement of* ***4•+SbCl$_6^-$***.

Empirical formula	$C_{32}H_{28}Cl_6N_2O_2Sb$
Formula weight	807.01
Temperature	100.0 K
Crystal system	Triclinic
Space group	P-1
a	7.9631(3) Å
b	10.0144(4) Å
c	11.2341(5) Å
α	100.421(2)º
β	95.385(2)º
γ	106.067(2)º
Volume	638.80(6) Å^3
Z	1
ρ_{calc}	1.601 g cm^{-3}
μ	1.336 mm^{-1}
F(000)	403.0
Crystal color	Blue
Crystal size	0.137 x 0.096 x 0.087 mm^3
Radiation	Mo Kα (λ = 0.71073 Å)
2Θ range for data collection	4.336 to 59.15º
Index ranges	$-11 \leq h \leq 11$, $-13 \leq k \leq 13$, $-15 \leq l \leq 15$
Reflections collected	45173
Independent collections	4678 [R_{int} = 0.0870, R_{sigma} = 0.0429]
Data/restraints/parameters	4678/0/197
Goodness-of-fit on F^2	1.002
Final R indexes [$I \geq 2\sigma$ (I)]	R_1 = 0.0327, wR_2 = 0.0704
Final R indexes [call data]	R_1 = 0.0461, wR_2 = 0.0750
Largest diff. peak/hole	0.76/-0.44 e Å^{-3}

Crystallographic Information for ***9•+SbCl$_6^-$***

See the attached .CIF file for the full crystal structure and experiment details. Carbons in the naphthyl ring were found to be disordered over two positions and were modeled using free variables. The occupancies found for the two positions were 0.476(9) and 0.524(9). In addition, one of the benzene rings in one of the biphenyl core substituents was found to be disordered over two positions. Modeling this disorder using free variables yielded occupancies of 0.45(3) and 0.55(3).

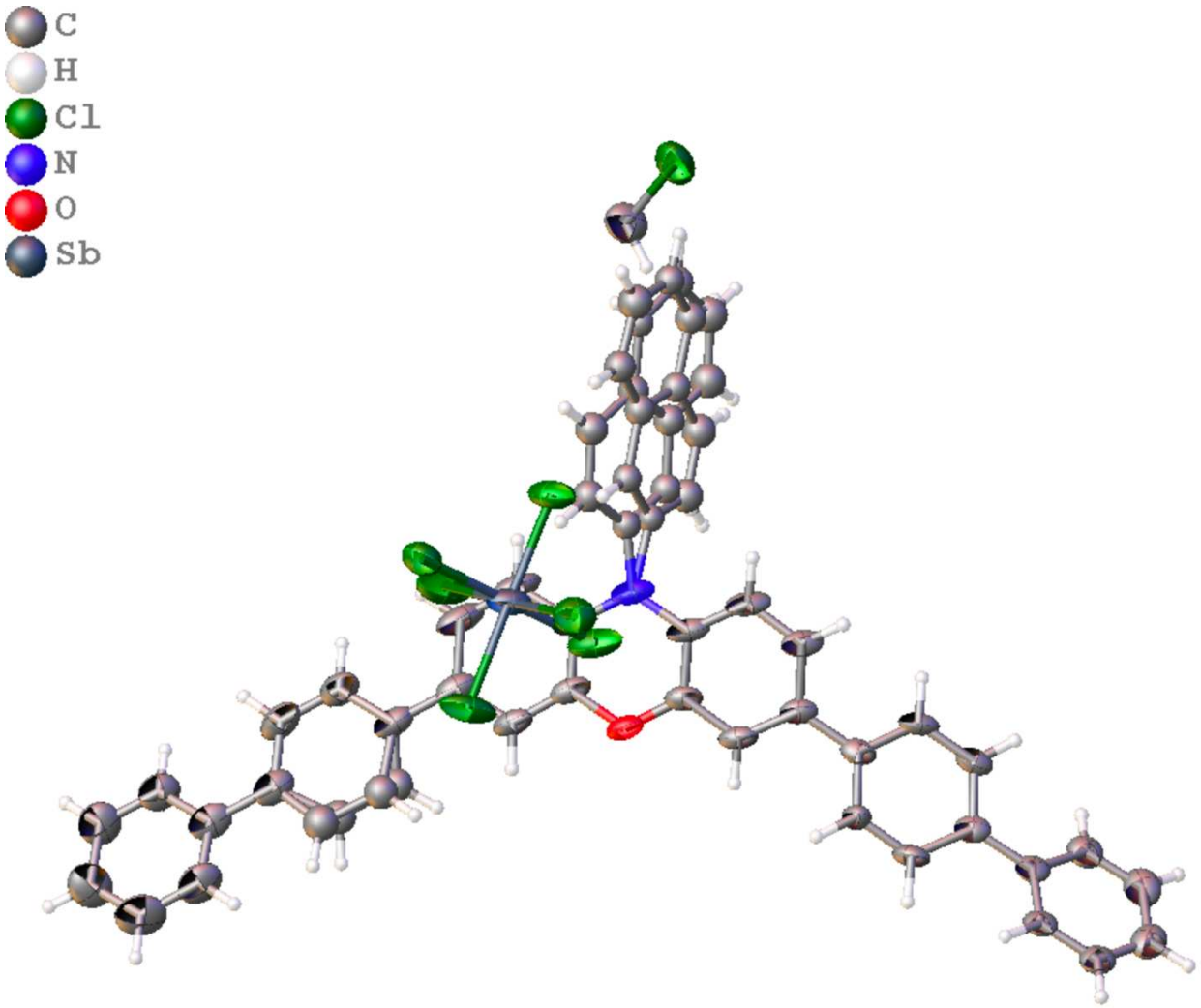

Figure 5.66. *Crystal structure of* ***9$^{\bullet+}$SbCl$_6^-$*** *shown as an ORTEP plot. Half of a DCM molecule is visible in this view due to disorder (i.e. the representation shown is only 50% occupancy).*

Table 5.8. *Crystallographic information for the structural refinement of* ***9•+SbCl6-***.

Empirical formula	$C_{46.5}H_{32}Cl_7NOSb$
Formula weight	990.63
Temperature	99.97 K
Crystal system	Monoclinic
Space group	$P2_1/n$
a	11.6418(5) Å
b	18.8802(7) Å
c	18.9143(7) Å
α	90º
β	91.686(2)º
γ	90º
Volume	4155.6(3) $Å^3$
Z	4
ρ_{calc}	1.583 g cm^{-3}
μ	1.152 mm^{-1}
F(000)	1984.0
Crystal color	Brown
Crystal size	0.094 x 0.063 x 0.056 mm^3
Radiation	Mo Kα (λ = 0.71073 Å)
2Θ range for data collection	3.048 to 50.058º
Index ranges	$-13 \leq h \leq 13$, $-22 \leq k \leq 22$, $-22 \leq l \leq 22$
Reflections collected	151177
Independent collections	7336 [R_{int} = 0.0919, R_{sigma} = 0.0283]
Data/restraints/parameters	7336/67/504
Goodness-of-fit on F^2	1.185
Final R indexes [$I \geq 2\sigma$ (I)]	R_1 = 0.0650, wR_2 = 0.1344
Final R indexes [call data]	R_1 = 0.0990, wR_2 = 0.1520
Largest diff. peak/hole	1.10/-0.78

Radical Cation Stability Studies

General Procedure

All solutions were prepared in an air-free quartz cuvette with a Teflon screw cap, under a nitrogen atmosphere, and under minimal lighting. In each case, a stock solution of $PC^{\bullet+}$ was prepared and diluted to a final concentration of 0.036 mM. To do this, the $PC^{\bullet+}$ stock was combined with solvent in the cuvette to a final volume of 3 mL, after which the cuvette was sealed and immediately transported to the UV-Vis for measurement. Experiments conducted in the dark were

left in the spectrometer between spectra, whereas those conducted under irradiation were removed from the spectrometer and irradiated in a white LED well between spectra.

Stability in N,N-Dimethylacetamide

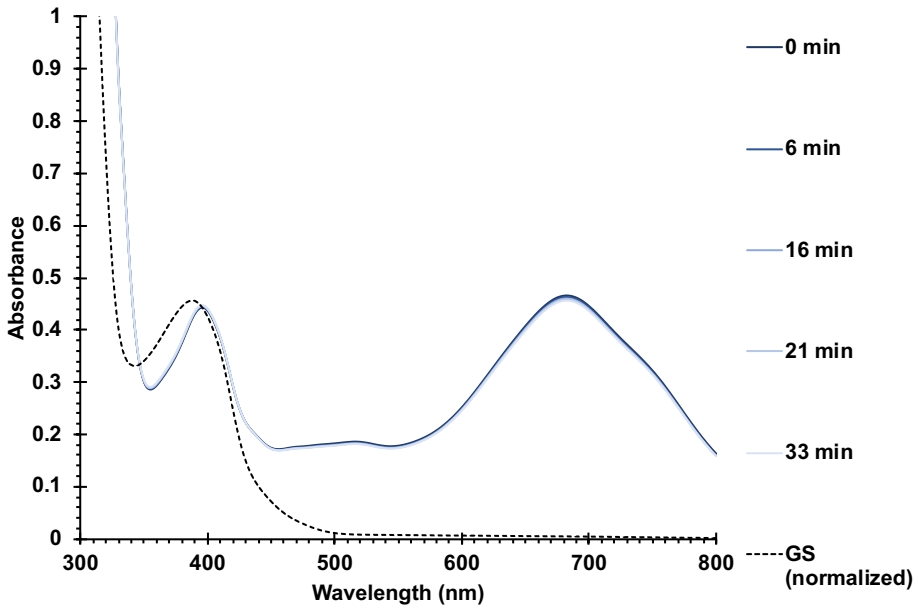

Figure 5.67. *UV-Vis spectra tracking the disappearance of* ***5***$^{\bullet+}$ *in DMAc in the absence of irradiation. Spectrum labeled GS corresponds to the neutral ground state PC spectrum.*

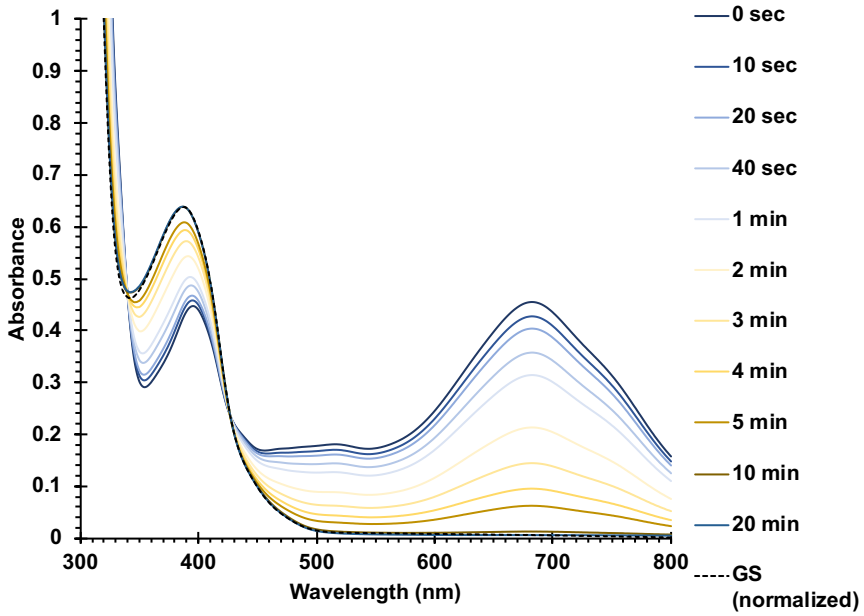

Figure 5.68. *UV-Vis spectra tracking the disappearance of* ***5***$^{\bullet+}$ *in DMAc under irradiation in a white LED well. Times shown represent the amount of time irradiated and do not include the time between irradiation periods during which the spectra were collected. Spectrum labeled GS corresponds to the neutral ground state PC spectrum.*

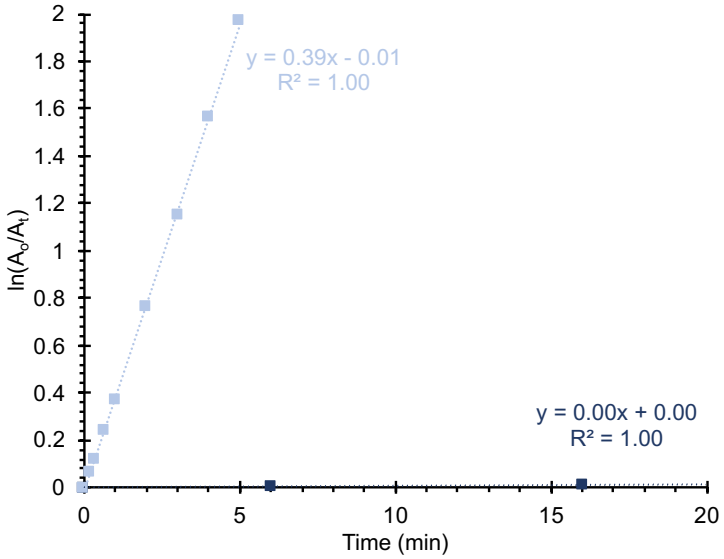

Figure 5.69. *Pseudo-first-order kinetics following the disappearance of* ***5***$^{\bullet+}$ *in DMAc with (light blue) and without (dark blue) irradiation. For the experiment under irradiation, the time represents time under irradiation (i.e. not including time in the dark during spectra collection).*

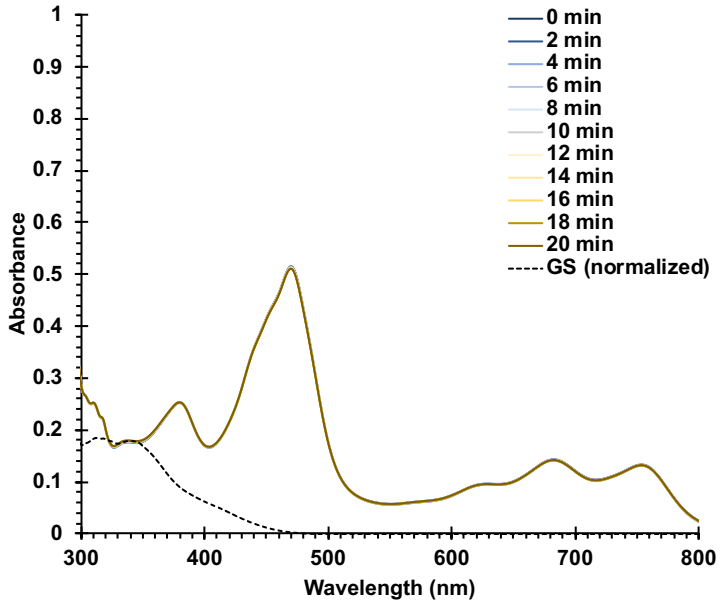

Figure 5.70. *UV-Vis spectra tracking the disappearance of* ***3***$^{\bullet+}$ *in DMAc in the absence of irradiation. Spectrum labeled GS corresponds to the neutral ground state PC spectrum.*

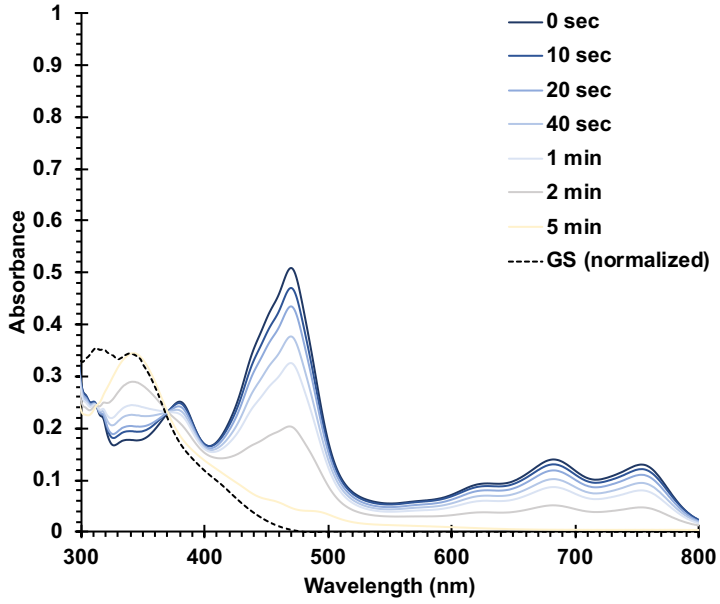

Figure 5.71. *UV-Vis spectra tracking the disappearance of* ***3***$^{\bullet+}$ *in DMAc under irradiation in a white LED well. Times shown represent the amount of time irradiated and do not include the time between irradiation periods during which the spectra were collected. Spectrum labeled GS corresponds to the neutral ground state PC spectrum.*

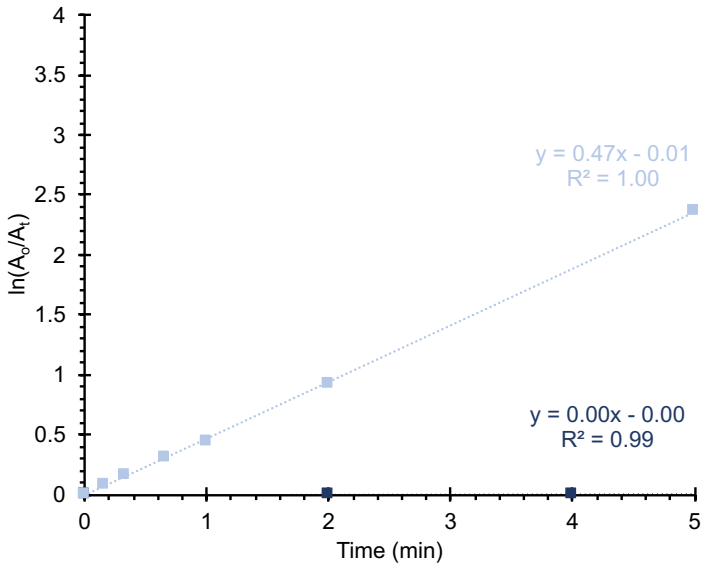

Figure 5.72. *Pseudo-first-order kinetics following the disappearance of* ***3***$^{\bullet+}$ *in DMAc with (light blue) and without (dark blue) irradiation. For the experiment under irradiation, the time represents time under irradiation (i.e. not including time in the dark during spectra collection).*

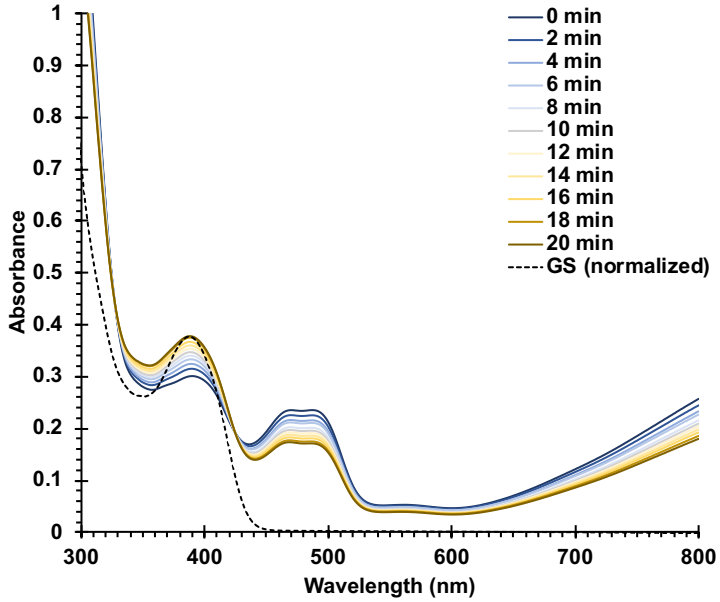

Figure 5.73. *UV-Vis spectra tracking the disappearance of* ***10***$^{\bullet+}$ *in DMAc in the absence of irradiation. Spectrum labeled GS corresponds to the neutral ground state PC spectrum.*

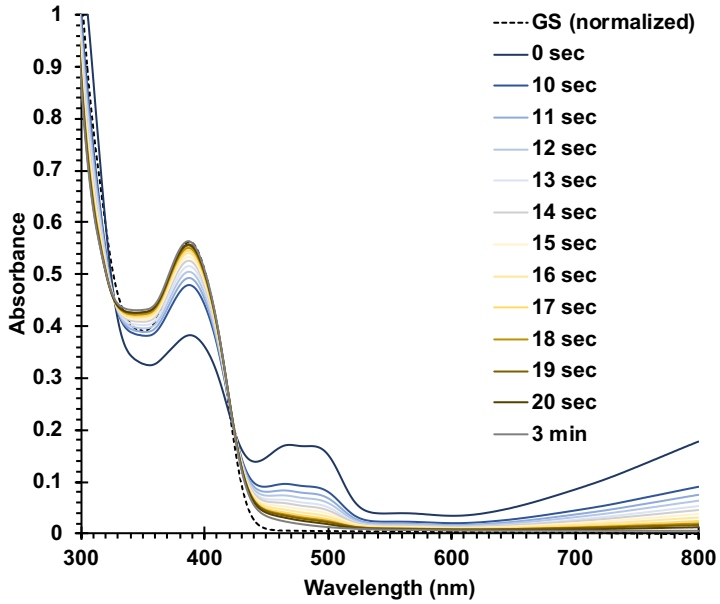

Figure 5.74. *UV-Vis spectra tracking the disappearance of* ***10***$^{\bullet+}$ *in DMAc under irradiation in a white LED well. Times shown represent the amount of time irradiated and do not include the time between irradiation periods during which the spectra were collected. Spectrum labeled GS corresponds to the neutral ground state PC spectrum.*

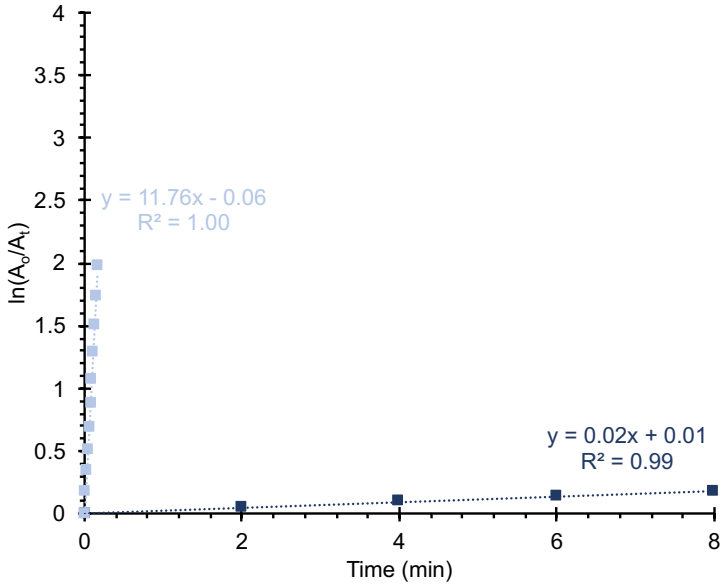

Figure 5.75. *Pseudo-first-order kinetics following the disappearance of* ***3***$^{\bullet+}$ *in DMAc with (light blue) and without (dark blue) irradiation. For the experiment under irradiation, the time represents time under irradiation (i.e. not including time in the dark during spectra collection).*

Stability in Ethyl Acetate

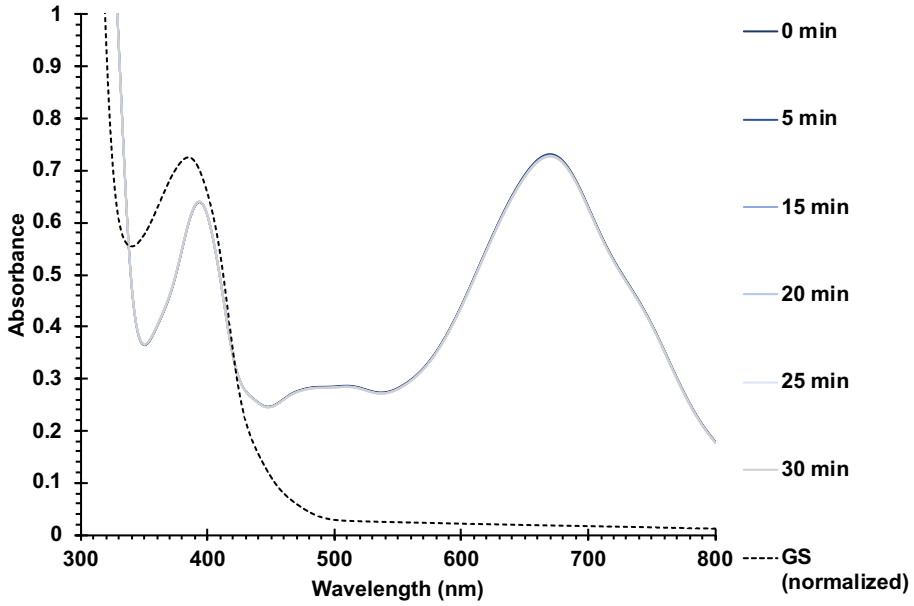

Figure 5.76. *UV-Vis spectra tracking the disappearance of* ***5***$^{\bullet+}$ *in EtAc in the absence of irradiation. Spectrum labeled GS corresponds to the neutral ground state PC spectrum.*

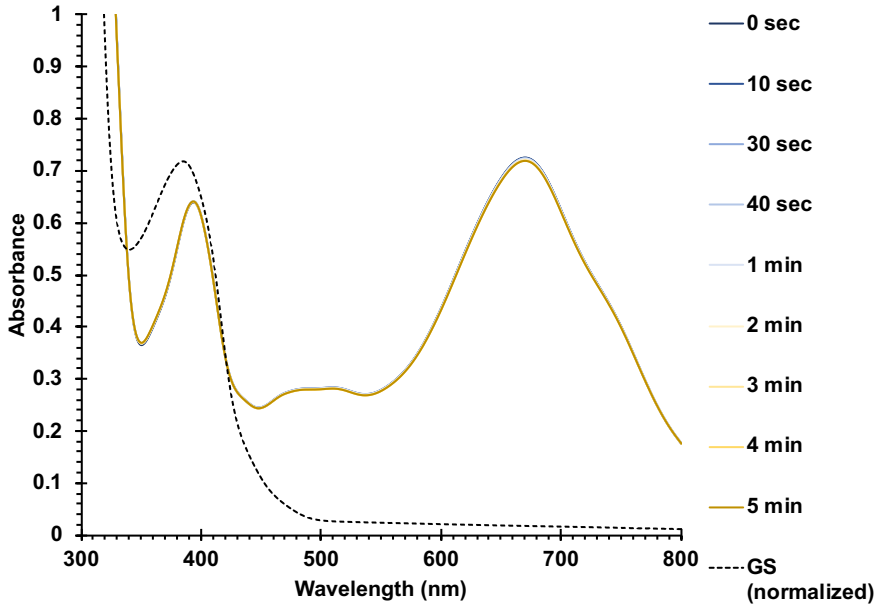

Figure 5.77. *UV-Vis spectra tracking the disappearance of* ***5***$^{\bullet+}$ *in EtAc under irradiation in a white LED well. Times shown represent the amount of time irradiated and do not include the time between irradiation periods during which the spectra were collected. Spectrum labeled GS corresponds to the neutral ground state PC spectrum.*

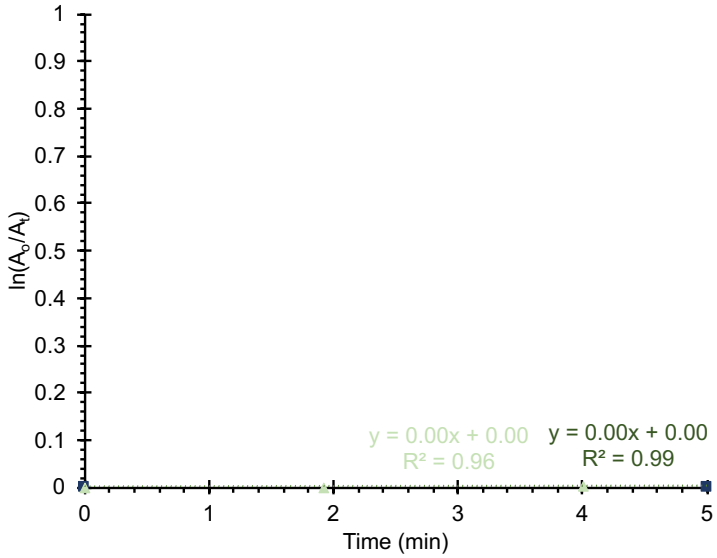

Figure 5.78. *Pseudo-first-order kinetics following the disappearance of* ***5***$^{\bullet+}$ *in EtAC with (light green) and without (dark green) irradiation. For the experiment under irradiation, the time represents time under irradiation plus time in the dark during spectra collection.*

Investigation of PF_6^- Stability

To investigate the stability of the PF_6^- anion, a solution of **5**$^{\bullet+}$**PF**$_6^-$ was prepared in d_7-DMF and irradiated in a white LED well. The solution gradually changed from dark blue to yellow, after which it was analyzed by ^{19}F NMR (Figure 5.79). The results are consistent with the presence of PF_6^-, indicating this anion did not undergo reaction during the decomposition of **5**$^{\bullet+}$.

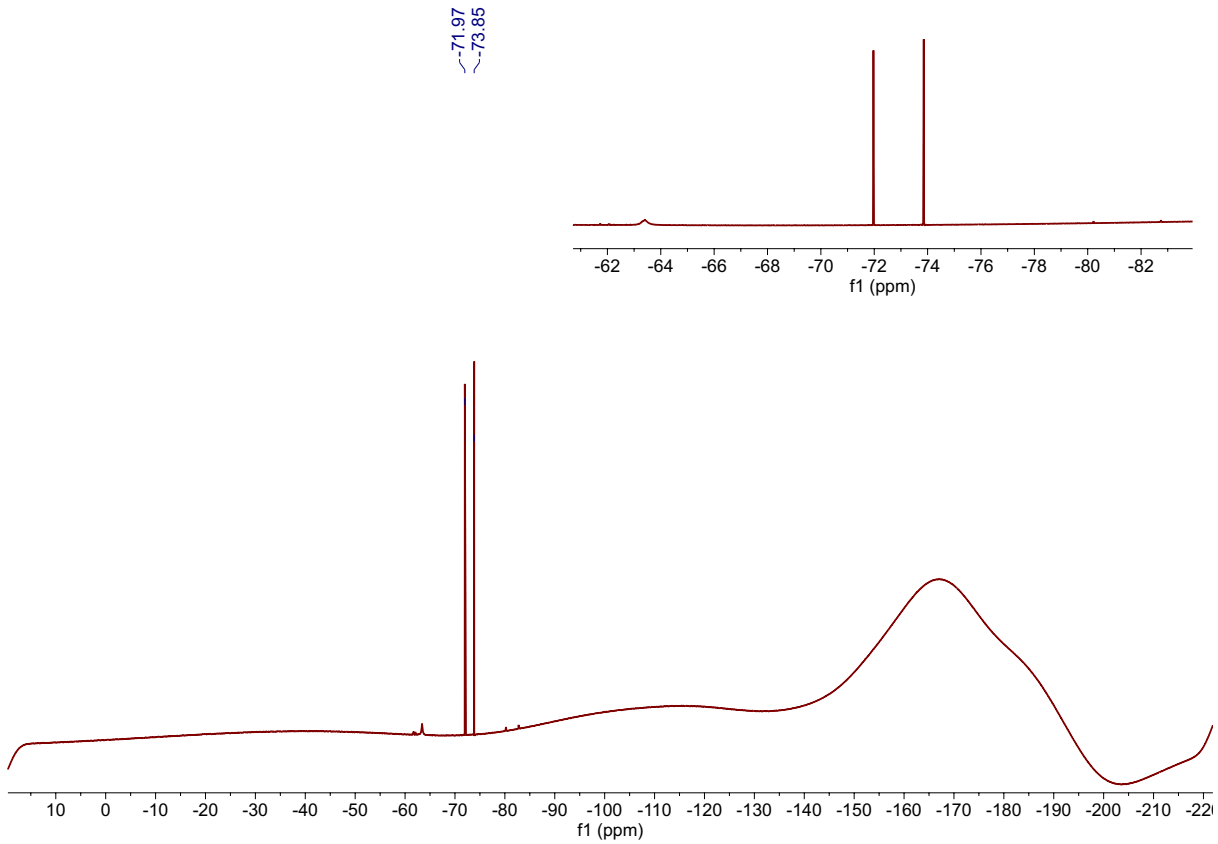

Figure 5.79. *^{19}F NMR of decomposed* ***5$^{\bullet+}$PF$_6^-$*** *in d_7-DMF. Figure inset shows spectrum zoomed in on PF_6^- peaks.*

Kinetic Isotope Effect in the Oxidation of N,N-Dimethylformamide

To further investigate the role of DMAc in the decomposition of **5**$^{\bullet+}$, a kinetic isotope study was undertaken. Given the structural similarities between DMAc and DMF, we hypothesized **5**$^{\bullet+}$ would exhibit similar instability in the presence of DMF as observed in the presence of DMAc. As such, stability studies were performed according to the general procedure described above using 0.7 mL DMF in 2.3 mL EtAc as the solvent. Under these conditions, the gradual disappearance of **5**$^{\bullet+}$ was observed by UV-Vis and analyzed assuming pseudo-first-order kinetics (Figure 5.80). To investigate the role of isotopic substitution on this reaction, the same experiment was carried out using d_7-DMF, at which point a significant increase in the rate of **5**$^{\bullet+}$ disappearance was observed.

Table 5.9 shows the results of these experiments, which indicate an inverse kinetic isotope effect under irradiation and a primary kinetic isotope effect in the dark. The presence of these isotope effects is consistent with the direct involvement of DMF in the decomposition reaction for $\mathbf{5}^{\bullet+}$, both in the dark and under irradiation.

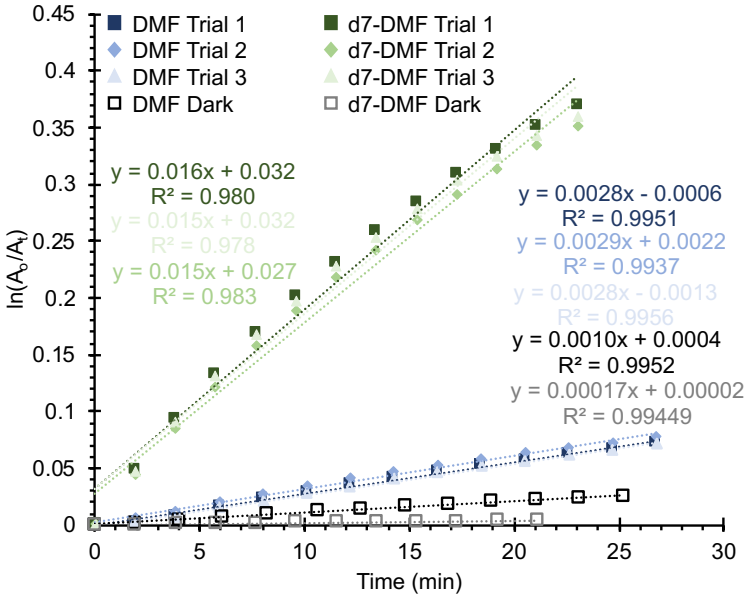

Figure 5.80. *Pseudo-first-order kinetics of* $\mathbf{5}^{\bullet+}$ *disappearance in the presence of DMF (blue) and* d_7*-DMF (green).*

Table 5.9. *Results from the decomposition of* ***5***$^{\bullet+}$ *in the presence of DMF and* d_7*-DMF.*

$k_{H,\,avg}$ **(M^{-1} s^{-1})**	0.0028 ± 0.0001
$k_{H,\,dark}$ **(M^{-1} s^{-1})**	0.0010
$k_{D,\,avg}$ **(M^{-1} s^{-1})**	0.015 ± 0.0004
$k_{D,\,dark}$ **(M^{-1} s^{-1})**	0.00017
k_H **/** k_D **(light)**	**0.18 ± 0.04**
k_H **/** k_D **(dark)**	**5.88**

Investigation of Solvent Impurities

The purity of DMF and d_7-DMF used in the kinetic isotope effect study (see above) was evaluated using gas chromatography. In each case, 1 μL pure solvent was injected directly into the instrument. The injector temperature was 100 ºC, and the initial column temperature was 75 ºC. The column temperature was maintained constant for 1 min, then ramped at a rate of 10 ºC min^{-1} to 180 ºC, and finally ramped at 100 ºC min^{-1} to 250 ºC and held there for 3 min. No significant differences were observed in the chromatograms of DMF and d_7-DMF, indicating no significant difference in volatile impurities that can account for the observed results with these reagents.

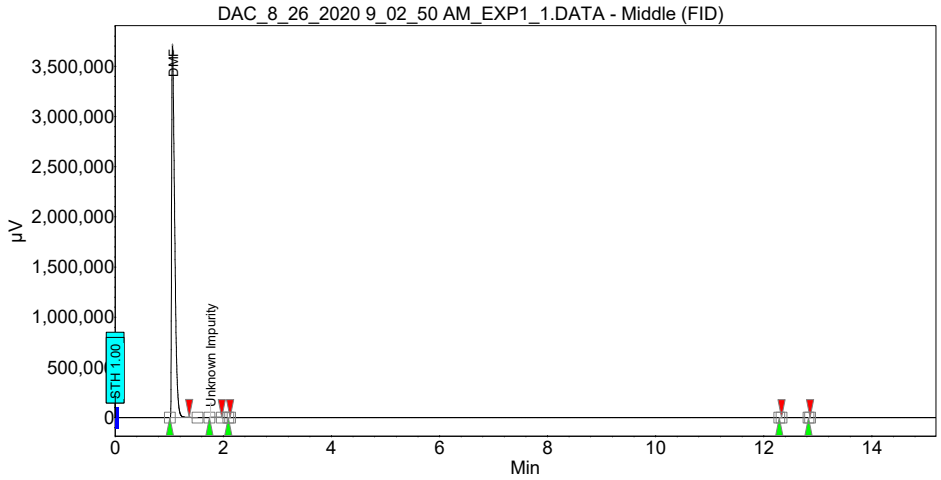

Peak results :

Index	Name	Time [Min]	Quantity [mM]	Height [µV]	Area [µV.Min]	Area % [%]
1	DMF	1.06	0.00	3719558.1	244792.4	99.910
2	Unknown Impurity	1.76	0.00	2166.4	206.1	0.084
3	UNKNOWN	2.10	0.00	565.1	10.3	0.004
4	UNKNOWN	12.30	0.00	137.4	1.9	0.001
5	UNKNOWN	12.84	0.00	110.1	1.3	0.001
Total			0.00	3722537.2	245011.9	100.000

Figure 5.81. *Gas chromatogram for DMF.*

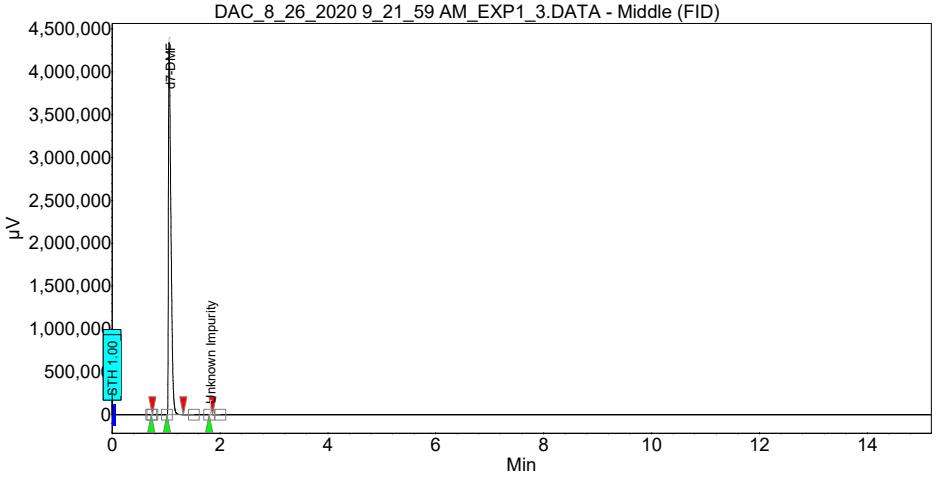

Peak results :

Index	Name	Time [Min]	Quantity [mM]	Height [µV]	Area [µV.Min]	Area % [%]
1	UNKNOWN	0.74	0.00	128.2	0.4	0.000
2	d7-DMF	1.06	0.00	4346556.9	232539.0	99.978
3	Unknown Impurity	1.82	0.00	949.1	50.5	0.022
Total			0.00	4347634.2	232589.9	100.000

Figure 5.82. *Gas chromatogram for d_7-DMF.*

Investigation of Radical Cation Excited State Reactivity

General Procedure

To further investigate possible reactivity from the excited state of $\mathbf{5}^{\bullet+}$, a series of reactions were performed in the presence of substrates with increasing oxidation potentials. Ethyl acetate was chosen for these studies due to the stability of $\mathbf{5}^{\bullet+}$ in this solvent, although the rate of disappearance of $\mathbf{5}^{\bullet+}$ was still quantified so reactions with substrates could be distinguished from any background decomposition of $\mathbf{5}^{\bullet+}$ (Table 5.10). In each case, the reactions were explored under irradiation with white LEDs and in the dark, and the kinetics of each reaction were monitored using UV-Vis to follow the disappearance of $\mathbf{5}^{\bullet+}$ (Table 5.10).

All solutions were prepared in an air-free quartz cuvette with a Teflon screw cap, under a nitrogen atmosphere, and under minimal lighting. In each case, substrates (100 or 10,000 eq relative to $\mathbf{5}^{\bullet+}\mathbf{PF_6}^-$) were dissolved in EtAc and transferred to the air-free cuvette. A stock solution of $PC^{\bullet+}$ was then prepared and diluted to a final concentration of 0.036 mM in the cuvette (final volume = 3 mL). The cuvette was wrapped in aluminum foil and quickly transported to the UV-Vis spectrometer for analysis. Experiments conducted in the dark were left in the spectrometer between spectra, whereas those conducted under irradiation were removed from the spectrometer and irradiated in a white LED well between spectra.

For each substrate, a control experiment was conducted in which neutral **5** was irradiated in the presence of substrate to rule out any background reaction that might interfere with kinetics experiments. However, no reactivity was observed by UV-Vis between **5** and any of the substrates used in these experiments.

For initial investigations, reactions were performed with 100 equivalents of substrate relative to $\mathbf{5}^{\bullet+}$. For substrates with lower oxidation potentials – o-phenylenediamine, *N,N*-

dimethylaniline, *N*-methylaniline, and aniline – the measured kinetics for the disappearance of $\mathbf{5}^{\bullet+}$ were clearly distinguishable from the slow background decomposition of the radical cation. However, the same kinetics were observed under irradiation and in the dark, indicating a ground state mechanism is likely dominant with these substrates. For substrates with oxidation potentials greater than aniline, no reactivity was observed either in the dark or under irradiation. Interestingly, even when DMAc was employed as a substrate under these conditions (100 equivalents dissolved in ethyl acetate), no reactivity was observed beyond the slow background reaction of $\mathbf{5}^{\bullet+}$.

As a clear difference in the reactivity of $\mathbf{5}^{\bullet+}$ had been previously observed when DMAc was used as the solvent, it was hypothesized that the substrates in these reactions were too dilute to enable an excited state reaction. In particular, the concentration of the substrates could be an important factor if the lifetime of photoexcited $\mathbf{5}^{\bullet+}$ is very short, in which case photophysical relaxation processes would likely occur faster than diffusion of photoexcited $\mathbf{5}^{\bullet+}$ to a substrate molecule. To address this possibility, similar experiments were performed using 10,000 equivalents of substrate relative to $\mathbf{5}^{\bullet+}$. Under these conditions, a reaction with DMAc was distinguishable from the background decomposition of $\mathbf{5}^{\bullet+}$, and a clear difference in reactivity was observed under irradiation versus in the dark. However, experiments with other substrates at this concentration still did not exhibit any evidence for reactivity from the excited state of $\mathbf{5}^{\bullet+}$.

Table 5.10. *Observed pseudo-first-order rate constants for the oxidation of various substrates by* $\mathbf{5}^{\bullet+}$ *with and without irradiation.*

Substrate	$E^o(S^+/S)$ (V vs. SCE)	$E^o_{calc}(S^+/S)$ (V vs. SCE)[a]	$K_{obs,\ light}$ ($M^{-1}\ s^{-1}$)	$K_{obs,\ dark}$ ($M^{-1}\ s^{-1}$)
None (Ethyl Acetate)	-	3.33	$4.0 \pm 1.0 \times 10^{-4}$	1.9×10^{-4}
o-Phenylenediamine	0.48[b]	0.42	$1.5 \pm 0.2 \times 10^{-1}$	1.3×10^{-1}
N,N-Dimethylaniline	0.851[c]	0.57	$4.9 \pm 0.4 \times 10^{-3}$	4.1×10^{-3}
N-Methylaniline	0.928[c]	0.68	$8.6 \pm 1.5 \times 10^{-3}$	7.5×10^{-3}
Aniline	1.038[c]	0.62	$2.2 \pm 0.3 \times 10^{-3}$	2.2×10^{-3}
3-Methylindole	1.085[c]	0.81	$4.3 \pm 1.8 \times 10^{-4}$	2.4×10^{-4}
1-Methylindole	1.184[c]	0.94	$5.1 \pm 0.3 \times 10^{-4}$	2.8×10^{-4}
Indole	1.254[c]	1.04	$4.5 \pm 1.1 \times 10^{-4}$	3.2×10^{-4}
1,2-Dimethoxybenzene	1.415[c]	1.14	$6.4 \pm 0.3 \times 10^{-4}$	6.9×10^{-5}
N-Methylacetanilide	1.753[c]	1.63	$2.1 \pm 0.3 \times 10^{-4}$	6.1×10^{-5}
N,N-Dimethylacetamide	1.97[d]	1.98	$1.7 \pm 0.2 \times 10^{-4}$	1.6×10^{-4}
1-Methylindole[e]	1.184[c]	0.94	$7.0 \pm 0.3 \times 10^{-3}$	6.4×10^{-3}
1,2-Dimethoxybenzene[e]	1.415[c]	1.14	$8.7 \pm 1.1 \times 10^{-4}$	4.1×10^{-4}
N-Methylacetanilide[e]	1.753[c]	1.63	$7.5 \pm 0.9 \times 10^{-4}$	3.5×10^{-4}
N,N-Dimethylacetamide[e]	1.97[d]	1.98	$1.5 \pm 0.04 \times 10^{-3}$	2.2×10^{-4}
N,N-Dimethyltrifluoroacetamide[e]	2.73[d]	2.78	$6.5 \pm 1.0 \times 10^{-3}$	3.7×10^{-3}
N,N-Dimethylacetamide[f]	1.97[d]	1.98	3.9×10^{-1}	6.4×10^{-4}

[a]Oxidation potential determined by DFT using the method reported in ref. 58. [b]Oxidation potential obtained from ref. 58. [c]Oxidation potential obtained from ref. 59. [d]Estimated using the $E_{p/2}(S^+/S)$ *as measured by cyclic voltammetry. [e]10,000 eq substrate. [f]Substrate = solvent =* 3.3×10^5 *eq. See Section 5 of Experimental for full experimental and computational details.*

With 100 Equivalents of Substrate

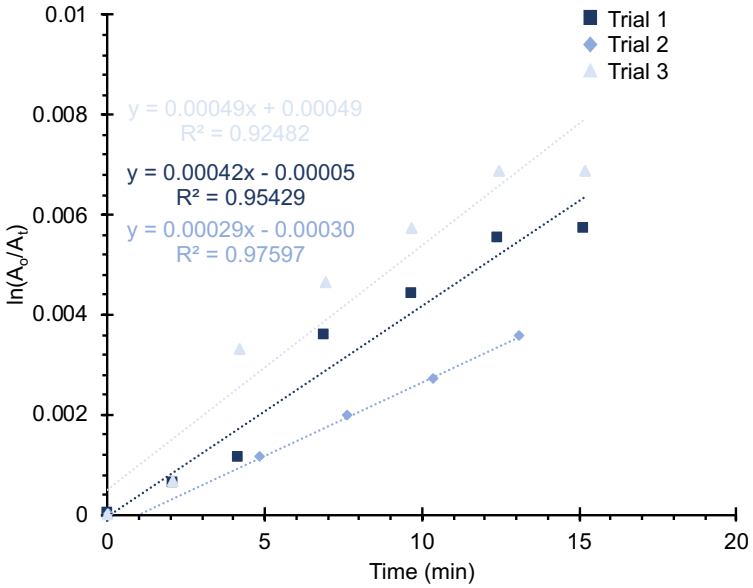

Figure 5.83. *Pseudo-first-order kinetics plot for the disappearance of* ***5***$^{\bullet+}$ *(0.036 mM) in EtAc in the absence of an added substrate. Experiments under irradiation (filled shapes) performed in triplicate.*

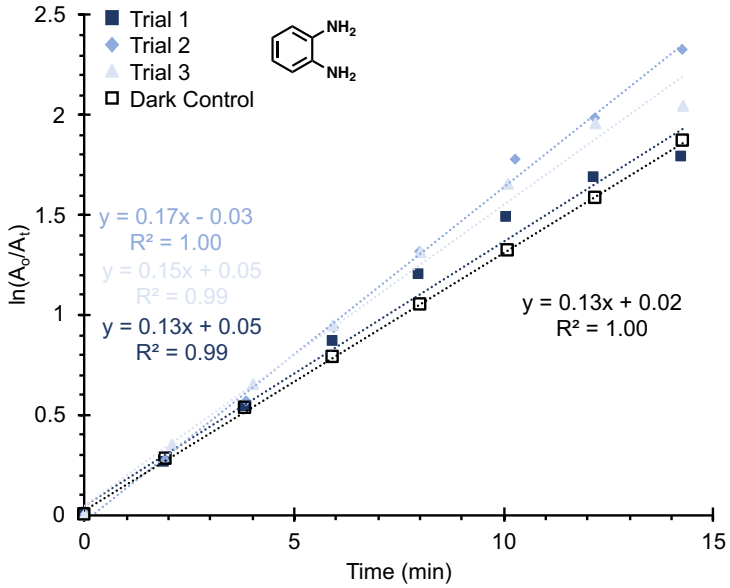

Figure 5.84. *Pseudo-first-order kinetics plot for the disappearance of* ***5***$^{\bullet+}$ *(0.036 mM) in EtAc in the presence of 100 equivalents o-phenylenediamine. Experiments under irradiation (filled shapes) performed in triplicate, while a control experiment in the dark (hollow squares) was performed once.*

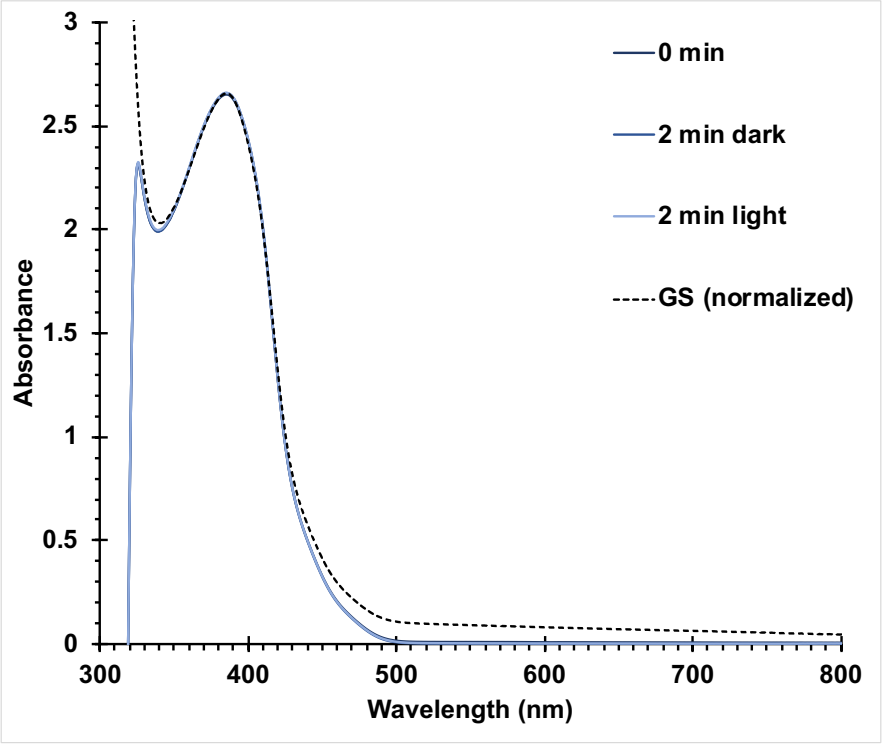

Figure 5.85. *UV-Vis of* ***5*** *in the presence of o-phenylenediamine before (solid, dark blue) and after (solid, light blue) 5 min of irradiation in a white LED well. Spectrum labeled GS corresponds to the spectrum of* ***5*** *in pure EtAc for reference.*

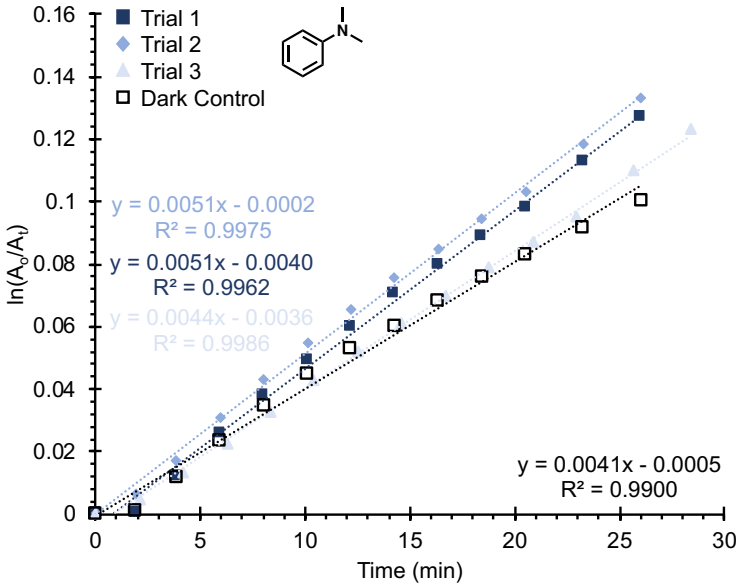

Figure 5.86. *Pseudo-first-order kinetics plot for the disappearance of* ***5***$^{\bullet+}$ *(0.036 mM) in EtAc in the presence of 100 equivalents of N,N-dimethylaniline. Experiments under irradiation (filled shapes) performed in triplicate, while a control experiment in the dark (hollow squares) was performed once.*

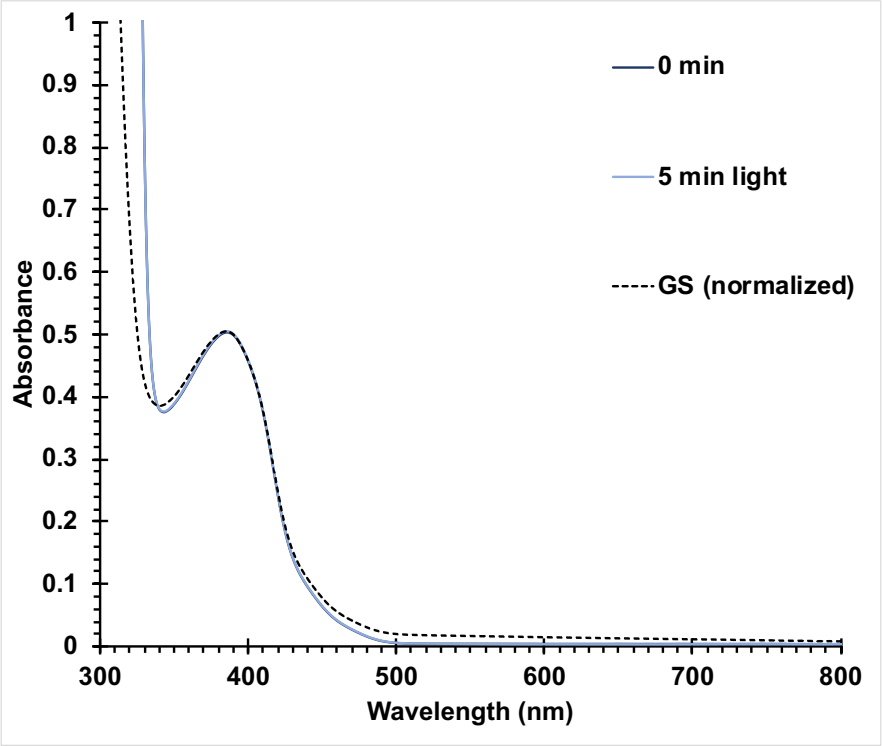

Figure 5.87. *UV-Vis of* ***5*** *in the presence of N,N-dimethylaniline before (solid, dark blue) and after (solid, light blue) 5 min of irradiation in a white LED well. Spectrum labeled GS corresponds to the spectrum of* ***5*** *in pure EtAc for reference.*

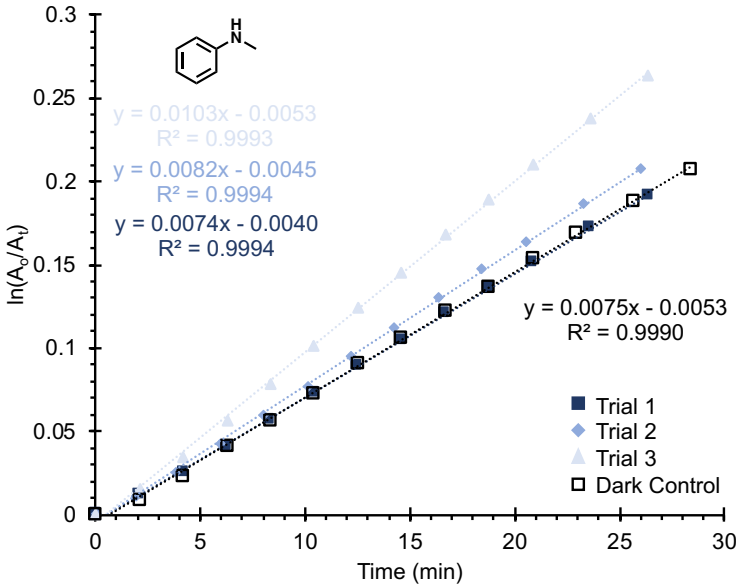

Figure 5.88. *Pseudo-first-order kinetics plot for the disappearance of* ***5***$^{\bullet+}$ *(0.036 mM) in EtAc in the presence of 100 equivalents of N-methylaniline. Experiments under irradiation (filled shapes) performed in triplicate, while a control experiment in the dark (hollow squares) was performed once.*

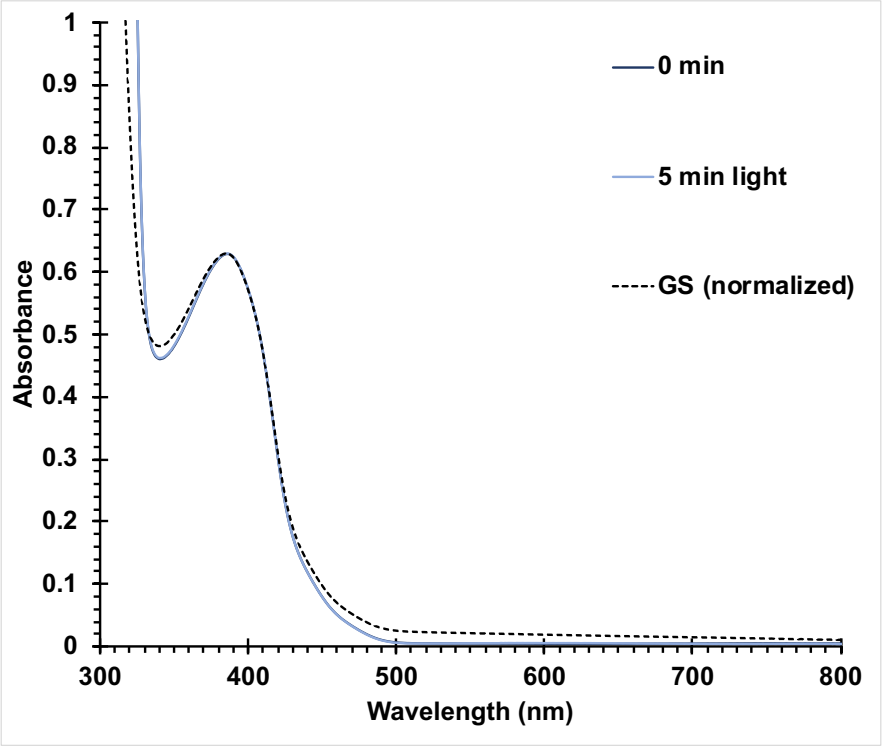

Figure 5.89. *UV-Vis of* ***5*** *in the presence of N-methylaniline before (solid, dark blue) and after (solid, light blue) 5 min of irradiation in a white LED well. Spectrum labeled GS corresponds to the spectrum of* ***5*** *in pure EtAc for reference.*

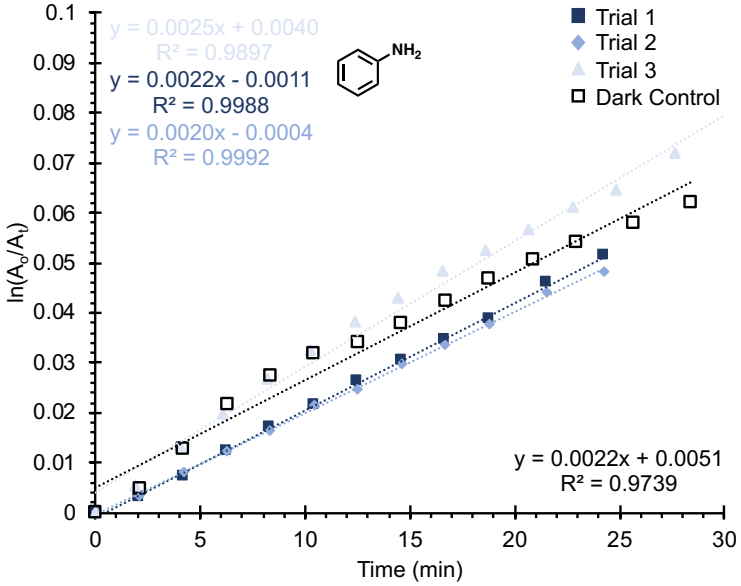

Figure 5.90. *Pseudo-first-order kinetics plot for the disappearance of* ***5***$^{\bullet+}$ *(0.036 mM) in EtAc in the presence of 100 equivalents of aniline. Experiments under irradiation (filled shapes) performed in triplicate, while a control experiment in the dark (hollow squares) was performed once.*

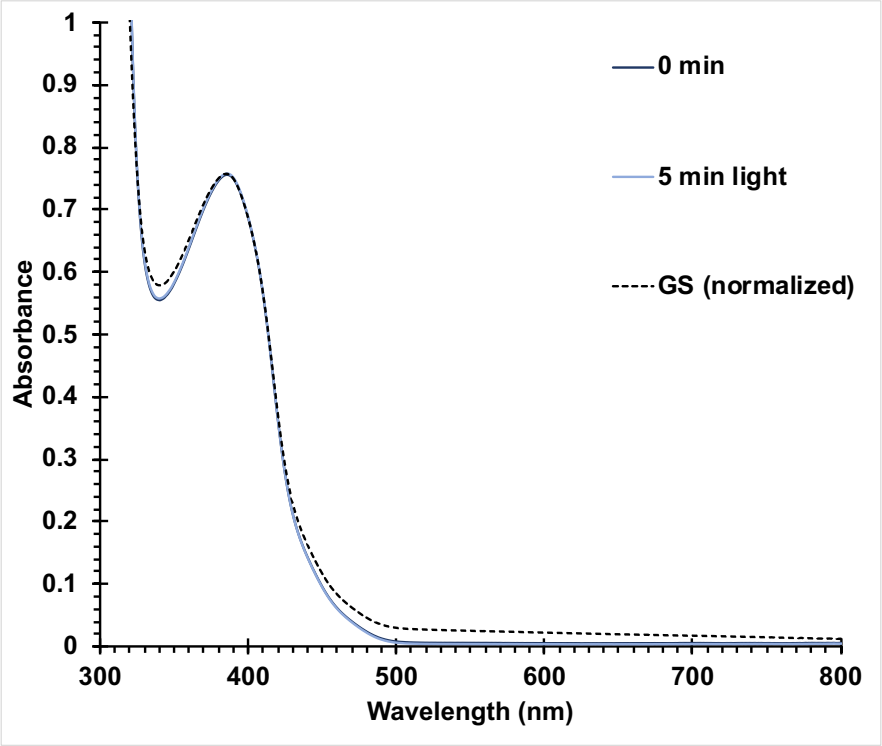

Figure 5.91. *UV-Vis of* ***5*** *in the presence of aniline before (solid, dark blue) and after (solid, light blue) 5 min of irradiation in a white LED well. Spectrum labeled GS corresponds to the spectrum of* ***5*** *in pure EtAc for reference.*

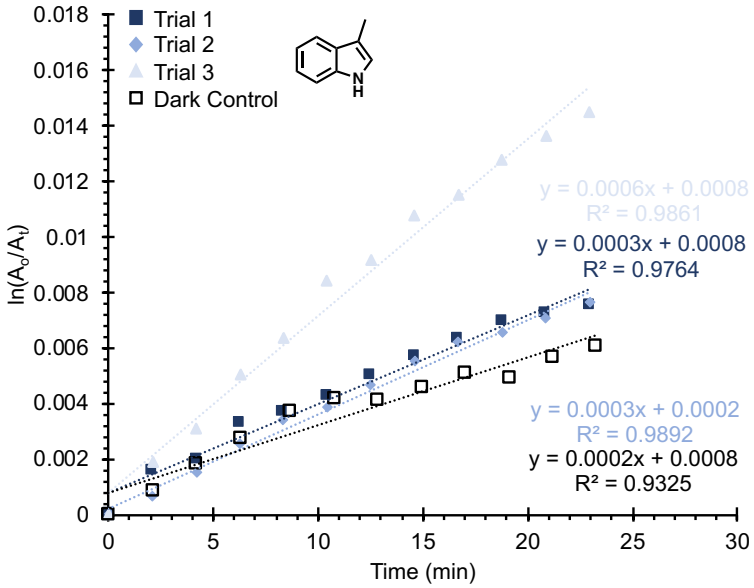

Figure 5.92. *Pseudo-first-order kinetics plot for the disappearance of* ***5***$^{\bullet+}$ *(0.036 mM) in EtAc in the presence of 100 equivalents of 3-methylindole. Experiments under irradiation (filled shapes) performed in triplicate, while a control experiment in the dark (hollow squares) was performed once.*

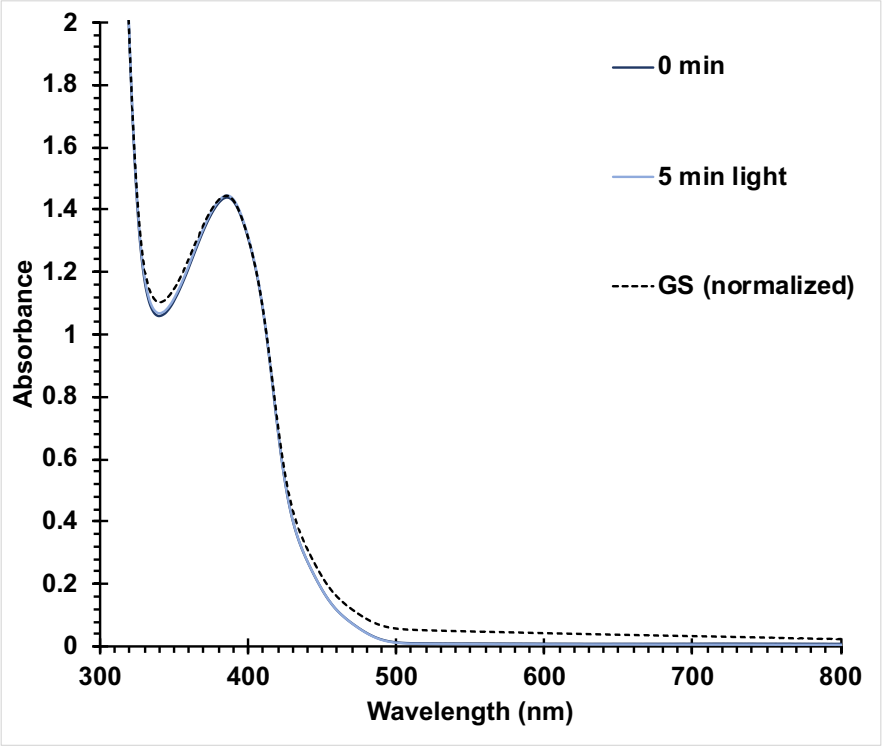

Figure 5.93. *UV-Vis of* ***5*** *in the presence of 3-methylindole before (solid, dark blue) and after (solid, light blue) 5 min of irradiation in a white LED well. Spectrum labeled GS corresponds to the spectrum of* ***5*** *in pure EtAc for reference.*

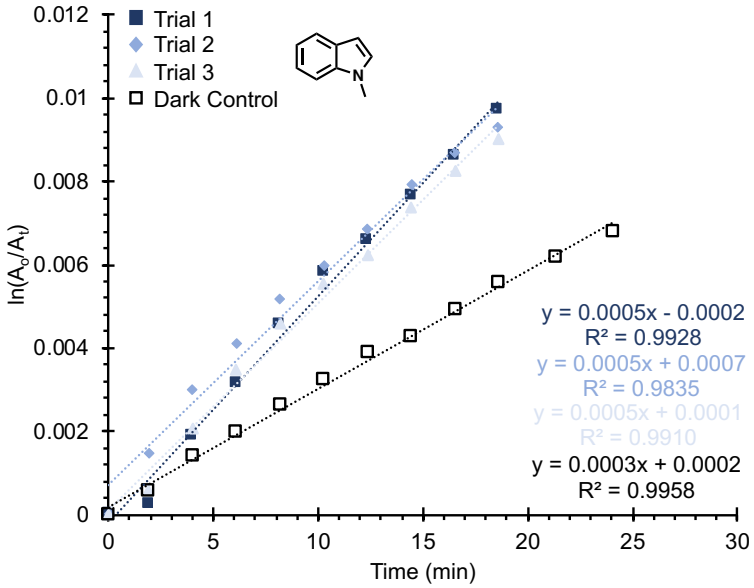

Figure 5.94. *Pseudo-first-order kinetics plot for the disappearance of* ***5***$^{\bullet+}$ *(0.036 mM) in EtAc in the presence of 100 equivalents of 1-methylindole. Experiments under irradiation (filled shapes) performed in triplicate, while a control experiment in the dark (hollow squares) was performed once.*

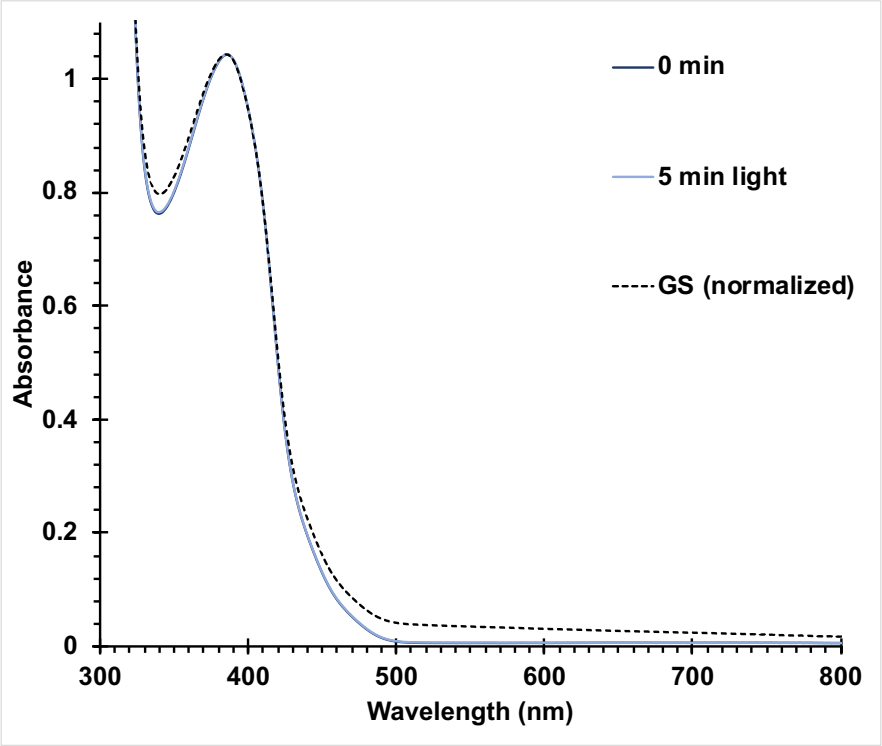

Figure 5.95. *UV-Vis of* ***5*** *in the presence of 1-methylindole before (solid, dark blue) and after (solid, light blue) 5 min of irradiation in a white LED well. Spectrum labeled GS corresponds to the spectrum of* ***5*** *in pure EtAc for reference.*

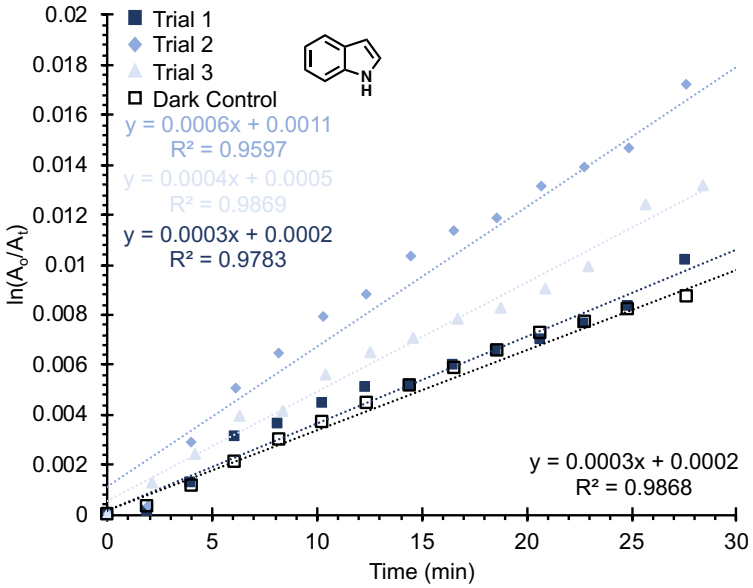

Figure 5.96. *Pseudo-first-order kinetics plot for the disappearance of* ***5***$^{\bullet+}$ *(0.036 mM) in EtAc in the presence of 100 equivalents of indole. Experiments under irradiation (filled shapes) performed in triplicate, while a control experiment in the dark (hollow squares) was performed once.*

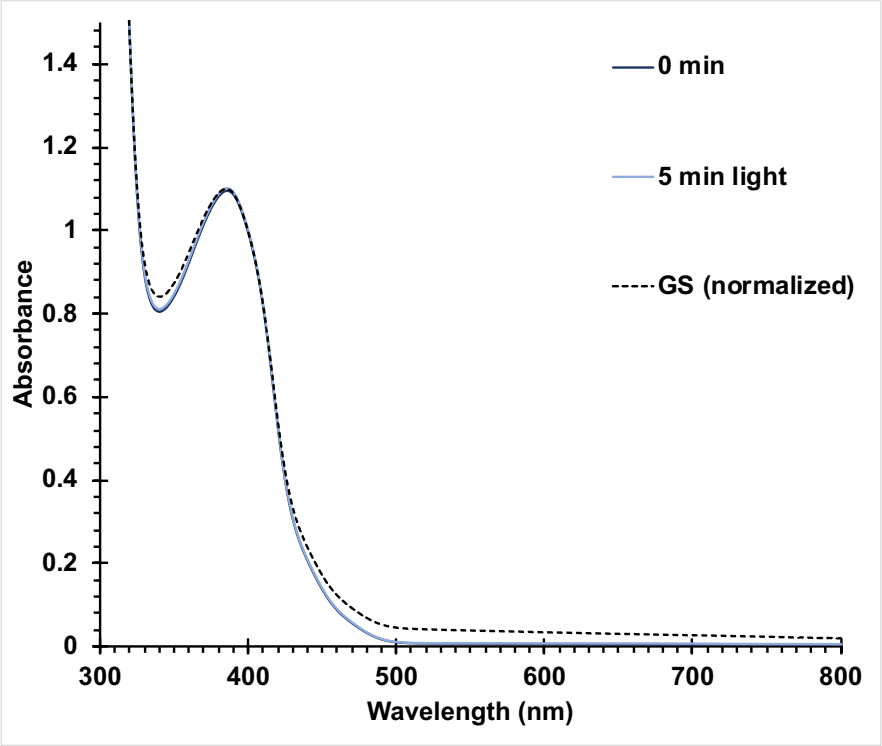

Figure 5.97. *UV-Vis of* ***5*** *in the presence of indole before (solid, dark blue) and after (solid, light blue) 5 min of irradiation in a white LED well. Spectrum labeled GS corresponds to the spectrum of* ***5*** *in pure EtAc for reference.*

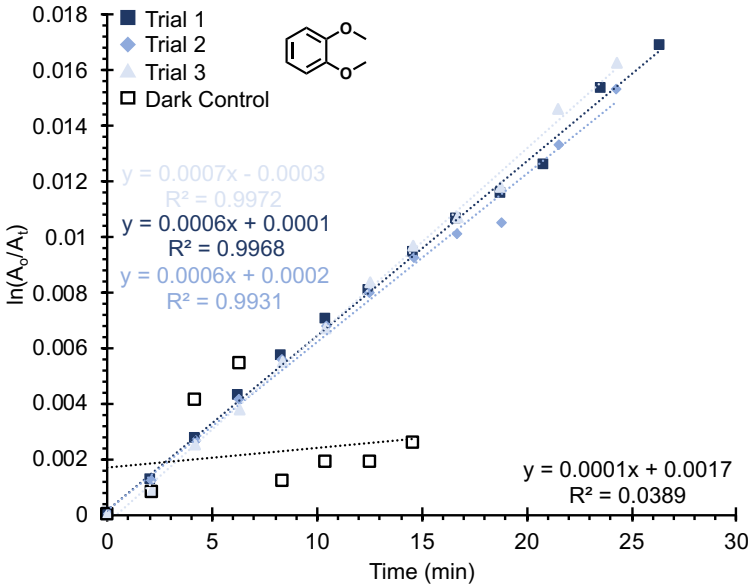

Figure 5.98. *Pseudo-first-order kinetics plot for the disappearance of* ***5***$^{\bullet+}$ *(0.036 mM) in EtAc in the presence of 100 equivalents of 1,2-dimethoxybenzene. Experiments under irradiation (filled shapes) performed in triplicate, while a control experiment in the dark (hollow squares) was performed once.*

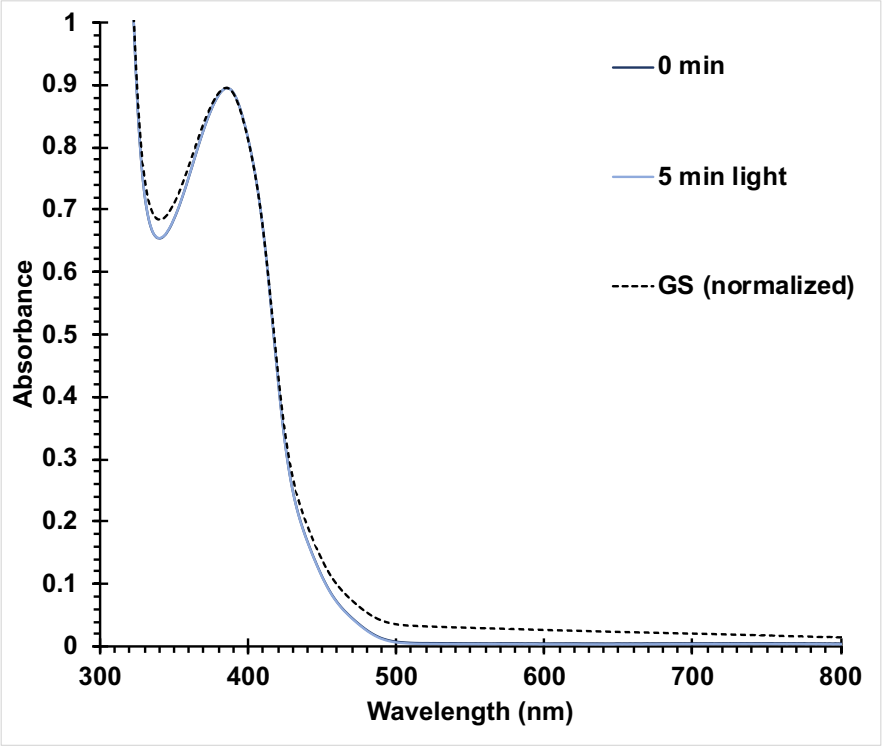

Figure 5.99. *UV-Vis of* ***5*** *in the presence of 1,2-dimethoxybenzene before (solid, dark blue) and after (solid, light blue) 5 min of irradiation in a white LED well. Spectrum labeled GS corresponds to the spectrum of* ***5*** *in pure EtAc for reference.*

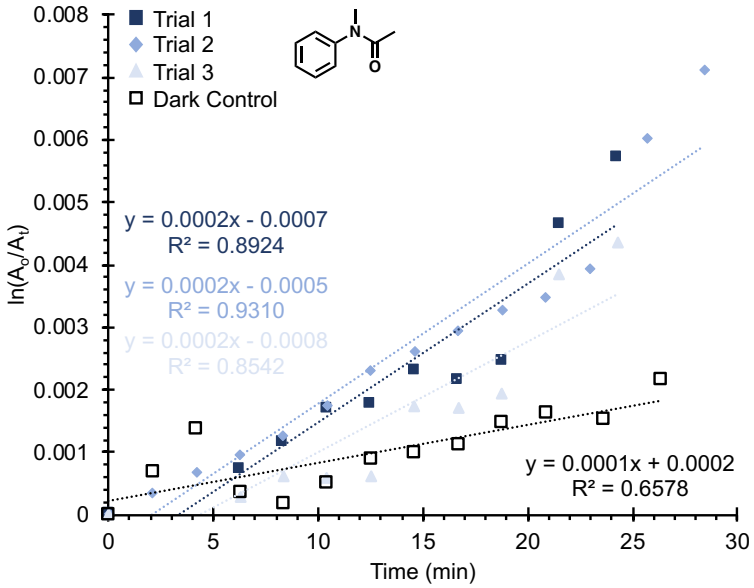

Figure 5.100. *Pseudo-first-order kinetics plot for the disappearance of* ***5***$^{\bullet+}$ *(0.036 mM) in EtAc in the presence of 100 equivalents of N-methylacetanilide. Experiments under irradiation (filled shapes) performed in triplicate, while a control experiment in the dark (hollow squares) was performed once.*

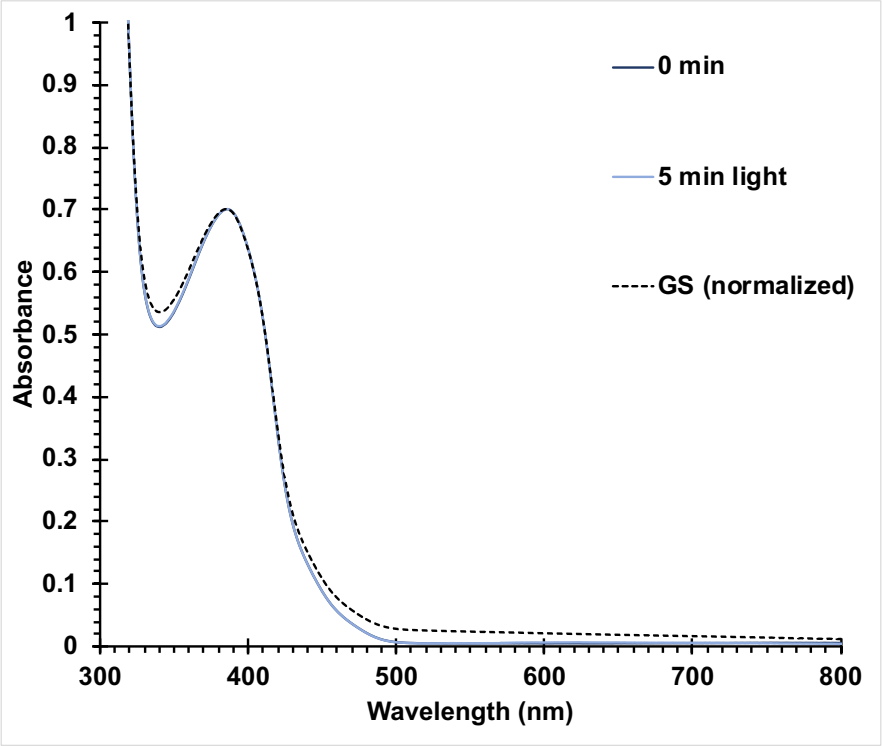

Figure 5.101. *UV-Vis of* ***5*** *in the presence of N-methylacetanilide before (solid, dark blue) and after (solid, light blue) 5 min of irradiation in a white LED well. Spectrum labeled GS corresponds to the spectrum of* ***5*** *in pure EtAc for reference.*

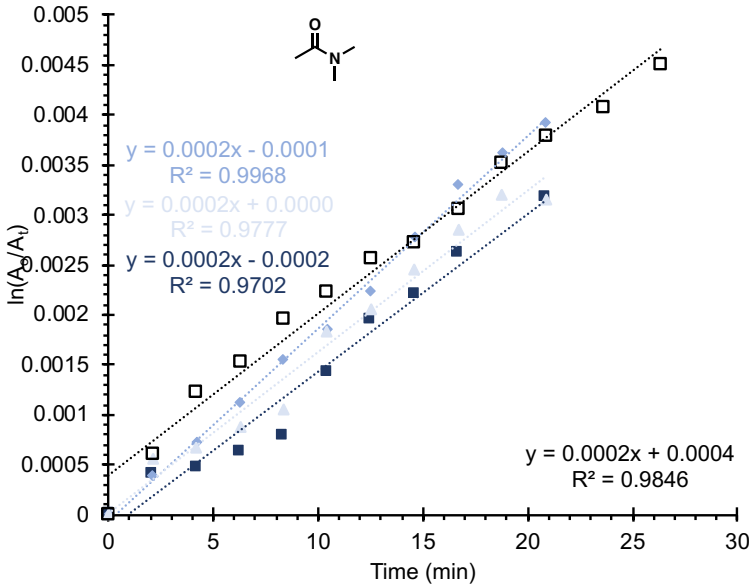

Figure 5.102. *Pseudo-first-order kinetics plot for the disappearance of* ***5***$^{\bullet+}$ *(0.036 mM) in EtAc in the presence of 100 equivalents of N,N-dimethylacetamide. Experiments under irradiation (filled shapes) performed in triplicate, while a control experiment in the dark (hollow squares) was performed once.*

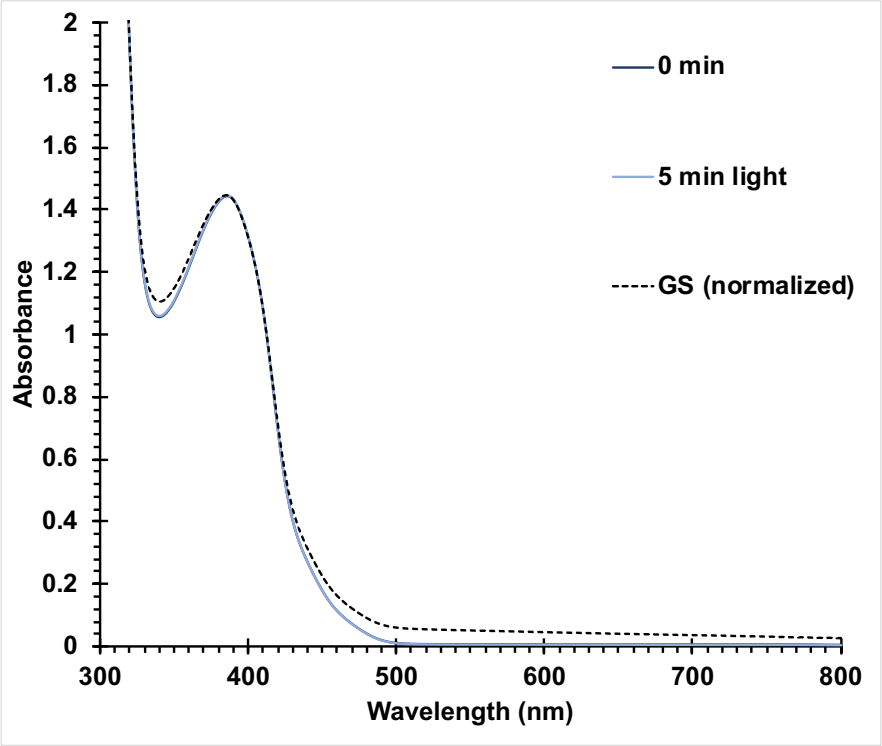

Figure 5.103. *UV-Vis of* ***5*** *in the presence of N,N-dimethylacetamide before (solid, dark blue) and after (solid, light blue) 5 min of irradiation in a white LED well. Spectrum labeled GS corresponds to the spectrum of* ***5*** *in pure EtAc for reference.*

With 10,000 Equivalents of Substrate

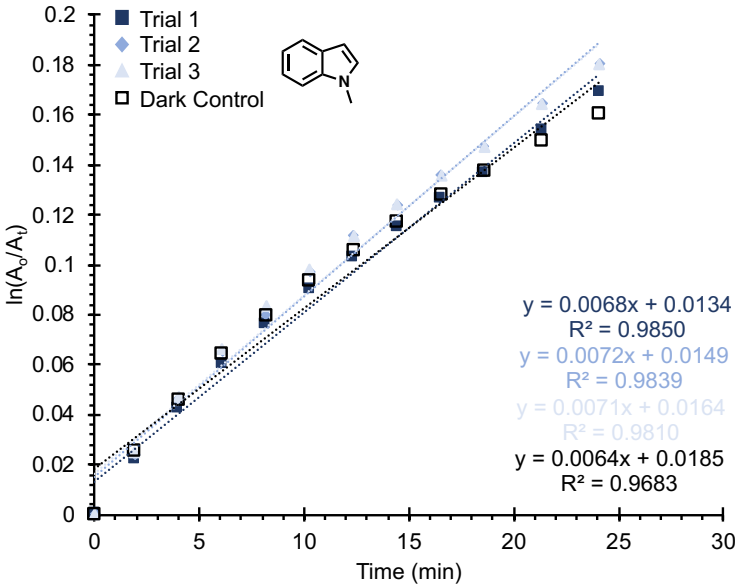

Figure 5.104. *Pseudo-first-order kinetics plot for the disappearance of* ***5***$^{\bullet+}$ *(0.036 mM) in EtAc in the presence of 10,000 equivalents of 1-methylindole. Experiments under irradiation (filled shapes) performed in triplicate, while a control experiment in the dark (hollow squares) was performed once.*

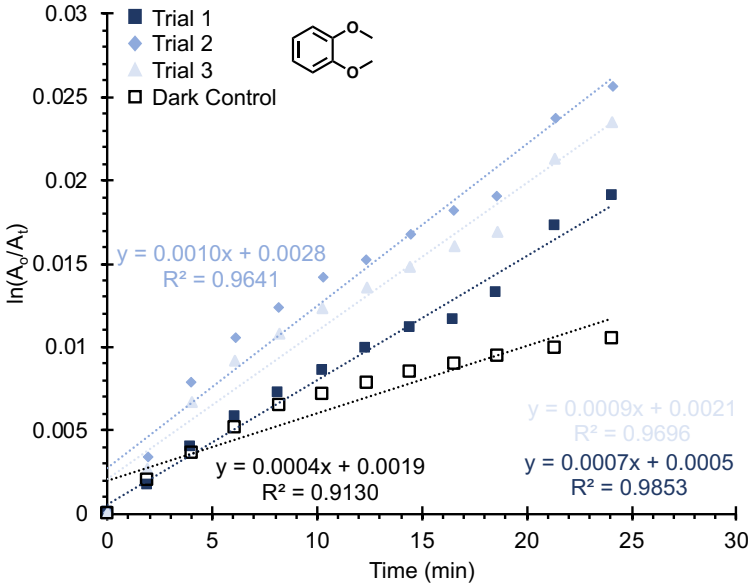

Figure 5.105. *Pseudo-first-order kinetics plot for the disappearance of* ***5***$^{\bullet+}$ *(0.036 mM) in EtAc in the presence of 10,000 equivalents of 1,2-dimethoxybenzene. Experiments under irradiation (filled shapes) performed in triplicate, while a control experiment in the dark (hollow squares) was performed once.*

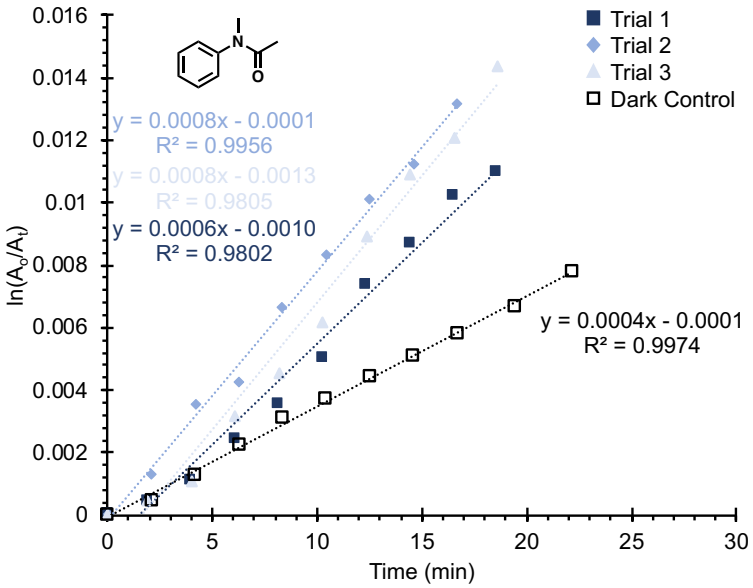

Figure 5.106. *Pseudo-first-order kinetics plot for the disappearance of* ***5***$^{\bullet+}$ *(0.036 mM) in EtAc in the presence of 10,000 equivalents of N-methylacetanilide. Experiments under irradiation (filled shapes) performed in triplicate, while a control experiment in the dark (hollow squares) was performed once.*

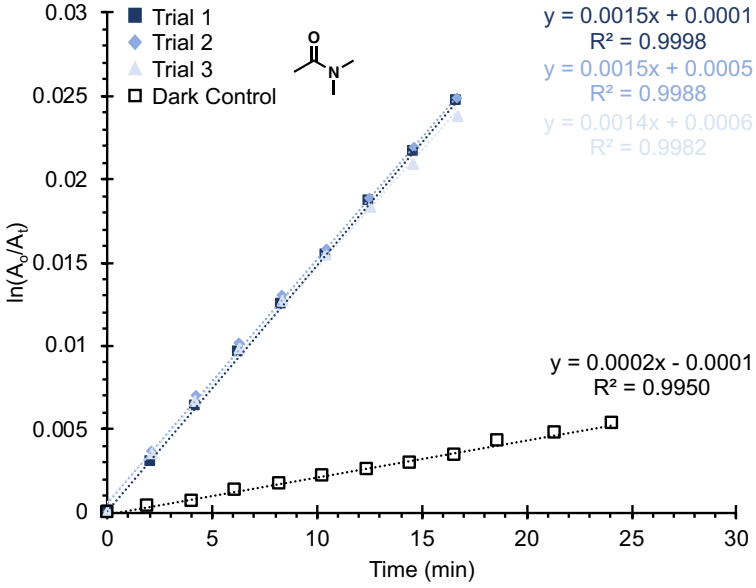

Figure 5.107. *Pseudo-first-order kinetics plot for the disappearance of* ***5***$^{\bullet+}$ *(0.036 mM) in EtAc in the presence of 10,000 equivalents of N,N-dimethylacetamide. Experiments under irradiation (filled shapes) performed in triplicate, while a control experiment in the dark (hollow squares) was performed once.*

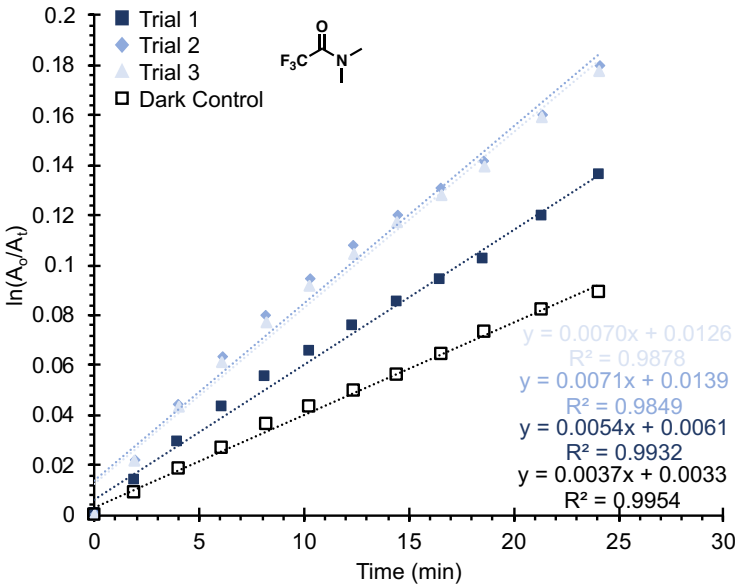

Figure 5.108. *Pseudo-first-order kinetics plot for the disappearance of* ***5***$^{\bullet+}$ *(0.036 mM) in EtAc in the presence of 10,000 equivalents of N,N-dimethyltrifluoroacetamide. Experiments under irradiation (filled shapes) performed in triplicate, while a control experiment in the dark (hollow squares) was performed once.*

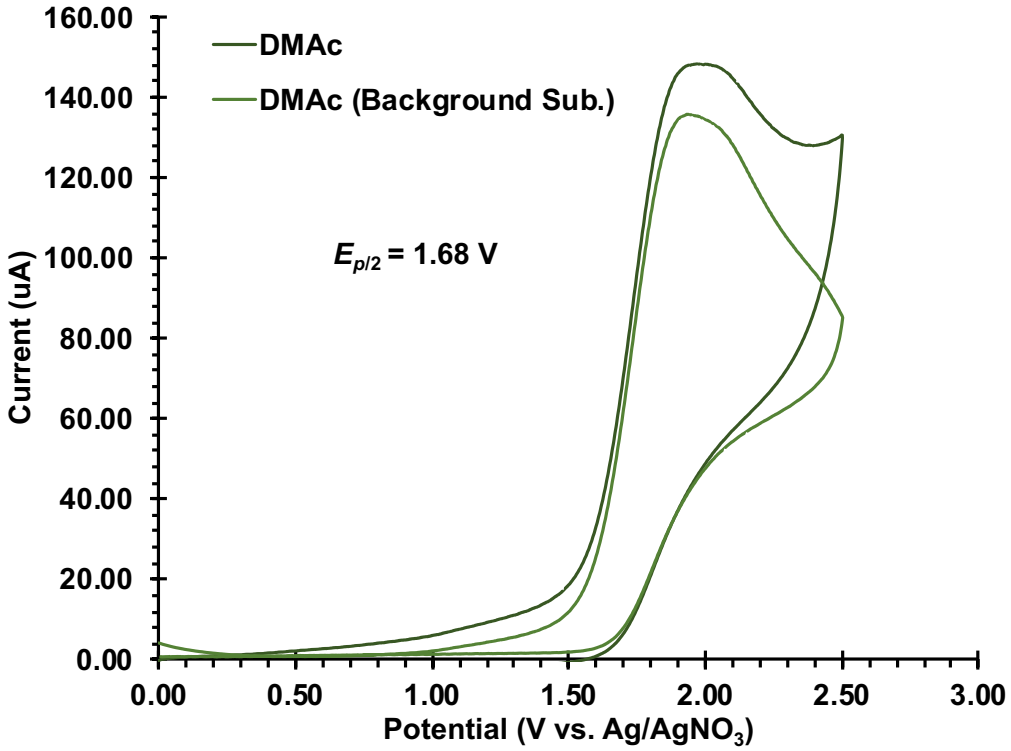

Figure 5.109. *Cyclic voltammogram of N,N-dimethylacetamide in MeCN (scan rate = 100 mV s^{-1}).*

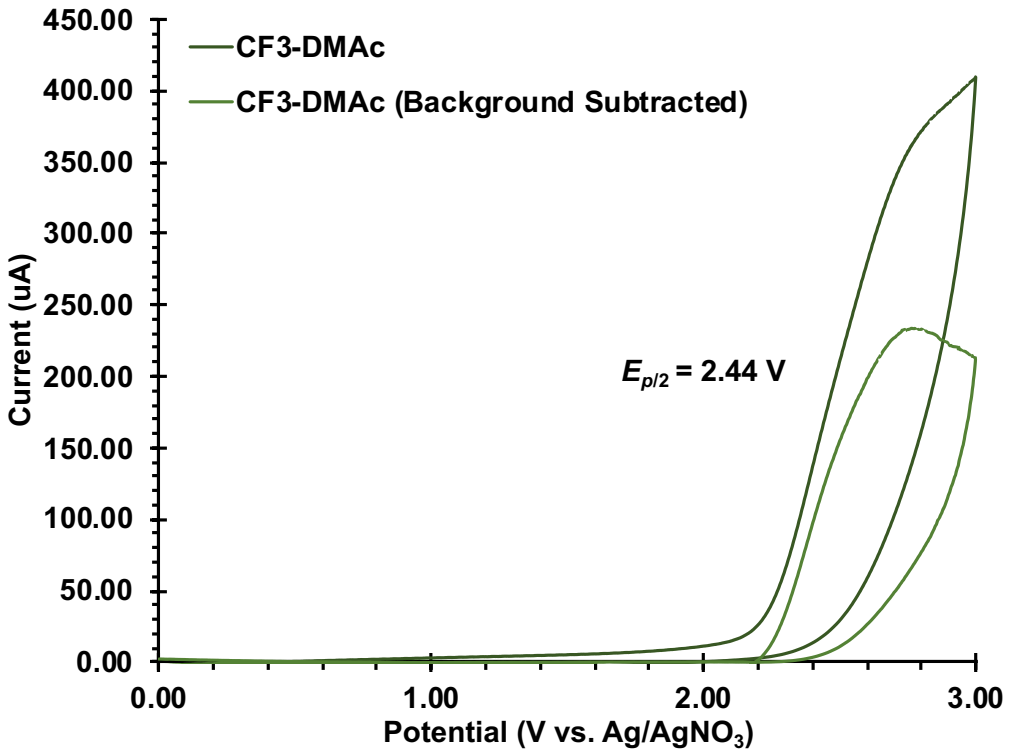

Figure 5.110. *Cyclic voltammogram of N,N-dimethyltrifluoroacetamide in MeCN (scan rate = 100 mV s^{-1}).*

Estimation of Substrate Oxidation Potentials by Density Functional Theory

Oxidation potential of substrates employed in these studies were computed using the method outlined by Nicewicz and coworkers[58]. All density functional theory (DFT) calculations were performed using the GAUSSIAN 16 version C.01 computational chemistry package.

Structures of the substrates and corresponding radical cations were optimized at the B3LYP/6-31+G** level of theory in CPCM-acetonitrile. The resulting computed free energies of the substrate (G[sub]) and radical cation (G[rad-cat]) were used to calculate the standard oxidation potential of the substrate in the following manner. The free energy change for the oxidation was calculated as ΔG_{ox} = G[rad-cat] – G[sub]. Since the free energies obtained by DFT are in units of Hartrees, they were converted to kcal mol^{-1} using the conversion factor 627.51 kcal mol^{-1} $Hartree^{-1}$. To reference this value versus the standard hydrogen electrode (SHE), a value of -100.5 kcal/mol

was assumed for the reduction free energy of the SHE. As such, $E_{ox} = (\Delta G_{ox} - 100.5) / (n*F)$, where n = 1 for a one electron oxidation and F = 23.061 kcal mol^{-1} V^{-1}. Finally, E_{ox} was referenced versus the saturated calomel electrode (SCE) by subtracting 0.24 V, the conversion factor for SHE to SCE. Molecular coordinates of all computed structures are provided at the end.

Radical Cation Reactivity Towards Halides

UV-Vis Experiments in the Presence of Bromide

All solutions were prepared in an air-free quartz cuvette with a Teflon screw cap, under a nitrogen atmosphere, and under minimal lighting. In each case, LiBr was dissolved in EtAc or DMAc and transferred to the cuvette, such that the final solution would be 0.1 M in LiBr. A stock solution of $PC^{\bullet+}$ in the same solvent was then prepared and diluted to a final concentration of 0.036 mM in the cuvette (final volume = 3 mL). The cuvette was wrapped in aluminum foil and quickly transported to the UV-Vis spectrometer for analysis. Experiments conducted in the dark were left in the spectrometer between spectra, whereas those conducted under irradiation were removed from the spectrometer and irradiated in a white LED well between spectra.

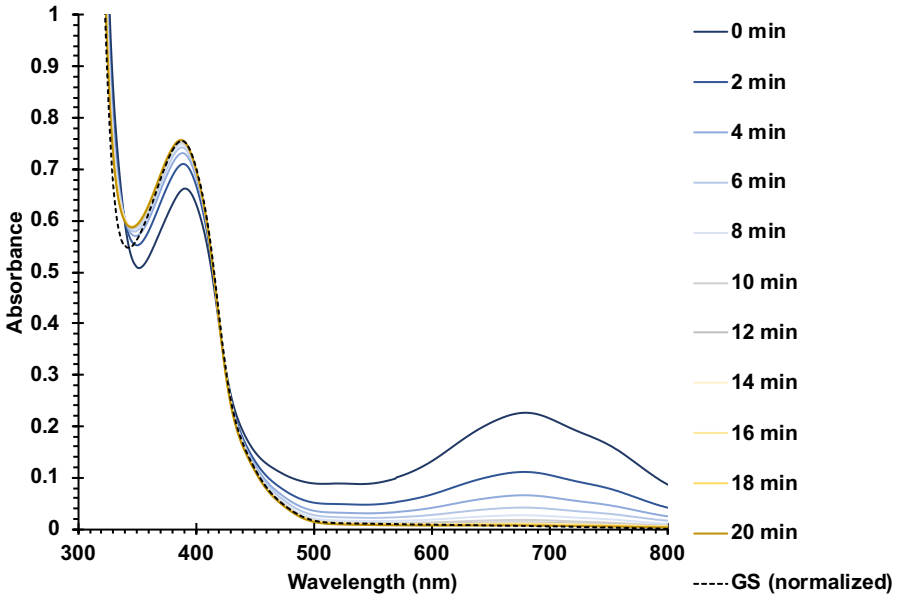

Figure 5.111. *Representative example of UV-Vis spectra following the disappearance of* $\mathbf{5}^{\bullet+}$ *in the presence of 0.1 M LiBr in DMAc in the dark. Spectrum labeled GS corresponds to the neutral ground state PC spectrum.*

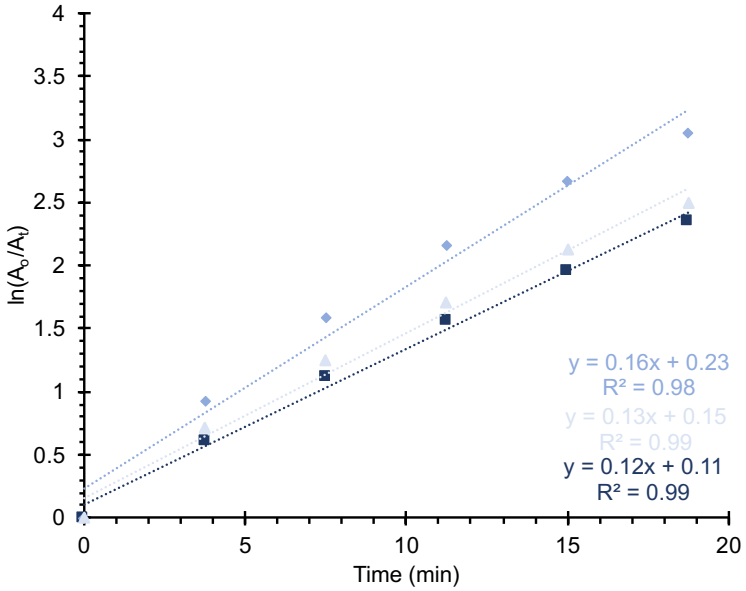

Figure 5.112. *Pseudo-first-order kinetics following the disappearance of* $\mathbf{5}^{\bullet+}$ *in the presence of 0.1 M LiBr in DMAc in the dark. Average* $k_{obs} = 0.14 \pm 0.02\ M^{-1}s^{-1}$.

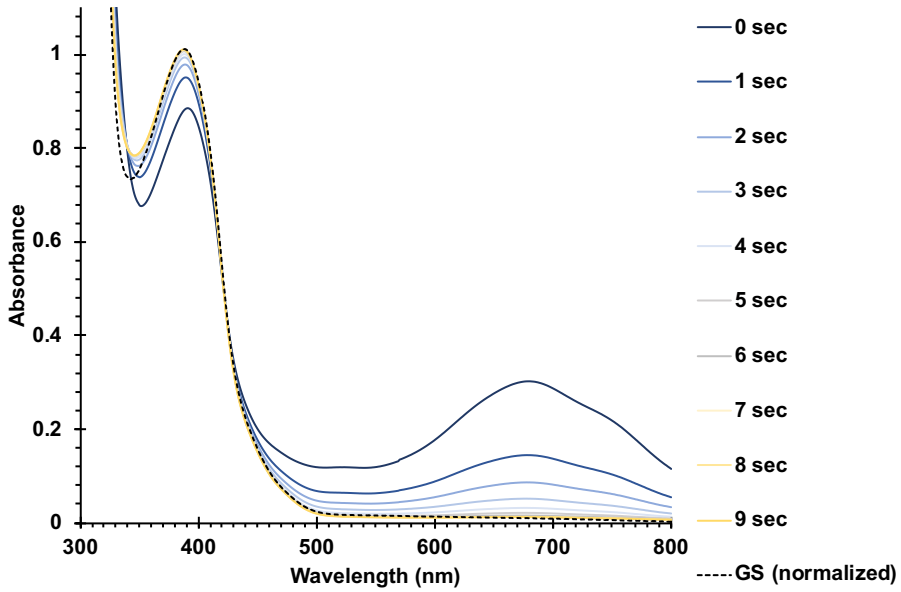

Figure 5.113. *Representative example of UV-Vis spectra following the disappearance of* $\mathbf{5}^{\bullet+}$ *in the presence of 0.1 M LiBr in DMAc under irradiation in a white LED well. Spectrum labeled GS corresponds to the neutral ground state PC spectrum.*

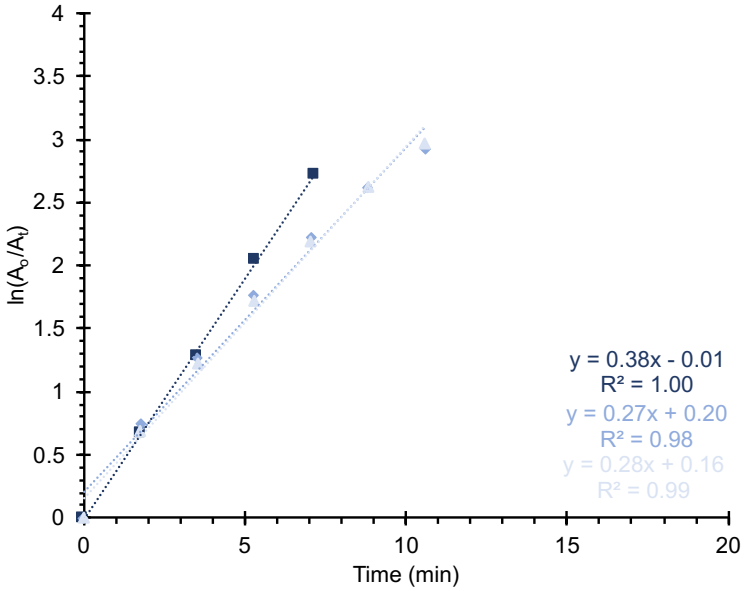

Figure 5.114. *Pseudo-first-order kinetics following the disappearance of* $\mathbf{5}^{\bullet+}$ *in the presence of 0.1 M LiBr in DMAc under irradiation in a white LED well. The time represents total time (i.e. under irradiation and in the dark). Average* $k_{obs} = 0.31 \pm 0.06\ M^{-1}s^{-1}$.

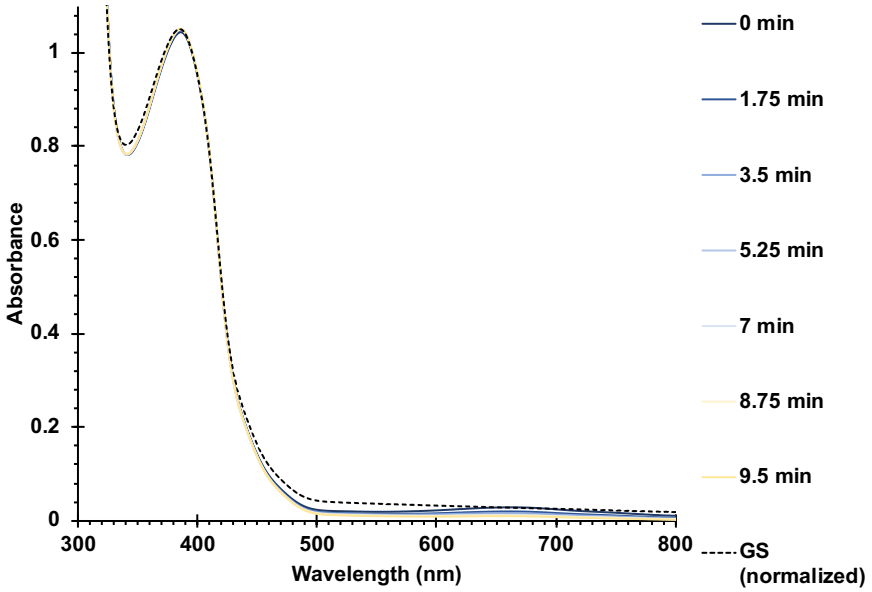

Figure 5.115. *UV-Vis spectra following the disappearance of* ***5***$^{\bullet+}$ *in the presence of 0.1 M LiBr in EtAc in the dark. Spectrum labeled GS corresponds to the neutral ground state PC spectrum.*

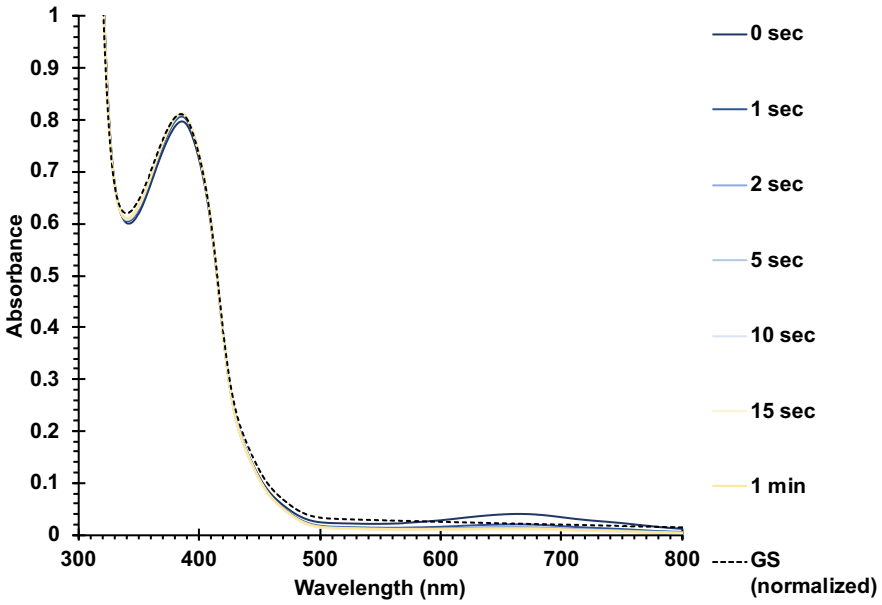

Figure 5.116. *UV-Vis spectra following the disappearance of* ***5***$^{\bullet+}$ *in the presence of 0.1 M LiBr in EtAc under irradiation in a white LED well. Spectrum labeled GS corresponds to the neutral ground state PC spectrum.*

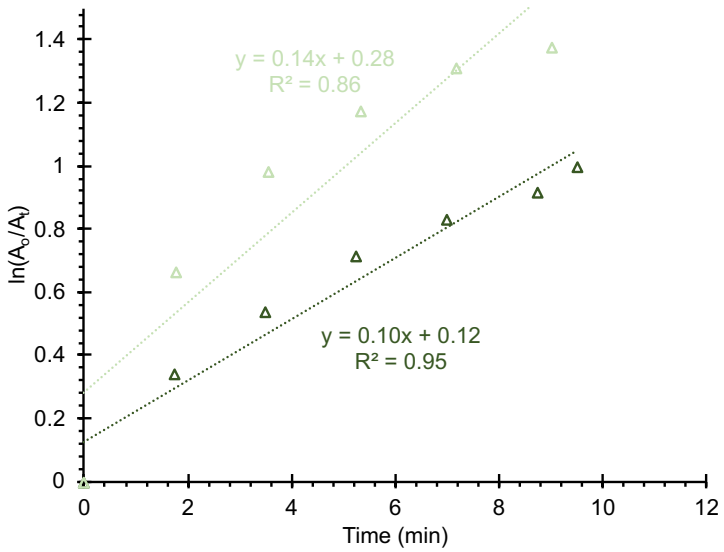

Figure 5.117. *Pseudo-first-order kinetics following the disappearance of* ***5***$^{\bullet+}$ *in 0.1 M LiBr in EtAc with (light green) and without (dark green) irradiation. For the experiment under irradiation, the time represents total time (i.e. time under irradiation plus time in the dark).*

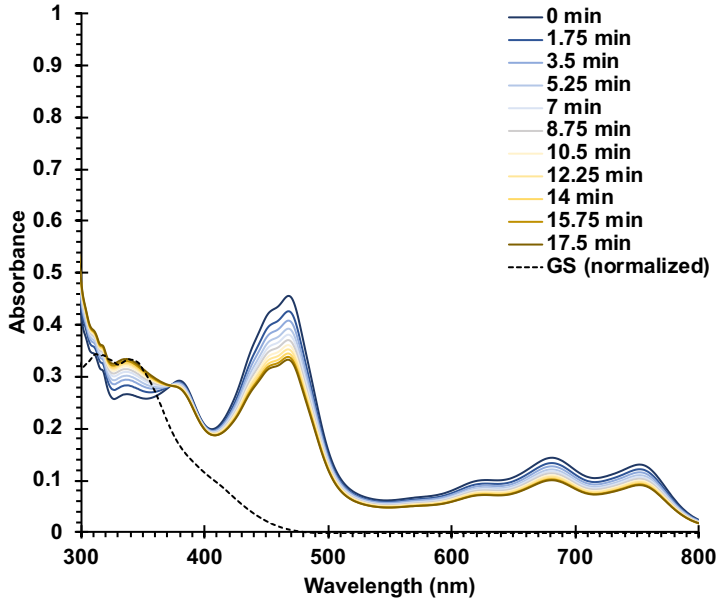

Figure 5.118. *UV-Vis spectra following the disappearance of* ***3***$^{\bullet+}$ *in the presence of 0.1 M LiBr in DMAc in the dark. Spectrum labeled GS corresponds to the neutral ground state PC spectrum.*

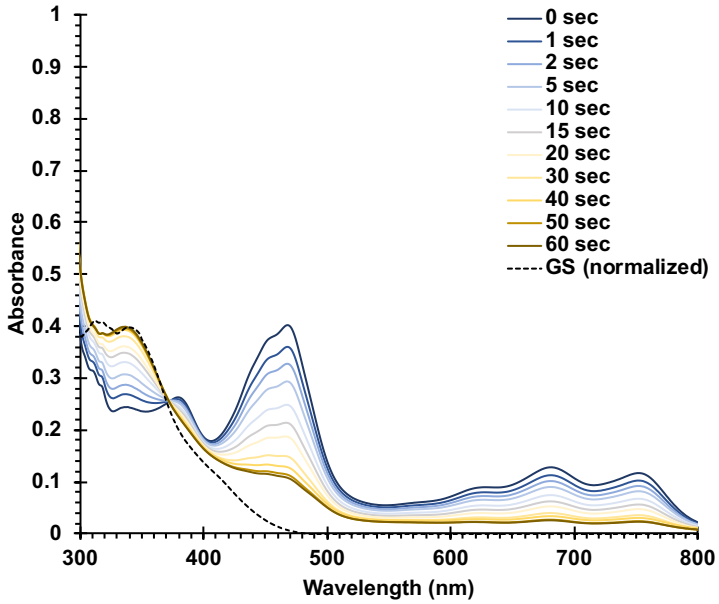

Figure 5.119. *UV-Vis spectra following the disappearance of* ***3***$^{\bullet+}$ *in the presence of 0.1 M LiBr in DMAc under irradiation in a white LED well. Spectrum labeled GS corresponds to the neutral ground state PC spectrum.*

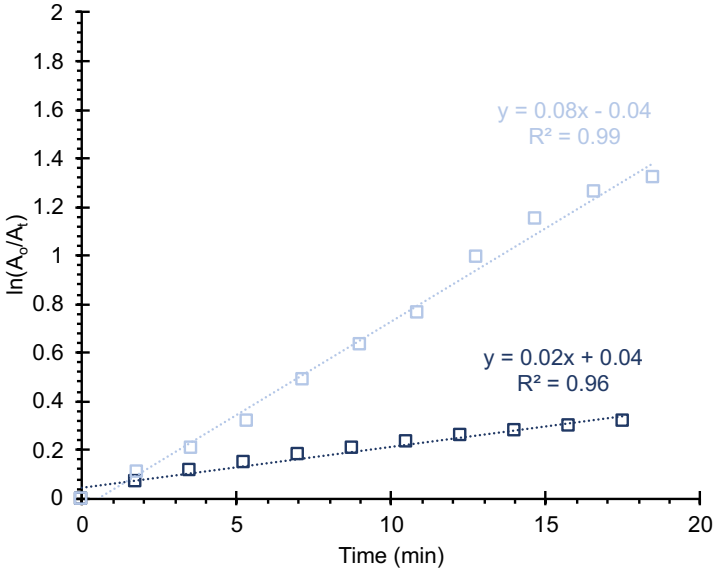

Figure 5.120. *Pseudo-first-order kinetics following the disappearance of* ***3***$^{\bullet+}$ *in 0.1 M LiBr in DMAc with (light blue) and without (dark blue) irradiation. For the experiment under irradiation, the time represents total time (i.e. time under irradiation plus time in the dark).*

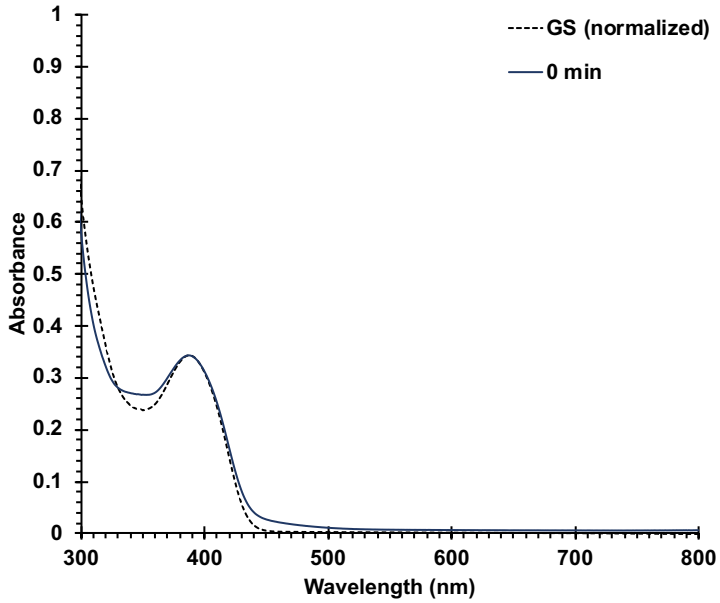

Figure 5.121. *UV-Vis spectra following the disappearance of* ***10***$^{\bullet+}$ *in the presence of 0.1 M LiBr in DMAc in the dark. Spectrum labeled GS corresponds to the neutral ground state PC spectrum.*

Bromine Radical Trapping Experiment

Following the reaction of $PC^{\bullet+}$ in the presence of Br^- by UV-Vis showed evidence that one product of this reaction was the neutral PC. We hypothesized this reaction also generated Br• through electron transfer from Br^- to $PC^{\bullet+}$. However, further experimentation was necessary to support this hypothesis. To support the formation of Br•, the radical halogenation of alkanes was used as a probe into the presence of halogen radicals in these reactions.

To conduct this experiment, $\mathbf{5}^{\bullet+}\mathbf{PF_6}^-$ (1.1 mg, 0.00089 mmol, 1 eq) was dissolved in a solution of 0.1 M LiBr and cyclohexane (1.9 µL, 0.0178 mmol, 20 eq) in deuterated MeCN (0.5 mL). The solution was transferred to an NMR tube, the tube sealed, and the reaction irradiated in a white LED well for several hours. A yellow precipitate formed, after which the reaction was analyzed by ^{1}H NMR (Figure 5.122, top). The ^{1}H NMR spectrum of bromocyclohexane is provided for reference (Figure 5.122, bottom). Agreement between the two spectra supports the

formation of Br• during the decomposition of $\mathbf{5}^{\bullet+}$, which in turn leads to the formation of bromocyclohexane by the scheme shown in Figure 5.123.

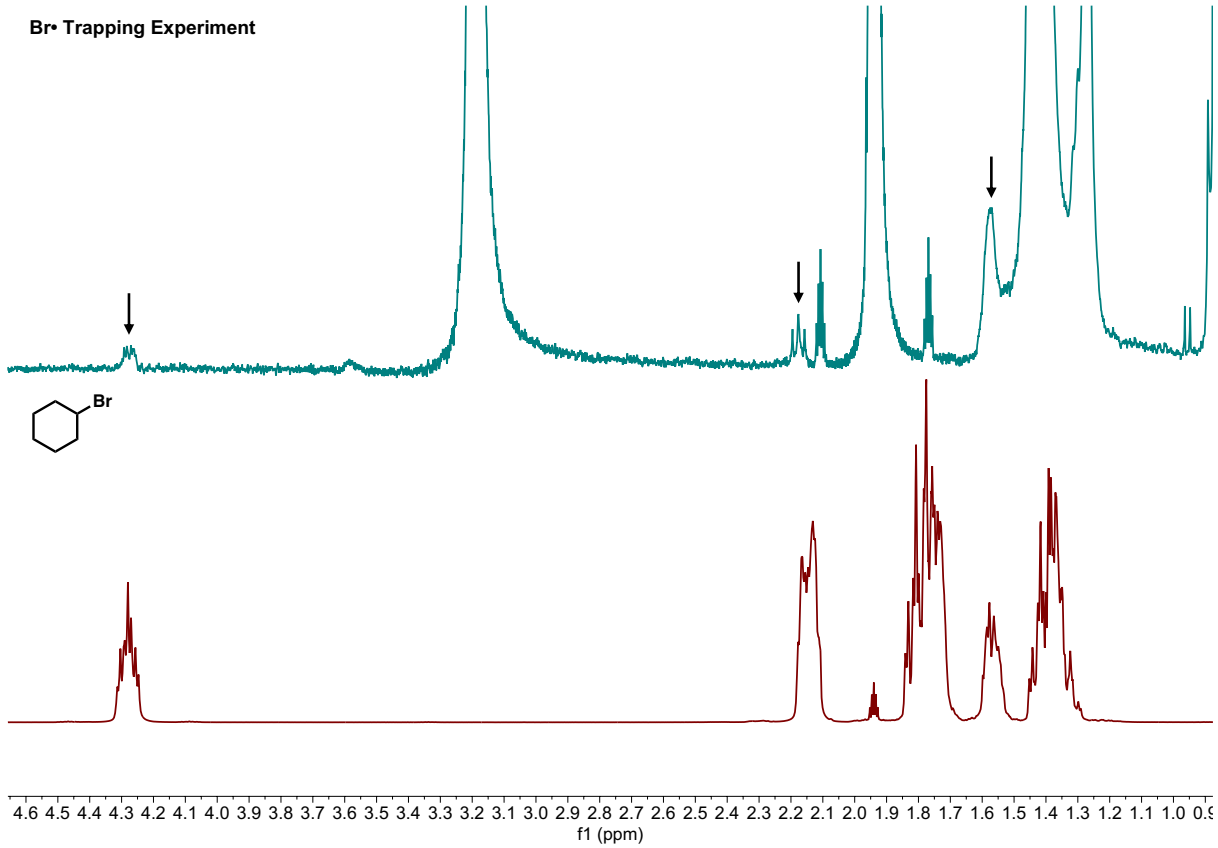

Figure 5.122. *^{1}H NMR spectra of bromocyclohexane (bottom) and the products of the reaction between $\mathbf{5}^{\bullet+}$ and Br^- in the presence of cyclohexane. Both spectra were collected in deuterated MeCN.*

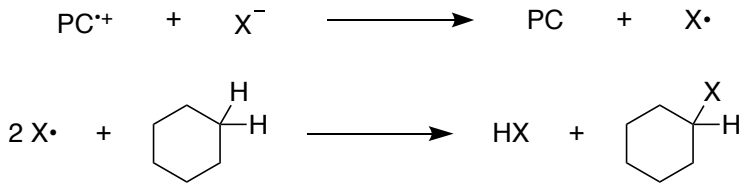

Figure 5.123. *Scheme for Br• trapping experiments using cyclohexane.*

UV-Vis Experiments in the Presence of Chloride

Experiments were conducted in the same manner as with LiBr (see above) using $\mathbf{5}^{\bullet+}\mathbf{PF}_6^-$ as the radical cation.

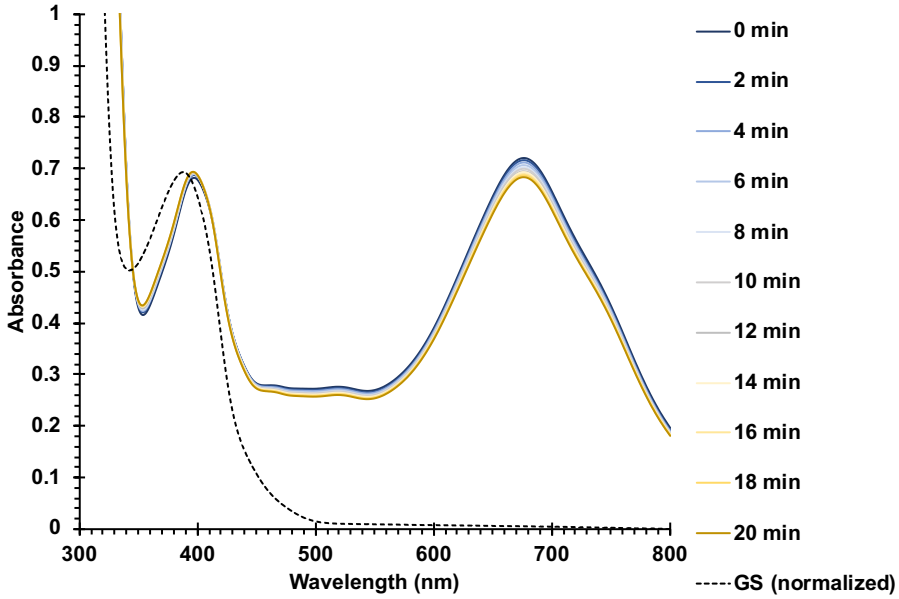

Figure 5.124. *Representative example of UV-Vis spectra following the disappearance of* $\mathbf{5}^{\bullet+}$ *in the presence of 0.1 M LiCl in DMAc in the dark. Spectrum labeled GS corresponds to the neutral ground state PC spectrum.*

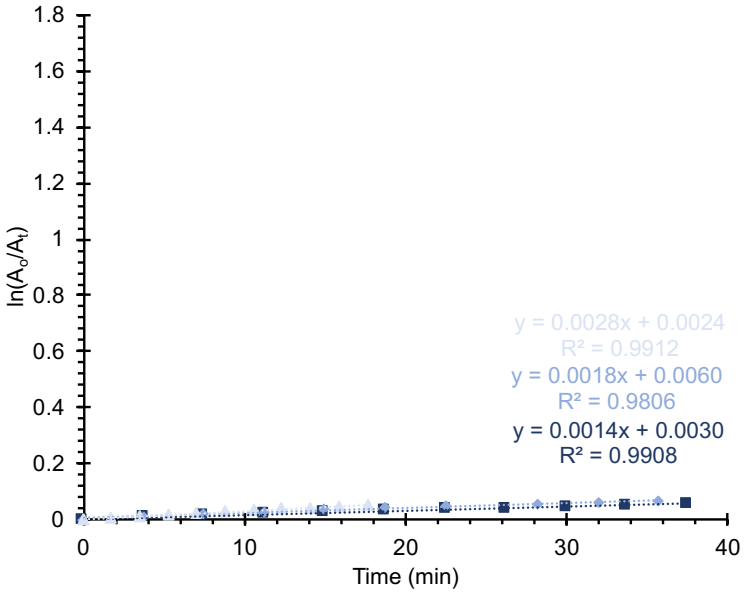

Figure 5.125. *Pseudo-first-order kinetics following the disappearance of* $\mathbf{5}^{\bullet+}$ *in the presence of 0.1 M LiCl in DMAc in the dark. Average* $k_{obs} = 0.0020 \pm 0.0007\ M^{-1}s^{-1}$.

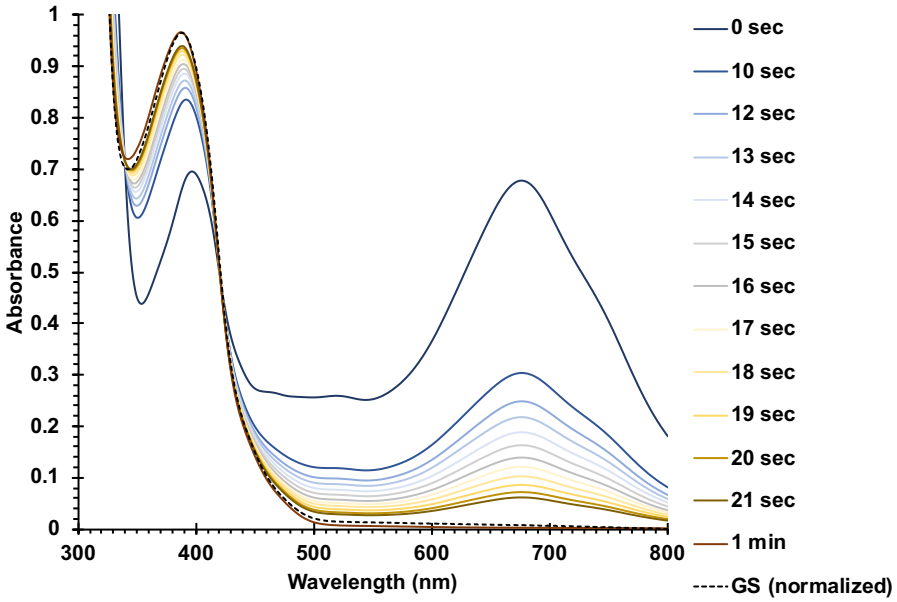

Figure 5.126. *Representative example of UV-Vis spectra following the disappearance of* ***5***$^{\bullet+}$ *in the presence of 0.1 M LiCl in DMAc under irradiation in a white LED well. Spectrum labeled GS corresponds to the neutral ground state PC spectrum.*

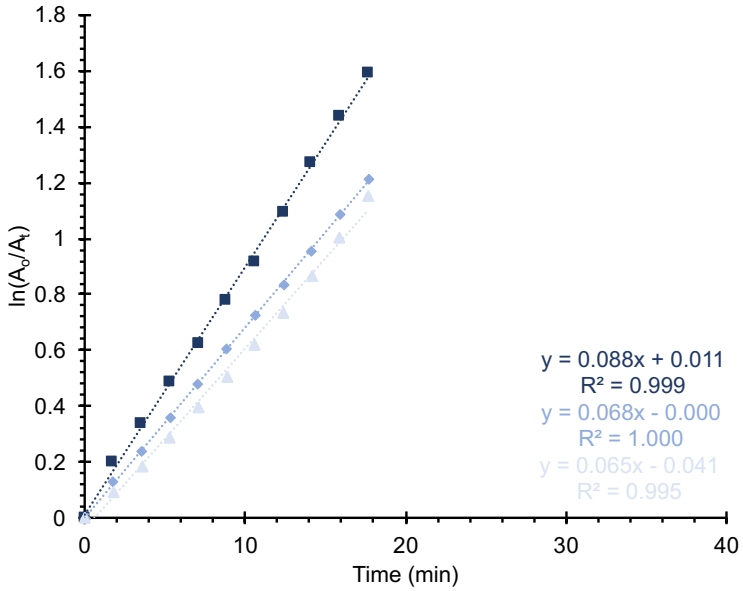

Figure 5.127. *Pseudo-first-order kinetics following the disappearance of* ***5***$^{\bullet+}$ *in the presence of 0.1 M LiCl in DMAc under irradiation in a white LED well. The time represents total time (i.e. under irradiation and in the dark). Average* $k_{obs} = 0.074 \pm 0.013\ M^{-1}s^{-1}$.

Chlorine Radical Trapping Experiments

Experiments similar to those described above for trapping Br• with cyclohexane were performed, except using LiCl instead of LiBr. Due to the poor solubility of LiCl in deuterated MeCN, experiments were also attempted in d_7-DMF and deuterated DMSO. However, no evidence was observed by ^{1}H NMR in either case for the formation of chlorocyclohexane in these experiments.

Deactivation of Alkyl Radicals by Radical Cations

Identification of the Deactivation Product in a Model Reaction

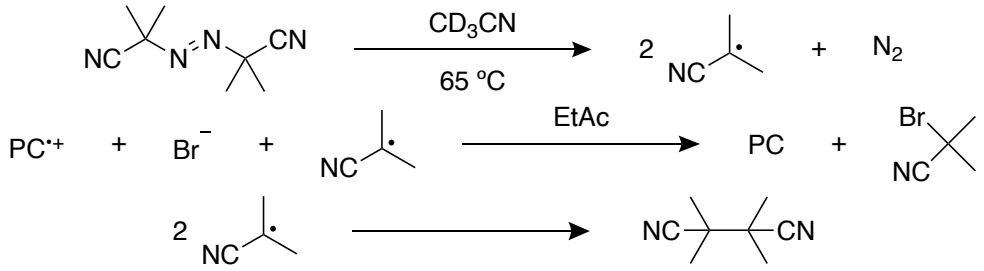

Figure 5.128. *Scheme for deactivation model reactions using AIBN as a thermal radical source.*

5$^{\bullet+}$**PF**$_6^-$ (1.2 mg, 0.001 mmol, 1 eq) was dissolved in a solution of LiBr (0.5 mg, 0.005 mmol, 5 eq) and AIBN (1.5 mg, 0.001 mmol, 1 eq) in deuterated MeCN (0.5 mL). The solution was transferred to an NMR tube, the tube sealed and wrapped in aluminum foil, and the reaction mixture heated at 65 ºC for one day. After one day, a yellow precipitate had formed. The reaction was then analyzed by ^{1}H NMR to identify the products of the reaction (Figure 5.129). To identify the product of the deactivation reaction, 2-bromo-2-methylpropanenitrile was also analyzed by ^{1}H NMR in deuterated MeCN (Figure 5.130, middle).

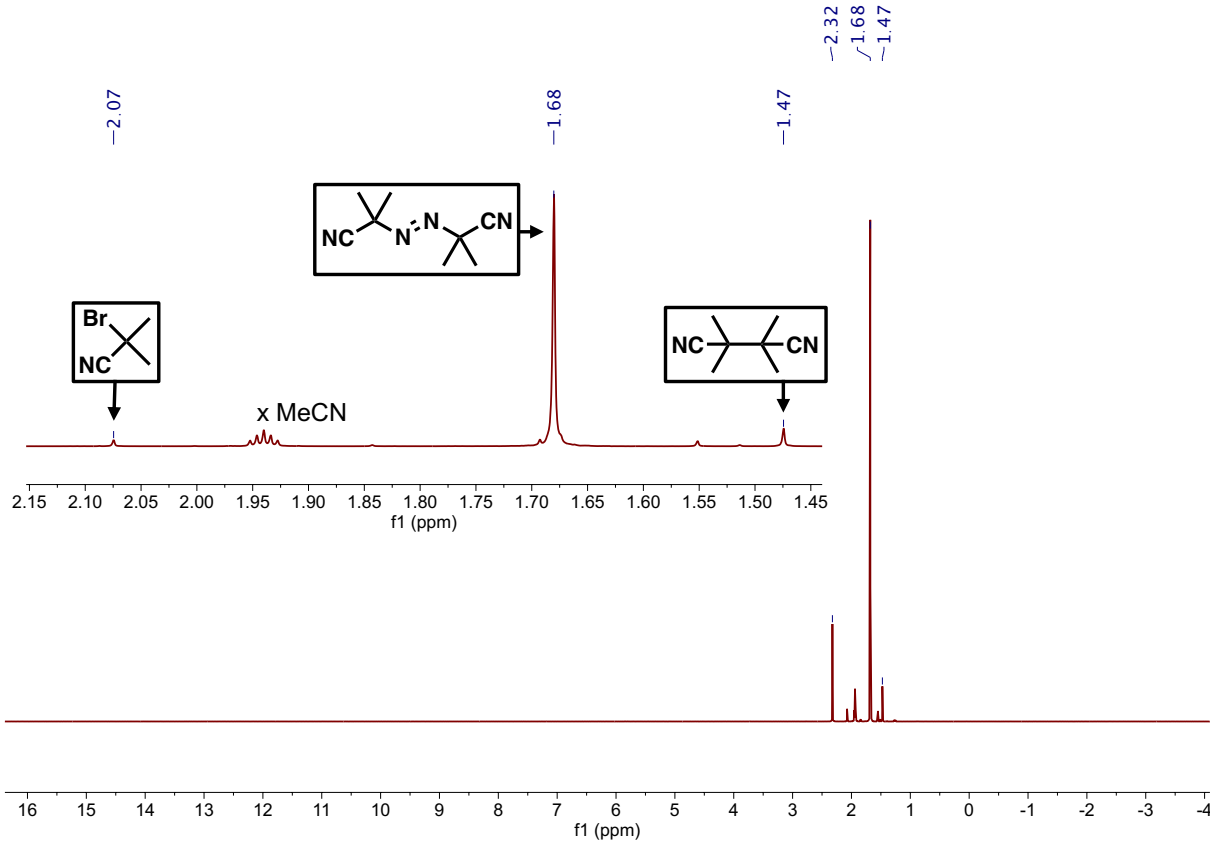

Figure 5.129. *^{1}H NMR of the products of a model deactivation reaction using* ***5$^{\bullet+}$PF$_6^-$*** *in deuterated MeCN.*

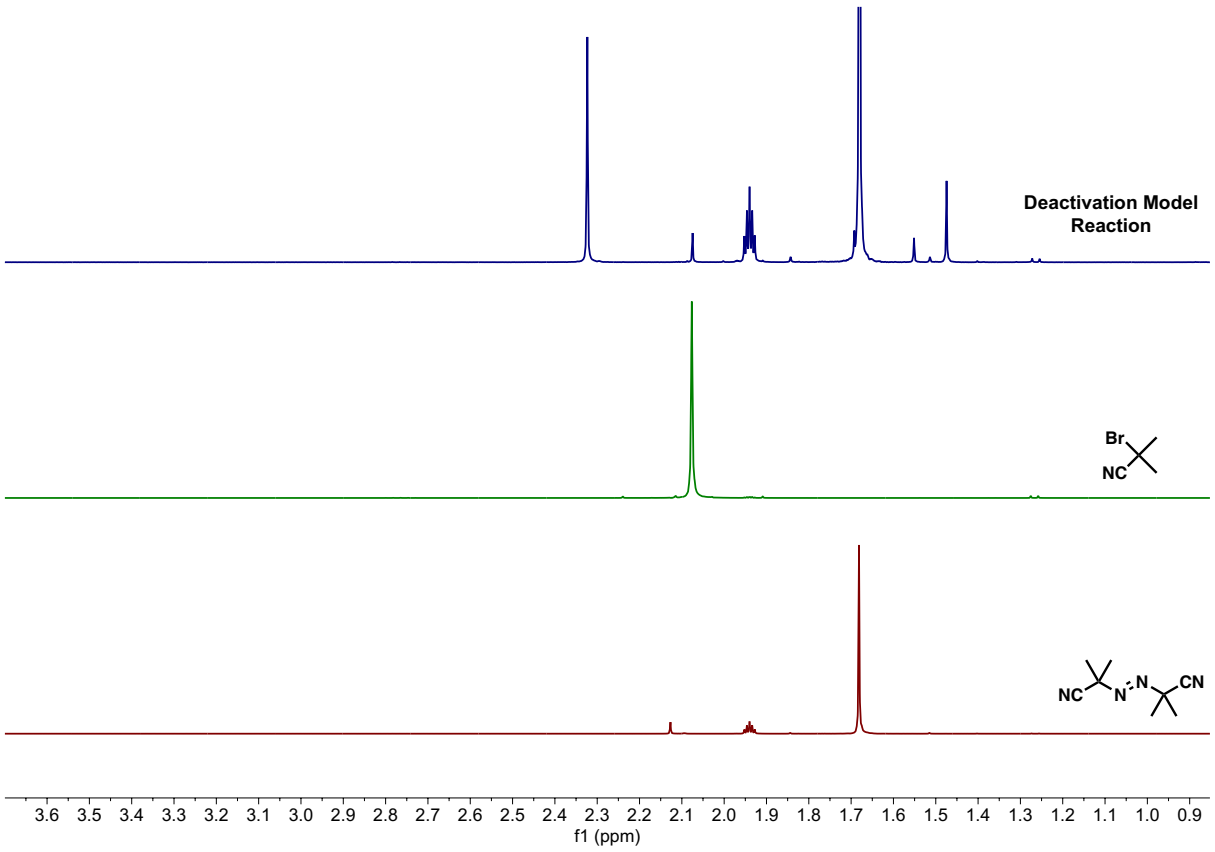

Figure 5.130. *Stacked ^{1}H NMR spectra in deuterated MeCN of AIBN (red), 2-bromo-2-methylpropanenitrile (green), and a deactivation model reaction using* ***5***$^{\bullet+}$***PF***$_6^-$ *(blue).*

Deactivation in the Presence of a Bromine Radical Trap

To probe whether free Br• forms during deactivation, which would be consistent with a stepwise deactivation mechanism, a deactivation model reaction was performed in the presence of cyclohexane. We hypothesized that significant bromocyclohexane formation would only be observed if free Br• forms during deactivation. For details regarding the deactivation model reaction and the Br• trapping reaction, see Figures 5.128 and 5.123, respectively.

In this experiment, **5**$^{\bullet+}$**PF**$_6^-$ (1.1 mg, 0.001 mmol, 1 eq) was dissolved in a solution of LiBr (0.4 mg, 0.005 mmol, 5 eq), AIBN (1.6 mg, 0.001 mmol, 1 eq), and cyclohexane (1.1 µL, 0.01 mmol, 10 eq) in deuterated MeCN (0.5 mL). The solution was transferred to an NMR tube, the

tube sealed and wrapped in aluminum foil, and the reaction mixture heated at 65 ºC for one day. The reaction was then analyzed by ^{1}H NMR to identify the products of the reaction (Figure 5.131).

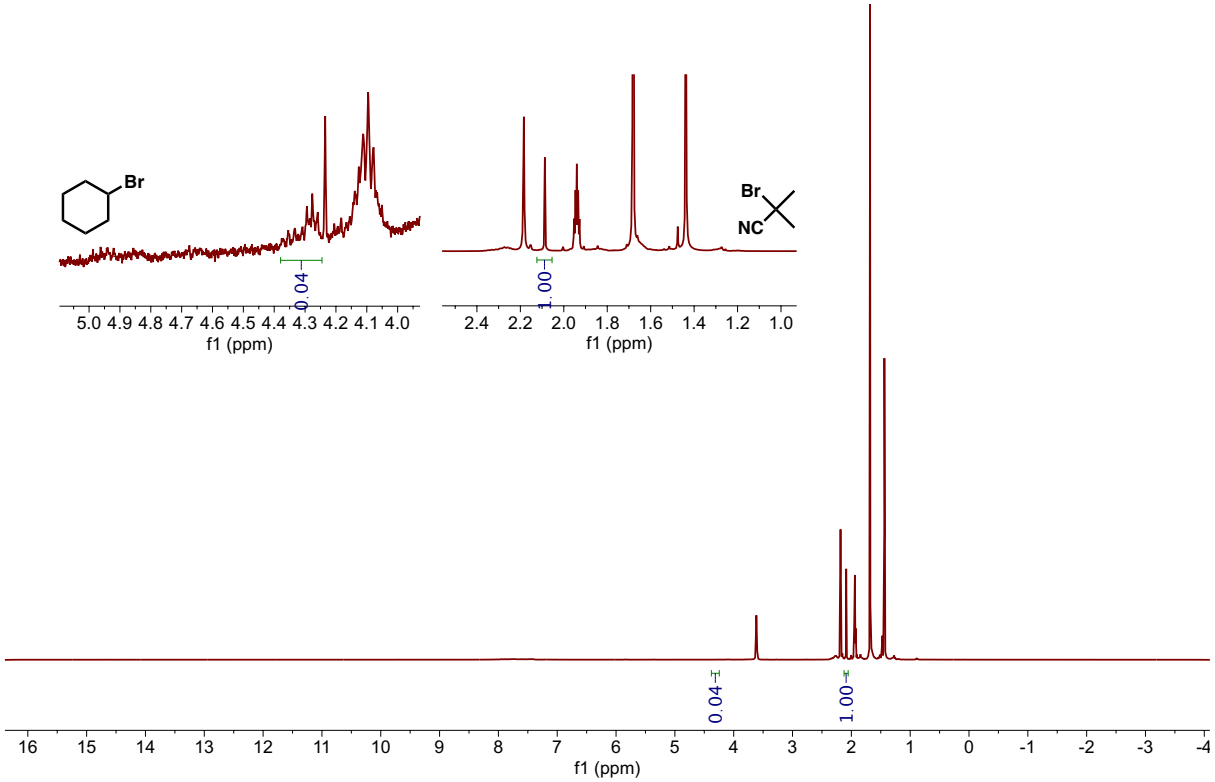

Figure 5.131. *^{1}H NMR of a deactivation model reaction in the presence of cyclohexane in deuterated MeCN.*

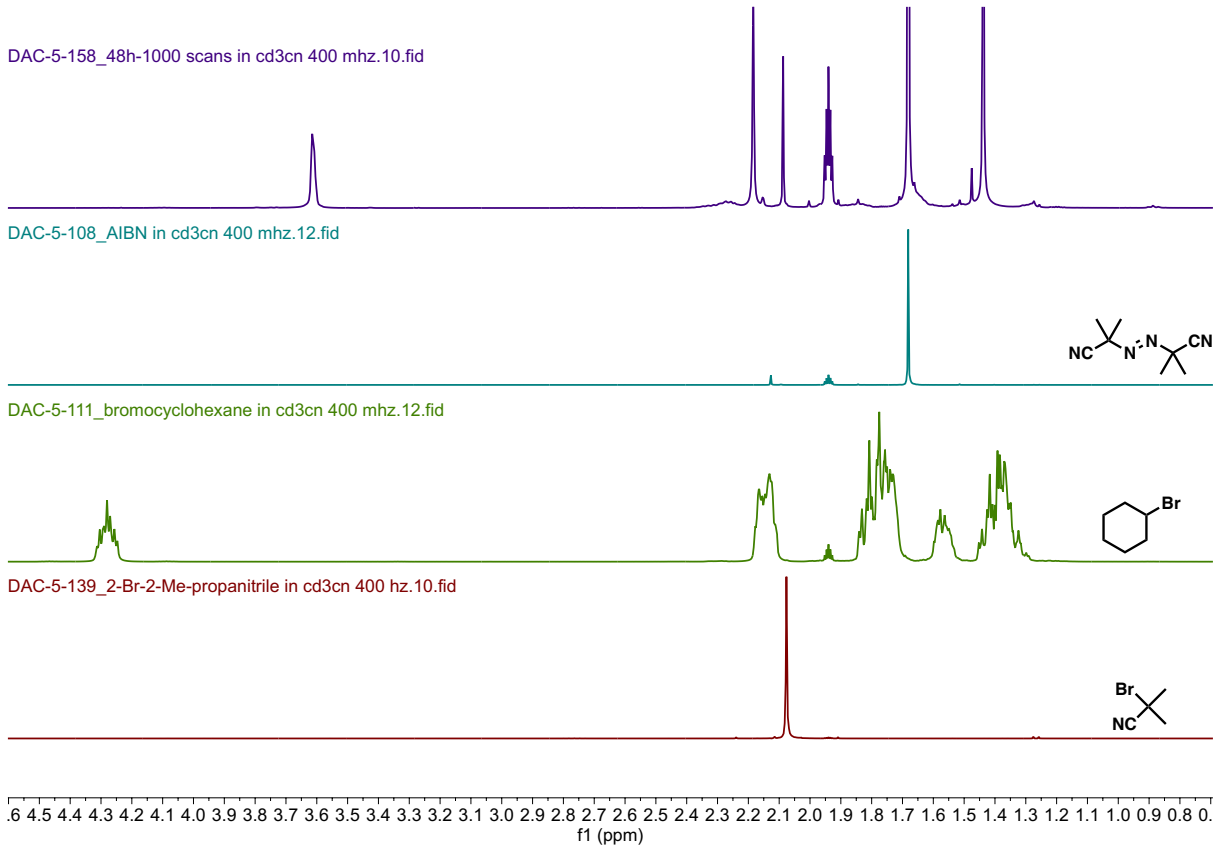

Figure 5.132. *Stacked ^{1}H NMR spectra in deuterated MeCN of a deactivation model reaction in the presence of cyclohexane (purple), AIBN (blue), bromocyclohexane (green), and 2-bromo-2-methylpropanenitrile (red).*

Impact of Bromide vs. Chloride

To investigate the impact of different variables on the rate of deactivation, the deactivation model reaction described above (Figure 5.138) was performed in EtAc and monitored *in-situ* by UV-Vis spectroscopy to follow the disappearance of $PC^{\bullet+}$. A picture of the apparatus used in these studies is provided in Figure 5.133, although during experiments the vent needle was removed, the solution heated to 65 ºC in the oil bath, and the entire apparatus was covered in aluminum foil to eliminate irradiation of the solution.

Figure 5.133. *Photograph of the apparatus used in kinetics experiments following the deactivation of alkyl radicals in a model reaction. Note that during the experiment, no vent needle was present, the flask was submerged in the oil bath, and the entire reaction was covered with aluminum foil to eliminate light exposure.*

To investigate the rate of deactivation in the presence Br^- (Figure 5.134, blue), a three-neck flask was charged with AIBN (2.6 mg, 0.016 mmol, 10 eq). The reaction apparatus was assembled and degassed by positive nitrogen flow for 15 min. Degassed EtAc (12 mL) and a stock solution of LiBr (0.28 mg, 0.0032 mmol, 2 eq, in 0.2 mL EtAc) were added to the flask, after which the flask was covered in aluminum foil and heated to 65 ºC. Upon reaching the target temperature, $\mathbf{5}^{\bullet+}\mathbf{PF_6}^-$ (1.8 mg, 0.0016 mmol, 1 eq, in 2.8 mL EtAC) was added to the flask under rapid stirring. The disappearance of $\mathbf{5}^{\bullet+}$ was then monitored *in-situ* using a UV-Vis fiber optic probe.

To investigate the rate of deactivation in the presence Cl^- (Figure 5.134, red), the same procedure was followed, except LiCl (0.14 mg, 0.0032 mmol, 2 eq, in 0.2 mL EtAC) was substituted for LiBr. Instead, to obtain a baseline measurement for the disappearance of $\mathbf{5}^{\bullet+}$ in the absence of a halide (Figure 5.134, grey), no LiBr or LiCl was added to the reaction, and $\mathbf{5}^{\bullet+}\mathbf{PF_6}^-$ was dissolved in 3 mL EtAC rather than 2.8 mL.

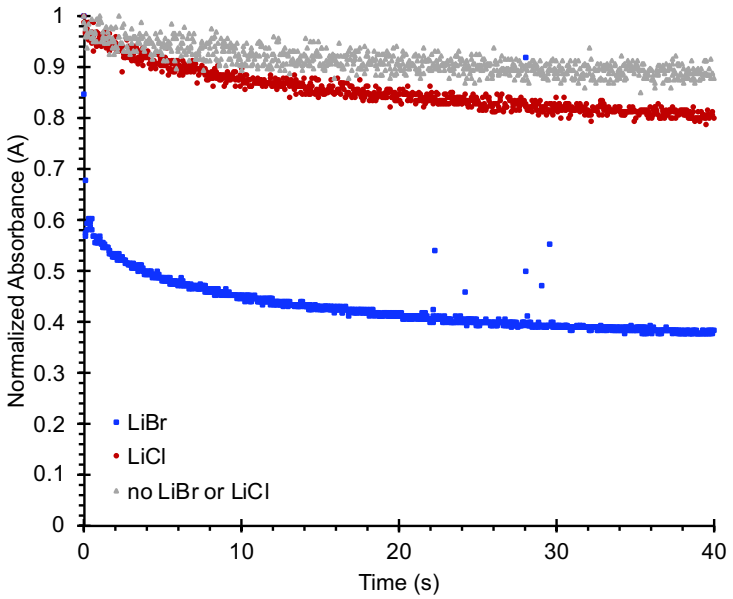

Figure 5.134. *Comparison of deactivation kinetics for* $\mathbf{5}^{\bullet+}$ *in the presence of LiBr (blue), LiCl (red), and no halide (grey). All kinetic traces are normalized to A = 1 at the time of* $\mathbf{5}^{\bullet+}\mathbf{PF_6}^-$ *injection.*

Impact of the Catalyst Oxidation Potential

To investigate the rate of deactivation in the presence of different radical cations with varying oxidation potentials, a three-neck flask was charged with AIBN (2.6 mg, 0.016 mmol, 10 eq). The reaction apparatus was assembled and degassed by positive nitrogen flow for 15 min. Degassed EtAc (12 mL) and a stock solution of LiBr (0.28 mg, 0.0032 mmol, 2 eq, in 0.2 mL EtAc) were added to the flask, after which the flask was covered in aluminum foil and heated to

65 ºC. Upon reaching the target temperature, $\mathbf{1}^{\bullet+}\mathbf{PF_6}^-$ (1.0 mg, 0.0016 mmol, 1 eq, in 2.8 mL EtAC), $\mathbf{3}^{\bullet+}\mathbf{PF_6}^-$ (0.9 mg, 0.002 mmol, 1 eq, in 2.8 mL EtAC), or $\mathbf{4}^{\bullet+}\mathbf{PF_6}^-$ (0.9 mg, 0.002 mmol, 1 eq, in 2.8 mL EtAC) was added to the flask under rapid stirring. The disappearance of $PC^{\bullet+}$ was then monitored *in-situ* using a UV-Vis fiber optic probe (Figure 5.135).

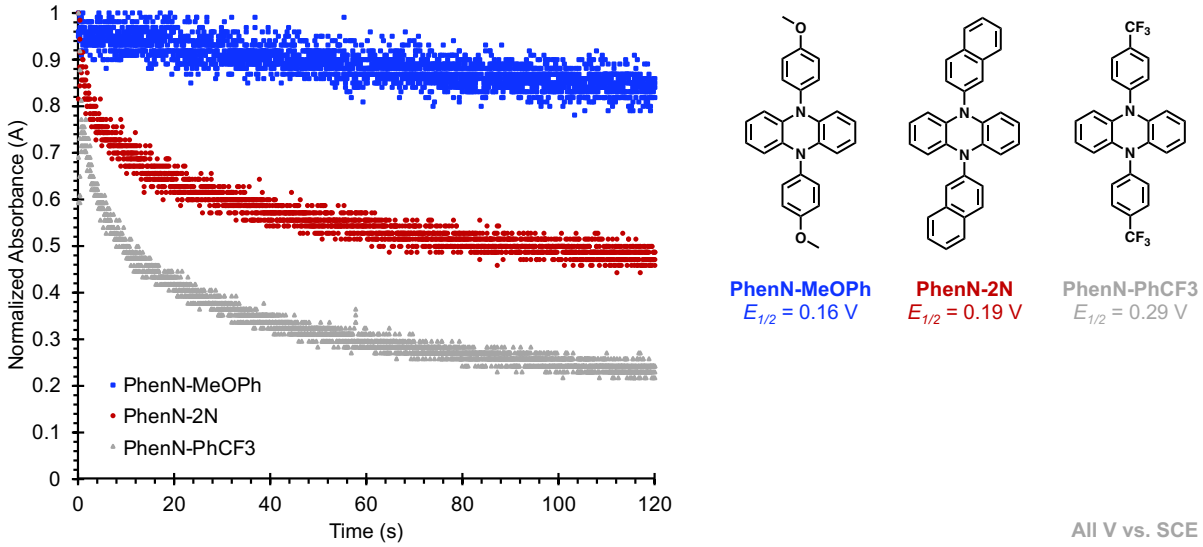

Figure 5.135. *Comparison of deactivation kinetics in the presence of LiBr for* $\boldsymbol{1}^{\bullet+}\boldsymbol{PF_6}^-$ *(grey),* $\boldsymbol{3}^{\bullet+}\boldsymbol{PF_6}^-$ *(red), and* $\boldsymbol{4}^{\bullet+}\boldsymbol{PF_6}^-$ *(blue).*

Previously, we have hypothesized that dihydrophenazine PCs can be substituted by alkyl radicals at the core, which in O-ATRP might explain why these PCs suffer from generally low I^*.[d] In these experiments, such a side reaction could impact the observed kinetics for the disappearance of $PC^{\bullet+}$. As such, control experiments were performed in the absence of LiBr with each $PC^{\bullet+}$ to monitor for reactions between $PC^{\bullet+}$ and AIBN (or the radicals derived from AIBN).

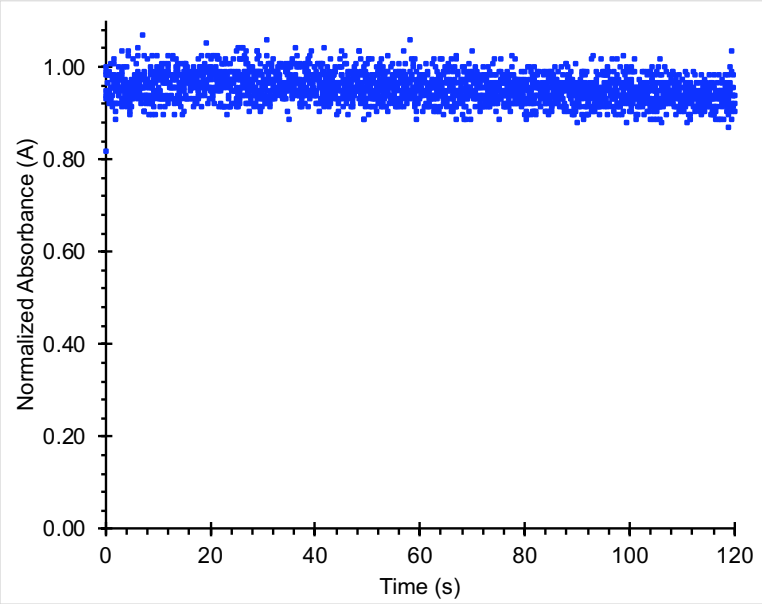

Figure 5.136. *Control reaction following the disappearance of* $\mathbf{1}^{\bullet+}$ *in the presence of AIBN at 65 ºC.*

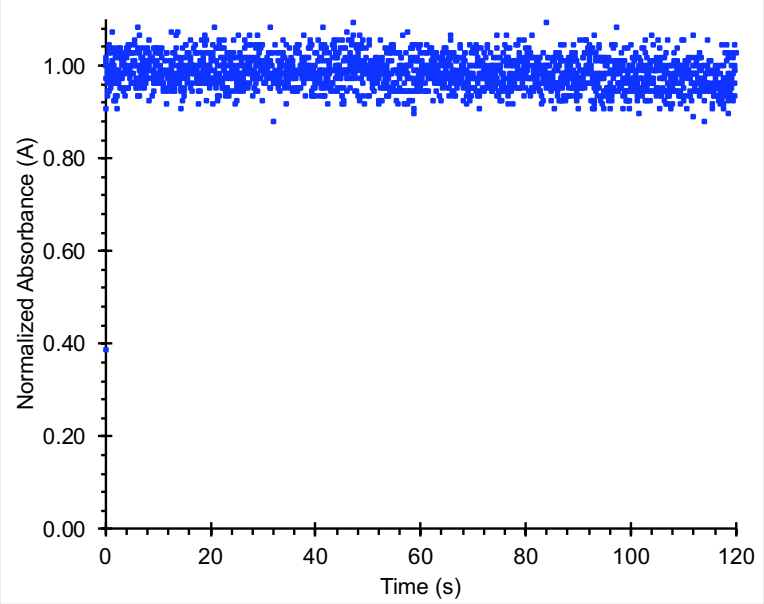

Figure 5.137. *Control reaction following the disappearance of* $\mathbf{3}^{\bullet+}$ *in the presence of AIBN at 65 ºC.*

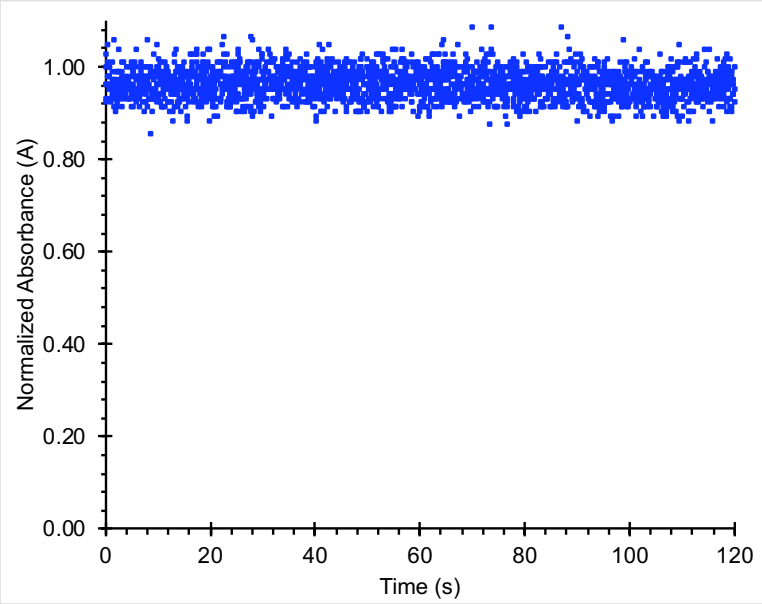

Figure 5.138. *Control reaction following the disappearance of* $\mathbf{4}^{\bullet+}$ *in the presence of AIBN at 65 ºC.*

Deactivation in the Presence of Phenoxazine Radical Cations

To investigate the rate of deactivation in the presence or phenoxazine radical cations, a three-neck flask was charged with AIBN (2.6 mg, 0.016 mmol, 10 eq). The reaction apparatus was assembled and degassed by positive nitrogen flow for 15 min. Degassed EtAc (12 mL) and a stock solution of LiBr (0.28 mg, 0.0032 mmol, 2 eq, in 0.2 mL EtAc) were added to the flask, after which the flask was covered in aluminum foil and heated to 65 ºC. Upon reaching the target temperature, $\mathbf{6}^{\bullet+}\mathbf{PF_6}^-$ (1.2 mg, 0.0016 mmol, 1 eq, in 2.8 mL EtAC), $\mathbf{7}^{\bullet+}\mathbf{PF_6}^-$ (1.0 mg, 0.0016 mmol, 1 eq, in 2.8 mL EtAC), or $\mathbf{8}^{\bullet+}\mathbf{PF_6}^-$ (1.1 mg, 0.0016 mmol, 1 eq, in 2.8 mL EtAC) was added to the flask under rapid stirring. The disappearance of $PC^{\bullet+}$ was then monitored *in-situ* using a UV-Vis fiber optic probe (Figure 5.139). In all three cases, the deactivation reaction was too rapid to be effectively monitored by this approach.

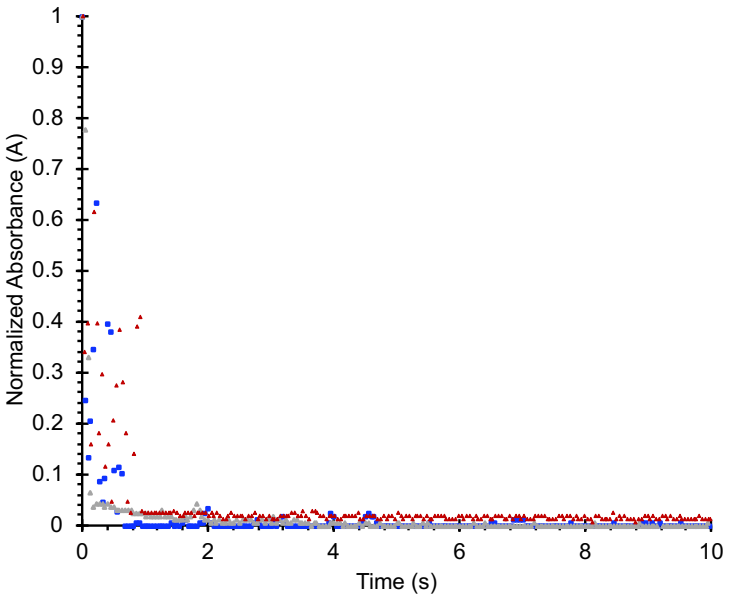

Figure 5.139. *Comparison of deactivation kinetics in the presence of LiBr for* ***6•+PF6-*** *(blue),* ***7•+PF6-*** *(grey), and* ***8•+PF6-*** *(red).*

Investigation of Hydrogen Atom Abstraction Side Reactions

Description of the Collector-Generator Experiment

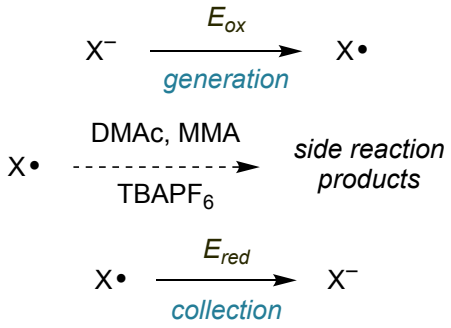

Figure 5.140. *General scheme for collector-generator experiments to probe halogen radical side reactions.*

A collector-generator experiment is an electrochemical experiment employing a rotating ring-disk electrode to probe the reactivity of a species generated at an electrode. The electrode in this experiment is a dual electrode consisting of a disk-shaped electrode surrounded by a ring-shaped electrode, with a non-conductive plastic layer separating the two. When the electrode is

immersed in solution and rotated rapidly, convective currents pull the solution up towards the center of the electrode and then push it out towards the edges of the electrode. As a result, an electrochemically active species can be oxidized (or reduced) at the disk to "generate" a reactive species, which then travels to the ring where it is reduced (or oxidized) back to its original form, or "collected."

The amount of substrate collected at the ring relative to how much was generated at the disk is referred to as the collection efficiency and can be expressed as a percentage of the limiting current observed at the ring relative by the limiting current at the disk. In this case, the limiting current refers to the value of the current response curve where the curve plateaus (see below for examples of current response curves), which represents the current achieved under diffusion limited conditions. Even in an ideal system, where the oxidized or reduced substrate is stable and does not undergo side reactions, only a fraction of the species generated at the disk will be collected at the ring due to solution mixing. This ideal collection efficiency can be calculated according to the geometry of the electrode,[60] or alternatively it can also be determined by calibration using an ideal system.

Regardless, this electrochemical method is particularly useful when the species generated at the disk is reactive, as the degree of reactivity can be evaluated based on the measured collection efficiency for the system. As such, a collector-generator experiment was used in this work to estimate the degree of side reactions undergone by Br• versus Cl• under O-ATRP conditions.

Evaluation of Ideal Collection Efficiency

The ideal collection efficiency for our apparatus was measured using a 6 mM $FeCl_3$ solution in 2 M HCl. A rotation rate of 1000 rpm was employed. Under these conditions, a collection efficiency of 37.0% was observed.

In addition, the expected collection efficiency for our electrode at a rotation rate of 1000 rpm was calculated using the program reported by Prater and Bard,[60] which was translated to run in MatLab for this work. This calculation gave an expected collection efficiency of 38.1%, which agrees well with the value measured above for $FeCl_3$.

General Procedure

A solution of LiBr or LiCl was prepared by dissolving LiBr (40.6 mg, 0.467 mmol, 1 eq) or LiCl (19.8 mg, 0.467 mmol, 1 eq) in MMA (50 mL, 468 mmol, 1000 eq) and DMAc (50 mL). These conditions were chosen to mimic conditions found in O-ATRP while being suitable for electrochemical analysis. Bu_4NPF_6 (969 mg, 0.1 M) was added to the solution as a supporting electrolyte in each case. The solution was then transferred to an electrochemical cell, the counter and reference electrodes inserted in the solution, and the working electrode submerged about 1 cm below the surface of the solution. Experiments reported herein were conducted with a rotation rate of 5000 rpm. In addition, to ensure maximum accuracy and eliminate the possibility of a liquid junction potential at the reference electrode, the reference electrode in these experiments was 0.01 M $AgNO_3$ in 50/50 DMAc and MMA with 0.1 M Bu_4NPF_6.

Cyclic Voltammetry of Halides Under O-ATRP Conditions

To determine the potential at which the disk electrode should be set to achieve rapid oxidation of each halide ion, cyclic voltammetry was performed on each solution prior to the collector-generator experiment (Figure 5.141). In addition, given the unusual nature of the solvent system and reference electrode used in these experiments, potentials were reference vs. the ferrocene/ferrocenium redox couple (Figure 5.142).

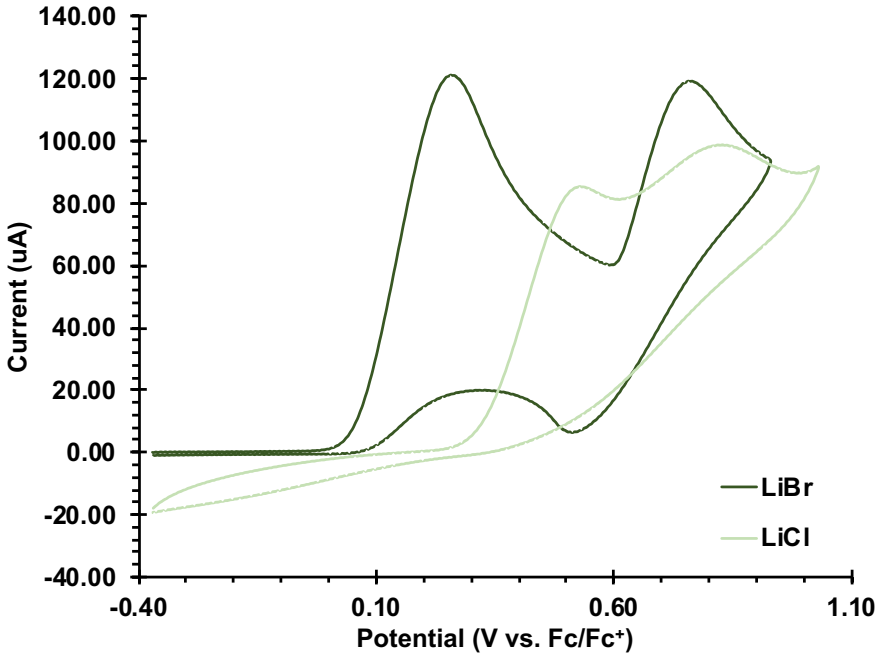

Figure 5.141. *Cyclic voltammograms of LiBr (dark green) and LiCl (light green) in 50/50 DMAc and MMA with 0.1 M Bu_4NPF_6 at a scan rate of 100 mV s^{-1}.*

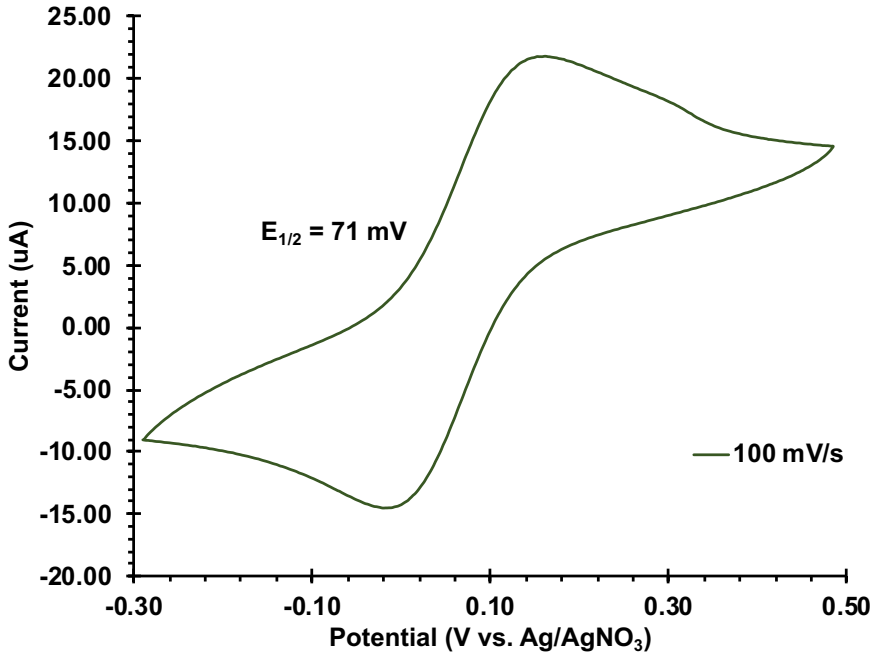

Figure 5.142. *Cyclic voltammetry of ferrocene in 50/50 DMAc and MMA with 0.1 M Bu_4NPF_6 using an $Ag/AgNO_3$ reference electrode in 50/50 DMAc and MMA with 0.1 M.*

Current Response Curves and Data Analysis

In the most ideal collector-generator experiment, the current response should increase until the diffusion limited regime is entered, at which point the current response should level off to a steady value. This final value is taken as the limiting current. However, a more realistic scenario is one where the current response continues to increase, but at a reduced rate (see Figure 5.143 for an example). In such a case, determination of the limiting current is still possible, although this process is more complicated. Specifically, the limiting current can be determined by extrapolating back from the final portion of the current response curve and determining the value on this extrapolation at the potential where the current response curve experiences an inflection point.

To perform this analysis quantitatively, a MatLab script was written (see supporting documents) to import the raw current response data, fit the data with a smoothing spline such that a derivative of the data could be taken, and then fit the derivative of the data such that the maximum (or minimum) value of the derivative could be found. Since the maximum (or minimum) of the derivative of a curve corresponds to the inflection point of that curve, the potential at which this maximum (or minimum) occurs corresponds to the potential at the inflection point. This potential was then inserted into the equation for the extrapolation line previously fit to the current response curve to find the limiting current at each electrode. Figure 5.144 below shows an example of the output of this analysis for the $FeCl_3$ system used to calibrate the collection efficiency of our apparatus.

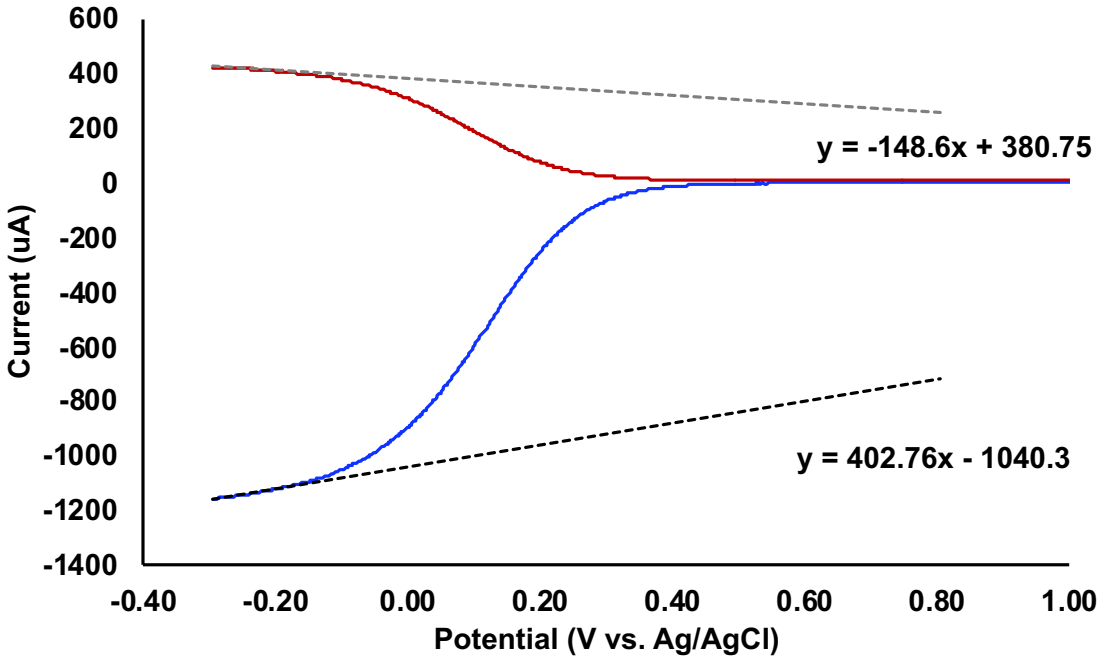

Figure 5.143. *Current response curves for a collector-generator experiment with 6 mM $FeCl_3$ in 2 M HCl at a rotation rate of 1000 RPM.*

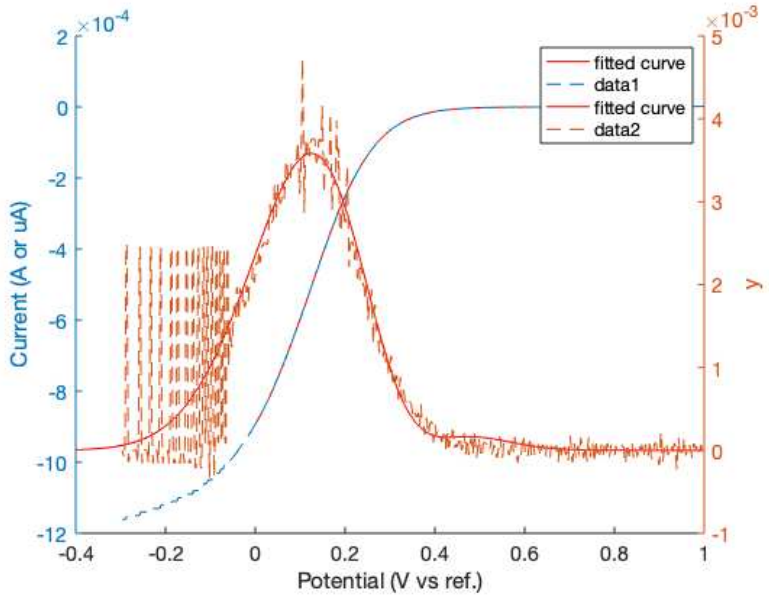

Figure 5.144. *Example output from our MatLab script for determining the limiting disk current in the $FeCl_3$ system. The blue dashed line corresponds to the raw current response data, whereas the red dashed line corresponds to the derivative data.*

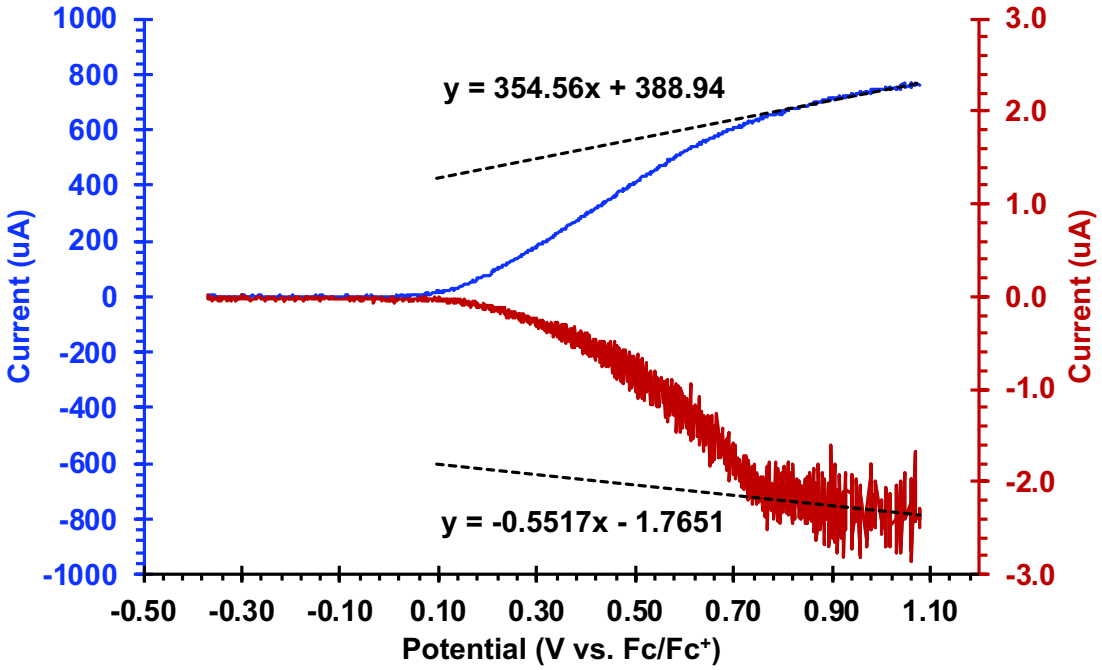

Figure 5.145. *Current response curves for a collector-generator experiment with LiBr in 50/50 DMAc and MMA at a rotation rate of 5000 RPM. Inflection points occur at 0.397 V (disk) and 0.723 V (ring), both vs. Fc/Fc$^+$. Collection efficiency = 0.7%.*

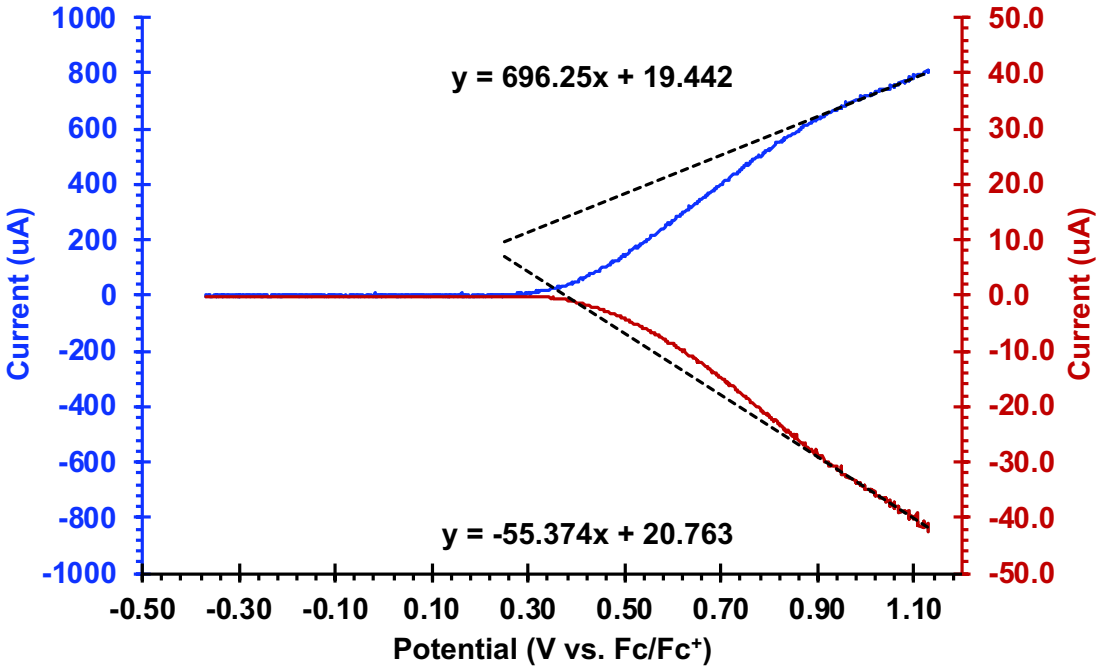

Figure 5.146. *Current response curves for a collector-generator experiment with LiCl in 50/50 DMAc and MMA at a rotation rate of 5000 RPM. Inflection points occur at 0.789 V (disk) and 0.957 V (ring), both vs. Fc/Fc$^+$. Collection efficiency = 5.9%.*

Ion Pairing in Radical Cation Hexafluorophosphate Salts

General Procedure

For all conductometry experiments, measurements were performed in triplicate on separately prepared samples at a minimum of five different concentrations. In each case, samples were weighed into 20 mL amber glass vials (for minimum light exposure) and dissolved immediately prior to their measurement. During each measurement, the solution was stirred using a magnetic stir bar and the temperature was maintained at 30 ± 1 ºC.

For analysis of the data and determination of the association equilibrium constant (K_{assoc}), an equation relating the dissociation equilibrium constant (K_{diss}) to the conductivity of the radical cation was derived from the expression for K_{diss} (Eq. 5.5).

$$K_{diss} = \frac{[PC^{\cdot+}][Br^-]}{[PC^{\cdot+}Br^-]} \qquad \text{(Eq. 5.5)}$$

First, the equation for K_{diss} was generalized and written in terms of the degree of dissociation (α) and the initial solute concentration (c_o):

$$K_{diss} = \frac{\alpha^2}{1-\alpha} \cdot c_o \qquad \text{(Eq. 5.6)}$$

However, α can be expressed in terms of conductivity (Λ, [S cm^2]) as the ratio of the equivalent conductivity (Λ_{eq} = Λ normalized to concentration, [S cm^2 mol^{-1}]) to the limiting equivalent conductivity ($\Lambda_o = \Lambda_{eq}$ extrapolated to infinite dilution):

$$\alpha = \frac{\Lambda_{eq}}{\Lambda_o} \qquad \text{(Eq. 5.7)}$$

Plugging this expression into Eq. 5.6, we get:

$$K_{diss} = \frac{\Lambda_{eq}^2}{(\Lambda_o - \Lambda_{eq}) \cdot \Lambda_o} \cdot c_o \qquad \text{(Eq. 5.8)}$$

Finally, this expression can be rearranged into an equation with a linear form (Eq. 5.9), making it useful for analyzing conductometry data and determining Λ_o and K_{diss}.

$$\frac{1}{\Lambda_{eq}} = \frac{1}{\Lambda_o} + \frac{\Lambda_{eq} \cdot c_o}{K_{diss} \cdot \Lambda_o^2} \qquad \text{(Eq. 5.9)}$$

From this equation, K_{assoc} can be easily determined by taking the inverse of K_{diss}.

Evaluation of Accuracy with Tetra-n-butylammonium Bromide

To evaluate how accurately this approach could determine K_{assoc}, we performed conductometry with tetra-n-butylammonium bromide (Bu_4NBr) in DMAc according to the general procedure described above. Figure 5.147 shows the data from this measurement, and Table 5.11 shows the results of this experiment compared to published literature values for Bu_4NBr.

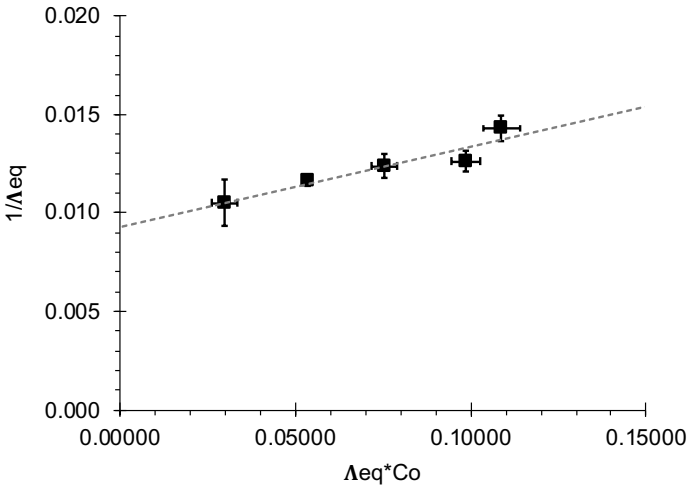

Figure 5.147. *Conductometry data for Bu_4NBr in DMAc at 30 ºC.*

Table 5.11. *Results from the conductometry of Bu_4NBr.*

	K_{assoc} (M^{-1})	Delta G (kcal/mol)
Experimental	4.27×10^2	-3.65
Literature[61]	4.52×10^1	-2.29

Impact of Radical Cation Structure

To evaluate whether the structure of $PC^{\bullet+}$ has a significant impact on ion pairing, conductometry was performed on each of the $PC^{\bullet+}PF_6^-$ salts synthesized. Below is the data for each of these measurements.

Table 5.12. *Conductometry data and derived association equilibrium constants for various $PC^{\bullet+}PF_6^-$ in DMAc.*

$PC^{\bullet+}$	Λ_o ($\mu S\ cm^2\ mmol^{-1}$)	K_{assoc} (M^{-1})	ΔG_{assoc} (kcal mol^{-1})
1$^{\bullet+}$	92.4	3×10^2	-3.4
2$^{\bullet+}$	106.1	7×10^2	-3.9
3$^{\bullet+}$	124.9	1×10^3	-4.3
4$^{\bullet+}$	139.1	2×10^3	-4.6
5$^{\bullet+}$	157.8	9×10^3	-5.4
6$^{\bullet+}$	158.9	5×10^3	-5.1
7$^{\bullet+}$	95.5	4×10^2	-3.6
8$^{\bullet+}$	137.2	2×10^3	-4.6
10$^{\bullet+}$	112.4	2×10^3	-4.5
11$^{\bullet+}$	130.0	1×10^3	-4.1

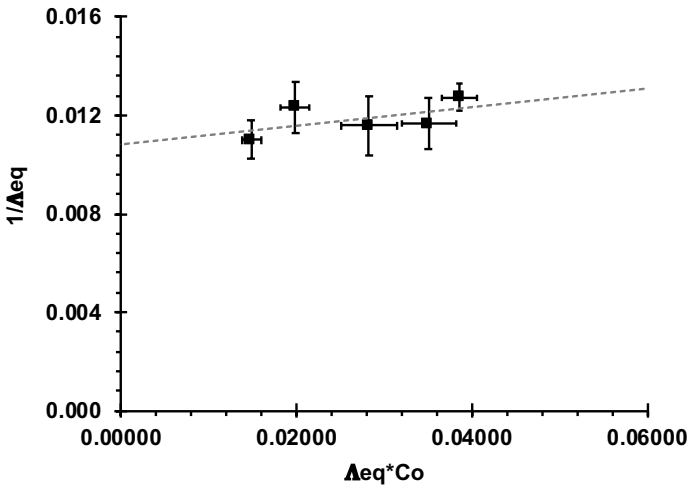

Figure 5.148. *Conductometry data for* ***1$^{\bullet+}$PF$_6^-$*** *in DMAc at 30 ºC.*

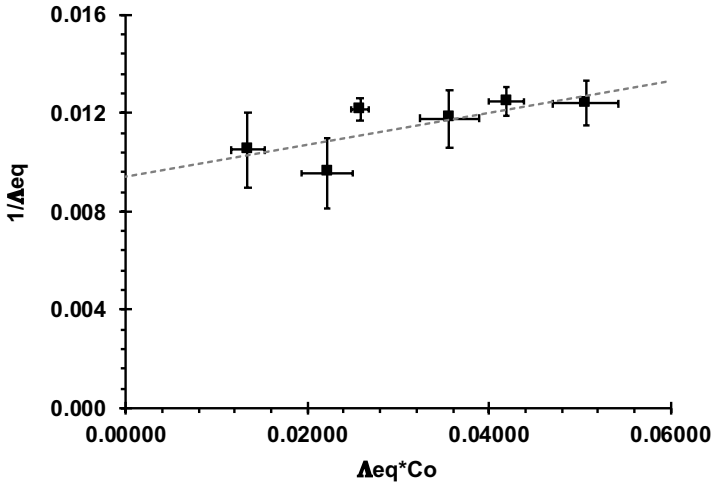

Figure 5.149. *Conductometry data for* ***2$^{\bullet+}$PF$_6^-$*** *in DMAc at 30 ºC.*

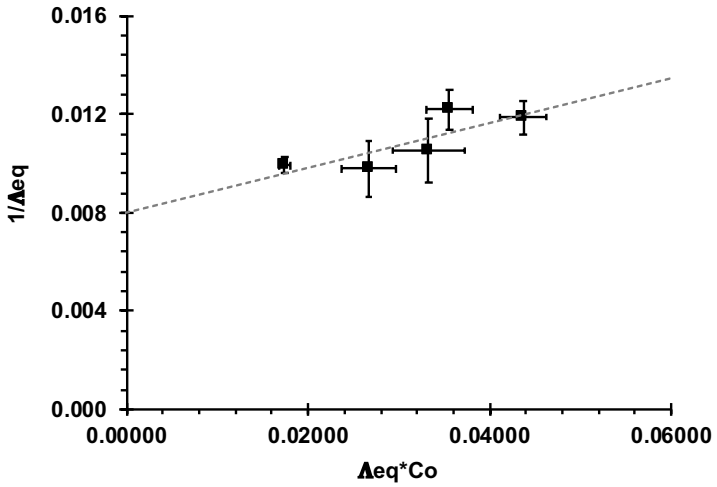

Figure 5.150. *Conductometry data for* ***3$^{\bullet+}$PF$_6^-$*** *in DMAc at 30 ºC.*

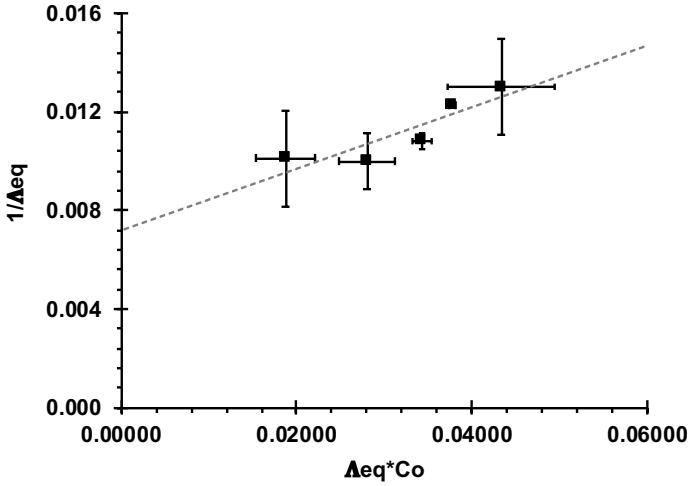

Figure 5.151. *Conductometry data for* ***4$^{\bullet+}$PF$_6^-$*** *in DMAc at 30 ºC.*

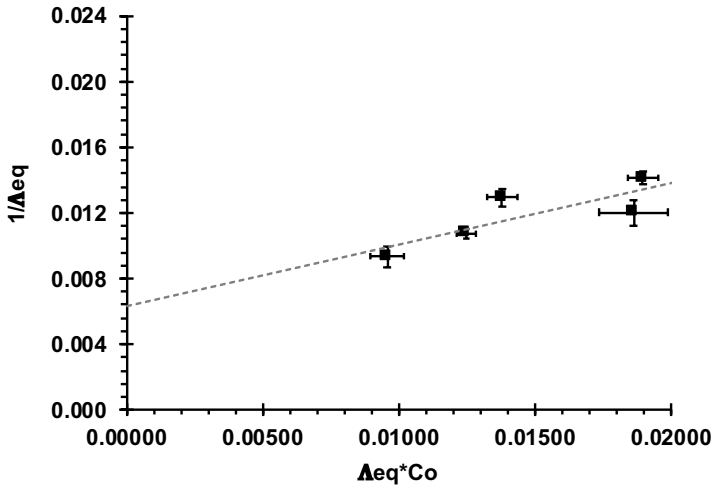

Figure 5.152. *Conductometry data for* ***5***$^{\bullet+}$***PF₆***$^{-}$ *in DMAc at 30 ºC.*

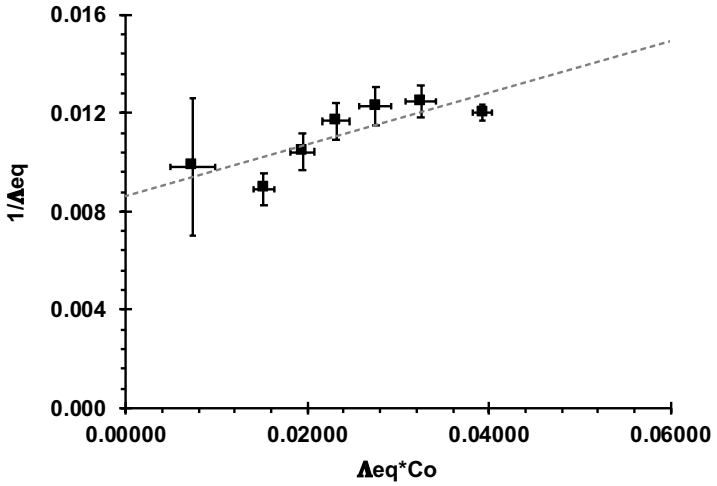

Figure 5.153. *Conductometry data for* ***6***$^{\bullet+}$***PF₆***$^{-}$ *in DMAc at 30 ºC.*

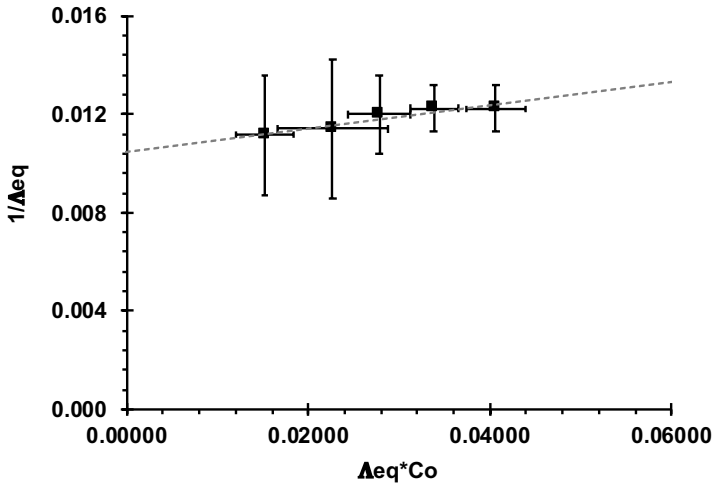

Figure 5.154. *Conductometry data for* ***7•+PF6-*** *in DMAc at 30 ºC.*

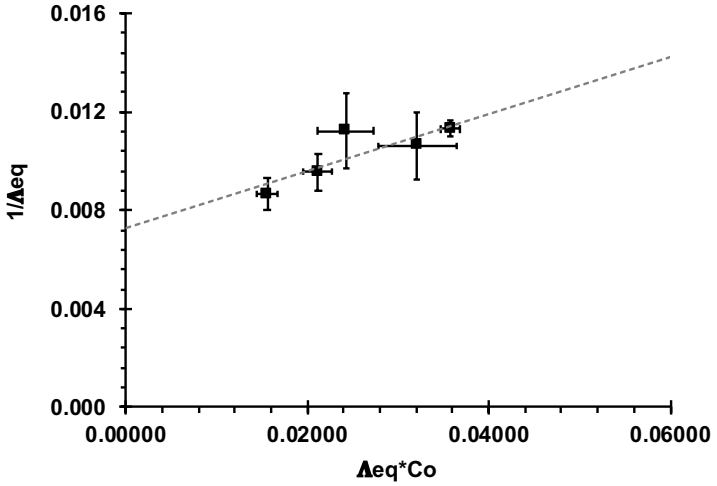

Figure 5.155. *Conductometry data for* ***8•+PF6-*** *in DMAc at 30 ºC.*

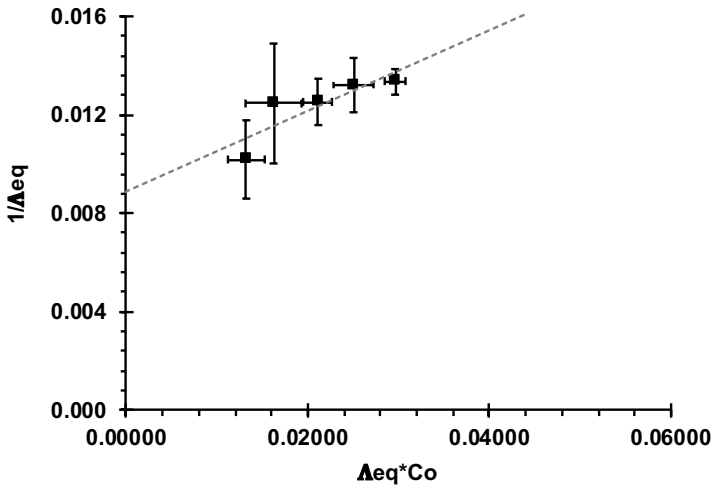

Figure 5.156. *Conductometry data for* ***10$^{\bullet+}$PF$_6^-$*** *in DMAc at 30 ºC.*

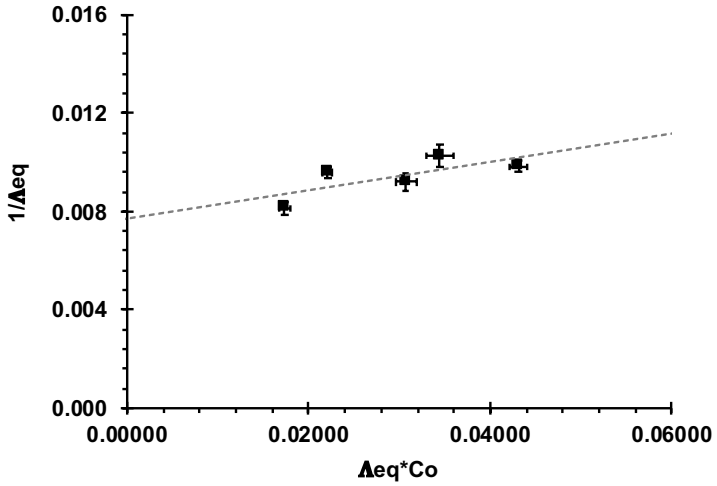

Figure 5.157. *Conductometry data for* ***11$^{\bullet+}$PF$_6^-$*** *in DMAc at 30 ºC.*

Impact of Solvent Polarity

The impact of solvent polarity on ion pairing was evaluated by performing conductometry in different solvent systems. In each case, the dielectric constant (ε_r) of the solvent system was used as an estimate of solvent polarity. Table 5.13 shows the results of these measurements. In addition, theory developed by Fuoss (Eq. 5.10) predicts that the ln(K_{assoc}) should change linearly

as an inverse function of ε_r.[38] As such, Figure 5.158 shows a plot of $\ln(K_{assoc})$ vs. ε_r exhibiting this behavior.

Table 5.13. *Results from conductometry using* ***1$^{\bullet+}$PF$_6^-$*** *in four different solvent systems.*

	ε_r	Λ_o (uS cm^2 mmol^{-1})	K_{assoc} (M^{-1})	ΔG_{assoc} (kcal mol^{-1})
THF	7.58	235.3	1 x 10^6	-8.3
57% Acetone, 43% EtAc[a]	14.4[b]	341.8	1 x 10^4	-5.6
Acetone	20.7	271.7	8 x 10^2	-4.0
DMAc	37.8	92.4	3 x 10^2	-3.4

[a]*Mol percent.* [b]*Calculated as the weighted average of the individual solvents' dielectric constants.*

$$lnK_{assoc} = \frac{1}{\varepsilon_r} \cdot \frac{e^2}{\alpha kT} \cdot ln\left(\frac{4\pi N\alpha^3}{3000}\right) \qquad \text{(Eq. 5.10)}$$

Where α is the ionic diameter, k is Boltzmann's constant, T is absolute temperature, and N is Avogadro's number.

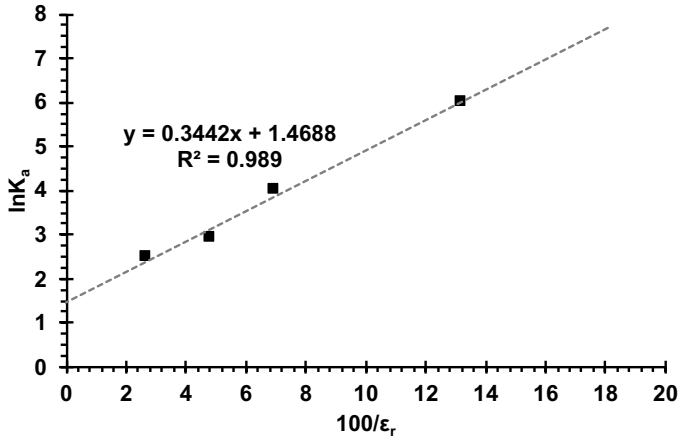

Figure 5.158. *Analysis of the impact of solvent polarity on ion pairing in* ***1$^{\bullet+}$PF$_6^-$***.

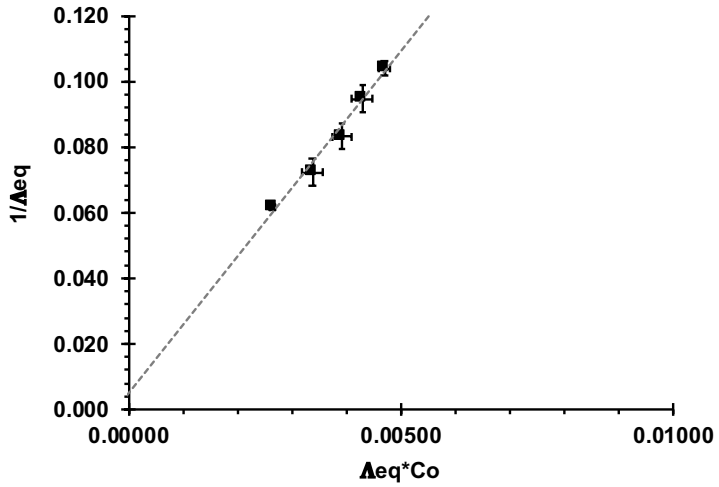

Figure 5.159. *Conductometry data for* ***1•+PF6-*** *in THF at 30 ºC.*

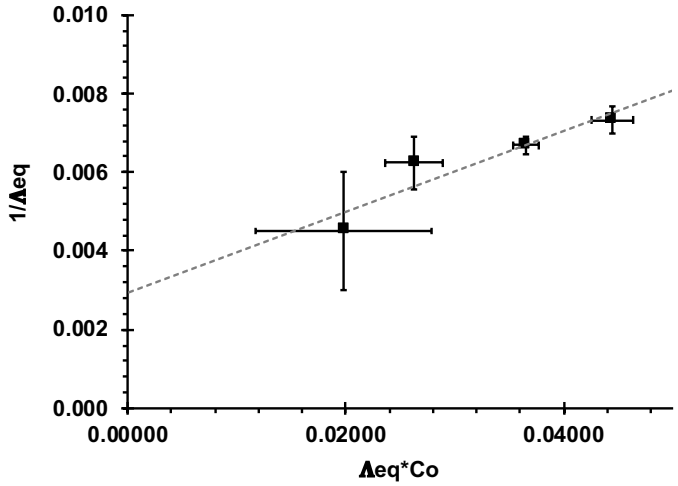

Figure 5.160. *Conductometry data for* ***1•+PF6-*** *in 57% acetone, 43% EtAc (mol percent) at 30 ºC.*

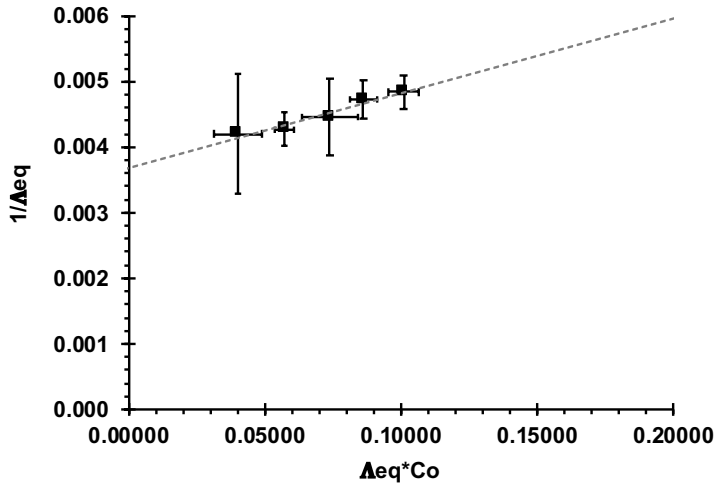

Figure 5.161. *Conductometry data for* ***1•+PF6-*** *in acetone at 30 ºC.*

Reproducibility of Measurement

To evaluate the precision and reproducibility of these measurements, conductometry was performed three separate times with **2•+PF6-** according to the general procedure described above. Table 5.14 shows the results of these experiments.

Table 5.14. *Results of conductometry with* ***2•+PF6-*** *on three different occasions.*

	Trial 1	Trial 2	Trial 3	**Average**	**Standard Deviation**
Λ_o (uS cm^2 mmol^{-1})	106.1	125.3	158.5	**130.0**	**26.5**
K_{assoc} (M^{-1})	7 x 10^2	1 x 10^3	3 x 10^3	**2 x 10^3**	**1 x 10^3**
ΔG_{assoc} (kcal mol^{-1})	-3.9	-4.3	-4.7	**-4.3**	**0.4**

General Polymerization Procedures

For Analysis of Kinetics and Molecular Weight Growth

To monitor polymerizations, 0.1 mL aliquots were removed periodically using a nitrogen

purged syringe and needle. Aliquots were quenched in a deuterated chloroform containing 250 ppm butylated hydroxytoluene (BHT). These solutions were then transferred to an NMR tube for ^{1}H NMR analysis to determine the extent of monomer conversion. Afterwards, solutions were dried and dissolved in unstabilized THF for GPC analysis to obtain number average molecular weight and dispersity.

For the Polymerization of Methyl Methacrylate

For polymerizations performed by O-ATRP with supplemental deactivator targeting a molecular weight of 10 kDa, **5**, $\mathbf{5^{\bullet+}PF_6^-}$, and LiBr were weighted into scintillation vials and pumped into a nitrogen glovebox. Under a nitrogen atmosphere, stock solutions of **5**, $\mathbf{5^{\bullet+}PF_6^-}$, and LiBr were prepared in EtAc. These stock solutions were then added, in the appropriate quantities, to a 20 mL scintillation vial along with MMA (1 mL, 9.35 mmol, 1000 eq), DBMM (17.9 μL, 0.0935 mmol, 10 eq), and a magnetic stir bar. If necessary, further EtAc was added to the vial to reach a total volume of 2 mL (1 mL total EtAc). The vials were then sealed and irradiated in a white LED beaker with a fan blowing over the beaker for temperature control.

For polymerizations performed by O-ATRP or reverse O-ATRP targeting a molecular weight of 50, 75, or 100 kDa, **5**, $\mathbf{5^{\bullet+}PF_6^-}$, and LiBr were weighted into scintillation vials and pumped into a nitrogen glovebox. Under a nitrogen atmosphere, stock solutions of **5**, $\mathbf{5^{\bullet+}PF_6^-}$, and LiBr were prepared in EtAc. These stock solutions were then added, in the appropriate quantities, to a 20 mL scintillation vial along with MMA (1 mL, 9.35 mmol, 1000 eq), DBMM (quantities varied depending on $M_{n,target}$) and a magnetic stir bar. If necessary, further EtAc was added to the vial to reach a total volume of 2 mL (1 mL total EtAc). The vials were then sealed and irradiated in a white LED beaker with a fan blowing over the beaker for temperature control.

For the Polymerization of Methyl Acrylate

For polymerizations performed by O-ATRP with supplemental deactivator using a total catalyst loading (PC + $PC^{\bullet+}$) of 100 ppm, **5**, $\mathbf{5^{\bullet+}PF_6^-}$, and LiBr were weighted into scintillation vials and pumped into a nitrogen glovebox. Under a nitrogen atmosphere, stock solutions of **5**, $\mathbf{5^{\bullet+}PF_6^-}$, and LiBr were prepared in EtAc. These stock solutions were then added, in the appropriate quantities, to a 20 mL scintillation vial along with MA (1 mL, 11.1 mmol, 1000 eq), DBMM (21.2 μL, 0.111 mmol, 10 eq), and a magnetic stir bar. If necessary, further EtAc was added to the vial to reach a total volume of 2 mL (1 mL total EtAc). The vials were then sealed and irradiated in a white LED beaker with a fan blowing over the beaker for temperature control.

For polymerizations performed by O-ATRP or reverse using a catalyst loading (PC or $PC^{\bullet+}$) greater than 100 ppm, **5** and $\mathbf{5^{\bullet+}PF_6^-}$ were weighed into 20 mL scintillation vials with magnetic stir bars. LiBr was weighted into a scintillation vial, and all vials were pumped into a nitrogen glovebox. Under a nitrogen atmosphere, a stock solution of LiBr was prepared in EtAc. MA (1 mL, 11.1 mmol, 1000 eq), DBMM (21.2 μL, 0.111 mmol, 10 eq), and the LiBr stock solution (quantities varied to match catalyst loadings) was added to the reaction vials. If necessary, further EtAc was added to reach a total volume of 2 mL (1 mL total EtAc). The vials were then sealed and irradiated in a white LED beaker with a fan blowing over the beaker for temperature control.

For the Polymerization of Other Acrylates

For the polymerization of various acrylate monomers by O-ATRP using $\mathbf{5^{\bullet+}}$, $\mathbf{5^{\bullet+}PF_6^-}$ (2.5 mg, 0.00222 mmol, 0.2 eq) was weighed into a 20 mL scintillation vial and equipped with a magnetic stir bar. LiBr was weighed into a scintillation vial. All vials were pumped into a nitrogen filled glovebox, in which all subsequent manipulations were performed. Monomer (11.1 mmol,

1000 eq), DBMM (21.2 μL, 0.111 mmol, 10 eq), and LiBr (0.193 mg, 0.00222 mmol, 0.2 eq, added by stock solution in EtAc) were added to the reaction vial. Finally, additional EtAc was added reach 1 mL total of EtAc in the reaction. The vials were then sealed and irradiated in white LED beakers with a fan blowing over the beakers for temperature control.

*For the Synthesis of Poly(Methyl Acrylate) Macroinitiator by O-ATRP using **5***

A 20 mL scintillation vial was charged with **5** (2.2 mg, 0.00222 mmol, 0.2 eq) and a magnetic stir bar. LiBr was weighed into a scintillation vial. All vials were pumped into a nitrogen filled glovebox, in which all subsequent manipulations were performed. MA (1 mL, 11.1 mmol, 1000 eq), DBMM (21.2 μL, 0.111 mmol, 10 eq), and LiBr (0.193 mg, 0.00222 mmol, 0.2 eq, added by stock solution in EtAc) were added to the reaction vial. Finally, additional EtAc was added reach 1 mL total of EtAc in the reaction. The vials were then sealed and irradiated for 30 min in white LED beakers with a fan blowing over the beakers for temperature control. The volatiles were then removed under vacuum and the product polymer further dried in a vacuum oven at 60 ºC for two days prior to subsequent characterization and use in O-ATRP.

*For the Synthesis of Poly(Methyl Acrylate) Macroinitiator by O-ATRP using **5**$^{\bullet+}$*

A 20 mL scintillation vial was charged with $\mathbf{5}^{\bullet+}\mathbf{PF_6}^-$ (2.5 mg, 0.00222 mmol, 0.2 eq) and a magnetic stir bar. LiBr was weighed into a scintillation vial. All vials were pumped into a nitrogen filled glovebox, in which all subsequent manipulations were performed. MA (1 mL, 11.1 mmol, 1000 eq), DBMM (21.2 μL, 0.111 mmol, 10 eq), and LiBr (0.193 mg, 0.00222 mmol, 0.2 eq, added by stock solution in EtAc) were added to the reaction vial. Finally, additional EtAc was added reach 1 mL total of EtAc in the reaction. The vials were then sealed and irradiated for 14 h

in white LED beakers with a fan blowing over the beakers for temperature control. The volatiles were then removed under vacuum and the product polymer further dried in a vacuum oven at 60 ºC for two days prior to subsequent characterization and use in O-ATRP.

For Chain Extensions and Block Copolymer Synthesis

A scintillation vial was charged with **5** (1.0 mg, 0.0010 mmol, 0.2 eq). A separate 20 mL scintillation vial was charged with pMA macroinitiator (M_n = 24.8 kDa, 0.2588 g, 0.0104 mmol, 2 eq) and a magnetic stir bar, and LiBr was weighed into another scintillation vial. All vials were pumped into a nitrogen filled glovebox, in which all subsequent manipulations were performed. EtAc was added to the macroinitiator vial and allowed to stir until the macroinitiator was completely dissolved. MA (0.47 mL, 5.22 mmol, 1000 eq) and LiBr (0.090 mg, 0.0010 mmol, 0.2 eq, added by stock solution in EtAc) were added to the vial containing **5**. Finally, the mixture was transferred to the vial containing the macroinitiator and EtAc (1 mL EtAc total). The vial was then sealed and irradiated for 24 h in a white LED beaker with a fan blowing over the beaker for temperature control. The volatiles were then removed under forced air and the product polymer further dried in a vacuum oven at 60 ºC for two days prior to subsequent characterization. Yield = 0.1550 g (31.2%).

A scintillation vial was charged with $\mathbf{5}^{\bullet+}\mathbf{PF_6}^-$ (1.0 mg, 0.00091 mmol, 0.2 eq). A separate 20 mL scintillation vial was charged with pMA macroinitiator (M_n = 4.21 kDa, 0.1909 g, 0.0453 mmol, 10 eq) and a magnetic stir bar, and LiBr was weighed into another scintillation vial. All vials were pumped into a nitrogen filled glovebox, in which all subsequent manipulations were performed. EtAc was added to the macroinitiator vial and allowed to stir until the macroinitiator was completely dissolved. MA (0.41 mL, 4.53 mmol, 1000 eq) and LiBr (0.079 mg, 0.00091

mmol, 0.2 eq, added by stock solution in EtAc) were added to the vial containing $\mathbf{5}^{\bullet+}\mathbf{PF_6}^-$. Finally, the mixture was transferred to the vial containing the macroinitiator and EtAc (1 mL EtAc total). The vial was then sealed and irradiated for 14 h in a white LED beaker with a fan blowing over the beaker for temperature control. The volatiles were then removed under forced air and the product polymer further dried in a vacuum oven at 60 ºC for two days prior to subsequent characterization. Yield = 0.2122 g (45.9%).

A scintillation vial was charged with **5** (1.7 mg, 0.0018 mmol, 0.2 eq). A separate 20 mL scintillation vial was charged with pMA macroinitiator (M_n = 14.2 kDa, 0.2544 g, 0.0179 mmol, 2 eq) and a magnetic stir bar, and LiBr was weighed into another scintillation vial. All vials were pumped into a nitrogen filled glovebox, in which all subsequent manipulations were performed. EtAc was added to the macroinitiator vial and allowed to stir until the macroinitiator was completely dissolved. tBA (1.15 mL, 8.96 mmol, 1000 eq) and LiBr (0.16 mg, 0.0018 mmol, 0.2 eq, added by stock solution in EtAc) were added to the vial containing **5**. Finally, the mixture was transferred to the vial containing the macroinitiator and EtAc (1 mL EtAc total). The vial was then sealed and irradiated for 24 h in a white LED beaker with a fan blowing over the beaker for temperature control. The volatiles were then removed under forced air and the product polymer further dried in a vacuum oven at 60 ºC for two days prior to subsequent characterization. Yield = 0.4295 g (58.6%).

A scintillation vial was charged with $\mathbf{5}^{\bullet+}\mathbf{PF_6}^-$ (1.5 mg, 0.0014 mmol, 0.2 eq). A separate 20 mL scintillation vial was charged with pMA macroinitiator (M_n = 2.96 kDa, 0.2035 g, 0.0688 mmol, 10 eq) and a magnetic stir bar, and LiBr was weighed into another scintillation vial. All vials were pumped into a nitrogen filled glovebox, in which all subsequent manipulations were performed. EtAc was added to the macroinitiator vial and allowed to stir until the macroinitiator

was completely dissolved. tBA (1.01 mL, 6.88 mmol, 1000 eq) and LiBr (0.12 mg, 0.0014 mmol, 0.2 eq, added by stock solution in EtAc) were added to the vial containing $\mathbf{5}^{\bullet+}\mathbf{PF}_6^-$. Finally, the mixture was transferred to the vial containing the macroinitiator and EtAc (1 mL EtAc total). The vial was then sealed and irradiated for 24 h in a white LED beaker with a fan blowing over the beaker for temperature control. The volatiles were then removed under forced air and the product polymer further dried in a vacuum oven at 60 ºC for two days prior to subsequent characterization. Yield = 0.4186 g (55.4%).

Supplemental Data for the Polymerization of Methyl Methacrylate

Initial Polymerization Experiments

To probe the impact of adding $\mathbf{5}^{\bullet+}$ to O-ATRP catalyzed by **5**, polymerizations were carried out in which the total catalyst loading (**5** + $\mathbf{5}^{\bullet+}$) was held constant but the ratio of [**5**]:[$\mathbf{5}^{\bullet+}$] was varied from 1:0 to 0:1.

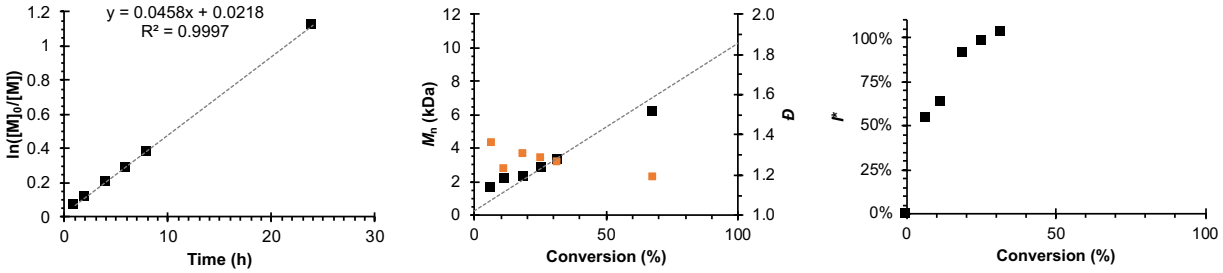

Figure 5.162. *O-ATRP of MMA with* ***5*** *in the absence of LiBr. [MMA]:[DBMM]:[**5** + $\mathbf{5}^{\bullet+}$]:[LiBr] = [1000]:[10]:[0.1]:[0]; [**5**]:[$\mathbf{5}^{\bullet+}$] = 1:0; 1 mL MMA, 1 mL EtAc; irradiated in a white LED beaker. (Left) Pseudo-first-order kinetics plot. (Middle) Evolution of polymer molecular weight (black) and Đ (orange) as a function of monomer conversion; grey dashed line represents the theoretical molecular weight growth. (Right) Initiator efficiency as a function of monomer conversion.*

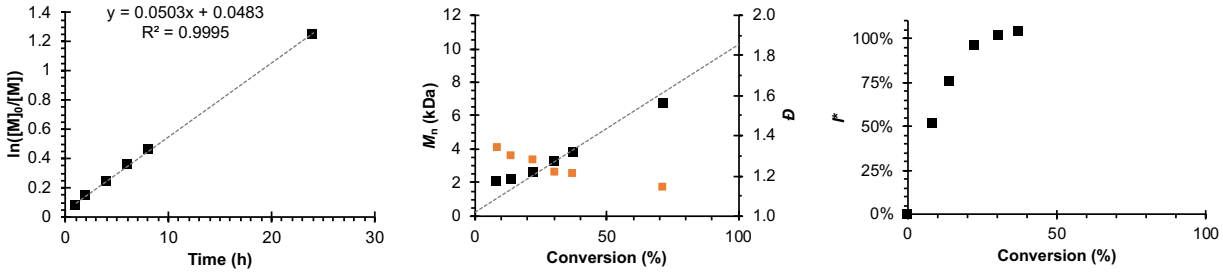

Figure 5.163. *O-ATRP of MMA with* ***5*** *and LiBr. [MMA]:[DBMM]:[****5*** *+* ***5***$^{\bullet+}$*]:[LiBr] = [1000]:[10]:[0.1]:[0.1]; [****5****]:[****5***$^{\bullet+}$*] = 1:0; 1 mL MMA, 1 mL EtAc; irradiated in a white LED beaker. (Left) Pseudo-first-order kinetics plot. (Middle) Evolution of polymer molecular weight (black) and Đ (orange) as a function of monomer conversion; grey dashed line represents the theoretical molecular weight growth. (Right) Initiator efficiency as a function of monomer conversion.*

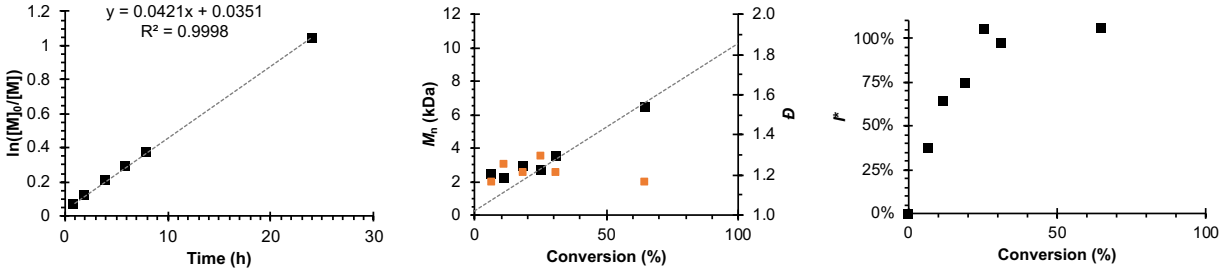

Figure 5.164. *O-ATRP of MMA with* ***5****,* ***5***$^{\bullet+}$*, and LiBr. [MMA]:[DBMM]:[****5*** *+* ***5***$^{\bullet+}$*]:[LiBr] = [1000]:[10]:[0.1]:[0.1]; [****5****]:[****5***$^{\bullet+}$*] = 3:1; 1 mL MMA, 1 mL EtAc; irradiated in a white LED beaker. (Left) Pseudo-first-order kinetics plot. (Middle) Evolution of polymer molecular weight (black) and Đ (orange) as a function of monomer conversion; grey dashed line represents the theoretical molecular weight growth. (Right) Initiator efficiency as a function of monomer conversion.*

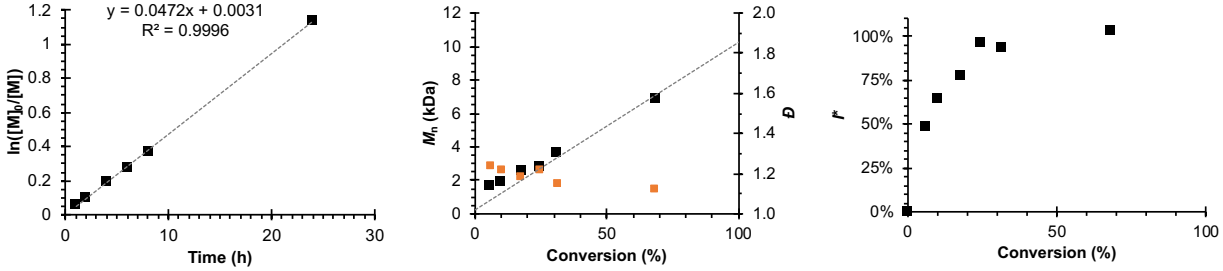

Figure 5.165. *O-ATRP of MMA with* ***5****,* ***5***$^{\bullet+}$*, and LiBr. [MMA]:[DBMM]:[****5*** *+* ***5***$^{\bullet+}$*]:[LiBr] = [1000]:[10]:[0.1]:[0.1]; [****5****]:[****5***$^{\bullet+}$*] = 1:1; 1 mL MMA, 1 mL EtAc; irradiated in a white LED beaker. (Left) Pseudo-first-order kinetics plot. (Middle) Evolution of polymer molecular weight (black) and Đ (orange) as a function of monomer conversion; grey dashed line represents the theoretical molecular weight growth. (Right) Initiator efficiency as a function of monomer conversion.*

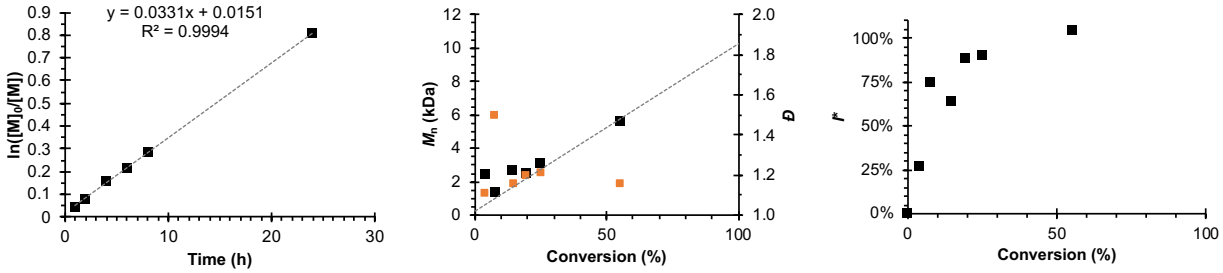

Figure 5.166. *O-ATRP of MMA with* ***5****,* ***5***$^{\bullet+}$*, and LiBr. [MMA]:[DBMM]:[****5*** *+* ***5***$^{\bullet+}$*]:[LiBr] = [1000]:[10]:[0.1]:[0.1]; [****5****]:[****5***$^{\bullet+}$*] = 1:3; 1 mL MMA, 1 mL EtAc; irradiated in a white LED beaker. (Left) Pseudo-first-order kinetics plot. (Middle) Evolution of polymer molecular weight (black) and Đ (orange) as a function of monomer conversion; grey dashed line represents the theoretical molecular weight growth. (Right) Initiator efficiency as a function of monomer conversion.*

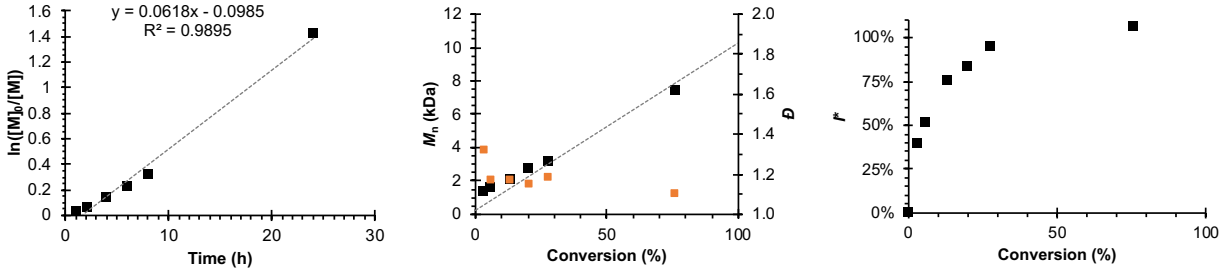

Figure 5.167. *O-ATRP of MMA with* ***5***$^{\bullet+}$ *and LiBr. [MMA]:[DBMM]:[****5*** *+* ***5***$^{\bullet+}$*]:[LiBr] = [1000]:[10]:[0.1]:[0.1]; [****5****]:[****5***$^{\bullet+}$*] = 0:1; 1 mL MMA, 1 mL EtAc; irradiated in a white LED beaker. (Left) Pseudo-first-order kinetics plot. (Middle) Evolution of polymer molecular weight (black) and Đ (orange) as a function of monomer conversion; grey dashed line represents the theoretical molecular weight growth. (Right) Initiator efficiency as a function of monomer conversion.*

Control Experiments

To investigate the impact of each reaction component in the O-ATRP of MMA using **5**$^{\bullet+}$**PF**$_6^-$, control reactions were performed systematically eliminating one reaction variable at a time (Table 5.15). Figure 5.168 shows photographs of some of the control reactions after 8 h. From the images, it can be seen that in the absence of LiBr the solution remains dark blue even after irradiation, indicating the presence of a significant quantity of **5**$^{\bullet+}$. Instead, under standard

conditions (in the presence of LiBr), the solution gradually turns green and then yellow as a result of the reaction between $\mathbf{5}^{\bullet+}$ and Br^- to form **5**. Finally, in the absence of LiBr and $\mathbf{5}^{\bullet+}\mathbf{PF_6}^-$ (Table 5.15, Entry S2), no change in the solution can be observed visually, suggesting minimal background polymerization has occurred.

Table 5.15. *Control reactions for the O-ATRP of MMA using* $\mathbf{5}^{\bullet+}$.

Entry	[MMA]:[DBMM]:[$5^{\bullet+}$]:[LiBr]	Time (h)	Conv. (%)	$M_{n,\,theo}$ (kDa)	$M_{n,\,exp}$ (kDa)[a]	$Đ^a$	I^* (%)[b]
S1	[1000]:[10]:[0.2]:**[0]**	8	8.3	1.08	2.13	2.40	51
S2	[1000]:[10]:**[0]**:**[0]**	8	2.0	0.45	36.7	2.34	1
S3	[1000]:**[0]**:[0.2]:[0.2]	8	13.0	-	163	1.78	-
S4[c]	[1000]:[10]:[0.2]:[0.2]	8	0	-	-	-	-
S5[c]	[1000]:[10]:**[0]**:[0.2]	8	0	-	-	-	-

[a]Determined by GPC. [b]Initiator efficiency (I) = ($M_{n,\,theo}$ / $M_{n,\,exp}$)•100%. [c]Reaction performed in the dark.*

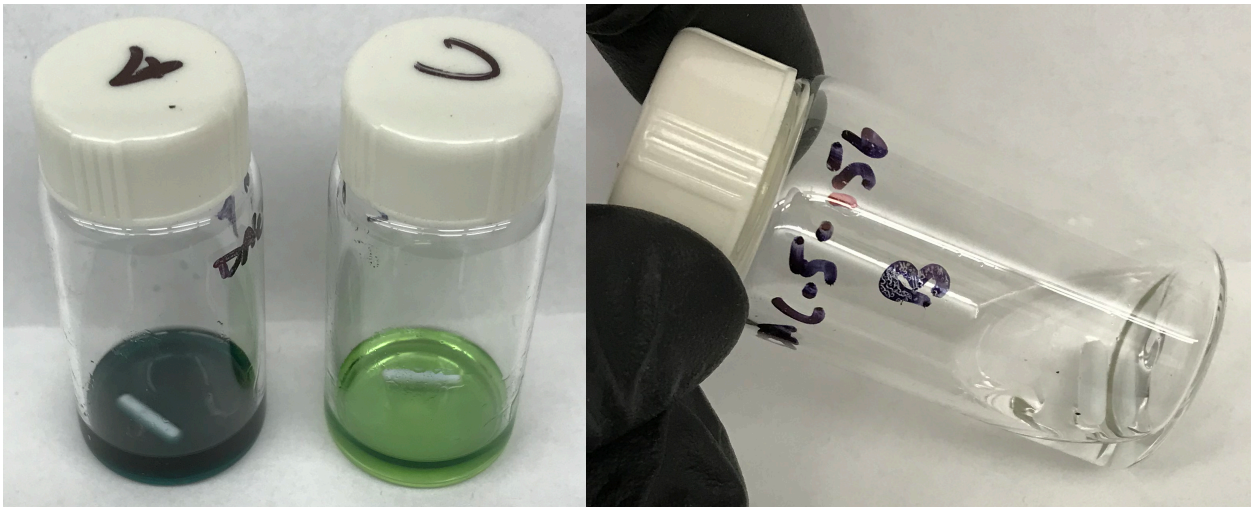

Figure 5.168. *Photographs of control reactions after 8 h of irradiation in a white LED beaker.*

For the Synthesis of High Molecular Weight Polymers

In an attempt to synthesize high molecular weight PMMA, polymerizations were carried under the same conditions used in initial MMA polymerizations. To vary the polymer target molecular weight, the initiator loading was altered.

Table 5.16. *Polymerization results for the attempted synthesis of high molecular weight pMMA using* ***5*** *or* ***5***$^{\bullet+}$.

Entry	[5]:[5$^{\bullet+}$]	$M_{n,target}$ (kDa)	Time (h)	Conv. (%)[a]	$M_{n,theo}$ (kDa)	$M_{n,exp}$ (kDa)[b]	$Đ$[b]	I^* (%)[c]
S6	1:0	50	38	73.9	37.24	29.0	1.17	128
S7	0:1	50	38	81.0	40.8	29.1	1.22	140
S8	1:0	75	38	76.0	57.3	45.1	1.19	127
S9	0:1	75	38	68.5	51.7	36.1	1.14	143
S10	1:0	100	38	68.6	68.9	42.5	1.26	162
S11	0:1	100	38	71.3	71.7	41.0	1.22	175

*For all polymerizations, [MMA]:[**5**/**5**$^{\bullet+}$]:[LiBr] = [1000]:[0.1]:[0.1], and $M_{n,target}$ was adjusted by varying the initiator loading while keeping all other conditions constant (see Section 11 of Experimental for full experiment details).* [a]*Determined by* ^{1}*H NMR.* [b]*Determined by GPC.* [c]*Initiator efficienty (I*) =* $(M_{n,theo} / M_{n,exp})$*•100%.*

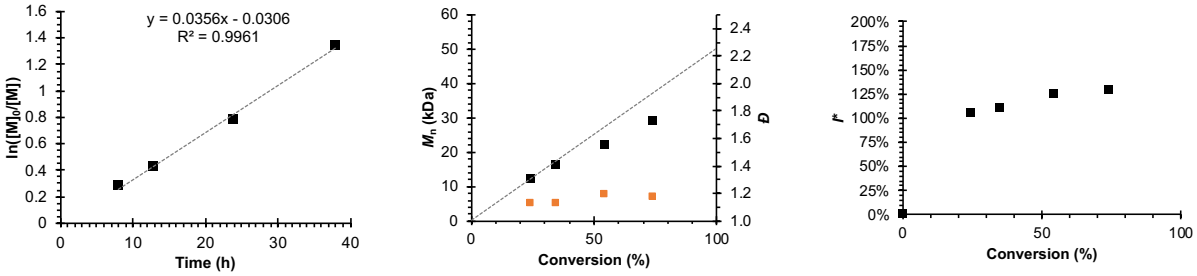

Figure 5.169. *O-ATRP of MMA with* ***5*** *and LiBr ($M_{n,target}$ = 50). [MMA]:[DBMM]:[**5** + **5**$^{\bullet+}$]:[LiBr] = [1000]:[2]:[0.1]:[0.1]; [**5**]:[**5**$^{\bullet+}$] = 1:0; 1 mL MMA, 1 mL EtAc; irradiated in a white LED beaker. (Left) Pseudo-first-order kinetics plot. (Middle) Evolution of polymer molecular weight (black) and Đ (orange) as a function of monomer conversion; grey dashed line represents the theoretical molecular weight growth. (Right) Initiator efficiency as a function of monomer conversion.*

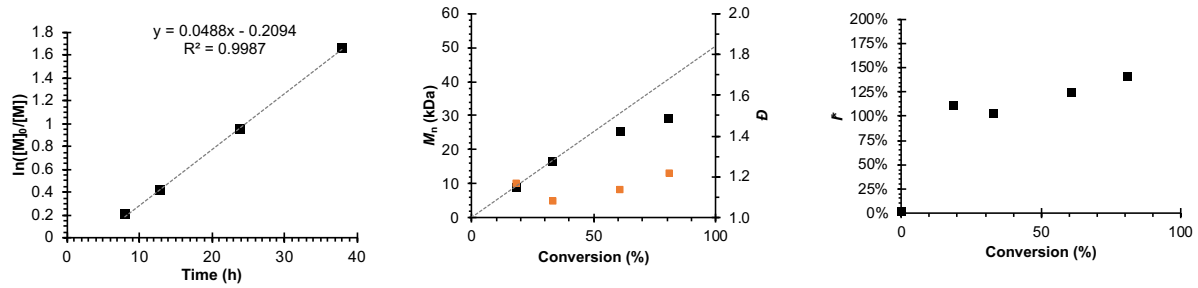

Figure 5.170. *O-ATRP of MMA with* ***5***$^{\bullet+}$ *and LiBr (*$M_{n,target}$ *= 50). [MMA]:[DBMM]:[****5*** *+* ***5***$^{\bullet+}$*]:[LiBr] = [1000]:[2]:[0.1]:[0.1]; [****5****]:[****5***$^{\bullet+}$*] = 0:1; 1 mL MMA, 1 mL EtAc; irradiated in a white LED beaker. (Left) Pseudo-first-order kinetics plot. (Middle) Evolution of polymer molecular weight (black) and Đ (orange) as a function of monomer conversion; grey dashed line represents the theoretical molecular weight growth. (Right) Initiator efficiency as a function of monomer conversion.*

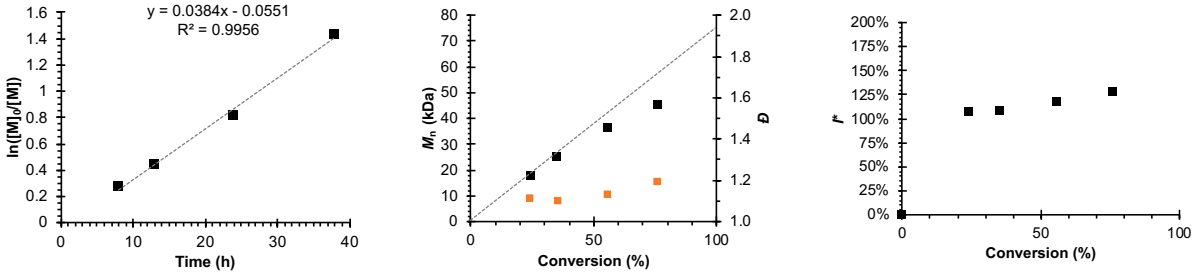

Figure 5.171. *O-ATRP of MMA with* ***5*** *and LiBr (*$M_{n,target}$ *= 75). [MMA]:[DBMM]:[****5*** *+* ***5***$^{\bullet+}$*]:[LiBr] = [1000]:[1.33]:[0.1]:[0.1]; [****5****]:[****5***$^{\bullet+}$*] = 1:0; 1 mL MMA, 1 mL EtAc; irradiated in a white LED beaker. (Left) Pseudo-first-order kinetics plot. (Middle) Evolution of polymer molecular weight (black) and Đ (orange) as a function of monomer conversion; grey dashed line represents the theoretical molecular weight growth. (Right) Initiator efficiency as a function of monomer conversion.*

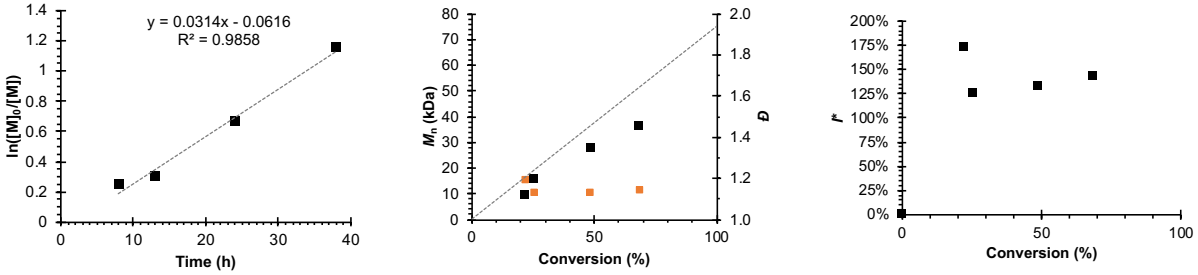

Figure 5.172. *O-ATRP of MMA with* ***5***$^{\bullet+}$ *and LiBr (*$M_{n,target}$ *= 75). [MMA]:[DBMM]:[****5*** *+* ***5***$^{\bullet+}$*]:[LiBr] = [1000]:[1.33]:[0.1]:[0.1]; [****5****]:[****5***$^{\bullet+}$*] = 0:1; 1 mL MMA, 1 mL EtAc; irradiated in a white LED beaker. (Left) Pseudo-first-order kinetics plot. (Middle) Evolution of polymer molecular weight (black) and Đ (orange) as a function of monomer conversion; grey dashed line represents the theoretical molecular weight growth. (Right) Initiator efficiency as a function of monomer conversion.*

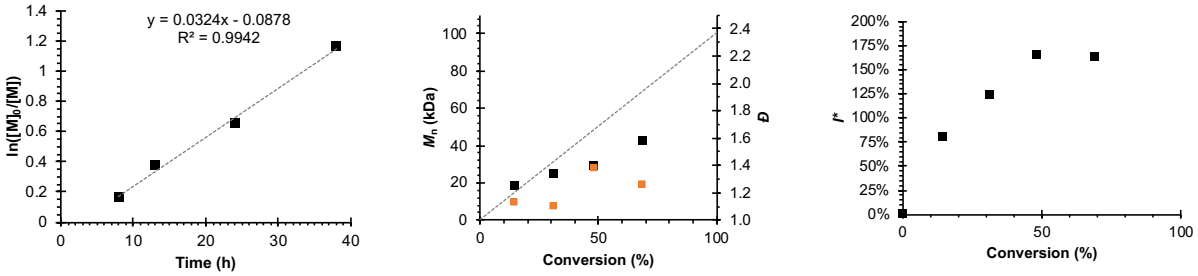

Figure 5.173. *O-ATRP of MMA with* ***5*** *and LiBr ($M_{n,target}$ = 100). [MMA]:[DBMM]:[**5** + **5**$^{\bullet+}$]:[LiBr] = [1000]:[1]:[0.1]:[0.1]; [**5**]:[**5**$^{\bullet+}$] = 1:0; 1 mL MMA, 1 mL EtAc; irradiated in a white LED beaker. (Left) Pseudo-first-order kinetics plot. (Middle) Evolution of polymer molecular weight (black) and Đ (orange) as a function of monomer conversion; grey dashed line represents the theoretical molecular weight growth. (Right) Initiator efficiency as a function of monomer conversion.*

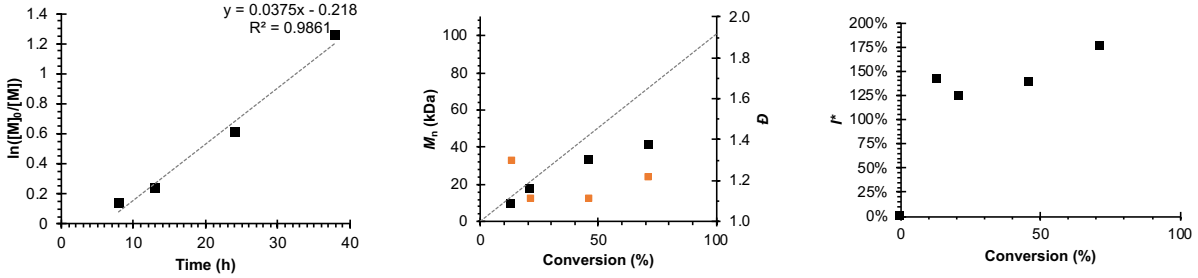

Figure 5.174. *O-ATRP of MMA with* ***5***$^{\bullet+}$ *and LiBr ($M_{n,target}$ = 100). [MMA]:[DBMM]:[**5** + **5**$^{\bullet+}$]:[LiBr] = [1000]:[1]:[0.1]:[0.1]; [**5**]:[**5**$^{\bullet+}$] = 0:1; 1 mL MMA, 1 mL EtAc; irradiated in a white LED beaker. (Left) Pseudo-first-order kinetics plot. (Middle) Evolution of polymer molecular weight (black) and Đ (orange) as a function of monomer conversion; grey dashed line represents the theoretical molecular weight growth. (Right) Initiator efficiency as a function of monomer conversion.*

Since effective deactivation is essential to prevent termination reactions at high monomer conversions and achieve high molecular weight polymers, two approaches were investigated to improve polymerization control: varying the LiBr loading (Table 5.17) and varying the **5**$^{\bullet+}$ loading (Table 5.18). However, neither approach enabled the synthesis of polymers with molecular weights above 45 kDa.

Table 5.17. *Results from the O-ATRP of MMA with* ***5***$^{\bullet+}$ *and LiBr ($M_{n,target}$ = 100) varying the LiBr loading. 1 mL MMA, 1 mL EtAc; irradiated in a white LED beaker.*

Entry	[MMA]:[DBMM]:[$5^{\bullet+}$]:[LiBr]	Time (h)	Conv. (%)	$M_{n,\,theo}$ (kDa)	$M_{n,\,exp}$ (kDa)[a]	$Đ^a$	I^* (%)[b]
S12	[1000]:[1]:[0.1]:**[1]**	38	63.8	64.1	41.3	1.24	155
S13	[1000]:[1]:[0.1]:**[0.5]**	38	68.6	68.9	41.3	1.26	167
S14	[1000]:[1]:[0.1]:**[0.1]**	38	74.2	74.6	44.6	1.33	167
S15	[1000]:[1]:[0.1]:**[0.05]**	48	59.7	60.0	43.1	1.11	139
S16	[1000]:[1]:[0.1]:**[0.01]**	72	81.3	81.66	48.1	1.15	170

[a]*Determined by GPC.* [b]*Initiator efficiency (I*) = ($M_{n,\,theo}$ / $M_{n,\,exp}$)•100%.*

Table 5.18. *Results from the O-ATRP of MMA with* ***5***$^{\bullet+}$ *and LiBr ($M_{n,target}$ = 100) varying the loading of* ***5***$^{\bullet+}$*. 1 mL MMA, 1 mL EtAc; irradiated in a white LED beaker.*

Entry	[$5^{\bullet+}$] (ppm)	Time (h)	Conv. (%)	$M_{n,\,theo}$ (kDa)	$M_{n,\,exp}$ (kDa)[a]	$Đ^a$	I^* (%)[b]
S17	100	38	71.3	71.7	41.0	1.22	175
S18	150	72	69.5	69.9	41.3	1.19	169
S19	200	72	77.5	77.9	38.2	1.37	204
S20	250	95	70.5	70.8	39.1	1.24	181

[a]*Determined by GPC.* [b]*Initiator efficiency (I*) = ($M_{n,\,theo}$ / $M_{n,\,exp}$)•100%.*

Supplemental Data for the Polymerization of Methyl Acrylate

Initial Experiments

To probe the impact of adding $\mathbf{5}^{\bullet+}$ to O-ATRP catalyzed by **5**, polymerizations were carried out in which the total catalyst loading (**5** + $\mathbf{5}^{\bullet+}$) was held constant but the ratio of [**5**]:[$\mathbf{5}^{\bullet+}$] was varied from 1:0 to 0:1.

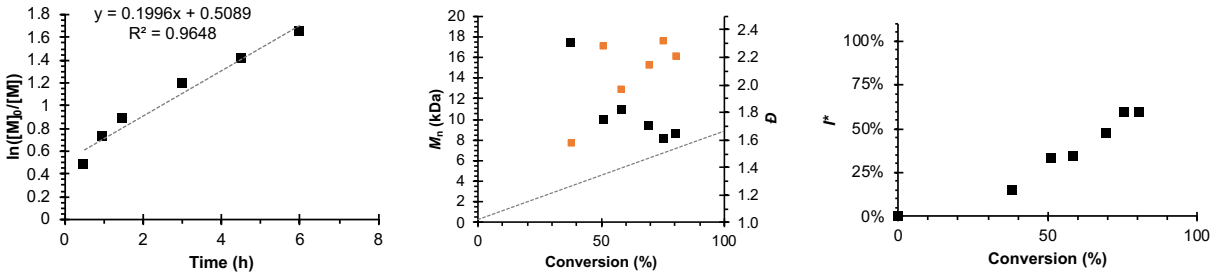

Figure 5.175. *O-ATRP of MA with* ***5*** *in the absence of LiBr. [MA]:[DBMM]:[****5*** *+* $\mathbf{5}^{\bullet+}$*]:[LiBr] = [1000]:[10]:[0.1]:[0]; [****5****]:[*$\mathbf{5}^{\bullet+}$*] = 1:0; 1 mL MA, 1 mL EtAc; irradiated in a white LED beaker. (Left) Pseudo-first-order kinetics plot. (Middle) Evolution of polymer molecular weight (black) and Đ (orange) as a function of monomer conversion; grey dashed line represents the theoretical molecular weight growth. (Right) Initiator efficiency as a function of monomer conversion.*

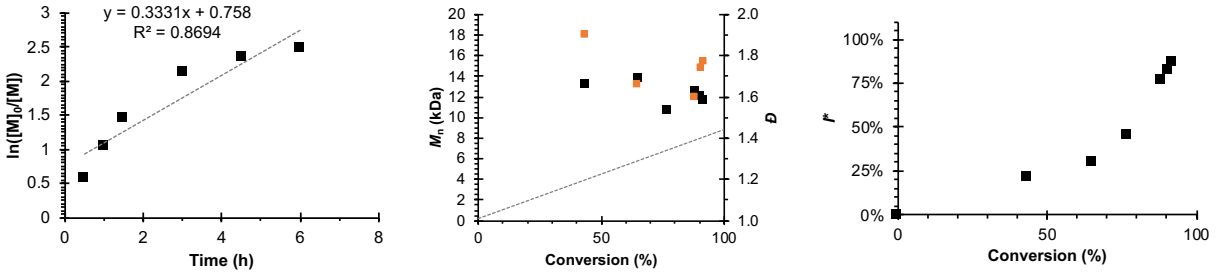

Figure 5.176. *O-ATRP of MA with* ***5*** *and LiBr. [MA]:[DBMM]:[****5*** *+* $\mathbf{5}^{\bullet+}$*]:[LiBr] = [1000]:[10]:[0.1]:[0.1]; [****5****]:[*$\mathbf{5}^{\bullet+}$*] = 1:0; 1 mL MA, 1 mL EtAc; irradiated in a white LED beaker. (Left) Pseudo-first-order kinetics plot. (Middle) Evolution of polymer molecular weight (black) and Đ (orange) as a function of monomer conversion; grey dashed line represents the theoretical molecular weight growth. (Right) Initiator efficiency as a function of monomer conversion.*

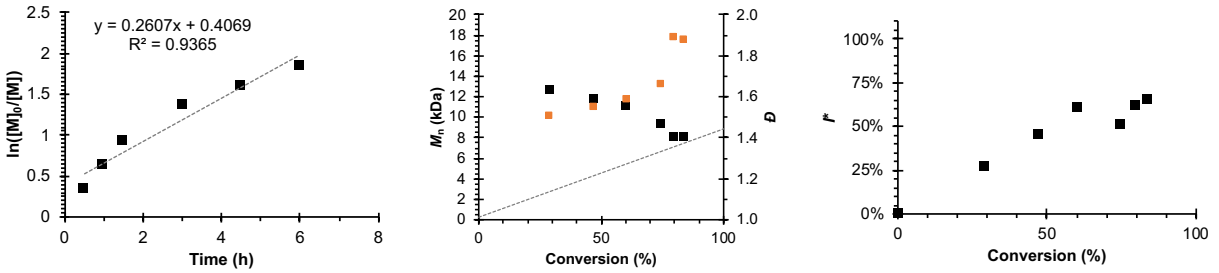

Figure 5.177. *O-ATRP of MA with* ***5****,* ***5***$^{\bullet+}$*, and LiBr. [MA]:[DBMM]:[****5*** *+* ***5***$^{\bullet+}$*]:[LiBr] = [1000]:[10]:[0.1]:[0.1]; [****5****]:[****5***$^{\bullet+}$*] = 3:1; 1 mL MA, 1 mL EtAc; irradiated in a white LED beaker. (Left) Pseudo-first-order kinetics plot. (Middle) Evolution of polymer molecular weight (black) and Đ (orange) as a function of monomer conversion; grey dashed line represents the theoretical molecular weight growth. (Right) Initiator efficiency as a function of monomer conversion.*

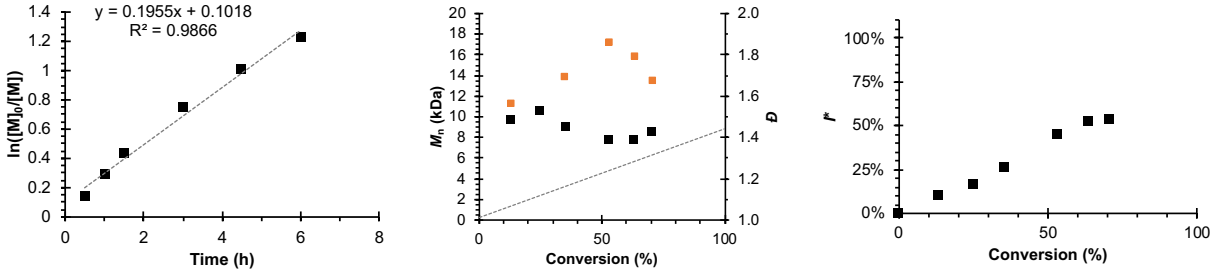

Figure 5.178. *O-ATRP of MA with* ***5****,* ***5***$^{\bullet+}$*, and LiBr. [MA]:[DBMM]:[****5*** *+* ***5***$^{\bullet+}$*]:[LiBr] = [1000]:[10]:[0.1]:[0.1]; [****5****]:[****5***$^{\bullet+}$*] = 1:1; 1 mL MA, 1 mL EtAc; irradiated in a white LED beaker. (Left) Pseudo-first-order kinetics plot. (Middle) Evolution of polymer molecular weight (black) and Đ (orange) as a function of monomer conversion; grey dashed line represents the theoretical molecular weight growth. (Right) Initiator efficiency as a function of monomer conversion.*

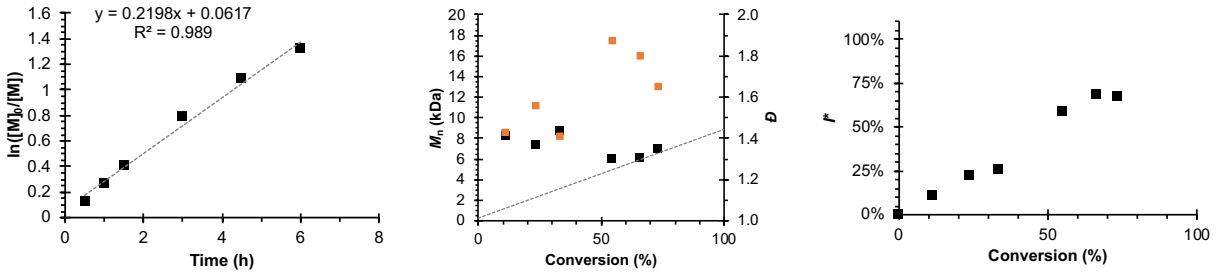

Figure 5.179. *O-ATRP of MA with* ***5****,* ***5***$^{\bullet+}$*, and LiBr. [MA]:[DBMM]:[****5*** *+* ***5***$^{\bullet+}$*]:[LiBr] = [1000]:[10]:[0.1]:[0.1]; [****5****]:[****5***$^{\bullet+}$*] = 1:3; 1 mL MA, 1 mL EtAc; irradiated in a white LED beaker. (Left) Pseudo-first-order kinetics plot. (Middle) Evolution of polymer molecular weight (black) and Đ (orange) as a function of monomer conversion; grey dashed line represents the theoretical molecular weight growth. (Right) Initiator efficiency as a function of monomer conversion.*

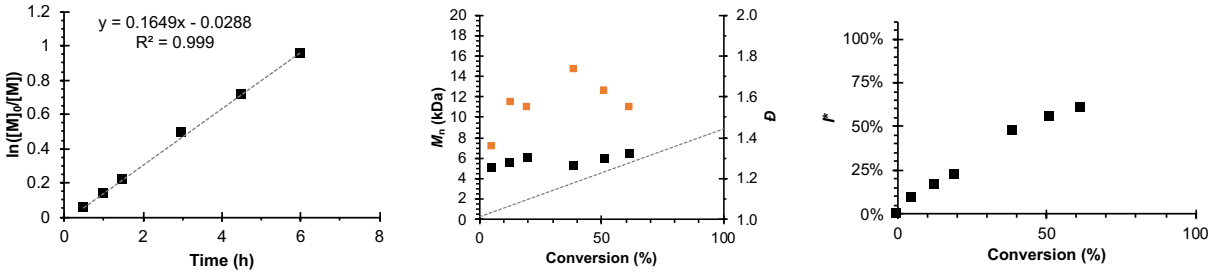

Figure 5.180. *O-ATRP of MA with* ***5***$^{\bullet+}$ *and LiBr. [MA]:[DBMM]:[****5*** *+* ***5***$^{\bullet+}$*]:[LiBr] = [1000]:[10]:[0.1]:[0.1]; [****5****]:[****5***$^{\bullet+}$*] = 0:1; 1 mL MA, 1 mL EtAc; irradiated in a white LED beaker. (Left) Pseudo-first-order kinetics plot. (Middle) Evolution of polymer molecular weight (black) and Đ (orange) as a function of monomer conversion; grey dashed line represents the theoretical molecular weight growth. (Right) Initiator efficiency as a function of monomer conversion.*

Since the polymerization performed with 100 ppm **5**$^{\bullet+}$ showed the best control but still left room for improvement, several additional polymerizations were performed with increasing **5**$^{\bullet+}$ loadings to investigate whether improved polymerization control could be achieved in this manner. To verify that changes in polymerization control were due to improved deactivation and not simply higher catalyst loadings, the same polymerizations were performed with **5** for comparison.

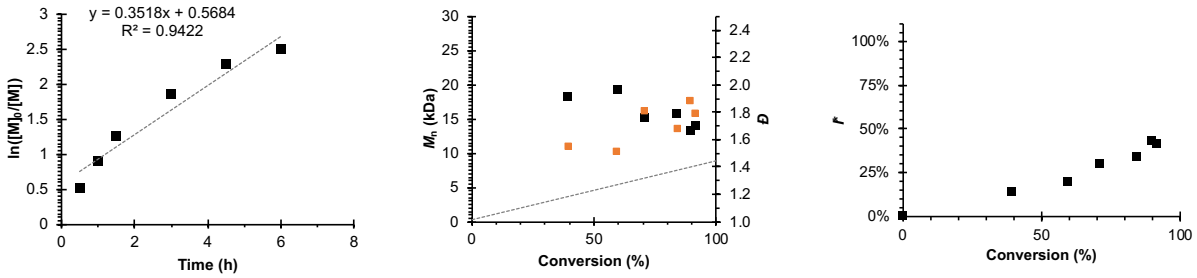

Figure 5.181. *O-ATRP of MA with* ***5*** *and LiBr. [MA]:[DBMM]:[****5****]:[LiBr] = [1000]:[10]:[0.15]:[0.15] (150 ppm* ***5****); 1 mL MA, 1 mL EtAc; irradiated in a white LED beaker. (Left) Pseudo-first-order kinetics plot. (Middle) Evolution of polymer molecular weight (black) and Đ (orange) as a function of monomer conversion; grey dashed line represents the theoretical molecular weight growth. (Right) Initiator efficiency as a function of monomer conversion.*

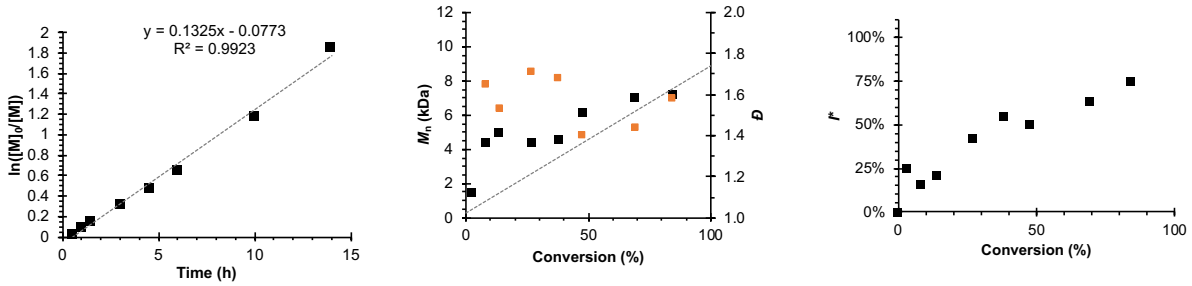

Figure 5.182. *O-ATRP of MA with* ***5***$^{\bullet+}$ *and LiBr. [MA]:[DBMM]:[****5***$^{\bullet+}$*]:[LiBr] = [1000]:[10]:[0.15]:[0.15] (150 ppm* ***5***$^{\bullet+}$*); 1 mL MA, 1 mL EtAc; irradiated in a white LED beaker. (Left) Pseudo-first-order kinetics plot. (Middle) Evolution of polymer molecular weight (black) and Đ (orange) as a function of monomer conversion; grey dashed line represents the theoretical molecular weight growth. (Right) Initiator efficiency as a function of monomer conversion.*

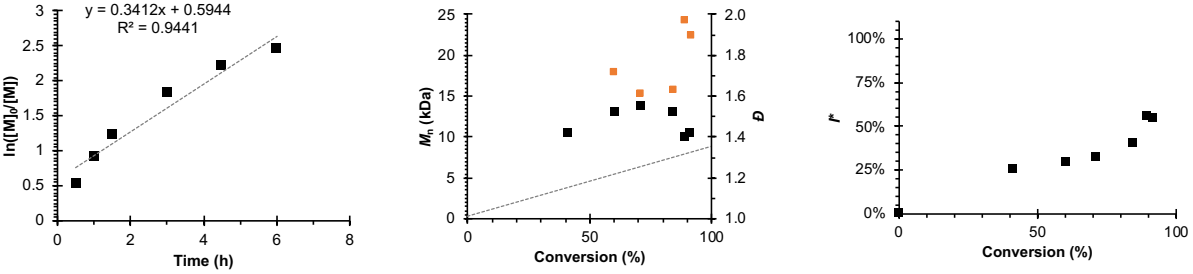

Figure 5.183. *O-ATRP of MA with* ***5*** *and LiBr. [MA]:[DBMM]:[****5****]:[LiBr] = [1000]:[10]:[0.2]:[0.2] (200 ppm* ***5****); 1 mL MA, 1 mL EtAc; irradiated in a white LED beaker. (Left) Pseudo-first-order kinetics plot. (Middle) Evolution of polymer molecular weight (black) and Đ (orange) as a function of monomer conversion; grey dashed line represents the theoretical molecular weight growth. (Right) Initiator efficiency as a function of monomer conversion.*

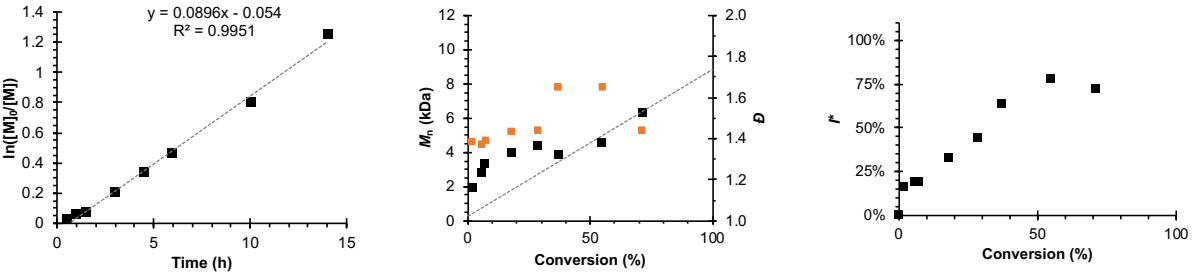

Figure 5.184. *O-ATRP of MA with* ***5***$^{\bullet+}$ *and LiBr. [MA]:[DBMM]:[****5***$^{\bullet+}$*]:[LiBr] = [1000]:[10]:[0.2]:[0.2] (200 ppm* ***5***$^{\bullet+}$*); 1 mL MA, 1 mL EtAc; irradiated in a white LED beaker. (Left) Pseudo-first-order kinetics plot. (Middle) Evolution of polymer molecular weight (black) and Đ (orange) as a function of monomer conversion; grey dashed line represents the theoretical molecular weight growth. (Right) Initiator efficiency as a function of monomer conversion.*

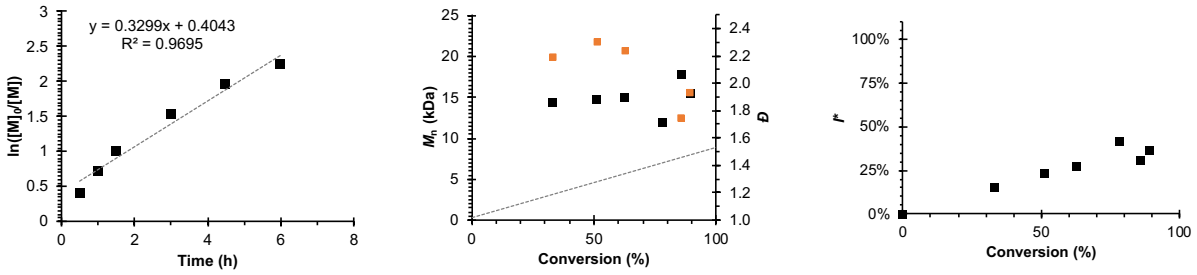

Figure 5.185. *O-ATRP of MA with* ***5*** *and LiBr. [MA]:[DBMM]:[****5****]:[LiBr] = [1000]:[10]:[0.25]:[0.25] (250 ppm* ***5****); 1 mL MA, 1 mL EtAc; irradiated in a white LED beaker. (Left) Pseudo-first-order kinetics plot. (Middle) Evolution of polymer molecular weight (black) and Đ (orange) as a function of monomer conversion; grey dashed line represents the theoretical molecular weight growth. (Right) Initiator efficiency as a function of monomer conversion.*

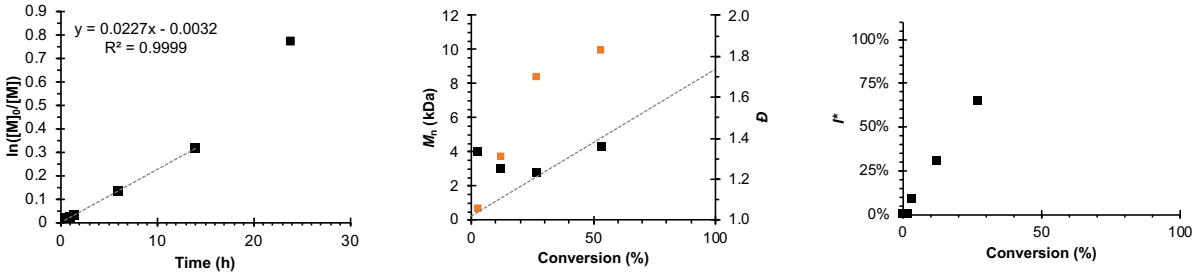

Figure 5.186. *O-ATRP of MA with* ***5***$^{\bullet+}$ *and LiBr. [MA]:[DBMM]:[****5***$^{\bullet+}$*]:[LiBr] = [1000]:[10]:[0.25]:[0.25] (250 ppm* ***5***$^{\bullet+}$*); 1 mL MA, 1 mL EtAc; irradiated in a white LED beaker. (Left) Pseudo-first-order kinetics plot. (Middle) Evolution of polymer molecular weight (black) and Đ (orange) as a function of monomer conversion; grey dashed line represents the theoretical molecular weight growth. (Right) Initiator efficiency as a function of monomer conversion.*

Control Experiments

To investigate the impact of each reaction component in the O-ATRP of MA using **5**$^{\bullet+}$**PF**$_6^-$, control reactions were performed systematically eliminating one reaction variable at a time (Table 5.19). Interestingly, significant background polymerization was observed in the absence of **5**$^{\bullet+}$**PF**$_6^-$ and LiBr (Entry S22). Figure 5.187 shows photographs of some of these control reactions after 14 h of irradiation. For the polymerization without LiBr (Entry S21), the polymerization remained dark blue after irradiation, suggesting the presence of a significant quantity of **5**$^{\bullet+}$. By comparison, the polymerization in the absence of DBMM (with LiBr) turned green after 14h, supporting the

presence of a reaction between $\mathbf{5}^{\bullet+}$ and Br^- to for **5** over time. Finally, the reaction in the absence of $\mathbf{5}^{\bullet+}\mathbf{PF_6}^-$ and LiBr (Entry S22) showed significant gelling after 14h, supporting the presence of a background, uncontrolled polymerization.

Table 5.19. *Control reactions for the O-ATRP of MA using 200 ppm* $\mathbf{5}^{\bullet+}\mathbf{PF_6}^-$.

Entry	[MA]:[DBMM]:[$5^{\bullet+}$]:[LiBr]	Time (h)	Conv. (%)	$M_{n,\,theo}$ (kDa)	$M_{n,\,exp}$ (kDa)[a]	$Đ^a$	I^* (%)[b]
S21	[1000]:[10]:[0.2]:**[0]**	14	9.1	1.04	3.97	1.70	26
S22	[1000]:[10]:**[0]**:**[0]**	14	57.1	5.17	467	1.06	1
S23	[1000]:**[0]**:[0.2]:[0.2]	14	55.4	-	0.51	1.71	-
S24	[1000]:[10]:[0.2]:[0.2]	14	0	-	-	-	-
S25[c]	[1000]:[10]:**[0]**:[0.2]	14	0	-	-	-	-

[a]Determined by GPC. [b]Initiator efficiency (I) = ($M_{n,\,theo}$ / $M_{n,\,exp}$)•100%. [c]Reaction performed in the dark.*

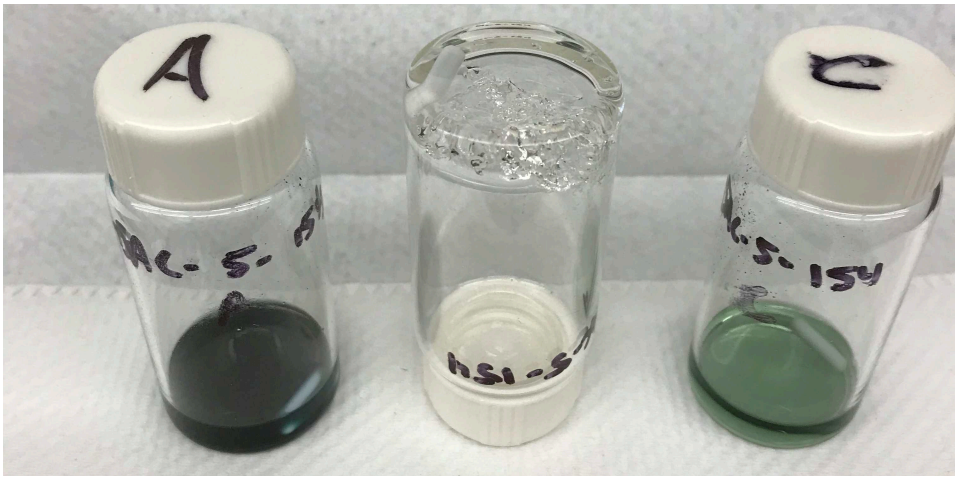

Figure 5.187. *Photographs of MA control reactions after 14 h of irradiation in a white LED beaker.*

Polymerization Optimization

In an attempt to improve polymerization control to an even greater degree in O-ATRP

using **5**$^{\bullet+}$, several reaction variables were tuned. First, a solvent screen was performed, in which THF and DMAc were investigated. While polymerization results in THF were similar to those in EtAc, polymerizations in DMAc exhibited very poor control, presumably due to the poor stability of **5**$^{\bullet+}$ in DMAc.

Table 5.20. *Results for the O-ATRP of MA using* ***5***$^{\bullet+}$ *in three different solvents.*

Entry	5$^{\bullet+}$ or 5	Solvent	Time (h)	Conv. (%)	$M_{n,\,theo}$ (kDa)	$M_{n,\,exp}$ (kDa)[a]	$Đ^a$	I^* (%)[b]
S26	**5**	EtAc	6	91.4	8.12	10.4	1.90	78
S27	**5**$^{\bullet+}$	EtAc	14	71.3	6.39	6.25	1.44	102
S28	**5**	THF	14	93.0	8.26	5.50	1.97	150
S29	**5**$^{\bullet+}$	THF	14	66.1	5.94	4.82	1.46	123
S30	**5**	DMAc	14	98.9	8.77	8.87	2.52	99
S31	**5**$^{\bullet+}$	DMAc	14	99.9	8.86	6.97	2.05	127

[a]*Determined by GPC.* [b]*Initiator efficiency (I*) =* $(M_{n,\,theo} / M_{n,\,exp})$*•100%.*

In addition, it was hypothesized that a higher LiBr loading might further improve deactivation, and therefore polymerization control, in O-ATRP using **5**$^{\bullet+}$. Alternatively, a higher LiBr loading could also lead to faster disappearance of **5**$^{\bullet+}$, leading to poor polymerization control due to a loss of the deactivator. To test these hypotheses, five different LiBr loadings were investigated.

Table 5.21. *Results from the O-ATRP of MA using* ***5***$^{\bullet+}$ *with different LiBr loadings.*

Entry	[MA]:[DBMM]:[5$^{\bullet+}$]:[LiBr]	Time (h)	Conv. (%)	$M_{n,\,theo}$ (kDa)	$M_{n,\,exp}$ (kDa)[a]	$Đ^a$	I^* (%)[b]
S32	[1000]:[10]:[0.2]:**[2]**	47	59.2	5.35	3.89	1.90	137
S33	[1000]:[10]:[0.2]:**[1]**	47	70.7	6.34	5.66	1.58	112
S34	[1000]:[10]:[0.2]:**[0.2]**	47	89.9	8.00	8.25	1.49	97
S35	[1000]:[10]:[0.2]:**[0.1]**	47	85.5	7.61	7.72	1.78	99
S36	[1000]:[10]:[0.2]:**[0.02]**	47	74.6	6.67	5.89	2.68	113

[a]*Determined by GPC.* [b]*Initiator efficiency (I*) =* $(M_{n,\,theo} / M_{n,\,exp})$*•100%.*

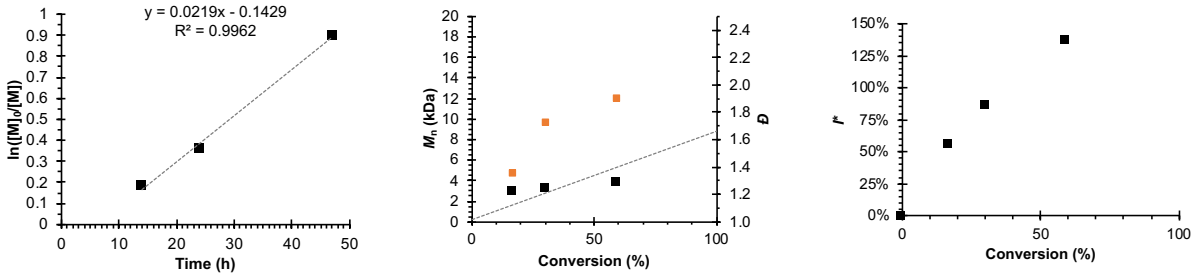

Figure 5.22. *O-ATRP of MA with* $\mathbf{5}^{\bullet+}$ *and LiBr. [MA]:[DBMM]:[*$\mathbf{5}^{\bullet+}$*]:[LiBr] = [1000]:[10]:[0.2]:[2]; 1 mL MA, 1 mL EtAc; irradiated in a white LED beaker. (Left) Pseudo-first-order kinetics plot. (Middle) Evolution of polymer molecular weight (black) and Đ (orange) as a function of monomer conversion; grey dashed line represents the theoretical molecular weight growth. (Right) Initiator efficiency as a function of monomer conversion.*

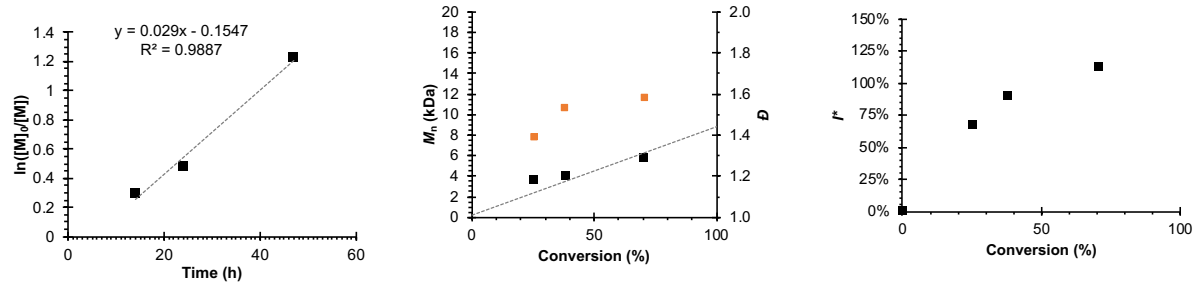

Figure 5.189. *O-ATRP of MA with* $\mathbf{5}^{\bullet+}$ *and LiBr. [MA]:[DBMM]:[*$\mathbf{5}^{\bullet+}$*]:[LiBr] = [1000]:[10]:[0.2]:[1]; 1 mL MA, 1 mL EtAc; irradiated in a white LED beaker. (Left) Pseudo-first-order kinetics plot. (Middle) Evolution of polymer molecular weight (black) and Đ (orange) as a function of monomer conversion; grey dashed line represents the theoretical molecular weight growth. (Right) Initiator efficiency as a function of monomer conversion.*

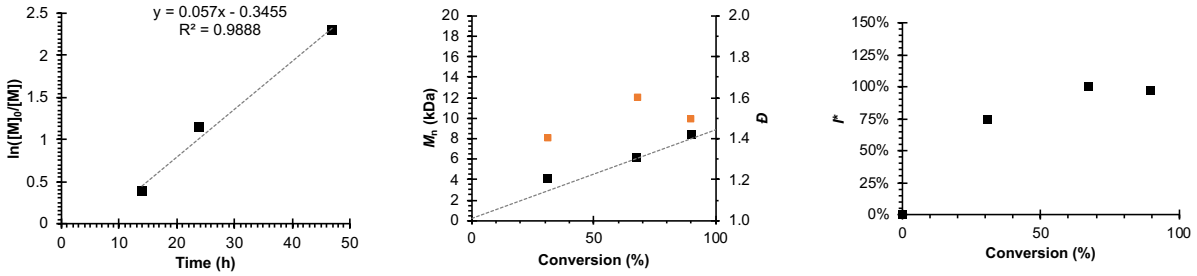

Figure 5.190. *O-ATRP of MA with* $\mathbf{5}^{\bullet+}$ *and LiBr. [MA]:[DBMM]:[*$\mathbf{5}^{\bullet+}$*]:[LiBr] = [1000]:[10]:[0.2]:[0.2]; 1 mL MA, 1 mL EtAc; irradiated in a white LED beaker. (Left) Pseudo-first-order kinetics plot. (Middle) Evolution of polymer molecular weight (black) and Đ (orange) as a function of monomer conversion; grey dashed line represents the theoretical molecular weight growth. (Right) Initiator efficiency as a function of monomer conversion.*

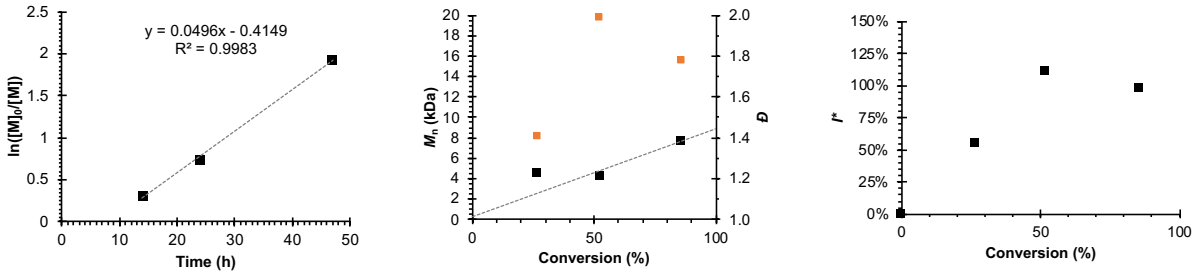

Figure 5.191. *O-ATRP of MA with* ***5***$^{\bullet+}$ *and LiBr. [MA]:[DBMM]:[****5***$^{\bullet+}$*]:[LiBr] = [1000]:[10]:[0.2]:[0.1]; 1 mL MA, 1 mL EtAc; irradiated in a white LED beaker. (Left) Pseudo-first-order kinetics plot. (Middle) Evolution of polymer molecular weight (black) and Đ (orange) as a function of monomer conversion; grey dashed line represents the theoretical molecular weight growth. (Right) Initiator efficiency as a function of monomer conversion.*

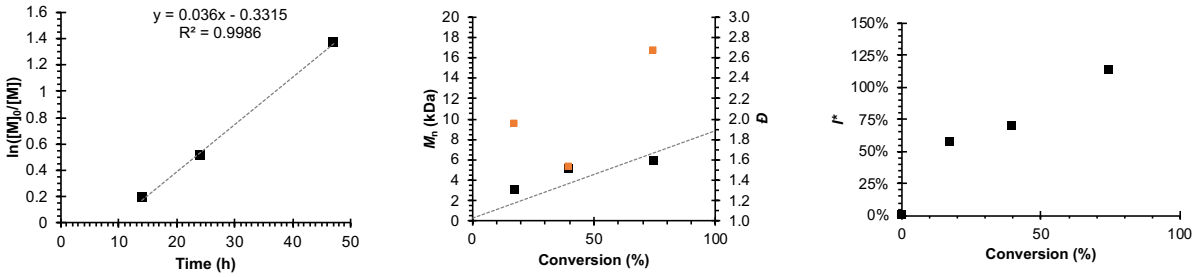

Figure 5.192. *O-ATRP of MA with* ***5***$^{\bullet+}$ *and LiBr. [MA]:[DBMM]:[****5***$^{\bullet+}$*]:[LiBr] = [1000]:[10]:[0.2]:[0.02]; 1 mL MA, 1 mL EtAc; irradiated in a white LED beaker. (Left) Pseudo-first-order kinetics plot. (Middle) Evolution of polymer molecular weight (black) and Đ (orange) as a function of monomer conversion; grey dashed line represents the theoretical molecular weight growth. (Right) Initiator efficiency as a function of monomer conversion.*

Acrylate Monomer Screen

Five acrylate monomers (Figure 5.193) with different substituents were investigated in O-ATRP using **5**$^{\bullet+}$. Figures 5.194 – 5.198 show the full data sets for each polymerization.

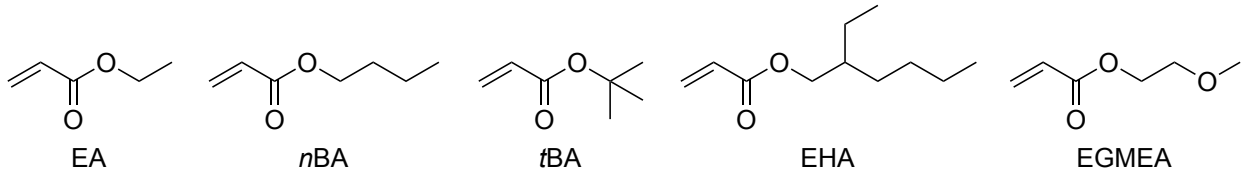

Figure 5.193. *Structures of acrylate monomers polymerized by O-ATRP using* ***5***$^{\bullet+}$.

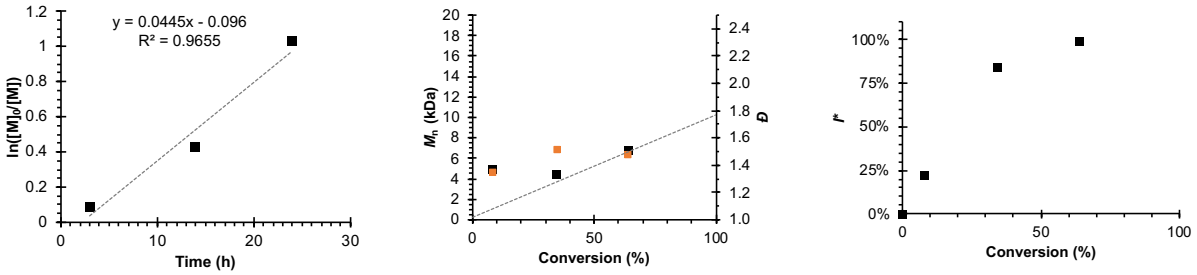

Figure 5.194. *O-ATRP of EA with* $\mathbf{5}^{\bullet+}$ *and LiBr. [EA]:[DBMM]:[*$\mathbf{5}^{\bullet+}$*]:[LiBr] = [1000]:[10]:[0.2]:[0.2]; 1.21 mL EA, 1 mL EtAc; irradiated in a white LED beaker. (Left) Pseudo-first-order kinetics plot. (Middle) Evolution of polymer molecular weight (black) and Đ (orange) as a function of monomer conversion; grey dashed line represents the theoretical molecular weight growth. (Right) Initiator efficiency as a function of monomer conversion.*

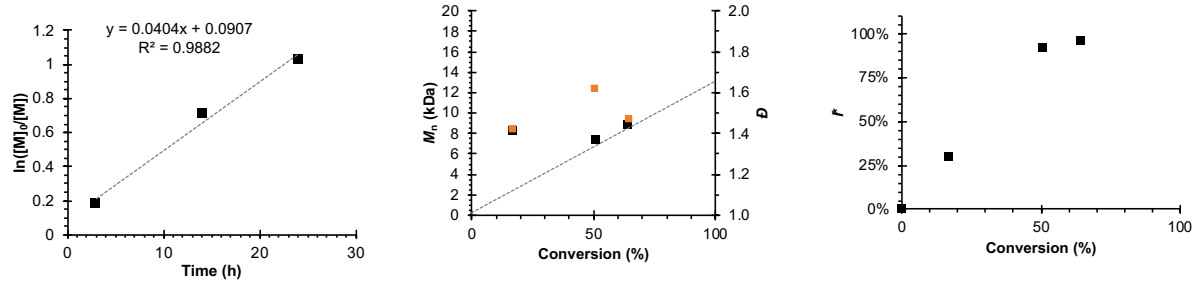

Figure 5.195. *O-ATRP of nBA with* $\mathbf{5}^{\bullet+}$ *and LiBr. [nBA]:[DBMM]:[*$\mathbf{5}^{\bullet+}$*]:[LiBr] = [1000]:[10]:[0.2]:[0.2]; 1.59 mL nBA, 1 mL EtAc; irradiated in a white LED beaker. (Left) Pseudo-first-order kinetics plot. (Middle) Evolution of polymer molecular weight (black) and Đ (orange) as a function of monomer conversion; grey dashed line represents the theoretical molecular weight growth. (Right) Initiator efficiency as a function of monomer conversion.*

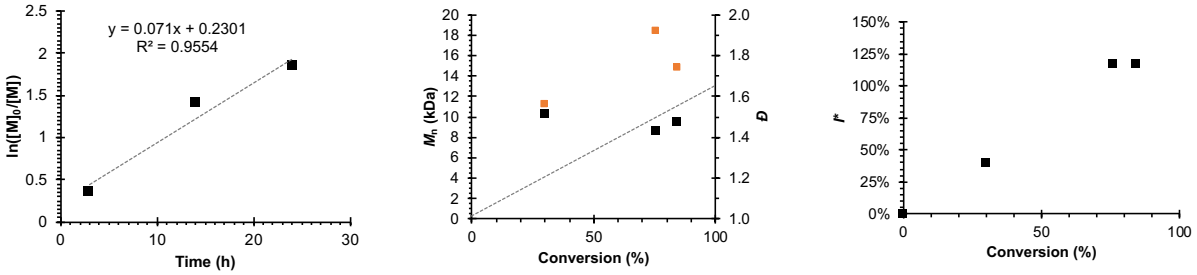

Figure 5.196. *O-ATRP of tBA with* $\mathbf{5}^{\bullet+}$ *and LiBr. [tBA]:[DBMM]:[*$\mathbf{5}^{\bullet+}$*]:[LiBr] = [1000]:[10]:[0.2]:[0.2]; 1.63 mL tBA, 1 mL EtAc; irradiated in a white LED beaker. (Left) Pseudo-first-order kinetics plot. (Middle) Evolution of polymer molecular weight (black) and Đ (orange) as a function of monomer conversion; grey dashed line represents the theoretical molecular weight growth. (Right) Initiator efficiency as a function of monomer conversion.*

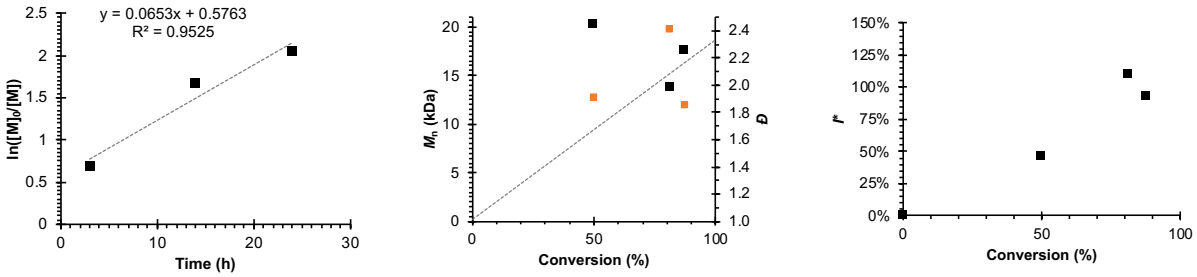

Figure 5.197. *O-ATRP of EHA with* $\mathbf{5}^{\bullet+}$ *and LiBr. [EHA]:[DBMM]:[*$\mathbf{5}^{\bullet+}$*]:[LiBr] = [1000]:[10]:[0.2]:[0.2]; 2.31 mL EHA, 1 mL EtAc; irradiated in a white LED beaker. (Left) Pseudo-first-order kinetics plot. (Middle) Evolution of polymer molecular weight (black) and Đ (orange) as a function of monomer conversion; grey dashed line represents the theoretical molecular weight growth. (Right) Initiator efficiency as a function of monomer conversion.*

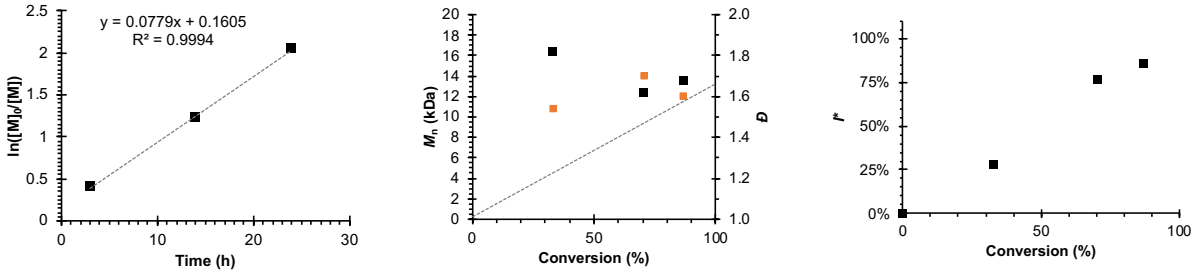

Figure 5.198. *O-ATRP of EGMEA with* $\mathbf{5}^{\bullet+}$ *and LiBr. [EGMEA]:[DBMM]:[*$\mathbf{5}^{\bullet+}$*]:[LiBr] = [1000]:[10]:[0.2]:[0.2]; 1.43 mL EGMEA, 1 mL EtAc; irradiated in a white LED beaker. (Left) Pseudo-first-order kinetics plot. (Middle) Evolution of polymer molecular weight (black) and Đ (orange) as a function of monomer conversion; grey dashed line represents the theoretical molecular weight growth. (Right) Initiator efficiency as a function of monomer conversion.*

Characterization of Poly(Methyl Acrylate) Macroinitiators

Isolated and dried pMA macroinitiators synthesized by O-ATRP with **5** or $\mathbf{5}^{\bullet+}$ were first characterized by GPC and ^{1}H NMR to verify their identity and determined their molecular weights. The consistency in the results for O-ATRP with $\mathbf{5}^{\bullet+}$ highlights the reproducibility of this method.

Table 5.22. *Characterization of pMA macroinitiators synthesized by O-ATRP with* ***5*** *and* ***5***$^{\bullet+}$.

Entry	5 or 5$^{\bullet+}$	Time (h)	Conv. (%)[a]	$M_{n,\,theo}$ (kDa)	$M_{n,\,exp}$ (kDa)[b]	$Đ^{b}$	I^{*} (%)[c]
S37	**5**	0.5	21.9	2.14	24.2	1.60	9
S38	**5**$^{\bullet+}$	14	29.6	2.80	4.02	1.34	70
S39	**5**	0.5	33.3	3.12	15.6	1.86	20
S40	**5**$^{\bullet+}$	14	33.3	3.12	4.36	1.34	72
S41	**5**	0.5	32.0	3.01	18.7	1.58	16
S42	**5**$^{\bullet+}$	14	28.1	2.67	3.93	1.36	68

[a]*Determined by taking an aliquot at the end of the polymerization prior to drying the product polymer.* [b]*Determined by GPC.* [c]*Initiator efficiency (I*) =* $(M_{n,\,theo} / M_{n,\,exp})\bullet 100\%$.

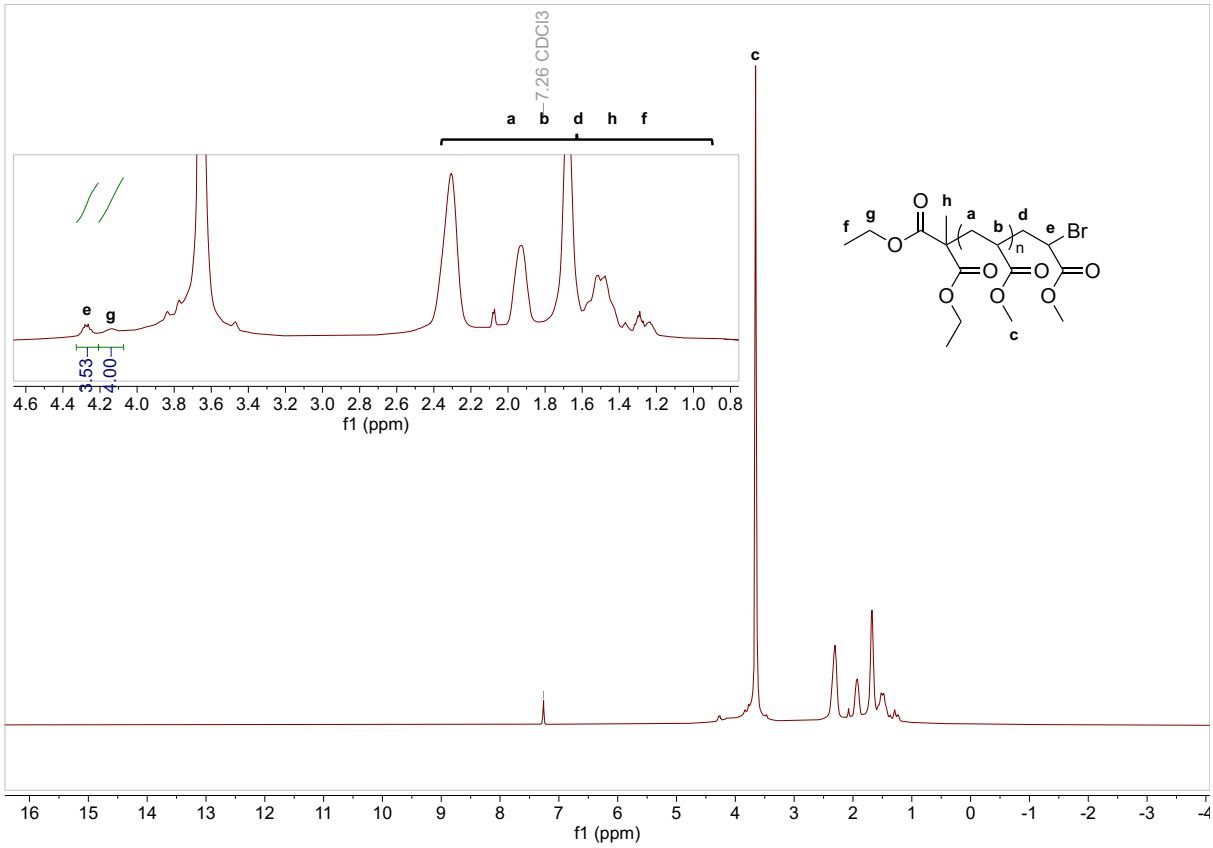

Figure 5.199. *[1]H NMR of pMA macroinitiator synthesized by O-ATRP using* ***5****.*

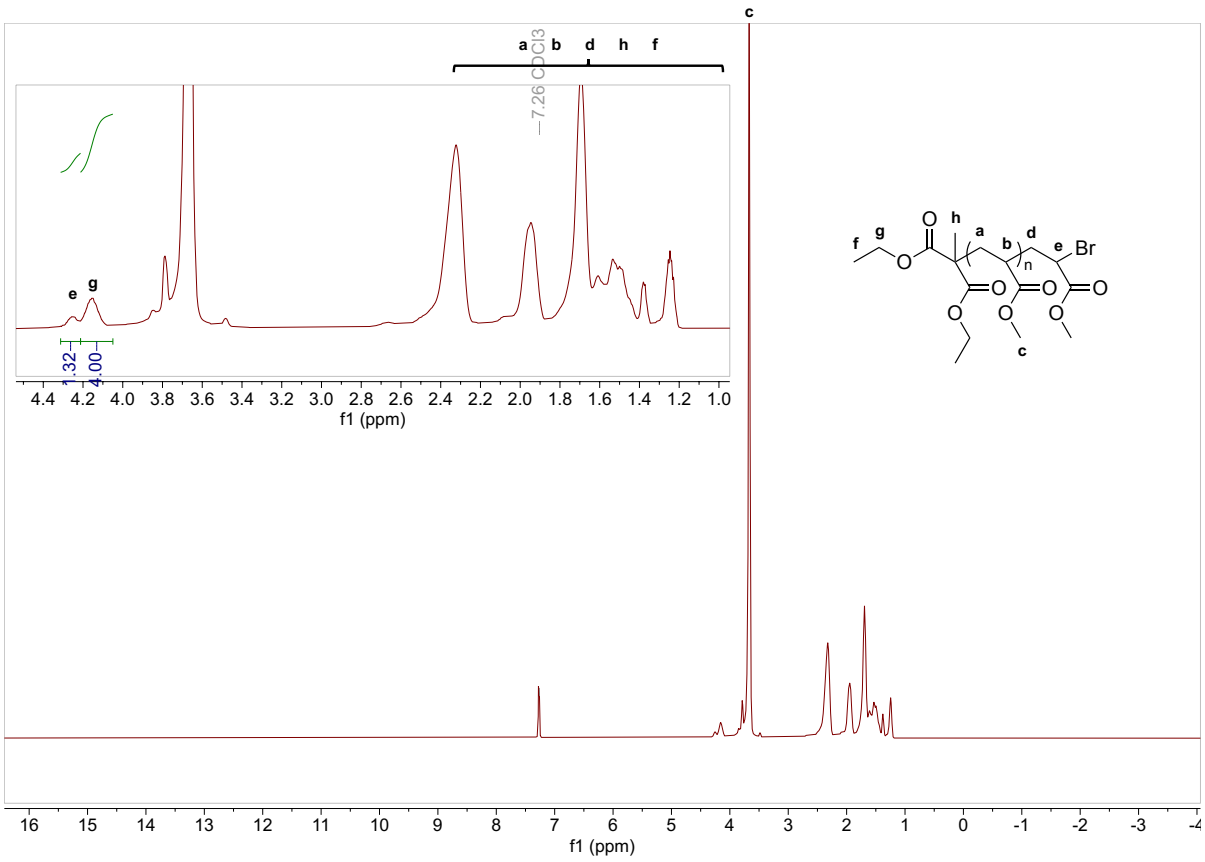

Figure 5.200. *^{1}H NMR of pMA macroinitiator synthesized by O-ATRP using* ***5***$^{\bullet+}$.

To determine the end-groups present in each of the macroinitiators, matrix assisted laser desorption ionization time of flight mass spectrometry (MALDI-TOF-MS) was performed. Samples were prepared according to the following modified literature procedure:[62]

4-hydroxybenzilidenemalononitrile was used as the matrix and prepared in THF as a 20 mg/mL solution. Sodium trifluoroacetate (NaTFA) was used as a cationic complexing agent and prepared in THF as a 1 mg/mL solution. Poly(methyl acrylate) macroinitiators were dissolved in THF at a concentration of 2 mg/mL. The three solutions were mixed in a 10:5:5 volume ratio of matrix to NaTFA to pMA, after which 0.5 µL was spotted onto a MALDI spot plate.

To determine the mass of the end-groups – and thereby estimate the end-group structure – a plot of m/z versus number of repeat units was generated. The data was then fit with a linear trend

line and extrapolated to zero repeat units, at which the y-intercept should correspond to the mass of the end-groups present on the polymer chains.

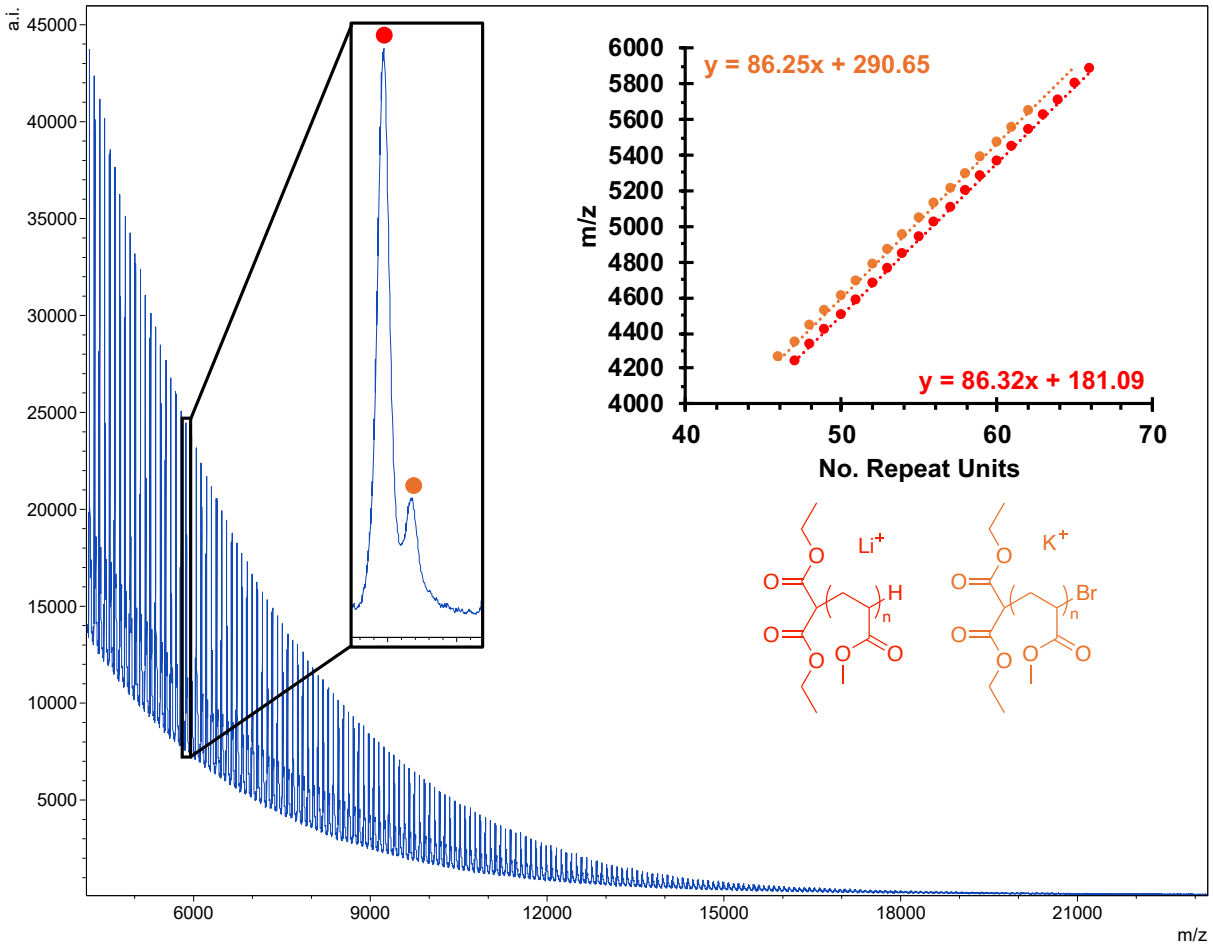

Figure 5.201. *MALDI-TOF mass spectrum of pMA synthesized by O-ATRP using* ***5****. Figure insets show a zoomed in view of the peak pattern (left), a plot used for end-group analysis (top right), and polymer structures determined by this method (bottom right). This sample was run in linear mode due to the higher molecular weight of the polymer ($M_{n,GPC}$ = 15.6 kDa).*

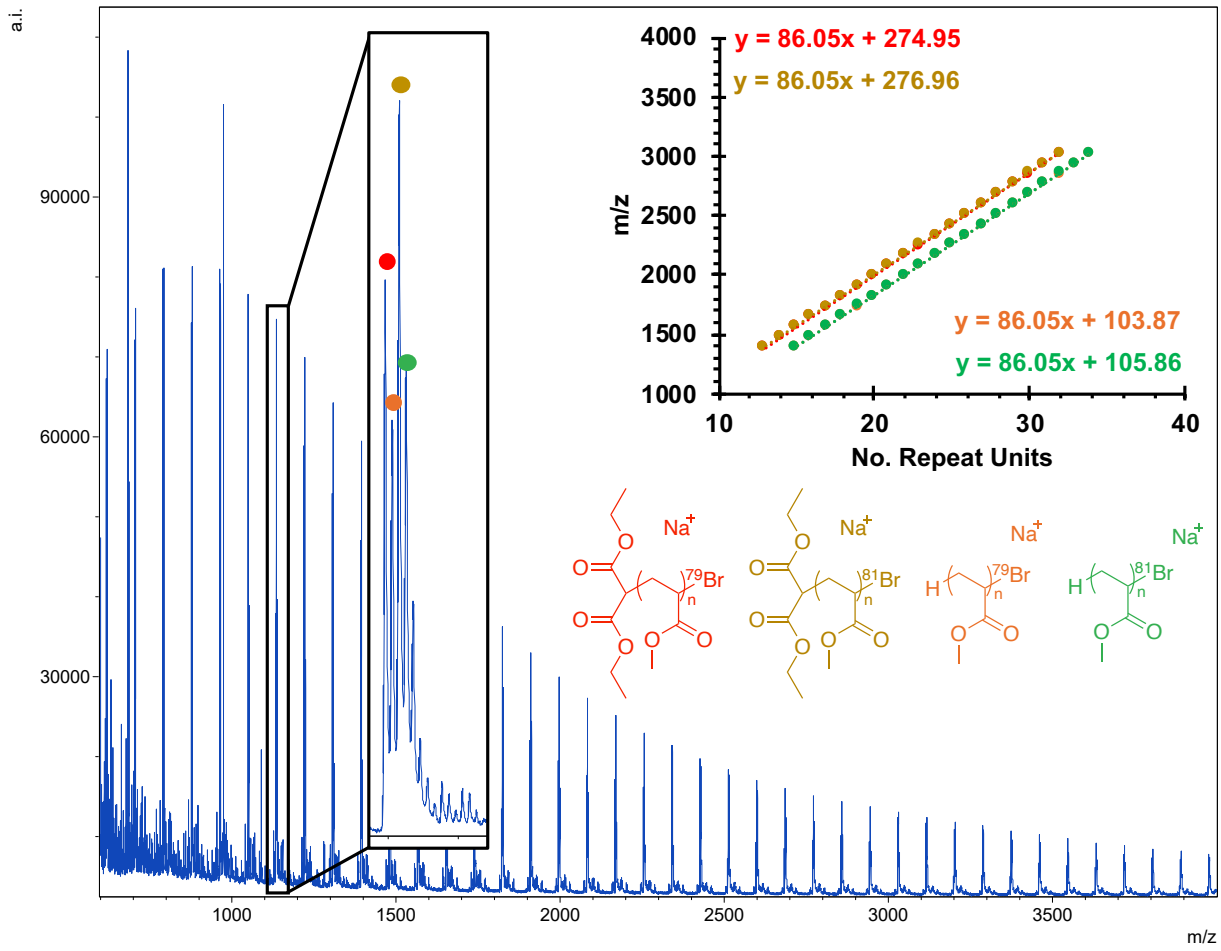

Figure 5.202. *MALDI-TOF mass spectrum of pMA synthesized by O-ATRP using* ***5****•+. Figure insets show a zoomed in view of the peak pattern (left), a plot used for end-group analysis (top right), and polymer structures determined by this method (bottom right). This sample was run in reflector mode to achieve better sensitivity, which was possible due to the low molecular weight of the polymer sample ($M_{n,GPC}$ = 4.36 kDa).*

Chain Extensions and Block Copolymer Synthesis

The macroinitiators synthesized in Entries S39 – S42 of Table 5.22 were employed in the synthesis of block copolymers with MA and *t*BA. Similar to before, the polymers were isolated and dried prior to being characterized by GPC and ^{1}H NMR.

Table 5.23. *Characterization of block copolymers synthesized by O-ATRP using* ***5*** *or* ***5***$^{\bullet+}$.

Entry	Copolymer	5 or 5$^{\bullet+}$	Conv. (%)[a]	$M_{n,\,theo}$ (kDa)	$M_{n,\,exp}$ (kDa)[b]	$Đ^{b}$	I^{*} (%)[c]
S43	pMA-*b*-pMA	**5**	26.3	47.5	16.8	1.91	283
S44		**5**$^{\bullet+}$	61.7	10.2	7.80	1.30	130
S45	pMA-*b*-p*t*BA	**5**	47.6	44.7	15.1	2.69	296
S46		**5**$^{\bullet+}$	62.5	11.0	13.1	1.36	84

[a]*Determined by taking an aliquot at the end of the polymerization prior to drying the product polymer.* [b]*Determined by GPC.* [c]*Initiator efficiency (I*) =* $(M_{n,\,theo} / M_{n,\,exp})\bullet 100\%$.

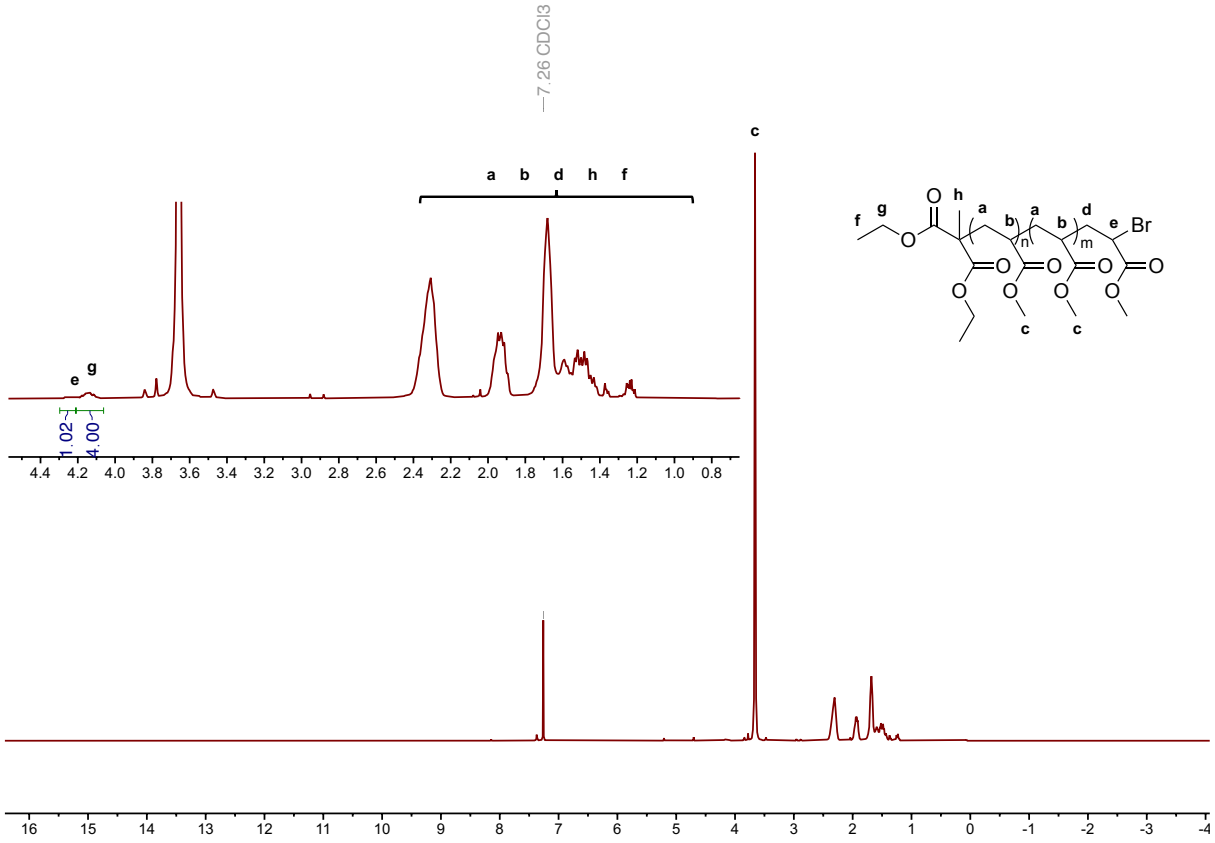

Figure 5.203. *^{1}H NMR spectrum of pMA-b-pMA synthesized by O-ATRP using* ***5****.*

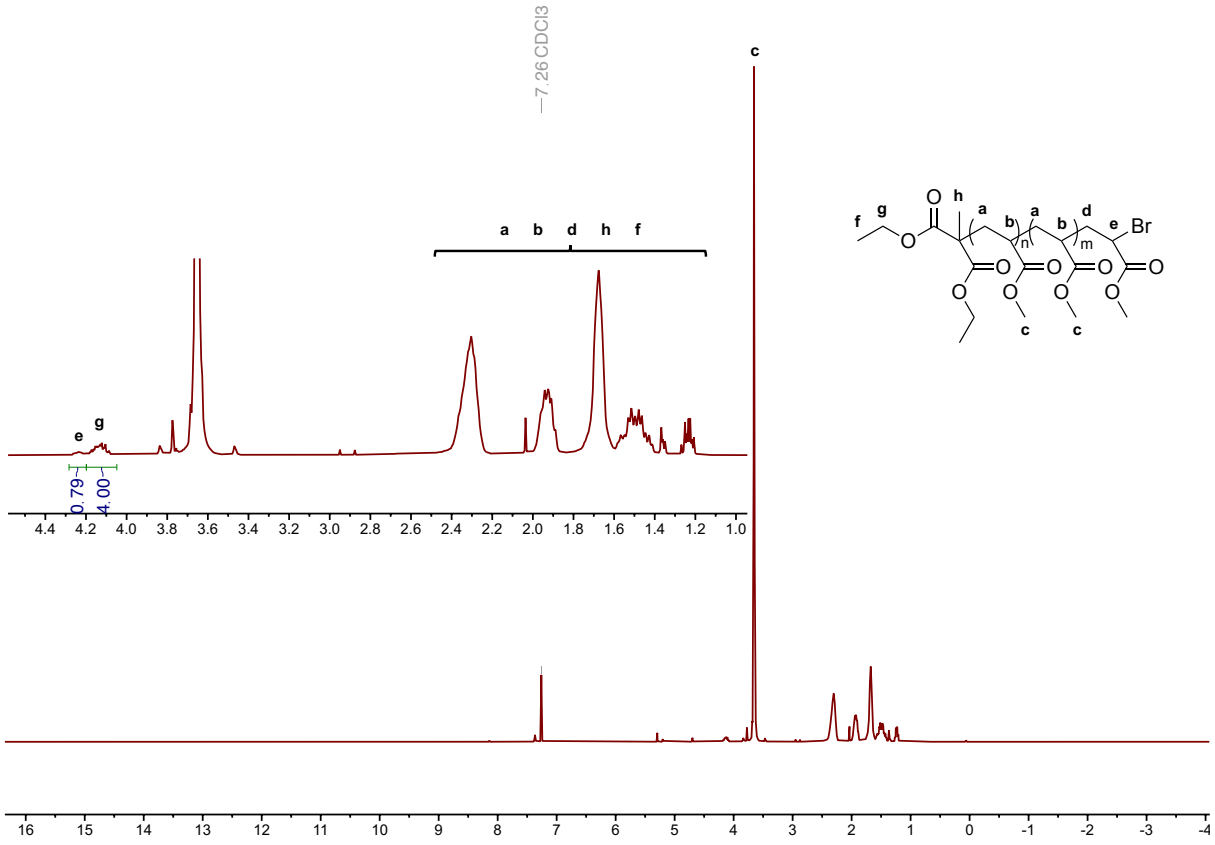

Figure 5.204. *^{1}H NMR spectrum of pMA-b-pMA synthesized by O-ATRP using* ***5***$^{\bullet+}$.

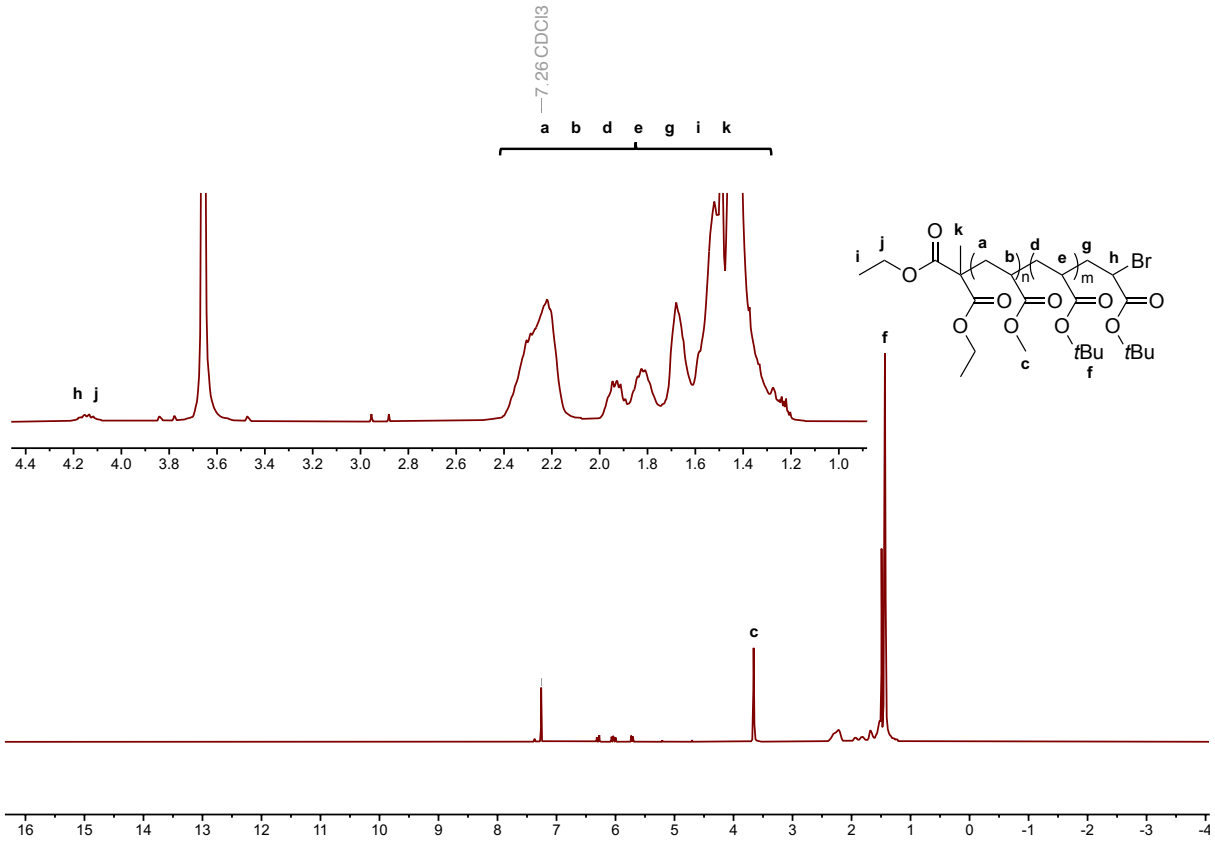

Figure 5.205. *^{1}H NMR spectrum of pMA-b-ptBA synthesized by O-ATRP using* ***5***

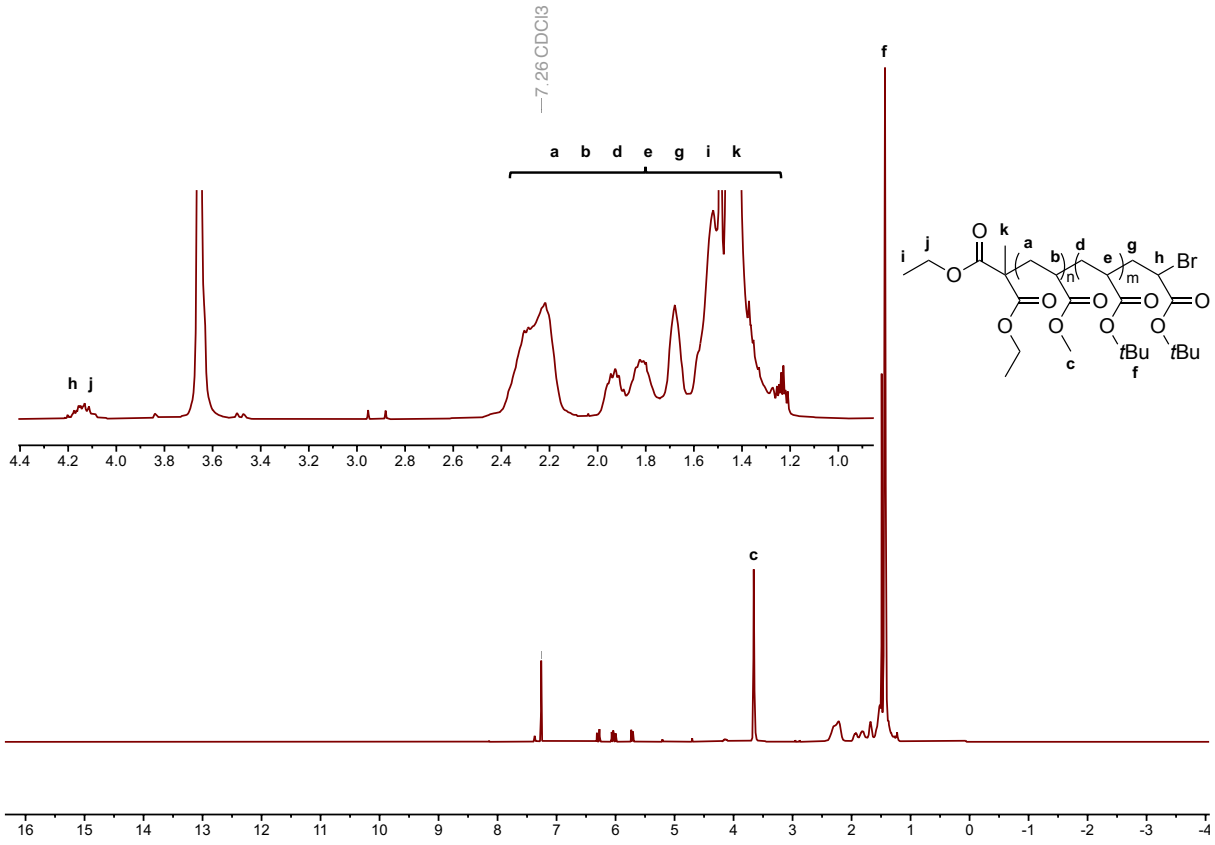

Figure 5.206. *^{1}H NMR spectrum of pMA-b-ptBA synthesized by O-ATRP using* ***5***$^{\bullet+}$.

Molecular Coordinates for Substrate Oxidation Calculations

Structures of the substrates and corresponding radical cations were optimized at the B3LYP/6-31+G** level of theory in CPCM-acetonitrile. All coordinates are reported as XYZ Cartesian coordinates. Reported free energies are stated in Hartrees units. Oxidation potentials are reported in V vs. SCE. All energies reported were calculated using the GAUSSIAN 16 version C.01 computational chemistry package.

Ethyl Acetate

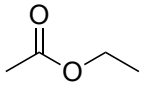

G[substrate] = -307.65407 hartrees

G[radical cation] = -307.362622 hartrees

E_{ox} = 3.33 V vs. SCE

Substrate Molecular Coordinates:

C -3.49649300 0.81576300 -0.62357600

O -3.16887100 1.70980200 -1.38895700

C -4.61732800 0.90121800 0.37977100

H -5.11931300 1.86425600 0.29080300

H -5.33357100 0.09138100 0.21366500

H -4.21840800 0.78610300 1.39226700

O -2.88047000 -0.37906500 -0.57943200

C -1.76939700 -0.59348500 -1.49635500

C -1.24449900 -1.99578300 -1.26087400

H -1.00870500 0.16701700 -1.29935900

H -2.13559100 -0.45964000 -2.51800300

H -0.40660100 -2.18638000 -1.93889200

H -0.88800400 -2.11613400 -0.23337200

H -2.01882700 -2.74433800 -1.45430200

Radical Cation Molecular Coordinates:

C -3.05654800 0.71769100 0.33926800

O -2.86327700 1.36068300 1.41779800

C -4.36171400 1.06091000 -0.31937000

H -4.13922400 1.41572700 -1.33146600

H -4.96746300 0.14814500 -0.34082000

H -4.89304800 1.83762400 0.23294200

O -2.17894300 -0.11264400 -0.05693300

C -2.34607900 -0.89707000 -1.33767400

C -1.17408600 -1.84246000 -1.40057500

H -2.34800000 -0.16143500 -2.14197700

H -3.30544900 -1.40897700 -1.26755100

H -1.26678600 -2.42024500 -2.32581800

H -0.22657300 -1.29955300 -1.42649400

H -1.17888900 -2.53768100 -0.55794700

Ortho-Phenylenediamine

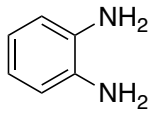

G[substrate] = -342.898917 hartrees

G[radical cation] = -342.714648 hartrees

E_{ox} = 0.42 V vs. SCE

Substrate Molecular Coordinates:

C -1.93358100 -0.14969900 -0.25095700

C -0.55537300 -0.10655600 -0.49123200

C 0.18643100 1.05437800 -0.24022700

C -0.47896000 2.20975800 0.23972300

C -1.85514600 2.15033600 0.49196300

C -2.58385100 0.97948300 0.25300300

H -2.48638500 -1.06329800 -0.44870300

H -0.04041500 -0.98736800 -0.86784500

H -2.35867000 3.03776200 0.86846400

H -3.65127800 0.95952900 0.45190800

N 1.56602900 1.13338900 -0.51561900

H 2.09485500 1.63908000 0.18914800

H 1.99574000 0.23132200 -0.68609800

N 0.28161800 3.36373900 0.51388600

H 0.98243800 3.56833200 -0.19255200

H -0.28316900 4.18755800 0.68639200

Radical Cation Molecular Coordinates:

C -1.74848100 -0.11015600 -0.08937500

C -0.37912700 -0.11935100 -0.16981500

C 0.36430400 1.09089200 -0.07401600

C -0.36082800 2.34617500 0.07117300

C -1.78080800 2.30753600 0.16762900

C -2.45711100 1.11680300 0.08860900

H -2.29920200 -1.04200200 -0.15543400

H 0.16550900 -1.04931200 -0.29487800

H -2.31418100 3.24406800 0.29335400

H -3.53936000 1.10533100 0.15621600

N 1.70662000 1.05188700 -0.12076700

H 2.30678500 1.85168300 0.01741300

H 2.18187200 0.16385300 -0.21811400

N 0.27704500 3.52754800 0.11595300

H 1.27128400 3.64335200 -0.01129700

H -0.25176200 4.38422100 0.21653800

N,N-Dimethylaniline

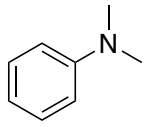

G[substrate] = -366.109699 hartrees

G[radical cation] = -365.91991 hartrees

E_{ox} = 0.57 V vs. SCE

Substrate Molecular Coordinates:

C -1.63291300 0.00208000 0.82350500

C -0.24414800 -0.13094400 0.85916900

C 0.59050400 0.71223300 0.08225400

C -0.04745200 1.66745100 -0.74933600

C -1.43783000 1.78614900 -0.77195600

C -2.24944300 0.96111100 0.01332200

H -2.23709000 -0.66139200 1.43697900

H 0.18726100 -0.89277700 1.49639400

H 0.53882000 2.32374400 -1.38031000

H -1.88768700 2.53369200 -1.42032900

H -3.33046000 1.05707600 -0.01160300

N 1.97643000 0.61799600 0.14607300

C 2.57789200 -0.54188500 0.79439900

H 2.31614200 -1.48985000 0.29792600

H 3.66282800 -0.43307900 0.77766600

H 2.27009100 -0.60887800 1.84246400

C 2.77914200 1.30065700 -0.86240500

H 2.60114700 2.38030400 -0.84122100

H 3.83499200 1.13816200 -0.64339600

H 2.57660300 0.93881200 -1.88303100

Radical Cation Molecular Coordinates:

C -1.66641700 -0.02790200 0.72375300

C -0.30254700 -0.24566300 0.71344100

C 0.56027800 0.64744700 0.00029400

C -0.01761500 1.76216900 -0.68802400

C -1.38343800 1.96477900 -0.65062100

C -2.21948700 1.07554500 0.04878000

H -2.31298800 -0.71939100 1.25267200

H 0.10100200 -1.11334200 1.21764500

H 0.61077500 2.47054300 -1.21048500

H -1.80973500 2.82129200 -1.16119500

H -3.29142700 1.24076800 0.06746900

N 1.90373500 0.43905300 -0.02198800

C 2.55655000 -0.55269600 0.84179900

H 2.53739100 -1.53513300 0.35726900

H 3.59317700 -0.24974900 0.98289500

H 2.06633000 -0.60525400 1.81185200

C 2.80242900 1.18794700 -0.90842100

H 2.30417600 1.44861600 -1.83910200

H 3.15001100 2.09476400 -0.40099500

H 3.66263000 0.55687400 -1.13047100

N-Methylaniline

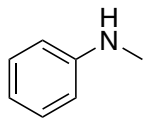

G[substrate] = -326.83101 hartrees

G[radical cation] = -326.636905 hartrees

E_{ox} = 0.68 V vs. SCE

Substrate Molecular Coordinates:

C -1.65034600 -0.19829600 -0.63883800

C -0.28705200 -0.45054300 -0.50979400

C 0.56640000 0.48656800 0.11731800

C -0.00285800 1.67776800 0.61500200

C -1.37367100 1.91907200 0.47424500

C -2.21068500 0.99099800 -0.15040000

H -2.28179200 -0.93774900 -1.12434800

H 0.13332600 -1.37590800 -0.89670600

H 0.61914600 2.41655400 1.10813500

H -1.78632000 2.84559900 0.86500300

H -3.27396600 1.18431300 -0.25293000

N 1.92985000 0.23140600 0.19230300

H 2.17987700 -0.74156000 0.08008100

C 2.80617700 0.98524300 1.07633200

H 2.46961200 0.97610000 2.12433500

H 3.80505500 0.54784900 1.02833300

H 2.88248700 2.02841000 0.75175800

Radical Cation Molecular Coordinates:

C -1.53597600 -0.20740700 0.22654100

C -0.17663400 -0.22060300 0.45625400

C 0.57552700 0.98313200 0.26823400

C -0.08937100 2.18160700 -0.15781900

C -1.44928100 2.16597800 -0.37961600

C -2.18250900 0.97677300 -0.18990500

H -2.11359100 -1.11425500 0.36731600

H 0.31826400 -1.12940800 0.77546200

H 0.49015600 3.08849200 -0.29820600

H -1.95568800 3.06960500 -0.69981400

H -3.25292900 0.97044400 -0.36537300

N 1.89940800 1.02549200 0.48270700

H 2.36015800 1.91791300 0.32758200

C 2.74624300 -0.07695100 0.92799200

H 2.71021100 -0.89823600 0.20697900

H 3.76723000 0.29039300 1.00584500

H 2.41402300 -0.43714700 1.90564800

Aniline

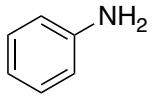

G[substrate] = -287.540711 hartrees

G[radical cation] = -287.348876 hartrees

E_{ox} = 0.62 V vs. SCE

Substrate Molecular Coordinates:

C -1.46447600 -0.25103400 0.00006800

C -0.06639800 -0.25676400 0.00063500

C 0.65122300 0.94990900 0.00011900

C -0.05451600 2.15894200 -0.00095200

C -1.45421300 2.16650700 -0.00151400

C -2.16317300 0.96170200 -0.00102100

H -2.00692400 -1.19234200 0.00046900

H 0.47512700 -1.19935700 0.00146500

H 0.50389600 3.09024200 -0.00133800

H -1.98770400 3.11281400 -0.00234600

H -3.24925600 0.96613700 -0.00146100

N 2.09664500 0.99314100 0.00068900

H 2.46518100 0.50370500 0.81410900

H 2.46583800 0.50321100 -0.81213600

Radical Cation Molecular Coordinates:

C -1.49738800 -0.27816900 -0.12246000

C -0.12385000 -0.35368600 -0.10870500

C 0.64587100 0.85370400 0.00970000

C -0.01759600 2.12361700 0.11412500

C -1.39253600 2.16820400 0.09703700

C -2.14276700 0.97572000 -0.02100400

H -2.08891100 -1.18223100 -0.21244500

H 0.39060500 -1.30551100 -0.18739500

H 0.57430600 3.02802500 0.20585400

H -1.90398000 3.12098900 0.17463000

H -3.22630900 1.02340700 -0.03382200

N 1.97718700 0.79401000 0.02291200

H 2.54732800 1.62925900 0.10484800

H 2.46929100 -0.09052500 -0.04648900

3-Methylindole

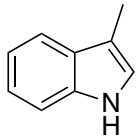

G[substrate] = -403.048926 hartrees

G[radical cation] = -402.85022 hartrees

E_{ox} = 0.81 V vs. SCE

Substrate Molecular Coordinates:

C 1.06942500 -0.65384700 0.00278900

C -0.35674700 -0.65360600 0.00457400

C -1.10407100 0.53206600 0.00247400

C -0.40230300 1.73604700 -0.00149500

C 1.01132300 1.76072200 -0.00320800

C 1.74982900 0.57985200 -0.00101900

C 1.50028100 -2.03185200 0.00548100

H -2.19024600 0.51392000 0.00388100

H -0.95218100 2.67286800 -0.00321200

H 1.52582100 2.71754900 -0.00626900

H 2.83619700 0.61092700 -0.00239600

N -0.76419700 -1.97024400 0.00873100

C 0.35216200 -2.79003100 0.00903500

H 0.23872000 -3.86569400 0.01176900

C 2.91554800 -2.53101400 0.00486700

H 3.46711300 -2.18431600 -0.87794900

H 3.46928700 -2.18043200 0.88479900

H 2.94534500 -3.62476300 0.00724400

H -1.72044100 -2.29121800 0.00959700

Radical Cation Molecular Coordinates:

C 1.07938900 -0.64199600 0.00247200

C -0.34117600 -0.64530800 0.00448100

C -1.09554600 0.50735500 0.00259900

C -0.38464100 1.73182800 -0.00138400

C 1.01410000 1.77094600 -0.00338400

C 1.76451900 0.58920800 -0.00144500

C 1.51409900 -2.00049300 0.00496200

H -2.17990600 0.49026800 0.00428100

H -0.94611900 2.66005200 -0.00289900

H 1.52201800 2.72899000 -0.00651300

H 2.84881900 0.62204100 -0.00307500

N -0.74870200 -1.99373100 0.00902100

C 0.31754800 -2.79004600 0.00920400

H 0.22506300 -3.86734700 0.01229800

C 2.90081700 -2.53131900 0.00445500

H 3.44902900 -2.17278800 -0.87509300

H 3.44900500 -2.17385800 0.88452900

H 2.91331100 -3.62233200 0.00396900

H -1.71076300 -2.31453600 0.01121400

1-Methylindole

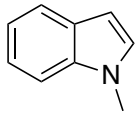

G[substrate] = -403.039053 hartrees

G[radical cation] = -402.835692 hartrees

E_{ox} = 0.94 V vs. SCE

Substrate Molecular Coordinates:

C 1.06459100 -0.67309000 0.00433800

C -0.36317900 -0.67200400 0.00275800

C -1.10938700 0.51579200 -0.00101600

C -0.40559200 1.71865700 -0.00333000

C 1.00804400 1.74089200 -0.00178100

C 1.74569300 0.55996500 0.00208600

C 1.47462900 -2.04988700 0.00801600

H -2.19505500 0.50446700 -0.00217800

H -0.95373900 2.65640500 -0.00629700

H 1.52368100 2.69707400 -0.00362500

H 2.83220500 0.58791000 0.00319600

H 2.48608000 -2.43203300 0.00985300

N -0.78848300 -1.98638300 0.00557900

C 0.32500000 -2.80560500 0.00869800

H 0.20241500 -3.88023200 0.01120700

C -2.17470200 -2.42668800 0.00556100

H -2.69821000 -2.06233400 0.89530500

H -2.69728000 -2.06478900 -0.88571100

H -2.19882500 -3.51693000 0.00703400

Radical Cation Molecular Coordinates:

C 1.06070900 -0.66264600 0.00384300

C -0.36292500 -0.66138100 0.00303200

C -1.10605100 0.49604900 -0.00011600

C -0.38416800 1.71946700 -0.00255000

C 1.01313100 1.75155000 -0.00179400

C 1.75636400 0.56456500 0.00133900

C 1.47056500 -2.01444400 0.00753800

H -2.19012500 0.49743900 -0.00088100

H -0.94150600 2.65005100 -0.00509300

H 1.52602500 2.70679600 -0.00364300

H 2.84106800 0.58386400 0.00200500

H 2.47773600 -2.40669000 0.00917800

N -0.78947100 -2.01386700 0.00558900

C 0.28414800 -2.80342500 0.00840800

H 0.19230900 -3.88060900 0.01105200

C -2.18523500 -2.44786500 0.00545500

H -2.68586600 -2.06342500 0.89667700

H -2.68428300 -2.06817400 -0.88868900

H -2.21453800 -3.53606600 0.00834000

Indole

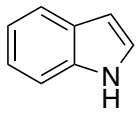

G[substrate] = -363.753167 hartrees

G[radical cation] = -363.545851 hartrees

E_{ox} = 1.04 V vs. SCE

Substrate Molecular Coordinates:

C 1.06537600 -0.66652400 0.00463700

C -0.36120100 -0.65902200 0.00498100

C -1.10414300 0.52983200 0.00120700

C -0.39703200 1.72978000 -0.00311000

C 1.01731500 1.74748200 -0.00348400

C 1.75112500 0.56496000 0.00043700

C 1.47411600 -2.04593700 0.00892700

H -2.19027800 0.51606100 0.00157500

H -0.94182600 2.66943900 -0.00615800

H 1.53552900 2.70222000 -0.00686000

H 2.83763400 0.58914000 0.00008300

H 2.48615000 -2.42658200 0.00980900

H -1.73661600 -2.28766700 0.01041600

N -0.77736100 -1.97497700 0.00973900

C 0.32714400 -2.80426300 0.01188400

H 0.20249100 -3.87793600 0.01561000

Radical Cation Molecular Coordinates:

C 1.06342200 -0.66074300 0.00429800

C -0.36306300 -0.65378700 0.00502800

C -1.10251800 0.50492700 0.00172800

C -0.37563900 1.72635600 -0.00266400

C 1.02403700 1.75655300 -0.00359200

C 1.76328200 0.57085500 -0.00017300

C 1.47370300 -2.00779000 0.00885000

H -2.18694900 0.50357500 0.00234300

H -0.93032300 2.65857000 -0.00541200

H 1.53734600 2.71141600 -0.00697100

H 2.84796400 0.58676500 -0.00076500

H 2.48117900 -2.39889500 0.00980900

H -1.74105600 -2.31543200 0.01048600

N -0.77747000 -1.99919500 0.00937000

C 0.28633100 -2.80039700 0.01179000

H 0.18817600 -3.87677200 0.01556600

1,2-Dimethoxybenzene

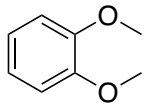

G[substrate] = -461.195583 hartrees

G[radical cation] = -460.984889 hartrees

E_{ox} = 1.14 V vs. SCE

Substrate Molecular Coordinates:

C -0.70179400 0.15736400 -0.07795600

C 0.68810600 0.14181800 0.01168500

C 1.39982700 1.35477500 0.16608500

C 0.69098300 2.56174300 0.21145300

C -0.70714000 2.56220800 0.11658300

C -1.40885300 1.36540500 -0.02386500

H -1.21942000 -0.79115100 -0.18637400

H 1.21650400 3.50197100 0.32813400

H -1.23870900 3.50826600 0.15732100

H -2.49209000 1.36445000 -0.09326300

O 1.35109500 -1.06908900 0.01857300

O 2.75675900 1.24754400 0.27155100

C 3.52387600 2.44379900 0.43415300

H 4.56304300 2.12088500 0.49642700

H 3.39883300 3.11348500 -0.42385000

H 3.24759600 2.96835400 1.35546500

C 2.05766700 -1.38632000 -1.19462900

H 2.52161900 -2.36051400 -1.03163400

H 1.35880600 -1.44910100 -2.03693900

H 2.82964900 -0.64047700 -1.40541400

Radical Cation Molecular Coordinates:

C -0.91947000 0.28516400 -0.33064900

C 0.49620700 0.19360700 -0.39641500

C 1.30040600 1.36083200 -0.04044600

C 0.65195800 2.54678100 0.35413300

C -0.72725000 2.59301200 0.40310600

C -1.51894700 1.45520200 0.05905400

H -1.49164200 -0.59542600 -0.59847500

H 1.23569500 3.41834700 0.61875900

H -1.21901800 3.51008800 0.70846200

H -2.59981500 1.52293700 0.10786200

O 0.95996500 -0.97433200 -0.78359200

O 2.60972700 1.20872300 -0.11776300

C 3.50671100 2.30138600 0.21018600

H 4.50398400 1.89488600 0.06162500

H 3.32800800 3.13919800 -0.46654600

H 3.36276600 2.59678500 1.25123000

C 2.35479000 -1.35528100 -0.95292500

H 2.87916100 -1.27391600 -0.00140400

H 2.30169700 -2.38937400 -1.28486400

H 2.82142300 -0.72320500 -1.70783000

N-Methylacetanilide

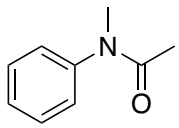

G[substrate] = -479.470051 hartrees

G[radical cation] = -479.24099 hartrees

E_{ox} = 1.63 V vs. SCE

Substrate Molecular Coordinates:

C -0.28174900 0.46481700 -0.09747800

C 1.09692700 0.64789500 0.06370500

C 1.61246900 1.92890600 0.29142900

C 0.75022500 3.02863300 0.33665200

C -0.62623900 2.84904000 0.16766800

C -1.14073700 1.56573800 -0.04716100

H -0.67173200 -0.53421600 -0.26814400

H 2.68163800 2.05954700 0.42911200

H 1.15412200 4.02201300 0.50753700

H -1.29484400 3.70383400 0.20458400

H -2.20890200 1.42129600 -0.17859200

N 1.97550600 -0.49246300 0.04446400

C 2.12316700 -1.23202800 1.30385300

H 2.56730400 -2.20398800 1.09358500

H 2.76684700 -0.68773200 2.00501600

H 1.13968400 -1.36592400 1.75955900

C 2.75353400 -0.81705500 -1.03294600

O 3.58327300 -1.73884100 -0.98032200

C 2.56709100 -0.01087400 -2.30498700

H 1.51897200 0.21734300 -2.50977700

H 3.10558900 0.93977000 -2.22979400

H 2.98957200 -0.58188100 -3.13244000

Radical Cation Molecular Coordinates:

C 0.01960300 0.79676300 -0.76893700

C 1.13718100 0.73339700 0.12878100

C 1.30627900 1.76944600 1.10547800

C 0.42324200 2.82635900 1.14529000

C -0.66415600 2.88164900 0.24853800

C -0.85974000 1.85515000 -0.69781800

H -0.17259300 -0.01329100 -1.45992900

H 2.15368700 1.74790100 1.77774100

H 0.57226400 3.62357300 1.86468000

H -1.35709500 3.71503700 0.29170000

H -1.71648400 1.88636900 -1.36122700

N 2.00199600 -0.31880900 0.09584600

C 2.84633000 -0.65181100 1.26010500

H 3.12514400 -1.69928700 1.17279500

H 3.74973000 -0.03445200 1.25055400

H 2.28721800 -0.49481900 2.18037400

C 2.18312500 -1.18967800 -1.07815900

O 2.44397500 -2.35224500 -0.87546300

C 2.16047800 -0.56479900 -2.44709400

H 1.33400800 -0.98184900 -3.03010200

H 2.09940500 0.52147300 -2.43902500

H 3.08811900 -0.87224800 -2.93860400

N,N-Dimethylacetamide

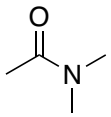

G[substrate] = -287.767482 hartrees

G[radical cation] = -287.525873 hartrees

E_{ox} = 1.98 V vs. SCE

Substrate Molecular Coordinates:

C -4.39671100 1.26107200 -0.42581700

H -4.78809800 2.21429000 -0.79477700

H -4.04589900 0.68542600 -1.28809100

H -5.20533400 0.71301500 0.05739600

C -3.29520100 1.46406200 0.60264000

O -3.43728200 1.02651800 1.75976500

N -2.17065300 2.12936200 0.21987900

C -1.07845300 2.33763200 1.16657100

H -0.16343400 1.86052800 0.79638300

H -0.88508300 3.40975500 1.28735600

H -1.34807200 1.90695200 2.12837500

C -1.92783000 2.66065600 -1.11821900

H -2.78601100 2.51207800 -1.76828500

H -1.71976700 3.73515200 -1.05936400

H -1.05868100 2.16650600 -1.56866200

Radical Cation Molecular Coordinates:

C -4.27145900 1.02250500 -0.47926500

H -4.68120500 1.95801300 -0.86905500

H -3.84618500 0.46007800 -1.31680900

H -5.06643300 0.43335900 -0.02444600

C -3.23353800 1.27252100 0.56632200

O -3.20040800 0.78670100 1.67379300

N -2.13774900 2.19494600 0.22421600

C -1.15989500 2.53325100 1.23061300

H -0.19559300 2.09896300 0.92691500

H -1.03687200 3.62226200 1.24041100

H -1.46330200 2.14610200 2.19847500

C -2.01321100 2.77058900 -1.09689000

H -2.76361800 3.57008300 -1.19880000

H -1.01900400 3.19560900 -1.21867700

H -2.21803800 2.01802000 -1.86165100

N,N-Dimethyltrifluoroacetamide

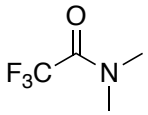

G[substrate] = -585.518651 hartrees

G[radical cation] = -585.253891 hartrees

E_{ox} = 2.78 V vs. SCE

Substrate Molecular Coordinates:

C -4.43983400 1.29815300 -0.35284800

C -3.26340700 1.48799400 0.65600600

O -3.42869500 1.04532700 1.79431300

N -2.15978300 2.11906600 0.21380600

C -1.04088700 2.31191500 1.14130700

H -0.15006200 1.81236500 0.74785400

H -0.83158500 3.38138700 1.24244700

H -1.29643300 1.89478900 2.11241100

C -1.92741500 2.65124700 -1.13309500

H -2.77720000 2.49516200 -1.78924000

H -1.72934900 3.72518300 -1.06501700

H -1.05271700 2.15815900 -1.56798900

F -4.07641100 0.56096200 -1.43306100

F -5.45945600 0.65866400 0.23756200

F -4.92045500 2.48267800 -0.80931200

Radical Cation Molecular Coordinates:

C -4.47645700 1.32645800 0.39334300

C -3.27807200 1.39721400 -0.60156100

O -3.32245700 0.85981500 -1.67604700

N -2.10290800 2.12759800 -0.20679800

C -1.93460900 2.72606500 1.10185500

H -0.86956100 2.81444800 1.31363300

H -2.36757700 3.74027100 1.06170100

H -2.45135800 2.15475300 1.87108300

C -1.03042100 2.24578100 -1.17059500

H -1.39331500 2.05045900 -2.17594200

H -0.57714300 3.23466300 -1.06521800

H -0.26522400 1.49702900 -0.90346800

F -5.50849400 0.75282400 -0.21661900

F -4.14517400 0.59668100 1.47448600

F -4.83092000 2.55899300 0.79529200

REFERENCES

(1) Flory, P. J. Molecular size distribution in ethylene oxide polymers. *J. Am. Chem. Soc.* **1940**, *62*, 1561–1565.

(2) Szwarc, M. Living polymers. *Nature* **1956**, *178*, 1168–1169.

(3) Matyjaszewski, K.; Muller, A. H. E. 50 Years of living polymerization. *Prog. Polym. Sci.* **2006**, *31*, 1039–1040.

(4) Grubbs, R. B.; Grubbs, R. H. 50th Anniversary perspective: living polymerization-emphasizing the molecule in macromolecules. *Macromolecules* **2017**, *50*, 6979–6997.

(5) Hawker, C. J.; Wooley, K. L. The convergence of synthetic organic and polymer chemistries. *Science* **2005**, *309*, 1200–1205.

(6) Kato, M.; Kamigaito, M.; Sawamoto, M.; Higashimura, T. Polymerization of methyl-methacrylate with the carbon-tetrachloride dichlorotris(triphenylphosphine)ruthenium(ii) methylaluminum bis(2,6-di-tert-butylphenoxide) initiating system - possibility of living radical polymerization. *Macromolecules* **1995**, *28*, 1721–1723.

(7) Wang, J. S.; Matyjaszewski, K. Controlled living radical polymerization - atom-transfer radical polymerization in the presence of transition-metal complexes. *J. Am. Chem. Soc.* **1995**, *117*, 5614–5615.

(8) Solomon, D. H.; Rizzardo, E.; Cacioli, P. Polymerization process and polymers produced thereby. US 4581429, July 11, 1984.

(9) Chiefari, J.; Chong, Y. K.; Ercole, F.; Krstina, J.; Jeffery, J.; Le, T. P. T.; Mayadunne, R. T. A.; Meijs, G. F.; Moad, C. L.; Moad, G.; Rizzardo, E.; Thang, S. H. Living free-radical polymerization by reversible addition-fragmentation chain transfer: the RAFT process. *Macromolecules* **1998**, *31*, 5559–5562.

(10) Miyake, G. M.; Theriot, J. C. Perylene as an organic photocatalyst for the radical polymerization of functionalized vinyl monomers through oxidative quenching with alkyl bromides and visible light. *Macromolecules* **2014**, *47*, 8255–8261.

(11) Treat, N. J.; Sprafke, H.; Kramer, J. W.; Clark, P. G.; Barton, B. E.; de Alaniz, J. R.; Fors, B. P.; Hawker, C. J. Metal-free atom transfer radical polymerization. *J. Am. Chem. Soc.* **2014**, *136*, 16096–16101.

(12) Krys, P.; Matyjaszewski, K. Kinetics of atom transfer radical polymerization. *Eur. Polym. J.* **2017**, *89*, 482–523.

(13) Matyjaszewski, K. Atom transfer radical polymerization (ATRP): current status and future perspectives. *Macromolecules* **2012**, *45*, 4015–4039.

(14) Matyjaszewski, K. Advanced materials by atom transfer radical polymerization. *Adv. Mater.* **2018**, *30*, 1706441.

(15) Pan, X. C.; Lamson, M.; Yan, J. J.; Matyjaszewski, K. Photoinduced metal-free atom transfer radical polymerization of acrylonitrile. *ACS Macro Lett.* **2015**, *4*, 192–196.

(16) Theriot, J. C.; Lim, C. H.; Yang, H.; Ryan, M. D.; Musgrave, C. B.; Miyake, G. M. Organocatalyzed atom transfer radical polymerization driven by visible light. *Science* **2016**, *352*, 1082–1086.

(17) Pearson, R. M.; Lim, C. H.; McCarthy, B. G.; Musgrave, C. B.; Miyake, G. M. Organocatalyzed atom transfer radical polymerization using *N*-aryl phenoxazines as photoredox catalysts. *J. Am. Chem. Soc.* **2016**, *138*, 11399–11407.

(18) Chen, D. F.; Boyle, B. M.; McCarthy, B. G.; Lim, C. H.; Miyake, G. M. Controlling polymer composition in organocatalyzed photoredox radical ring-opening polymerization of vinylcyclopropanes. *J. Am. Chem. Soc.* **2019**, *141*, 13268–13277.

(19) Su, X.; Jessop, P. G.; Cunningham, M. F. Versatility of organocatalyzed atom transfer radical polymerization and CO_2-switching for preparing both hydrophobic and hydrophilic polymers with the recycling of a photocatalyst. *Macromolecules* **2019**, *52*, 6725–6733.

(20) McCarthy, B.; Sartor, S.; Cole, J.; Damrauer, N.; Miyake, G. M. Solvent effects and side reactions in organocatalyzed atom transfer radical polymerization for enabling the controlled polymerization of acrylates catalyzed by diaryl dihydrophenazines. *Macromolecules* **2020**, *53*, 9208–9219.

(21) Buss, B. L.; Lim, C.-H.; Miyake, G. M. Dimethyl dihydroacridines as photocatalysts in organocatalyzed atom transfer radical polymerization of acrylate monomers. *Angew. Chem. Int. Ed.* **2020**, *59*, 3209–3217.

(22) Corbin, D. A.; McCarthy, B. G.; Miyake, G. M. Impacts of performing electrolysis during organocatalyzed atom transfer radical polymerization. *Polym. Chem.* **2020**, *11*, 4978–4985.

(23) Jockusch, S.; Yagci, Y. The active role of excited states of phenothiazines in photoinduced metal free atom transfer radical polymerization: singlet or triplet excited states? *Polym. Chem.* **2016**, *7*, 6039–6043.

(24) Koyama, D.; Dale, H. J. A.; Orr-Ewing, A. J. Ultrafast observation of a photoredox reaction mechanism: photoinitiation in organocatalyzed atom-transfer radical polymerization. *J. Am. Chem. Soc.* **2018**, *140*, 1285–1293.

(25) Lewis-Borrell, L.; Sneha, M.; Bhattacherjee, A.; Clark, I. P.; Orr-Ewing, A. J. Mapping the multi-step mechanism of a photoredox catalyzed atom-transfer radical polymerization reaction by direct observation of the reactive intermediates. *Chem. Sci.* **2020**, *11*, 4475–4481.

(26) Pan, X. C.; Fang, C.; Fantin, M.; Malhotra, N.; So, W. Y.; Peteanu, L. A.; Isse, A. A.; Gennaro, A.; Liu, P.; Matyjaszewskit, K. Mechanism of photoinduced metal-free atom transfer radical

polymerization: experimental and computational studies. *J. Am. Chem. Soc.* **2016**, *138*, 2411–2425.

(27) Sartor, S. M.; McCarthy, B. G.; Pearson, R. M.; Miyake, G. M.; Damrauer, N. H. Exploiting charge-transfer states for maximizing intersystem crossing yields in organic photoredox catalysts. *J. Am. Chem. Soc.* **2018**, *140*, 4778–4781.

(28) Sartor, S. M.; Lattke, Y. M.; McCarthy, B. G.; Miyake, G. M.; Damrauer, N. H. Effects of naphthyl connectivity on the photophysics of compact organic charge-transfer photoredox catalysts. *J. Phys. Chem. A* **2019**, *123*, 4727–4736.

(29) Sartor, S. M.; Chrisman, C. H.; Pearson, R. M.; Miyake, G. M.; Damrauer, N. H. Designing high-triplet-yield phenothiazine donor-acceptor complexes for photoredox catalysis. *J. Phys. Chem. A* **2020**, *124*, 817–823.

(30) Lim, C. H.; Ryan, M. D.; McCarthy, B. G.; Theriot, J. C.; Sartor, S. M.; Damrauer, N. H.; Musgrave, C. B.; Miyake, G. M. Intramolecular charge transfer and ion pairing in *N,N*-diaryl dihydrophenazine photoredox catalysts for efficient organocatalyzed atom transfer radical polymerization. *J. Am. Chem. Soc.* **2017**, *139*, 348–355.

(31) Connelly, N. G.; Geiger, W. E. Chemical redox agents for organometallic chemistry. *Chem. Rev.* **1996**, *96*, 877–910.

(32) Christensen, J. A.; Phelan, B. T.; Chaudhuri, S.; Acharya, A.; Batista, V. S.; Wasielewski, M. R. Phenothiazine radical cation excited states as super-oxidants for energy-demanding reactions. *J. Am. Chem. Soc.* **2018**, *140*, 5290–5299.

(33) Parkin, G., Applications of deuterium isotope effects for probing aspects of reactions involving oxidative addition and reductive elimination of H-H and C-H bonds. *J. Labelled Compd. Rad.* **2007**, *50*, 1088–1114.

(34) Kolthoff, I. M.; Coetzee, J. F. Polarography in acetonitrile .2. Metal ions which have significantly different polarographic properties in acetonitrile and in water - anodic waves - voltammetry at rotated platinum electrode. *J. Am. Chem. Soc.* **1957**, *79*, 1852–1858.

(35) Espenson, J. H. *Chemical kinetics and reaction mechanisms.* 2nd ed.; McGraw-Hill: New York, NY, 2002.

(36) Luo, Y.-R. *Comprehensive handbook of chemical bond energies*. CRC Press: Boca Raton, 2007.

(37) Theriot, J. C.; McCarthy, B. G.; Lim, C. H.; Miyake, G. M. Organocatalyzed atom transfer radical polymerization: perspectives on catalyst design and performance. *Macromol. Rapid Commun.* **2017**, *38*, 1700040.

(38) Fuoss, R. M. Ionic association .3. The equilibrium between ion pairs and free ions. *J. Am. Chem. Soc.* **1958**, *80*, 5059–5061.

(39) Cole, J. P.; Federico, C. R.; Lim, C. H.; Miyake, G. M., Photoinduced organocatalyzed atom transfer radical polymerization using low ppm catalyst loading. *Macromolecules* **2019**, *52*, 747–754.

(40) Carmean, R. N.; Becker, T. E.; Sims, M. B.; Sumerlin, B. S. Ultra-high molecular weights via aqueous reversible-deactivation radical polymerization. *Chem* **2017**, *2*, 93–101.

(41) Xu, J. T.; Jung, K.; Atme, A.; Shanmugam, S.; Boyer, C. A robust and versatile photoinduced living polymerization of conjugated and unconjugated monomers and its oxygen tolerance. *J. Am. Chem. Soc.* **2014**, *136*, 5508–5519.

(42) Gong, H. H.; Gu, Y.; Zhao, Y. C.; Quan, Q. Z.; Han, S. T.; Chen, M. Precise synthesis of ultra-high-molecular-weight fluoropolymers enabled by chain-transfer-agent differentiation under visible-light irradiation. *Anew. Chem. Int. Ed.* **2020**, *59*, 919–927.

(43) Mueller, L.; Jakubowski, W.; Matyjaszewski, K.; Pietrasik, J.; Kwiatkowski, P.; Chaladaj, W.; Jurczak, J. Synthesis of high molecular weight polystyrene using AGET ATRP under high pressure. *Eur. Polym. J.* **2011**, *47*, 730–734.

(44) Percec, V.; Guliashvili, T.; Ladislaw, J. S.; Wistrand, A.; Stjerndahl, A.; Sienkowska, M. J.; Monteiro, M. J.; Sahoo, S. Ultrafast synthesis of ultrahigh molar mass polymers by metal-catalyzed living radical polymerization of acrylates, methacrylates, and vinyl chloride mediated by SET at 25 degrees C. *J. Am. Chem. Soc.* **2006**, *128*, 14156–14165.

(45) Rzayev, J.; Penelle, J., HP-RAFT: A free-radical polymerization technique for obtaining living polymers of ultrahigh molecular weights. *Angew. Chem. Int. Ed.* **2004**, *43*, 1691–1694.

(46) Matyjaszewski, K. Comparison and classification of controlled/living radical polymerizations. In *Controlled/living radical polymerization: progress in ATRP, NMP, and RAFT.* Matyjaszewski, K.; ACS Symposium Series, Vol. 768; American Chemical Society, 2000; pp 2-26.

(47) Kwiatkowski, P.; Jurczak, J.; Pietrasik, J.; Jakubowski, W.; Mueller, L.; Matyjaszewski, K. High molecular weight polymethacrylates by AGET ATRP under high pressure. *Macromolecules* **2008**, *41*, 1067–1069.

(48) Ryan, M. D.; Theriot, J. C.; Lim, C. H.; Yang, H. S.; Lockwood, A. G.; Garrison, N. G.; Lincoln, S. R.; Musgrave, C. B.; Miyake, G. M. Solvent effects on the intramolecular charge transfer character of *N,N*-diaryl dihydrophenazine catalysts for organocatalyzed atom transfer radical polymerization. *J. Polym. Sci. Part A Polym. Chem.* **2017**, *55*, 3017–3027.

(49) Beuermann, S.; Buback, M. Rate coefficients of free-radical polymerization deduced from pulsed laser experiments. *Prog. Polym. Sci.* **2002**, *27*, 191–254.

(50) Penzel, E.; Goetz, N. Solution Ptoperties of Polyacrylic Esters. *Die Angewandte Makromolekulare Chemie* **1990**, *178*, 191–200.

(51) Coelho, J. F. J.; Gois, J.; Fonseca, A. C.; Carvalho, R. A.; Popov, A. V.; Percec, V.; Gil, M. H. Synthesis of Poly(2-methoxyethyl acrylate) by Single Electron Transfer–Degenerative Transfer Living Radical Polymerization Catalyzed by $Na_2S_2O_4$ in Water. *J. Polym. Sci. Part A Polym. Chem.* **2009**, *47*, 4454–4463.

(52) Sheldrick, G. M. Program for Empirical Absorption Correction of Area Detector Data. *SADABS* **1996**.

(53) Sheldrick, G. M. SHELXT – Integrated Space-Group and Crystal-Structure Determination. *Acta Crystallogr. Sect. Found. Adv.* **2015**, *71*, 3–8.

(54) Sheldrick, G. M. Crystal Structure Refinement with SHELXL. *Acta Crystallogr. Sect. C Struct. Chem.* **2015**, *71*, 3–8.

(55) Dolomanov, O. V.; Bourhis, L. J.; Gildea, R. J.; Howard, J. A. K.; Puschmann, H. OLEX2: A Complete Structure Solution, Refinement, and Analysis Program. *J. Appl. Cryst.* **2009**, *42*, 339–341.

(56) McCarthy, B. G.; Pearson, R. M.; Lim, C.-H.; Sartor, S. M.; Damrauer, N. H.; Miyake, G. M. Structure–Property Relationships for Tailoring Phenoxazines as Reducing Photoredox Catalysts. *J. Am. Chem. Soc.* **2018**, *140*, 5088–5101.

(57) Elrishi, N.; Rountree, K. J.; McCarthy, B. D.; Rountree, E. S.; Eisenhart, T. T.; Dempsey, J. L. A Practical Beginner's Guide to Cyclic Voltammetry. *J. Chem. Educ.* **2018**, *95*, 197–206.

(58) Roth, H. G.; Romero, N. A.; Nicewicz, D. A. Experimental and calculated electrochemical potentials of common organic molecules for applications to single-electron redox chemistry. *Synlett* **2016**, *27*, 714–723.

(59) Luo, P.; Feinberg, A. M.; Guirado, G.; Farid, S.; Dinnocenzo, J. P. Accurate oxidation potentials of 40 benzene and biphenyl derivatives with heteroatom substituents. *J. Org. Chem.* **2014**, *79*, 9297–9304.

(60) Prater, K. B.; Bard, A. J. Rotating Ring-Disk Electrodes. I. Fundamentals of the Digital Simulation Approach. Disk and Ring Transients and Collection Efficiencies. *J. Electrochem. Soc.* **1970**, *117*, 207–213.

(61) Marcus, Y.; Hefter, G. Ion Pairing. *Chem. Rev.* **2006**, *106*, 4585–4621.

(62) Hart-Smith, G.; Lammens, M.; Du Prez, F. E.; Guilhaus, M.; Barner-Kowollik, C., ATRP Poly(Acrylate) Star Formation: A Comparative Study Between MALDI and ESI Mass Spectrometry. *Polymer* **2009**, *50*, 1986–2000.

CHAPTER 6.

RADICAL ADDITION TO *N,N*-DIARYL DIHYDROPHENAZINE PHOTOREDOX CATALYSTS AND IMPLICATIONS IN PHOTOINDUCED ORGANOCATALYZED ATOM TRANSFER RADICAL POLYMERIZATION

Overview

Photoinduced organocatalyzed Atom Transfer Radical Polymerization (O-ATRP) is a controlled radical polymerization methodology catalyzed by organic photoredox catalysts (PCs). In an efficient O-ATRP system, good control over molecular weight with an initiator efficiency ($I^* = M_{n,\,theo} / M_{n,\,exp} \times 100\%$) near unity is achieved, and the synthesized polymers possess a low dispersity ($Đ$). *N,N*-diaryl dihydrophenazine catalysts typically produce polymers with low dispersity ($Đ < 1.3$), but with less than unity molecular weight control ($I^* \sim 60$ to 80%). This work explores the termination reactions that lead to decreased control over polymer molecular weight and identifies a reaction leading to radical addition to the phenazine core. This reaction can occur with radicals generated through reduction of the ATRP initiator or the polymer chain-end. In addition to causing a decrease in I^*, this reactivity modifies the properties of the PC, ultimately impacting polymerization control in O-ATRP. With this insight in mind, a new family of core substituted *N,N*-diaryl dihydrophenazines is synthesized from commercially available ATRP initiators and employed in O-ATRP. These new core substituted PCs improve both I^* and $Đ$ in the O-ATRP of MMA, while minimizing undesired side reactions during the polymerization. Further, the ability of one core substituted PC to operate at low catalyst loadings is demonstrated, with minimal loss of polymerization control down to 100 ppm (weight average molecular weight [M_w]

= 10.8 kDa, $Đ$ = 1.17, I^* = 104% versus M_w = 8.26, $Đ$ = 1.10, I^* = 107% at 1000 ppm) and signs of a controlled polymerization down to 10 ppm of catalyst (M_w = 12.1 kDa, $Đ$ = 1.36, I^* = 107%).

Introduction

Photoredox catalysis has broadly impacted the synthesis of small molecules and polymers through enabling diverse and challenging reactions under mild reaction conditions.[1-5] Much of the progress in photoredox catalysis has leveraged well-established precious metal complexes based on ruthenium or iridium as photoredox catalysts (PCs).[2, 6] While these PCs have certainly been effective in promoting a wide range of transformations, they also have raised concerns regarding the scarcity of these precious metals and the environmental impacts associated with their mining, use, and disposal.[7] Our interest in photoredox catalysis has centered upon the development of strongly reducing organic photoredox catalysts as sustainable alternatives to precious metal-based PCs, especially for application in organocatalyzed atom transfer radical polymerization (O-ATRP).[8-13]

Since its introduction in 1995,[14, 15] ATRP has blossomed into one of the most popular controlled radical polymerizations for the synthesis of polymers with targeted molecular weights and low dispersity ($Đ$).[16-21] Most commonly, traditional ATRP employs a transition metal catalyst – often copper or ruthenium – to mediate a reversible activation-deactivation mechanism. During this process, a polymer with a terminal C-X (X = halide) bond is activated to generate a reactive radical capable of chain propagation through reaction with a vinyl monomer. However, the radicals produced can also react with each other, leading to irreversible termination reactions that hinder polymerization control. As such, a key feature of ATRP is reversible deactivation, which regenerates the dormant C-X bond to lower the concentration of radicals in solution and kinetically

limit undesirable termination reactions. While O-ATRP employs an organic catalyst instead, the same general mechanism is mediated during the polymerization (Figure 6.1).[8, 22, 23]

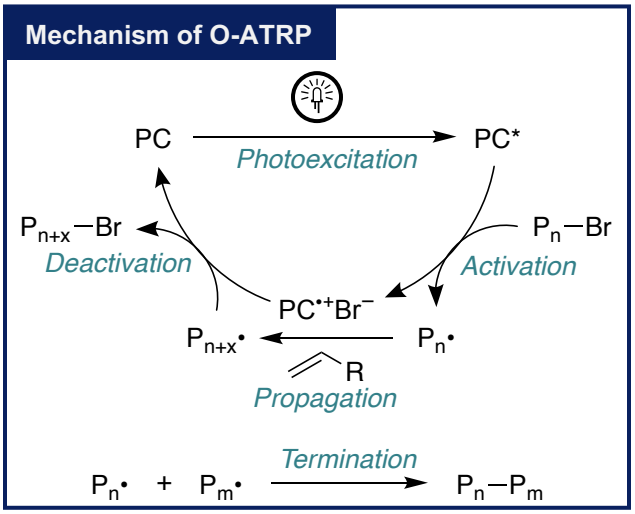

Figure 6.1. *Proposed mechanism of organocatalyzed atom transfer radical polymerization proceeding through an oxidative quenching photoredox cycle.*

Although traditional ATRP has been used to polymerize a wide variety of monomers and produce polymers with highly tunable structures and architectures,[18-20] its application in metal-sensitive systems has been limited by its dependence on metal-based catalysts. For example, in electronic applications, the presence of residual Cu catalyst trapped in the polymer matrix has been demonstrated to decrease the performance of the target polymer.[24] In addition, the polymerization of coordinating monomers can be challenging by metal-catalyzed ATRP, since coordination of the monomer to the catalyst can lead to a loss of desirable catalytic properties. By contrast, O-ATRP employs metal-free, organic catalysts, enabling its success in these metal-sensitive applications.[25-27]

Previously, much of the work in this field has focused on the identification of novel PCs capable of mediating O-ATRP, including phenothiazines,[22, 28-33] phenoxazines,[10, 12, 34-36]

dihydrophenazines,[9, 37-39] dihydroacridines,[13, 40] polyaromatic hydrocarbons,[8, 41-43] and xanthene dyes[44, 45]. While a number of these catalyst families have been demonstrated to produce polymers with a high degree of polymerization control, one of the most successful PC families has been the dihydrophenazines. Previous work with this catalyst family showed that the installation of *N*-aryl groups with electron withdrawing functionalities or extended conjugation (eg. naphthalene) could produce highly controlled polymers with $Đ < 1.1$,[9] consistent with the standards of ATRP.[16-20] Through computational and experimental investigations, it was shown that these *N*-aryl functionalities promote intramolecular charge transfer in the excited state, leading to the formation of long-lived triplet excited state species capable of catalysis.[9]

However, one limitation of dihydrophenazines PCs in O-ATRP is that they consistently exhibit low initiator efficiency ($I^* = M_{n,\,theo} / M_{n,\,exp} \times 100\%$, $I^* \sim 60\%$ to 80%).[9] Interestingly, when the dihydrophenazine core is further functionalized through installation of aryl substituents (Figure 6.2), this problem is alleviated and the resulting polymers from O-ATRP possess I^* near unity.[37] This observation led us to hypothesize that the low I^* seen with non-core substituted dihydrophenazines is a result of a side reaction between the initiator and the PC, which results in substitution of the PC core and consumption of the initiator prior to O-ATRP. In support of this hypothesis, recent work applying dihydrophenazines to the synthesis of poly(acrylates) showed evidence of this reactivity between diethyl-2-bromo-2-methylmalonate (DBMM) and 5,10-di(2-naphthyl)-5,10-dihydrophenazine.[39] Similar ligand substitution by radicals has also been observed with a polypyridal iridium complex, which altered the reactivity of the PC during the course of reaction.[46] However, the origin of this reactivity in dihydrophenazine PCs remains unknown, as does the impact of this core substitution on catalytic properties and successful O-ATRP.

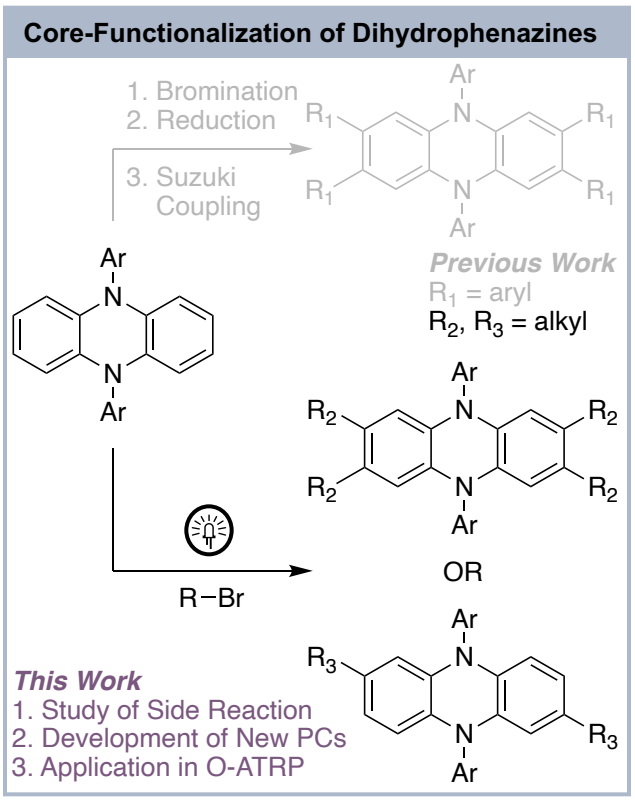

Figure 6.2. *Previous work allowed for substitution of the dihydrophenazine core through bromination followed by aryl cross-coupling. This work exploits a side reaction between the PC and ATRP initiators to achieve core substitution.*

In this work, we investigate the reaction of 5,10-di(4-triflouromethylphenyl)-5,10-dihydrophenazine (**1**) with several common ATRP initiators to gain insight into this potential side reactivity in O-ATRP that can detract from *I** and produce PCs that are not necessarily expected from the onset of the reaction. These core substituted derivatives are isolatable and reveal that this substitution impacts catalytically relevant properties of these molecules. As such, when used as PCs in O-ATRP, these alkyl core substituted PCs achieve non-equivalent levels of success in producing polymers with low *Đ* and near unity *I** in comparison to using non-core substituted PCs. This work highlights the importance of continued mechanistic understanding of O-ATRP and catalyst evolution to realize improved catalyst systems. Furthermore, this insight is broadly relevant to small molecule transformations, introduces further considerations regarding PC side

reactivity, and could lead to improved reaction systems by understanding the potential for the catalyst to be altered during the course of reaction. Lastly, this radical addition to the core of *N,N*-diaryl dihydrophenazines could serve as an efficient and atom-economical means to access new PC derivatives with tailored photophysical properties.

Results and Discussion

PC **1** is one of the first visible-light absorbing PCs reported for O-ATRP. Although it was demonstrated to produce polymers with relatively low dispersity ($Đ < 1.3$), I^* was typically less than 100% ($I^* \sim 60\%$ to 80%).[9] To explore the possibility of radical addition to this catalyst during O-ATRP, PC **1** was irradiated with a variety of common ATRP initiators in *N,N*-dimethylacetamide (DMAc), essentially mimicking O-ATRP conditions but in the absence of monomer (Figure 6.3). When PC **1** was reacted with 10 equivalents of ethyl α-bromophenylacetate (EBP) in DMAc, the reaction mixture was irradiated for two hours and characterized by electrospray ionization mass spectrometry (ESI-MS) (Figure 6.36 in *Experimental* section). The mass spectrum of the solution revealed peaks at m/z = 470.12, 632.19, 794.26, 956.33, and 1118.40,[47] consistent with zero to four equivalents of the ethyl phenylacetate fragment installed on the phenazine core.

In an effort to determine the positions of these new substituents by NMR, the irradiation time was increased to drive the reaction to higher conversion and reduce the number of products. After irradiating for 16 hours, the observed color of each solution was qualitatively different. In accord with the proposed single electron transfer reduction of the initiator, we hypothesized that the observed color change arose from formation of $^2PC^{\bullet+}Br^-$.[48] Supporting this hypothesis, the UV-

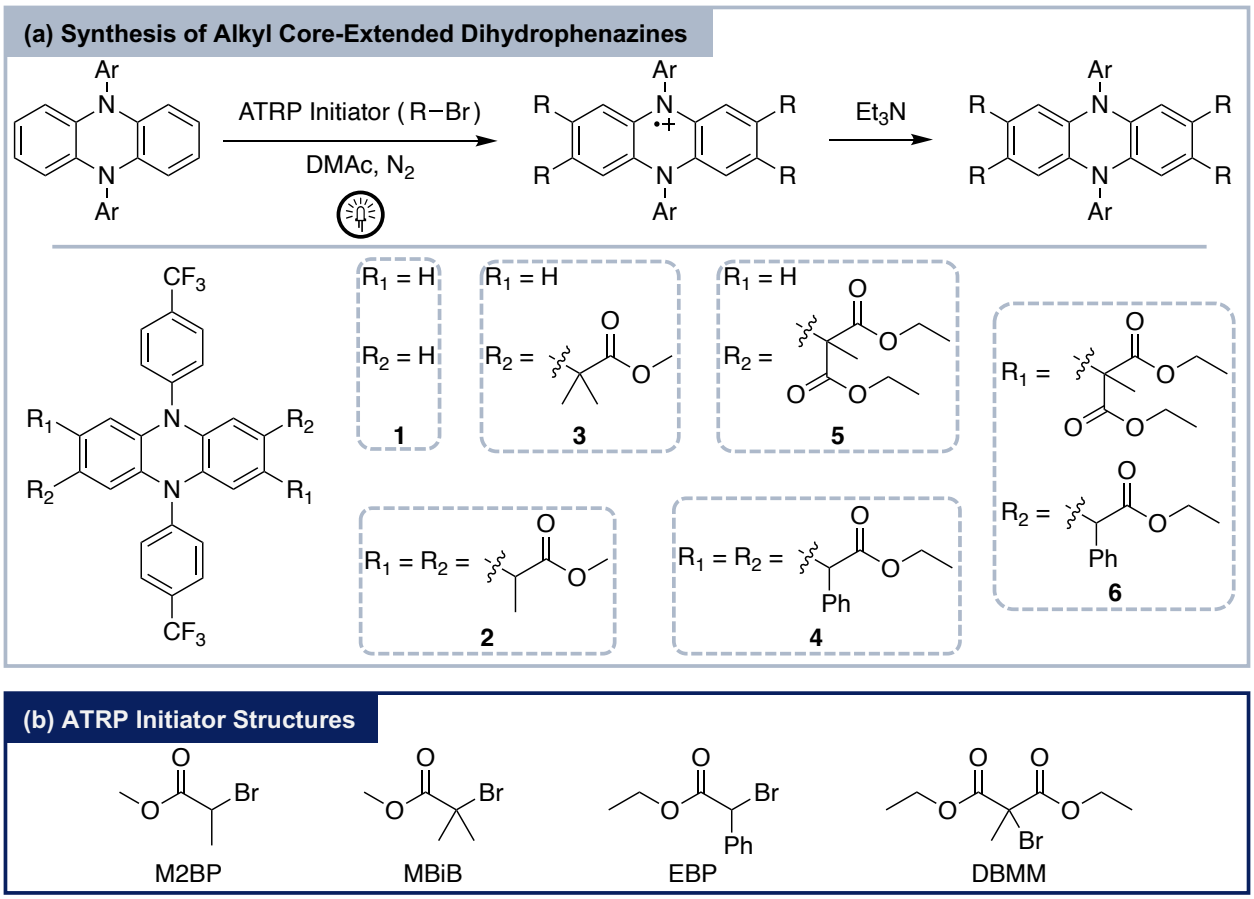

Figure 6.3. *Scheme for the synthesis of core-extended dihydrophenazines through reaction with ATRP initiators (top) and structures (bottom) of the PCs investigated in this work (a). Structures of ATRP initiators used in this work (b).*

visible absorption spectra of the reaction mixtures closely matched those of oxidized PCs generated electrochemically (Figure 6.4). Furthermore, electron paramagnetic resonance (EPR) spectroscopy confirmed the formation of a stable radical during the reaction of PC **1** with ATRP initiators. To convert these radical cation species to the neutral PCs, the reaction solutions were quenched using triethylamine (TEA) as a sacrificial electron donor. The resulting yellow or orange compounds were purified by column chromatography and isolated in yields of 67% to 92%. The structures of core substituted PCs **2** – **6** were assigned based on NMR, as well as single-crystal X-ray diffractometry (SCXRD) in the case of **4** (see *Supporting Information – Photocatalyst Characterization*). Alternatively, **2** – **6** could also be isolated by precipitation of the reduced

reaction solution in deionized water, followed by vacuum filtration, washing with cold methanol, and drying under high vacuum overnight.

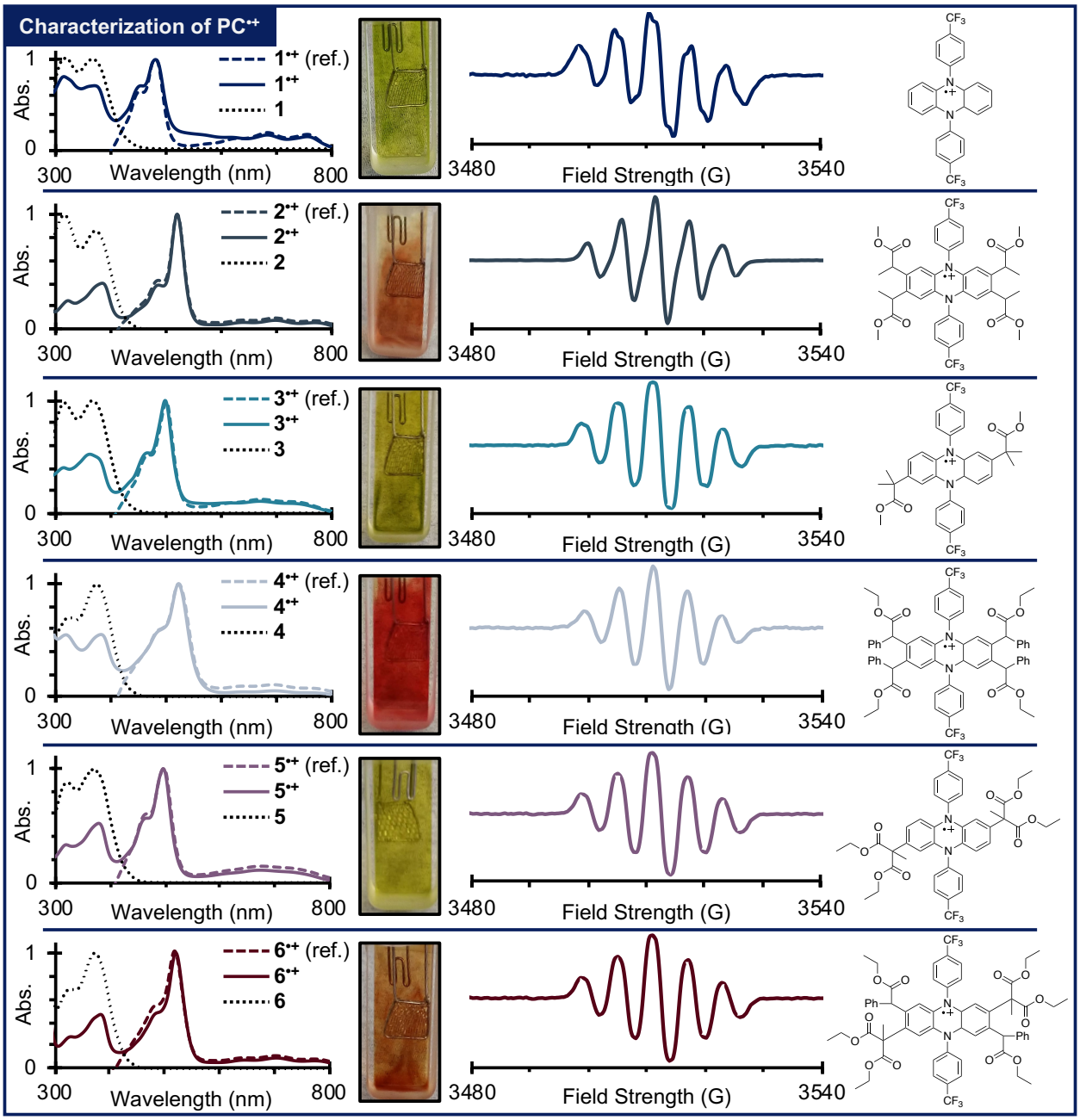

Figure 6.4. *Characterization of the radical cations of PC* ***1*** *–* ***6*** *using UV-Visible spectroscopy coupled with spectro-electrochemistry (left), showing spectra of the PC (small dash), the isolated radical cations (solid), and the radical cations obtained by spectro-electrochemistry (large dash). Photographs of solutions after spectro-electrochemistry (middle), and electron paramagnetic resonance spectroscopy (right).*

When ATRP initiators possessing a secondary bromide were employed (i.e. 2-methyl 2-bromopropionate [M2BP] and EBP), four substitutions at the 2-,3-,7-, and 8- positions of the dihydrophenazine core were observed. Instead, when ATRP initiators possessing a tertiary bromide were reacted with **1** (i.e. methyl α-bromoisobutyrate [MBiB] and DBMM), the resulting compounds exhibited only two core substituents (Figure 6.3). It should be noted that characterization of **3** and **5** revealed a mixture of regioisomers resulting from substitution at either the 2- and 7- positions or the 2- and 8- positions of the dihydrophenazine core (*see below*). However, these compounds could not be resolved by column chromatography, and figures in this report depict only one isomer for simplicity. We propose tetra- versus di-substitution is controlled by the sterics of the initiator (i.e. secondary versus tertiary bromide). In support of this hypothesis, when **5** was irradiated in the presence of EBP, further addition of the ethyl phenylacetyl radical ensued, resulting in the formation of **6** with four substituents on the dihydrophenazine core (Figure 6.3).

While these experiments support that radical addition to PC **1** is possible, they do not necessarily indicate that this reaction can occur during O-ATRP. To test this possibility, we performed O-ATRP using PC **1**, EBP, and methyl methacrylate (MMA). After 20 minutes, the reaction was stopped, the volatiles were removed, and the mixture was analyzed by ESI-MS (Figure 6.37 in *Experimental* section). As expected, this analysis revealed that the ATRP initiator can in fact add to the PC core during O-ATRP, consistent with the observations made in the absence of MMA. What was unexpected, however, was the observation of core substitution with poly(methyl methacrylate (PMMA) oligomers as well.[47] As such, this experiment reveals that a major termination reaction in O-ATRP can be radical addition to the PC, especially at early

reaction times. Ultimately, these experiments provide important insight into why *I** often deviates from 100 %, since ATRP initiators and oligomers are consumed through addition to the catalyst.

With this new reaction pathway in mind, PCs **2** – **6** were characterized to understand how core substitution impacts their catalytically relevant electrochemical and photophysical properties (Table 6.1). Using density functional theory (DFT), the electrochemical properties of key catalytic states (^{1}PC, ^{3}PC*, and ^{2}PC$^{\bullet+}$) were computed to gain insight into the impact of core substitution on PC thermodynamics. In each case, the computationally predicted excited state reduction [$E^o(^2PC^{\bullet+}/^3PC^*)$] and ground state oxidation [$E^o(^2PC^{\bullet+}/^1PC)$] potentials were similar to the parent compound. In addition, the photophysical and electrochemical properties of **1** – **6** were also experimentally determined. For **2** – **6**, the λ_{max} of absorption is redshifted 3–10 nm compared to the parent PC **1**. Interestingly, **4** and **6** both exhibit a significantly higher molar absorptivity (ε_{max}) than the parent PC **1**, possibly due to the added conjugation from the ethyl phenylacetate moiety. However, **2**, **3**, and **5** all possess a ε_{max} similar to that of **1**. With regard to the excited state properties of these compounds, core substitution generally leads to a shorter wavelength emission from the S_1 excited state, meaning that core substituted catalysts **2** – **6** have a higher energy singlet excited state ($E_{S1,exp}$) than **1**. Finally, core substitution also destabilized the radical cations of **4** and **5** relative to **1** [i.e. increased $E^o(^2PC^{\bullet+}/^1PC)$], while stabilizing those of **2**, **3**, and **6**.

Given the previous observation of stable radical cations for **1** – **6** by EPR, we sought to synthesize the radical cation salt of the parent PC **1** so that we could probe the mechanism of radical addition. Adding Br_2 to a solution of PC **1** in benzene (Figure 6.5) resulted in an immediate color change and precipitation of a dark green powder from solution, which was isolated by filtration. This solid was recrystallized from methanol, and SCXRD of the resulting crystals

Table 6.1. *Electrochemical and photophysical characterization of PCs **1** – **6**.*

PC	λ_{max} (nm)[a]	ε_{max} ($M^{-1}cm^{-1}$)[b]	$\lambda_{em,\ max}$ (nm)[c]	$E_{S1,\ exp}$ (eV)[d]	$E_{1/2}$ ($^2PC^{\bullet+}/^1PC$) (V vs. SCE)[e]	E^o_{ox} ($^2PC^{\bullet+}/^1PC$) (V vs. SCE)[f]	$E^{o*}_{S1,\ exp}$ ($^2PC^{\bullet+}/^1PC^*$) (V vs. SCE)[c]	$E^{o*}_{T1,\ calc}$ ($^2PC^{\bullet+}/^3PC^*$) (V vs. SCE)[f]
1	367	4600	611	2.02	0.28	0.21	-1.74	-2.17
2	373	5000	600	2.07	0.35	0.17	-1.72	-2.10
3	371	4300	611	2.02	0.30	0.15	-1.72	-2.10
4	377	7500	581	2.13	0.36	0.28	-1.77	-2.19
5	370	5000	602	2.06	0.36	0.23	-1.70	-1.99
6	372	6900	598	2.07	0.40	0.16	-1.67	-2.01

[a]Measured in N,N-dimethylacetamide (DMAc). λ_{max}, maximum absorption wavelength; [b]ε_{max}, molar absorptivity at λ_{max}; [c]$\lambda_{em,\ max}$, maximum emission wavelength; [d]$E^{0*}_{S1,\ exp}$, lowest singlet excited state energy determined from $\lambda_{em,\ max}$; [e]first oxidation potential determined in DMAc with NBu_4PF_6 as the electrolyte; [f]computationally predicted oxidation and reduction potentials (see Supporting Information for full computational details).

indicated the formation of the radical cation tribromide salt ($\mathbf{1}^{\bullet+}Br_3^-$). While this tribromide species was certainly an interesting discovery, it does not represent the proposed deactivator in O-ATRP ($\mathbf{1}^{\bullet+}Br^-$). In order to convert the Br_3^- anion to Br^- and obtain the monobromide salt, $\mathbf{1}^{\bullet+}Br_3^-$ was refluxed in methanol for four hours. The choice of methanol in this step proved to be crucial, as using benzene instead led to bromination of the PC core.[37] The isolated material was then recrystallized from methanol, and SCXRD revealed the monobromide $\mathbf{1}^{\bullet+}Br^-$ radical cation salt.[37]

***Figure 6.5**. Scheme for the synthesis of $\mathbf{1}^{\bullet+}Br^-$.*

To investigate the mechanism of core substitution with ATRP initiators, we explored the reactivity of **1** and $\mathbf{1}^{\bullet+}Br^-$ in the presence of free radicals generated by the thermal decomposition of azobisisobutyronitrile (AIBN) (Figure 6.6). Both **1** and $\mathbf{1}^{\bullet+}Br^-$ were each reacted with AIBN at 80 °C in DMAc in the dark to prevent unwanted photoexcitation of **1**. After one hour, ^{1}H NMR analysis revealed that the thermally generated isobutyronitrile radical had added to the dihydrophenazine core of $\mathbf{1}^{\bullet+}Br^-$ and generated the substituted neutral PC derivative. Instead, no reaction was observed between PC **1** and AIBN, suggesting that core substitution occurs exclusively to $\mathbf{1}^{\bullet+}Br^-$ and not **1**.

Based on these results, we propose the following mechanism for dihydrophenazine core substitution with ATRP initiators. Upon irradiation of **1**, **1*** activates the C-Br bond in the initiator to generate an alkyl radical and Br^-. After addition of the radical species to the 2- position of the PC core, the intermediate is deprotonated – possibly by Br^- – to restore aromaticity. The resulting species is a neutral, mono-substituted PC derivative that can likely re-enter the catalytic cycle,

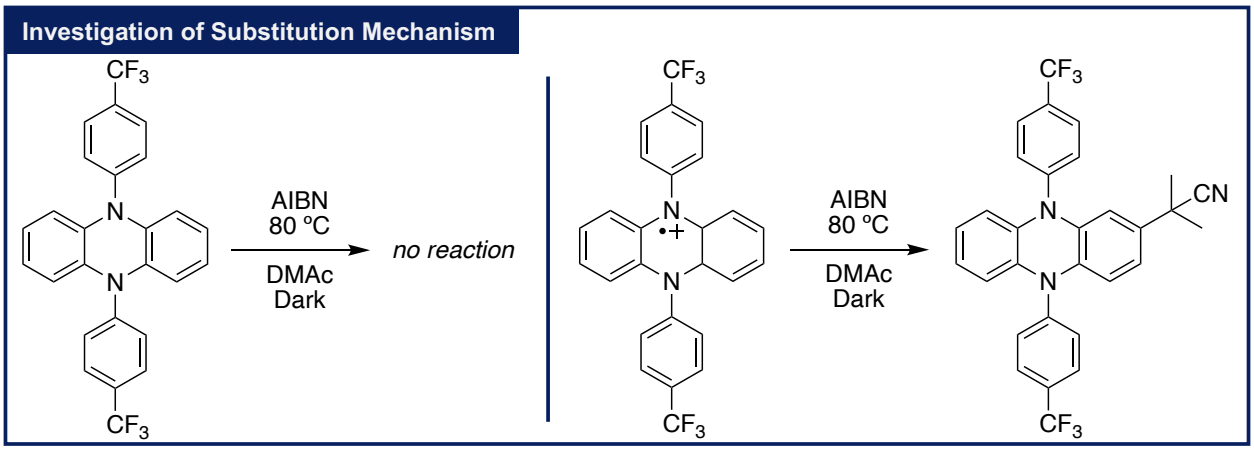

***Figure 6.6**. Model reactions reveal no reaction between thermally generated radicals with the ground state ^1PC (left), but radical addition occurs to $^2PC^{\bullet+}$ (right).*

where this process is repeated for further substitution of the PC core. Depending on the sterics of the radical, the core can be substituted either two or four times. However regardless of the identity of the initiator, when the final substitution occurs, the di- or tetra- substituted PC undergoes photoexcitation and reaction with a final equivalent of initiator. Since core substitution is no longer feasible, this process results in the formation of a stable radical cation species, which is later reduced by addition of a sacrificial electron donor to the reaction solution.

To understand how core substitution impacts catalytic performance in O-ATRP, PCs **1** – **6** were employed in the O-ATRP of MMA under standard conditions – using DBMM as the initiator, [MMA]:[DBMM]:[PC] = [1000]:[10]:[1], with 1 mL MMA, 1 mL DMAc as the solvent, and irradiated in a white LED beaker under N_2 atmosphere. In each case, all six PCs produced PMMA in a controlled fashion ($Đ \leq 1.5$, $I^* \sim 100\%$), although with varying levels of polymerization control (Table 6.2). In particular, PC **4** exhibited excellent polymerization control, producing PMMA with a weight average molecular weight (M_w) = 10.2 kDa, $Đ$ = 1.23, and I^* = 112% (entry 4). Interestingly, even PC **1** exhibited near unity I^* (I^* = 97%), although it should be noted that these polymerizations used DBMM as the initiator whereas previous work employed EBP.[9]

Nevertheless, PC **4** produced PMMA with lower $Đ$ than PC **1** ($Đ$ = 1.23 for **4** versus 1.32 for **1**), indicating superior performance in O-ATRP.

Table 6.2. *Results of the O-ATRP of MMA using PCs **1-6**.*

Entry	PC	Time (h)	Conversion (%)[a]	$M_{n,\,theo}$ (kDa)	$M_{n,\,exp}$ (kDa)	$M_{w,\,exp}$ (kDa)[b]	$Đ$[b]	I^* (%)[c]
1	**1**	8	78.3	8.09	8.38	11.1	1.32	97
2	**2**	8	73.0	7.57	7.35	10.1	1.37	103
3	**3**	8	88.6	9.12	8.47	12.0	1.42	108
4	**4**	8	89.9	9.25	8.26	10.2	1.23	112
5	**5**	8	83.3	8.59	8.40	11.0	1.31	102
6	**6**	8	96.1	9.88	8.02	9.94	1.24	123

Conditions: [MMA]:[DBMM]:[PC] = [1000]:[10]:[1]; 1 mL MMA, 1 mL DMAc. Solutions prepared in the dark and then irradiated in a white LED beaker for specified time (see Supporting Information – Supplemental Polymerization Data for full details). [a]Determined by 1H NMR. [b]Determined by GPC coupled with multi-angle light scattering. [c]Initiator efficiency (I) = ($M_{n,\,theo}$ / $M_{n,\,exp}$)•100%.*

We next sought to improve upon these results by modification of the reaction solvent. Previously, several reports have shown that solvent choice in O-ATRP – especially using dihydrophenazine PCs – can have a significant impact on polymerization control.[39, 49, 50] As such, solvents of varying polarity from DMSO to benzene were employed in the polymerization of MMA using **4** as the PC (Table 6.3). Consistent with previous findings,[49] this polymerization was most successful in less polar solvents such as ethyl acetate (EtAc: M_w = 5.16 kDa, $Đ$ = 1.11, I^* = 100%) and benzene (M_w = 6.26 kDa, $Đ$ = 1.12, I^* = 100%). Further, polymerizations in less polar solvents (i.e. EtAc, benzene) were significantly slower than those in more polar solvents (i.e. dimethyl sulfoxide [DMSO], DMAc), reaching roughly half as much monomer conversion in the same amount of time. This detail might indicate improved deactivation in less polar solvents, though the impact of solvent on polymerization control will be discussed in greater detail later (*see below)*. Regardless, since EtAc and benzene gave similar levels of polymerization control, EtAc

was chosen for subsequent polymerizations since it is a "green" solvent and less toxic than benzene.

Table 6.3. *Results from the O-ATRP of MMA using PC **4** in solvents of different polarity.*

Entry	Solvent	Time (h)	Conversion (%)[a]	$M_{n,\,theo}$ (kDa)	$M_{n,\,exp}$ (kDa)	$M_{w,\,exp}$ (kDa)[b]	$Đ$[b]	I^* (%)[c]
(4)	DMAc	8	89.9	9.25	8.26	10.2	1.23	112
7	DMSO	8	68.6	7.12	12.6	24.3	1.93	56
8	MeCN	8	27.5	3.01	4.95	6.73	1.36	61
9	THF	8	21.3	2.38	5.53	6.25	1.13	43
10	EtAc	8	43.8	4.64	4.65	5.16	1.11	100
11	Benzene	8	53.5	5.61	5.59	6.26	1.12	100

*Conditions: [MMA]:[DBMM]:[**4**] = [1000]:[10]:[1]; 1 mL MMA, 1 mL solvent. Solutions prepared in the dark and then irradiated in a white LED beaker for specified time (see Supporting Information – Supplemental Polymerization Data for full details).* [a]*Determined by 1H NMR.* [b]*Determined by GPC coupled with multi-angle light scattering.* [c]*Initiator efficiency (I*) = ($M_{n,\,theo}$ / $M_{n,\,exp}$)•100%.*

Since dihydrophenazines with aryl core substituents were previously shown to operate effectively in O-ATRP at ppm-level catalyst loadings,[37] the ability of PC **4** to mediate O-ATRP under similar conditions was also investigated. In particular, we questioned whether core substitution alone would enable the PC to operate at low catalyst loadings – possibly through minimization of side reactions – or if another property unique to the aryl core substituted PCs is key to this ability. As such, polymerizations with **4** were performed with systematically reduced catalyst loadings – from 1000 ppm to 1 ppm. The resulting polymers were characterized by ^{1}H NMR (to determine monomer conversion) and gel permeation chromatography (GPC) coupled with multi-angle light scattering (to determine the M_w, $Đ$, and I^*). Excitingly, polymerizations with as little as 100 ppm of **4** – an order of magnitude lower than standard conditions – showed almost no loss of polymerization control (Table 6.4), producing PMMA with low dispersity ($Đ$ = 1.17 at 100 ppm versus 1.10 at 1000 ppm) and near-quantitative initiator efficiency (I^* = 104% at

100 ppm versus 107% at 1000 ppm). Moreover, polymerization control was maintained at loadings as low as 10 ppm of **4**, where $Đ$ = 1.36 and I^* = 107.

Table 6.4. *Results from the O-ATRP of MMA using PCs **1** and **4** at decreasing catalyst loadings.*

Entry	[MMA]:[DBMM]:[PC]	[PC] (ppm)	Time (h)	Conv. (%)[a]	$M_{n,\,theo}$ (kDa)	$M_{n,\,exp}$ (kDa)	$M_{w,\,exp}$ (kDa)[b]	$Đ$[b]	I^* (%)[c]
			*Polymerizations with PC **4***						
12	[1000]:[10]:[**1**]	1000	24	77.5	8.01	7.51	8.26	1.10	107
13	[1000]:[10]:[**0.75**]	750	24	81.9	8.45	7.60	8.66	1.14	111
14	[1000]:[10]:[**0.5**]	500	24	85.5	8.82	8.29	9.37	1.13	106
15	[1000]:[10]:[**0.25**]	250	24	90.5	9.31	8.71	10.0	1.15	107
16	[1000]:[10]:[**0.1**]	100	24	93.1	9.58	9.22	10.8	1.17	104
17	[1000]:[10]:[**0.05**]	50	24	94.1	9.68	8.94	11.1	1.24	108
18	[1000]:[10]:[**0.025**]	25	24	95.1	9.77	9.18	11.7	1.27	106
19	[1000]:[10]:[**0.01**]	10	24	92.0	9.47	8.89	12.1	1.36	107
20	[1000]:[10]:[**0.005**]	5	24	82.7	8.53	8.07	12.5	1.55	106
21	[1000]:[10]:[**0.001**]	1	24	56.1	5.87	9.92	17.2	1.73	59
			*Polymerizations with PC **1***						
22	[1000]:[10]:[**1**]	1000	24	72.1	7.48	8.68	9.81	1.13	86
23	[1000]:[10]:[**0.5**]	500	24	82.2	8.48	8.86	10.2	1.15	96
24	[1000]:[10]:[**0.1**]	100	24	91.6	9.42	8.20	10.7	1.30	115
25	[1000]:[10]:[**0.05**]	50	24	95.5	9.81	8.85	12.6	1.42	111
26	[1000]:[10]:[**0.025**]	25	24	94.8	9.74	9.34	14.5	1.55	104
27	[1000]:[10]:[**0.01**]	10	24	79.6	8.23	8.20	14.5	1.77	100
28	[1000]:[10]:[**0.005**]	5	24	69.8	7.24	10.3	18.8	1.83	70
29	[1000]:[10]:[**0.001**]	1	24	34.6	3.72	18.3	32.8	1.79	20

Conditions: [MMA]:[DBMM]:[PC] = [1000]:[10]:[X]; 1 mL MMA, 1 mL solvent. Solutions prepared in the dark and then irradiated in a white LED beaker for specified time (see Supporting Information – Supplemental Polymerization Data for full details). [a]*Determined by 1H NMR.* [b]*Determined by GPC coupled with multi-angle light scattering.* [c]*Initiator efficiency (I^*) = ($M_{n,\,theo}$ / $M_{n,\,exp}$)•100%.*

Since previous polymerizations with dihydrophenazines were often performed in DMAc,[9, 37] we wondered whether the ability of **4** to mediate O-ATRP at such low catalyst loadings was due to core substitution or alternatively the choice of solvent. To test the influence of the solvent,

similar polymerizations at reduced catalyst loadings were performed with **1**. Interestingly, this experiment revealed that **1** can also operate effectively at significantly reduced catalyst loadings, although not matching the performance of PC **4**. At 100 ppm, **1** still produced well controlled PMMA (M_w = 10.7 kDa, $Đ$ = 1.30, I^* = 115% versus M_w = 9.81 kDa, $Đ$ = 1.13, I^* = 86% at 1000 ppm), though **4** exhibited a higher degree of polymerization control at this concentration (M_w = 10.8 kDa, $Đ$ = 1.17, I^* = 104%). In the case of **1**, the increase in I^* upon lowering [**1**] can likely be attributed to the fact that at lower catalyst loading (but with the same amount of initiator), less initiator is consumed through core substitution of the PC. At 100 ppm of **4**, the quantity of initiator consumed by core substitution is likely within the error for I^*. In addition, signs of a controlled polymerization are observed with catalyst loadings as low as 50 ppm of **1** (M_w = 12.6 kDa, $Đ$ = 1.42, I^* = 111%), a significant improvement over previous results in DMAc[37].

To understand how changing the polymerization solvent enables such dramatic improvements in polymerization control, several previous reports have investigated the impact of different solvents in O-ATRP. For example, previous work with dihydrophenazine PCs showed that less polar solvents can alter the excited state energy, as observed through blue shifting of their fluorescence. In addition, computations showed that ion pairing in $PC^{\bullet+}Br^-$ should be stronger in less polar solvents, favoring the formation of this ion pair.[50] Since we hypothesize $PC^{\bullet+}Br^-$ is the deactivator in O-ATRP, the choice of less polar solvents may improve deactivation and thereby polymerization control. Macroscopically, this effect of solvent polarity on polymerization control has been observed on several occasions,[39, 49, 50] as well as in this work.

In addition, solvent polarity can have drastic impacts on the photophysics and electrochemical properties of the PC, both of which can directly influence catalysis. In the case of 5,10-di(2-naphthyl)-5,10-dihydrophenazine, comprehensive investigation of these influences

revealed that lowering the solvent polarity can: (1) decrease non-radiative decay of the singlet excited state; (2) increase intersystem crossing to the triplet excited state, which we propose is most catalytically active in O-ATRP; (3) increase the lifetime of both the singlet and triplet excited states; (4) increase the excited state energy; and (5) increase the oxidation potential of the radical cation [$E^o(^2PC^{\bullet+}/^1PC)$].[39] Each of these changes to the PC properties should ultimately improve catalysis in O-ATRP. In particular, decreasing non-radiative decay, increasing intersystem crossing, and increasing the excited state lifetimes should favor activation. In turn, the concentration of $PC^{\bullet+}$ during early reaction times should be greater, leading to effective deactivation sooner in the polymerization. In addition, increasing $E^o(^2PC^{\bullet+}/^1PC)$ increases the driving force for deactivation, which in turn increases the rate of deactivation in O-ATRP.

Therefore, considering each of these reported solvent effects, the improvement in polymerization control and catalytic performance for both **1** and **4** in EtAc relative to DMAc can be rationalized. It should still be noted, though, that PC **4** did successfully mediate O-ATRP in a controlled fashion at lower catalyst loadings than PC **1**. This result, however, can likely be explained by the differences in photophysical and electrochemical properties of **1** and **4** outlined in Table 6.1. Most notably, **4** features stronger visible light absorption, observed as both a red shifted absorption (λ_{max} = 377 nm for **4** and 367 nm for **1**) and higher molar absorptivity (ε_{max} = 7,500 $M^{-1}cm^{-1}$ for **4** and 4,600 $M^{-1}cm^{-1}$ for **1**). Further, while the excited state reduction potentials [$E^o(^2PC^{\bullet+}/^3PC^*)$ and $E^o(^2PC^{\bullet+}/^1PC^*)$] of **1** and **4** are similar, the radical cation of **4** is more oxidizing [i.e. higher $E^o(^2PC^{\bullet+}/^1PC)$] than that of **1**. As such, **4** should be more effective than **1** in both activation and deactivation, leading to overall better catalysis in O-ATRP as observed.

Conclusion

This work investigated the possibility of radical addition to the organic photoredox catalyst 5,10-di(4-trifluormethylphenyl)-5,10-dihydrophenazine (PC **1**) under conditions relevant to O-ATRP. Common ATRP initiators were reacted with **1** under irradiation, which revealed that fragments resulting from the reduction of the ATRP initiator by **1** could add to the PC core. Depending upon reaction time and the sterics of the ATRP initiator, up to four fragments could be installed on the PC core, and these derivatives could be isolated in good to excellent yields. If this reaction is performed in the presence of monomer, oligomeric species can also add to the PC core, revealing an important termination reaction in O-ATRP.

Through isolation of the radical cation of **1**, it was determined that radical addition occurs to $\mathbf{1}^{\bullet+}$ and not **1**. Further, these substitutions generate compounds with different photophysical and electrochemical properties that can impact catalysis. As such, if these core substituted dihydrophenazines are employed as catalysts in the O-ATRP of MMA, they macroscopically perform non-equivalently in regard to control over the polymerization, as observed through the production of PMMA with varying molecular weights, $Đ$, and I*. In particular, PC **4** – formed through the reaction of **1** with EBP – showed excellent polymerization control, producing PMMA with $Đ$ as low as 1.10 and I* = 100%. Through optimization of the reaction solvent, this PC could mediate a controlled polymerization of PMMA in EtAc down to 10 ppm of catalyst (M_w = 12.1 kDa, $Đ$ = 1.36, I* = 107%), whereas **1** operated effectively down to 50 ppm of catalyst (M_w = 12.6 kDa, $Đ$ = 1.42, I* = 111%).

Finally, the insight gained through this work has broad implications in the field of photoredox catalysis. First, a new route to functionalizing diaryl dihydrophenazines is presented that enables the ability to not only further tailor the physical properties of this family of PCs but

also minimize undesired side reactivity. Second, new catalyst design principles are introduced that emphasize designing PCs that minimize side-reactions. Lastly, this work highlights the importance of understanding potential side reactions that a catalyst may undergo during the course of a reaction, especially when they can alter the identity of the catalyst, modify the catalyst properties, and ultimately impact the success of the reaction.

Experimental

Materials and Methods

Purchased Chemicals

Phenazine Reduction. Phenazine and sodium hydrosulfite were purchased from Alfa Aesar. Reagent grade alcohol was purchased from Fisher.

*For the synthesis of **1**.* Sodium tert-butoxide, 2-Dicyclohexylphosphino-2′,6′-diisopropoxybiphenyl (RuPhos), RuPhos Pd G4, 4-bromobenzotrifluoride, and dioxane were all purchased from Sigma Aldrich.

*For the synthesis of **2** – **6**.* Methyl 2-bromopropionate (M2BP), methyl α-bromoisobutyrate (MBiB), ethyl α-bromophenylacetate, diethyl-2-bromo-2-methylmalonate, triethylamine, and *N,N*-dimethylacetamide (DMAc) were purchased from Sigma Aldrich.

*For the synthesis of **1**$^{\bullet+}$**Br**$^{-}$.* Molecular bromine, benzene, and methanol were purchased from Sigma Aldrich.

For electrochemistry. Tetra-n-butylammonium hexafluorophosphate (NBu_4PF_6), silver nitrate, acetonitrile, and DMAc were purchased from Sigma Aldrich.

For Polymerizations. Methyl methacrylate (MMA), DMAc, dimethyl sulfoxide (DMSO), acetonitrile (MeCN), tetrahydrofuran (THF), ethyl acetate (EtAc), M2BP, MBiB, EBP, DBMM,

and ethyl α-chlorophenylacetate (EClP) were purchased from Sigma Aldrich. Benzene was purchased from TCI America.

Chemical Preparation and Storage

For Polymerizations. All solvents were purchased anhydrous and degassed and used as received. MMA, M2BP, MBiB, EBP, EClP, and DBMM were dried overnight using calcium hydride, distilled under reduced pressure, and freeze-pump-thawed three times. These chemicals were stored at -40ºC, in the dark, and under N_2 atmosphere when not in use. They were then warmed to room temperature prior to use each time.

Experimental Equipment

Electrochemistry. For all electrochemistry performed in this work, 0.1 M Bu_4NPF_6 was used as the supporting electrolyte. Cyclic voltammetry and spectro-electrochemistry were performed using a three-electrode cell. Cyclic voltammetry was performed with a glassy carbon working electrode, platinum counter electrode, and a silver/silver nitrate (0.01 M $AgNO_3$ in MeCN with 0.1 M Bu_4NPF_6) reference electrode. For spectro-electrochemistry, the working electrode was a platinum mesh. As appropriate, potentials were referenced to a saturated calomel electrode (SCE) by adding 0.29 V to the potential vs. $AgNO_3$.

Light Reactors. The following LEDs were used in the construction of light reactors for this work. For light beakers, strips of white LEDs were purchased from Creative Lighting Solutions (item no. CL-FRS1210-5M-12V-WH). Reactors were constructed by wrapping a 400 mL beaker (10.0 cm tall, 8.5 cm diameter) with aluminum foil and wrapping LED strips (9 LED segments,

16” total) around the inside of the reactor (Figure 6.7). Figure 6.8 shows the qualitative emission spectrum of the LEDs used in this work.

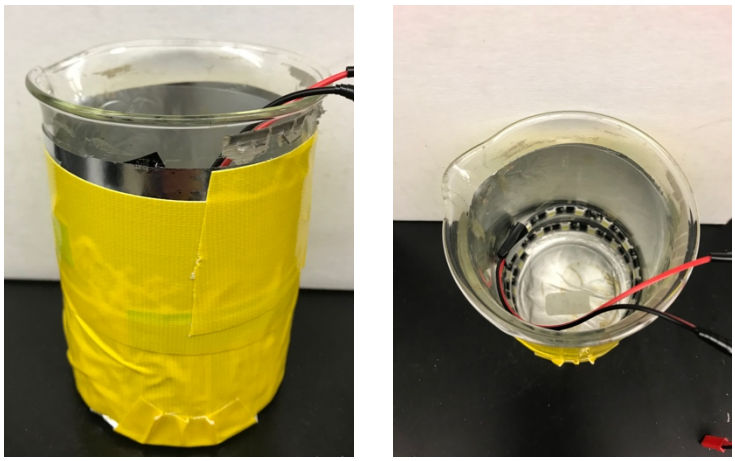

Figure 6.7. *Photographs showing a side view (left) and top view (right) of the light beakers used in this work.*

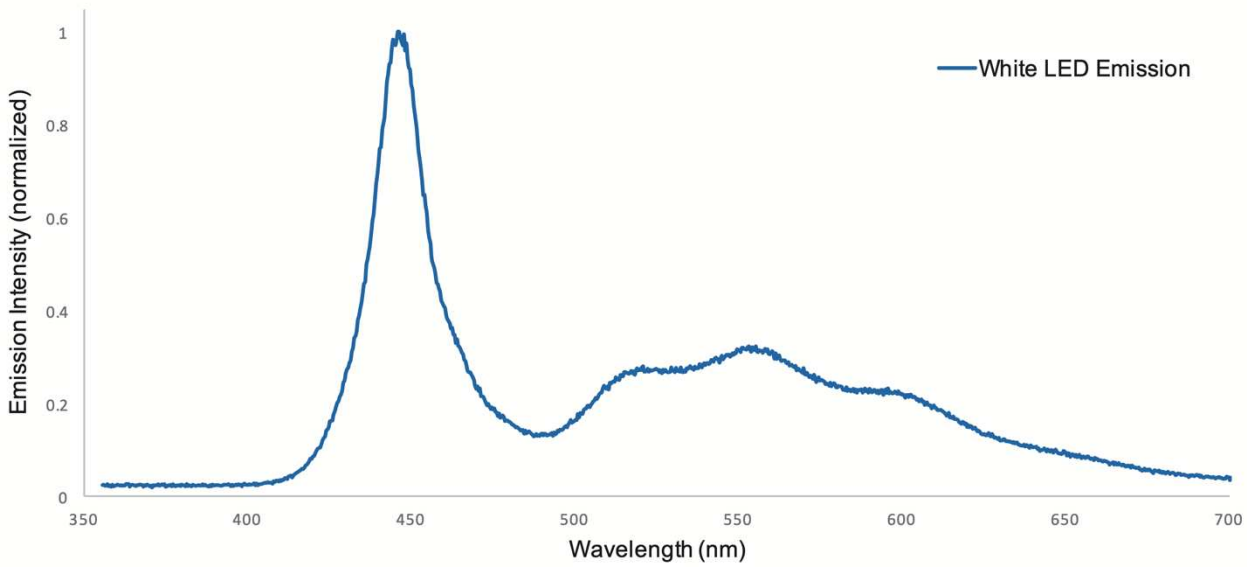

Figure 6.8. *Emission spectrum of the LEDs used in this work.*

Instrumentation

Nuclear magnetic resonance (NMR) spectroscopy was performed using either a Bruker US 400 MHZ spectrometer or a Bruker Ascend 400 MHZ spectrometer. All ^{1}H NMR spectra are

reported in **δ** units, parts per million (ppm), and are referenced to residual chloroform (7.26 ppm) or benzene (7.15 ppm) signals. Electron paramagnetic resonance (EPR) spectroscopy was performed using a Bruker ESR-300 spectrometer. EPR data for $\mathbf{1}^{\bullet+}Br^-$ was simulated using EasySpin.[51] Analysis of polymer molecular weights were performed via gel permeation chromatography (GPC) coupled with multi-angle light scattering (MALS), using an Agilent HPLC fitted with one guard column, three PLgel 5 μm MIXED-C gel permeation columns, a Wyatt Technology TrEX differential refractometer, and a Wyatt Technology miniDAWN TREOS light scattering detector, using THF as the eluent at a flow rate of 1.0 mL/min. For molecular weight analysis of PMMA, a d*n*/dc value of 0.084 was used. Electrochemical measurements were performed using either a Gamry Interface 1010B or 1010E potentiostat. UV-Visible spectroscopy was performed using an Agilent Cary 5000 UV-Vis-NIR spectrometer. Fluorescence spectroscopy was performed using an FS5 Spectrofluorometer from Edinburgh Instruments. Measurements of LED emission were made using an Olympus IX73 inverted microscope connected to a Horiba iHR 550 spectrometer with a Horiba Synapse back-illuminated CCD camera and a 1200 blaze/mm grating. For qualitative measurements of LED emission intensity, light sources were placed in the same configuration and the light directed into an opening in the microscope. Single crystal X-ray diffractometry was performed using a Bruker D8 Quest ECO single-crystal X-ray diffractometer equipped with Mo Kα (λ = 0.71073 Å). Data was collected and integrated using the Bruker APEX 3 software. Absorption correction were applied using SADABS.[52] Crystal structures were solved using SHELXT and refined with the aid of successive difference Fourier maps by SHELXL operated in conjunction with Bruker APEX 3.[53,54] Hydrogen atoms were placed in ideal positions and refined using a riding model for all structures. Mass spectrometry was performed using a Thermo-Finnigan LTQ LC/MS-MS spectrometer equipped with a linear ion trap.

Procedures

Synthesis of Photocatalysts

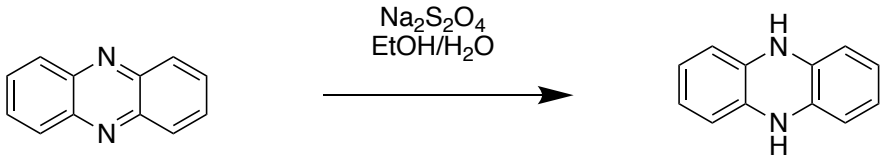

Figure 6.9. *Scheme for the synthesis of dihydrophenazine.*

Synthesis of 5,10-Dihydrophenazine. This synthesis was performed using a modified literature procedure.[55] Phenazine (2.0 g, 0.011 mol) was dissolved in 70 mL of EtOH that had been sparged with N_2 for 30 min. This mixture was brought to reflux under N_2 and $Na_2S_2O_4$ dissolved in degassed water was added. The solution was then refluxed for 3 hrs and subsequently cooled to room temperature. The solid was collected using a swivel frit under N_2 and washed with sparged H_2O (3 x 100 mL). The solid was then dried overnight under vacuum before being brought into an N_2 filled glovebox. Yield: 1.90 g (95%). ^{1}H NMR (400 MHz, C_6D_6): δ 8.31-8.23 (m, 4H), 7.91-7.83 (m, 4H).

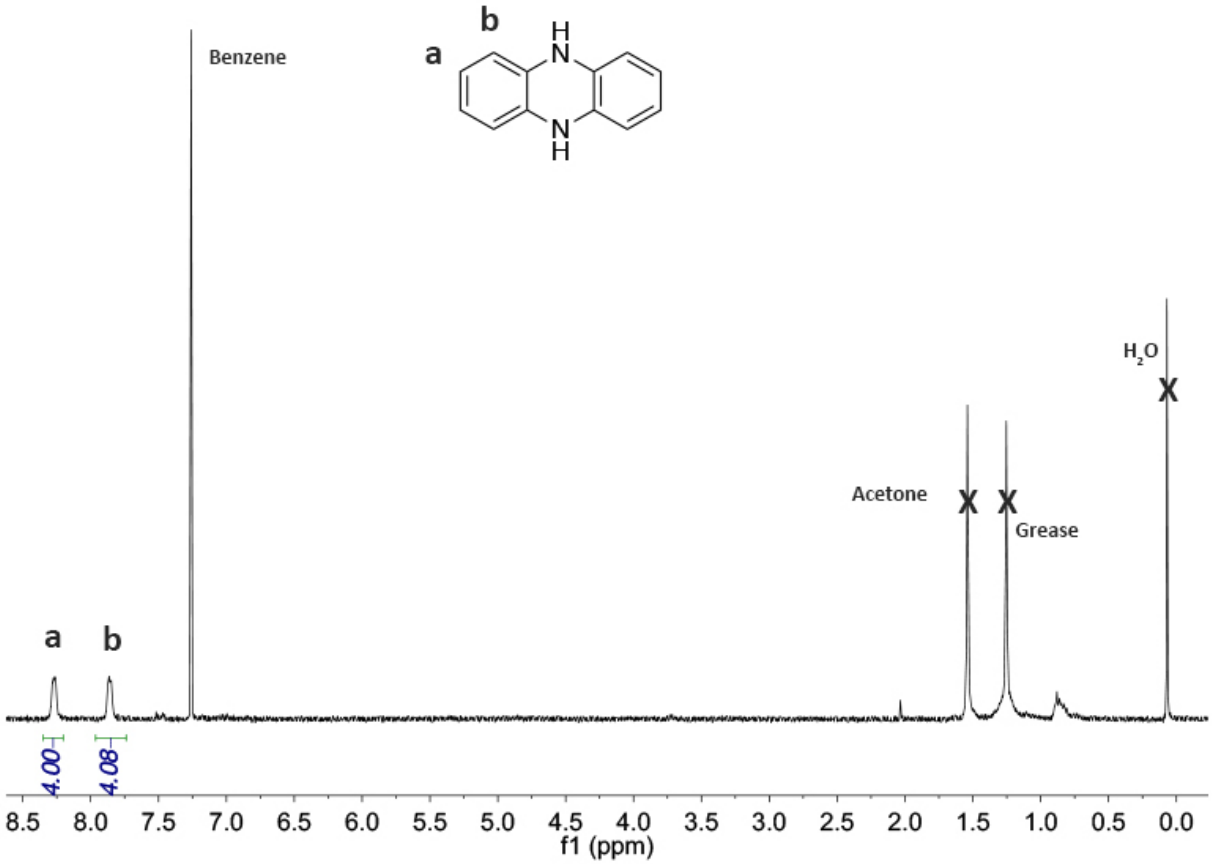

Figure 6.10. *^{1}H NMR spectrum of dihydrophenazine in C_6D_6.*

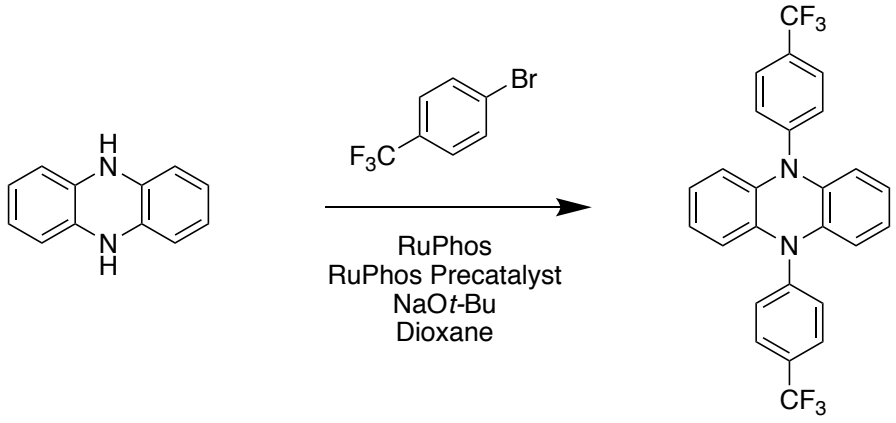

Figure 6.11. *Scheme for the synthesis of **1**.*

*Synthesis of 5,10-di(4-trifluoromethylphenyl)-5,10-dihydrophenazine (**1**).* This synthesis was performed using a modified literature procedure.[9] Bromobenzotrifluoride was sparged with N_2 over ice for 15 minutes. 5,10-dihydrophenazine (2.00 g, 0.011 mol), RuPhos Pd G4 precatalyst (0.373 g, 0.000439 mol), and dioxane (16 mL) were added to an oven dried Schlenk flask in an N_2 filled glovebox. The flask was brought out of the glovebox and NaO*t*-Bu (4.22 g, 0.0439 mol), RuPhos (0.205 g, 0.000439 mol), and sparged bromobenzotrifluoride (6.15 mL, 0.0439 mol) were added under N_2. This mixture was refluxed overnight and subsequently cooled to room temperature. 600 mL of DCM and 300 mL of water were added. The product crashed out of solution over several minutes. Both layers were filtered and the solid was collected. The product was then recrystallized from boiling DCM/MeOH to yield yellow crystals. Yield: 4.2 g (81%). ^{1}H NMR (400 MHz, C_6D_6): δ 7.33-7.24 (m, 4H), 6.94-6.88 (m, 4H), 6.33-6.24 (m, 4H), 5.66-5.59 (m, 4H). ^{13}C NMR (101 MHz, C_6D_6): δ 136.01, 131.32, 128.48-127.49 (unresolvable from solvent), 121.70, 113.39. ^{19}F NMR (376 MHz): δ -62.26. Abs. λ_{max}: 367 nm. ε = 5200 $M^{-1}\cdot cm^{-1}$. Em. λ_{max}: 611 nm.

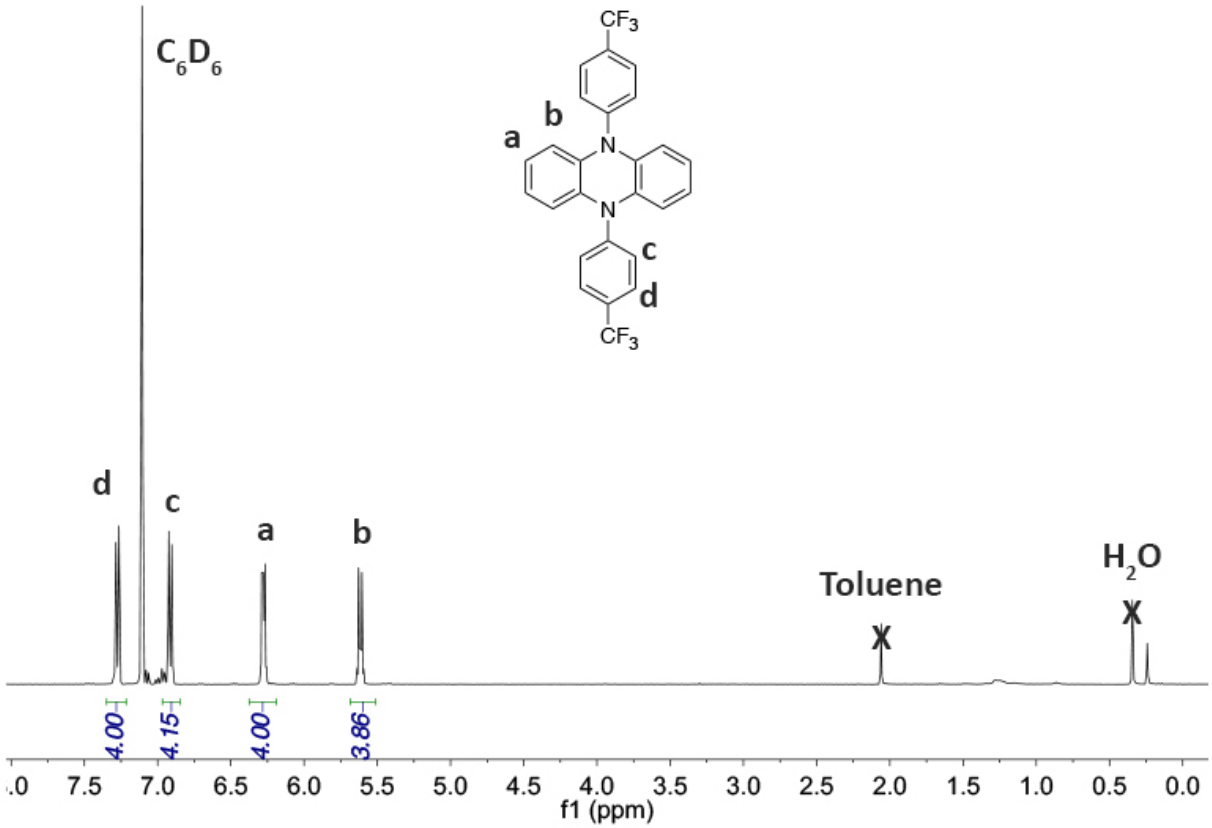

Figure 6.12. *^{1}H NMR spectrum of **1** in C_6D_6.*

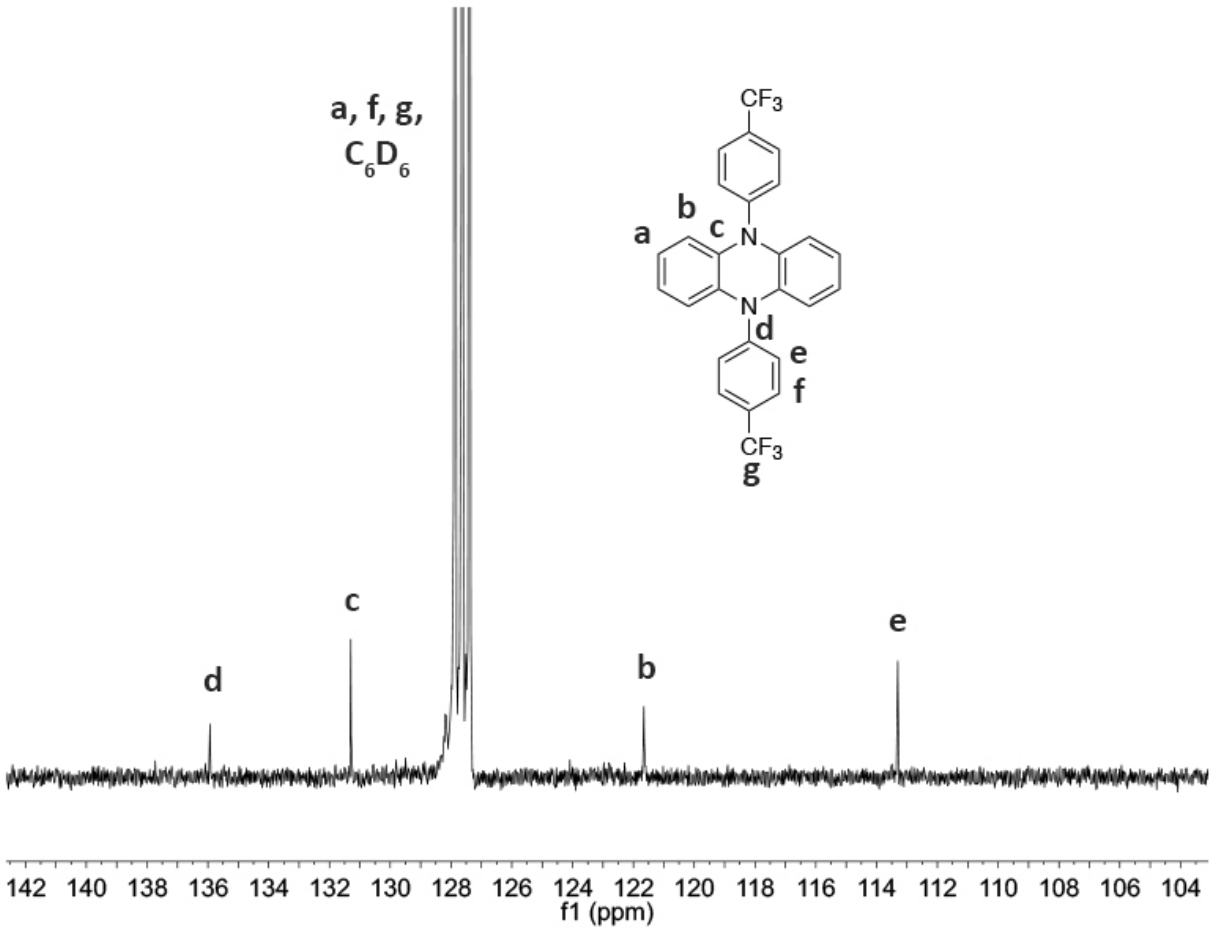

Figure 6.13. *^{13}C NMR spectrum of **1** in C_6D_6.*

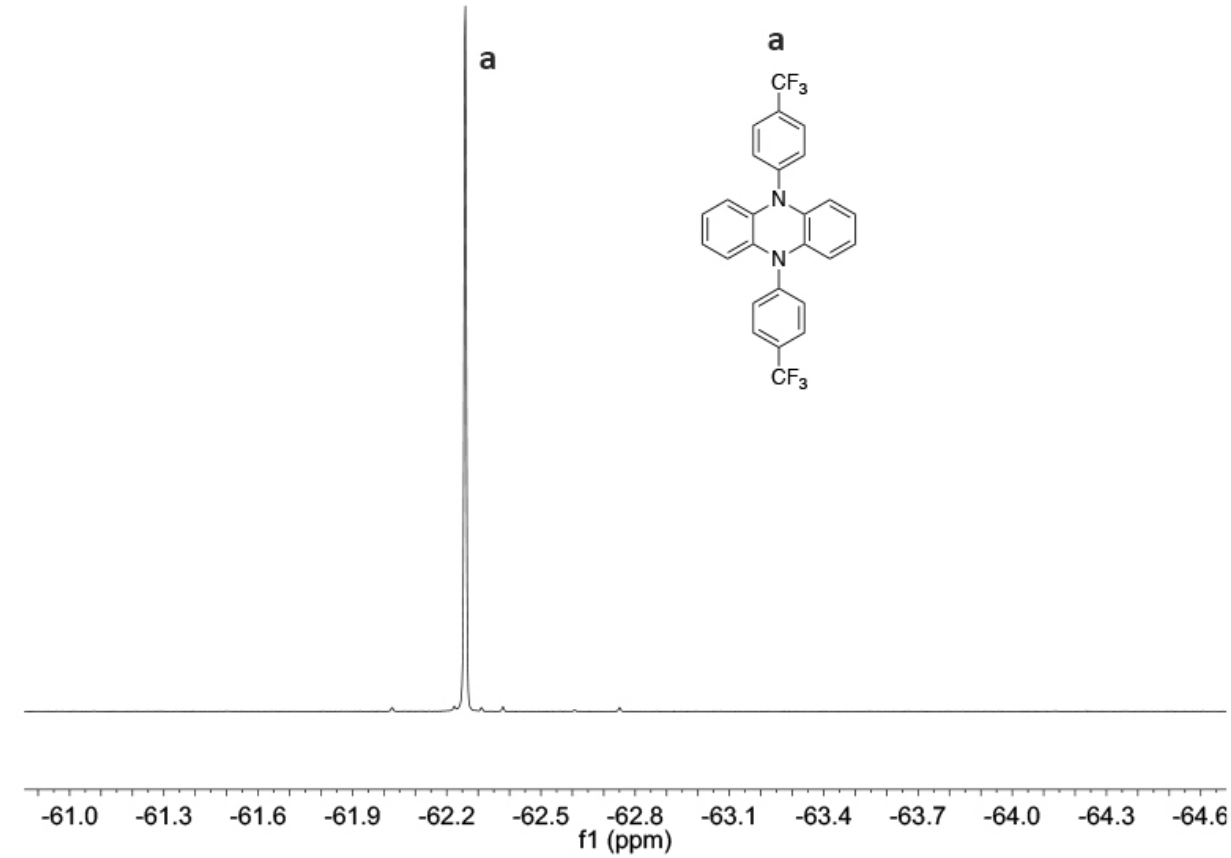

Figure 6.14. *^{19}F NMR spectrum of **1** in C_6D_6.*

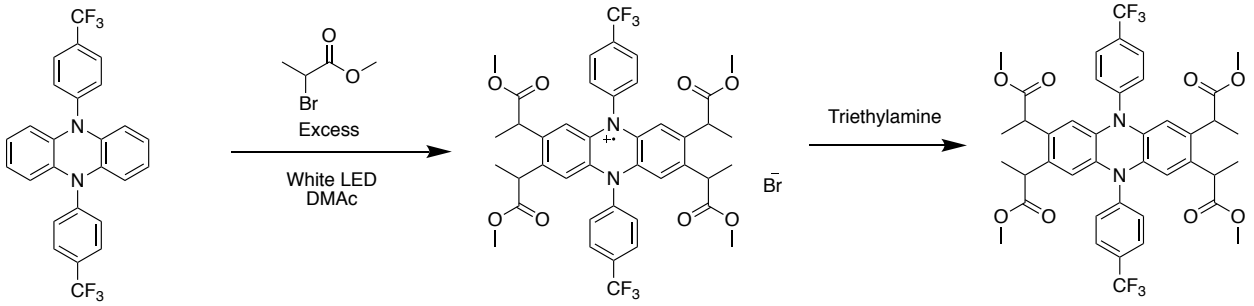

Figure 6.15. *Scheme for the synthesis of **2**.*

*Synthesis of 2,3,7,8-tetra(methylpropionoate-yl)-5,10-di(4-trifluoromethylphenyl)-5,10-dihydrophenazine (**2**).* 5,10-di(4-trifluoromethylphenyl)-5,10-dihydrophenazine (0.400 g, 0.000851 mol) was added to 40 mL of DMAc in a 100 mL vacuum flask in an N_2 filled glovebox.

Methyl 2-bromopropionoate (0.55 mL, 0.00425 mol) was added and the solution was stirred and irradiated with white LEDs overnight. Then the flask was removed from the box, opened to air and 20 mL of radical cation solution was removed for further study. To the remaining solution, 2 mL of triethylamine was added. This solution was then stirred for 5 minutes and the volatiles were subsequently removed by rotary evaporation and dry-loaded onto silica gel. The compound was purified by flash chromatography using a gradient of 0-30% EtOAc in hexanes with 5% triethylamine. Yield: 0.233 g (67.1%). ^{1}H NMR (400 MHz, C_6D_6): δ 7.42-7.32 (m, 4H), 7.10-7.04 (m, 4H (unresolvable from solvent)), 6.08-5.99 (m, 4H), 3.66 (q (*J* = 7.04 Hz), 2H), 3.58 (q (*J* = 7.07 Hz), 2H), 3.23-3.18 (m, 12H), 1.24-1.16 (m, 12H). ^{13}C NMR (101 MHz, C_6D_6): δ 173.99, 144.44, 135.22, 132.42, 130.21, 113.71, 113.19, 51.22, 40.90, 40.67, 18.63. ^{19}F NMR (376 MHz, C_6D_6): δ -62.21. Abs. λ_{max}: 373 nm. ε = 4600 $M^{-1}\cdot cm^{-1}$. Em. λ_{max}: 600 nm.

Alternatively, the product could also be isolated after reduction with triethylamine by precipitation into DI water, resulting in the formation of a yellow solid. The solid was collected by vacuum filtration, washed with excess DI water and cold methanol (~20 mL), and then dried overnight under high vacuum. When 1.1 g of 5,10-di(4-trifluoromethylphenyl)-5,10-dihydrophenazine starting material was used, 1.1 g (57%) of **2** was recovered using this method. Characterization matched that reported above.

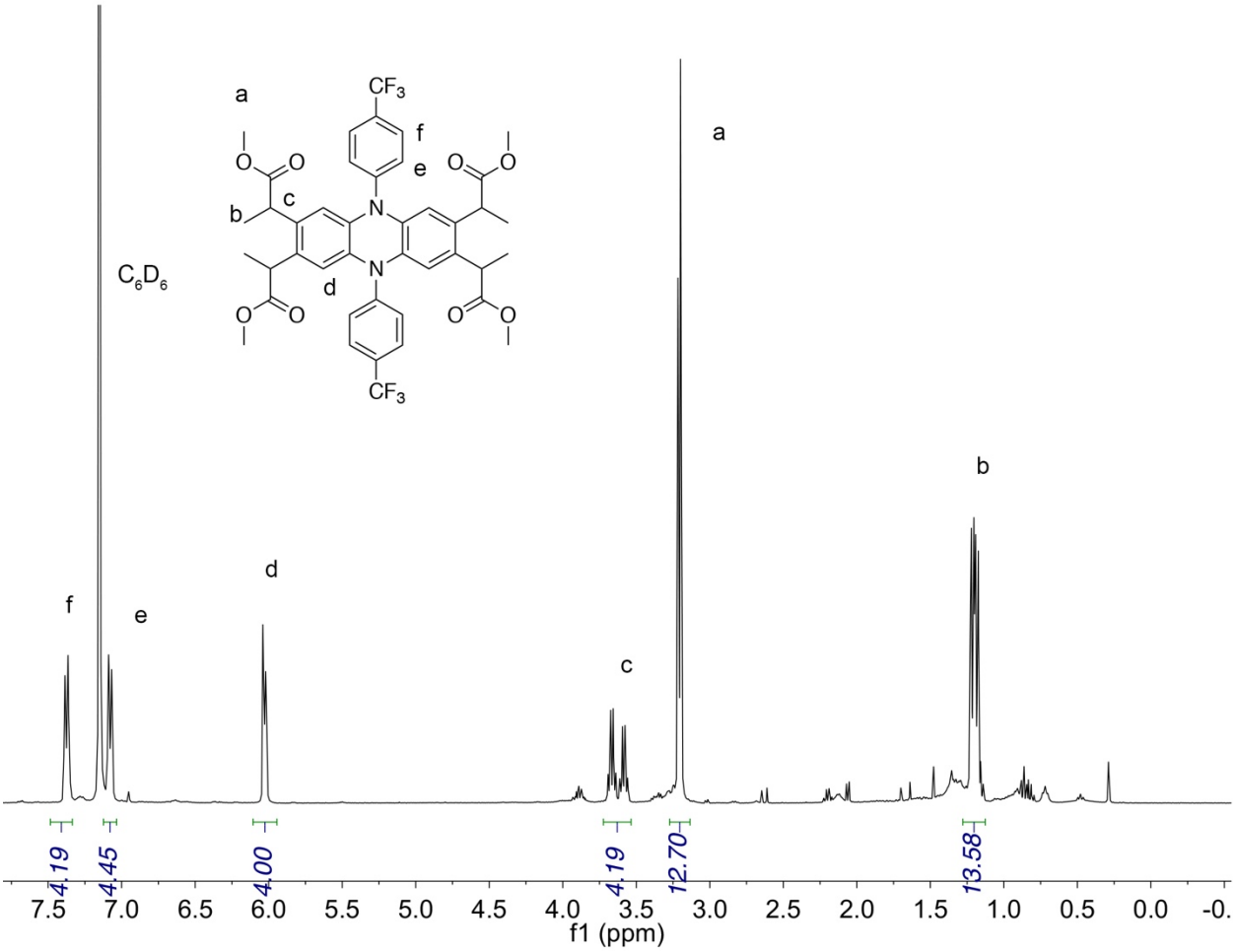

Figure 6.16. *^{1}H NMR spectrum of **2** in C_6D_6.*

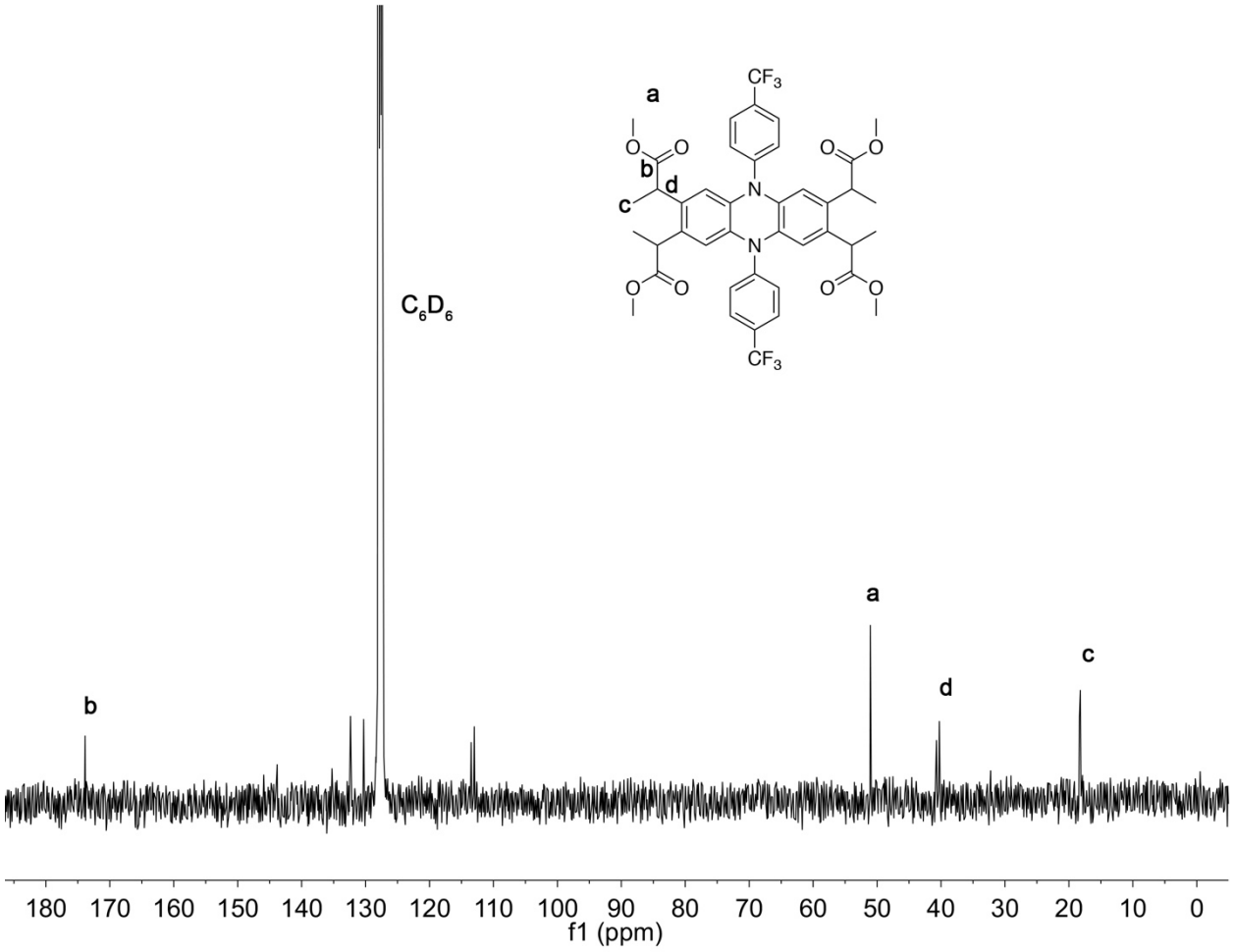

Figure 6.17. *^{13}C NMR spectrum of **2** in C_6D_6.*

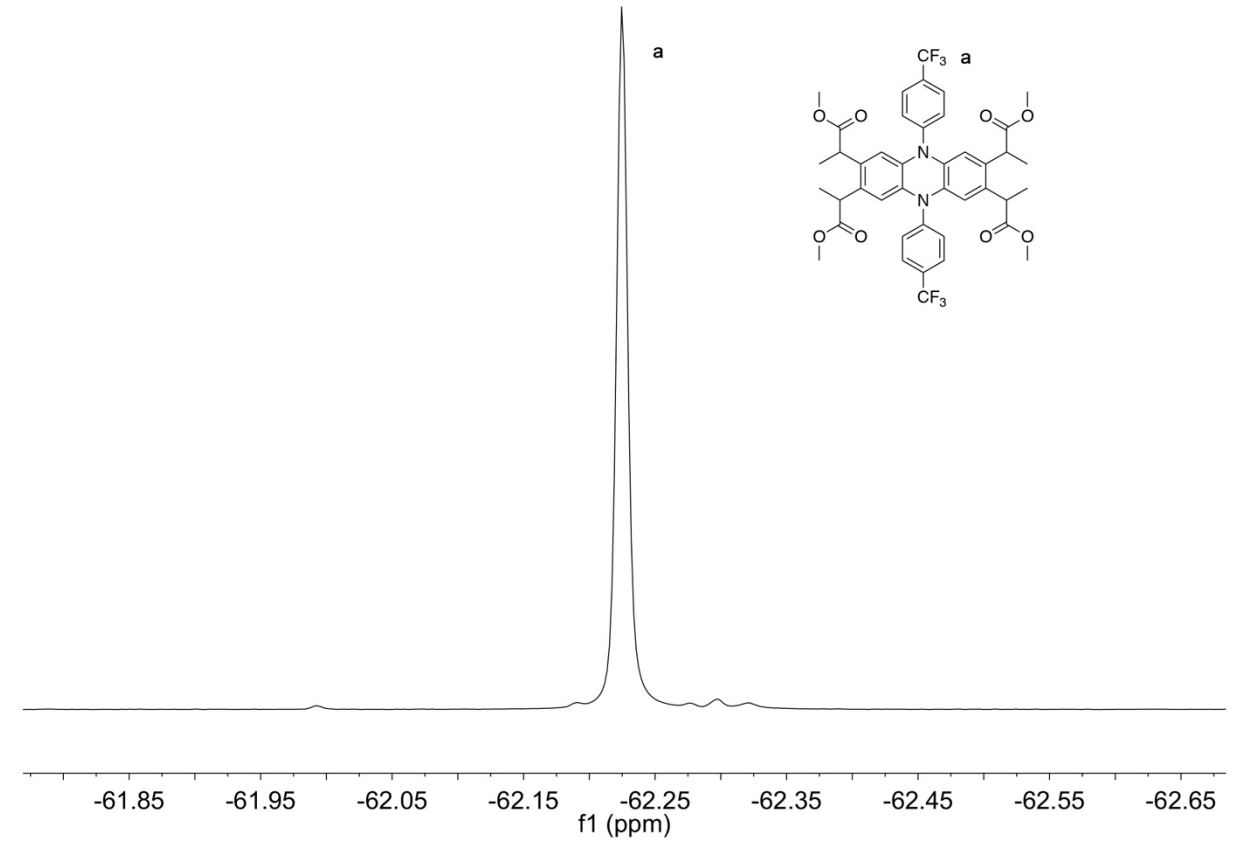

Figure 6.18. *^{19}F NMR spectrum of **2** in C_6D_6.*

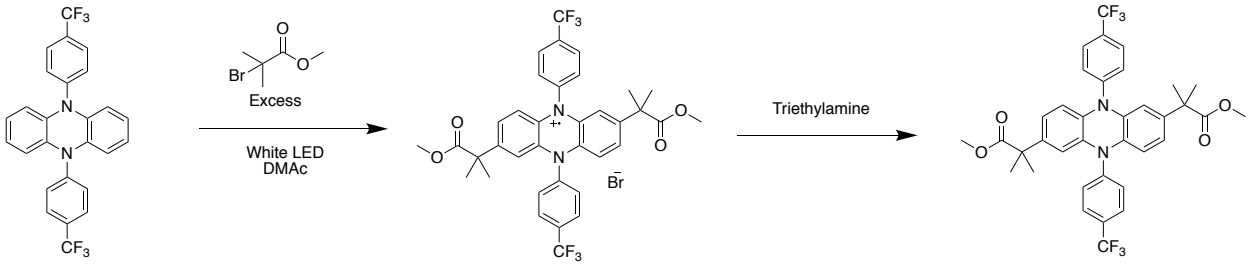

Figure 6.19. *Scheme for the synthesis of **3**.*

*Synthesis of 2,7-di(methylisobutyrate-yl)-5,10-di(4-trifluoromethylphenyl)-5,10-dihydrophenazine (**3**).* 5,10-di(4-trifluoromethylphenyl)-5,10-dihydrophenazine (0.200 g, 0.000425 mol) was added to 20 mL of DMAc in a scintillation vial in an N_2 filled glovebox. Methyl-α-bromoisobutyrate (0.55 mL, 0.00425 mol) was added and the solution was stirred and

irradiated with white LEDs overnight. Then the scintillation vial was removed from the box, opened to air and 1 mL of triethylamine was added. The solution was then stirred for 5 minutes and the volatiles were subsequently removed by rotary evaporation. The residue was dissolved in EtOAc and dry-loaded onto silica gel. The compound was purified by flash chromatography using a gradient of 0-30% EtOAc in hexanes with 5% triethylamine. Yield: 0.218 g (76.5 %). ^{1}H NMR (400 MHz, C_6D_6): δ 7.22-7.14 (m, 4H), 6.87-6.76 (m, 4H), 6.29-6.20 (m, 2H), 5.85-5.75 (m, 2H), 5.52-5.40 (m, 2H), 3.03 (s, 6H), 1.15 (s, 12H). ^{13}C NMR (101 MHz, C_6D_6): δ 175.86, 143.95, 138.62, 135.85, 135.40, 135.10, 134.61, 131.21, 130.86, 130.19, 119.05, 118.83, 113.75, 113.27, 112.33, 111.58, 51.16, 45.56, 26.01. ^{19}F NMR (376 MHz, C_6D_6): δ -62.22. Abs. λ_{max}: 371 nm. ε = 4400 $M^{-1}\cdot cm^{-1}$. Em. λ_{max}: 611 nm.

Alternatively, the product could also be isolated after reduction with triethylamine by precipitation into DI water, resulting in the formation of a yellow solid. The solid was collected by vacuum filtration, washed with excess DI water and cold methanol (~20 mL), and then dried overnight under high vacuum. When 1.1072 g of 5,10-di(4-trifluoromethylphenyl)-5,10-dihydrophenazine starting material was used, 1.1466 g (72.6%) of **3** was recovered using this method. Characterization matched that reported above.

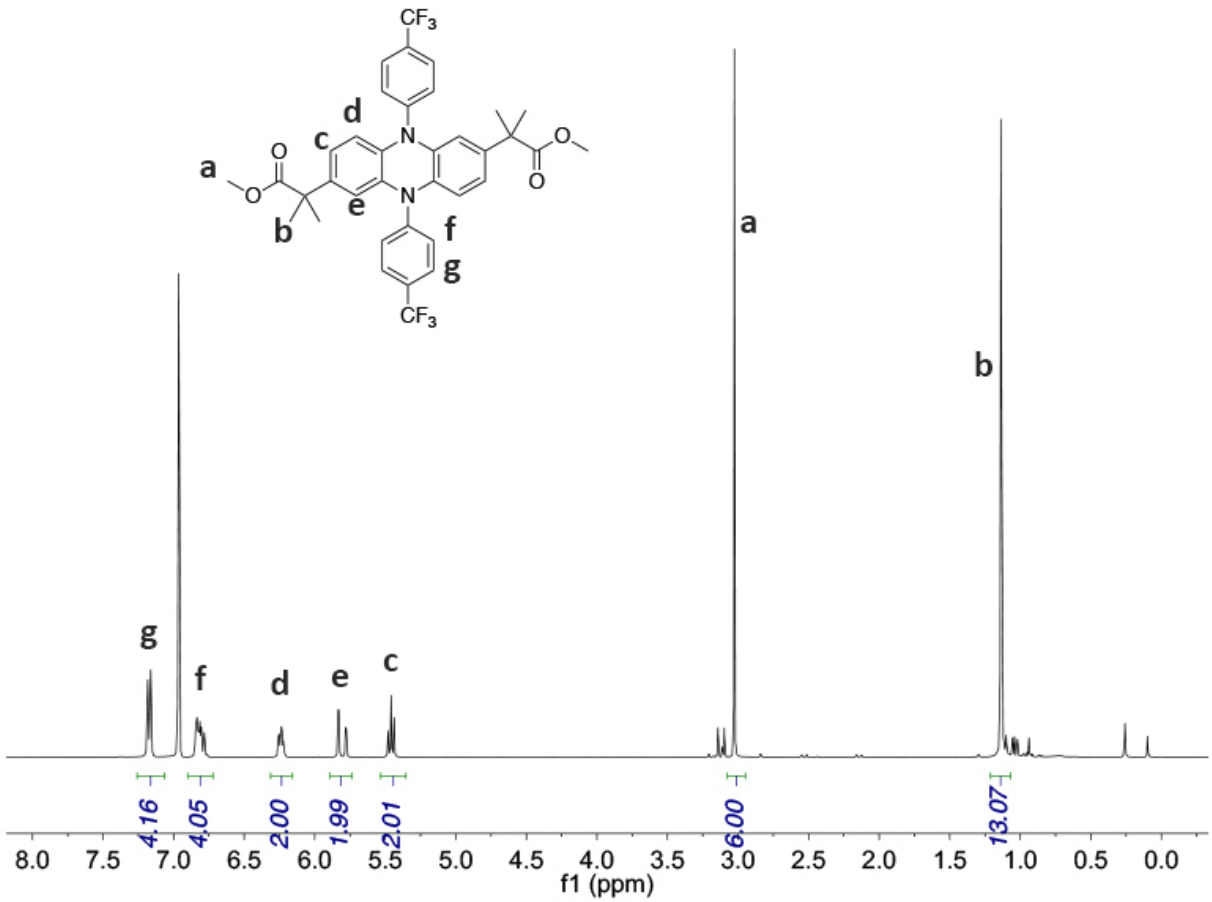

Figure 6.20. *^{1}H NMR spectrum of **3** in C_6D_6.*

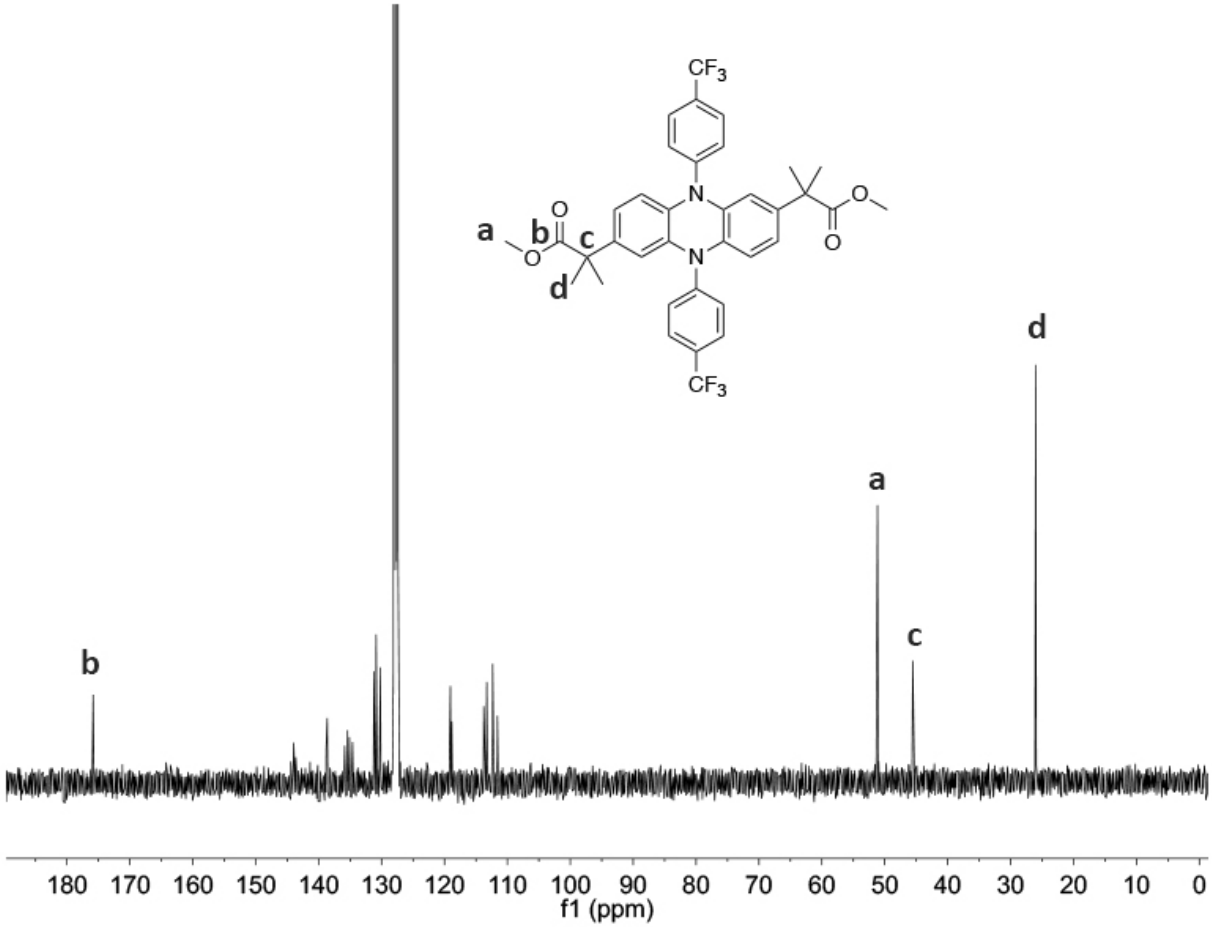

Figure 6.21. *^{13}C NMR spectrum of **3** in C_6D_6.*

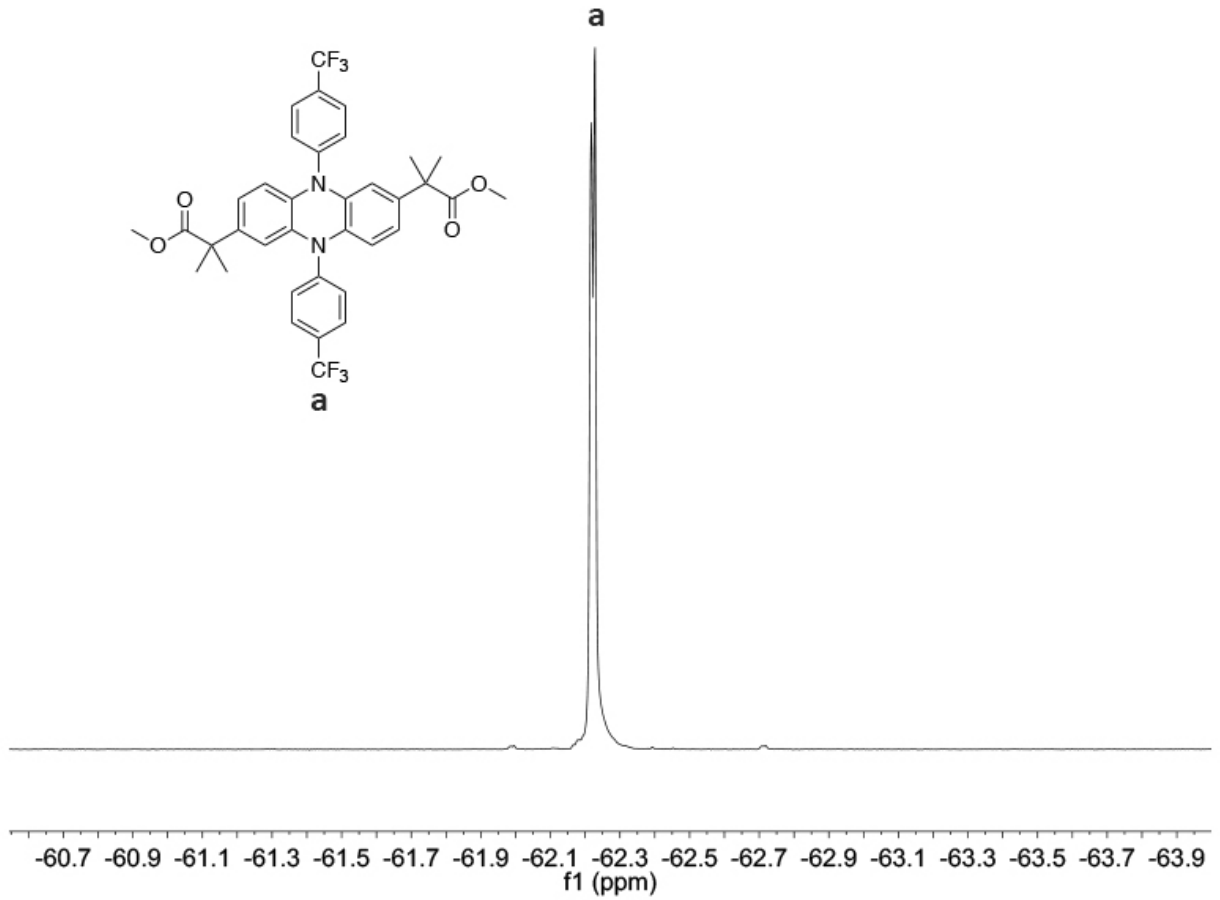

Figure 6.22. *^{19}F NMR spectrum of **3** in C_6D_6.*

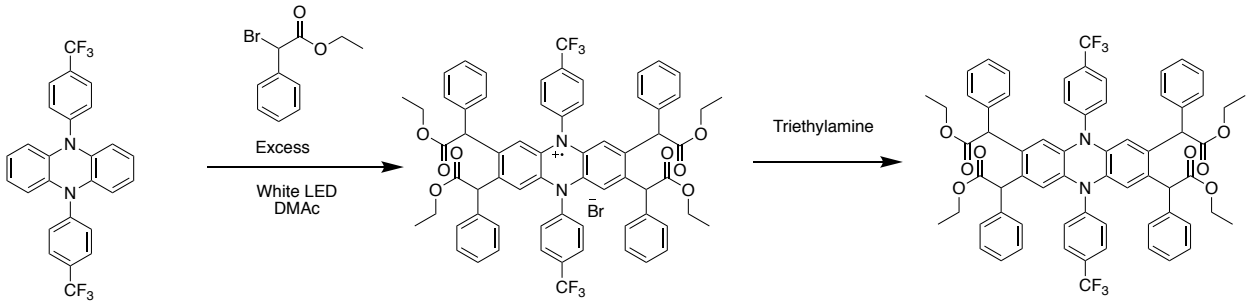

Figure 6.23. *Scheme for the synthesis of **4**.*

*Synthesis of 2,3,7,8-tetra(ethylphenylacetate-yl)-5,10-di(4-trifluoromethylphenyl)-5,10-dihydrophenazine (**4**).* 5,10-di(4-trifluoromethylphenyl)-5,10-dihydrophenazine (0.200 g, 0.000425 mol) was added to 20 mL of DMAc in a scintillation vial in an N_2 filled glovebox. Ethyl-

α-bromophenylacetate (0.743 mL, 0.00425 mol) was added and the solution was stirred and irradiated with white LEDs overnight. Then the scintillation vial was removed from the box, opened to air and 2 mL of triethylamine were added. The solution was then stirred for 5 minutes and the volatiles were subsequently removed by rotary evaporation. The residue was dissolved in EtOAc and dry-loaded onto silica gel. The compound was purified by flash chromatography using a gradient of 0-50% EtOAc in hexanes with 5% triethylamine. The first yellow fraction was isolated as the compound named above. Yield: 0.423 g (88.7 %). ^{1}H NMR (400 MHz, C_6D_6): δ 7.07-6.94 (m, indistinguishable from solvent), 6.90-6.62 (m, 20H), 5.77-5.61 (m, 4H), 5.10-4.98 (m, 4H), 3.75-3.43 (m, 8H), 0.67-0.49 (m, 12H) ^{13}C NMR (101 MHz, C_6D_6): δ 171.48, 171.30, 143.01, 138.57, 134.93, 130.87, 128.57, 128.27, 127.82, 127.56, 126.95, 125.56, 122.88, 114.80, 60.78, 52.50, 13.69. ^{19}F NMR (376 MHz, C_6D_6): δ -62.33 Abs. λ_{max}: 377 nm. ε = 8500 $M^{-1}\cdot cm^{-1}$. Em. λ_{max}: 581 nm.

Alternatively, the product could also be isolated after reduction with triethylamine by precipitation into DI water, resulting in the formation of an orange solid. The solid was collected by vacuum filtration, washed with excess DI water and cold methanol (~20 mL), and then dried overnight under high vacuum. When 1.1167 g of 5,10-di(4-trifluoromethylphenyl)-5,10-dihydrophenazine starting material was used, 1.4200 g (53.4%) of **4** was recovered using this method. Characterization matched that reported above.

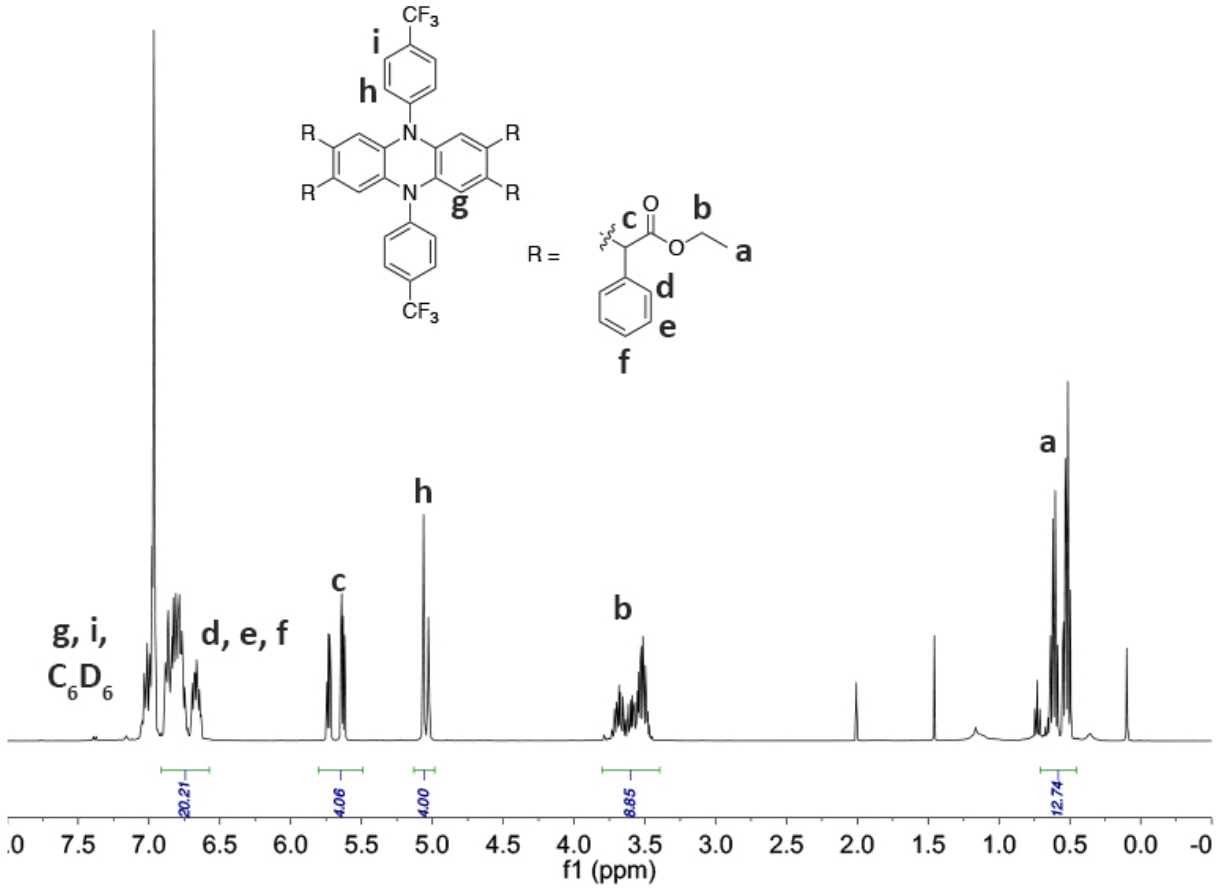

Figure 6.24. *^{1}H NMR spectrum of **4** in C_6D_6.*

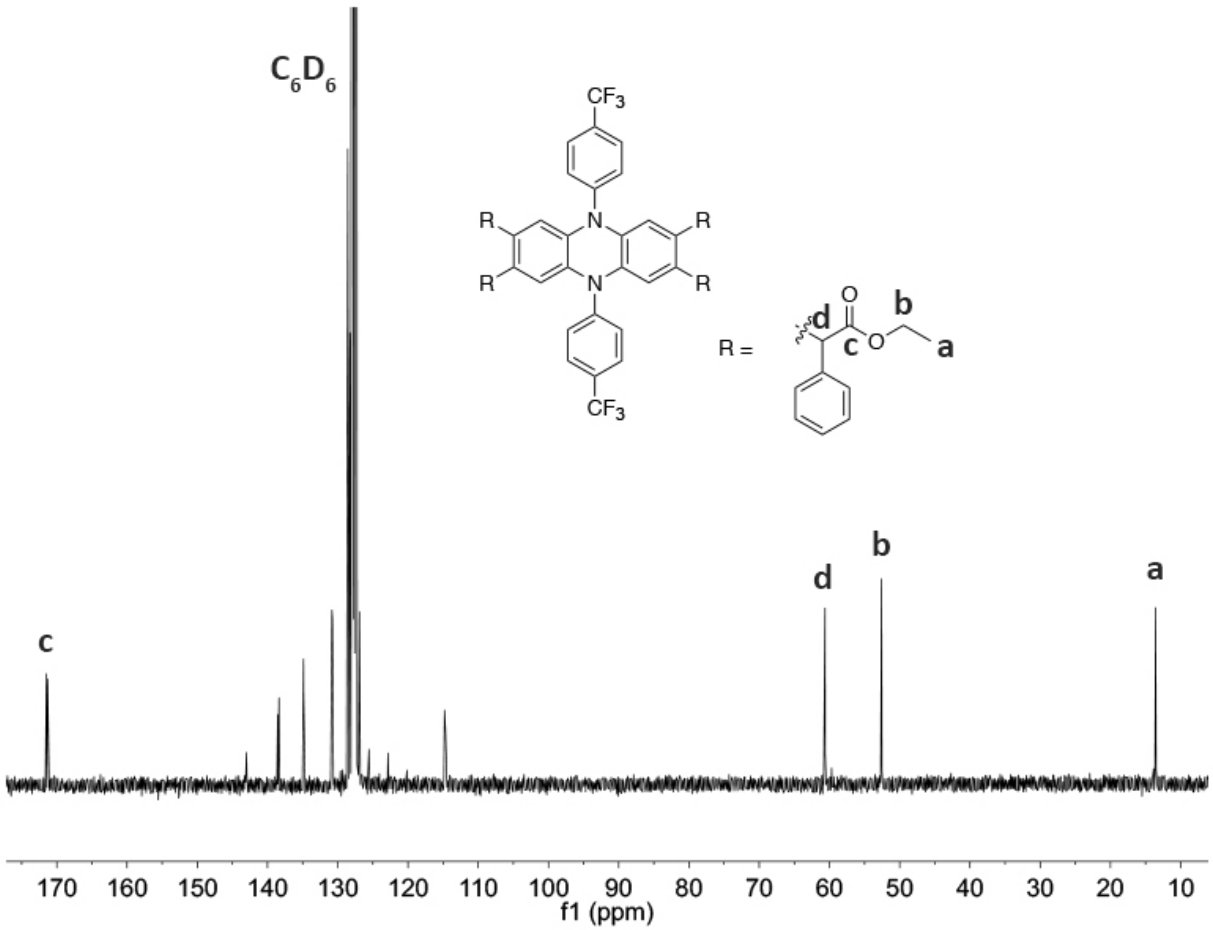

Figure 6.25. *^{13}C NMR spectrum of **4** in C_6D_6.*

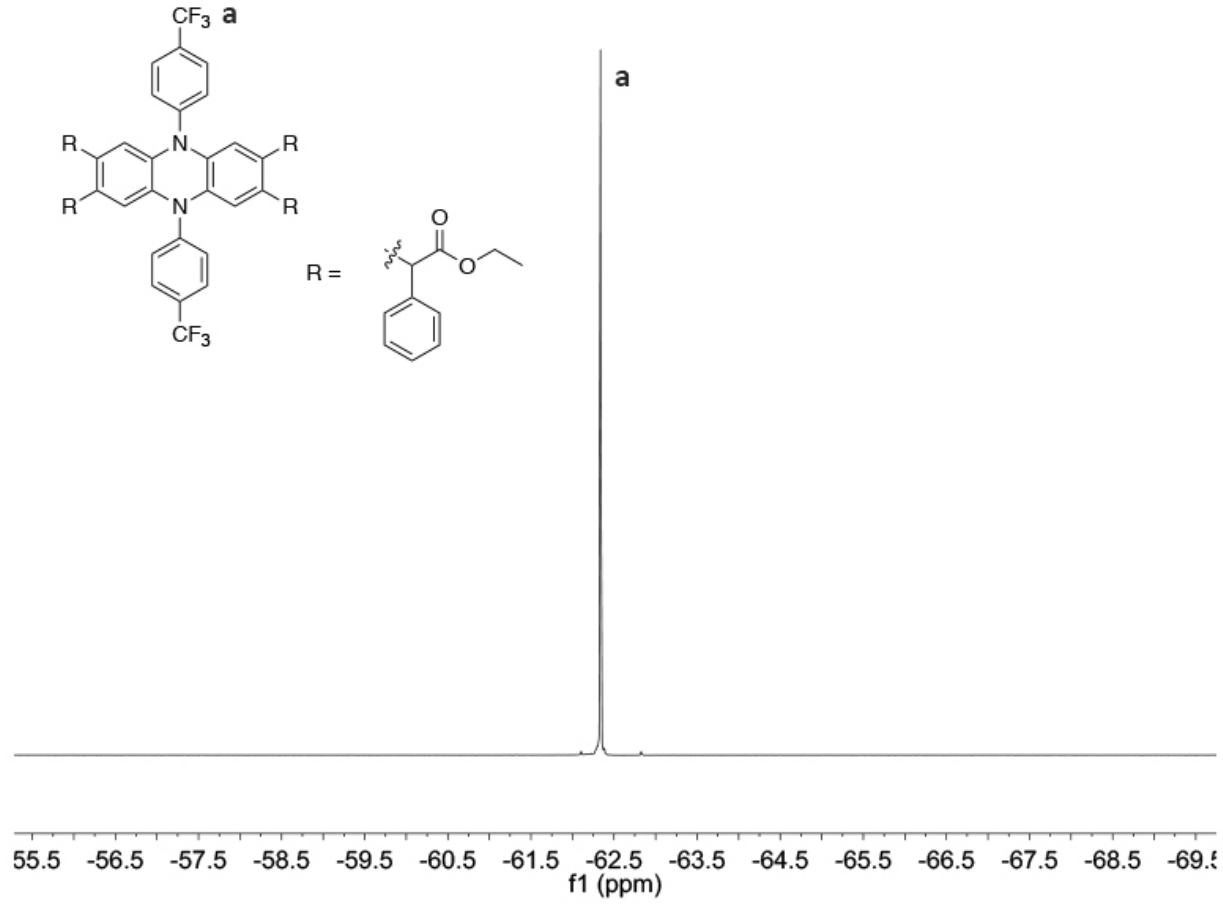

Figure 6.26. *^{19}F NMR spectrum of **4** in C_6D_6.*

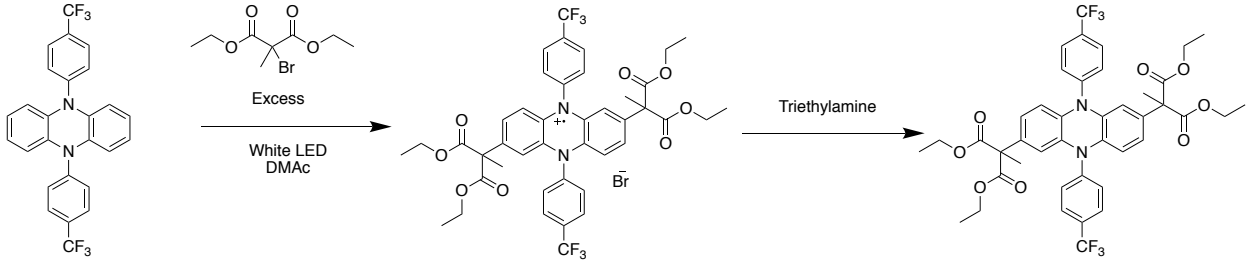

Figure 6.27. *Scheme for the synthesis of **5**.*

*Synthesis of 2,7-di(diethyl-2-methymalonate-yl)-5,10-di(4-trifluoromethylphenyl)-5,10-dihydrophenazine (**5**).* 5,10-di(4-trifluoromethylphenyl)-5,10-dihydrophenazine (0.400 g, 0.000851 mol) was added to 40 mL of DMAc in a 100 mL vacuum flask in an N_2 filled glovebox.

Diethyl-2-bromo-2-methylmalonate (1.63 mL, 0.00851 mol) was added and the solution was stirred and irradiated with white LEDs overnight. Then the flask was removed from the box, opened to air and 20 mL of radical cation solution was removed for further study. To the remaining solution, 2 mL of triethylamine was added. This solution was then stirred for 5 minutes and the volatiles were subsequently removed by rotary evaporation and dry-loaded onto silica gel. The compound was purified by flash chromatography using a gradient of 0-30% EtOAc in hexanes with 5% triethylamine. Yield: 0.320 g (92.2%). ^{1}H NMR (400 MHz, C_6D_6): δ 7.41-7.30 (m, 4H), 7.13-6.90 (m, 4H (unresolvable from solvent)), 6.56-6.47 (m, 2H), 6.21-6.04 (m, 2H), 5.67-5.58 (m, 2H), 3.92-3.67 (m, 8H), 1.87-1.72 (s, 6H), 0.84-0.78 (m, 12H). ^{13}C NMR (101 MHz, C_6D_6): δ 170.93, 143.76, 135.69, 135.36, 135.09, 132.30, 131.47, 131.32, 130.77, 120.81, 120.68, 114.54, 113.75, 113.00, 112.63, 61.15, 57.98, 21.90, 13.61. ^{19}F NMR (376 MHz, C_6D_6): δ -62.23, -62.31, -62.35. Abs. λ_{max}: 373 nm. $\varepsilon = 4600\ M^{-1}\cdot cm^{-1}$. Em. λ_{max}: 602 nm.

Alternatively, the product could also be isolated after reduction with triethylamine by precipitation into DI water, resulting in the formation of a yellow solid. The solid was collected by vacuum filtration, washed with excess DI water and cold methanol (~20 mL), and then dried overnight under high vacuum. When 1.145 g of 5,10-di(4-trifluoromethylphenyl)-5,10-dihydrophenazine starting material was used, 1.090 g (93.9%) of **5** was recovered using this method. Characterization matched that reported above.

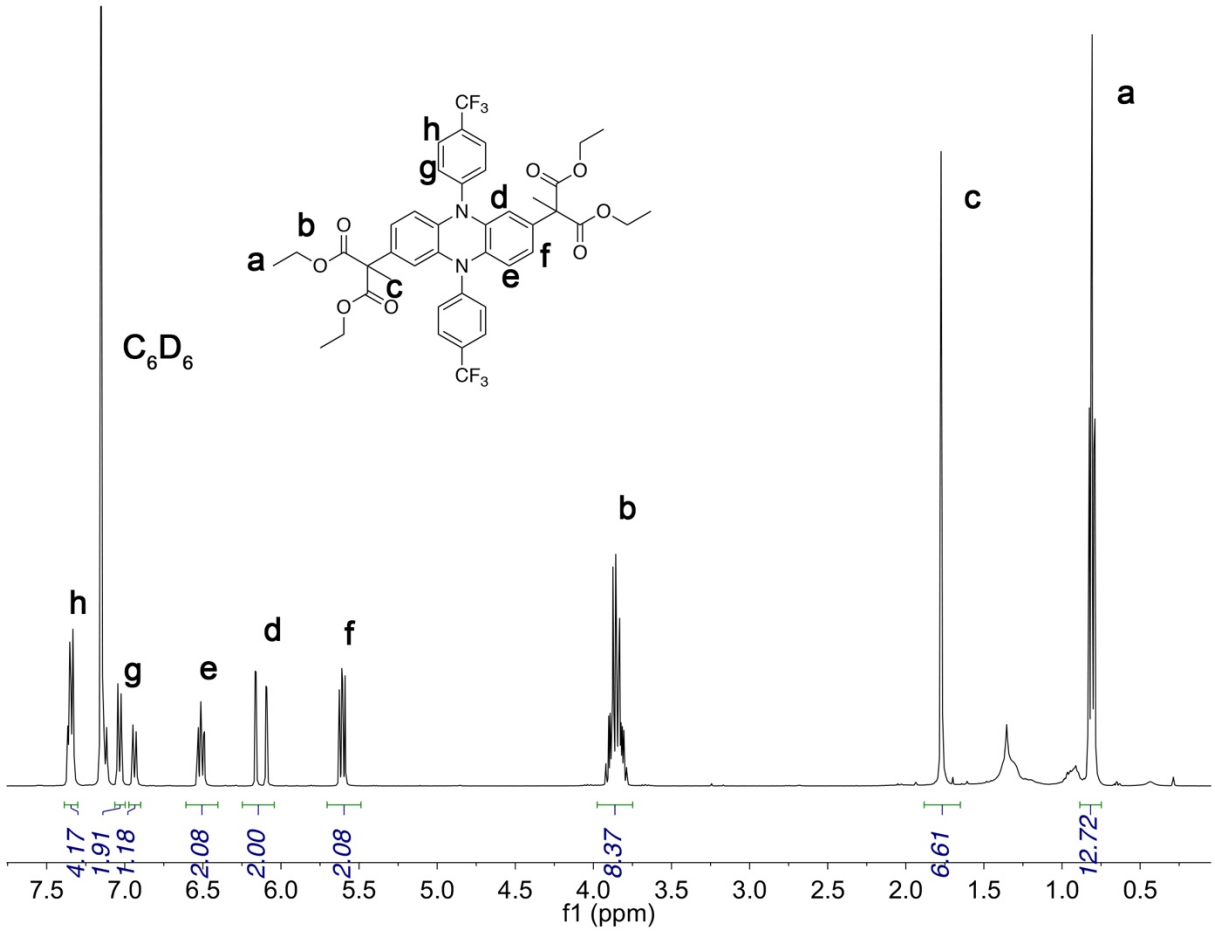

Figure 6.28. *^{1}H NMR spectrum of **5** in C_6D_6.*

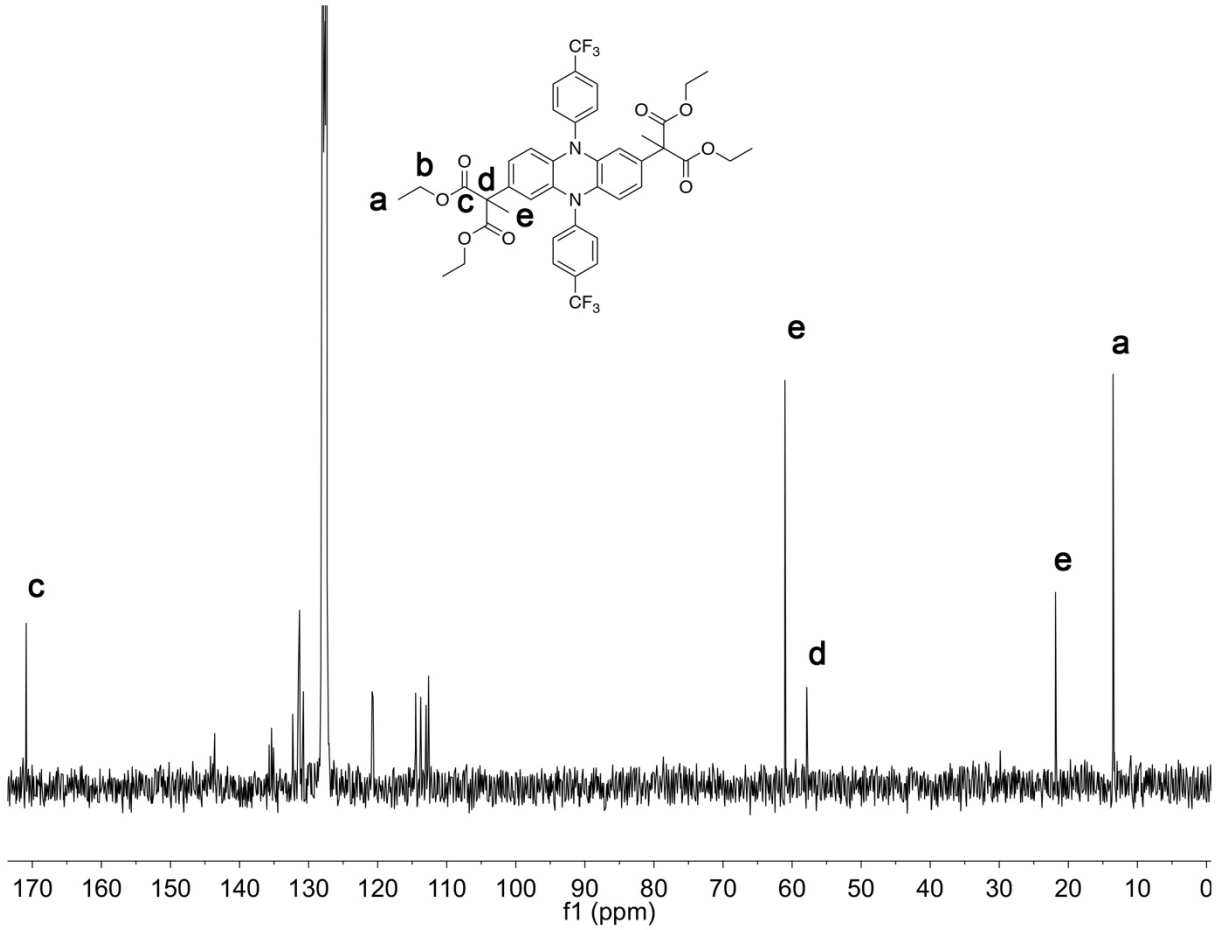

Figure 6.29. *^{13}C NMR spectrum of **5** in C_6D_6.*

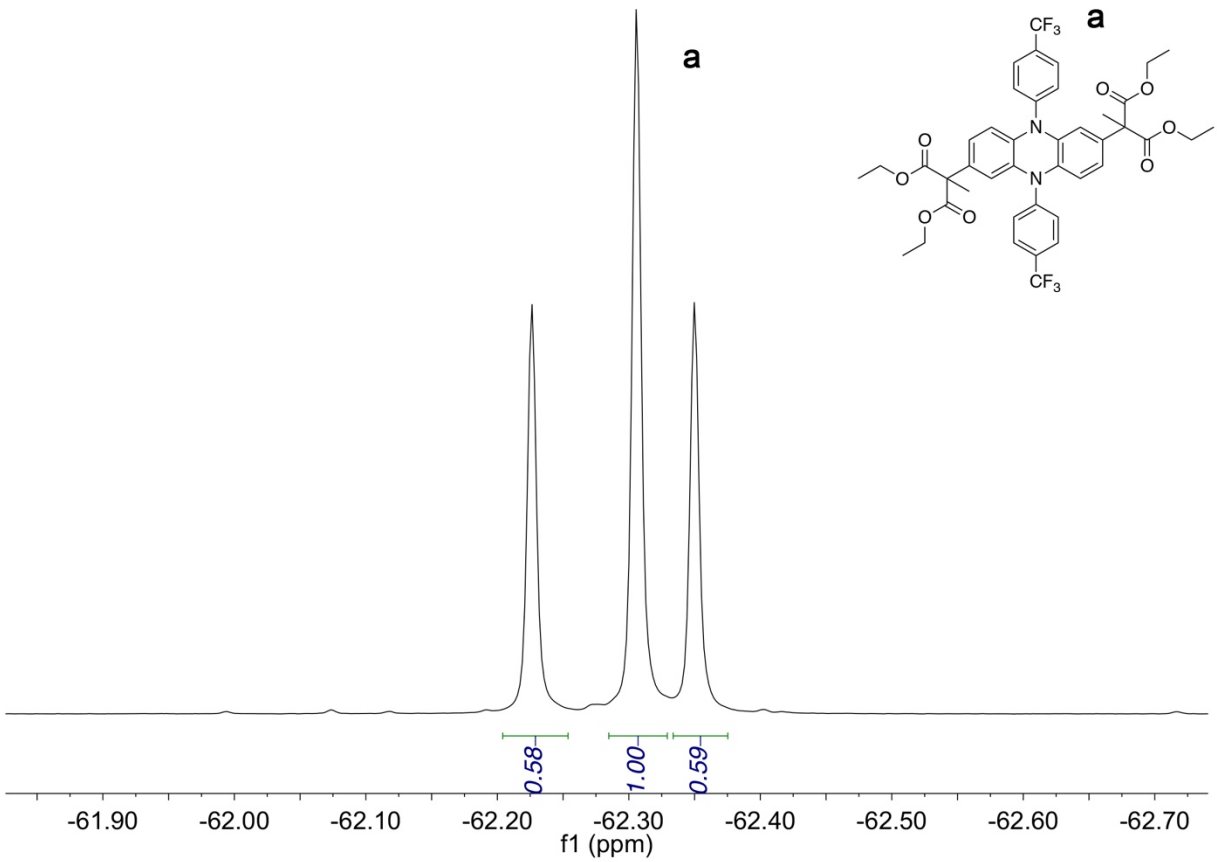

Figure 6.30. *^{19}F NMR spectrum of **5** in C_6D_6.*

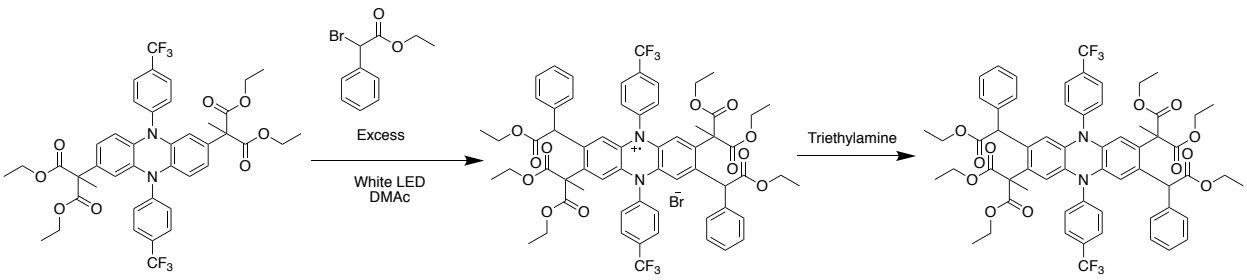

Figure 6.31. *Scheme for the synthesis of **6**.*

*Synthesis of 2,7-di(diethyl-2-methymalonate-yl)-3,8 di (ethyl phenylacetate-yl)-5,10-di(4-trifluoromethylphenyl)-5,10-dihydrophenazine (**6**).* 2,7-di(diethyl-2-methymalonate-yl)-5,10-di(4-trifluoromethylphenyl)-5,10-dihydrophenazine (0.277 g, 0.00034 mol) was added to 20 mL of DMAc in a scintillation vial in an N_2 filled glovebox. Ethyl-α-bromophenylacetate (0.60 mL,

0.0034 mol) was added and the solution was stirred and irradiated with white LEDs overnight. Then the flask was removed from the box, opened to air. Then, 2 mL of triethylamine was added. This solution was then stirred for 5 minutes and the volatiles were subsequently removed by rotary evaporation and dry-loaded onto silica gel. The compound was purified by flash chromatography using a gradient of 0-50% EtOAc in hexanes with 5% triethylamine. Yield: 0.320 g (92.2%). ^{1}H NMR (400 MHz, C_6D_6): δ 7.38-7.20 (m, 8H), 7.08-6.83 (m, 10H), 6.27-6.04 (m, 2H), 5.77-5.60 (m, 2H), 5.23 (s, 2H), 3.97-3.64 (m, 12H), 2.00-1.90 (m, 6H), 0.90-0.71 (m, 18H. ^{13}C NMR (101 MHz, C_6D_6): δ 171.38, 171.12, 139.99, 134.58, 132.19, 131.92, 131.23, 130.60, 130.09, 126.74, 118.84, 118.33, 112.36, 61.38, 60.63, 59.31, 52.87, 23.66, 13.54. ^{19}F NMR (376 MHz, C_6D_6): δ -62.25, -62.35, -62.43. Abs. λ_{max}: 372 nm. ε = 7200 $M^{-1}\cdot cm^{-1}$. Em. λ_{max}: 598 nm.

Alternatively, the product could also be isolated after reduction with triethylamine by precipitation into DI water, resulting in the formation of an orange solid. The solid was collected by vacuum filtration, washed with excess DI water and cold methanol (~20 mL), and then dried overnight under high vacuum. When 1.7978 g of **5** was used, 1.0895 g (38.9%) of **6** was recovered using this method. Characterization matched that reported above.

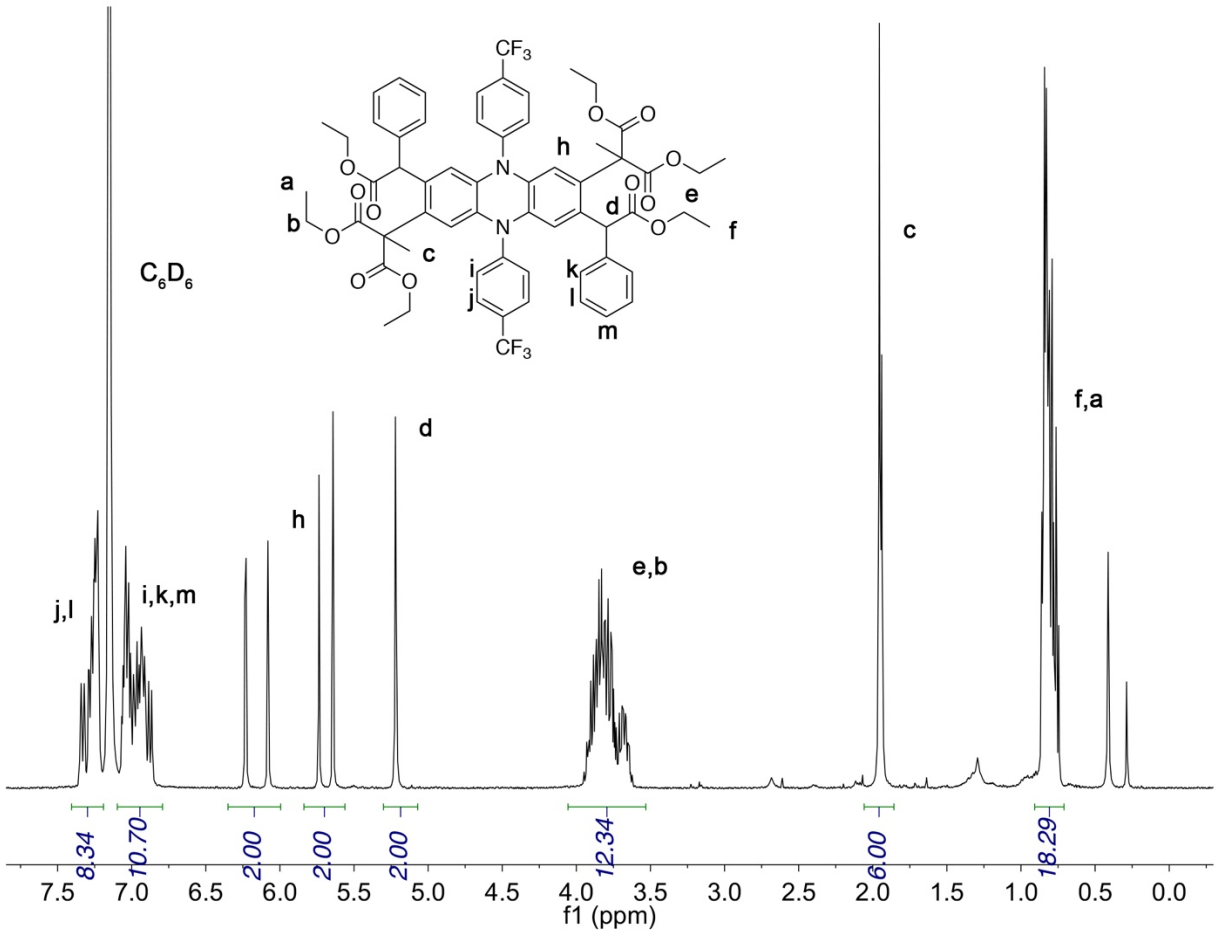

Figure 6.32. *^{1}H NMR spectrum of **6** in C_6D_6.*

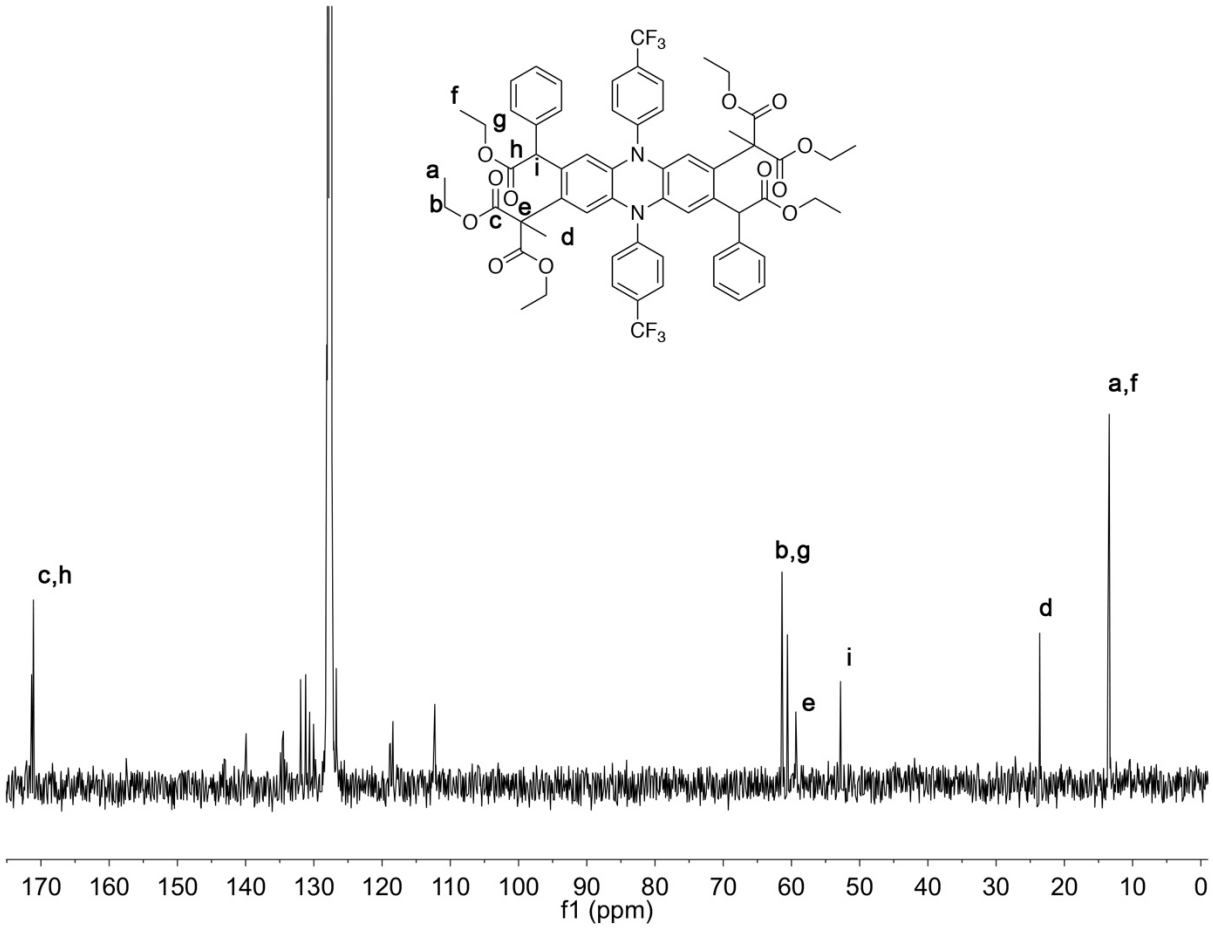

Figure 6.33. *^{13}C NMR spectrum of **6** in C_6D_6.*

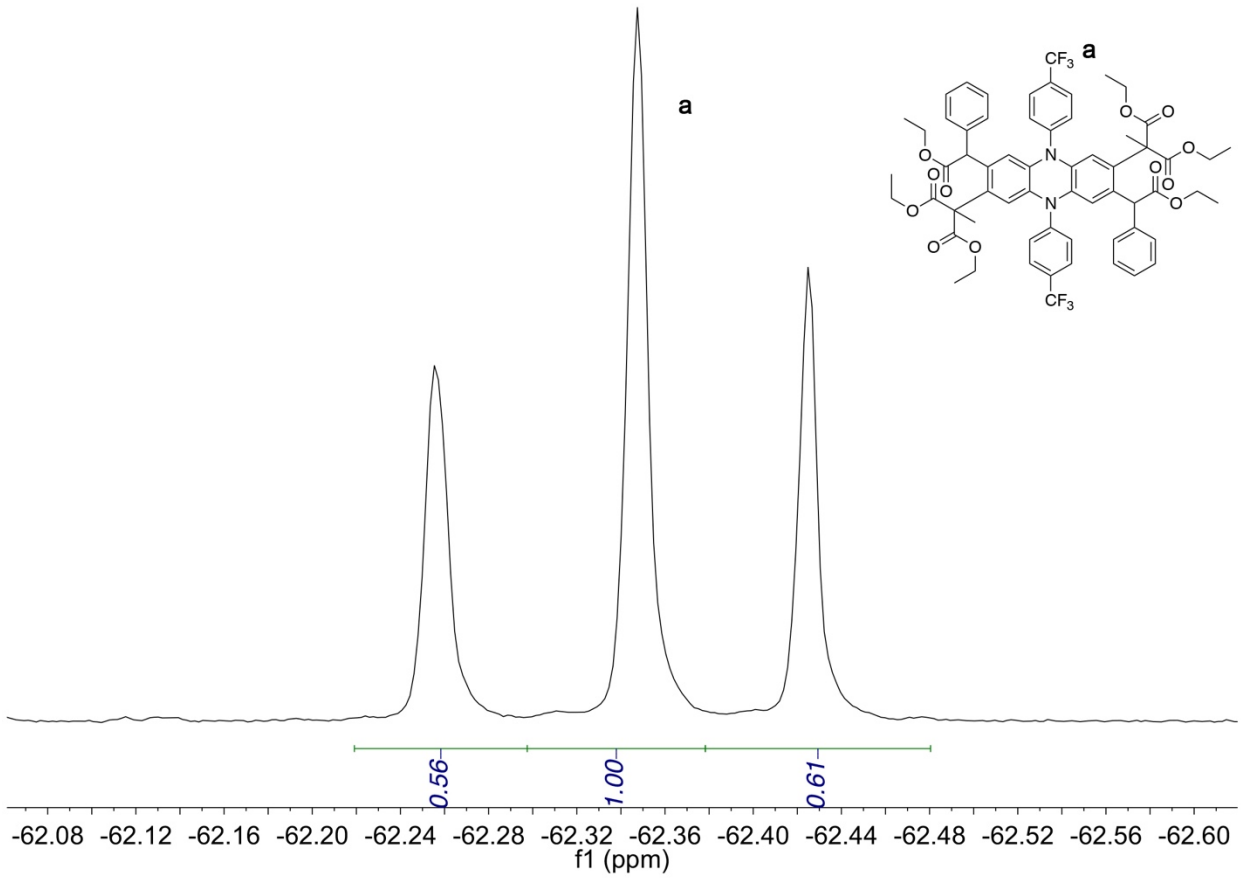

Figure 6.34. *^{19}F NMR spectrum of* ***6*** *in C_6D_6.*

Synthesis of Radical Cations

For UV-Vis, aliquots containing each radical cation were removed from the PC synthesis reaction mixture prior to the addition of triethyl amine.

For EPR spectroscopy of **1**$^{\bullet+}$ – **6**$^{\bullet+}$ as presented in the main text, radical cations of **1** – **6** were synthesized using 1 eq nitrosonium tetrafluoroborate. Oxidation of **1** – **6** was performed in DCM, after which the resulting radical cations were dissolved in DMAc and measured by EPR spectroscopy.

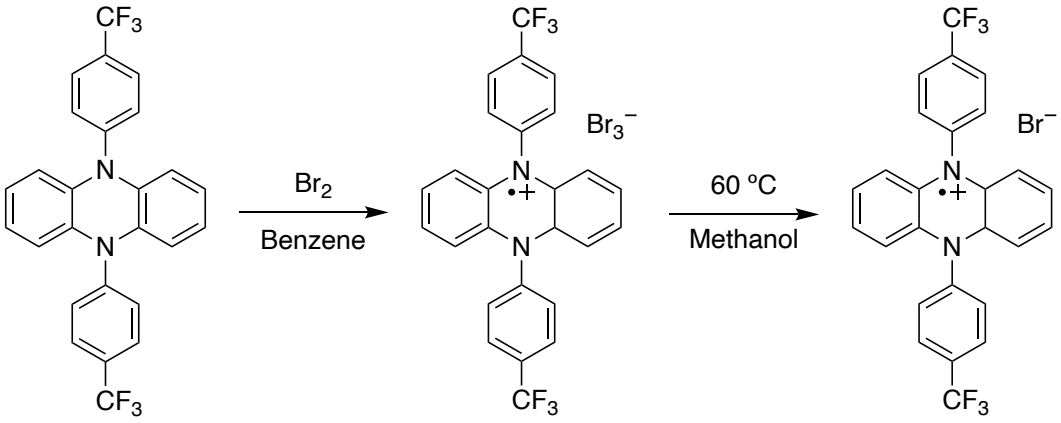

Figure 6.35. *Scheme for the synthesis of* $\mathbf{1}^{\bullet+}Br^{-}$.

Synthesis of 5,10-di(4-trifluorobenzo)-5,10-dihydrophenazinium tribromide ($\mathbf{1}^{\bullet+}\mathbf{Br_3}^{-}$*).* Alternatively, **1** (0.100 g, 0.213 mmol, 1 eq) was dissolved in 80 mL benzene and stirred vigorously. Molecular bromine (5.5 µL, 0.106 mmol, 0.5 eq) was added to the solution, which caused immediate precipitation of a dark green powder. The powder was collected by vacuum filtration and dried under high vacuum. The same product as above was obtained.

Synthesis of 5,10-di(4-trifluorobenzo)-5,10-dihydrophenazinium bromide ($\mathbf{1}^{\bullet+}\mathbf{Br}^{-}$*).* **1** (0.200 g, 0.425 mmol, 1 eq) was dissolved in 80 mL benzene and stirred vigorously. Molecular bromine (43 µL, 0.851 mmol, 2 eq) was added to the solution, which caused immediate precipitation of a dark green powder. The powder was collected by vacuum filtration and recrystallized from methanol. Crystallography revealed the presence of a tribromide anion, so the product was heated in methanol for 4 h, causing the solution to turn from green to red. The solution was placed in a freezer at -25 ºC, which ultimately yielded green crystals of $\mathbf{1}^{\bullet+}\mathbf{Br}^{-}$ (characterized by crystallography in reference 37).

Investigation of Radical Addition to ***1*** *and* $\mathbf{1}^{\bullet+}$

Addition of EBP to ***1*** *in the absence of MMA.* A 20 mL vial was charged with 5 mg (0.01

mmol, 1.00 eq.) **1** and a stir-bar and brought into a nitrogen atmosphere glovebox. To this vial was added 1.00 mL DMAc and 10.0 eq. ATRP initiator EBP. The vial was then sealed and placed in a photoreactor on a stir-plate. After 2 hours, the vial was removed from the glovebox and the volatiles were removed under reduced pressure. The sample was then analyzed by ESI-MS.[47]

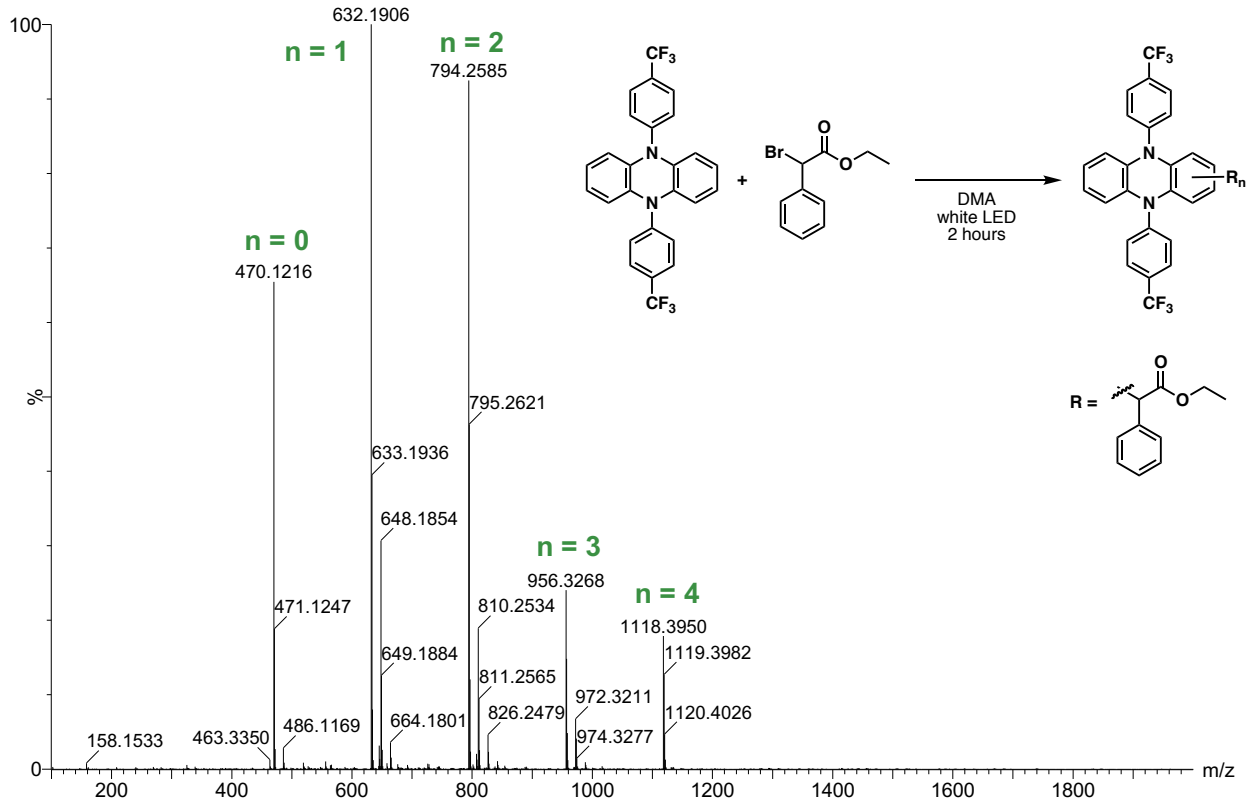

Figure 6.36. *ESI mass spectrum of the residue of a core substitution reaction irradiated for 2h.*[47]

*Radical addition to **1** in the presence of MMA.* A 20 mL vial was charged with 5 mg (0.01 mmol, 1.00 eq.) **1** and a stirbar and brought into a nitrogen atmosphere glovebox. To this vial was added 1.00 mL DMAc, 25.8 mg (0.106 mmol, 10.0 eq.) EBP, and 1.06 g MMA (10.6 mmol, 1000 eq.). The vial was then sealed and placed in a photoreactor on a stir-plate. After 20 minutes, the vial was removed from the glovebox and the volatiles were removed under reduced pressure. The sample was then analyzed by ESI-MS.[47]

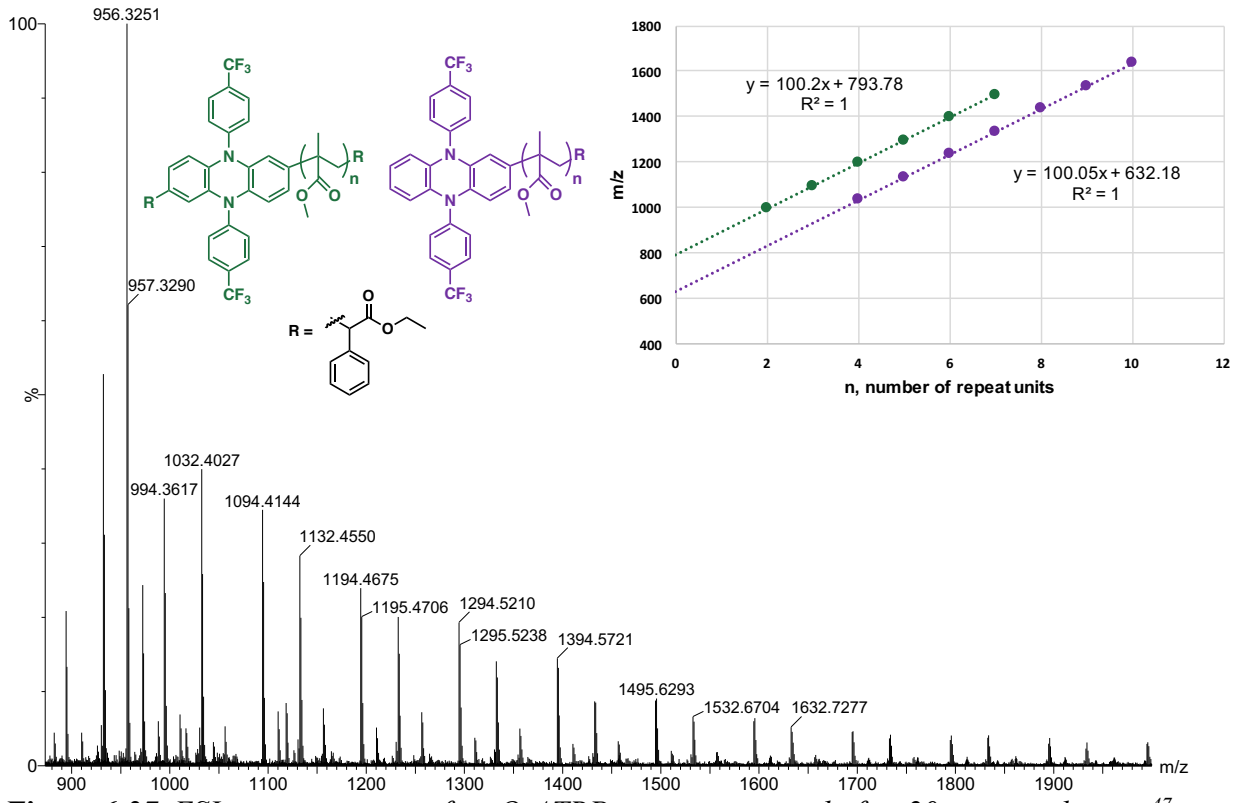

Figure 6.37. *ESI mass spectrum of an O-ATRP reaction stopped after 20 min irradiation.*[47]

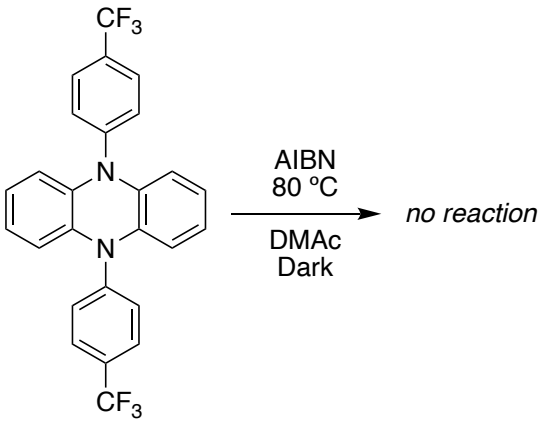

Figure 6.38. *Scheme for the reaction of* ***1*** *with AIBN in deuterated DMAc.*

*Investigation of core substitution with AIBN and **1**.* **1** (20 mg, 0.0425 mmol, 1 eq) and AIBN (0.139 g, 0.851 mmol, 20 eq) were dissolved in deuterated (d_9) DMAc (1 mL). The ^{1}H NMR spectrum of the solution was acquired, and then the solution was heated to 80 ºC for 1h. After

heating, the ^{1}H NMR spectrum of the solution was once again taken to analyze the products of the reaction. No change to the PC spectrum was evident (Figure 6.40).

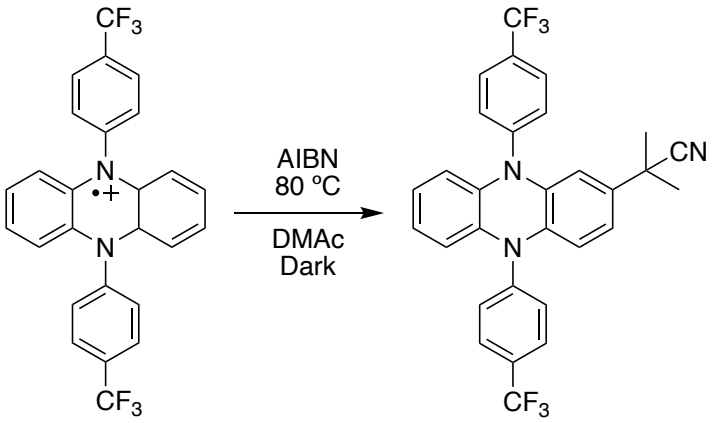

Figure 6.39. *Scheme for the reaction of* ***1***$^{\bullet+}$*Br*$^-$ *with AIBN in deuterated DMAc.*

Investigation of core substitution with AIBN and ***1***$^{\bullet+}$. **1**$^{\bullet+}$Br$^-$ (20 mg, 0.0364 mmol, 1 eq) and AIBN (0.119 g, 0.729 mmol, 20 eq) were dissolved in deuterated (d_9) DMAc (1 mL). The ^{1}H NMR spectrum of the solution was acquired, and then the solution was heated to 80 ºC for 1h. After heating, the ^{1}H NMR spectrum of the solution was once again taken to analyze the products of the reaction (Figure 6.40).

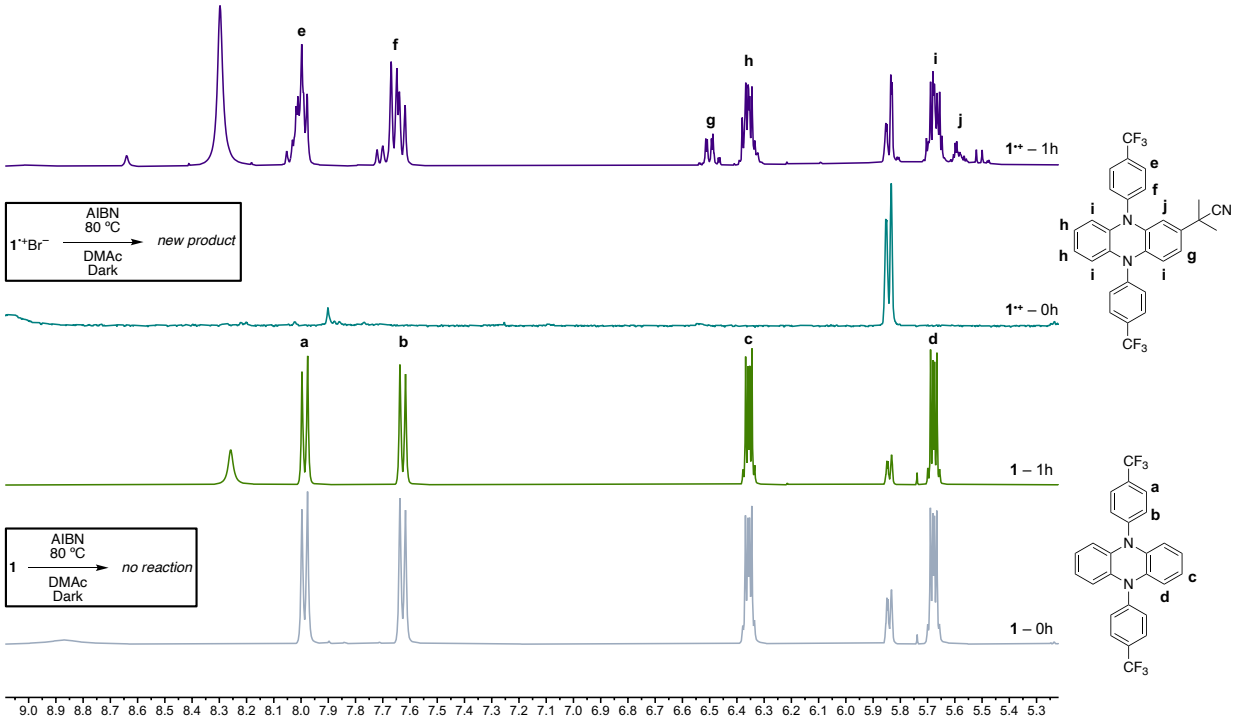

Figure 6.40. *^{1}H NMR spectra of **1** (bottom) and **1**$^{\bullet+}$Br$^-$ (top) reactions with AIBN at 0h and 1h.*

General Polymerization Procedure

For polymerizations performed by O-ATRP with greater than 100 ppm PC, the PCs were weighted into scintillation vials and pumped into a nitrogen glovebox with a magnetic stir bar. Under a nitrogen atmosphere, solvent (1 mL), MMA (1 mL, 9.35 mmol, 1000 eq), and DBMM (17.9 µL, 0.0935 mmol, 10 eq) were added to the vials. The vials were then sealed and irradiated in a white LED beaker with a fan blowing over the beaker for temperature control.

For polymerizations performed by O-ATRP with less than 100 ppm PC, the PCs were weighted into scintillation vials and pumped into a nitrogen glovebox. Under a nitrogen atmosphere, stock solutions of the PCs were made in EtAc and transferred to 20 mL scintillation vials with magnetic stir bars. Extra solvent (to reach a total of 1 mL solvent), MMA (1 mL, 9.35 mmol, 1000 eq), and DBMM (17.9 µL, 0.0935 mmol, 10 eq) were then added to the vials. The

vials were sealed and irradiated in a white LED beaker with a fan blowing over the beaker for temperature control.

To monitor polymerizations, 0.1 mL aliquots were removed periodically. Aliquots were quenched in a deuterated chloroform containing 250 ppm butylated hydroxytoluene (BHT). These solutions were then transferred to an NMR tube for ^{1}H NMR analysis to determine the extent of monomer conversion. Afterwards, solutions were dried and dissolved in unstabilized THF for GPC analysis to obtain number average molecular weight and dispersity.

Photocatalyst Characterization

UV-Visible Absorption Spectroscopy

For determination of the molar absorptivity of **1** – **6**, a stock solution of **1** – **6** was prepared in DMAc. This stock solution was then diluted to form each of the measurement solutions prior to analysis by UV-Vis.

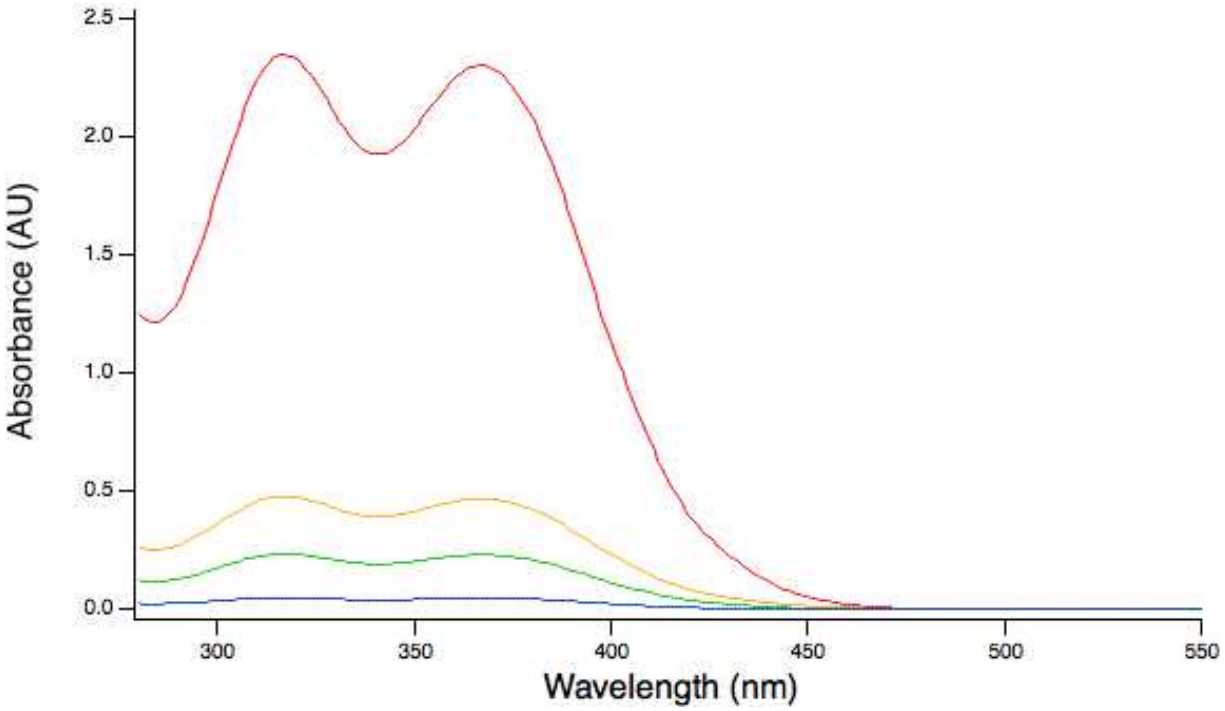

Figure 6.41. *UV-Vis spectrum of* ***1*** *at four concentrations in DMAc.*

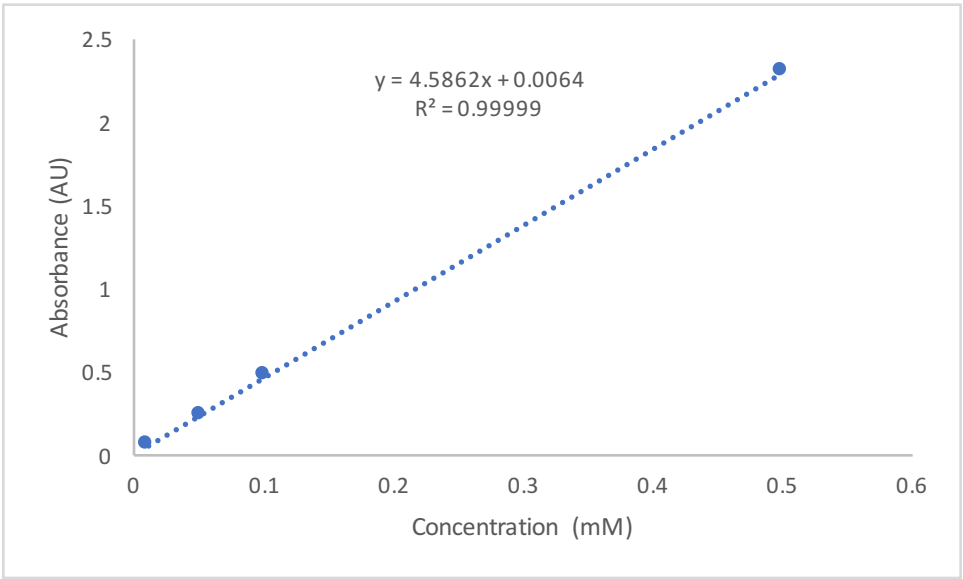

Figure 6.42. *Beer's law plot for the determination of the molar absorptivity of* ***1*** *in DMAc at* λ_{max} *= 367 nm.*

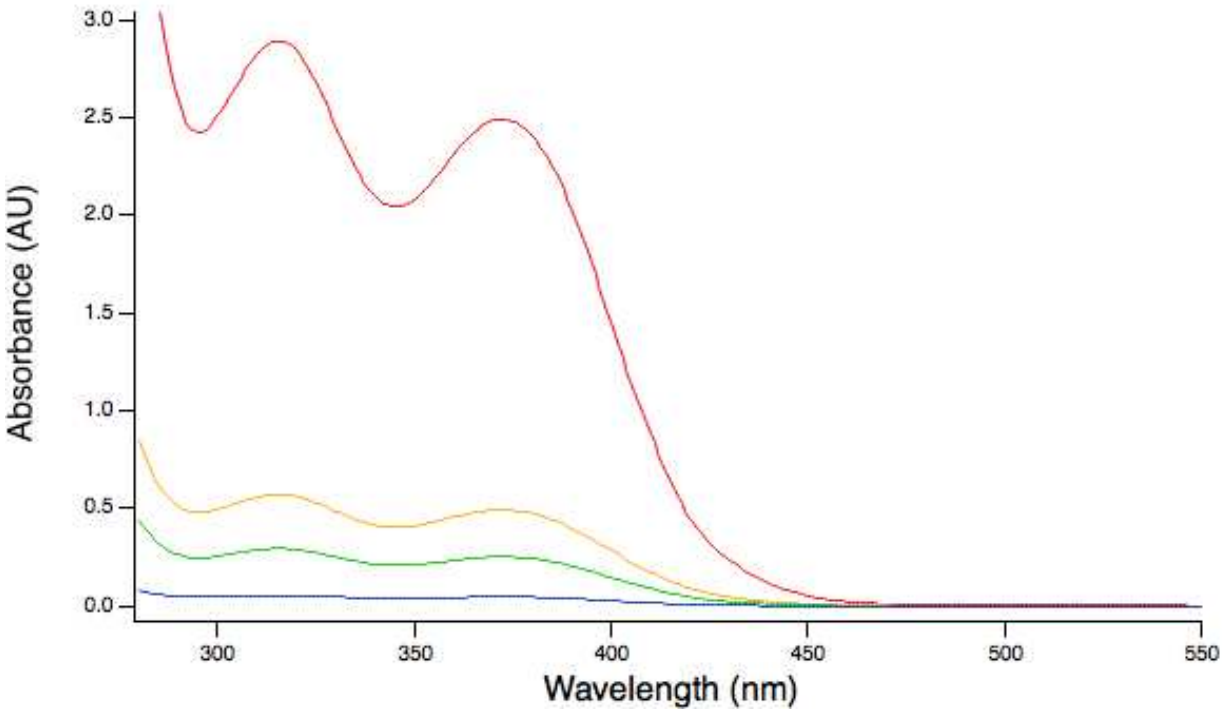

Figure 6.43. *UV-Vis spectrum of* ***2*** *at four concentrations in DMAc.*

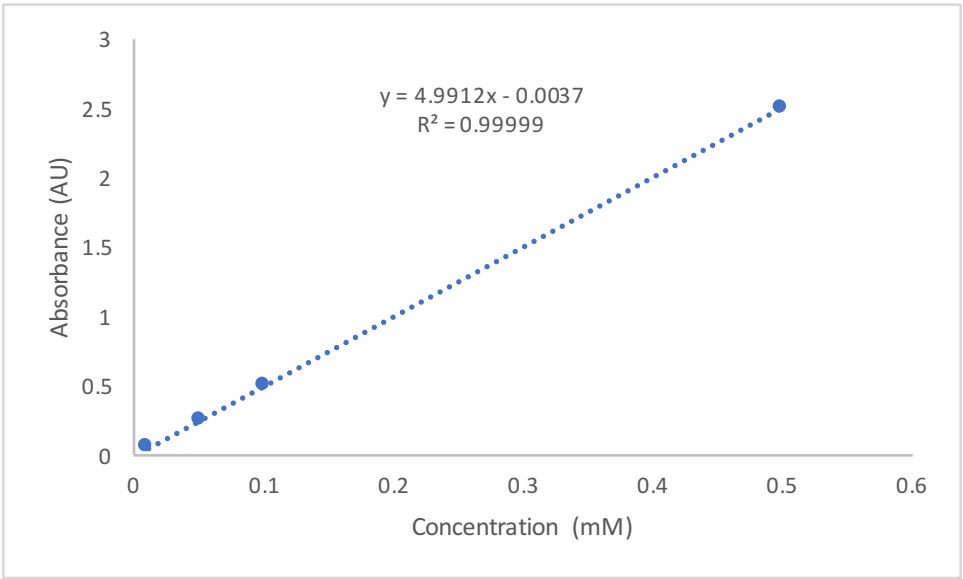

Figure 6.44. *Beer's law plot for the determination of the molar absorptivity of* ***2*** *in DMAc at* λ_{max} *= 373 nm.*

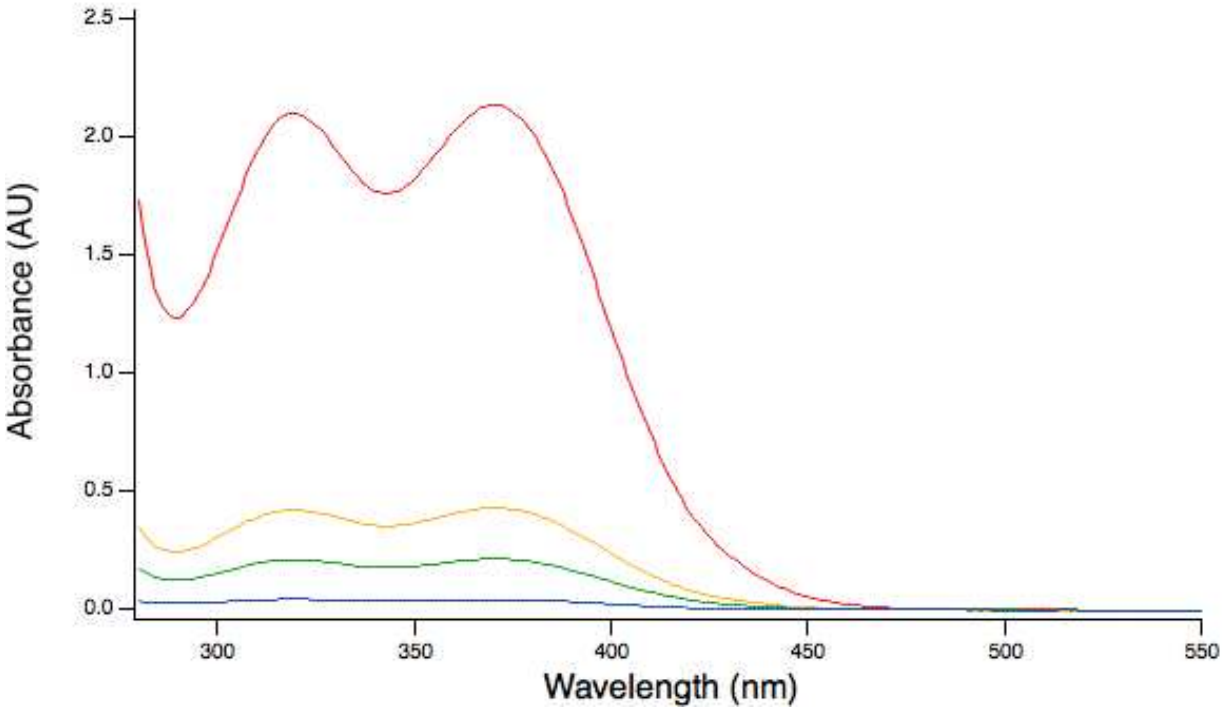

Figure 6.45. *UV-Vis spectrum of* ***3*** *at four concentrations in DMAc.*

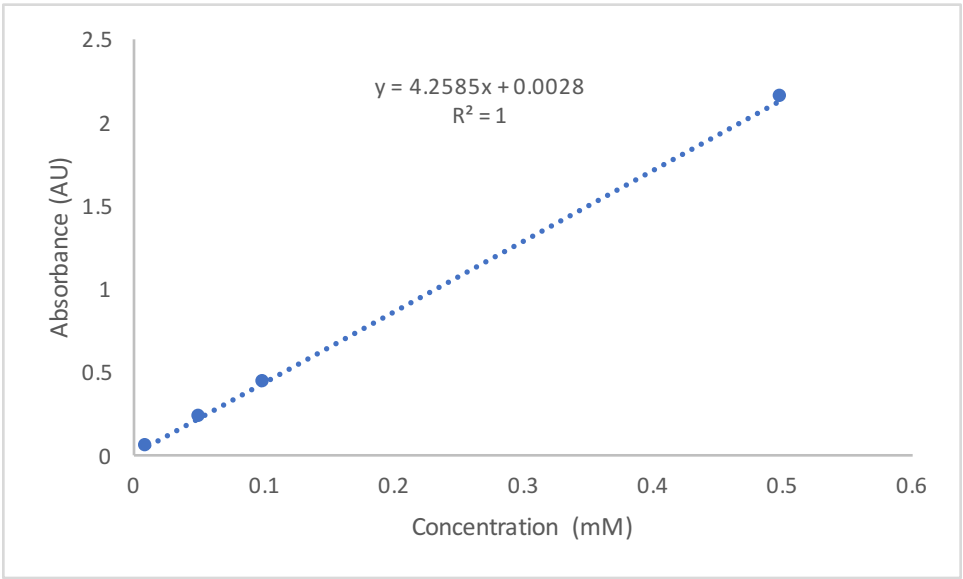

Figure 6.46. *Beer's law plot for the determination of the molar absorptivity of* ***3*** *in DMAc at* λ_{max} *= 371 nm.*

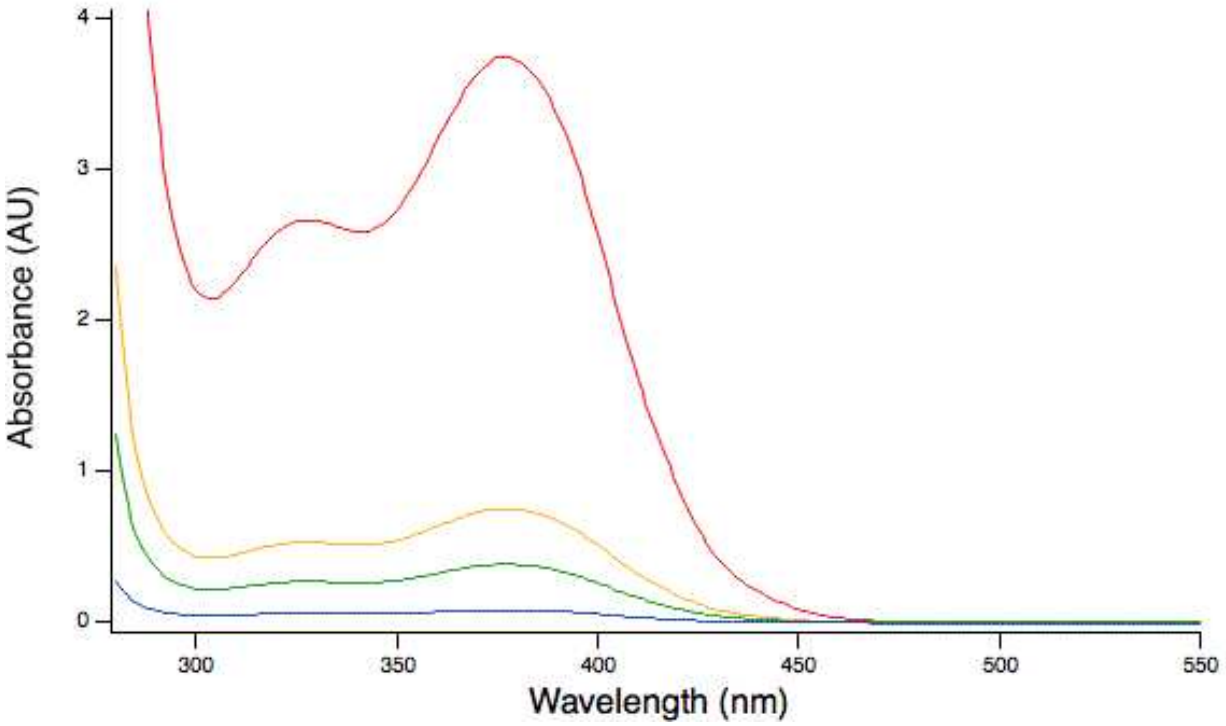

Figure 6.47. *UV-Vis spectrum of* ***4*** *at four concentrations in DMAc.*

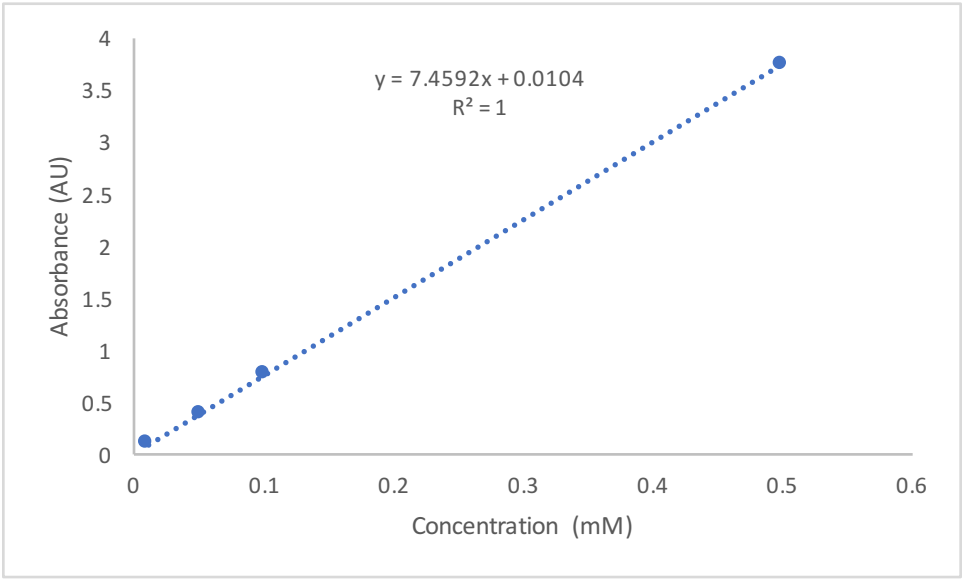

Figure 6.48. *Beer's law plot for the determination of the molar absorptivity of* ***4*** *in DMAc at* λ_{max} *= 377 nm.*

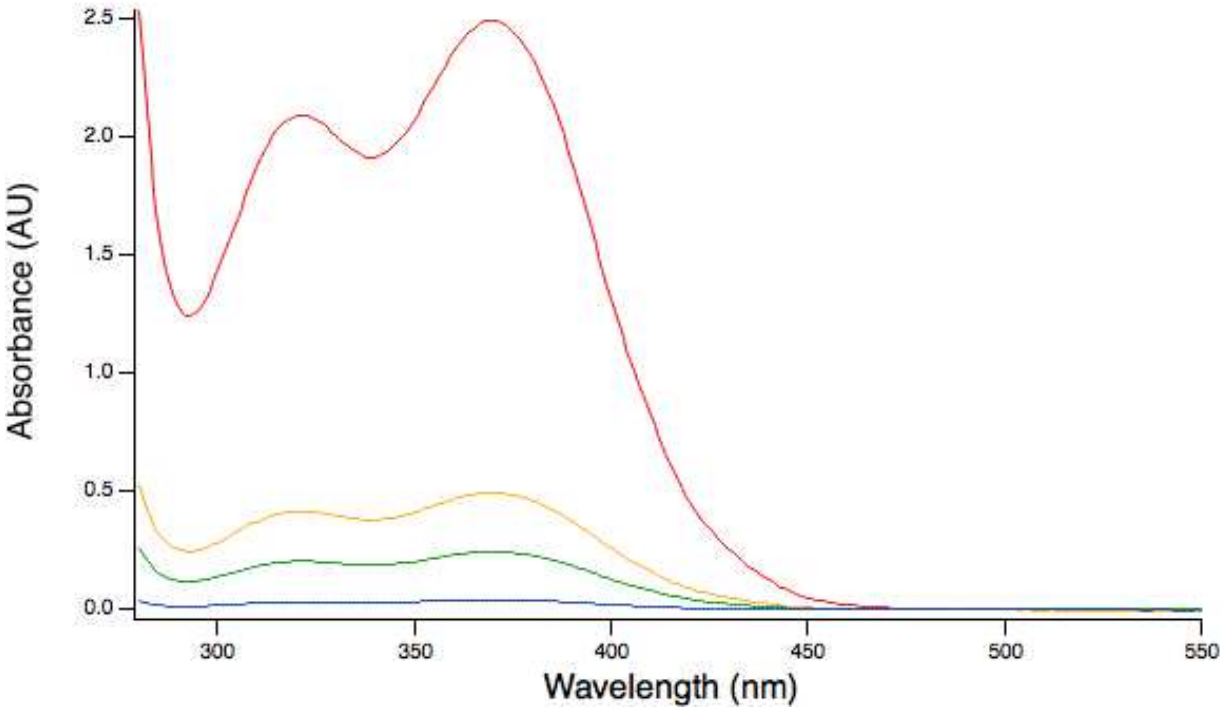

Figure 6.49. *UV-Vis spectrum of* ***5*** *at four concentrations in DMAc.*

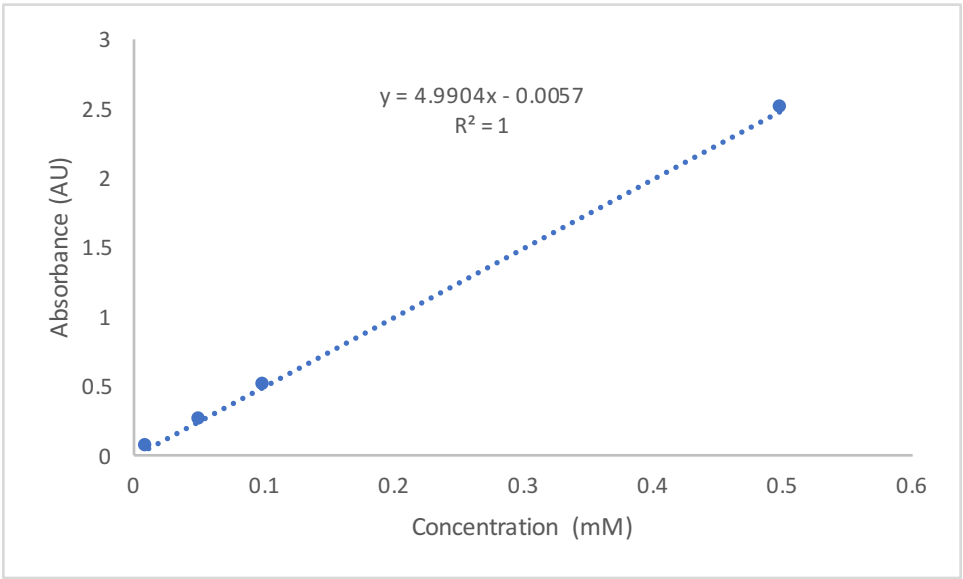

Figure 6.50. *Beer's law plot for the determination of the molar absorptivity of* ***5*** *in DMAc at* λ_{max} *= 370 nm.*

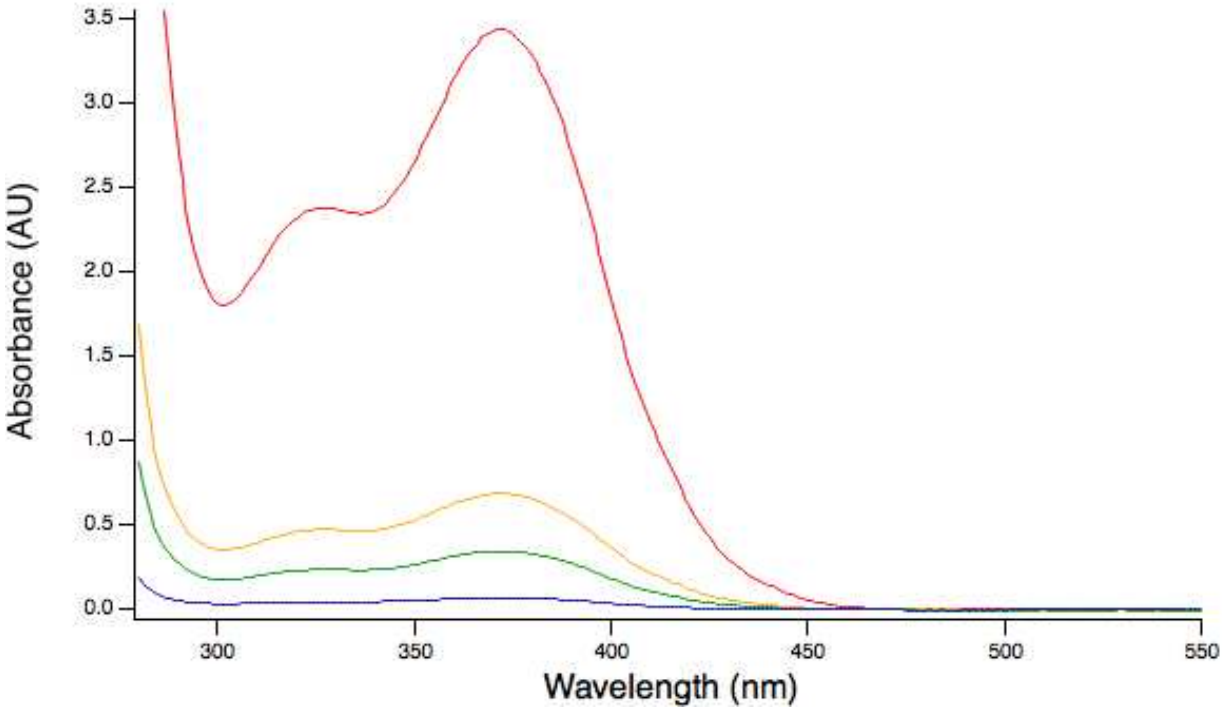

Figure 6.51. *UV-Vis spectrum of* ***6*** *at four concentrations in DMAc.*

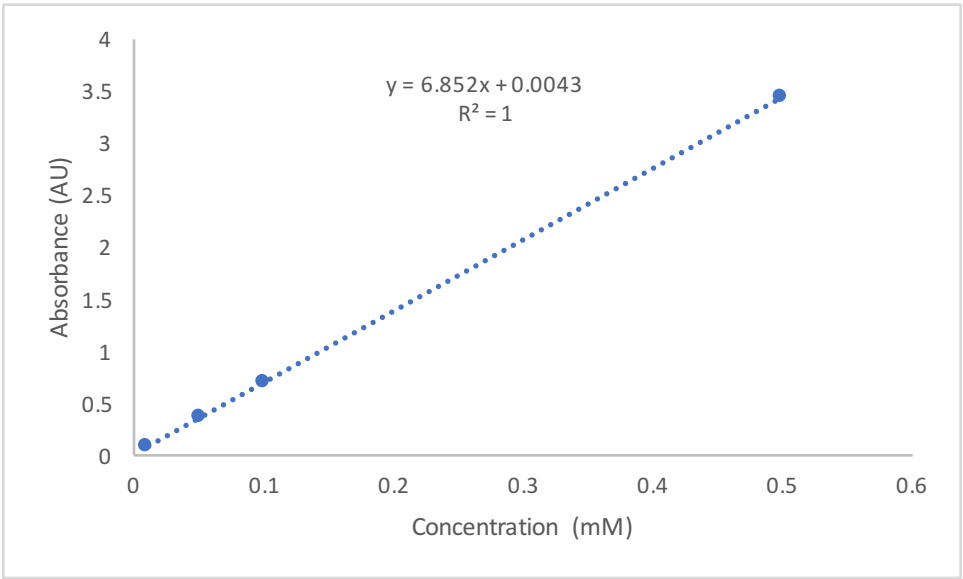

Figure 6.52. *Beer's law plot for the determination of the molar absorptivity of* ***6*** *in DMAc at* λ_{max} *= 372 nm.*

Emission Spectroscopy

For measurement of the emission spectra of **1** – **6**, stock solutions of the PCs were prepared in DMAc. The stock solution was measured by emission spectroscopy and then diluted several times to prepare the other concentrations reported.

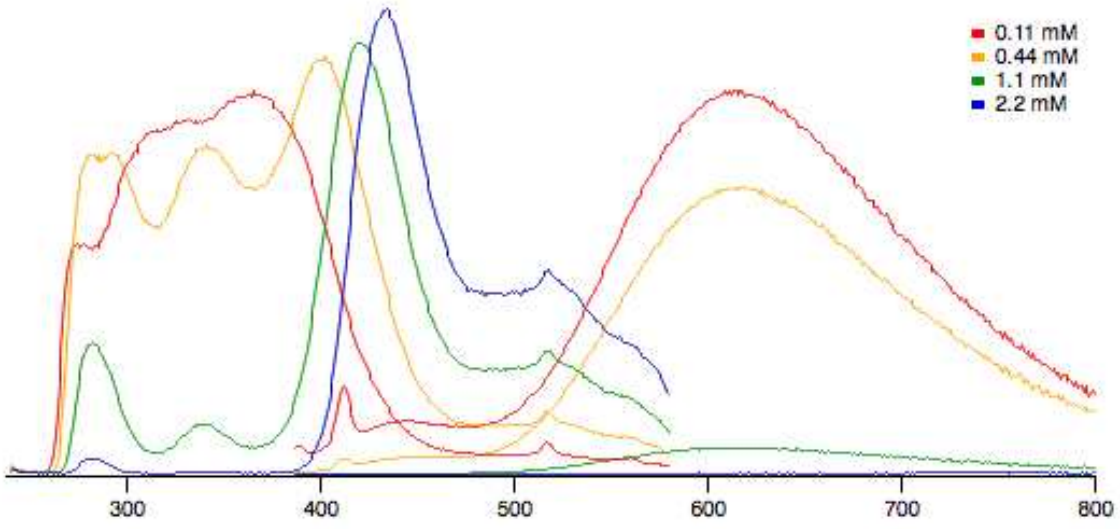

Figure 6.53. *Emission (right) and excitation (left) spectra of* ***1*** *in DMAc at various concentrations.*

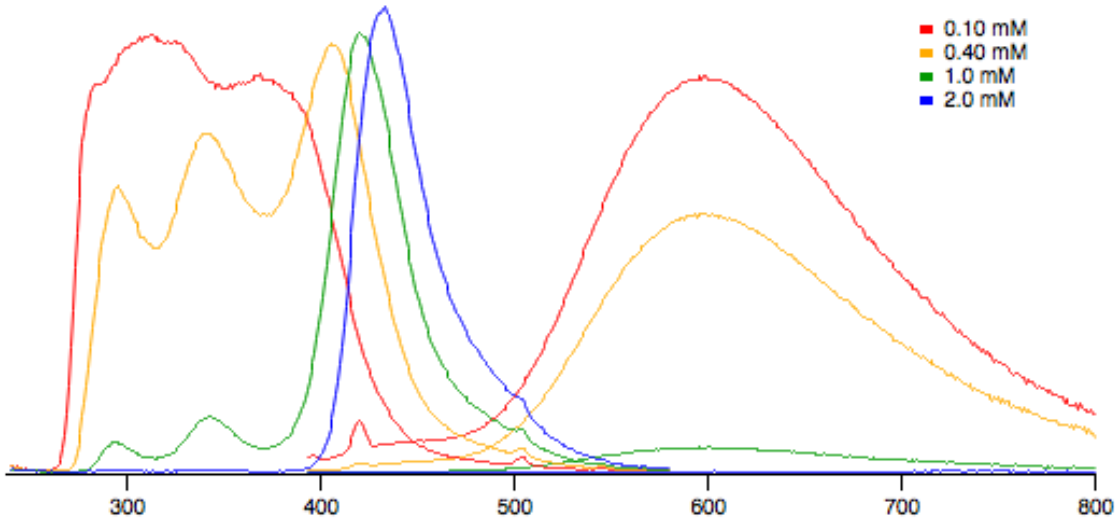

Figure 6.54. *Emission (right) and excitation (left) spectra of* ***2*** *in DMAc at various concentrations.*

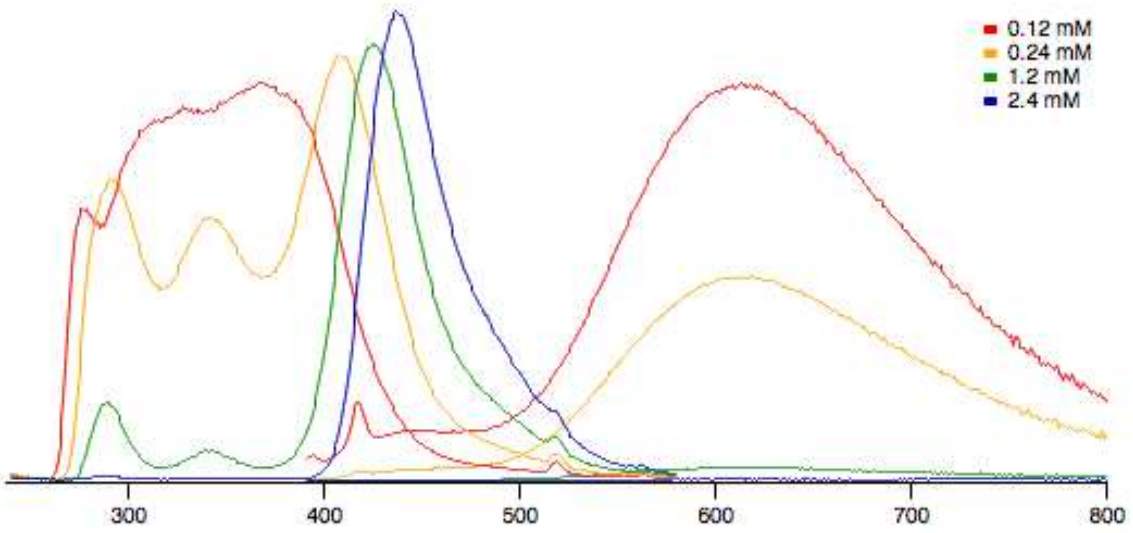

Figure 6.55. *Emission (right) and excitation (left) spectra of* ***3*** *in DMAc at various concentrations.*

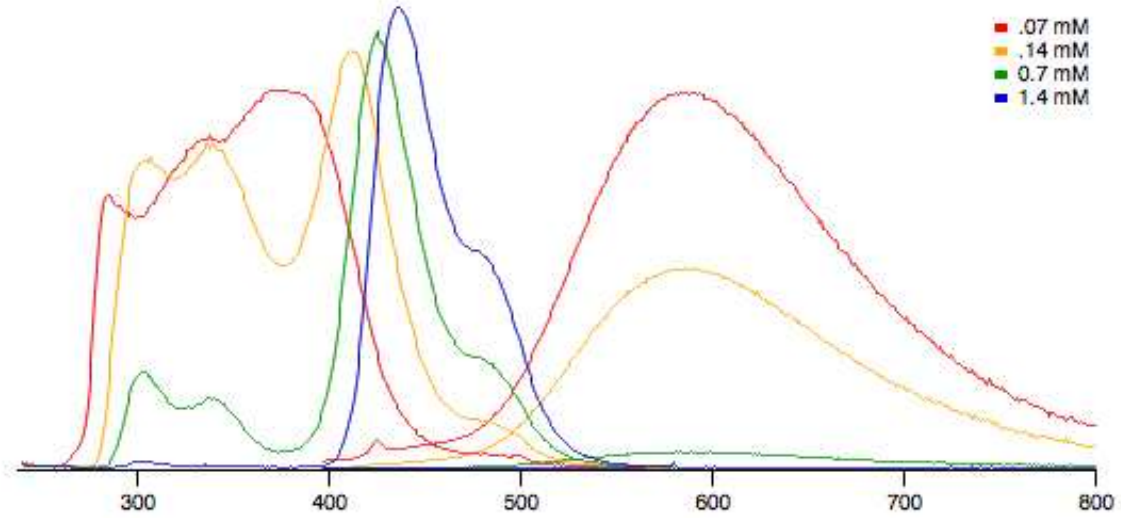

Figure 6.56. *Emission (right) and excitation (left) spectra of* ***4*** *in DMAc at various concentrations.*

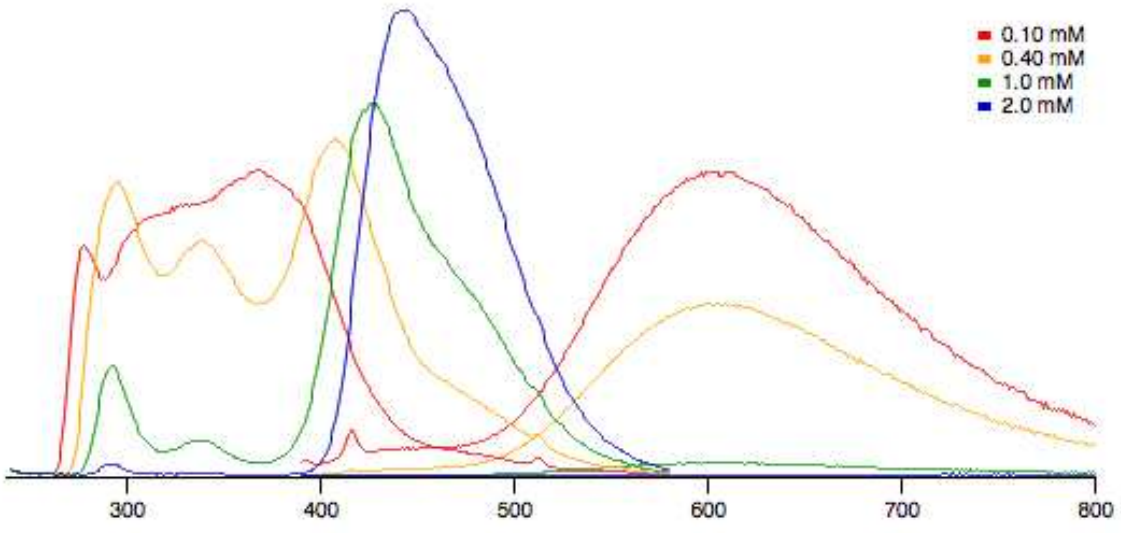

Figure 6.57. *Emission (right) and excitation (left) spectra of* ***5*** *in DMAc at various concentrations.*

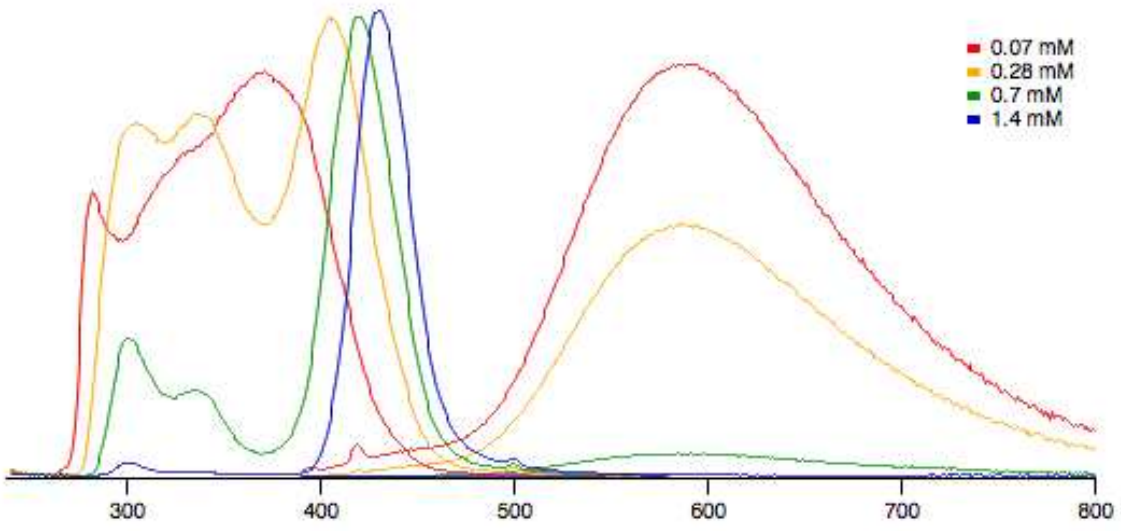

Figure 6.58. *Emission (right) and excitation (left) spectra of* ***6*** *in DMAc at various concentrations.*

Cyclic Voltammetry

See *Experimental Equipment* above for details regarding the reagents and electrodes used in these measurements. For each compound, solutions were prepared in DMAc with 0.1 M NBu_4PF_6 and degassed by nitrogen bubbling prior to measurement.

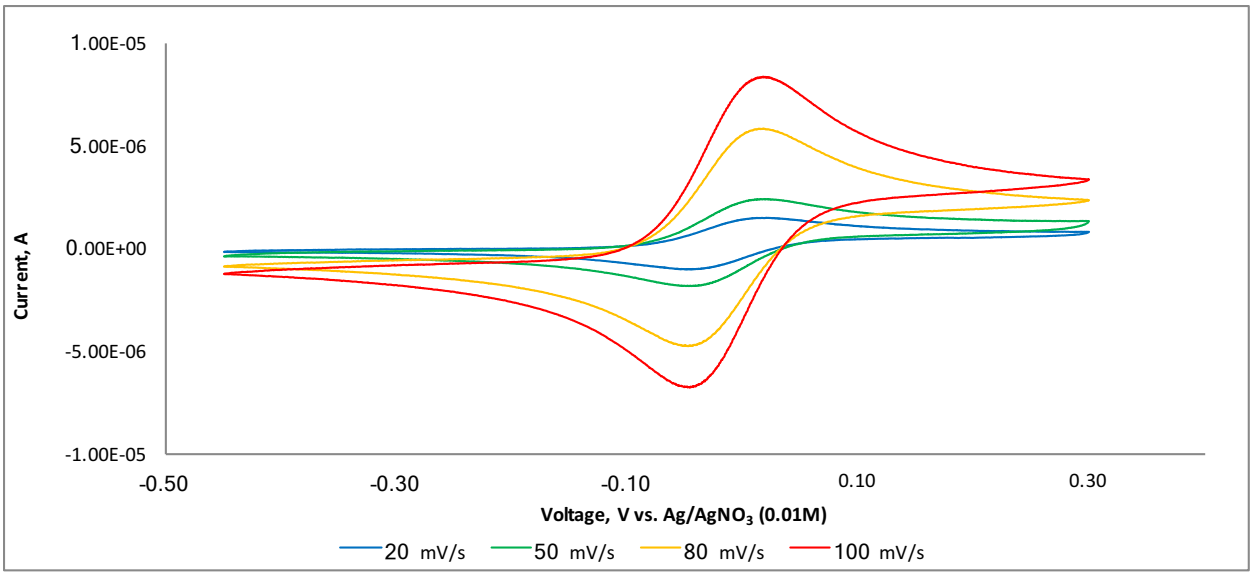

Figure 6.59. *Cyclic voltammogram of* ***1*** *in DMAc with 0.1 M NBu_4PF_6 supporting electrolyte scanning in the positive potential direction (potentials versus 0.01 M $Ag/AgNO_3$ reference electrode in acetonitrile with 0.1 M NBu_4PF_6).*

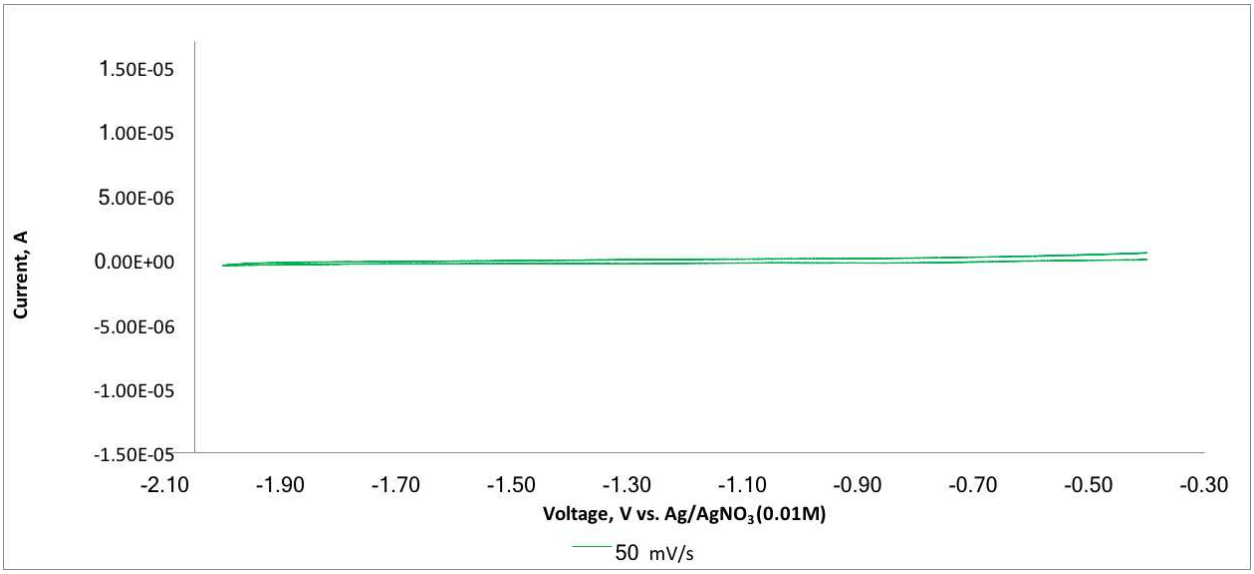

Figure 6.60. *Cyclic voltammogram of* ***1*** *in DMAc with 0.1 M NBu_4PF_6 supporting electrolyte scanning in the negative potential direction (potentials versus 0.01 M $Ag/AgNO_3$ reference electrode in acetonitrile with 0.1 M NBu_4PF_6).*

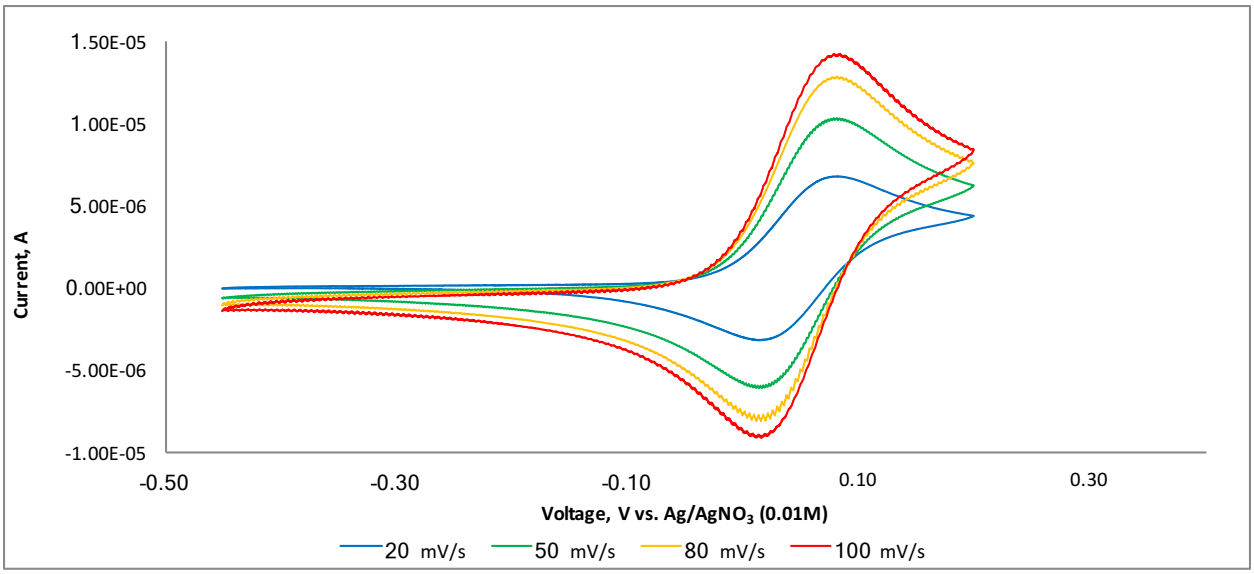

Figure 6.61. *Cyclic voltammogram of* ***2*** *in DMAc with 0.1 M NBu_4PF_6 supporting electrolyte scanning in the positive potential direction (potentials versus 0.01 M $Ag/AgNO_3$ reference electrode in acetonitrile with 0.1 M NBu_4PF_6).*

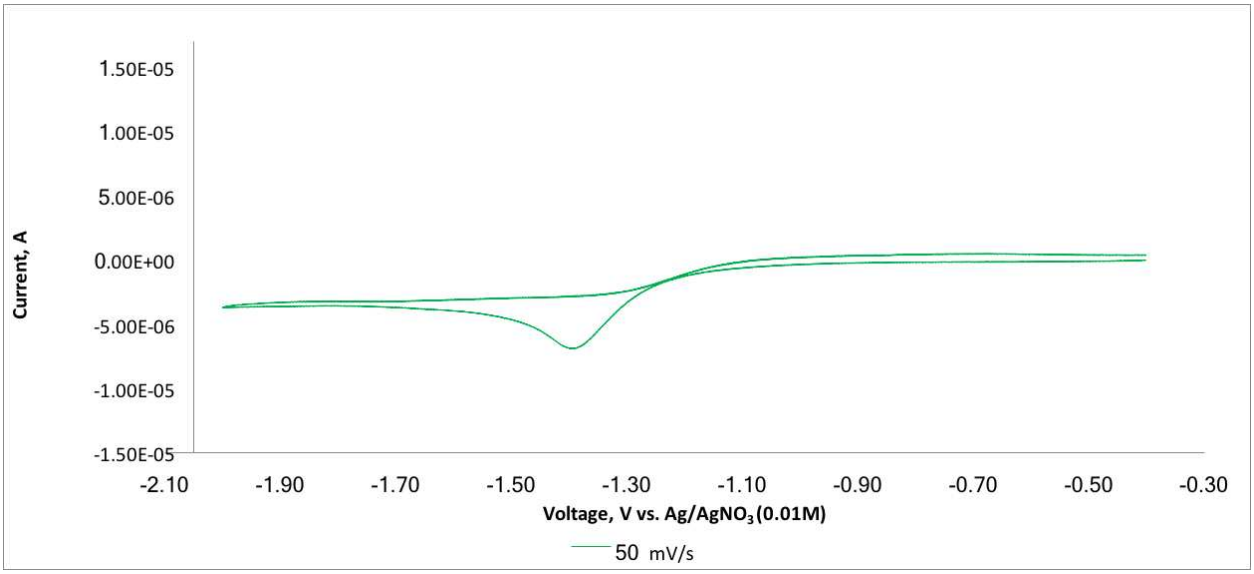

Figure 6.62. *Cyclic voltammogram of* ***2*** *in DMAc with 0.1 M NBu_4PF_6 supporting electrolyte scanning in the negative potential direction (potentials versus 0.01 M $Ag/AgNO_3$ reference electrode in acetonitrile with 0.1 M NBu_4PF_6).*

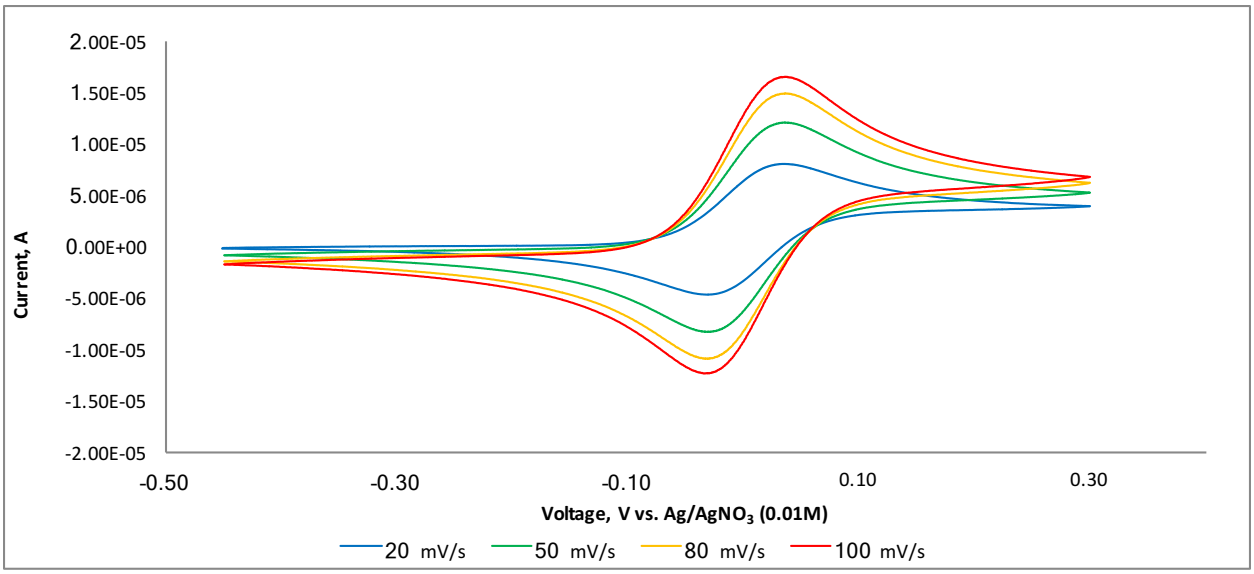

Figure 6.63. *Cyclic voltammogram of* ***3*** *in DMAc with 0.1 M NBu_4PF_6 supporting electrolyte scanning in the positive potential direction (potentials versus 0.01 M $Ag/AgNO_3$ reference electrode in acetonitrile with 0.1 M NBu_4PF_6).*

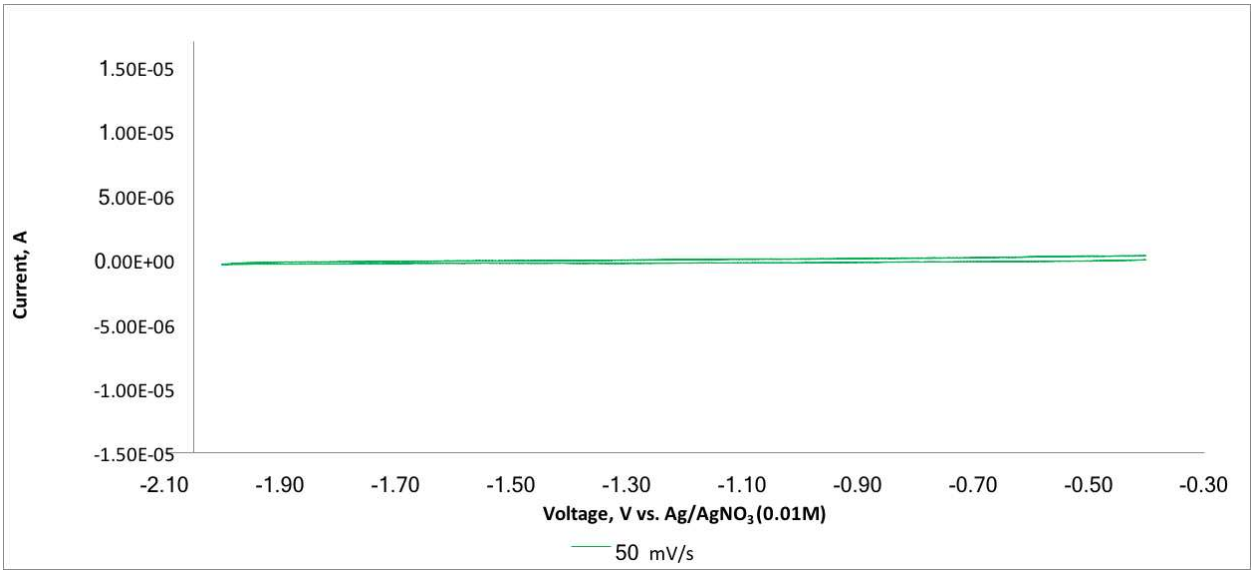

Figure 6.64. *Cyclic voltammogram of* ***3*** *in DMAc with 0.1 M NBu_4PF_6 supporting electrolyte scanning in the negative potential direction (potentials versus 0.01 M $Ag/AgNO_3$ reference electrode in acetonitrile with 0.1 M NBu_4PF_6).*

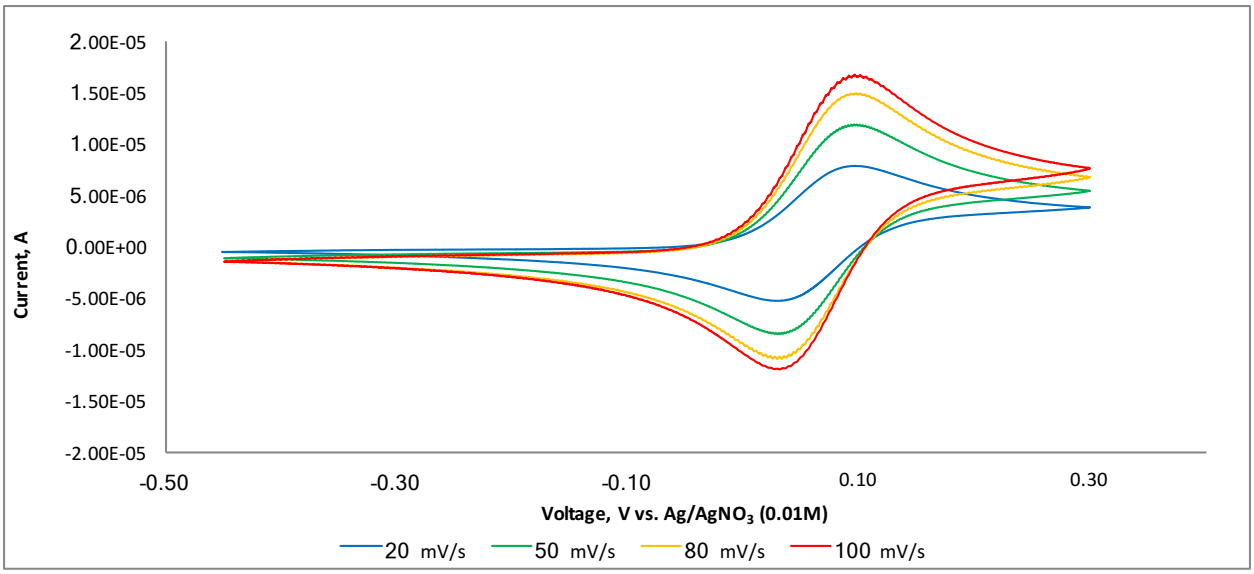

Figure 6.65. *Cyclic voltammogram of* ***4*** *in DMAc with 0.1 M NBu_4PF_6 supporting electrolyte scanning in the positive potential direction (potentials versus 0.01 M $Ag/AgNO_3$ reference electrode in acetonitrile with 0.1 M NBu_4PF_6).*

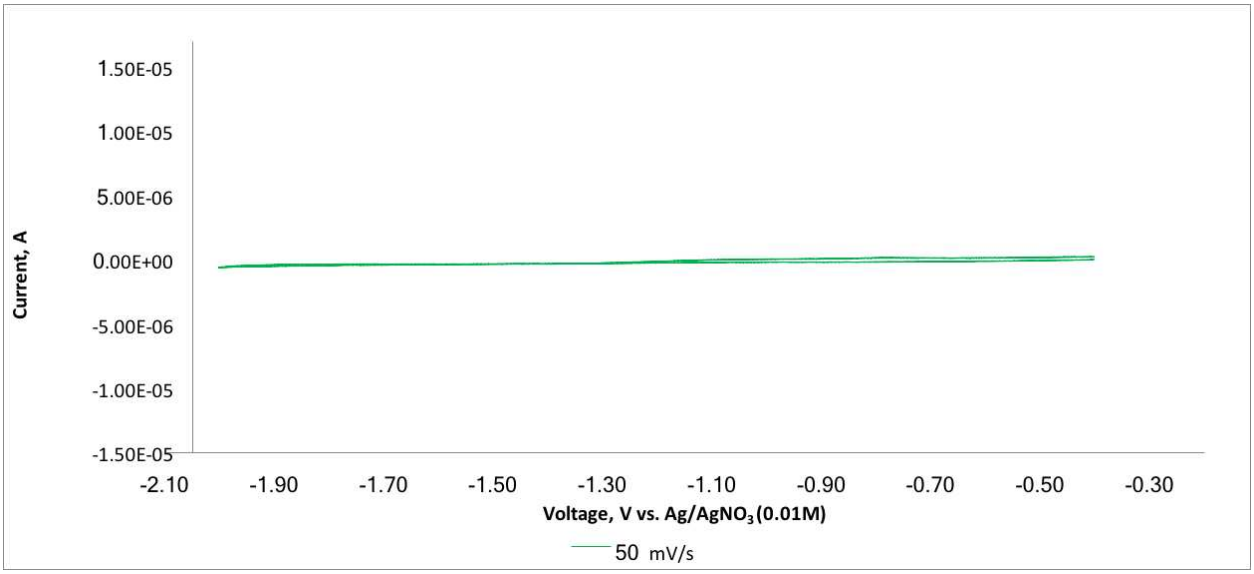

Figure 6.66. *Cyclic voltammogram of* ***4*** *in DMAc with 0.1 M NBu_4PF_6 supporting electrolyte scanning in the negative potential direction (potentials versus 0.01 M $Ag/AgNO_3$ reference electrode in acetonitrile with 0.1 M NBu_4PF_6).*

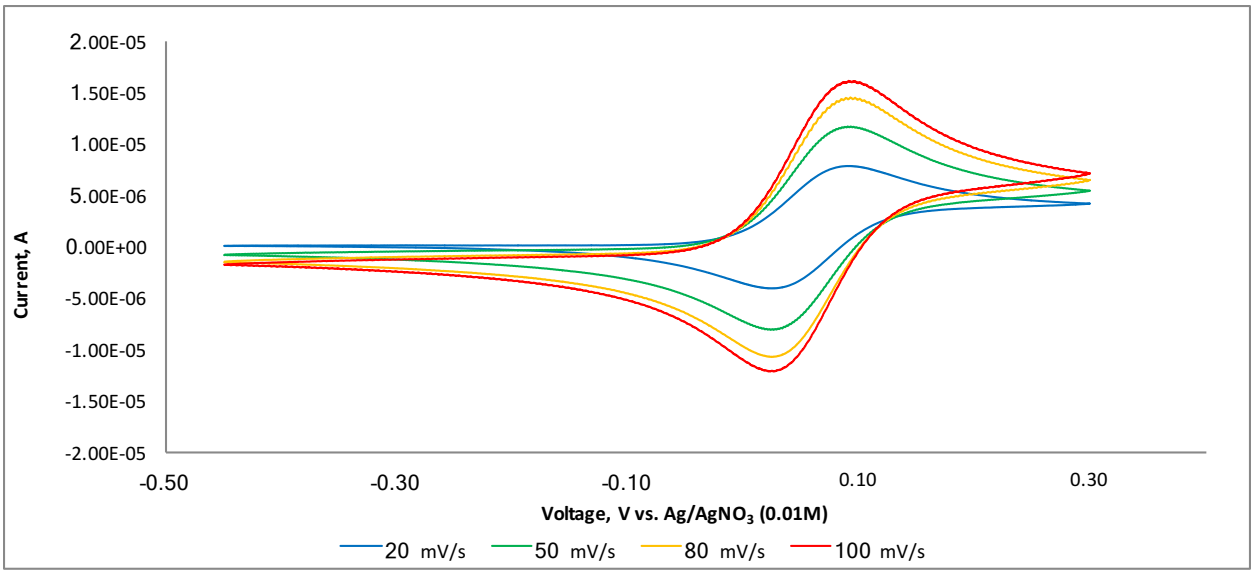

Figure 6.67. *Cyclic voltammogram of* ***5*** *in DMAc with 0.1 M NBu_4PF_6 supporting electrolyte scanning in the positive potential direction (potentials versus 0.01 M $Ag/AgNO_3$ reference electrode in acetonitrile with 0.1 M NBu_4PF_6).*

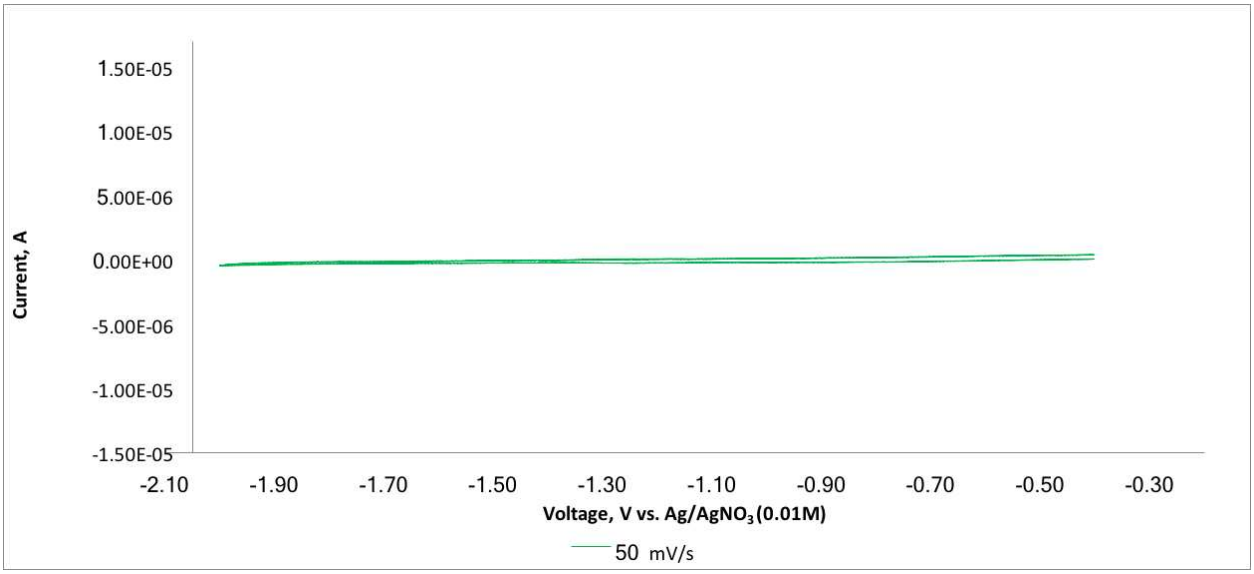

Figure 6.68. *Cyclic voltammogram of* ***5*** *in DMAc with 0.1 M NBu_4PF_6 supporting electrolyte scanning in the negative potential direction (potentials versus 0.01 M $Ag/AgNO_3$ reference electrode in acetonitrile with 0.1 M NBu_4PF_6).*

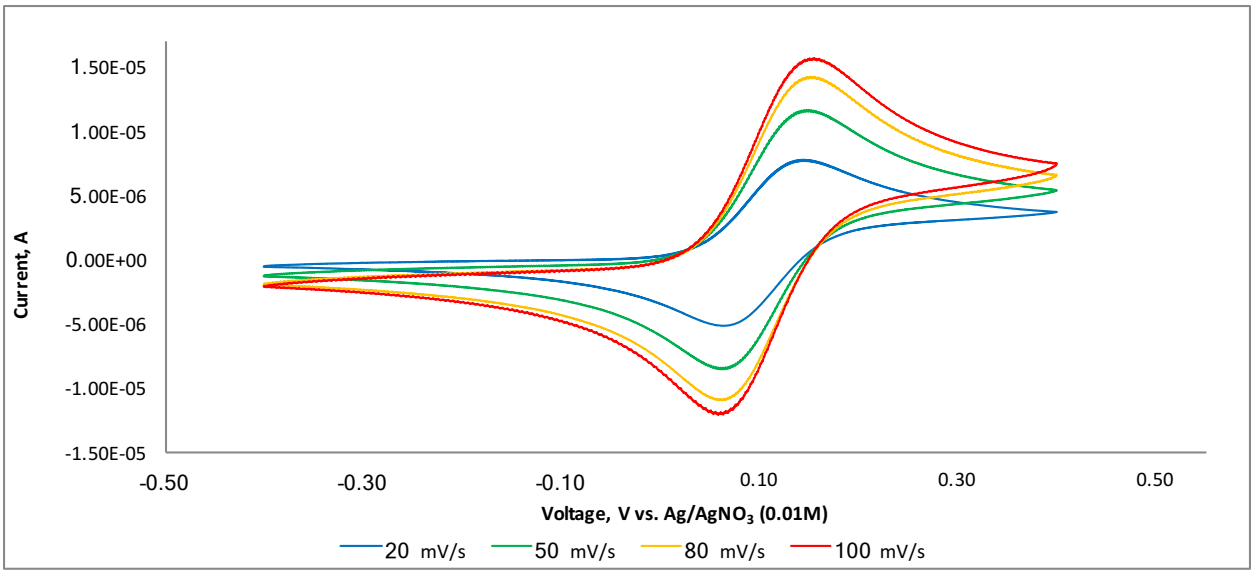

Figure 6.69. *Cyclic voltammogram of* ***6*** *in DMAc with 0.1 M NBu_4PF_6 supporting electrolyte scanning in the positive potential direction (potentials versus 0.01 M $Ag/AgNO_3$ reference electrode in acetonitrile with 0.1 M NBu_4PF_6).*

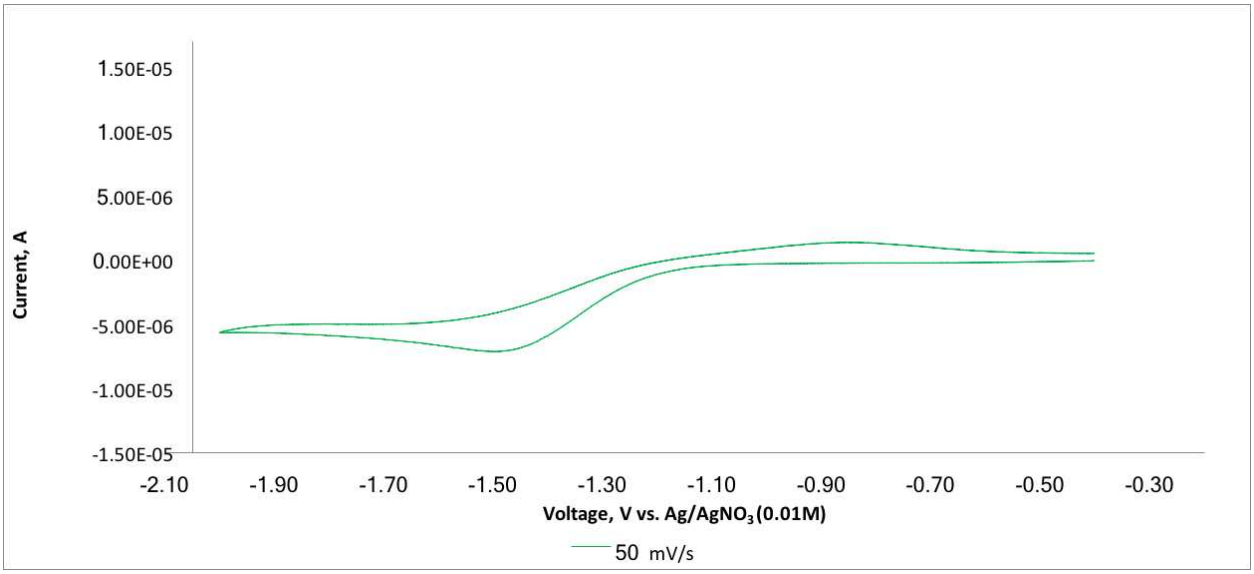

Figure 6.70. *Cyclic voltammogram of* ***6*** *in DMAc with 0.1 M NBu_4PF_6 supporting electrolyte scanning in the negative potential direction (potentials versus 0.01 M $Ag/AgNO_3$ reference electrode in acetonitrile with 0.1 M NBu_4PF_6).*

Crystallographic Information for ***4***

Crystals of **4** for X-ray diffraction were grown by diffusion of hexanes into benzene. The obtained crystal structure is shown below (hydrogens omitted for clarity).

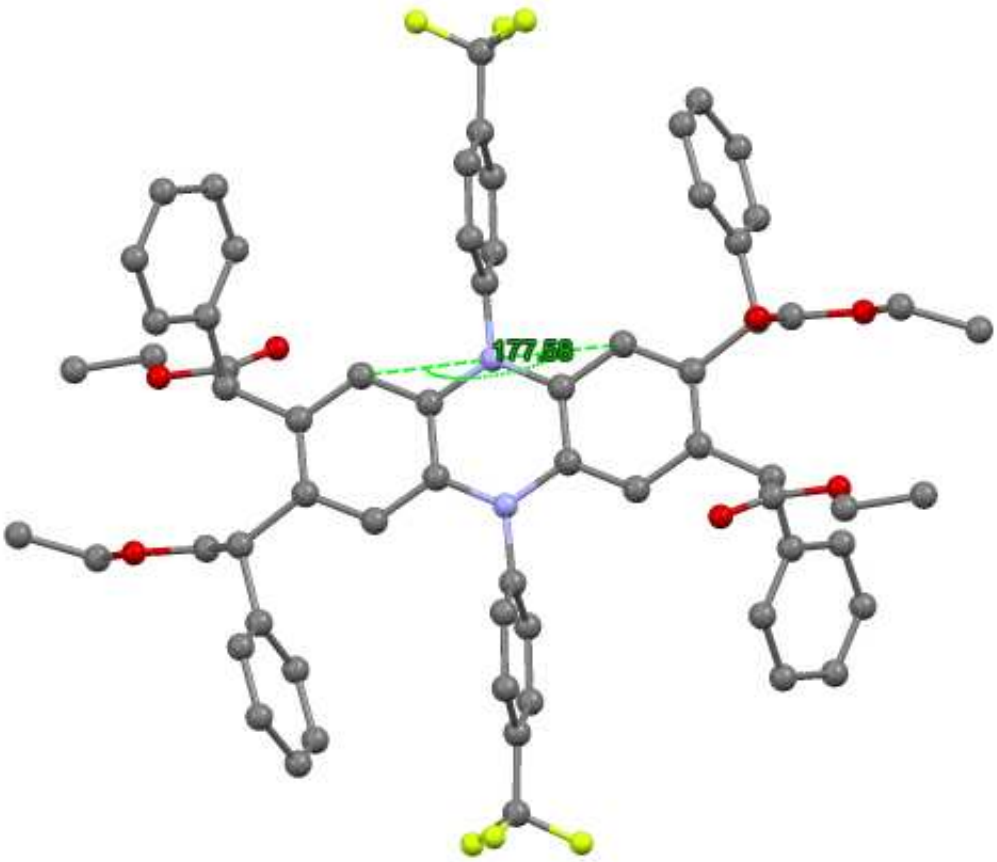

Figure 6.71. *Crystal structure of PC* ***4*** *(hydrogens omitted for clarity).*

Table 6.5. *Crystallographic information for the structural refinement of* ***4****.*

Identification code	gm15_PhenN-PhCF3-EBP4_report
Empirical formula	$C_{66}H_{56}F_6N_2O_8$
Formula weight	1119.12
Temperature/K	104.(2)
Crystal system	triclinic
Space group	P-1
a/Å	6.5181(6)
b/Å	14.7409(12)
c/Å	16.2314(13)
α/°	114.080(4)
β/°	93.910(4)
γ/°	102.462(4)
Volume/Å^3	1368.8(2)
Z	1
ρ_{calc}g/cm^3	1.358
μ/mm^{-1}	0.102
F(000)	584.0
Crystal size/mm^3	0.108 × 0.049 × 0.026
Radiation	Mo Kα (λ = 0.71073)
2Θ range for data collection/°	5.02 to 50.06
Index ranges	$-7 \leq h \leq 7$, $-17 \leq k \leq 17$, $-19 \leq l \leq 19$
Reflections collected	51869
Independent reflections	4844 [R_{int} = 0.1100, R_{sigma} = 0.0563]
Data/restraints/parameters	4844/0/372
Goodness-of-fit on F^2	1.014
Final R indexes [I>=2σ (I)]	R_1 = 0.0568, wR_2 = 0.1310
Final R indexes [all data]	R_1 = 0.1041, wR_2 = 0.1563
Largest diff. peak/hole / e Å^{-3}	0.41/-0.23

Radical Cation Characterization

Electron Paramagnetic Resonance Spectroscopy

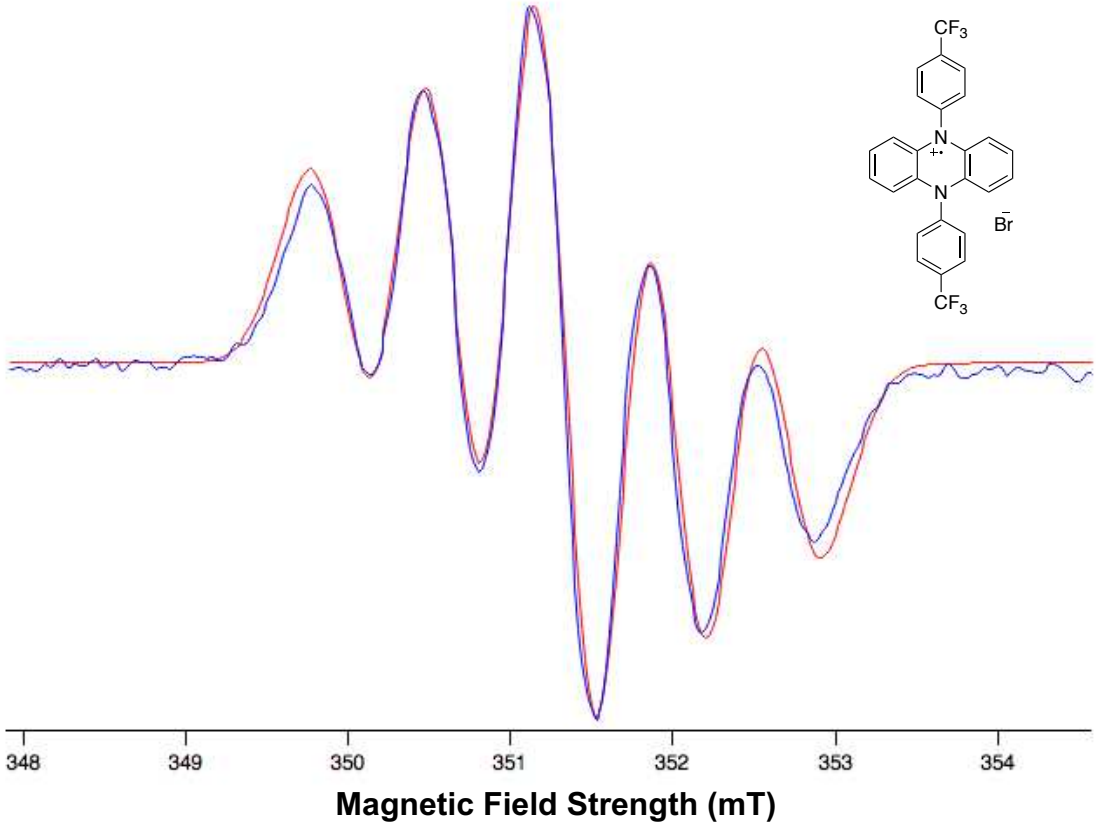

Figure 6.72. *EPR spectrum of* ***1***$^{\bullet+}$*Br*$^{-}$ *(blue) and simulated EPR spectrum (red).*

Table 6.6. *Parameters used in the simulation of the EPR spectrum of* ***1***$^{\bullet+}$*Br*$^{-}$*.*

Nuclei	n	g	A	Line width
^{14}N	2	2.00331	18.5657	
^{1}H	8	2.00092	1.59	.54367
C	12	1.9987	.031	

Spectro-Electrochemistry

Solutions for spectro-electrochemistry were prepared in the same manner as described for cyclic voltammetry. After degassing by nitrogen bubbling for 10 min, the cuvettes were placed in

the UV-Vis spectrometer and a baseline spectrum collected. This spectrum was subtracted from subsequent spectra to subtract the PC signal and isolate that of the radical cation.

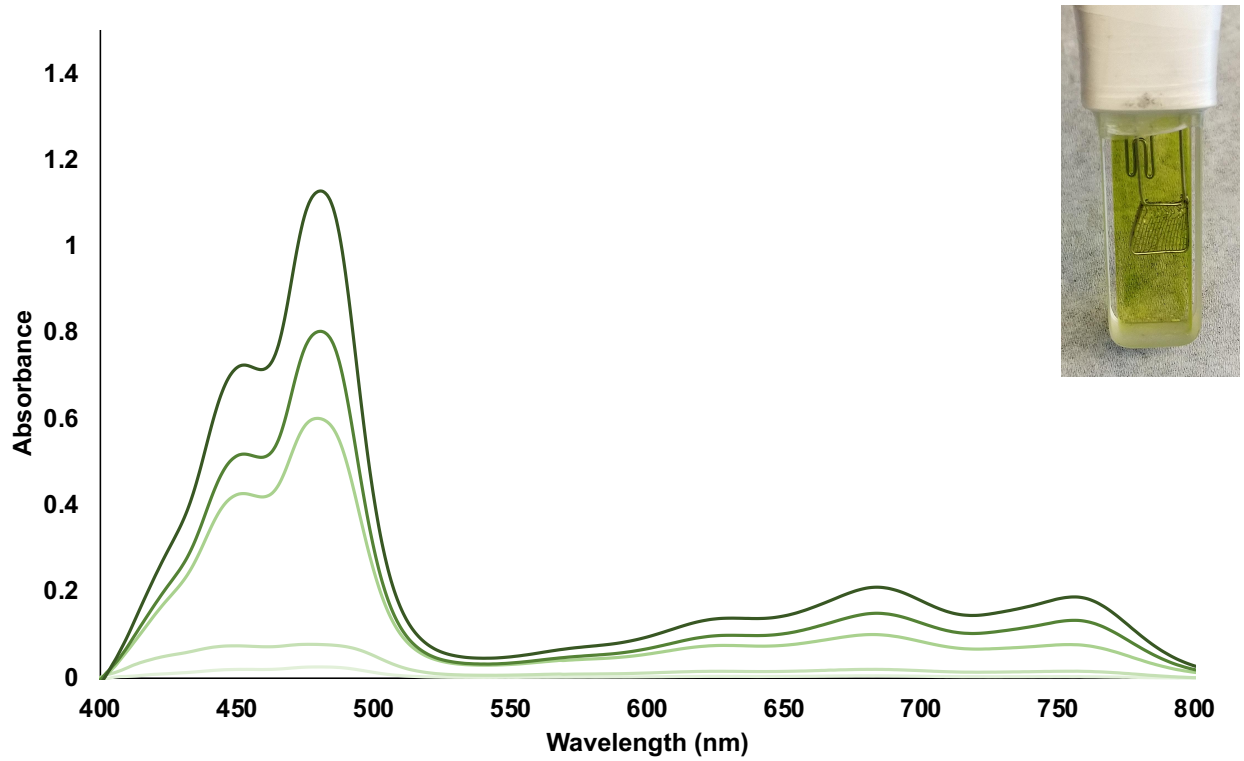

Figure 6.73. *Spectro-electrochemistry of* ***1*** *to* $\mathbf{1}^{\bullet+}$ *(spectrum of* ***1*** *subtracted) in DMAc with 0.1 M* NBu_4PF_6. E_{app} = 0.09 V vs. $Ag/AgNO_3$ *(0.01 M in acetonitrile with 0.1 M* NBu_4PF_6*). Figure inset shows the reaction solution after electrolysis.*

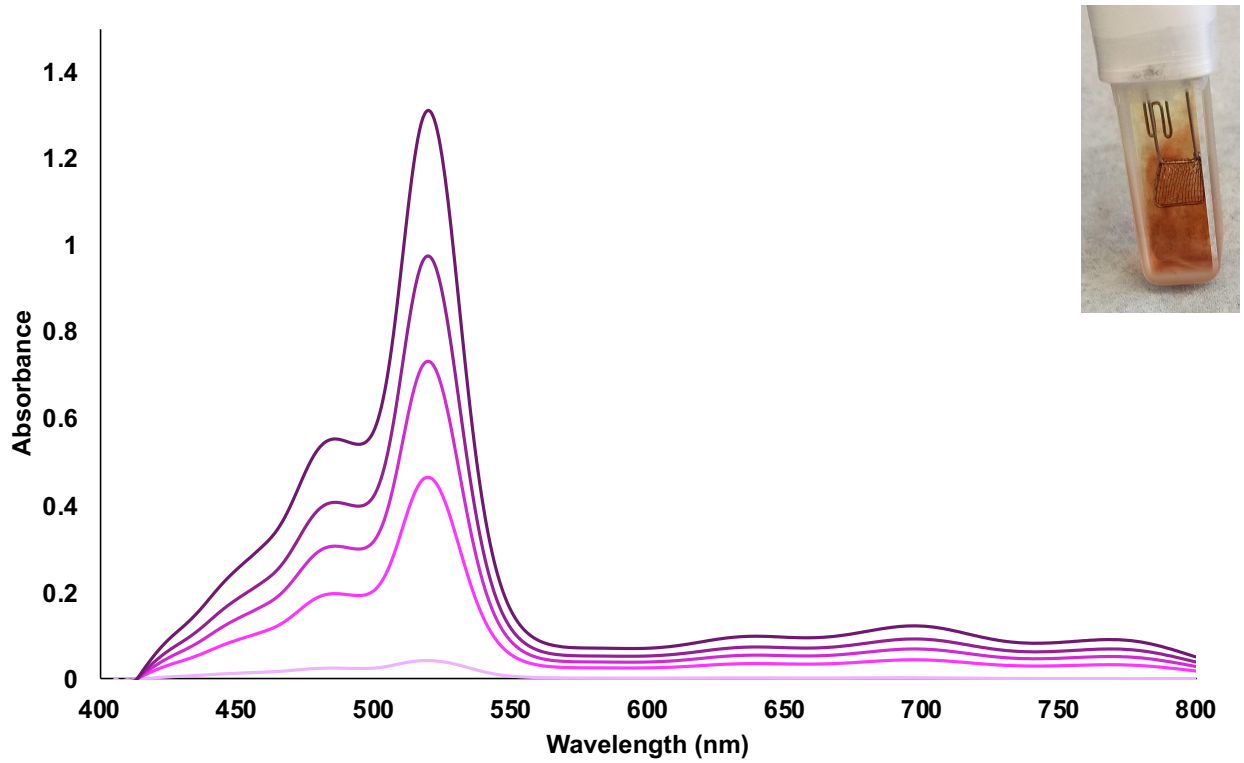

Figure 6.74. *Spectro-electrochemistry of* ***2*** *to* $\mathbf{2}^{\bullet+}$ *(spectrum of* ***2*** *subtracted) in DMAc with 0.1 M* NBu_4PF_6. E_{app} = 0.13 V vs. $Ag/AgNO_3$ *(0.01 M in acetonitrile with 0.1 M* NBu_4PF_6*). Figure inset shows the reaction solution after electrolysis.*

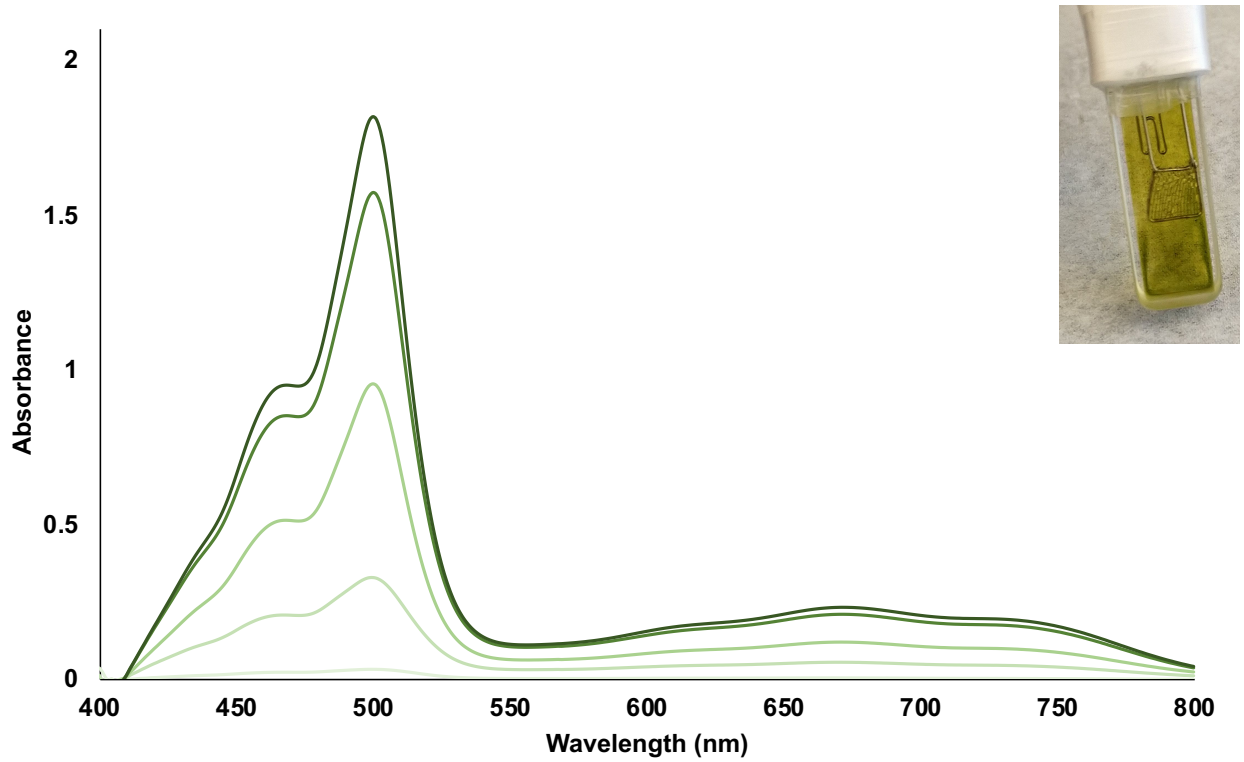

Figure 6.75. *Spectro-electrochemistry of **3** to **3**$^{\bullet+}$ (spectrum of **3** subtracted) in DMAc with 0.1 M NBu_4PF_6. E_{app} = 0.09 V vs. $Ag/AgNO_3$ (0.01 M in acetonitrile with 0.1 M NBu_4PF_6). Figure inset shows the reaction solution after electrolysis.*

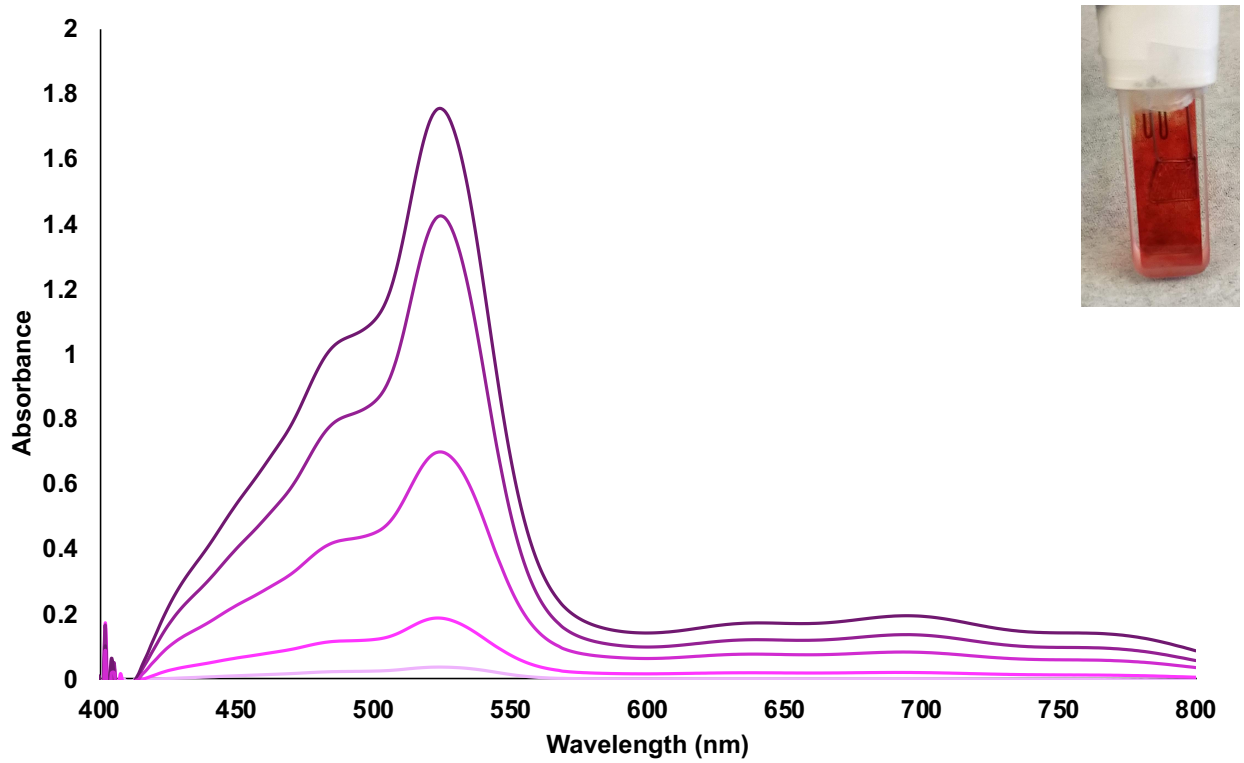

Figure 6.76. *Spectro-electrochemistry of* ***4*** *to* $\mathbf{4}^{\bullet+}$ *(spectrum of* ***4*** *subtracted) in DMAc with 0.1 M* NBu_4PF_6. E_{app} = 0.12 V vs. $Ag/AgNO_3$ *(0.01 M in acetonitrile with 0.1 M* NBu_4PF_6*). Figure inset shows the reaction solution after electrolysis.*

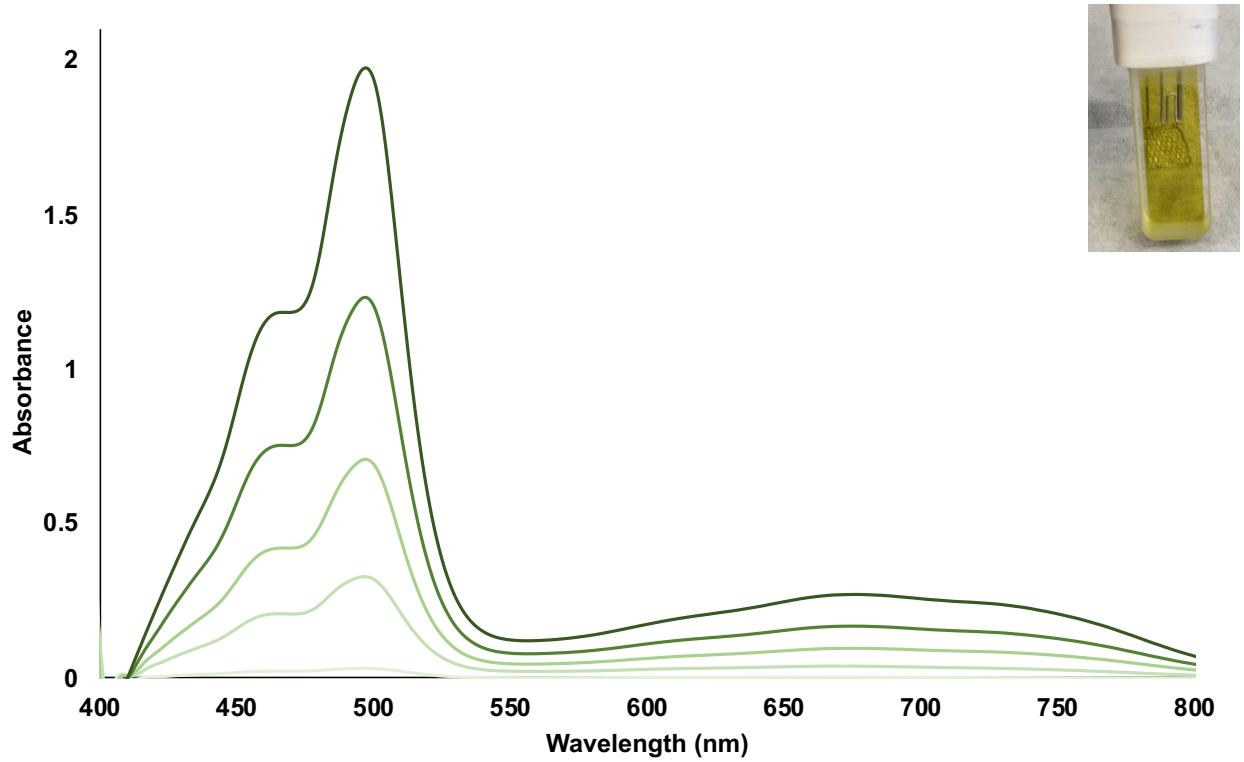

Figure 6.77. *Spectro-electrochemistry of* ***5*** *to* $\mathbf{5}^{\bullet+}$ *(spectrum of* ***5*** *subtracted) in DMAc with 0.1 M* NBu_4PF_6. E_{app} = 0.14 V vs. $Ag/AgNO_3$ *(0.01 M in acetonitrile with 0.1 M* NBu_4PF_6*). Figure inset shows the reaction solution after electrolysis.*

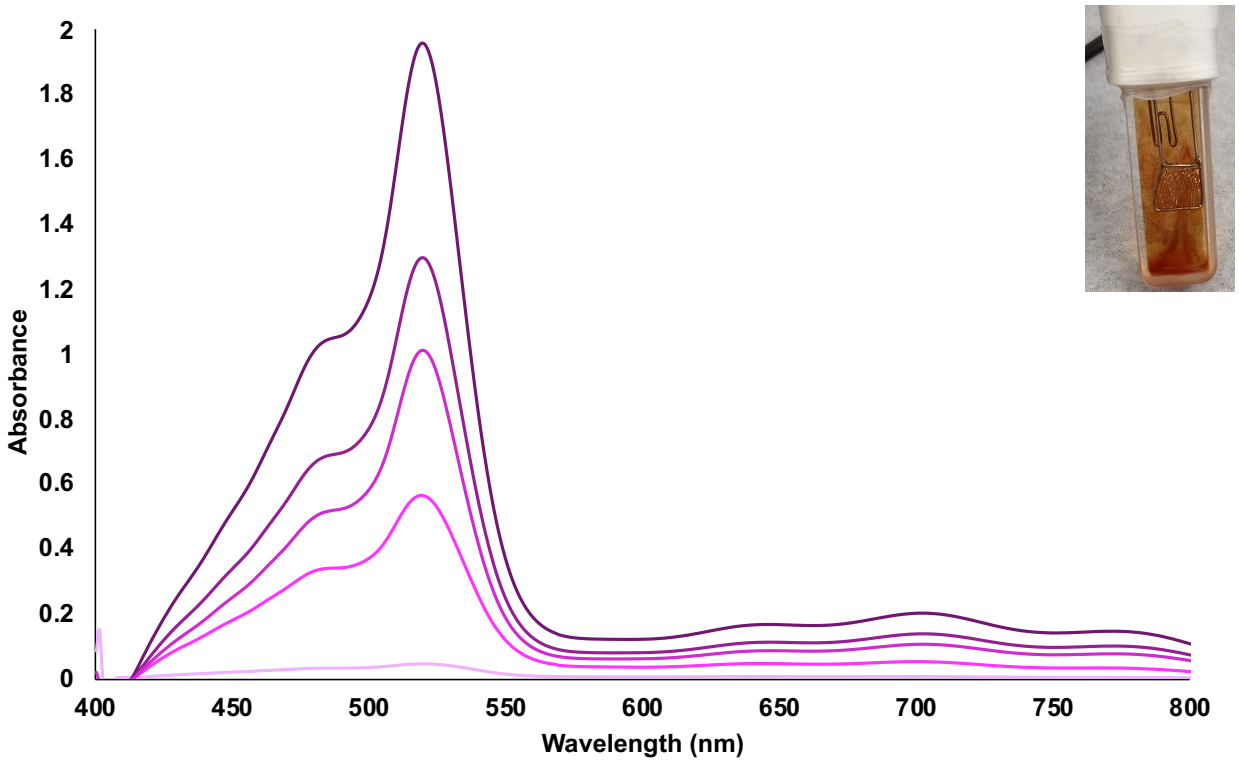

Figure 6.78. *Spectro-electrochemistry of* ***6*** *to* $\mathbf{6}^{\bullet+}$ *(spectrum of* ***6*** *subtracted) in DMAc with 0.1 M* NBu_4PF_6. E_{app} = 0.17 V vs. $Ag/AgNO_3$ *(0.01 M in acetonitrile with 0.1 M* NBu_4PF_6*). Figure inset shows the reaction solution after electrolysis.*

UV-Visible Absorption Spectroscopy

UV-Vis spectra of the radical cations were obtained by removing an aliquot from the reaction solution after the synthesis of each PC but before addition of triethyl amine. Those spectra are shown below, along with the spectra of the neutral PCs and the radical cation spectra obtained by spectro-electrochemistry.

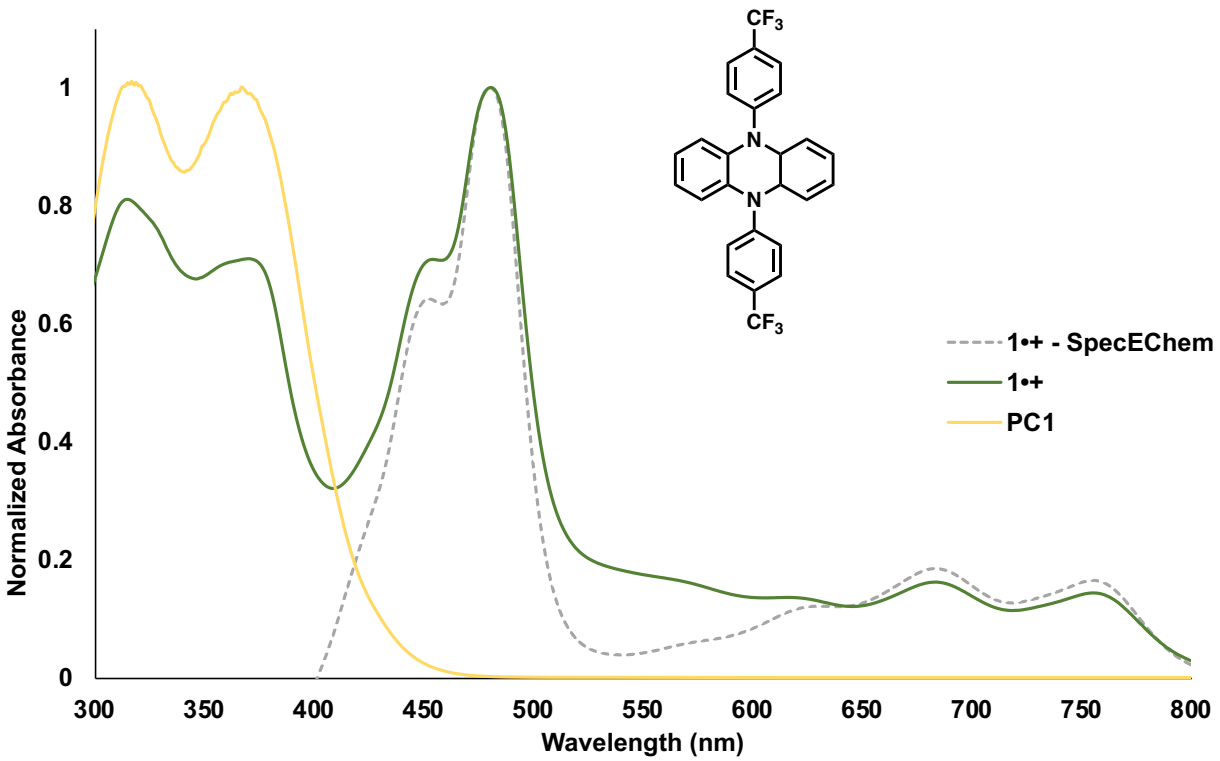

Figure 6.79. *Overlapped UV-vis absorption spectra of* ***1*** *(solid yellow),* ***1***$^{\bullet+}$ *generated during core substitution and removed after the reaction (solid green), and* ***1***$^{\bullet+}$ *generated by spectro-electrochemistry (dashed grey).*

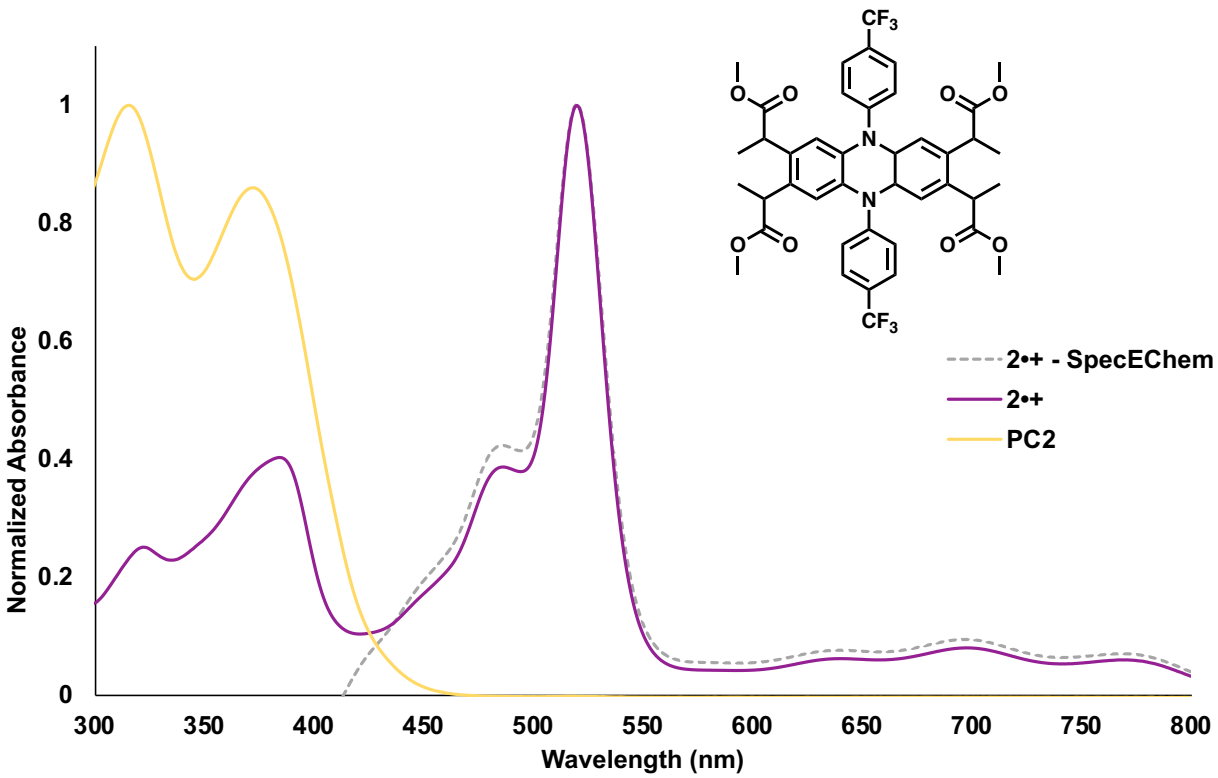

Figure 6.80. *Overlapped UV-vis absorption spectra of* ***2*** *(solid yellow),* $\mathbf{2}^{\bullet+}$ *generated during core substitution and removed after the reaction (solid purple), and* $\mathbf{2}^{\bullet+}$ *generated by spectro-electrochemistry (dashed grey).*

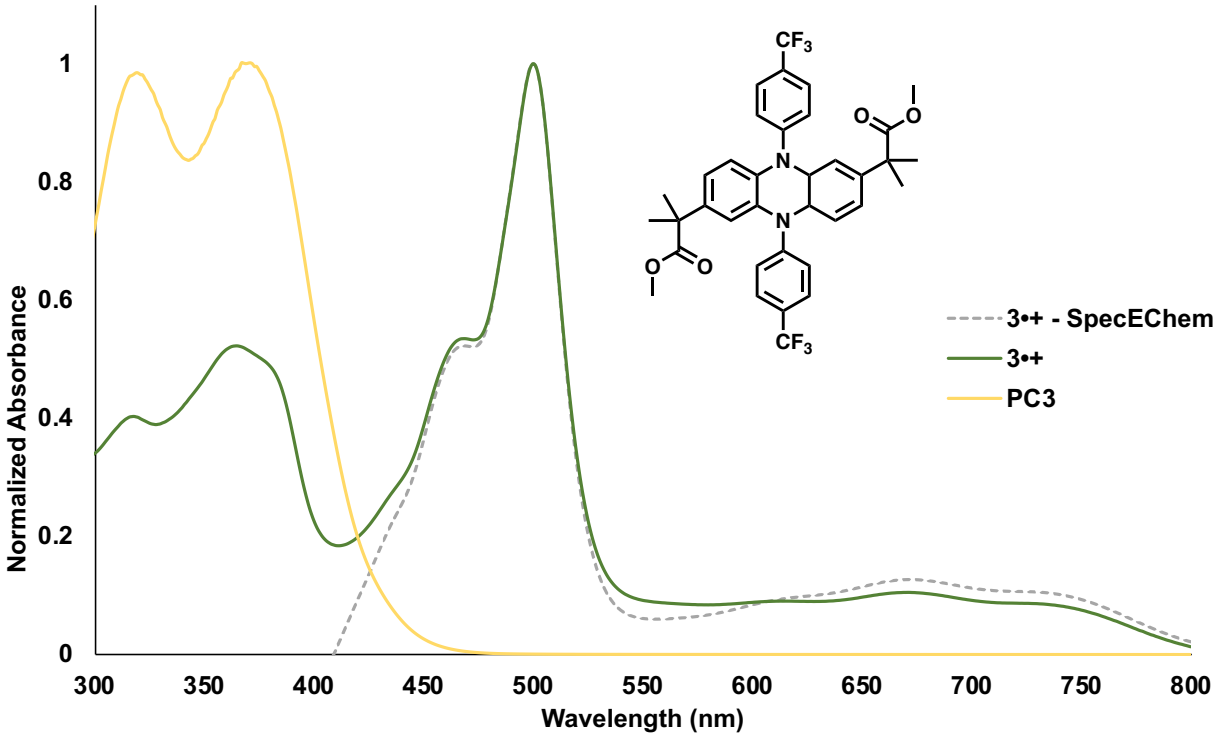

Figure 6.81. *Overlapped UV-vis absorption spectra of* ***3*** *(solid yellow),* ***3***$^{\bullet+}$ *generated during core substitution and removed after the reaction (solid green), and* ***3***$^{\bullet+}$ *generated by spectro-electrochemistry (dashed grey).*

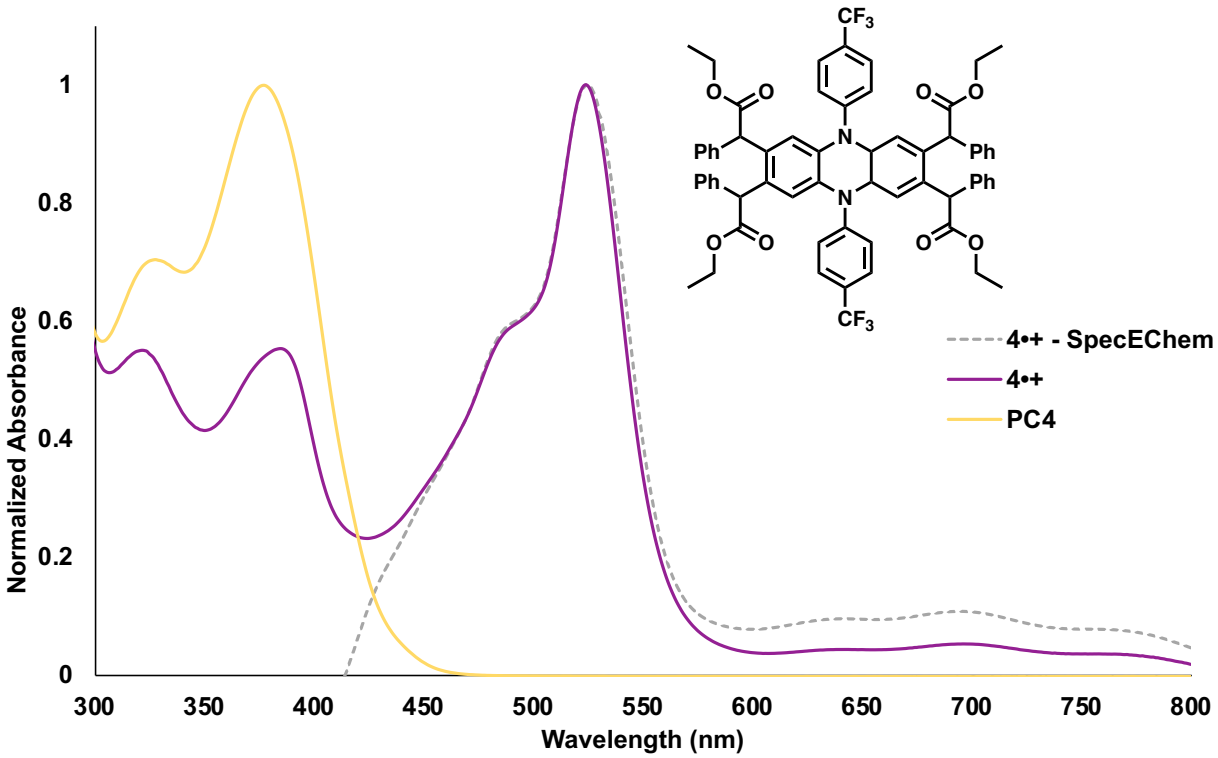

Figure 6.82. *Overlapped UV-vis absorption spectra of* ***4*** *(solid yellow),* ***4***$^{\bullet+}$ *generated during core substitution and removed after the reaction (solid purple), and* ***4***$^{\bullet+}$ *generated by spectro-electrochemistry (dashed grey).*

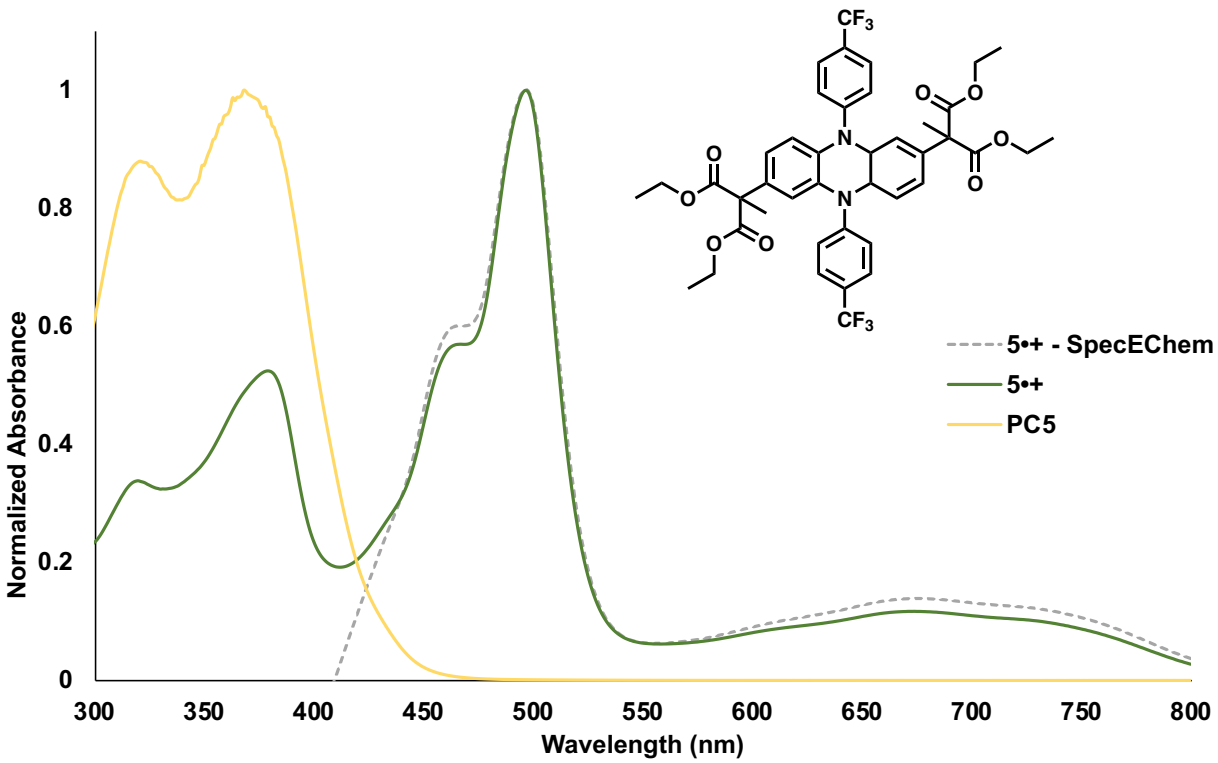

Figure 6.83. *Overlapped UV-vis absorption spectra of* ***5*** *(solid yellow),* ***5***$^{\bullet+}$ *generated during core substitution and removed after the reaction (solid green), and* ***5***$^{\bullet+}$ *generated by spectro-electrochemistry (dashed grey).*

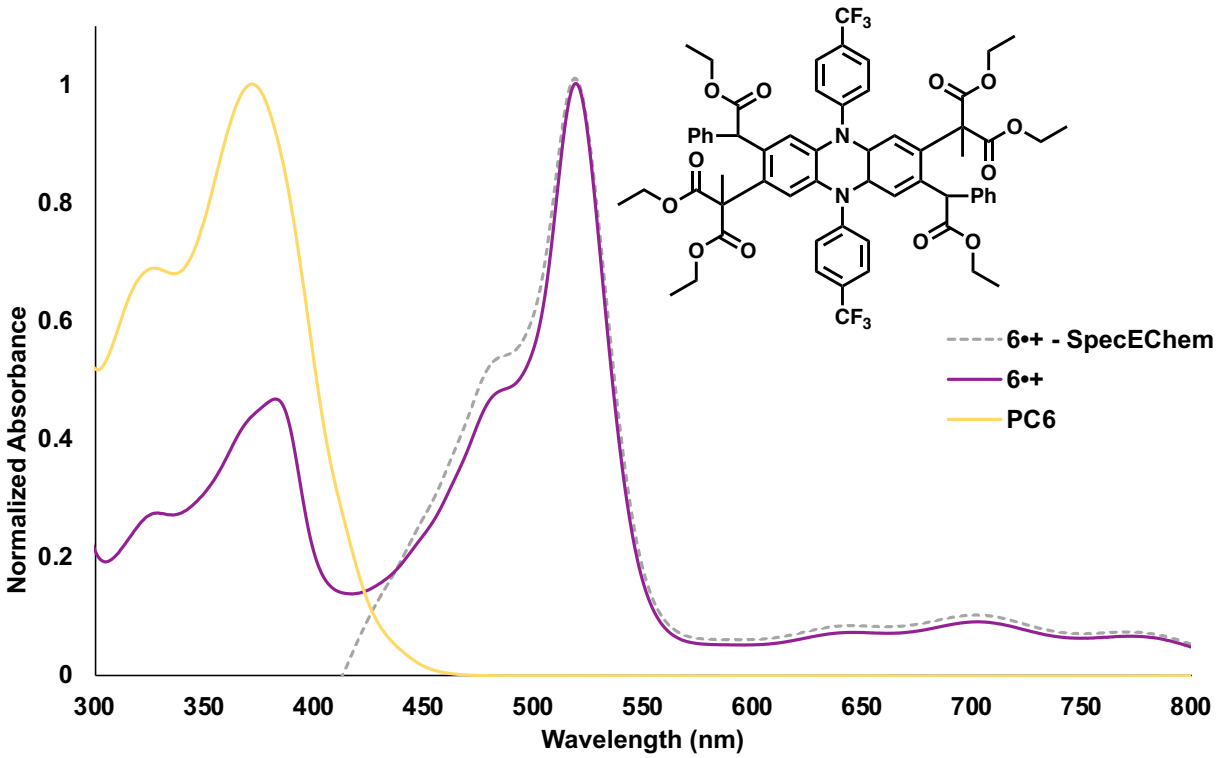

Figure 6.84. *Overlapped UV-vis absorption spectra of* ***6*** *(solid yellow),* ***6***$^{\bullet+}$ *generated during core substitution and removed after the reaction (solid purple), and* ***6***$^{\bullet+}$ *generated by spectro-electrochemistry (dashed grey).*

Crystallographic Information for ***1***$^{\bullet+}Br_3^-$

Crystals of **1**$^{\bullet+}$Br$_3^-$ for X-ray diffraction were grown by dissolving the radical cation in methanol and layering with benzene. The obtained crystal structure is shown below (hydrogens omitted for clarity). It should be noted that while the quality of this crystal structure is poor and does not provide strong evidence for the structure of the radical cation, it does show formation of the tribromide ion, necessitating further treatment to obtain a monobromide anion. While the poor quality of this crystal structure would normally impede its publication, we emphasize its inclusion in this work simply to show evidence for the formation of the tribromide anion. In comparison to other tribromide compounds published in the Cambridge Structural Database (CSD), the bond lengths and bond angle of the tribromide shown here is consistent with previous data published for

tribromides. As such, this crystal structure justifies further manipulation of this radical cation to obtain the desired anion, but it does not yield any reliable information regarding the structure of the radical cation itself. For this reason, and at the suggestion of the reviewers of this manuscript, this structure has been presented here but has not been deposited in the CSD.

Figure 6.85. *Crystal structure of* ***1***$^{\bullet+}Br_3^-$ *(hydrogens omitted for clarity).*

Table 6.7. *Crystallographic information for the structural refinement of* ***1***$^{\bullet+}Br_3^-$.

Identification code	gm20_PhenN-PhCF3-BR3_report
Empirical formula	$C_{26}H_{16}F_6Br_3N_2$
Formula weight	710.14
Temperature/K	100.(2)
Crystal system	triclinic
Space group	P-1
a/Å	7.7300(6)
b/Å	10.3469(9)
c/Å	16.7221(14)
α/°	78.825(3)
β/°	77.881(3)
γ/°	83.304(3)
Volume/Å^3	1278.83(18)
Z	2
ρ_{calc}g/cm^3	1.844
μ/mm^{-1}	4.795
F(000)	690.0
Crystal size/mm^3	0.517 × 0.295 × 0.278
Radiation	Mo Kα (λ = 0.71073)
2Θ range for data collection/°	5.06 to 52.74
Index ranges	-9 ≤ h ≤ 9, -12 ≤ k ≤ 12, -20 ≤ l ≤ 20
Reflections collected	36270
Independent reflections	5214 [R_{int} = 0.0290, R_{sigma} = 0.0206]
Data/restraints/parameters	5214/0/329
Goodness-of-fit on F^2	1.049
Final R indexes [I>=2σ (I)]	R_1 = 0.0712, wR_2 = 0.1867
Final R indexes [all data]	R_1 = 0.0834, wR_2 = 0.1961
Largest diff. peak/hole / e Å^{-3}	8.23/-0.57

Supplemental Polymerization Data

Initial Catalyst Screen in the O-ATRP of MMA

The following experiments were performed according to the *General Polymerization Procedure* outlined in the *Procedures* section of this document.

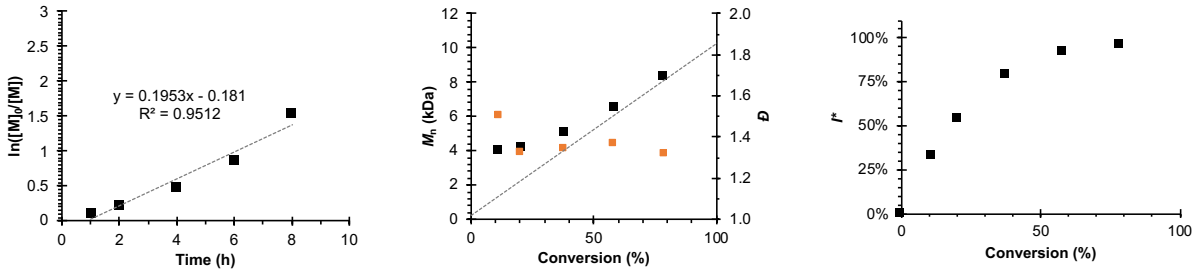

Figure 6.86. *O-ATRP of MMA with* ***1****. [MMA]:[DBMM]:[****1****] = [1000]:[10]:[1]; 1 mL MMA, 1 mL DMAc; irradiated in a white LED beaker. (Left) Pseudo-first-order kinetics plot. (Middle) Evolution of polymer molecular weight (black) and Đ (orange) as a function of monomer conversion; grey dashed line represents the theoretical molecular weight growth. (Right) Initiator efficiency as a function of monomer conversion.*

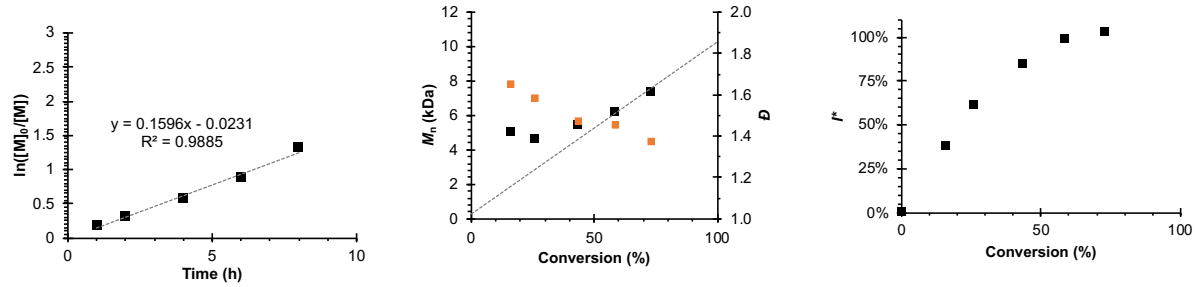

Figure 6.87. *O-ATRP of MMA with* ***2****. [MMA]:[DBMM]:[****2****] = [1000]:[10]:[1]; 1 mL MMA, 1 mL DMAc; irradiated in a white LED beaker. (Left) Pseudo-first-order kinetics plot. (Middle) Evolution of polymer molecular weight (black) and Đ (orange) as a function of monomer conversion; grey dashed line represents the theoretical molecular weight growth. (Right) Initiator efficiency as a function of monomer conversion.*

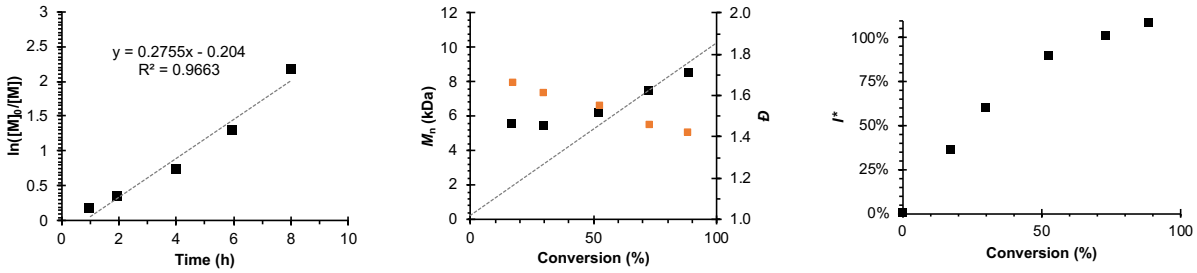

Figure 6.88. *O-ATRP of MMA with* ***3****. [MMA]:[DBMM]:[****3****] = [1000]:[10]:[1]; 1 mL MMA, 1 mL DMAc; irradiated in a white LED beaker. (Left) Pseudo-first-order kinetics plot. (Middle) Evolution of polymer molecular weight (black) and Đ (orange) as a function of monomer conversion; grey dashed line represents the theoretical molecular weight growth. (Right) Initiator efficiency as a function of monomer conversion.*

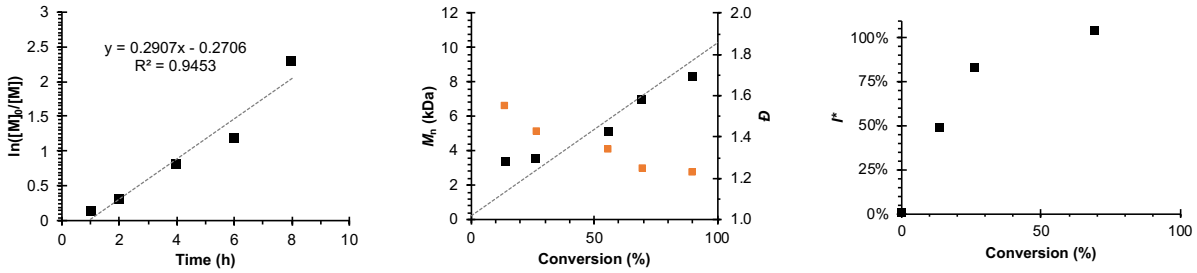

Figure 6.89. *O-ATRP of MMA with* ***4****. [MMA]:[DBMM]:[****4****] = [1000]:[10]:[1]; 1 mL MMA, 1 mL DMAc; irradiated in a white LED beaker. (Left) Pseudo-first-order kinetics plot. (Middle) Evolution of polymer molecular weight (black) and Đ (orange) as a function of monomer conversion; grey dashed line represents the theoretical molecular weight growth. (Right) Initiator efficiency as a function of monomer conversion.*

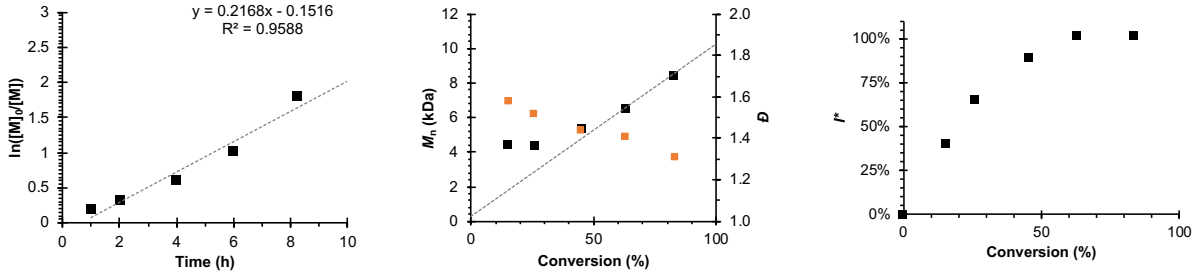

Figure 6.90. *O-ATRP of MMA with* ***5****. [MMA]:[DBMM]:[****5****] = [1000]:[10]:[1]; 1 mL MMA, 1 mL DMAc; irradiated in a white LED beaker. (Left) Pseudo-first-order kinetics plot. (Middle) Evolution of polymer molecular weight (black) and Đ (orange) as a function of monomer conversion; grey dashed line represents the theoretical molecular weight growth. (Right) Initiator efficiency as a function of monomer conversion.*

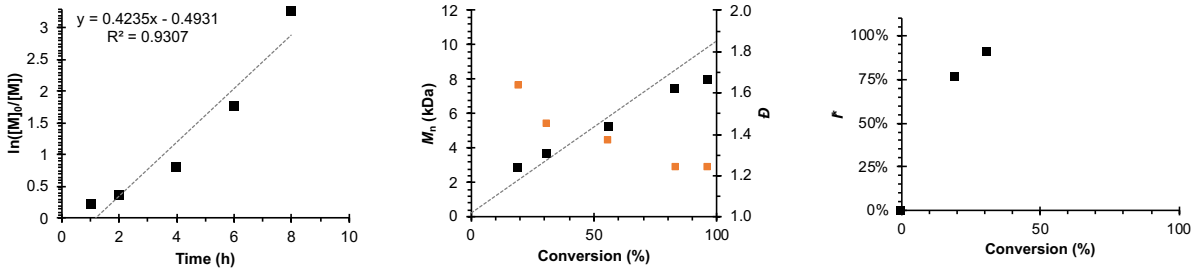

Figure 6.91. *O-ATRP of MMA with* ***6****. [MMA]:[DBMM]:[****6****] = [1000]:[10]:[1]; 1 mL MMA, 1 mL DMAc; irradiated in a white LED beaker. (Left) Pseudo-first-order kinetics plot. (Middle) Evolution of polymer molecular weight (black) and Đ (orange) as a function of monomer conversion; grey dashed line represents the theoretical molecular weight growth. (Right) Initiator efficiency as a function of monomer conversion.*

Solvent Screen

In an effort to improve upon the polymerization results above, polymerizations were performed in various solvents of different polarity. These polymerizations were performed according to the *General Polymerization Procedure* outlined in the *Procedures* section of this document. The results of these experiments are presented in Table 3 of the main text.

Initiator Screen

The ability of **4** to perform O-ATRP with different initiators was investigated. Polymerizations were setup and performed according to the *General Polymerization Procedure* outlined in the *Procedures* section of this document. In general, PC **4** showed excellent polymerization control with most alkyl bromide initiators investigated. When an alkyl chloride initiator was used instead (Table 6.8, entry S4), conversion was observed but with poor polymerization control, consistent with previous findings.[23]

Table 6.8. *Results from the initiator screen using PC **4**.*

Entry	Initiator	Time (h)	Conv. (%)[a]	$M_{n,\,theo}$ (kDa)	$M_{n,\,exp}$ (kDa)[b]	$Đ$[b]	I^* (%)[c]
S1	M2BP	24	79.6	8.14	7.15	1.11	114
S2	MBiB	24	89.6	9.15	5.12	1.10	179
S3	EBP	24	79.3	8.19	8.80	1.12	93
S4	EClP	24	100	10.20	10.20	1.49	100
S5	DBMM	24	77.5	8.01	7.25	1.08	110

[a]Determined by 1H NMR. [b]Determined by GPC coupled with multi-angle light scattering. [c]Initiator efficienty (I) = ($M_{n,\,theo}$ / $M_{n,\,exp}$)•100%.*

Gel Permeation Chromatography Traces

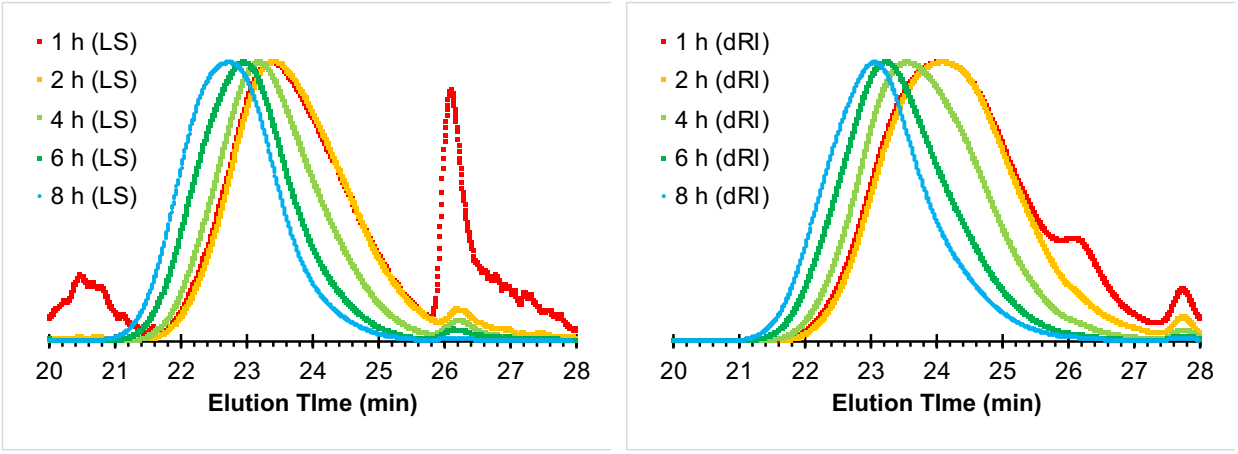

Figure 6.92. *GPC traces for O-ATRP of MMA with **1**. [MMA]:[DBMM]:[**1**] = [1000]:[10]:[1]; 1 mL MMA, 1 mL DMAc; irradiated in a white LED beaker. Detectors: multi-angle light scattering (left) and differential refractive index (right).*

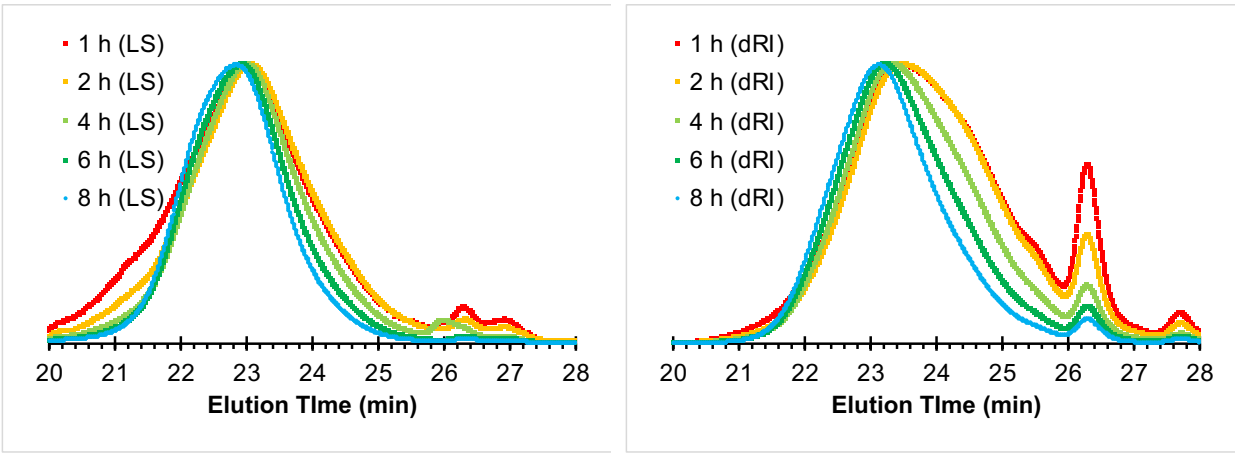

Figure 6.93. *GPC traces for O-ATRP of MMA with **2**. [MMA]:[DBMM]:[**2**] = [1000]:[10]:[1]; 1 mL MMA, 1 mL DMAc; irradiated in a white LED beaker. Detectors: multi-angle light scattering (left) and differential refractive index (right).*

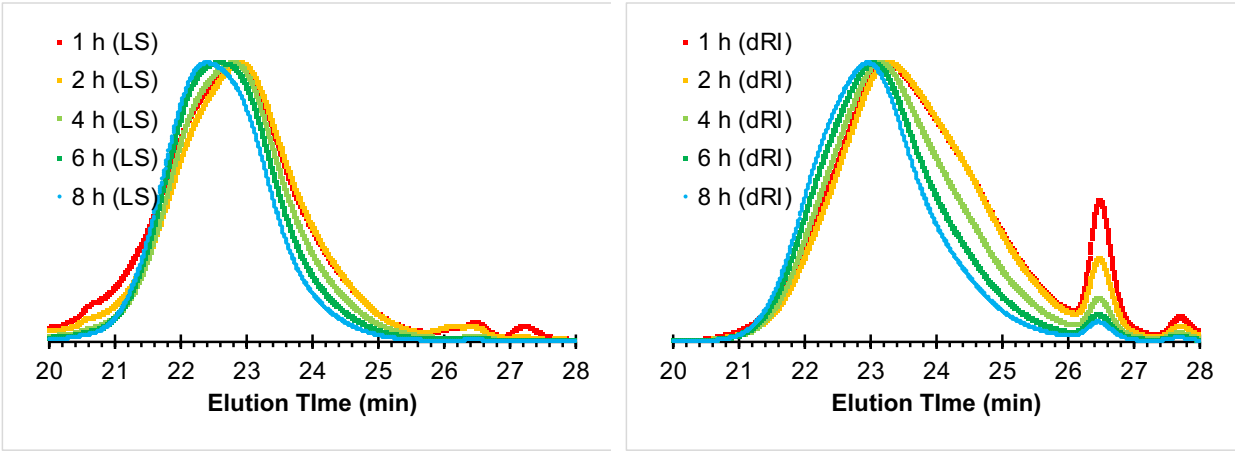

Figure 6.94. *GPC traces for O-ATRP of MMA with **3**. [MMA]:[DBMM]:[**3**] = [1000]:[10]:[1]; 1 mL MMA, 1 mL DMAc; irradiated in a white LED beaker. Detectors: multi-angle light scattering (left) and differential refractive index (right).*

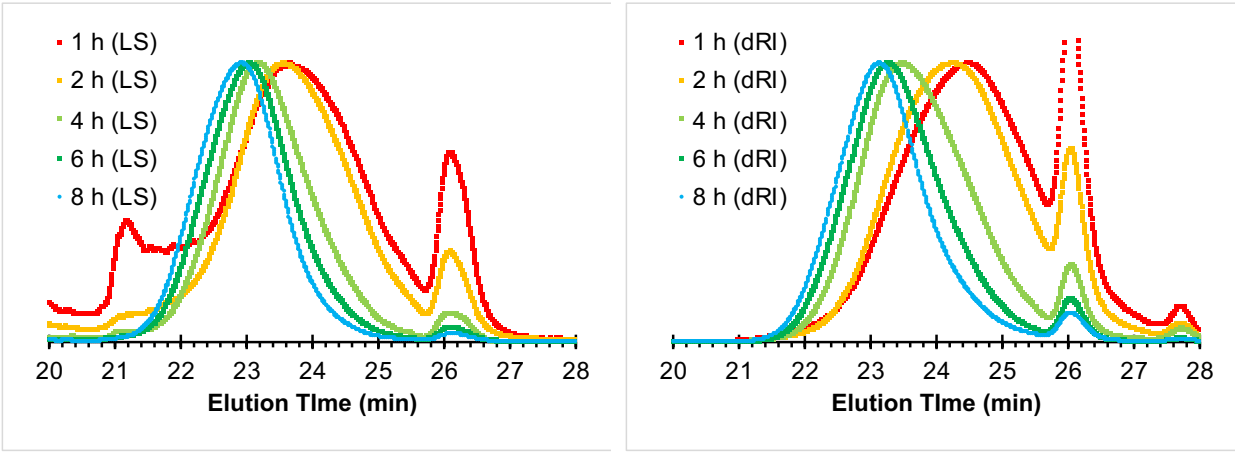

Figure 6.95. *GPC traces for O-ATRP of MMA with **4**. [MMA]:[DBMM]:[**4**] = [1000]:[10]:[1]; 1 mL MMA, 1 mL DMAc; irradiated in a white LED beaker. Detectors: multi-angle light scattering (left) and differential refractive index (right).*

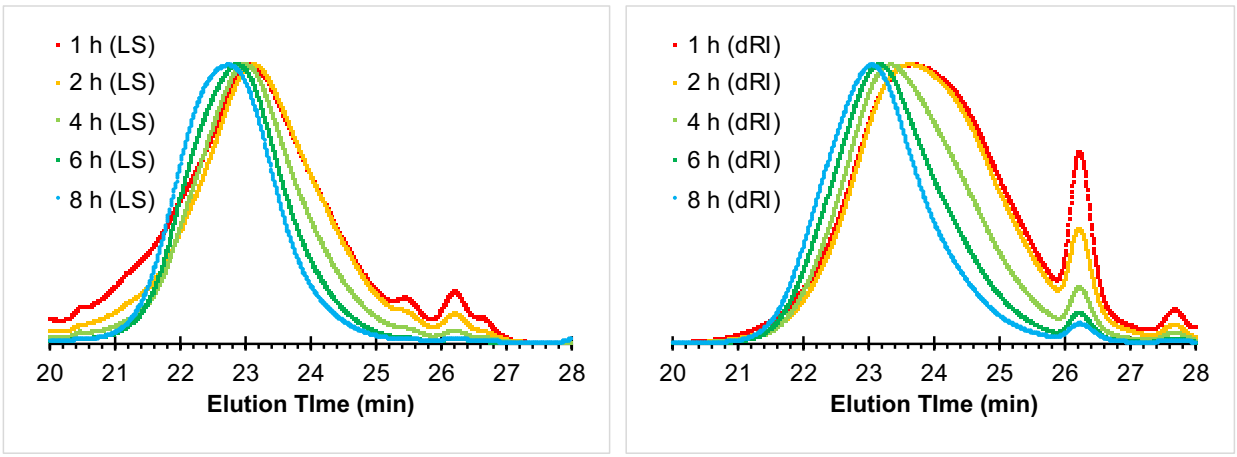

Figure 6.96. *GPC traces for O-ATRP of MMA with* ***5****. [MMA]:[DBMM]:[****5****] = [1000]:[10]:[1]; 1 mL MMA, 1 mL DMAc; irradiated in a white LED beaker. Detectors: multi-angle light scattering (left) and differential refractive index (right).*

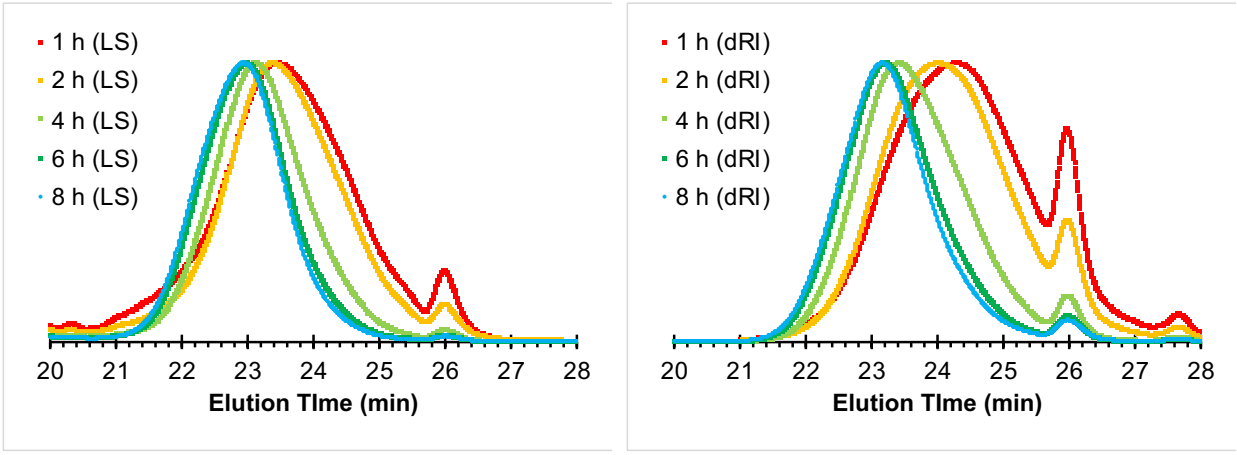

Figure 6.97. *GPC traces for O-ATRP of MMA with* ***6****. [MMA]:[DBMM]:[****6****] = [1000]:[10]:[1]; 1 mL MMA, 1 mL DMAc; irradiated in a white LED beaker. Detectors: multi-angle light scattering (left) and differential refractive index (right).*

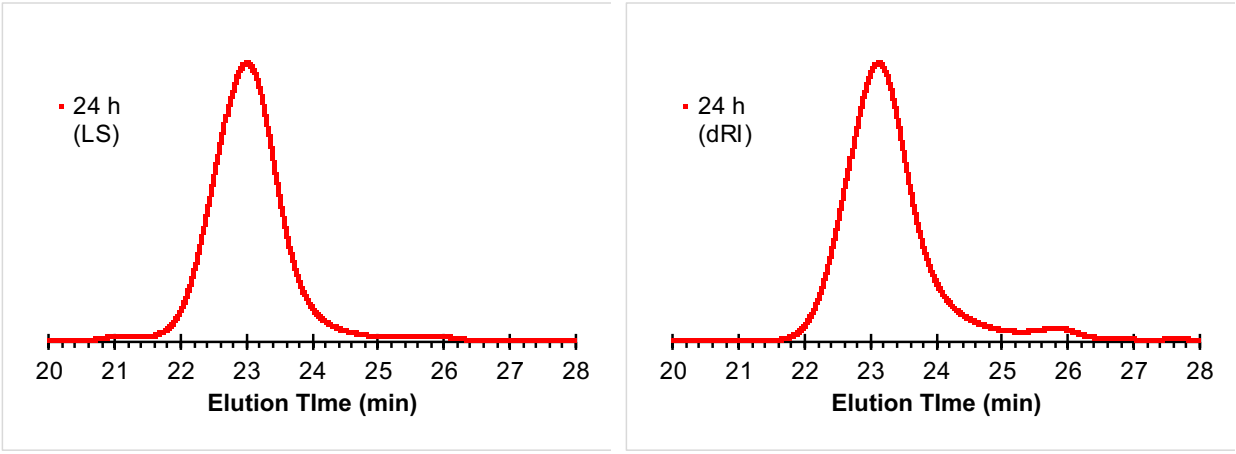

Figure 6.98. *GPC traces for O-ATRP of MMA with* ***1****. [MMA]:[DBMM]:[****1****] = [1000]:[10]:[1]; 1 mL MMA, 1 mL EtAc; irradiated in a white LED beaker. Detectors: multi-angle light scattering (left) and differential refractive index (right).*

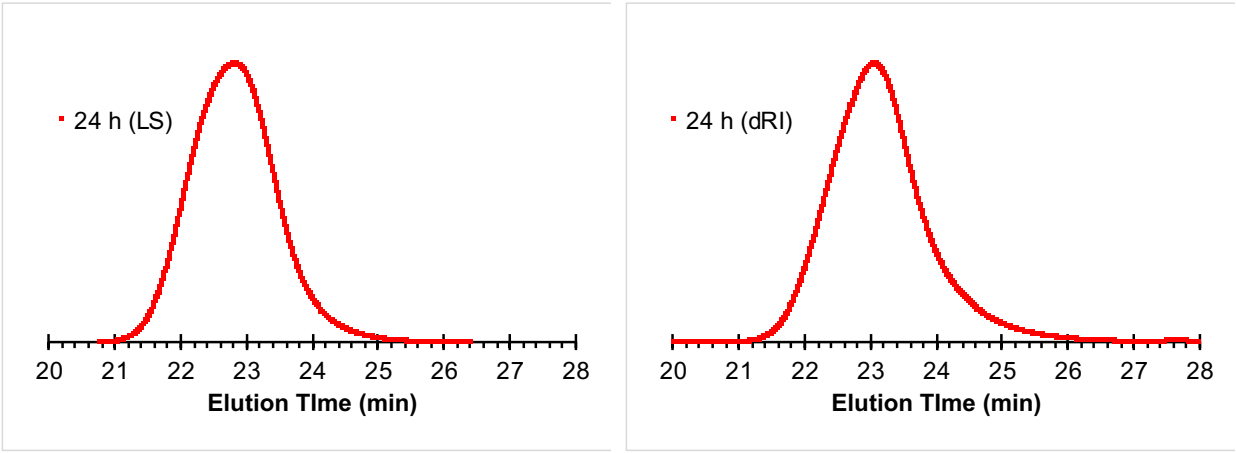

Figure 6.99. *GPC traces for O-ATRP of MMA with* ***1****. [MMA]:[DBMM]:[****1****] = [1000]:[10]:[0.1]; 1 mL MMA, 1 mL EtAc; irradiated in a white LED beaker. Detectors: multi-angle light scattering (left) and differential refractive index (right).*

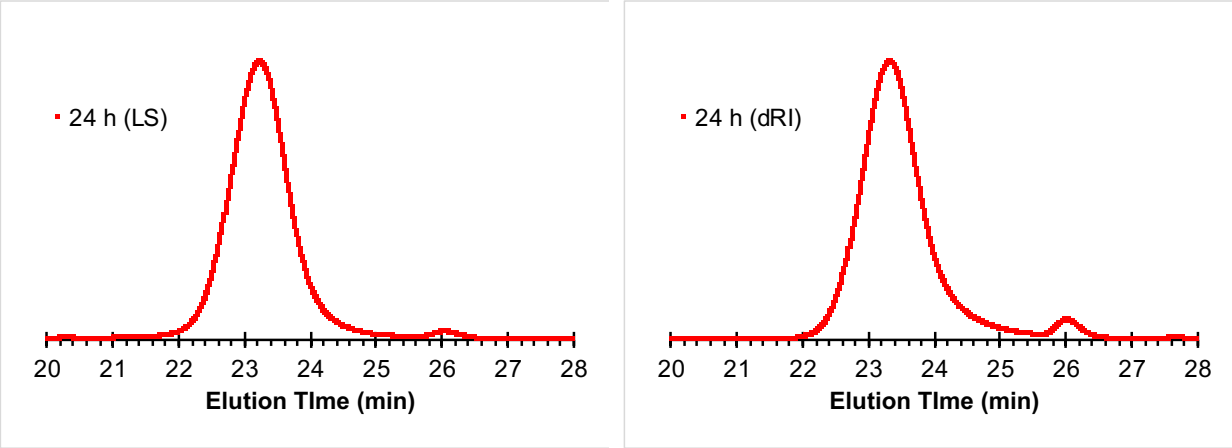

Figure 6.100. *GPC traces for O-ATRP of MMA with **4**. [MMA]:[DBMM]:[**4**] = [1000]:[10]:[1]; 1 mL MMA, 1 mL EtAc; irradiated in a white LED beaker. Detectors: multi-angle light scattering (left) and differential refractive index (right).*

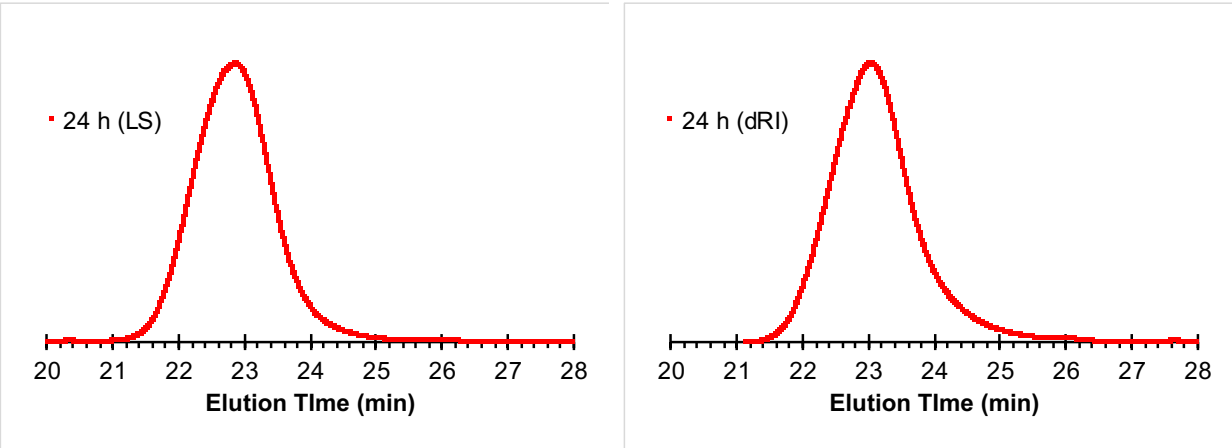

Figure 6.101. *GPC traces for O-ATRP of MMA with **4**. [MMA]:[DBMM]:[**4**] = [1000]:[10]:[0.1]; 1 mL MMA, 1 mL EtAc; irradiated in a white LED beaker. Detectors: multi-angle light scattering (left) and differential refractive index (right).*

Computational Details

Calculations were performed using the computational chemistry software package Gaussian 09 version D.01.[56] We acknowledge the use of computational resources provided by the XSEDE – Comet Supercomputer.

Standard reduction potentials (E^0) were calculated following previously reported procedure.[57-60] A value of -100.5 kcal/mol was assumed for the reduction free energy of the

standard hydrogen electrode (SHE). Thus, E^0 = (-100.5 - ΔG_{red})/23.06 (V vs. SHE); for E^0 ($^2PC^{\bullet+}/^3PC^*$), ΔG_{red} = G($^3PC^*$) - G($^2PC^{\bullet+}$) while for E^0 ($^2PC^{\bullet+/1}PC$), ΔG_{red} = G(^1PC) - G($^2PC^{\bullet+}$). The Gibbs free energies of $^3PC^*$, $^2PC^{\bullet+}$, and ^1PC were calculated at the unrestricted M06/6- 311+G** level of theory in CPCM-H2O solvent (single point energy) using geometries optimized at unrestricted M06/6-31+G** level of theory in CPCM-H2O solvent. The triple zeta basis set (6-311+G**) generally improves the E^0 ($^2PC^{\bullet+}/^1PC$) by ~0.1V relative to 6-31+G**, while the triplet energy is invariant for these two basis sets.

For PCs **4** and **6**, the structural complexity of these PCs prevented convergence during the structure optimization step of these calculations. To simplify these calculations, they were performed at the same level of theory and using the same basis set, but in the gas phase rather than with a CPCM solvent model.

To reference to the Saturated Calomel Electrode (SCE), E^0 (vs. SHE) is converted to E^0 (vs. SCE) using E^0 (vs. SCE) = E^0 (vs. SHE) - 0.24 V. Triplet energies (in eV) of PCs were obtained by [G($^3PC^*$) - G(^1PC), in kcal/mol]/23.06.

Based on the comparison of our experimental and computational data set, the choice of CPCM solvation model is justified as the computed reduction potential closely approximates the experimental values. For example, the computed ground state oxidation potentials between the $^2PC^{\bullet+}/^1PC$ redox couple is typically within ~0.15 to 0.25 V from the experimental values.

REFERENCES

(1) Narayanam, J. M. R.; Stephenson, C. R. J. Visible light photoredox catalysis: applications in organic synthesis. *Chem. Soc. Rev.* **2011**, *40*, 102–113.

(2) Prier, C. K.; Rankic, D. A.; MacMillan, D. W. C. Visible light photoredox catalysis with transition metal complexes: applications in organic synthesis. *Chem. Rev.* **2013**, *113*, 5322–5363.

(3) Romero, N. A.; Nicewicz, D. A. Organic photoredox catalysis. *Chem. Rev.* **2016**, *116*, 10075–10166.

(4) Corrigan, N.; Shanmugam, S.; Xu, J. T.; Boyer, C. Photocatalysis in organic and polymer synthesis. *Chem. Soc. Rev.* **2016**, *45*, 6165–6212.

(5) Shaw, M. H.; Twilton, J.; MacMillan, D. W. C. Photoredox catalysis in organic chemistry. *J. Org. Chem.* **2016**, *81*, 6898–6926.

(6) Arias-Rotondo, D. M.; McCusker, J. K. The photophysics of photoredox catalysis: a roadmap for catalyst design. *Chem. Soc. Rev.* **2016**, *45*, 5803–5820.

(7) Ludwig, J. R.; Schindler, C. S. Catalyst: Sustainable Catalysis. *Chem* **2017**, *2*, 313–316.

(8) Miyake, G. M.; Theriot, J. C. Perylene as an organic photocatalyst for the radical polymerization of functionalized vinyl monomers through oxidative quenching with alkyl bromides and visible light. *Macromolecules* **2014**, *47*, 8255–8261.

(9) Theriot, J. C.; Lim, C. H.; Yang, H.; Ryan, M. D.; Musgrave, C. B.; Miyake, G. M. Organocatalyzed atom transfer radical polymerization driven by visible light. *Science* **2016**, *352*, 1082–1086.

(10) Pearson, R. M.; Lim, C. H.; McCarthy, B. G.; Musgrave, C. B.; Miyake, G. M. Organocatalyzed atom transfer radical polymerization using n-aryl phenoxazines as photoredox catalysts. *J. Am. Chem. Soc.* **2016**, *138*, 11399–11407.

(11) Du, Y.; Pearson, R. M.; Lim, C. H.; Sartor, S. M.; Ryan, M. D.; Yang, H. S.; Damrauer, N. H.; Miyake, G. M. Strongly reducing, visible-light organic photoredox catalysts as sustainable alternatives to precious metals. *Chem. Eur. J.* **2017**, *23*, 10962.

(12) McCarthy, B. G.; Pearson, R. M.; Lim, C. H.; Sartor, S. M.; Damrauer, N. H.; Miyake, G. M. Structure-property relationships for tailoring phenoxazines as reducing photoredox catalysts. *J. Am. Chem. Soc.* **2018**, *140*, 5088–5101.

(13) Buss, B. L.; Lim, C. H.; Miyake, G. M. Dimethyl dihydroacridines as photocatalysts in organocatalyzed atom transfer radical polymerization of acrylate monomers. *Angew. Chem. Int. Ed.* **2020**, *59*, 3209–3217.

(14) Wang, J. S.; Matyjaszewski, K. Controlled living radical polymerization - atom-transfer radical polymerization in the presence of transition-metal complexes. *J. Am. Chem. Soc.* **1995**, *117*, 5614–5615.

(15) Kato, M.; Kamigaito, M.; Sawamoto, M.; Higashimura, T. Polymerization of methyl-methacrylate with the carbon-tetrachloride dichlorotris(triphenylphosphine)ruthenium(II) methylaluminum bis(2,6-di-tert-butylphenoxide) initiating system - possibility of living radical polymerization. *Macromolecules* **1995**, *28*, 1721–1723.

(16) Matyjaszewski, K.; Xia, J. H. Atom transfer radical polymerization. *Chem. Rev.* **2001**, *101*, 2921–2990.

(17) Matyjaszewski, K.; Muller, A. H. E. 50 Years of living polymerization. *Prog. Polym. Sci.* **2006**, *31*, 1039–1040.

(18) Matyjaszewski, K. Atom transfer radical polymerization (ATRP): current status and future perspectives. *Macromolecules* **2012**, *45*, 4015–4039.

(19) Krys, P.; Matyjaszewski, K. Kinetics of atom transfer radical polymerization. Eur. Polym. J. **2017**, *89*, 482–523.

(20) Matyjaszewski, K. Advanced materials by atom transfer radical polymerization. Adv. Mater. **2018**, *30*, 22.

(21) Corrigan, N.; Jung, K.; Moad, G.; Hawker, C. J.; Matyjaszewski, K.; Boyer, C. Reversible-deactivation radical polymerization (controlled/living radical polymerization): from discovery to materials design and applications. *Prog. Polym. Sci.* **2020,** *111,* 101311.

(22) Treat, N. J.; Sprafke, H.; Kramer, J. W.; Clark, P. G.; Barton, B. E.; de Alaniz, J. R.; Fors, B. P.; Hawker, C. J. Metal-free atom transfer radical polymerization. *J. Am. Chem. Soc.* **2014**, *136*, 16096–16101.

(23) Pan, X. C.; Fang, C.; Fantin, M.; Malhotra, N.; So, W. Y.; Peteanu, L. A.; Isse, A. A.; Gennaro, A.; Liu, P.; Matyjaszewskit, K. Mechanism of photoinduced metal-free atom transfer radical polymerization: experimental and computational studies. *J. Am. Chem. Soc.* **2016**, *138*, 2411–2425.

(24) Tan, S. B.; Xiong, J.; Zhao, Y. F.; Liu, J. J.; Zhang, Z. C. Synthesis of poly(vinylidene fluoride-cochlorotrifluoroethylene)-g-poly(methyl methacrylate) with low dielectric loss by photo-induced metal-free ATRP. *J. Mater. Chem. C* **2018**, *6*, 4131–4139.

(25) Ramakers, G.; Krivcov, A.; Trouillet, V.; Welle, A.; Mobius, H.; Junkers, T. Organocatalyzed photo-atom transfer radical polymerization of methacrylic acid in continuous flow and surface grafting. *Macromol. Rapid Commun.* **2017**, *38*, 1700423.

(26) Chen, D. F.; Boyle, B. M.; McCarthy, B. G.; Lim, C. H.; Miyake, G. M. Controlling polymer composition in organocatalyzed photoredox radical ring-opening polymerization of vinylcyclopropanes. *J. Am. Chem. Soc.* **2019**, *141*, 13268–13277.

(27) Chen, D. F.; Bernsten, S.; Miyake, G. M. Organocatalyzed photoredox radical ring-opening polymerization of functionalized vinylcyclopropanes. *Macromolecules* **2020**, *53*, 8352–8359.

(28) Pan, X. C.; Lamson, M.; Yan, J. J.; Matyjaszewski, K. Photoinduced metal-free atom transfer radical polymerization of acrylonitrile. *ACS Macro Lett.* **2015**, *4*, 192–196.

(29) Dadashi-Silab, S.; Pan, X. C.; Matyjaszewski, K. Phenyl benzo[*b*]phenothiazine as a visible light photoredox catalyst for metal-free atom transfer radical polymerization. *Chem. Eur. J.* **2017**, *23*, 5972–5977.

(30) Zhao, Y. C.; Gong, H. H.; Jiang, K. M.; Yan, S. J.; Lin, J.; Chen, M. Organocatalyzed photoredox polymerization from aromatic sulfonyl halides: facilitating graft from aromatic C-H bonds. *Macromolecules* **2018**, *51*, 938–946.

(31) Nguyen, T. H.; Nguyen, L. T. T.; Nguyen, V. Q.; Phan, L. N. T.; Zhang, G.; Yokozawa, T.; Phung, D. T. T.; Nguyen, H. T. Synthesis of poly(3-hexylthiophene) based rod-coil conjugated block copolymers via photoinduced metal-free atom transfer radical polymerization. *Polym. Chem.* **2018**, *9*, 2484–2493.

(32) Tran, H. M.; Phan, L. N. T.; Le, T. V.; Truong, T. T.; Nguyen, T. H.; Truong, K. T.; Nguyen, L. T. T.; Phong, M. T.; Nguyen, H. T. Phenothiazine derivative as organic photocatalyst for metal free atom transfer radical polymerization. *Polym. Korea* **2019**, *43*, 496–502.

(33) Huang, W. J.; Zhai, J. L.; Hu, X.; Duan, J. D.; Fang, Z.; Zhu, N.; Guo, K. Continuous flow photoinduced phenothiazine derivatives catalyzed atom transfer radical polymerization. *Eur. Polym. J.* **2020**, *126*, 109565.

(34) McCarthy, B.; Miyake, G. M. Organocatalyzed atom transfer radical polymerization catalyzed by core modified n-aryl phenoxazines performed under air. *ACS Macro Lett.* **2018**, *7*, 1016–1021.

(35) Bian, C.; Zhou, Y. N.; Deetz, J. D.; Luo, Z. H. Experimental and computational investigation of oxidative quenching governed aqueous organocatalyzed atom transfer radical polymerization. *Chem. Eng. J.* **2019**, *362*, 721–730.

(36) Park, G. S.; Back, J.; Choi, E. M.; Lee, E.; Son, K. S. Visible light-mediated metal-free atom transfer radical polymerization with N-trifluoromethylphenyl phenoxazines. *Eur. Polym. J.* **2019**, *117*, 347–352.

(37) Cole, J. P.; Federico, C. R.; Lim, C.-H.; Miyake, G. M. Photoinduced organocatalyzed atom transfer radical polymerization using low ppm catalyst loading. *Macromolecules* **2019**, *52*, 747–754.

(38) Su, X.; Jessop, P. G.; Cunningham, M. F. Versatility of organocatalyzed atom transfer radical polymerization and CO_2-switching for preparing both hydrophobic and hydrophilic polymers with the recycling of a photocatalyst. *Macromolecules* **2019**, *52*, 6725–6733.

(39) McCarthy, B.; Sartor, S.; Cole, J.; Damrauer, N.; Miyake, G. M. Solvent effects and side reactions in organocatalyzed atom transfer radical polymerization for enabling the controlled polymerization of acrylates catalyzed by diaryl dihydrophenazines. *Macromolecules* **2020**, *53*, 9208–9219.

(40) Liu, Y. M.; Chen, Q.; Tong, Y. J.; Ma, Y. G. 9,9-Dimethyl dihydroacridine-based organic photocatalyst for atom transfer radical polymerization from modifying "unstable" electron donor. *Macromolecules* **2020**, *53*, 7053–7062.

(41) Allushi, A.; Jockusch, S.; Yilmaz, G.; Yagci, Y. Photoinitiated metal-free controlled/living radical polymerization using polynuclear aromatic hydrocarbons. *Macromolecules* **2016**, *49*, 7785–7792.

(42) Zeng, L. L.; Xie, W. Y.; Yang, C. X.; Liang, E. X.; Wang, G. X. Photomediated atom transfer radical polymerization of MMA under long-wavelength light irradiation. *Iran. Polym. J.* **2018**, *27*, 881–887.

(43) Ma, Q.; Song, J. S.; Zhang, X.; Jiang, Y.; Ji, L.; Liao, S. H. Metal-free atom transfer radical polymerization with ppm catalyst loading under sunlight. *Nat. Commun,* **2021**, *12*, DOI: 10.1038/s41467-020-20645-8.

(44) Liu, X. D.; Zhang, L. F.; Cheng, Z. P.; Zhu, X. L. Metal-free photoinduced electron transfer-atom transfer radical polymerization (PET-ATRP) via a visible light organic photocatalyst. *Polym. Chem.* **2016**, *7*, 689–700.

(45) Kutahya, C.; Aykac, F. S.; Yilmaz, G.; Yagci, Y. LED and visible light-induced metal free ATRP using reducible dyes in the presence of amines. *Polym. Chem.* **2016**, *7*, 6094–6098.

(46) Devery, J. J.; Douglas, J. J.; Nguyen, J. D.; Cole, K. P.; Flowers, R. A.; Stephenson, C. R. J. Ligand functionalization as a deactivation pathway in a fac-Ir(ppy)$^{(3)}$-mediated radical addition. *Chem. Sci.* **2015**, *6*, 537–541.

(47) Theriot, J. C. Organocatalyzed Atom Transfer Radical Polymerization: Development, Catalyst Design, and Mechanistic Investigation. Ph.D. Dissertation, University of Colorado, Boulder, CO, 2018.

(48) Brisar, R.; Unglaube, F.; Hollmann, D.; Jiao, H. J.; Mejia, E. Aerobic oxidative homo- and cross-coupling of amines catalyzed by phenazine radical cations. *J. Org. Chem.* **2018**, *83*, 13481–13490.

(49) Ryan, M. D.; Theriot, J. C.; Lim, C. H.; Yang, H. S.; Lockwood, A. G.; Garrison, N. G.; Lincoln, S. R.; Musgrave, C. B.; Miyake, G. M. Solvent effects on the intramolecular charge

transfer character of *N,N*-diaryl dihydrophenazine catalysts for organocatalyzed atom transfer radical polymerization. *J. Polym. Sci. Part A Polym. Chem.* **2017**, *55*, 3017–3027.

(50) Lim, C. H.; Ryan, M. D.; McCarthy, B. G.; Theriot, J. C.; Sartor, S. M.; Damrauer, N. H.; Musgrave, C. B.; Miyake, G. M. Intramolecular charge transfer and ion pairing in *N,N*-diaryl dihydrophenazine photoredox catalysts for efficient organocatalyzed atom transfer radical polymerization. *J. Am. Chem. Soc.* **2017**, *139*, 348–355.

(51) Stoll, S.; Schweiger, A. EasySpin, a Comprehensive Software Package for Spectral Simulation and Analysis in EPR. *J. Magn. Reson.* **2006**, *178*, 42–55.

(52) Sheldrick, G. M. Program for Empirical Absorption Correction of Area Detector Data. *SADABS* **1996**.

(53) Sheldrick, G. M. SHELXT – Integrated Space-Group and Crystal-Structure Determination. *Acta Crystallogr. Sect. Found. Adv.* **2015**, *71*, 3–8.

(54) Sheldrick, G. M. Crystal Structure Refinement with SHELXL. *Acta Crystallogr. Sect. C Struct. Chem.* **2015**, *71*, 3–8.

(55) Zheng, Z.; Dong, Q.; Gou, L.; Su, J.-H.; Huang, J. Novel hole transport materials based on N,N′-disubstituted-dihydrophenazine derivatives for electroluminescent diodes. *J. Mater. Chem. C* **2014**, *2*, 9858–9865.

(56) Gaussian 09, R. D., Frisch, M. J.; Trucks, G. W.; Schlegel, H. B.; Scuseria, G. E.; Robb, M. A.; Cheeseman, J. R.; Scalmani, G.; Barone, V.; Mennucci, B.; Petersson, G. A.; Nakatsuji, H.; Caricato, M.; Li, X.; Hratchian, H. P.; Izmaylov, A. F.; Bloino, J.; Zheng, G.; Sonnenberg, J. L.; Hada, M.; Ehara, M.; Toyota, K.; Fukuda, R.; Hasegawa, J.; Ishida, M.; Nakajima, T.; Honda, Y.; Kitao, O.; Nakai, H.; Vreven, T.; Montgomery, J. A., Jr.; Peralta, J. E.; Ogliaro, F.; Bearpark, M.; Heyd, J. J.; Brothers, E.; Kudin, K. N.; Staroverov, V. N.; Kobayashi, R.; Normand, J.;

Raghavachari, K.; Rendell, A.; Burant, J. C.; Iyengar, S. S.; Tomasi, J.; Cossi, M.; Rega, N.; Millam, J. M.; Klene, M.; Knox, J. E.; Cross, J. B.; Bakken, V.; Adamo, C.; Jaramillo, J.; Gomperts, R.; Stratmann, R. E.; Yazyev, O.; Austin, A. J.; Cammi, R.; Pomelli, C.; Ochterski, J. W.; Martin, R. L.; Morokuma, K.; Zakrzewski, V. G.; Voth, G. A.; Salvador, P.; Dannenberg, J. J.; Dapprich, S.; Daniels, A. D.; Farkas, Ö.; Foresman, J. B.; Ortiz, J. V.; Cioslowski, J.; Fox, D. J. Gaussian, Inc., Wallingford CT, 2009.

(57) He, H.; Zapol, P.; Curtiss, L. A. A Theoretical Study of CO_2 Anions on Anatase (101) Surface. *J. Phys. Chem. C,* **2010**, *114*, 21474.

(58) Winget, P.; Cramer, C. J.; Truhlar, D. G. Computation of equilibrium oxidation and reduction potentials for reversible and dissociative electron-transfer reactions in solution. *Theor. Chem. Acc.* ***2004****, 112,* 217 – 227.

(59) Tossell, J. A. Calculation of the properties of molecules in the pyridine catalyst system for the photochemical conversion of CO2 to methanol. *Comput. Theor. Chem.* **2011**, *977*, 123 –127.

(60) Zhao, Y.; Truhlar, D. The M06 suite of density functionals for main group thermochemistry, thermochemical kinetics, noncovalent interactions, excited states, and transition elements: two new functionals and systematic testing of four M06-class functionals and 12 other functionals. *Theor. Chem. Acc.* **2008**, *120*, 215 – 241.

CHAPTER 7.

SUMMARY

When the work described in this dissertation first started in 2017, little was known about the mechanism of O-ATRP and how the PCs that mediate this process function. Since then, significant progress has been made in both of these areas. In this dissertation, efforts to understand several crucial steps in the mechanism of O-ATRP were described (Figure 7.1). Much of this work focused on understanding deactivation and the intermediates responsible for this step ($PC^{\bullet+}$). As a result, we now have experimental evidence supporting the role of $PC^{\bullet+}$ in deactivation during O-ATRP, and factors influencing this mechanistic step as well as $PC^{\bullet+}$ side reactions are better understood.

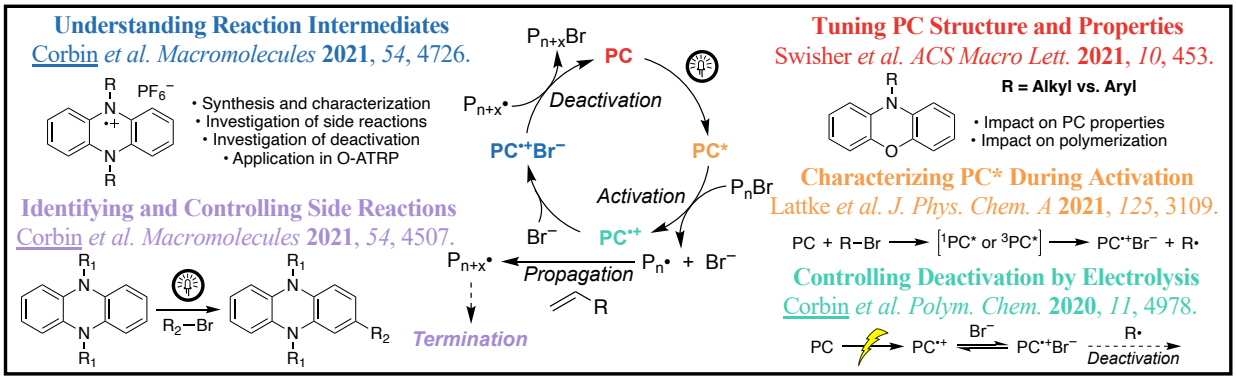

Figure 7.1. *Summary of work completed by the author of this dissertation on understanding the mechanism of O-ATRP, including work discussed in Chapters 4 (green), 5(blue), and 6 (purple), as well as previously published work that was not discussed in this dissertation (red and orange).*

These insights have allowed for $PC^{\bullet+}$ salts to be employed as reagents in O-ATRP, creating a new strategy for controlling deactivation during a polymerization simply by adding a reagent at the beginning of the reaction. In addition, the ability to control deactivation by electrolysis was

also demonstrated, and optimization of this method may now be feasible thanks to new insights into the deactivation mechanism in O-ATRP. Finally, the work described in this dissertation also identified new termination pathways that are unique to O-ATRP due to a side reaction between $PC^{\bullet+}$ and the alkyl radicals involved in polymer growth. With the knowledge of this process in hand, it is now possible to design PCs accordingly to avoid these termination pathways, thus increasing polymerization control in future systems and widening the scope of PCs available for O-ATRP.